Department of Mechanical Engineering

Mathematical Dynamics of Electromechanical Piezoelectric Energy Harvesters

Mikail F Lumentut

**This thesis is presented for the Degree of
Doctor of Philosophy**

of

**Curtin University
Australia**

November 2010

Declaration

To the best of my knowledge and belief this thesis contains no material previously published by any other person except where due acknowledgment has been made.

This thesis contains no material which has been accepted for the award of any other degree or diploma in any university.

Signature: ....

Date: ....8./.11./.2010......

Mathematical Dynamics of Electromechanical Piezoelectric Energy Harvesters

Mikail F Lumentut

Abstract

This research investigates vibration energy harvesting by modelling several piezoelectric-based structures. The usage of piezoelectric transduction under input vibration environments can be profitable for obtaining electrical energy for powering smart wireless sensor devices for health condition monitoring of rotating machines, structures and defence communication technology. The piezoelectric transduction shows strong prospect in the application of power harvesting because it can be applied at the microelectromechanical system design level in compact configuration with high sensitivity with respect to low input mechanical vibration. In this research work, the important aspects of the continuum thermopiezoelectric system associated with the laws of thermodynamics, Maxwell relations and Legendre transformations have been developed to explore the macroscopic thermopiezoelectric potential equations, the thermopiezoelectric equations of state and energy function forms. The application of the continuum thermopiezoelectric behaviour can be used to further formulate novel analytical methods of the electromechanical cantilevered piezoelectric bimorph beams with the tip mass using the weak and strong forms resulting from Hamiltonian's principle. The constitutive electromechanical dynamic equations of the piezoelectric bimorph beam under one or two input base excitations can be used to derive the equations of the coupled electromechanical dynamic response of transverse-longitudinal form (CEDRTL), the coupled electromechanical dynamic response of longitudinal form (CEDRL) and the coupled electromechanical

dynamic response of transverse form (CEDRT). The derivation of the constitutive electromechanical dynamic equations using the weak form of Hamiltonian's principle can be further derived using the Ritz method associated with orthonomality whereas the closed form or distributed parameter reduced from strong form of Hamiltonian's principle, can be further formulated using the convergent eigenfunction series with orthonormality. Laplace transformation can be used to give the solution in terms of the multi-mode transfer functions and multi-mode frequency response functions of dynamic displacement, velocity, electric voltage, current, power and optimal power. Moreover, the broadband multi-electromechanical bimorph beam with multi-resonance can also be explored showing the single- and multi-mode transfer functions and frequency response functions. A parametric case study of the piezoelectric bimorph beam with the tip mass and transverse input excitation is discussed to validate the weak and closed forms of the CEDRTL, under series and parallel connections, using the multi-mode frequency response functions with variable load resistance. A further case study of a broadband multi-electromechanical piezoelectric bimorph beam is also discussed using the weak form of the CEDRT to give the frequency response functions under variable load resistance. Finally, the piezoelectric bimorph beams with and without tip masses under transverse base input excitation are also comprehensively discussed using the weak forms of the CEDRTL and CEDRT models and compared with experimental results for variable load resistance. A piezoelectric bimorph beam with tip mass is investigated to show the close agreement between the CEDRTL model and experimental results using the polar amplitudes from the combined action of simultaneous longitudinal and transverse base input excitation.

Acknowledgements

I would like to express my indebtedness to A/Prof. Ian Howard who always gave the inspirational guidance, support and patience during my PhD study. Your dedication to being a research academic has truly inspired me and you have always been available to discuss many things both at the office and vibration laboratory. During my study, he would endorse me like his colleague and gave me opportunities to attend several international conferences.

I also would like to thank Curtin University of Technology for giving me research funding support during my study for three years and five months through the Curtin International Postgraduate Research Scholarships (CIPRS). Your support to my research in the Department of Mechanical Engineering was invaluable and I have realised that I still have many things to learn in my research career in the future.

Next, I also would like to thank Ms. Kim, the secretary of the department, who has been very helpful to manage the academic environment making it nice and friendly. She also provided information and organised the research activity and also several conferences registrations.

My family especially to my mother, Beatrix Wowor and in memory of my father, Hermanus Harry Lumentut, who have encouraged me with your great love, support and spirituality. I would express my deep gratitude to you. You have raised my life up and guided me to reach my dream.

Last, I would express my unlimited gratefulness to the Lord Almighty, who has guided me with His wings, held my hand when I fell down and lightened my heart when I was despairing. You are the one who has given me ability to shine my dream.

"Try not to become a man of success but rather to become a man of value."
 - Albert Einstein, quoted by William Miller in Life Magazine, 2 May 1955

"Research is to see what everybody else has seen, and to think what nobody else has thought" - Albert Szent-Gyorgyi

Table of Contents

List of Figures

List of Tables

CHAPTER
1
Introduction

In the last few years, the investigation of energy conversion techniques utilising ambient vibration has been of great interest for many researchers. The energy extracted from vibrating devices and structures can be utilised for powering electronic devices, supplying direct current into rechargeable batteries or electrical power storage devices. One of many applications being considered is for powering smart wireless sensor devices for health condition monitoring of rotating machines or structures and defence communication technology.

The action of mechanical vibration onto piezoelectric elements result in mechanical strain fields creating electric-polarity fields resulting in the generation of electric voltage. The input ambient vibration can be unused mechanical energies from numerous sources in industry, vehicles, airplane, humans' movement, piping structures, fluid flow and bridges, etc. The usage of piezoelectric material in the application of energy conversion requires knowledge of analytical methods, circuit components, material properties and geometrical structure. Piezoelectric materials have major benefits as they can give a reasonable prospect for microelectromechanical system design, compact configuration, high sensitivity with respect to low input mechanical vibration and are suitable to be used as a patch or embedded with other substructures.

An extensive review of piezoelectric element application for power harvesting has been discussed by Anton and Sodano [1] and Priya [2]. The piezoelectric bimorph beam represents a useful candidate for power harvesting as it gives high strain field due to the input vibration to induce the electrical field. The resulting extracted electrical energy can be optimised by utilising an electronic circuit capable of supplying the direct current into a rechargeable battery for the usage of wireless sensor communication, Roundy *et al* [3]. Moreover, there have been numerous

extensive analytical solutions of electromechanical piezoelectric systems associated with experimental validations. Smits and Choi [4] and Wang *et al* [5] derived an analytical solution for the static condition of the bending piezoelectric bimorph beam. However, their analytical methods cannot be applied to the vibration piezoelectric harvester due to the required coupled electromechanical response. Roundy and Wright [6] investigated the analytical solution using the electrical equivalent of the electromechanical transverse bending form for powering electrical devices but it was limited to the single mode. Some other investigations of analytical methods used the single mode of Rayleigh-Ritz's analytical approach of the electromechanical transverse bending form of the piezoelectric bimorph as shown by duToit *et al* [7]. The normalised single mode dynamic equation of piezoelectric power harvesting was shown by Shu and Lien [8] and the multi-mode frequency response using the closed-form method of the piezoelectric bimorph was derived by Erturk and Inman [9]. The parametric geometric consideration of the micromechanical piezoelectric unimorph beam using the Rayleigh-Ritz method with condense matrix equation form was shown by Goldschmidtboeing and Woias [10].

In this research work, novel analytical methods using the weak form and closed-form (reduced from strong form) Hamiltonian principle were considered. The coupled electromechanical dynamic response of the transverse-longitudinal model (CEDRTL), coupled electromechanical dynamic response of the transverse model (CEDRT) and coupled electromechanical dynamic response of the longitudinal model (CEDRL) of piezoelectric systems under two input base excitations will be developed mathematically in this dissertation. The derivations also include the single- and multi-mode transfer functions (TRs) and frequency response functions (FRFs). The analytical methods also provide the broadband multi-electromechanical piezoelectric bimorph beam with multi-frequency response for optimisation of the electrical output.

1.1. Objectives of the Dissertation

After reviewing the existing literature in the field of vibration energy harvesting and the applications for self-powered generators, it was found that the existing vibration power generators can be categorised into areas of piezoelectric, electromagnetic and electrostatic transductions. The aim of reviewing these types of

transductions are to discuss the comprehensive analytical and experimental methods, the characteristic materials, the primary areas of application, the electrical power output and the advantage and disadvantage of the various transductions. After reviewing the transduction mechanisms of energy harvesting, the piezoelectric transduction was chosen for further study focusing on developing novel theoretical methods for multi-directional input response. The primary objective of this dissertation was to review and investigate the state-of-the art energy methods using continuum piezoelectric element models and to present mathematical derivations of the multi-directional vibration induced electromechanical piezoelectric bimorph beam including experimental validations. The aim of formulating the continuum thermopiezoelectric behaviour was to establish the energy phenomena of piezoelectric material which results from the interrelationship between the physical properties of elasticity, electricity and entropy in order to obtain the thermopiezoelectric equations of state and thermopiezoelectric coefficients using Maxwell's relations and Legendre transformation. It was found that most researchers did not discuss the detail of the physical properties of thermopiezoelectricity. For the piezoelectric power harvester, the effect of electrical enthalpy of the thermopiezoelectric element under adiabatic and isothermal processes is presented.

Moreover, the analytical models of the electromechanical dynamic equations of the piezoelectric bimorph with the tip mass under two input base excitations are derived using the Hamiltonian principle to formulate three different methods, which are the strong form analytical method, weak form analytical approaches and closed-form boundary value methods. At this case, the weak form analytical approach derived from the strong form method was further derived using the Ritz method by introducing Ritz coefficients and space- and time-dependent Ritz eigenfunction series which were further formulated using orthonormalisation. The closed-form boundary value method derived from the strong form method was further formulated using a direct analytical solution with orthonormalisation by introducing the space- and time-dependent eigenfunction series into boundary conditions. The weak form method can be formulated to provide the coupled electromechanical dynamic response of the transverse and longitudinal forms (CEDRTL), the coupled electromechanical dynamic response of the longitudinal form (CEDRL) and the coupled electromechanical dynamic response of the transverse form (CEDRT). The

closed form method using the strong form derivation can be formulated to provide the coupled electromechanical dynamic response of the transverse and longitudinal forms (CEDRTL). In this dissertation, the transfer functions (TR) and frequency response functions (FRFs) using the CEDRTL and CEDRT models have been comprehensively established using Laplace transformations.

A further aim of this dissertation is to analyse the parametric case study of the piezoelectric bimorph under series and parallel electrical connections using the CEDRTL weak and strong forms. The results include the parametric FRF amplitudes including the multi-mode FRFs of tip absolute dynamic displacement, velocity, electrical voltage, current and power. Parametric analysis of the dynamic responses with respect to variations of load resistance, variations of bimorph geometry and the broadband multi-electromechanical piezoelectric beam with multi-frequency models are also presented. Moreover, the validations and comparison between the experimental and analytical results of the piezoelectric bimorph beam with and without tip masses are also discussed for the single- and multi-mode FRFs and the polar FRFs amplitudes.

1.2. Significance and Innovation

In this dissertation, the capabilities of the electromechanical response of the piezoelectric bimorph can be used to extract variable power from ambient vibration for future product applications of smart wireless sensor devices. The core research will be the mathematical study of the piezoelectric system and its application for vibration power harvesting. This includes the complete derivations of continuum thermopiezoeletricity to explore the macroscopic phenomena of thermopiezoelectric potential equations, the thermopiezoelectric equations of state and energy function forms. Moreover, the application of continuum thermopiezoelectricity can be utilised for deriving analytical equations of the electromechanical piezoelectric bimorph beam with the tip mass under input excitations using the Hamiltonian principle for analysing the transfer functions and frequency response functions with variable load resistance for predicting the tip displacement, velocity, electrical voltage, current and power outputs. Moreover, the complete derivations of series and parallel multi-electromechanical piezoelectric bimorph beams are discussed to analyse the broadband frequency response functions for optimisation study.

1.3. Research Method of the Dissertation

The vibration power harvester using the piezoelectric effect has been an emerging research field over the past few years. After investigating the comprehensive literature review, the research methodology of the electromechanical piezoelectric in this dissertation covers the extended concept of thermopiezoelectrical energy forms, the mathematical methods of electromechanical piezoelectric bimorph beam with two input base excitations, the parametric case study and experimental validations.

The piezoelectric behaviour underlies the macrostate thermodynamic principle covering the elasticity, quasi-static electrical energy and entropy. In this research method, the continuum thermopiezoelectricity representations are derived mathematically to establish the physical energy forms and thermopiezoelectric potentials of the Elastic-Electrical Gibbs Free Energy, Elastic Gibbs Free Energy, Electrical Helmholtz Free Energy, Elastic Helmholtz Free Energy, Elastic-Electrical Enthalpy and Electrical Enthalpy in terms of the entities of tensor thermopiezoelectric coefficients. The physical aspect of thermopiezoelectricity plays an important role in smart materials and structures. It was found that many researchers did not provide the in-depth interaction of the thermopiezoeletric equations of state based on the Maxwell' relation and Legendre transformation. The most common piezoelectric constitutive equations, derived from the electrical enthalpy under the adiabatic and isothermal processes, includes the direct and converse modes, which are used directly by many researchers without exploring the physical properties and other energy function forms of the macroscopic thermopiezoelectric tensor as mentioned above.

The vibration response of the piezoelectric bimorph beam with the tip mass under two input base excitations for power harvesting can be formulated using the potential energy from the substructure material (middle layer), electrical enthalpy of upper and lower layers of piezoelectric material, kinetic energy of the bimorph including the tip mass and external electrical energy into the piezoelectric element. The analytical methods, derived using the Hamiltonian principle, can be further formulated using three models. The first model represents strong form analytical method and the second model represents the analytical approach using the normalised Ritz

eigenfunction series (weak form) whereas the third model represents the closed-form analytical method using the normalised convergent eigenfunction series (reduced from strong form). Since the linear Lagrangian strain field of the piezoelectric bimorph associated with the two input base excitations is reduced from the kinematic of transverse and longitudinal displacement fields, the effect of coupled electromechanical dynamic behaviour of the bimorph based on the Hamiltonian principle are formulated into three further models. The first model represents the electromechanical dynamic response of the transverse-longitudinal form (CEDRTL), the second model represents the electromechanical dynamic response of the transverse form (CEDRT) and the third model represents the electromechanical dynamic response of the longitudinal form (CEDRL). The broadband frequency response of the multi-electromechanical piezoelectric bimorph beam is also derived analytically to analyse the frequency behaviour of the electrical current, voltage and power for optimisation study.

The frequency analysis reduced from the Laplace transforms of the electromechanical bimorph beams (weak and closed forms) can be used to formulate the single and multi-mode transfer functions (TRs) and frequency response functions (FRFs) of the CEDRTL, CEDRT and CEDRL models. The overarching vibration power harvesting of the piezoelectric bimorph beam reflects the interrelations of the electromechanical dynamic response between the input vibrations and the electrical current, voltage and power outputs associated with the mechanical displacement and velocity outputs. This understanding reflects the profound continuum electromechanical dynamic behaviour of vibration power harvesting for future applications of self-powered smart sensor devices to be used for condition health monitoring of rotating machines or structures.

The parametric case study of the piezoelectric bimorph beam with tip mass will be discussed according to the series and parallel electrical connections where two different analytical methods of the weak and closed forms of the multi-mode CEDRTL equations under series and parallel connections will be used to validate the results for variable load resistance. Moreover, the piezoelectric bimorph beam with and without tip masses using the weak forms of the CEDRTL and CEDRT equations can also be compared with experimental results. The trends between the CEDRTL

and CEDRT models and experiments are investigated over the frequency range. Programming code based on MATLAB was developed to model the theoretical simulations. In this dissertation, the experimental work was conducted in the vibration laboratory using equipment including the piezoelectric bimorph with and without tip mass, input base structure, FFT Analyzer, Laser vibrometer polytec PDV 100, B & K exciter, B & K impedance head, B & K charge amplifier, B & K power amplifier, wave function generator, and computer.

1.4. Layout of the Dissertation

This dissertation consists of seven chapters, detailing the mathematical analysis of continuum thermopiezoelectric behaviour covering the analytical methods of electromechanical piezoelectric bimorph beams for power harvesting. The validations of the piezoelectric vibration harvester are also provided by comparing two different analytical methods and experimental results. The detail and outline of each chapter is presented below:

Chapter 1 presents the general introduction of vibration power harvesting in the field of smart structures with applications of self-powering smart wireless sensor devices for the health condition monitoring of rotating machines. The major contribution of piezoelectric devices is the development of profitable power harvesting technology from simple structures, which can be used from macro- to micro-electromechanical scale to capture the vibration environment and convert the dynamic response into electrical energy. The concept of the research study is presented including the research objectives, significance and methodology.

Chapter 2 discusses the comprehensive review of the existing vibration power harvesting literature focusing on three major groups, represented by piezoelectric, electromagnetic and electrostatic generators. This review includes the physical aspect of the devices, mathematical models including the validations, analysis of the electromechanical dynamic system, implications for future smart sensor devices and the comparative modelling of the three different generators.

Chapter 3 provides the comprehensive theory of continuum thermopiezoelectricity to model the physical characteristics of the piezoelectric effect using the divergence field of quasi-electrical form, Gauss's electric displacement piezoelectric form,

piezoelectric polarisation, and thermodynamic laws associated with Maxwell relations and Legendre transforms to formulate the interrelationship of thermopiezoelectric potentials, thermopiezoelectric equations of states and energy function forms including the tensor coefficients.

Chapter 4 presents analytical methods for deriving the electromechanical dynamic equations of the piezoelectric bimorph beam with two input base excitations using the Hamiltonian principle. Since typical piezoelectric vibration power harvesting utilises the relatively thin bimorph beam, the Rayleigh and Euler-Bernoulli piezoelectric beam equations are formulated. The analytical methods are formulated using kinetic energy expressions for the bimorph and tip mass, the potential energy of the substructure, electrical enthalpy of the piezoelectric layers under adiabatic and isothermal processes and the applied mechanical and electrical work. The analytical derivations of the piezoelectric bimorph under series and parallel electrical connections can be split into three categories representing the strong form, weak form and closed form Hamiltonian principle. The weak form of the analytical method reduced from strong form can be further divided into three coupling electromechanical models (CEDRTL, CEDRT and CEDRL) for single- and multi-mode frequency analysis using the Ritz eigenfunction series. The closed-form analytical method was also reduced from the strong form Hamiltonian principle to give the multi-mode CEDRTL frequency analysis. The broadband multi-electromechanical piezoelectric bimorph beam is investigated to explore the multi-frequency behaviour response of the bimorph electrical output. Since the bimorph is connected to the external varying load resistance, each electromechanical coupling effect can be further formulated into transfer functions (TRs) and frequency response functions (FRFs) using Laplace transforms. This provides the relative and absolute transverse and longitudinal displacements including the velocity, electrical voltage, current and power. Moreover, the generalised time dependent absolute displacement and velocity including the FRF can also be formulated to give compatible results for comparing with the experimental setup.

Chapter 5 presents a parametric case study of a piezoelectric bimorph beam with tip mass and series and parallel electrical connection with varying load resistance. The CEDRTL weak form and closed form results can be compared to analyse the multi-

mode FRFs of tip absolute displacement and velocity, electrical voltage, current, and power harvesting. Moreover, the short and open circuit resonance frequencies with respect to the varying load resistances and geometrical parametric properties are presented. The broadband multi-frequency behaviour of three piezoelectric bimorph beam models with series and parallel electrical connections are also presented.

Chapter 6 presents the comparison between the analytical and experimental electromechanical dynamic response of the piezoelectric bimorph beam with and without tip mass. The CEDRTL and CEDRT weak form model results are investigated and compared with the experimental results from the bimorph with and without the tip mass. The single- and multi-mode FRFs of the tip absolute displacement and velocity, electrical voltage, current, and power relating to the input transverse excitation are presented. The two input base excitations of transverse and longitudinal excitations of the bimorph are also presented for discussion of the polar tip absolute displacement and velocity, electrical voltage, current and power under varying load resistance.

Chapter 7 presents the summary of the major research findings of the electromechanical piezoelectric system and presents the major conclusions of the dissertation.

The appendix provides the constitutive piezoelectric equations in matrix form, the mode shape of the piezoelectric bimorph and the MATLAB code developed and used in the research.

CHAPTER
2

Review of Electromechanical Vibration Power Harvester

The development of embedded permanent computing-based technology equipment has increased the demand from the engineering industry to monitor or control the health condition of structures and rotating machinery. The prevalent technological equipment still requires electrical power from the mains power supply or battery in order to read and transfer the electrical data signal via the wireless sensor nodes into the computer including data acquisition, instrument control and/or analyzers to monitor the rotating shafts, turbines, bearings, gearboxes, bridge structures, pipe etc. In that case, the convention battery systems have a limited lifespan for power production. The systems are still dependent upon the electrical power from the battery system or mains power supply for recharging. This leads to the tedious task of replacing the conventional battery from the smart sensor device often located in remote or inaccessible areas. This situation has revealed challenges for scientists to identify alternate low power systems for supporting smart sensor devices. Moreover, the emerging technology in the MEMS scale would facilitate future applications of smart sensor systems with wireless communication to monitor engines and other machinery located in remote areas. At the same time, the need for self-power systems with rechargeable thin battery technology will also inevitably increase. This research area is still ongoing and includes the development applications for scavenging power for long lifespan duration. To power the computing technologies such as small electronic devices with thin batteries and wireless capabilities, the mechanical energy sources from unused or wasted vibration energy from industrial machinery, airplane, automobile, bridge, human motion etc. can be utilised for micro-generator power harvesting. Table 2.1 shows an example of power consumption needed for electronic devices as found in Vullers *et al* [11]. Other power supplies from household tools, computers etc. in Roundy *et al* [3] are shown in Table 2.2. It should be noted that one of most realisable candidates for power scavenging are piezoelectric components,

even though some researchers still use electromagnetic and electrostatic systems. In this literature review, other sources of macro power supply such as gas turbine, wind turbine and nuclear power plants were not considered. It should be noted that other micro power supplies like photovoltaic cells, fuel cells and thermoelectric devices were also not discussed, as the main focus in this section was on the potential micro scale energy supply from piezoelectric, electromagnetic and electrostatic transductions for the use in future applications of smart sensor equipment as shown in Figure 2.1.

Table 2.1 Characteristic of battery operation system, [11]

Device type	Power Consumption	Energy autonomy
Smartphone	1 W	5 h
MP3 player	50 mW	15 h
Hearing aid	1 mW	5 days
Wireless sensor node	100 µW	Lifetime
Cardiac pacemaker	50 µW	7 years
Quartz watch	5 µW	5 years

Table 2.2 Acceleration magnitude and frequency of fundamental vibration, [3]

Vibration source	A (m/s^2)	F peak (Hz)
Car engine compartment	12	200
Base of 3-axis machine tool	10	70
Blender casing	6.4	121
Clothes dryer	3.5	121
Person nervously tapping their heel	3	1
Car instrument panel	3	13
Door frame just after door closes	3	125
Small microwave oven	2.5	121
HVAC vents in office building	0.2–1.5	60
Windows next to a busy road	0.7	100
CD on notebook computer	0.6	75
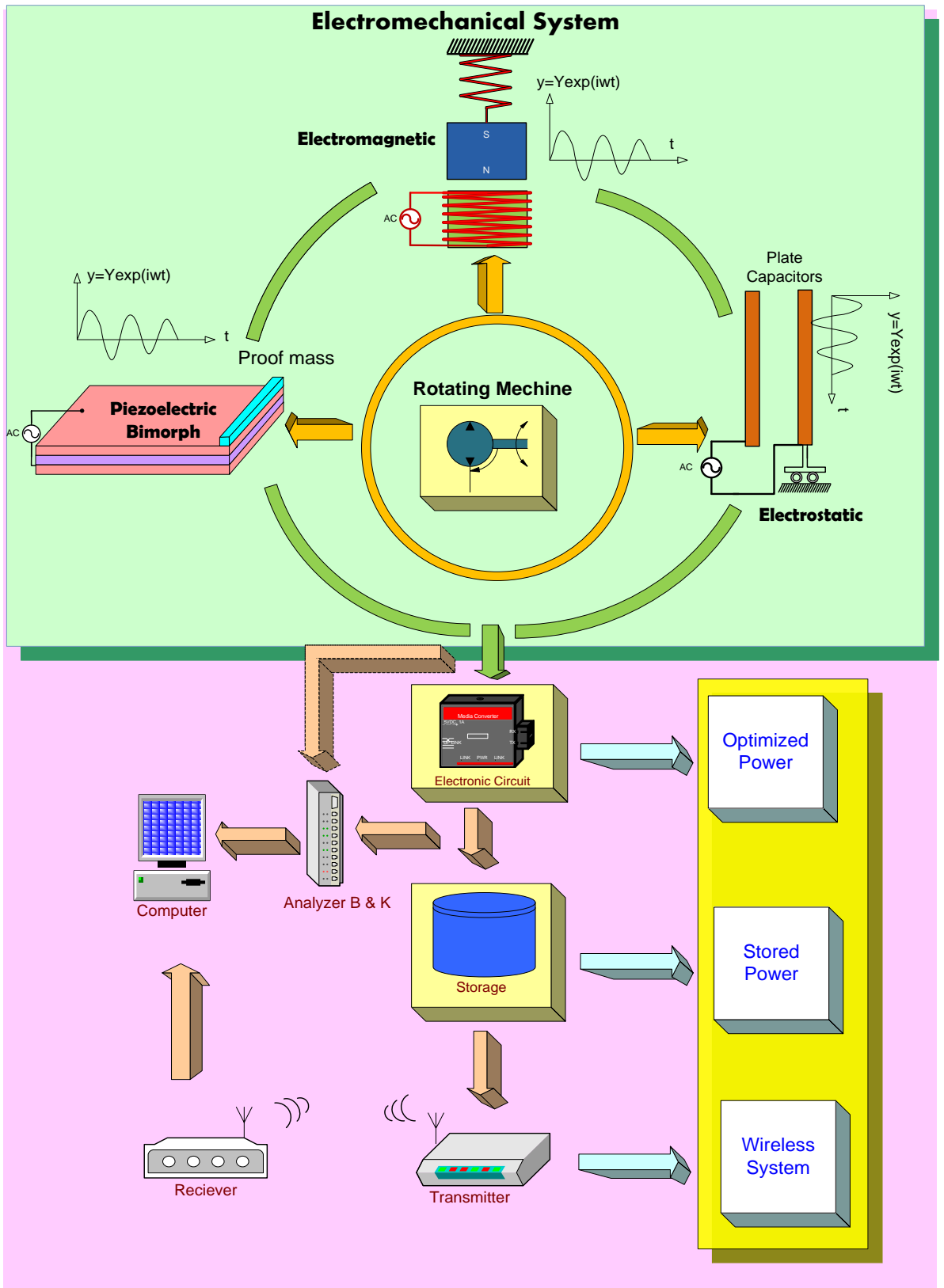
Figure 2.1 Schematic Electromechanical Power Harvesting System.
(Representation by Lumentut, 2010)

2.1. The Electromechanical Vibration-Based Piezoelectric Generator

The piezoelectric element, subjected to input motion from the vibration environment, can create the strain field to induce the polarity-electric field to generate useful electrical energy capable of being stored on electrical power storage devices such as batteries or capacitors. Such a technique is generally referred to as the energy harvesting technique by using the unused energies from the dynamic motion, fluid flow, human's motion, impact, etc.

Extensive experimental studies of the piezoelectric power generation, conducted by Inman's group at VirginiaTech, provided a comprehensive investigation of the performance of piezoelectric components. Sodano *et al* [12] investigated three different piezoelectric materials (MFC, Quick Pack and PZT) using the cantilever piezoelectric models under dynamic response for accumulating the electric voltage and charge flowing into various batteries. They found that PZT gave more efficient charging time for the battery than Quick Pack. Even though MFC gave higher electric voltage than PZT, it was found to provide inefficient current for charging compared with the two other piezoelectric materials. Further experimental investigation of power harvesting with different material properties has been reported by Sodano *et al* [13]. They proposed three piezoelectric devices (Quick Pack, MFC and Quick Pack IDE) bonded onto nearby clamped supports of a cantilevered aluminum beam as shown in Figure 2.2. Over the first three modes of frequency response, the Quick Pack had the highest power harvesting capability, followed by MFC and Quick Pack IDE as shown by the result given in Table 2.3 at the end of this section. However, each of the piezoelectric devices, bonded onto the aluminum beam had different geometrical structures making them unfit for comparison. Moreover, the capacitance of the MFC depended on the geometry of the capacitor cell between the interdigitated electrodes and this also affected the power harvesting performance. Sodano *et al* [14] demonstrated the cantilever piezoelectric beam under random and resonance input vibration environments for generating electrical voltage for subsequent storage into rechargeable batteries and capacitors. The piezoelectric element was circuited with a full rectifier, capacitor and rechargeable battery. It was found that the charging voltage under random vibration conditions generated increased output voltage to the capacitor. However, it did not give the continuous

voltage output signal from the capacitor during the discharge operation. The second test showed that the electrical voltage under the random input vibration took 1.5 hours to recharge the cell battery whereas the excited resonance frequency of the piezoelectric system charged the battery in around 20 minutes.
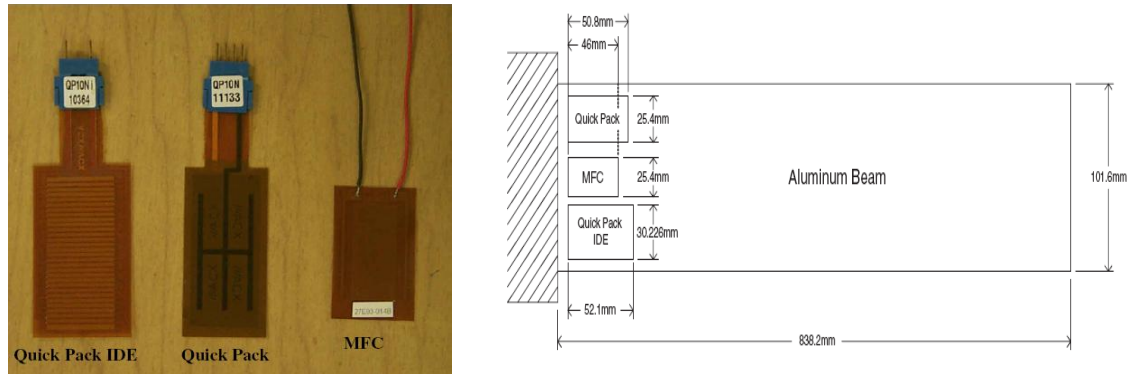
Figure 2.2 Piezoelectric transductions attached to the beam, [13].

The use of piezoelectric components in the application of human motion is of great interest to some researchers. Paradiso with his research group from MIT media Lab investigated several piezoelectric generators for human wearable electronic devices. Kymissis *et al* [15] discussed the application of piezoelectric PVDF and PZT components mounted between the insole and rubber sole of sport shoes, generating power harvesting from human walking as shown in Figure 2.3. The generated charge due to the mechanical contraction on the PVDF stave and the PZT of shoes during walking was investigated for optimisation of the electric voltage and energy harvesting, controlled using an electronic circuit to transmit the signal via radio transmitter. The average power during the brisk walk delivered by the PVDF stave at the shoe's toe at the frequency of 1 Hz using 250 kΩ, was 1.1 mW while the PZT element on the shoe's heel delivered an average power of 1.8 mW. Further improvement of piezoelectric power generation from a human walking was investigated by Shenck and Paradiso [16], where the PVDF stave placed in the insole of sports shoes delivered the average power of 1.3 mW at load resistance of 250 kΩ at 0.9 Hz during walking pace whereas the PZT bonded into the insole of US Navy boots generated the average power of 8.3 mW at 500 kΩ with the same frequency as shown in Figure 2.3.

Starner and Paradiso [17] further reviewed the improvement of computing electronics such as disc capacity, processor speed and computer memory with an

apparent increase of over 250 times with the available battery during 1990 and 2003. The power provided from the battery also has a limited lifespan and it is basic issue of the power storage for powering the electronic media. One of the trends in recovering the harvested power is that the piezoelectric sensor can act as a generator and be used to extract power due to the mechanical contraction from the human body. In Paradiso [18], this represents the well-known batteryless-based sensor model where the captured power never needs battery storage. This includes generating the harvested power from piezoelectric material bonded between the shoe insole and sole during human walking. Other researchers also completed similar work of scavenging power from human walking. The following work of the piezoelectric powered human walking was given by Mateu and Moll [19] where they optimised a bending piezoelectric beam in shoes using the simple support model. The typical layered piezoelectric beams of the homogeneous and heterogeneous bimorph as well as the heterogeneous unimorph were discussed under the application of point and distributed loads. Although the analytical dynamic response was not given, the author noticed that the triangular unimorph with the simple support provided the highest power under the distributed load. The subsequent study by Mateu and Moll [20] developed their research by using the capacitors as storage media with controls and regulators for powering a load. The current waveform was used to predict the voltage waveform, generating prolonged low energy to be stored in the storage media, which depended on the conversion of the strain of the embedded piezoelectric element in the insole of the shoe during walking.
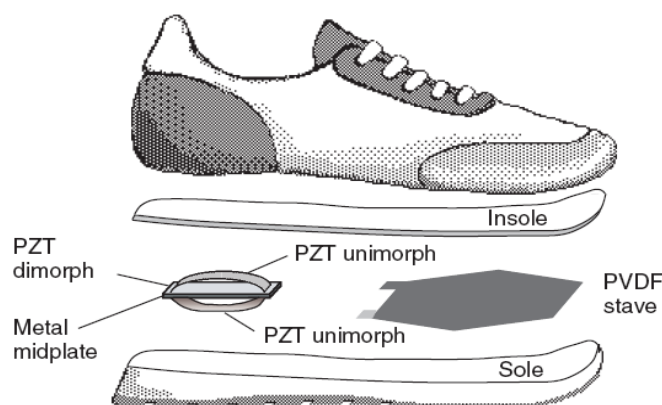
Figure 2.3 Wearable shoe power harvester, [16].

The investigations of power harvesters using cantilever piezoelectric models under base motion and optimisation of the current signal using an autonomous converter circuit model, transmitted to the load via wireless communication has been discussed

by Ferrari *et al* [21]. The rotational vibration generator was modelled to give high amplitude resonant response which could be used for power harvesting with varying load resistances and capacitive loads. Arms *et al* [22] from Microsystems inc. presented an autonomous design fabrication of a power harvester using the cantilevered MFC piezoelectric beam associated with an electronic circuit system and an electrochemical thin film rechargeable battery for powering the wireless temperature and humidity sensor as shown in Figure 2.4. The extracted electrical power from an input vibration level of 0.1 g achieved 2.8 mW with the modest strain level of 200 $\mu\varepsilon$, where the generated power was from the resonance frequency of the piezoelectric structure. Lin *et al* [23] presented a MEMS power generator using a silicon cantilever beam with an attached piezoelectric element. The silicon beam with a proof mass under input base acceleration of 10 m/s^2 at 100 Hz generated a power level of 2.59 μW. However, their result was not validated with the experiment and the analytical model of the piezoelectric beam failed to correctly model the coupled electromechanical dynamic system.
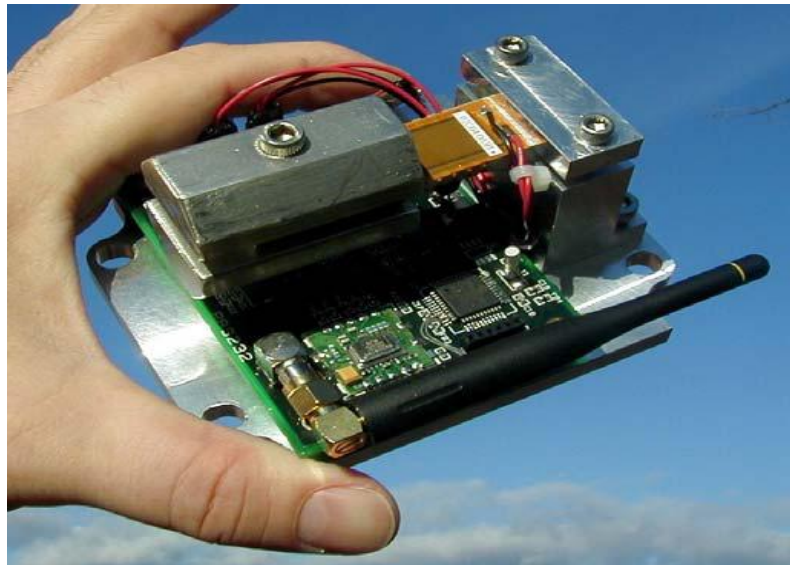
Figure 2.4. Fabricated piezoelectric vibration power harvester and wireless temperature and humidity sensing node, [22].

There have been numerous research studies of the development of analytical models and associated experimental results of the electromechanical vibration power harvester. Some researchers also applied ANSYS software for the numerical model. Many of the piezoelectric prototypes used the cantilevered beam under input transverse excitation and sliding mass impact. Other prototypes such as the

piezoelectric diaphragm and circular piezoelectric element under dynamic fluid pressure were also considered.

Shu and Lien [8] discussed a cantilevered bimorph piezoelectric beam coupled with an electrical circuit, AC-DC rectifier and load resistance under the action of a dynamic input force. Although, their analytical solution only considered the single mode frequency response, they derived the complete non-dimensional analytical equations to obtain the optimal parameters of displacement, voltage and electrical power under the short and open circuits' resonance frequency. The formulations also involved the coupling effect of electromechanical response and the uncoupling effect by ignoring the backward piezoelectric coupling. An analytical dynamic method with the curvature basis approach of the piezoelectric element bonded onto silicon layers has been discussed by Chen *et al* [24]. The cluster structure type was the unimorph model. The mathematical model was similar to dynamic admittance where the dynamic equation of the unimorph was developed without considering the coupling effect of piezoelectric behaviour as given in Table 2.3. However, the direct effect of the piezoelectric element was formulated to give the electrical voltage. This model showed the lack of mathematical components providing the interrelationship of direct and converse effects of the piezoelectric element for the multi-mode dynamic frequency response.

Wardle's group at MIT has investigated the cantilevered piezoelectric beam under the effect of load resistance and in duToit *et al* [7], they investigated a single mode of the mathematical model for scavenging low electrical power based on a range of frequency responses using the piezoelectric-based accelerometer and the cantilever piezoelectric models under input transverse base motion. In the analytical solution, the short and open circuit models of power harvesting were optimised to obtain power harvesting based on the frequency response under various load impedances. The strain effect from mechanical vibration of the cantilever piezoelectric beam structure gave more pronounce affect to the electrical power during the dynamic response. This situation depended on the series and parallel circuit systems of the bimorph piezoelectric beam and the {3-1} and {3-3} modes of operation as discussed by duToit *et al* [25]. They also further expanded their bimorph model using the cantilever piezoelectric element with the series connection of the bimorph beam

where the piezoelectric element was operating with the {3-1} mode. The comparison between the experiment and theory was also undertaken. However, the power at the resonance region seemed to give underpredicted results. Kim *et al* [26] further discussed the vibration energy harvester performance by considering the effects of geometrical tip mass onto the bimorph. The single mode of the electromechanical dynamic equations, stated as the scalar form given from duToit's representation, was modelled and the solution form of their analytical approach was based on the Rayleigh-Ritz's method. The trends of tip transverse displacement, voltage and power harvesting with and without tip masses were plotted with respect to the variation of load resistances where slight difference of results between the theoretical and experiment were found. They also noticed that the effect of geometrical tip mass, which created the offset centre of gravity from the bimorph tip, was an important issue affecting the dynamic behaviour of the piezoelectric beam. However, the authors did not provide the concentric bimorph proof mass to confirm the percentage difference of displacement and power from using the offset tip mass. In fact, the effect of proof mass onto the tip of bimorph was considered quite small for the power harvester application. This shows that the concentric bimorph tip mass should be preferable. The authors also did not provide the multi-mode FRFs of the electromechanical dynamic equations. Although, the purpose of simulation was the single mode FRFs, the multi-mode FRFs can provide a much more accurate representation and this can be adjusted through the graph to plot only the single mode simulation.

Ajitsaria *et al* [27] discussed the analytical model of the piezoelectric bimorph beam with the Euler-Bernoulli and Timoshenko types. The conservative energy of the piezoelectric beam was formulated to give the electrical voltage and transverse function of dynamic displacement. The authors also considered the electrical circuit response, including the AC-DC rectifier, capacitor and resistor to simulate the DC voltage and DC current. However, the derivation of constitutive formulations did not clearly represent the coupled electromechanical dynamic response such as the transfer function of dynamic displacement. In fact, the Euler-Bernoulli beam's dynamic equation was written with the misinterpretation. The research study led by Yang from the University of Nebraska, Jiang *et al* [28] discussed the single mode of the piezoelectric bimorph response using the method of boundary values to obtain

each coefficient of the dynamic equation to give the dynamic displacement and power density. In addition, the suggested analytical method did not gave the multi-mode frequency response of the bimorph and the experimental validation. Yang and Yang [29] discussed the exact analytical study of the two piezoelectric bimorph beams with tip masses connecting each other with the elastic spring. The solution form of this model was reduced by using the boundary values. However, the effect of elastic spring attached to the structure did not give optimise power output from each piezoelectric element although the tuning power of the piezoelectric element was the main purpose on their analytical study, as it was not validated with the experimental results. In fact, the aim of using two piezoelectric elements should be increased power output from the multi-frequency response where the result was also shown in Table 2.3.

Goldschmidtboeing and Woias [10] from IMTEK Germany investigated different shaped rectangle and truncated triangular piezoelectric beams with varying tip mass under base transverse excitation using Ritz-Rayleigh's method. They showed that varying the mass ratio between tip mass and piezoelectric mass and truncated ratio or shape ratio between the rectangle and triangular portion of the piezoelectric beam could tune the optimum power where the result was given in Table 2.3. They noticed that the triangular shaped beam provided the optimum power compared with the rectangular beam.

Renaud *et al* [30] discussed the unimorph piezoelectric beam under input impact load to generate the electric voltage. The sliding load was free to impact the tip of the piezoelectric element. A sliding mass of 750 mg moving along the piezoelectric beam with a distance of 1 cm produced the power of 40 μW for the first impact as shown in Figure 2.5. The input excitation to the piezoelectric harvester was 10 cm displacement. At this stage, the trend of transient responses from the experiment and theoretical were not given. Kuehne, *et at* [31] discussed a MEMS design of a circular piezoelectric plate diaphragm under dynamic motion from the inertia mass attached at the middle surface of the piezoelectric element. The Ritz method was used to establish the dynamic equation of the clamped circular piezoelectric plate to determine the charge and voltage. Minazara *et al* [32] discussed the coupled piezoelectric membrane and brass layer with a diameter of 25 mm under excitation

force from an actuator using the RLC circuit model controlled by a switching technique called synchronized switch harvesting on inductor (SSHI) where the result was given in Table 2.3. The power harvesting was found to increase 3 times at resonance regions compared with the normal system without SSHI. The maximised power obtained using the SSHI technique based on varying load impedances with the input force of 80 N gave power three times higher than using the standard technique. Further development of a piezoelectric disk for vibration-based energy harvester using the SSHI technique has been discussed by Lefeuvre *et al* [33]. The series-SSHI and parallel-SSHI techniques were optimised to maximise the power harvested from the piezoelectric element where the power output results gave a dramatic increase compared to that with the standard circuit techniques (bridge rectifier, capacitor and electrical load). Chao *et al* [34] optimised the harvested power from piezoelectric components under ambient vibration using the vibration tracking unit circuit to reduce the need of loss power, as it was known that the piezoelectric system provided only very low power from tens to hundreds of microwatts. This confirmed that power harvesting generated from the piezoelectric element can support the loss energy from the electronic circuit systems. Wang and Ko [35] presented the vibration energy harvester induced from fluid flow as shown in Figure 2.6. The fluid entered the chamber through a glass tube to create pressure onto the polydimethylsiloxane diaphragm where the piezoelectric beam was attached. When periodic pressure was applied onto the pressure chamber around with 1.196 kPa at a frequency of 26 Hz, the electric power generated was around 0.2 μW.
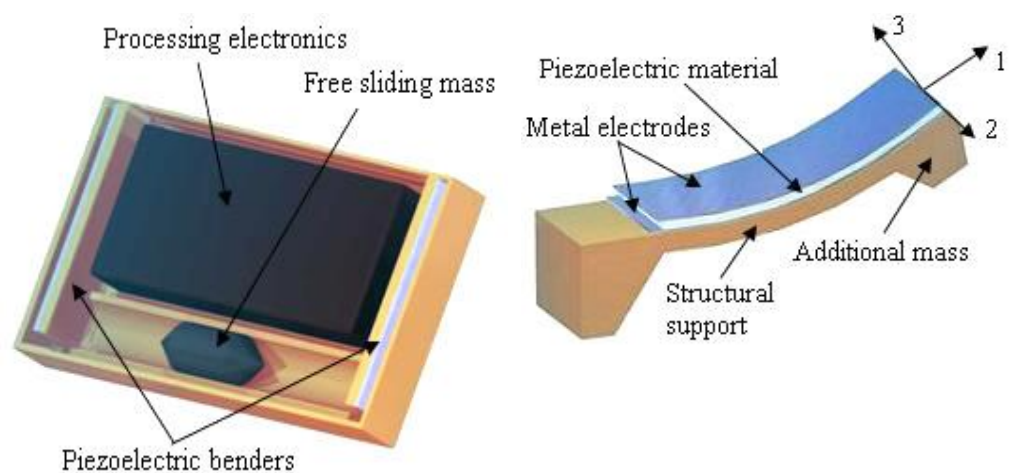
Figure 2.5 Piezoelectric beam under impact mass, [30].
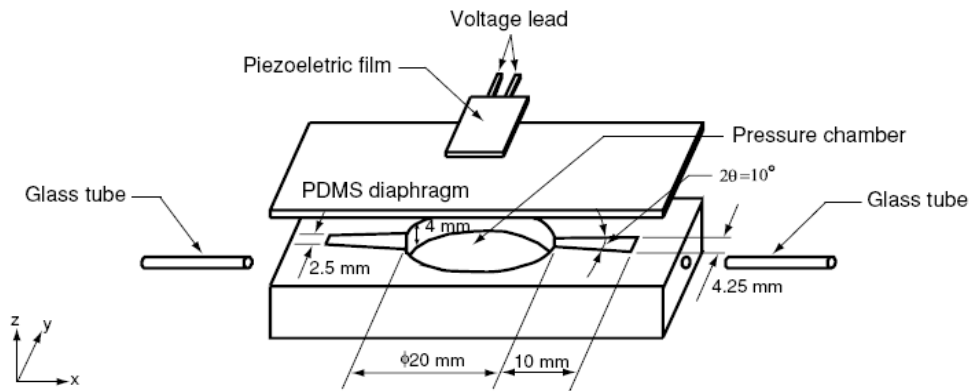
Figure 2.6 Piezoelectric film mounted onto the PDMS diaphragm under fluid
flow pressure, [35].

Erturk and Inman [9] discussed a mathematical model for a vibration power
harvester using the cantilever piezoelectric beam under input transverse excitation.
The normalised eigenfunction form was used to simplify the constitutive
electromechanical equations to give the frequency response analysis. The frequency
response electrical voltage and power using the analytical results showed good
agreement with the experimental results as given in Table 2.3. Feenstra *et al* [36]
investigated power harvesting from a backpack using the piezoelectric stack actuator
for the strap. The backpack model was analysed using Unigraphics CAD with Tetra4
Mesh to model the amplification of the strap of the piezoelectric stack actuator. The
amplified strap can be used to analyse the stack actuator using a single degree of
freedom to obtain the power harvesting.

The electrical equivalent representation of the electromechanical piezoelectric
structure has been discussed by some researchers. Roundy and Wright [6] discussed
the single mode of the piezoelectric beam with two different sizes of   tip mass in
order to investigate the trend of electrical voltage. The effect of centre of tip mass's
gravity referred to the offset from the end of the bimorph's length. Their analytical
model failed to consider the offset's length of bimorph due to the large tip mass
attached to the bimorph. Later work from duToit *et al* [7] however, further
considered the effect of the offset's length of the bimorph. Moreover, the equivalent
circuit model of the unimorph beam using ANSYS software for energy harvesting
has been reported by Yang and Tang [37]. They investigated each parameter of the
electromechanical system of the structure which could be converted into the
equivalent circuit. The SPICE electrical software was further used to analyse the

voltage and power output frequency responses. Although, the equivalent electrical circuit gave the simple alternative solution, it still needed to solve each of the electromechanical dynamic parameters based on the multi-mode frequency response. Moreover, their unimorph beam design using solid5 element ANSYS did not show the required number of element meshes in order to meet the convergent criteria where each element node was attached with wires and connected to the resistor. If the number of nodes increased, the number of wires also increased making the simulation much more complex.

Lee *et al* [38] discussed the utilisation of vibration environment from HVAC system (heating, ventilation, air conditioning) using the fabricated piezoelectric structure with the tip mass. The electrical circuit was also connected to the bimorph for supplying the electrical energy into the wireless sensors. The authors also provided the ANSYS simulation to analyse two different design optimisations from the rectangular and truncated triangular shapes of the piezoelectric element. They also provided the prototype model of a power harvester design. However, their design resulted in a complex model of a large attached tip mass located between two different shaped piezoelectric materials and also did not consider the mathematical computations to provide the electromechanical frequency responses. Yang *et al* [39] presented the application of a vibration power harvester using the three macro-fiber composites (MFC) patched onto the beam. Two MFCs were located nearby on the clamped beam support, extracting energy while another MFC acted as the input vibration to the beam (actuator). The electronic broadband measurement experimentally used an AC-DC rectifier and the storage capacitor to accumulate the electrical charge. The results were also validated with the electrical circuit simulation software, using the EDA software Multisim10.0. Although, the ABAQUS software was also used to simulate the strain distribution and voltage along the MFC patch with respect to the frequency response, their model only showed the prototype of energy harvesting without considering the mathematical implications.

Mathers *et al* [40] presented the fabricated micro-piezoelectric cantilever beam with the proof mass for predicting the vibration power harvesting. The use of piezoelectric material from the single crystal relaxor ferroelectric (PMN-PT) with the interdigitated electrode (IDE) as shown in Figure 2.7 was aimed to improve the

energy conversion efficiency where the use of varying proof mass from the polydimethylsiloxane (PDMS) aimed to tune the natural frequency. The analytical model of the elastic vibrating beam associated with the direct effect of the piezoelectric equation was used to give the electrical voltage frequency response. However, the electromechanical dynamic behaviour of the piezoelectric beam from the derivations failed to give the effect of backward piezoelectric coupling for the power harvesting or to model the multi-mode frequency responses of displacement, voltage and power. Although the voltage and power results versus the base input displacement amplitude achieved agreement between the theoretical and experiment, the predicted voltage and power under the frequency response from the experiments was not validated using their analytical models as given detail in Table 2.3. Song *et al* [41] discussed the energy harvester using a single PMN-PT patch onto the steel beam with a proof mass. The PMN-PT element with the integrated electrical circuit consisting of an AC-DC rectifier with resistor and capacitor was experimentally measured to generate the DC voltage, current and electrical power frequency response functions. However, there were no validations using the theoretical model as given in Table 2.3. The power output versus load resistor using the theoretical and experimental results for four different tip masses was given where the theoretical power result for the open circuit load resistance was beyond that found from the experimental prediction. Moreover, their analytical model of the PMN-PT patch on the steel beam failed to meet the mathematical continuity consideration because the length of the PMN-PT patch was much smaller than the steel beam, resulting in an oversimplification.
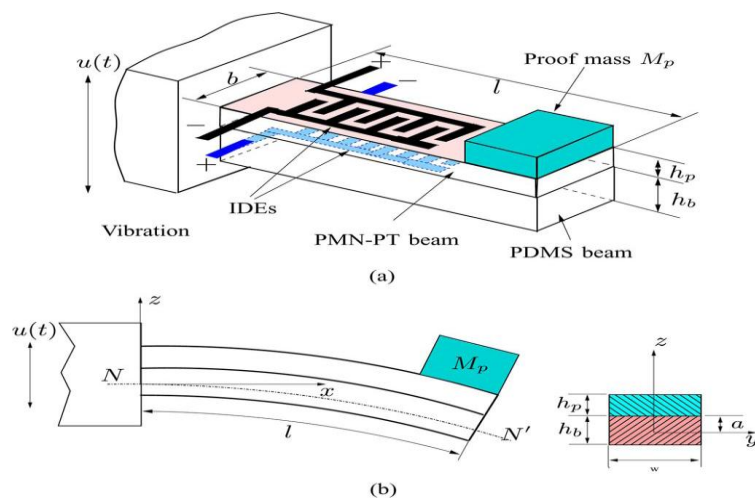
Figure 2.7 PMN-PT beam with proof mass under input transverse excitation, [40].

Jeon *et al* [42] explored the conversion energy of a micro power harvester cantilever piezoelectric model using the base-motion of the ambient vibration source from an exciter as shown in Figure 2.8. The generated voltage using the {3-3} piezoelectric mode operation was found to be higher compared with the {3-1} piezoelectric mode operation. The operational scheme indicated that the fabrication of the piezoelectric device was made by attaching its top surface on the interdigitated electrode to produce the {3-3} piezoelectric mode. The {3-3} piezoelectric mode gave a voltage at least 20 times higher than the {3-1} piezoelectric mode. The generated AC current from the cantilever piezoelectric was rectified using the bridge rectifier to obtain DC current where it was then stored using a capacitor.
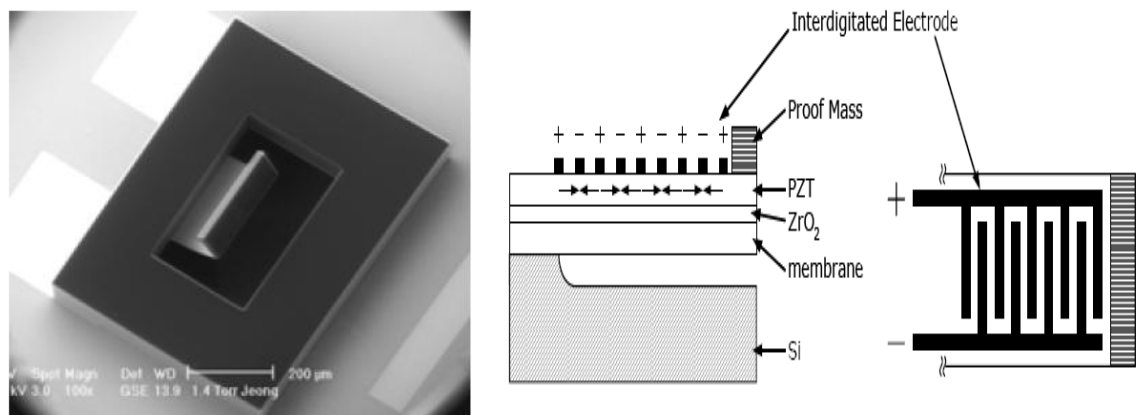
Figure 2.8 MEMS scale of interdigitated electrode of the Piezoelectric material, [42].

Song *et al* [43] discussed the mathematical and experimental models of a cantilever piezoelectric beam structure under harmonic vibration. The piezoelectric component which was bonded on the top and bottom of the beam structure, was made from macro-fiber composite where it was circuited using a full bridge rectifier, capacitor and load resistance. The optimised power harvesting, electric voltage and current was obtained using 3-1 (d_{31}) and 3-3 (d_{33}) poling directions where they found that the MFC with the {3-3} poling direction gave very high power harvesting and electric voltage compared with the {3-1} poling direction. On the other hand, the MFC with the {3-1} direction gave very high current, which was very useful for power storage. They also found that the varying thickness of the beam affected the strain and hence the maximum power harvesting and electric voltage results.

The broadband multi-piezoelectric beam with multi-frequency capability has also been investigated from some researchers. Ferrari *et al* [44] investigated an experimental multi-frequency array from three different bimorph beams using equivalent circuit systems. Each bimorph with different tip masses were connected to an AC-DC rectifier with the power stored into the single storage capacitor. Sharuz [45,46] from Berkeley Engineering Research Institute, attempted to discuss the analytical method of using mechanical band-pass filters of energy harvesting with the single mode multi-transverse bimorph beam effect with different lengths in order to maximise the frequency band. However, his mathematical method clearly failed to formulate the important issue of the coupled electromechanical strain and electric-polarity fields to provide the power harvesting under the broadband multi-frequency system because the piezoelectric transduction itself consists not only the mechanical field but also the electrical field. His two published papers from the Journal of Sound and Vibration and the Journal of Vibration and Acoustics failed to provide the mathematical formulation of the electromechanical multi-piezoelectric vibration power harvesting. The research group led by Wereley from the University of Maryland, Song *et al* [47] investigated three frequency power harvesters using the macro-fiber composite (MFC) bonded on the bottom and top of each beam with tip masses. They used the analytical assumed mode method with the single mode electromechanical response without considering the orthonormality condition and the experimental comparison showed the modelling tended to give overestimated results. Xue *et al* [48] provided the theoretical study of the multiple piezoelectric bimorphs with different thicknesses using mix-connection pattern (mix series and parallel connections) to widen the resonance frequency band. Their mathematical model was based on the boundary value system of the single mode piezoelectric beams.

Table 2.3. Summary of Piezoeletric Generator

reference	Frequency range (Hz)	Input vibration	Geometry (mm^3)	Damping	Output power/ voltage	Mathematical system	Detail
Sodano *et al*	1500		MFC :40.6×25.4×0.305 Quick Pack IDE :50.8×25.4×0.381 Quick Pack : 50.8×25.4×0.381	-	MFC : 60.7062 W/m^3, Quick Pack IDE : 60.7062 W/m^3, Quick Pack : 285.0246 W/m^3	-	Experiment given but no theoretical study. The power density output was plotted for the first twelve modes of frequency response.
Chen *et al*	250 -600	10 µm	Variance such as; Piezo length : 27,30, 33. Silicon subs. Length : 32, 35, 38. Piezo Thickness : 0.002, Silicon Thickness : 0.3	Variance of damping ratio :0.0067 to 0.0089	0.8 V (max)	Analytical method with curvature basis approach without converse piezoelectric coupling but having direct piezoelectric coupling	Validation with experiment. No tip mass and no multi-mode FRFs. Damping ratios were associated with the geometries
Yang & Yang	2x10^4 to 3.5x10^4	1 m/s^2	25×8×6 (each bimorph)	Quality factors of bimorph :10^2	2.5 W/m^3 (max)	Exact method with the boundary values to analyse two bimorphs coupled via elastic spring	No validation and only singe mode
Minazara *et al*	1710	80 N	Diameter and thickness of piezoelectric : 25 and 0.23, respectively	-	1.7 mW	Single mode of electromechanical equation	Experiment given including SSHI circuit system

Cont. from Table 2.3

Reference	Frequency range (Hz)	Input vibration	Geometry (mm^3)	damping	Output power/ voltage	Mathematical system	Detail
Goldschmi-dtboeing & Woias	4000	2.5 g	Rectangular :20×5×0.470 Truncated triangular: length : 30, width I : 20, width II: 3, thickness : 0.560	Rect. : α = 80 s^{-1}, β=3x10^{-6} s Triangular : α = 120 s^{-1} , β=1x10-6 s	Rect. : 4 V Triangular : 6 V (first mode)	Analytical approach by Rayleigh-Ritz method	Experiment, damping constants and tip mass were given. Rotary inertia from tip mass excluded
Erturk & Inman	30 to 70	1g	50.8×31.8×0.66	Damping ratio : 0.027	6.8 mW/g^2/cm^3(under short circuit resonance)	Analytical method with the solution form using the normalised eigenfunction series	Experiment given. Tip mass with its rotary included. Multi-mode FRFs also included
Mathers *et al*	1340	1.3 mm	PMN-PT :7.4×2×0.120	0.123	0.5 mW or 4.15 mW/cm^3	Analytical method without backward piezoelectric coupling	Experiment given. Tip mass without its rotary inertia. Single mode FRFs for the voltage & power
Song *et al*	60	0.2 g	Steel : 25.4×58.4×1.8 PMN-PT : 25×25×0.5	-	0.73 mW/cm^3	Analytical approach and no further derivations. No continuity criteria for the two different length of structures	PMN-PT bonded onto steel beam with tip mass without rotary inertia. Experiment was given. Single mode FRFs
Roundy & Wright	120	2.5 m/s^2	1000	0.015	375 µW/cm^3	Single mode analytical method	Analytical method using equivalent circuit for piezoelectric generation.

2.2. The Electromechanical Vibration-Based Electromagnetic Generator

The induced mechanical energy of a magnetic mass due to the vibration environment can create a change of magnetic flux through coils due to Faraday's law. As a result, electrical voltage from the coils can be generated having potential for powering batteries or capacitors through the circuit control system. Amirtharajah and Chandrakasan [49] demonstrated the use of ambient vibration to generate small electrical power, which was optimized using a DC-DC converter, and then controlled by DSP as a feedback signal. The DC Power obtained was 800 µW, which was then used as a feedback signal to a DSP with the input voltage sent to a regulator of 1 V. Further developments by Amirtharajah and Chandrakasan [50] used an electromagnetic coil transducer as a generator to convert ambient vibration to electrical energy, controlled by a DC regulator where the voltage output from the regulator was analysed using a DSP. The voltage output from the generator gave a peak level of 0.18 V which then abruptly dropped off to zero over a interval time of 15 ms. They also increased the number of coils and reduced the mass so that the output voltage could be increased. The maximum output power obtained was about 400 µW with the resonant frequency of the generator of 2 Hz.

Research led by Beeby from the University of Southampton, *et al* [51] discussed the electromagnetic micro-generator for energy harvesting. As shown in Figure 2.9, a cantilevered silicon beam with a tip mass of a copper coil, located at the middle between two-coupled NdFeB magnets under input vibration of 0.589 m/s^2, produced electrical power of 6 μW and power density of 307 μW/ m^3 with resonance frequency of 52 Hz. The power density was measured using the magnet volume of 0.15 cm^3 as given in Table 2.4. The optimised coils and magnets was also shown where the number of coil turns increased the electrical voltages with different load resistances. The optimised magnet was also found by changing the size where the electrical power increased with increasing magnet size.
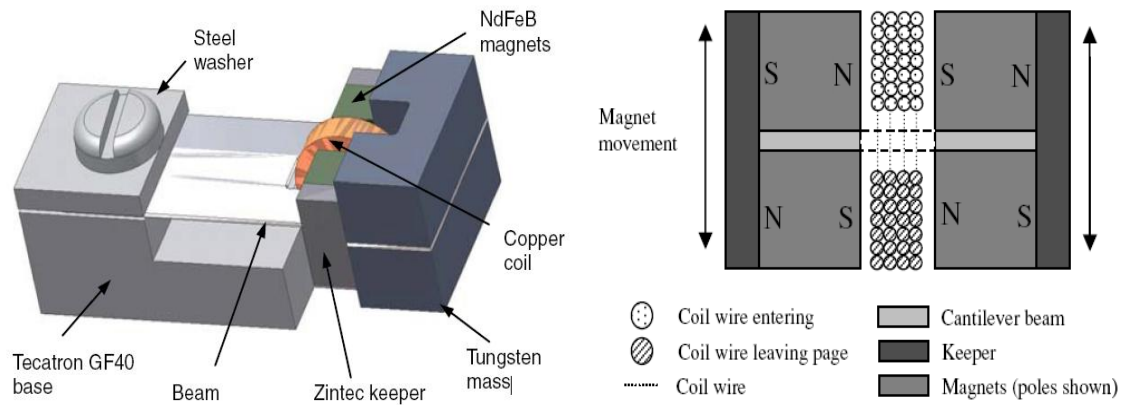
Figure 2.9 Cantilevered beam with the electromagnetic component, [51].

The work from Glynne-Jones *et al* [52]*,* presented fabricated electromagnetic power generators with two different prototypes as given in Table 2.4. The first prototype which was initially proposed by El-hami *et al* [53], had the coil located between two moving magnets, which were attached on the tip of the cantilevered beam. The difference was only in the geometrical structure and input vibration. The second prototype was the coil with four moving magnets. The first prototype with the beam volume of 0.84 cm^3 generated electrical power of 180 µW under resonance frequency of 322 Hz with the amplitude of beam motion of 0.85 mm as shown in Table 2.4. Moreover, the second prototype was tested on a car engine with a distance of 1.24 km under an average speed of 25 km/h where the average power generated was around 157 µW with the beam volume of 3.15 cm^3. The peak power achieved was around 3.9 mW. All results presented by authors were from the experimental study. The latest work from Beeby's research group, Zhu *et al* [54], included the addition of a tunable vibration system using the magnet with the micro-generator from Beeby *et al* [51]. The aim of this case was to adjust the resonance frequency from the generator where the resonance frequency shifted from 67.6 Hz to 98 Hz under input vibration of 0.59 m/s^2. The power generated also increased from 61.5 to 156.6 µW. However, the author stated that the electromagnetic generator was of small scale. The geometry of the beam and additional magnet for tuning the frequency also contributed to the larger size and weight. When the input vibration dropped drastically, the electromagnetic generator also drastically reduced its power output.

Sari *et al* [55] discussed the fabricated micro-electromagnetic power harvester using the multi-cantilever beam with printed planar coil and a magnet. The geometries of the beam and magnet size were given as 9.5×8×6 mm^3 and 6×6×6 mm^3, respectively. When the input vibration was given, the 20 beams with the planar coils vibrated around the magnet to induce the magnetic flux to create the electric charge. The number of coils printed on the beam was 16. The electrical power was measured experimentally giving around 56 pW for each cantilever under the vibration frequency of 3.4 kHz with the input displacement amplitude of 1 μm. At this stage, the authors did not provide the mathematical relationship of the coupled beam and electromagnetic system, but provided an oversimplified model of a single degree of freedom instead.

Yang *et al* [56] presented the fabricated electromagnetic system for multi-frequency power harvesting. The acrylic beam with three NdFeB magnets bonded along the beam span induced the magnetic flux due to the input vibration to create the electrical charge flowing into the printing planar copper coils located at the bottom of each magnet as shown in Figure 2.10. The beam length and distance between coils or magnets were given as 54 mm and 10 mm, respectively. The vector magnetic field and resonance frequencies were determined using ANSYS where the increase of gap between the magnet and coils was found to decrease the magnetic flux. The model under input vibration of 14 μm generated electrical power of 0.6 μW from the middle coil under the first mode and 3.2 μW from the first coil under the second mode. The total power under the series connection from the three coils was quoted as 1.157 μW under the first mode as given in Table 2.4. The first three modes of resonance frequencies from ANSYS was compared with the experiment with less than 6 % difference. However, the electrical voltage frequency response with the first three modes was only determined by experiment, where the electrical voltage under the first mode was given as 0.09 mV. Moreover, the theoretical model of the single degree of freedom system failed to show good agreement with the experimental results where the results showed significant difference of power versus the load resistance.
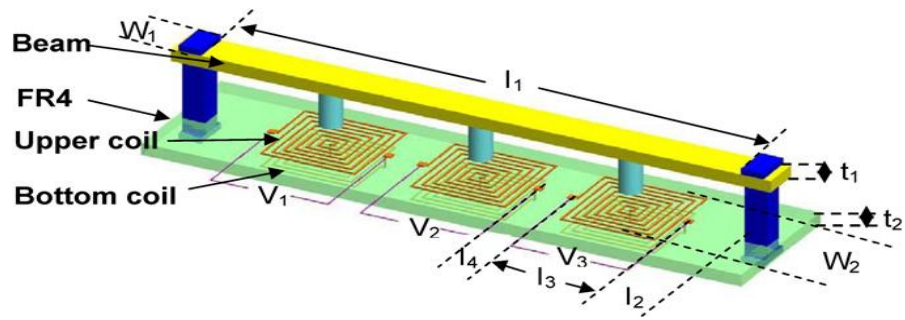
Figure 2.10 Beam with three poled magnets on the simple support beam, [56].

Saha *et al* [57] presented the generator tube for electromagnetic energy harvesting induced from human motion. The generator tube, which included a coil wound from the outer surface, consisted of moving magnets located between two permanent magnets as shown in Figure 2.11. The input vibration of the tube resulted in the magnetic flux from the magnet moving up and down to induce coil electric voltage. When the generator tube was placed onto the rucksack, the tube generator with the input acceleration of 0.5 g with frequency of 2 Hz generated power from 300 µW to 2.5 mW during walking and slow running. When the input acceleration from an exciter of 0.38259 m/s^2 under frequency of 7.6 Hz was applied onto the generator tube, the power generated was around 14.55 µW with the load resistance of 7.3 kΩ as given in Table 2.4.
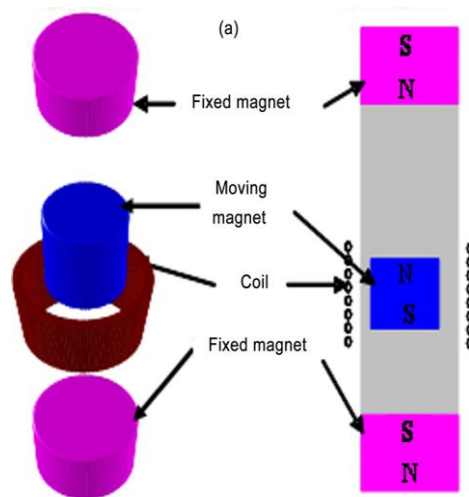
Figure 2.11 Tube Electromagnetic harvester with the moving magnet, [57].

Peter *et al* [58,59] from IMTEK Germany presented the tunable mechanical resonator using two piezoelectric actuators for controlling the vibrations as the electromagnetic system was attached for energy harvesting. One actuator was

clamped and another actuator was free. Both actuators were connected to each other by three hinges attached between the actuator. The input voltage of ±5 V for the actuators was applied to adjust the resonance frequency to provide a shift of ±15 % from the ambient vibration environment. As a result of this effect, the free actuator controlled the vibration in order to induce the fluctuating magnetic flux resulting in induced electrical voltage generated from the coils. Although, the concept of tuning the voltage of the piezoelectric control system for the electromagnetic power harvester was sophisticated, the structure model was complex and needed two piezoelectric actuators, which were much larger than the electromagnetic components. In addition, the piezoelectric actuators still needed the external voltage for tuning the mechanical system to adjust one resonance frequency.

Kim *et al* [60] presented two different electromagnetic power generators using wind flow as the input vibration as shown in Figure 2.12. The first generator was a windbelt power harvester using the strong air flow to vibrate the aeroelastic membrane inducing the magnet to create the magnetic flux where the electrical voltage was generated from the coil. The second generator was a Helmholtz resonator power harvester using the weaker airflow into the chamber to create audio acoustic response so that the electrical voltage was generated due to the moving resonator. Both the generators used the coupled magnet and coil as the electrical energy source. The windbelt generator provided the open circuit voltage of 81 mV at the frequency of 0.53 kHz whereas the Helmholtz resonator generated voltage response of 4 mV at the frequency of 1.4 kHz due to the acoustic response with the input airflow velocity of 5 m/s. However, both generators used the air pressure fluctuations to create enough vibration to move the magnets.
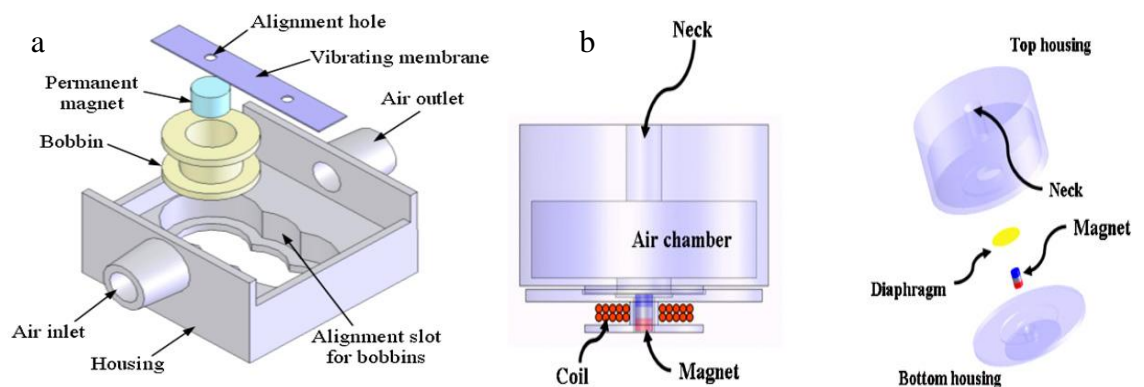
Figure 2.12 Wind flow of electromagnetic generator : a) Windbelt power harvester using the strong air flow , b) Helmholtz resonator using the weaker airflow, [60].

Park *et al* [61] presented the concept of a bulk-micro-electromagnetic power generator. The NdFeB magnet was attached to the centre of a silicon spiral spring directed to the centre of a copper coil where all parts were placed into the polydimethylsiloxane (PDMS) packaging mold as shown in Figure 2.13. The only difference between this model compared to others was the small scale of the bulk-micromachined silicon spiral spring with the volume scale of 8 x 8 x 0.04 mm^3 as it was only compatible for single degree of freedom response with the single poled magnet. The input vibration of 0.57 g onto the PDMS electromagnetic generator resulted in a power density of 590.4 μW/cm^3.g^{-2} at the frequency of 54 Hz as given in Table 2.4. Stephen [62] derived the mathematical model of an electromechanical system, which consisted of a seismic mass with constant stiffness and damping coefficients from the coupled mechanical and electrical parts under base excitation moving through an electromagnetic coil circuited with the electrical parts from load resistance and electromechanical coupling coefficient. For this case, the predicted power harvesting was optimised using the matching of load resistance and coil resistance, the matching of mechanical and electrical damping coefficients, and the matching of electrical analogue of mechanical damping.
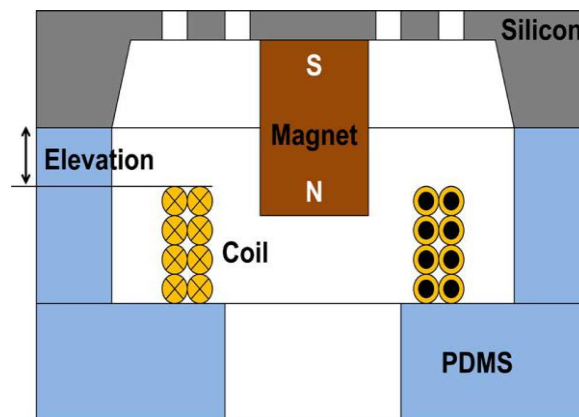
Figure 2.13 Single degree of freedom of electromagnetic generator with the plane spiral spring silicon, [61].

Table 2.4 Summary of Electromagnetic Generator

Reference	Frequency range (Hz)	Input vibration	Geometry (cm^3)	Damping	Output power/ voltage	Detail
Beeby *et al*	52	0.589 m/s^2	0.15 (Magnets)	-	307 μ W/ m^3	Beam with four poled magnets. Experiment only
Saha *et al*	7.6	0.38259 m/s^2	12.7 (Tube)	0.0277	14.55 μ W	Tube with two poled magnets. Experiment only
Glynne-Jones *et al*	322	2.7 m/s^2	0.84 (beam)		180 µW	Beam with two poled magnets. Experiment only
El-hami *et al*	322	25 µm	0.24	-	530 µW	Beam with two poled magnets. Experiment only
Yang *el al*	369	14 μ m	0.32 (beam)	-	1.157 μ W	Beam with three poled magnets. Experiment only
Park *et al*	54	0.57 g	0.6 (packaging mold)	0.03	590.4 µW/cm^3 .g^{-2}	Single poled Magnet attached on silicon spiral spring. Experiment and analysis of single degree of freedom

2.3. The Electromechanical Vibration-Based Electrostatic Generator

In the electrostatic generator, two parallel capacitors covering the electrode will polarise the electric charge when one of the plate capacitors is subjected to mechanical motion to overlap another capacitor periodically. The effect of polarised capacitors will vary the capacitance as it results in varying voltage and electrical current flow to the circuit. Roundy *et al* [6] discussed three basics prototypes of electrostatic energy generation as shown in Figure 2.14. The first prototype was an in-plane overlap converter. When the comb driven structure moved to change the overlapped area, the change of capacitance also varied. The second prototype was an in-plane gap closing converter. In this case, the capacitance changed due to the change of gap between two comb fingers. The third prototype was an out-of-plane

gap closing converter because the capacitance varied by changing the gap between the two large plates.
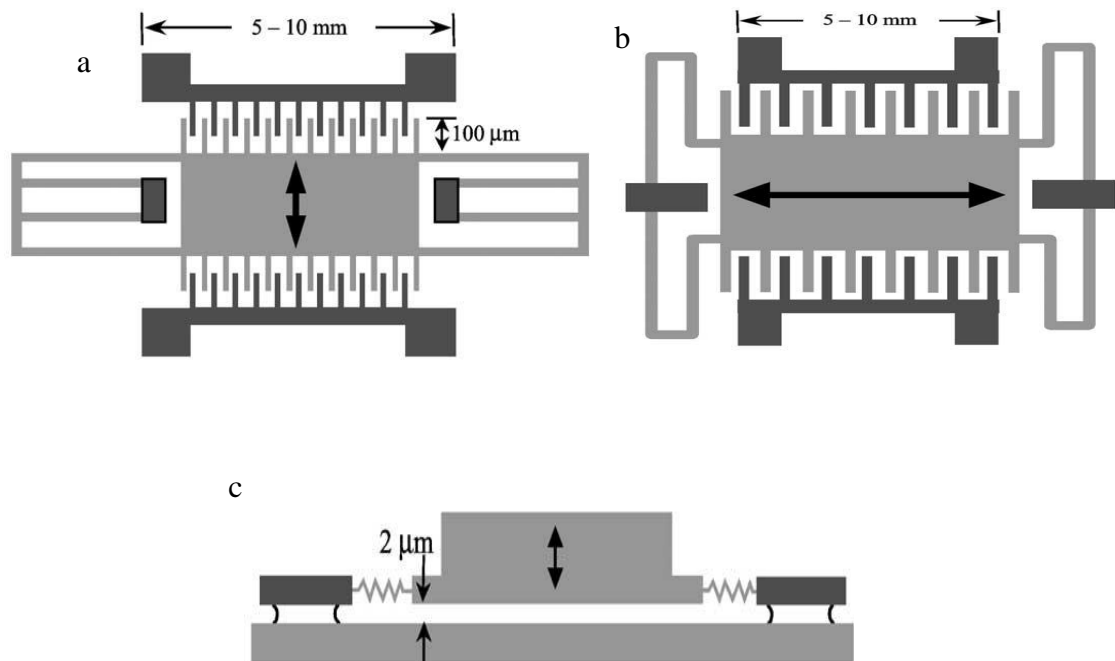
Figure 2.14 Types of Electrostatic generators: a) in-plane overlap converter, b) in-plane gap closing converter, c) out-of-plane gap closing converter, [6].

Starken *et al* [63] discussed the effect of the polarised electret of the micromachined electrostatic generator to produce the electrical charge due to the input mechanical motion. The basic prototype consisted of three wafers. The top wafer attached the electrets and the bottom wafer was used as the variable capacitor. The moving capacitor electrode was located at the middle wafer with the bonded seismic mass suspended by silicon spring. The result is shown in Table 2.5. The effect of the electret was expected to polarise the high voltage capacitor in order to generate high power where the resonance frequency was excited under the sinusoidal wave. In that case, the change of capacitance per micrometre displacement needed to be high. The numerical and experimental studies of the effect of the electret bonded at the base electrode surface was reported by Tsutsumino *et al* [64] where the moving electrode (counter electrode) was excited by the shaker to affect the polarisation of the electret. With the similar model of the electromechanical behaviour, Naruse *et al* [65] presented a new model for a micro-power electrostatic generator with two silicon substrates with the electret located at the middle between two glass substrates with collector electrodes as shown in Figure 2.15. The electrets with attached guard

electrodes, functioned as the dielectric material for the quasi-permanent electrical charge. The basic principle of their model was the moving silicon mass with two electrets, guided using the micro-bearing ball to keep the separation gap stable where the silicon mass was connected with the spring and supported at the fixed glass in order to control the vibration. Once the electrets moved away from one collector electrode to another electrode at the glass substrates, the electrical power with frequency of 2 Hz generated around 40 µW with input acceleration of 0.4 g as given in Table 2.5. The problem with their model was that the output power decreased when the mover underwent reciprocating motion and then collided with the edges of the device. The resulting power decreased dramatically.
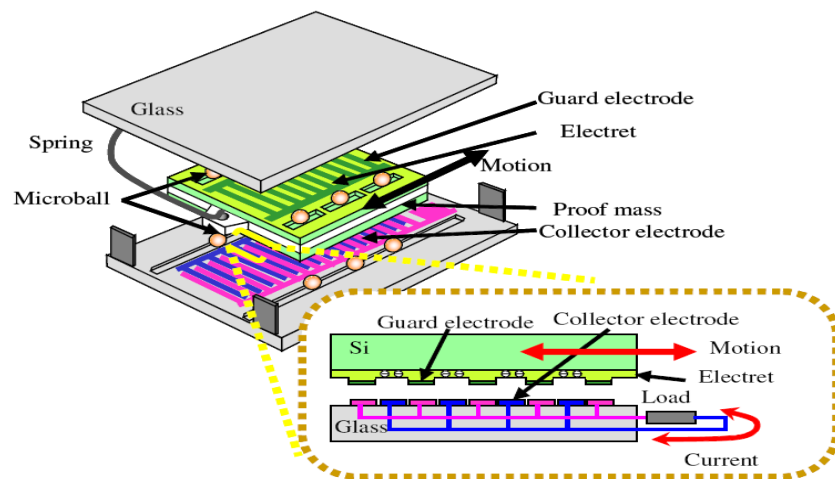
Figure 2.15 Electrostatic generators with moving electrets, [65].

Hoffmann *et al* [66] presented the concept of the Micro-electrostatic generator with the model of in-plane motion varying the overlap electrode area as shown in Figure 2.16. The comb mass with interdigitated electrodes moved the overlap area to create mechanical induction of the plate capacitors and electrical charges were generated due the change of capacitance as the results show in Table 2.5. Tvedt *et al* [67] also used the same model by introducing the equivalent circuit of linear and non-linear behaviour using the SPICE software. The mechanical stop was used in [66] and [67] to control the vibration of the comb mass. It was found that the power reduced because the impact of the comb mass with the mechanical stopper was strongly dependent on the acceleration excitation at the resonance frequency.
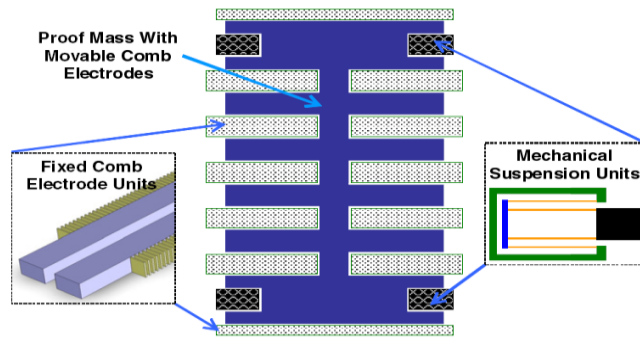
Figure 2.16 Electrostatic generators : in-plane overlap converter, [66].

Kiziroglou *et al* [68] from Imperial College London, presented the flexible substrate electrostatic plate generator using the rolling rod as the proof mass. The substrate material, which was mounted on a glass wafer, was made from a polyimide film wafer to allow for some flexibility as shown in Figure 2.17. The effect of the rolling rod on the different concave shape form of the substrate plate can change the capacitance to give higher power as it depended on the substrate curvature and allowed the rod to move periodically to induce the electrical voltage from the dielectric plate surface. However, their experiment only tested the rolling rod on the flat substrate. When the rod rolled over the flat dielectric-coated Cu plates, the capacitance varied periodically as it depended on the displacement of the rod. The input voltage of 20 V was needed for the substrate plate. When the rod rolled over the plate, the output voltage generated was around 48 V at the first peak which then decayed dramatically within 60 µs. With the similar model, Kiziroglou *et al* [69] also modified the shape of the substrate surface with low concave curvature of the plate which allowed the rod to roll periodically. The input voltage of 30 V into the substrate plate generated the peak voltage of 90 V that then abruptly decayed within 160 µs. During the rolling rod motion of the substrate plate, the output capacitance of 2 pF at the initial state increased up to 9 pF at the distance of 1.5 mm. The electrical power generated was around 0.5 µW at the frequency of 10 Hz.
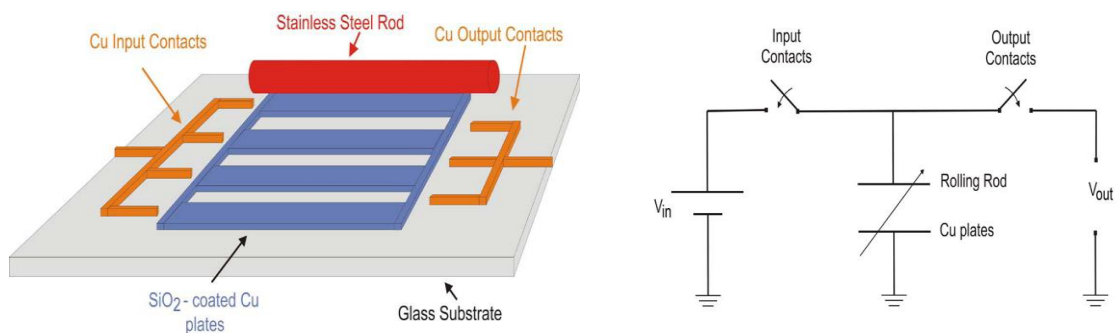
Figure 2.17 Electrostatic generator using moving rolling steel associated with the electrical equivalent, [68].

Table 2.5. Summary of Electrostatic Generator

Reference	Frequency range (Hz)	Input vibration	Geometry (cm^3)	Damping	Output power/ voltage	Detail
Naruse *et al*	2 Hz	0.4 g	0.28 (device)	-	40 μW (exp) 2232 µW (theory)	Electrets moved between two fixed collectors. Experiment and theory were given
Hoffmann *et al*	1300 Hz & 1500 Hz	13 g	0.2 (device)	5x10^{-5} N-s/m	3.5 μW (exp) 5.5 µW (theory)	Moving capacitors with in-plane varying overlap. Experiment and theory were given
Starken *et al*	500 Hz	1 g	-	-	5 µW	Electrets moved between two fixed collectors. Experiment given
Despesse *et al*	50 Hz	8.8 m/s^2	1.8 (device)	-	1052 µW	Moving capacitor with in-plane closing gap. Experiment given

2.4. Closing Remark

In this chapter, the review of electromechanical vibration power harvesters has been presented including those based on the piezoelectric, electromagnetic and electrostatic generators. The wasted or unused mechanical energy from machine vibration, fluid flow and human motion can be used to convert motion into electrical energy by designing a self-powered electromechanical system to support the development of smart wireless sensor devices for future technology applications. The conventional wired/wireless sensor devices still depend on the power supply from the battery where it is a tedious task to replace and time consuming for maintenance during the system operation. The power generators have scalability and show potential for long-term autonomous operation that can be used for many applications and these are included but not limited to :

1. Condition health monitoring such as of industrial rotating machines, bridge, pipe structure, automobile, airplane, train, ship, and etc.

2. Defense global positioning system for embedded application such as in boots and shoes, army shirt, gloves, tanks, radio frequency for water police and Navy, and etc.

3. Natural monitoring system: ocean wave for detecting ship smuggler and tsunami, wind flow to the leaves in the forest for detecting bush fire and etc.

Moreover, the summary of the three major transductions have advantages and disadvantages as given in Table 2.6. It is important to note here that the overall inherent mechanism of transductions depends on the material design, the nature of the vibration environment and strategies to increase the power through tuning the mechanical and electrical systems in order to maximise the power for the smart wireless sensor systems.

Table 2.6 Summary of Three Different Types of Generators

Type	Advanteges	Disadvantages
Piezoelectric	no external voltage no mechanical stop high power density high output voltage high sensitivity compatible with MEMS	depolarisation brittleness of piezoceramic materials high impedance
Electromagnetic	no external voltage no mechanical stop	difficult to integrate with MEMS low output voltage low sensitivity bulky size from the magnet and coil
Electrostatic	compatible with MEMS	need external voltage complex design for plate capacitor comb low power density need mechanical stop

However, unlike the electromagnetic and electrostatic transducers, the piezoelectric transducer has great capability for generating the highest electrical voltage and power as it has compact configuration, compatibility with MEMS standard and high sensitivity to capture the motion. Indeed, the coupling of an electromagnetic and piezoelectric power generator can be a good potential device, but it is still difficult for MEMS because the electromagnetic system results in a natural bulky size with the magnet and coil. However, in this thesis; the piezoelectric power harvester represents the major purpose of investigations not only for the chosen aspect of the profound material mechanism but also by providing novel analytical methods for

modelling the electromechanical system and the experimental study as given in the forthcoming chapters. In the next chapter, the exploration of continuum thermopiezoelectricity theory will be comprehensively presented to provide the indispensable relationships of the piezoelectric properties in terms of the thermopiezoelectric potentials, the thermopiezoelectric equations of state and energy function forms with the tensor coefficients.

CHAPTER

3

Theory of Continuum Thermopiezoelectricity

This chapter deals with the energy phenomenon of piezoelectric materials. Piezoelectric elements have unique behaviours for energy generation depending upon either the induced mechanical, electrical or even thermal loads. Under these circumstances, the piezoelectric element exhibits elongations or contractions in three dimensional space. The elongations of the piezoelectric element are due to the reaction of changes of the ion crystalline structure from random domain polarization to aligned polarization. This creates net dipole moments to align the electric field and generate electric voltage during the application of dynamic loads onto any face of the piezoelectric element. Piezoelectric materials display important properties in the engineering field which can be derived using thermodynamic relationships where the energy phenomenon can be used to explore the interrelationship between properties with different physical treatments in order to obtain the thermopiezoelectric coefficients.

This section mainly focuses on the mathematical continuum thermodynamic equations of the macroscopic piezoelectric element and develops the defining interrelationships between electricity, elasticity and entropy using Legendre's transform and Maxwell's theorem of thermopiezoelectricity. From basic thermodynamics, the concepts of macroscopic properties such as piezoelectricity, consisting of the stress, mass, and strain is found. From the perspective of microscopic properties, the piezoelectric element itself also has the nature of molecules of atoms. Moreover, the interactions between molecules of atoms in the system can be formulated at the macroscopic level using the concept of continuum thermopiezoelectricity instead of the quantum statistical thermodynamic equations as long as the thermodynamic coefficients can be determined. Sometimes these can be measured and derived in exact differential forms where these can be found from thermodynamic potentials. In other words, the macroscopic properties consist of the

numbers of molecules of atoms in the microscopic levels interacting to form the continuum energies, Desloge [70]. Apart from that, the solid macroscopic piezoelectric properties can be developed using the concepts of quasi-equilibrium thermodynamics or thermopiezoelectric equilibrium.

3.1. Quasi-Electrical Energy of Piezoelectricity

The basic concept is that the forces acting between two charges are proportional with the product of the magnitudes of each of the charges and the square of the distance between the charges $\sim 1/r^2$. The force is also proportional with the electric field E, resulting in the positive test charge heading toward the negative charge resulting in equipotential, Hayt and Buck [71]. The resulting simple electric force relationship is,

$$F = Q.E \qquad . \tag{3.1}$$

From this perspective, the applied work dW can be quantified due to the exerted force moving the charge Q along the path with distance dL, where the exerted force brings the charge opposite to the direction of the electric field E, creating the work W as shown in Figure (3.1). In this case, equation (3.1) can be formulated into the form of differential work done against the electric field by multiplying with the differential distance to give,

$$dW = -QE.dL \quad . \tag{3.2}$$

Figure (3.1) shows the moving charge along the path *i-a-b-c-f* with the direction of the electric field vector, Hayt and Buck [71]. The charge moving through each path or the change rate of direction dL contains the same magnitude of electric field to create the electrical work. Integrating Eq. (3.2) using line integration from the initial state to the final state gives,

$$W_{if} = -Q \int_i^f E.dL \qquad . \tag{3.3}$$

The electrical work for each section of the path shown in Figure 3.1 can be written as,

$$W_{if} = -Q \left[\int_i^a E_{ia}dL_{ia} + \int_a^b E_{ab}dL_{ab} + \int_b^c E_{bc}dL_{bc} + \int_c^f E_{cf}dL_{cf} \right] . \tag{3.4}$$
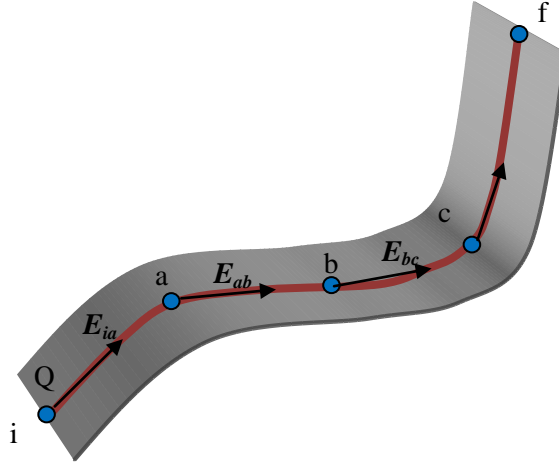
Figure 3.1 Illustration of the Work Done by the electric field moving a
charge from point i to f

The work done on this path depends on the position vector of the charge's displacement and electric field based on the initial and final states, Stratton [72]. Equation (3.4) can be reformulated into Eq. (3.5) to reflect the change in total electrical work,

$$W_{if} = -Q\left[\boldsymbol{E}_{ia}.\Delta\boldsymbol{L}_{ia} + \boldsymbol{E}_{ab}.\Delta\boldsymbol{L}_{ab} + \boldsymbol{E}_{bc}.\Delta\boldsymbol{L}_{bc} + E_{cf}.\Delta\boldsymbol{L}_{cf}\right], \qquad (3.5)$$

that can also be written as,

$$W_{if} = -Q\boldsymbol{E}\left[\Delta\boldsymbol{L}_{ia} + \Delta\boldsymbol{L}_{ab} + \Delta\boldsymbol{L}_{bc} + \Delta\boldsymbol{L}_{cf}\right], \qquad (3.6)$$

assuming the electric field along the path remains constant with magnitude $\boldsymbol{E}$,

$$\boldsymbol{E}_{ia} = \boldsymbol{E}_{ab} = \boldsymbol{E}_{bc} = \boldsymbol{E}_{cf} = \boldsymbol{E}.$$

The work done can also be expressed in terms of the total displacement function from i to f as,

$$W_{if} = -Q\boldsymbol{E}.\Delta\boldsymbol{L}_{if}.$$

or it can be stated using the general expression,

$$\Delta W = -Q\boldsymbol{E}.\Delta\boldsymbol{L} \qquad (3.7)$$

Equation (3.7) can be modified to yield the potential field as a result of the dot product between electric field and differential vector distance as,

$$\left[\frac{W}{Q}\right]_{i \to f} = -\int_{i}^{f} \boldsymbol{E}.\,\mathrm{d}\boldsymbol{L} \qquad , \qquad (3.8)$$

That can also be expressed as,

$$\Phi_{if} = - \int_i^f \boldsymbol{E}.\,\mathrm{d}\boldsymbol{L} \quad . \tag{3.9}$$

Where the Potential at point i is given as Φ_i and point f, Φ_f, the change of potential can be written as,

$$\Phi_i - \Phi_f = - \int_i^f \boldsymbol{E}.\,\mathrm{d}\boldsymbol{L} \quad , \tag{3.10}$$

or formulated to obtain,

$$\Delta\Phi = - \boldsymbol{E}.\,\Delta\boldsymbol{L} \quad . \tag{3.11}$$

From the previous basic formulation of the work done in moving the charge, the infinitesimal coordinate system can be used to demonstrate the differential work on the charge as shown in Figure (3.2).
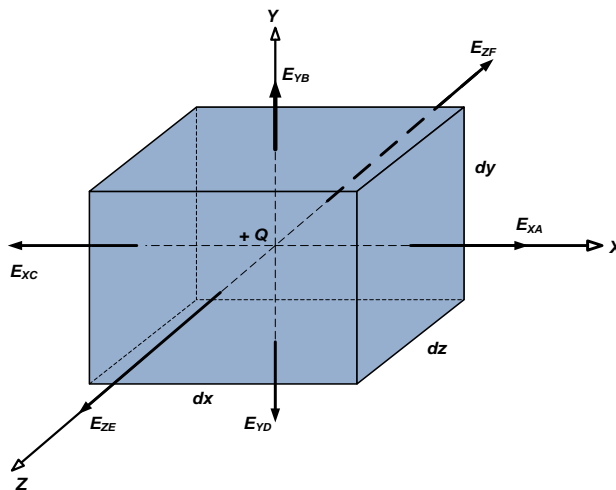
Figure 3.2 Components of electric field vector on the Infinitesimal element due to positive charge located in the middle of the element

The electric field vector can be written in terms of the field strength E and the first order approximation of the space rate of change of axes $(\mathrm{d}x/2 , \mathrm{d}y/2,$ and $\mathrm{d}z/2)$ using Taylor's series. The displacement vector can also be similarly expressed to give,

$$\boldsymbol{E}_{XA} = \boldsymbol{E}\left(X + \frac{\mathrm{d}X}{2}\right) = \boldsymbol{E}_X + \frac{\partial \boldsymbol{E}_X}{\partial X}\frac{\mathrm{d}X}{2} \quad , \boldsymbol{L}_{XA} = \boldsymbol{L}\left(X + \frac{\mathrm{d}X}{2}\right) = \boldsymbol{L}_X + \frac{\partial \boldsymbol{L}_X}{\partial X}\frac{\mathrm{d}X}{2} ,$$

$$\boldsymbol{E}_{XC} = \boldsymbol{E}\left(X - \frac{\mathrm{d}X}{2}\right) = \boldsymbol{E}_X - \frac{\partial \boldsymbol{E}_X}{\partial X}\frac{\mathrm{d}X}{2} \quad , \boldsymbol{L}_{XC} = \boldsymbol{L}\left(X - \frac{\mathrm{d}X}{2}\right) = \boldsymbol{L}_X - \frac{\partial \boldsymbol{L}_X}{\partial X}\frac{\mathrm{d}X}{2} ,$$

$$E_{YB} = E\left(Y + \frac{\mathrm{d}Y}{2}\right) = E_Y + \frac{\partial E_Y}{\partial Y}\frac{\mathrm{d}Y}{2}, \quad L_{YB} = L\left(Y + \frac{\mathrm{d}Y}{2}\right) = L_Y + \frac{\partial L_Y}{\partial Y}\frac{\mathrm{d}Y}{2}, \quad (3.12)$$

$$E_{YD} = E\left(Y - \frac{\mathrm{d}Y}{2}\right) = E_Y - \frac{\partial E_Y}{\partial Y}\frac{\mathrm{d}Y}{2}, \quad L_{YD} = L\left(Y - \frac{\mathrm{d}Y}{2}\right) = L_Y - \frac{\partial L_Y}{\partial Y}\frac{\mathrm{d}Y}{2},$$

$$E_{ZE} = E\left(Y + \frac{\mathrm{d}Y}{2}\right) = E_Z + \frac{\partial E_Z}{\partial Z}\frac{\mathrm{d}Z}{2}, \quad L_{ZE} = L\left(Z + \frac{\mathrm{d}Z}{2}\right) = L_Z + \frac{\partial L_Z}{\partial Z}\frac{\mathrm{d}Z}{2},$$

$$E_{ZF} = E\left(Y - \frac{\mathrm{d}Y}{2}\right) = E_Z - \frac{\partial E_Z}{\partial Z}\frac{\mathrm{d}Z}{2}, \quad L_{ZF} = L\left(Z - \frac{\mathrm{d}Z}{2}\right) = L_Z - \frac{\partial L_Z}{\partial Z}\frac{\mathrm{d}Z}{2}.$$

It should be noted that the negative sign because the work is done against electric field. In this case, the work on the charge moving through the infinitesimal space element can be written to yield the total differential work as,

$$\delta W = -Q\left[\int E_{XA}\delta L_{XA} - \int E_{XC}\delta L_{XC} + \int E_{YB}\delta L_{YB} - \int E_{YD}\delta L_{YD}\right.$$
$$\left. + \int E_{ZE}\delta L_{ZE} - \int E_{ZF}\delta L_{ZF}\right]. \quad (3.13)$$

Substituting each electric field and distance from Eq. (3.12) into Eq. (3.13) yields,

$$\delta W = -Q\left[\int \left(E_X + \frac{\partial E_X}{\partial X}\frac{\mathrm{d}X}{2}\right)\delta\left(L_X + \frac{\partial L_X}{\partial X}\frac{\mathrm{d}X}{2}\right)\right.$$
$$- \int \left(E_X - \frac{\partial E_X}{\partial X}\frac{\mathrm{d}X}{2}\right)\delta\left(L_X - \frac{\partial L_X}{\partial X}\frac{\mathrm{d}X}{2}\right)$$
$$+ \int \left(E_Y + \frac{\partial E_Y}{\partial Y}\frac{\mathrm{d}Y}{2}\right)\delta\left(L_Y + \frac{\partial L_Y}{\partial Y}\frac{\mathrm{d}Y}{2}\right)$$
$$- \int \left(E_Y - \frac{\partial E_Y}{\partial Y}\frac{\mathrm{d}Y}{2}\right)\delta\left(L_Y - \frac{\partial L_Y}{\partial Y}\frac{\mathrm{d}Y}{2}\right)$$
$$+ \int \left(E_Z + \frac{\partial E_Z}{\partial Z}\frac{\mathrm{d}Z}{2}\right)\delta\left(L_Z + \frac{\partial L_Z}{\partial Z}\frac{\mathrm{d}Z}{2}\right)$$
$$\left. - \int \left(E_Z - \frac{\partial E_Z}{\partial Z}\frac{\mathrm{d}Z}{2}\right)\delta\left(L_Z - \frac{\partial L_Z}{\partial Z}\frac{\mathrm{d}Z}{2}\right)\right]. \quad (3.14)$$

Equation (3.14) can be further simplified by applying the total differential partial where the products of different terms are ignored. As an example, consider,

$$\delta L_X = \delta\left(L_X + \frac{\partial L_X}{\partial X}\frac{\mathrm{d}X}{2}\right). \quad (3.15)$$

which can be expanded to give,

$$\delta L_X = \delta L_X + \frac{1}{2}\delta\left(\frac{\partial L_X}{\partial X}\right)\mathrm{d}X + \frac{1}{2}\frac{\partial L_X}{\partial X}\delta(\mathrm{d}X). \quad (3.16)$$

The last term can be assumed to be negligible because it is too small. Simplifying Eq. (3.16) by neglecting the products of differentials gives,

$$\delta L_X = \delta L_X + \frac{1}{2}\delta\left(\frac{\partial L_X}{\partial X}\right)dX \quad . \tag{3.17}$$

Equation (3.14) can then be written as a function of the differential distances as,

$$
\begin{aligned}
\delta W = -Q\Bigg[&\int\left(E_X + \frac{1}{2}\left(\frac{\partial E_X}{\partial X}\right)dX\right)\left(\delta L_X + \frac{1}{2}\delta\left(\frac{\partial L_X}{\partial X}\right)dX\right) \\
&-\int\left(E_X - \frac{1}{2}\left(\frac{\partial E_X}{\partial X}\right)dX\right)\left(\delta L_X - \frac{1}{2}\delta\left(\frac{\partial L_X}{\partial X}\right)dX\right) \\
&+\int\left(E_Y + \frac{1}{2}\left(\frac{\partial E_Y}{\partial Y}\right)dY\right)\left(\delta L_Y + \frac{1}{2}\delta\left(\frac{\partial L_Y}{\partial Y}\right)dY\right) \\
&-\int\left(E_Y - \frac{1}{2}\left(\frac{\partial E_Y}{\partial Y}\right)dY\right)\left(\delta L_Y - \frac{1}{2}\delta\left(\frac{\partial L_Y}{\partial Y}\right)dY\right) \\
&+\int\left(E_Z + \frac{1}{2}\left(\frac{\partial E_Z}{\partial Z}\right)dZ\right)\left(\delta L_Z + \frac{1}{2}\delta\left(\frac{\partial L_Z}{\partial Z}\right)dZ\right) \\
&-\int\left(E_Z - \frac{1}{2}\left(\frac{\partial E_Z}{\partial Z}\right)dZ\right)\left(\delta L_Z - \frac{1}{2}\delta\left(\frac{\partial L_Z}{\partial Z}\right)dZ\right)\Bigg] \quad . \tag{3.18}
\end{aligned}
$$

Multiplying the two components of the vector field in the bracket from each term of integrals of Eq. (3.17) gives,

$$
\begin{aligned}
\delta W = -Q\Bigg[&\int E_X\,\delta\left(\frac{\partial L_X}{\partial X}\right)dX + \int E_Y\delta\left(\frac{\partial L_Y}{\partial Y}\right)dY + \int E_Z\delta\left(\frac{\partial L_Z}{\partial Z}\right)dZ \\
&+ \int\left(\frac{\partial E_X}{\partial X}\right)\delta L_X dX + \int\left(\frac{\partial E_X}{\partial Y}\right)\delta L_Y dY + \int\left(\frac{\partial E_Z}{\partial Z}\right)\delta L_Z dZ\Bigg] \quad . \tag{3.19}
\end{aligned}
$$

Equation (3.19) can be modified to give the form,

$$\delta W = -Q\left[\int\frac{\partial(E_X\cdot\partial L_X)}{\partial X}dX + \int\frac{\partial(E_Y\cdot\partial L_Y)}{\partial Y}dY + \int\frac{\partial(E_Z\cdot\partial L_Z)}{\partial Z}dZ\right]. \tag{3.20}$$

By taking consideration of the operator δ in equation (3.20) which is the same as the ∂ operator in the differential equations. Equation (3.20) can be reformulated to yield,

$$\delta W = -Q\left[\int\frac{\partial\Phi_X}{\partial X}dX + \int\frac{\partial\Phi_Y}{\partial Y}dY + \int\frac{\partial\Phi}{\partial Z}dZ\right]. \tag{3.23}$$

This can be manipulated to give,

$$\delta W = -Q\int\left(\frac{\partial\Phi_X}{\partial X}e_x + \frac{\partial\Phi_Y}{\partial Y}e_y + \frac{\partial\Phi_Z}{\partial Z}e_z\right)\cdot\left(e_x dX + e_y dY + e_z dZ\right). \tag{3.24}$$

This can also be restated as,

$$\delta W = -Q\left(\frac{\partial \Phi_X}{\partial X}\mathbf{e}_x + \frac{\partial \Phi_Y}{\partial Y}\mathbf{e}_y + \frac{\partial \Phi_Z}{\partial Z}\mathbf{e}_z\right).\left(\mathbf{e}_x\delta X + \mathbf{e}_y\delta Y + \mathbf{e}_z\delta Z\right). \qquad (3.25)$$

Equation (3.25) can now be written,

$$\delta W = -Q\mathbf{E}.\delta \mathbf{L} \quad , \qquad (3.26)$$

where, $\quad \delta \mathbf{L} = \left(\mathbf{e}_x\delta X + \mathbf{e}_y\delta Y + \mathbf{e}_z\delta Z\right) \quad .$

Considering Eqs. (3.25) and (3.26) for δW, the electric field can now be written proportional to potential field terms, Hayt and Buck [71],

$$\mathbf{E} = -\left(\frac{\partial \Phi_X}{\partial X}\mathbf{e}_x + \frac{\partial \Phi_Y}{\partial Y}\mathbf{e}_y + \frac{\partial \Phi_Z}{\partial Z}\mathbf{e}_z\right) \quad . \qquad (3.27)$$

Equation (3.27) can be simplified using the gradient operator (grad) or nabla ($\boldsymbol{\nabla}$) to give,

$$\mathbf{E} = -\boldsymbol{\nabla}V = -grad\,(V) \quad . \qquad (3.28)$$

It is clear that the gradient operator for the infinitesimal element in rectangular coordinates indicate the vector form of the solution whereas the potential fields provide a scalar representation of the electric field. At this point, two different solutions for cylindrical and spherical coordinates can be formulated. In cylindrical form, the electric field can be formulated as,

$$\mathbf{E} = -\boldsymbol{\nabla}V = -\left(\frac{\partial \Phi}{\partial r}\mathbf{e}_r + \frac{1}{r}\frac{\partial \Phi}{\partial \phi}\mathbf{e}_\phi + \frac{\partial \Phi}{\partial z}\mathbf{e}_z\right). \qquad (3.29)$$

In spherical form, the electric field can also be obtained as,

$$\mathbf{E} = -\boldsymbol{\nabla}V = -\left(\frac{\partial \Phi}{\partial r}\mathbf{e}_r + \frac{1}{r}\frac{\partial \Phi}{\partial \theta}\mathbf{e}_\theta + \frac{1}{rsin\theta}\frac{\partial \Phi}{\partial \phi}\mathbf{e}_\phi\right) \quad . \qquad (3.30)$$

3.2. Electric Displacement of Piezoelectricity

Another vector term that can be developed for the piezoelectric element is the electric displacement field. The positive electric charge located at the centre from an arbitrary piezoelectric field can be considered a continuous function. Consider an arbitrary surface vector $\mathrm{d}\mathbf{S}$ with unit vector normal $\mathbf{n}$ on the area surface $\mathrm{d}S$ which has an electric displacement $\mathbf{D}_s$ upwards from the surface as shown in Figure (3.3). In this case, the electrical charge can be formulated in terms of Gauss' theorem to give,

$$Q = \oint \boldsymbol{D}_{s.} \mathrm{d}\boldsymbol{S} = \oint \boldsymbol{D}_{s.} \boldsymbol{n} \mathrm{d}S = \int_v \rho_v \mathrm{d}V = \int_s \rho_s \mathrm{d}S \quad , \tag{3.31}$$

where, ρ_v = charge per unit volume and ρ_s = charge per unit surface. The general vector form of electric displacement can then be formulated in terms of the vector component in rectangular coordinates as $\boldsymbol{D}_s = D_s \boldsymbol{e}_s = D_x \boldsymbol{e}_x + D_y \boldsymbol{e}_y + D_z \boldsymbol{e}_z$.
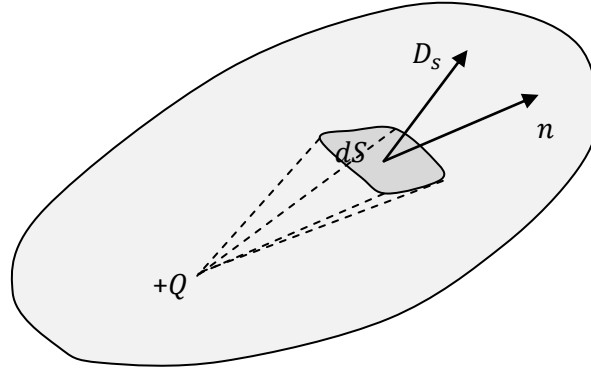
Figure 3.3 Outward electric displacement vector at element surface due to positive charge

Maxwell's electric displacement theorem can be shown in terms of Eq. (3.31) using the rectangular coordinate system. Consider each electrical displacement $\boldsymbol{D}$ together with surface vector $\boldsymbol{S}$ on the infinitesimal element face of the rectangular box to give the function of rectangular axes, (*x, y* and *z*) as shown in Figure (3.4). The space rate of change of axes $(\mathrm{d}x/2 , \mathrm{d}y/2 , \text{and } \mathrm{d}z/2)$ is located in the R^3 space, where $\boldsymbol{D}$ is a continuous function on the closed surface whereas d$\boldsymbol{S}$ is a continuous derivative to the vector surface where $\forall \boldsymbol{D}_{xo}, \boldsymbol{D}_{yo}, \boldsymbol{D}_{zo}, \Delta \boldsymbol{S} \in \{ \boldsymbol{D} , \boldsymbol{S} \subset R^3 \rightarrow R^2 \}$. The functional plane of $\boldsymbol{D}$ can be solved initially using the first two terms of the Taylor's series where the higher order series are very small for the differential electric displacement and can be neglected.
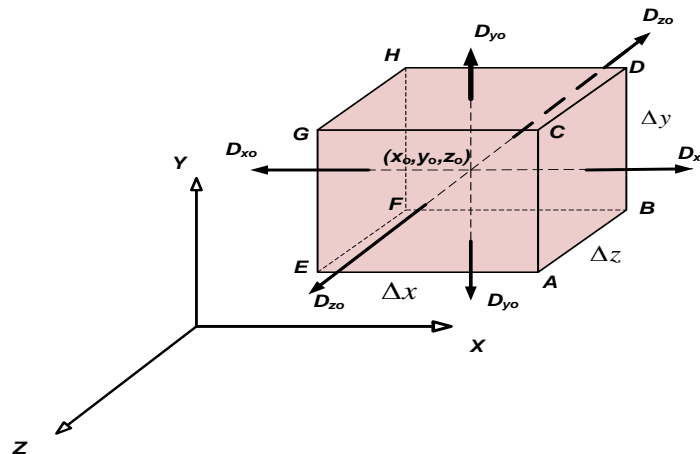
Figure 3.4 Outward electric displacement vector at the surface of the infinitesimal rectangular box due to positive charge

It should be noted that the component vector of electrical displacement can be formulated as,

$$D(x_o, y_o, z_o) = D_{xo}e_x + D_{yo}e_y + D_{zo}e_z. \qquad (3.32)$$

Applying Taylor's series while only considering the first two terms for Eq.(3.32) gives,

$$D_{xo}(ABCD) = D\left(x_o + \frac{\Delta x}{2}, y_o, z_o\right) = \left(D_{xo} + \frac{\Delta x}{2}\frac{\partial D_{xo}}{\partial x}\right)e_x \quad ; \quad \Delta S(ABCD)$$

$$= \Delta y \Delta z. \, e_x \, ,$$

$$D_{xo}(EFGH) = D\left(x_o - \frac{\Delta x}{2}, y_o, z_o\right) = \left(D_{xo} - \frac{\Delta x}{2}\frac{\partial D_{xo}}{\partial x}\right)e_x \quad ; \quad \Delta S(EFGH)$$

$$= -\Delta y \Delta z. \, e_x \, ,$$

$$D_{yo}(CDGH) = D\left(x_o, y_o + \frac{\Delta y}{2}, z_o\right) = \left(D_{yo} + \frac{\Delta y}{2}\frac{\partial D_{yo}}{\partial y}\right)e_y \quad ; \quad \Delta S(CDGH)$$

$$= \Delta x \Delta z. \, e_y \, ,$$

$$D_{yo}(ABEF) = D\left(x_o, y_o - \frac{\Delta y}{2}, z_o\right) = \left(D_{yo} - \frac{\Delta y}{2}\frac{\partial D_{yo}}{\partial y}\right)e_y \quad ; \quad \Delta S(ABEF)$$

$$= -\Delta x \Delta z. \, e_y \, ,$$

$$D_{zo}(AECG) = D\left(x_o, y_o, z_o + \frac{\Delta z}{2}\right) = \left(D_{zo} + \frac{\Delta z}{2}\frac{\partial D_{zo}}{\partial z}\right)e_z \quad ; \quad \Delta S(AECG)$$

$$= \Delta x \Delta y. \, e_z \, ,$$

$$D_{zo}(BFDH) = D\left(x_o, y_o, z_o - \frac{\Delta z}{2}\right) = \left(D_{zo} - \frac{\Delta z}{2}\frac{\partial D_{zo}}{\partial z}\right)e_z \quad ; \quad \Delta S(BFDH)$$

$$= -\Delta x \Delta y. \, e_z \, .$$

Using Maxwell's electrical displacement form in terms of Gauss' theorem gives,

$$Q = \oint D_{s.} \mathrm{d}S = \int_{ABCD} D_{s.} \mathrm{d}S + \int_{EFGH} D_{s.} \mathrm{d}S + \int_{CDGH} D_{s.} \mathrm{d}S$$

$$+ \int_{ABEF} D_{s.} \mathrm{d}S + \int_{AECG} D_{s.} \mathrm{d}S + \int_{BFDH} D_{s.} \mathrm{d}S \quad . \qquad (3.33)$$

Solving each face of the infinitesimal element face of the rectangular box gives,

Face ABCD

$$\int\limits_{ABCD} \boldsymbol{D}_{s.}\mathrm{d}\boldsymbol{S} \;=\; \boldsymbol{D}_{xo}(ABCD).\Delta\boldsymbol{S}(ABCD)$$

$$= \left(D_{xo} + \frac{\Delta x}{2}\frac{\partial D_{xo}}{\partial x}\right)\Delta y\Delta z\boldsymbol{e}_x.\boldsymbol{e}_x$$

$$\int\limits_{ABCD} \boldsymbol{D}_{s.}\mathrm{d}\boldsymbol{S} \;=\; \left(D_{xo} + \frac{\Delta x}{2}\frac{\partial D_{xo}}{\partial x}\right)\Delta y\Delta z \qquad , \qquad (3.34)$$

Face EFGH

$$\int\limits_{EFGH} \boldsymbol{D}_{s.}\mathrm{d}\boldsymbol{S} \;=\; \boldsymbol{D}_{xo}(EFGH).\Delta\boldsymbol{S}(EFGH)$$

$$= \left(D_{xo} - \frac{\Delta x}{2}\frac{\partial D_{xo}}{\partial x}\right)(-\Delta y\Delta z\boldsymbol{e}_x.\boldsymbol{e}_x)$$

$$\int\limits_{EFGH} \boldsymbol{D}_{s.}\mathrm{d}\boldsymbol{S} \;=\; \left(-D_{xo} + \frac{\Delta x}{2}\frac{\partial D_{xo}}{\partial x}\right)\Delta y\Delta z \qquad , \qquad (3.35)$$

Face $CDGH$

$$\int\limits_{CDGH} \boldsymbol{D}_{s.}\mathrm{d}\boldsymbol{S} \;=\; \boldsymbol{D}_{yo}(CDGH).\Delta\boldsymbol{S}(CDGH)$$

$$= \left(D_{yo} + \frac{\Delta y}{2}\frac{\partial D_{yo}}{\partial y}\right)\Delta x\Delta z\boldsymbol{e}_y.\boldsymbol{e}_y$$

$$\int\limits_{CDGH} \boldsymbol{D}_{s.}\mathrm{d}\boldsymbol{S} \;=\; \left(D_{yo} + \frac{\Delta y}{2}\frac{\partial D_{yo}}{\partial y}\right)\Delta x\Delta z \qquad , \qquad (3.36)$$

Face $ABEF$

$$\int\limits_{ABEF} \boldsymbol{D}_{s.}\mathrm{d}\boldsymbol{S} \;=\; \boldsymbol{D}_{yo}(ABEF).\Delta\boldsymbol{S}(ABEF) \;=\; \left(D_{yo} - \frac{\Delta y}{2}\frac{\partial D_{yo}}{\partial y}\right)(-\Delta x\Delta z\boldsymbol{e}_y.\boldsymbol{e}_y)$$

$$\int\limits_{ABEF} \boldsymbol{D}_{s.}\mathrm{d}\boldsymbol{S} \;=\; \left(-D_{yo} + \frac{\Delta y}{2}\frac{\partial D_{yo}}{\partial y}\right)\Delta x\Delta z \qquad , \qquad (3.37)$$

Face $AECG$

$$\int\limits_{AECG} \boldsymbol{D}_{s.}\mathrm{d}\boldsymbol{S} \;=\; \boldsymbol{D}_{zo}(AECG).\Delta\boldsymbol{S}(AECG) \;=\; \left(D_{zo} + \frac{\Delta z}{2}\frac{\partial D_{zo}}{\partial z}\right)\Delta x\Delta y\boldsymbol{e}_z.\boldsymbol{e}_z$$

$$\int_{AECG} \boldsymbol{D}_s.\mathrm{d}\boldsymbol{S} = \left(D_{zo} + \frac{\Delta z}{2}\frac{\partial D_{zo}}{\partial z}\right)\Delta x \Delta y \quad , \qquad (3.38)$$

Face $BFDH$

$$\int_{BFDH} \boldsymbol{D}_s.\mathrm{d}\boldsymbol{S} = \boldsymbol{D}_{zo}(BFDH).\Delta\boldsymbol{S}(BFDH) = \left(D_{zo} - \frac{\Delta z}{2}\frac{\partial D_{zo}}{\partial z}\right)(-\Delta x \Delta y \boldsymbol{e}_z.\boldsymbol{e}_z)$$

$$\int_{BFDH} \boldsymbol{D}_s.\mathrm{d}\boldsymbol{S} = \left(-D_{zo} + \frac{\Delta z}{2}\frac{\partial D_{zo}}{\partial z}\right)\Delta x \Delta y \quad , \qquad (3.39)$$

Substituting Eqs. (3.34) to (3.39) into Eq. (3.33) gives,

$$\oint \boldsymbol{D}_s.\mathrm{d}\boldsymbol{S} = \left(D_{xo} + \frac{\Delta x}{2}\frac{\partial D_{xo}}{\partial x}\right)\Delta y \Delta z + \left(-D_{xo} + \frac{\Delta x}{2}\frac{\partial D_{xo}}{\partial x}\right)\Delta y \Delta z$$

$$+ \left(D_{yo} + \frac{\Delta y}{2}\frac{\partial D_{yo}}{\partial y}\right)\Delta x \Delta z + \left(-D_{yo} + \frac{\Delta y}{2}\frac{\partial D_{yo}}{\partial y}\right)\Delta x \Delta z$$

$$+ \left(D_{zo} + \frac{\Delta z}{2}\frac{\partial D_{zo}}{\partial z}\right)\Delta x \Delta y + \left(-D_{zo} + \frac{\Delta z}{2}\frac{\partial D_{zo}}{\partial z}\right)\Delta x \Delta y . \qquad (3.40)$$

Simplifying Eq. (3.40) results in the expression,

$$\oint \boldsymbol{D}_s.\mathrm{d}\boldsymbol{S} = \left(\frac{\partial D_{xo}}{\partial x} + \frac{\partial D_{yo}}{\partial y} + \frac{\partial D_{zo}}{\partial z}\right)\Delta x \Delta y \Delta z$$

$$= \left(\frac{\partial D_{xo}}{\partial x} + \frac{\partial D_{yo}}{\partial y} + \frac{\partial D_{zo}}{\partial z}\right)\Delta V \quad . \qquad (3.41)$$

It can be seen that Gauss's theorem for electric displacement can be written as a divergence which is given as,

$$\oint \boldsymbol{D}_s.\mathrm{d}\boldsymbol{S} = (\nabla.\boldsymbol{D})\Delta V = Div \, \boldsymbol{D}.\Delta V \quad . \qquad (3.42)$$

This can be reformulated as,

$$\oint \boldsymbol{D}_s.\mathrm{d}\boldsymbol{S} = \int \nabla.\boldsymbol{D}\mathrm{d}V = \int \rho_v dV = Q \quad . \qquad (3.43)$$

Equation (3.43) for $\nabla.\boldsymbol{D}$ gives the electric charge per unit volume. This can be further manipulated to give,

$$\lim_{\Delta V \to 0} \frac{\oint \boldsymbol{D}_s.\mathrm{d}\boldsymbol{S}}{\Delta V} = Div \, \boldsymbol{D} = \rho_v \quad . \qquad (3.44)$$

The electric charge per unit volume has the relationship with electric displacement due to its continuous function on the closed surface in the space system. It can be seen that the limit ΔV approaching to zero gives the electric charge per unit volume from the divergence of electric displacement which is the well-known Maxwell's theorem, Hayt and Buck [71] and Stratton [72]. Maxwell's theorem for divergence of electric displacement has a relationship with Gauss's theorem for the closed surface integral. As shown in the derivations of infinitesimal element face of the rectangular box, it can obviously be expanded mathematically for other geometrical components such as for cylindrical and spherical surfaces.

For the cylindrical surface, the convergence of electrical displacement or electrical flux density can be formulated as,

$$Div.D = \frac{1}{r}\frac{\partial(rD_r)}{r} + \frac{1}{r}\frac{\partial D_\phi}{\partial \phi} + \frac{\partial D_z}{\partial z} \quad . \quad (3.45)$$

The convergence of electrical displacement for the spherical surface can also be formulated as,

$$Div.D = \frac{1}{r^2}\frac{\partial(rD_r)}{\partial r} + \frac{1}{rsin\theta}\frac{\partial(sin\theta D_\theta)}{\partial \theta} + \frac{1}{rsin\theta}\frac{\partial D_\phi}{\partial \phi} \quad . \quad (3.46)$$

As previously discussed, moving the charge in the path due to an applied force against an electric field requires work. The electrostatic energy of the piezoelectric element can be formulated in terms of the charge density and electric potential which has relationship with the Maxwell equation of electric displacement as given previously as,

$$W_e = \frac{1}{2}\int \rho_v \Phi dV = \frac{1}{2}\int (\nabla.\boldsymbol{D})\Phi dV \quad , \quad (3.47)$$

From Eq. (3.47), invoking operational multiplication of differential vector fields gives,

$$\nabla(\Phi\boldsymbol{D}) = \Phi(\nabla.\boldsymbol{D}) + D.(\nabla\Phi) \quad . \quad (3.48)$$

Inserting $\Phi(\nabla.\boldsymbol{D})$ from Eq. (3.48) into Eq. (3.47) obtains,

$$W_e = \frac{1}{2}\int (\nabla.\Phi\boldsymbol{D} - \boldsymbol{D}.\nabla\Phi)dV \quad . \quad (3.49)$$

where from Eq. (3.28) $E = -\nabla\Phi$, which can be inserted into Eq. (3.49) to give,

$$W_e = \frac{1}{2}\int (\nabla.\Phi D + D.E)dV \quad . \qquad (3.50)$$

The first integral is Gauss's theorem of divergence's volume integral, so it can be replaced using the closed surface integral from Gauss's theorem yielding,

$$W_e = \frac{1}{2}\oint \Phi D.\bar{n}\,dS + \frac{1}{2}\int D.E\,dV \quad . \qquad (3.51)$$

The first integral contains the electric voltage function, electric displacement and surface area which can be interpreted as the proportional function,

$$\Phi \sim \frac{1}{r} \quad , \qquad D \sim \frac{1}{r^2} \quad , \qquad dS \sim r^2 \quad . \qquad (3.52)$$

Corresponding to Eq. (3.52), applying the limit form at the first integral of Eq. (3.51) in terms of r approaching to infinity gives,

$$\lim_{r\to\infty} \Phi D.dS \quad \text{or} \quad \lim_{r\to\infty}\frac{1}{r}\frac{1}{r^2}r^2 \to 0 \quad . \qquad (3.53)$$

The resulting electrostatic energy of piezoelectricity then becomes,

$$W_e = \frac{1}{2}\int D.E\,dV \quad . \qquad (3.54)$$

Electric displacement D can be considered to obtain the relationship with electric field E and polarization P. Parameter D has a natural intensive property of the free space of permittivity ϵ_o whose property is proportional with extensive property of E which is further discussed in the next section,

$$D = \epsilon_o E \quad . \qquad (3.55)$$

Electric charge can now be further formulated by including polarization. In this case, the total charge flowing through the piezoelectric element in terms of the differential vector field of E and P can be written as,

$$Q = Q_t - Q_b = \oint \epsilon_o \nabla.E\,dS - \left(-\oint \nabla.P\,dS\right) \quad . \qquad (3.56)$$

The negative sign from the bracket indicates the opposite direction with respect to the electric field,

$$Q = \oint \epsilon_o \nabla . E \, dS + \oint \nabla . P \, dS \quad .$$

(3.57)

Modifying Eq. (3.57) gives,

$$Q = \oint \nabla \left(\epsilon_o E + P \right) dS \quad .$$

(3.58)

or it can formulated as,

$$Q = \oint \nabla . D \, dS \quad .$$

(3.59)

This can be compared with Eq. (3.43) solely having the relationship with electric field, polarisation and free space permittivity. Hence, the electric charge per unit volume also has a continuous function with polarization as proven in Eq. (3.56). The new formulation of electric displacement, Nye [73], can be written as,

$$D = \epsilon_o E + P \quad ,$$

(3.60)

or P can be formulated as,

$$P = x_e \epsilon_o E \quad ,$$

(3.61)

where x_e is the electric susceptibility of the piezoelectric material.

Substituting Eq. (3.61) into Eq.(3.71) gives,

$$D = \epsilon_o E + x_e \epsilon_o E \quad ,$$

(3.62)

and equation (3.62) can be written as,

$$D = (1 + x_e) \epsilon_o E \quad .$$

(3.63)

where $\epsilon_r = 1 + x_e$ is the relative permittivity. In this case, we can multiply the relative permittivity with the free space of permittivity to give,

$$\epsilon = \epsilon_r \epsilon_o \quad .$$

Finally, the electric displacement can be reformulated in terms of electric field, Stratton [72], Nye [73], Damjanovic [74] and Tiersten [75] as,

$$D = \epsilon_r \epsilon_o E = \epsilon E \quad . \tag{3.64}$$

It is noted that D in Eq. (3.64) can be specified as the first rank tensor and the electric field can also be specified as the first rank tensor. The relative permittivity can be specified as the second rank tensor. The electric displacement vector can be formulated in the tensor form as,

$$D_i = \epsilon_{ik} E_k \quad . \tag{3.65}$$

As can be seen, the quasi-electrical energy has been formulated using Maxwell's theorem in terms of the electric displacement with the application of Gauss's theorem.

3.3. Piezoelectric Effect

The unique electromechanical behaviour of piezoelectric material can be divided into two piezoelectric effects, i.e. direct and converse piezoelectric effects. When the applied stress is exerted on the material, the electric charge can be produced on the surface of the material due to the electric moment which is proportional to the applied stress to create polarization, Nye [73], Ikeda [76] and Cady [77]. The applied stress alters the polarisation to generate the electric voltage on the electrodes located between two faces of material with negative and positive charges. This situation is called the direct piezoelectric effect which is formulated as,

$$P = d\sigma \quad . \tag{3.66}$$

where P represents the polarization charge per unit area, d the piezoelectric modulus or piezoelectric constant and σ the applied stress. It should be noted that the polarisation P from the direct piezoelectric effect can be modified in terms of the electrical displacement D with the constant electric field, equation (3.60) to give,

$$P = D - \epsilon_o E \quad . \tag{3.67}$$

With the electric field kept constant, equation (3.66) can be modified in terms of Eq. (3.67) as,

$$D = d\sigma \quad . \tag{3.68}$$

This indicates that equations (3.67) and (3.68) have similar form for the direct effect. It is noted that P in Eq. (3.67) can be specified as a first rank tensor and stress can be specified as a second rank tensor. The piezoelectric modulus can then be specified as a third rank tensor. The direct piezoelectric effect in tensor form can be formulated as,

$$P_i = d_{ijk}\sigma_{jk} \quad . \tag{3.69}$$

When the electric field is applied onto the material, the shape of the material will change or deform due to the change of strain. This situation is called the converse piezoelectric effect which is formulated in tensor form as,

$$\varepsilon_{jk} = d_{ijk}E_i \quad . \tag{3.70}$$

where ε_{jk} indicates the second rank tensor of strain and E_i indicates the first rank tensor of electric field. The piezoelectric effects imply that the ratio between polarization and the applied stress in direct effect will be equal with the ratio between the change of strain and electric field in the converse effect.

3.4. Pyroelectric Effect

Certain piezoelectric materials have sensitivity with the change of temperature thereby forming the dipole moment to exhibit spontaneous polarisation with the constant electric field. This behaviour can be called the pyroelectric effect. Certain piezoelectric materials such as zinc oxide (ZnO), polyvinylidene fluoride (PVDF), lithium tantalate (LiTaO$_3$), lead magnesium niobate-lead titanate (PMN-PT) and lead zirconate titanate (PZT) also exhibit the pyroelectric effect whereas all pyroelectric materials can behave as piezoelectric materials, Damjanovic [74], Neumann *et al* [78], Ploss *et al* [79], Porter [80]. The pyroelectric effect can be formulated in terms of the changes of temperature and polarization or can be formulated in differential form as,

$$dP_i = p_i dT \quad , \tag{3.71}$$

where p_i represents the first rank tensor, pyroelectric coefficient (vector) P_i indicates spontaneous polarization and T indicates temperature. Equation (3.60) can be modified with second order polarisation which includes spontaneous polarisation P_i or P_s, Nye [73]. The electric displacement can then be formulated as,

$$D = (\epsilon_o E + P) + P_s = \epsilon E + P_s. \tag{3.72}$$

With respect to temperature, the pyroelectric coefficient can be obtained in differential form as,

$$\frac{\mathrm{d}\boldsymbol{D}}{\mathrm{d}T} = \boldsymbol{E}\frac{\mathrm{d}\epsilon}{\mathrm{d}T} + \frac{\mathrm{d}\boldsymbol{P}_s}{\mathrm{d}T} \ . \tag{3.73}$$

It is noted that the electric displacement not only depends on the pyroelectric coefficient but also on the electric field, and the change of permittivity with temperature. In this case, the effect of electric field can increase the transition of temperature on the pyroelectric effect and reduce the permittivity, Damjanovic [74]. If the effect of electric field was to be kept constant, the electric displacement will be equal with spontaneous polarisation as formulated by,

$$\frac{\mathrm{d}D_i}{\mathrm{d}T} = \frac{\mathrm{d}P_s}{\mathrm{d}T} = p_i \quad . \tag{3.74}$$

In the next section, theorems of thermodynamics in relation to properties of quasi-electrical energy, elastic strain energy and entropy are given in order to formulate the thermopiezoelectric equation of states in terms of Legendre's transform and Maxwell's relations.

3.5. Thermo-electric-elasticity of Piezoelectric Systems

The theory of thermodynamics plays an important role to identify all aspects of internal and external parameters of energies including mechanical work and heat affecting certain systems such as isolated, open and closed systems. The state of the system can be identified in the macroscopic properties because these properties include fundamental variables such as pressure P, temperature T, volume V, mole numbers N and so on. At the microscopic level, these properties consist of millions of molecules and structures at the atomic level that affect overall system dynamic behaviours because they interact with each other to move continually and consequently form the kinetic and potential energies at the macroscopic level, Desloge [70] and Sears and Salinger [81]. This shows that the macroscopic behaviour depends explicitly on the microscopic properties at the level of thermodynamics categories. This level relates to the continuum hypothesis of the macroscopic structure. At the in-depth study of microscopic level behaviour, statistical quantum physics should be used to explore the physical interactions between molecules or particles the quantum levels. At this point, continuum

thermodynamics is an appropriate tool to analyse many properties of systems at the macroscopic level, both experimental and mathematical, because the continuum thermodynamics is sometimes called the tangible physical study where it can identify clearly the level of energies in the internal system including the external energy from its surrounding.

Furthermore, the continuum thermodynamics studies the behaviour of interactions of properties in the system based on the laws of thermodynamics as discussed over the long term from many scientists. It is noted that the piezoelectric system can be analysed according to the closed system where the state of the system can be identified in fundamental variables such as stress σ, temperature T, strain ε and electric field E. The continuum thermodynamics of piezoelectricity has already been discussed experimentally and theoretically by Cady [77] and developed in tensor form by Nye [73], Munn [82], and Munn and Newham [83]. However in this chapter, the previous theories are reviewed and also discussed in more detail to present a clearer understanding of the constitutive equations of thermo piezoelectricity with its properties.

The thermodynamic properties can generally be divided into two classifications, i.e. intensive properties and extensive properties. These properties depend on macroscopic element interactions between the internal and external system. The extensive properties can be independent variables of the element size in the entire system and its surrounding whereas the intensive properties can be dependent variables of the element size in the entire system and its surrounding. At this point, the physical properties can be explained in the following theorems,

Theorem I. If X and Y indicate arbitrary intensive variables, then XY, X/Y, $\partial X/\partial Y$ and $X+Y$ should be intensive variables.

Theorem II. If X and Y indicate arbitrary extensive variables, then $X+Y$ give extensive variable, and X/Y and $\partial X/\partial Y$ should be intensive variables.

Theorem III. If X and Y indicate arbitrary intensive and extensive variables respectively, then XY, Y/X and $\partial Y/\partial X$ should be extensive variables.

Theorem IV. If $X(Y,Z)$ indicates extensive variable where Y and Z are also extensive variables, then exact differential form $dX = \partial X/\partial Z(dZ) + \partial X/\partial Y(dY)$ should be

extensive variable. As stated from theorem II, $\partial X/\partial Z$ and $\partial X/\partial Y$ indicate intensive variables.

Theorem V. As given in theorem IV, $\partial X/\partial Z = A$ and $\partial X/\partial Y = B$ indicate intensive variables. However, if A and B become the extended functional form stated as $A(Y,Z)$ and $B(Y,Z)$ where Y and Z are extensive variables based on theorem III, the exact differential forms of two functions $dA = \partial A/\partial Z(dZ) + \partial A/\partial Y(dY)$ and $dB = \partial B/\partial Z(dZ) + \partial B/\partial Y(dY)$ should be extensive variables where the parameters $\partial A/\partial Z$ and $\partial B/\partial Z$ indicate intensive variables based on theorem II.

To find other dependent intensive properties, Legendre transformation can be applied to obtain the interrelationship of internal energy with its independent extensive variables and other thermopiezoelectric potential. At this point, the thermodynamics properties can be further analysed from energy forms in the system using Maxwell's theorem based on the laws of thermodynamics.

The first law of thermodynamics, as proposed by Carnot, discusses the equilibrium process of the system under heat and work to form the transformation from initial to final states. In this case, whatever the change of heat and work under reversible or irreversible conditions, they should show the same summation results when the initial state moves to the final state. From the perspective of the second law of thermodynamics, it is impossible to construct the engine which will work for the complete cycle where the heat from a reservoir converts to mechanical work. This condition will allow us to discuss Clausius' theory for the reversible and irreversible processes in the entropy due to the heat change in the system.

In this case, the entropy is always positive real when the closed system is under irreversible process and the entropy will be zero for the reversible process. It should be noted that the change of entropy just depends on the transformation of heat from initial to final states. This means that the change of entropy for the reversible process will be equal with the change of entropy calculated using the irreversible process, as discussed by Kuiken [84].

The total entropy change can be stated as the exchange of heat and matter with external system $d_e S$ and the irreversible process in the internal system due to the

internal thermodynamic forces or dissipation energy $d_i S$, Verhas [85], Kondepudi and Prigogine [86] and Biot [87] to give,

$$dS = d_e S + d_i S \qquad .\tag{3.75}$$

The equation (3.75) should meet the second law of thermodynamics where the Clausius inequality entropy can be formulated in terms of the reversible and irreversible processes as,

$$dS \geq \frac{dQ}{T} \qquad .\tag{3.76}$$

Equation (3.76) reflects the arbitrary cycles of the heat process. The reversible and irreversible process of entropy for the closed system can be further stated as,

$$\oint \frac{dQ}{T} = 0 \quad , \quad d_e S = \frac{dQ}{T} \quad \text{for the reversible process}$$

and
$$\tag{3.77}$$

$$\oint \frac{dQ}{T} \geq 0 \quad , \quad d_i S \geq \frac{dQ}{T} \quad \text{for the irreversible process}$$

On this point, Gibbs considered $d_e S$ as a reversible process of heat and matter (open system) where he proposed the transformations of states in equilibrium thermodynamics in order to create the reversible process in the system whereas $d_e S$ (closed system) indicated the process of heat flow only excluding matter that could be positive and negative.

Total change of entropy from Eq. (3.76) gives the interrelationship of process states between reversible and irreversible. Since, the piezoelectric system considered as a closed form of solid system, is based on the change of entropy due to the reversible process for the entire transformation of state, Nye [73], there is no change of entropy due to the irreversibly internal piezoelectric system (parameter $d_i S$ is zero). The change of entropy for the closed system in terms of Eq. (3.75) can be formulated as,

$$dS = d_e S = \frac{dU + \sigma d\varepsilon}{T} \qquad .\tag{3.78}$$

As mentioned previously, the macroscopic field of piezoelectric thermodynamics presented here, is based solely on the basic theory of thermodynamics. In this case, the Maxwell's interrelation theorem from various differential partial extensive variables to give intensive variables will be further discussed where these can be

used to further define the Enthalpy property, Gibbs Free Energy, and Helmholtz Free Energy.

The first and second laws of thermodynamics were viewed as the equilibrium process of the changes of state in the system. The equilibrium process can be viewed as the macroscopic equilibrium properties of the system. The properties in the system in terms of thermodynamics potential such as internal energy U was a function of certain properties which were assumed as variable functions such as strain, entropy, and electric displacement. From this situation, other thermopiezoelectric potentials such as enthalpy H, Gibbs energy G, Helmholtz F can be achieved to obtain the interrelationship of independent state variables (intensive variables) and dependent state variables (extensive variables) in the equilibrium system. In this case, the macroscopic thermodynamics theory for continuum piezoelectricity can be further explored. The macroscopic piezoelectricity behaviour compounds the large numbers of microscopic matters like molecules of atoms bringing the positive and negative ions of the crystal lattice. The recent crystal structures in use were found to be polycrystalline such as barium titanate ($BaTiO_3$) and Lead zirconate titanate (PZT), Damjanovic [74]. Moreover, the macroscopic piezoelectricity can be formulated in terms of thermopiezoelectric potentials.

The internal energy of the system should be established first in terms of the laws of thermodynamics in order to explore other thermopiezoelectric potentials. The classical thermodynamic models gave the basic concepts to encounter the case of thermodynamics potentials of piezoelectricity which was affected from the thermal, mechanical and electrical interactions of the piezoelectric system. As mentioned previously, piezoelectricity can be viewed as a solid element structure based on the theories of elasticity, quasi-electrical energy and heat. In this theory, the interrelationship of different states of the thermopiezoelectric potentials in the system of infinitesimal piezoelectric element will be further developed using Legendre's transform in order to obtain intensive and extensive properties using Maxwell's relations in partial differential forms in terms of Figure (3.5), Nye [73].
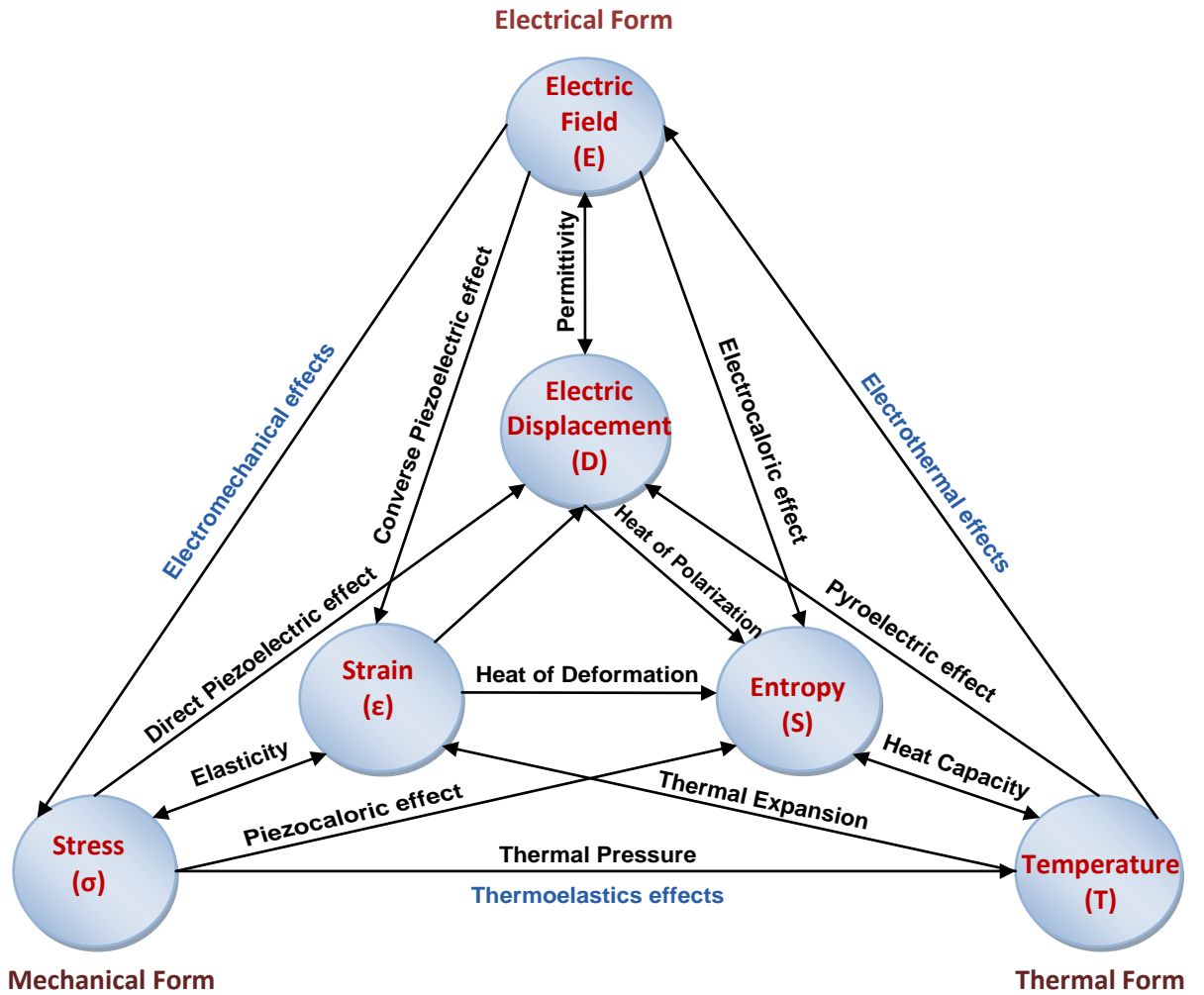
Figure 3.5 The Relationship between Mechanical, Thermal and Electrical Effects
of the Piezoelectric element, [73]

The first and second laws of thermodynamics of the piezoelectric element can be
stated in terms of the internal energy as one of thermodynamic potentials which is a
function of characteristic independent variables of strain ε_{ij}, electric displacement D_i
and entropy S as,

$$U = U(\varepsilon_{ij}, D_i, S) \qquad . \qquad (3.79)$$

Equation (3.79) needs to be proven to fulfill the first law of thermodynamics of the
macroscopic piezoelectric element as,

$$dU = \left(\frac{\partial U}{\partial \varepsilon_{ij}}\right)_{S,D} d\varepsilon_{ij} + \left(\frac{\partial U}{\partial D_i}\right)_{S,\varepsilon} dD_i + \left(\frac{\partial U}{\partial S}\right)_{\varepsilon,D} dS \qquad . \qquad (3.80)$$

Intensive properties from Eq. (3.79) can be stated as,

$$\left(\frac{\partial U}{\partial S}\right)_{\varepsilon,D} = T \quad , \quad \left(\frac{\partial U}{\partial \varepsilon}\right)_{S,D} = \sigma_{ij} \quad , \quad \left(\frac{\partial U}{\partial D_i}\right)_{S,\varepsilon} = E_i \quad . \qquad (3.81)$$

The macroscopic piezoelectric element can be viewed as a closed system which was in a state of thermal equilibrium with the surroundings. The system was presumed to undergo heat changes between initial to final states where this situation was called the reversible process of entropy as stated in Eqs. (3.77a) and (3.78). In this case, equation (3.80) can now be reformulated as,

$$dU = TdS + \sigma_{ij}d\varepsilon_{ij} + E_i dD_i \ .$$
(3.82)

Maxwell's relations can then be used to obtain,

$$\left(\frac{\partial T}{\partial \varepsilon_{ij}}\right)_{S,D} = \left(\frac{\partial \sigma_{ij}}{\partial S}\right)_{\varepsilon,D}, \left(\frac{\partial \sigma_{ij}}{\partial D_i}\right)_{\varepsilon,S} = \left(\frac{\partial E_i}{\partial \varepsilon_{ij}}\right)_{D,S}, \left(\frac{\partial E_i}{\partial S}\right)_{D,\varepsilon} = \left(\frac{\partial T}{\partial D_i}\right)_{S,\varepsilon}.$$
(3.83)

Equations (3.79) to (3.83) provided the basic formulations from the first and second laws of thermodynamics of piezoelectricity which can be used to develop the intensive and extensive properties from other thermodynamic potentials such as Gibbs Free Energy of elasticity, Electro-Elasticity Gibbs Free Energy, Helmholtz Free Energy, Enthalpy of Electro-Elasticity, and Electrical Helmholtz Free Energy. These energies can be explored using Legendre's Transformation and Maxwell's relations as further discussed in the next section. At this stage, the three base components of the exact differential energy forms for the piezoelectric system need to be established first before these energy forms can be developed into thermodynamic potentials. The exact differential elastic strain energy form can be formulated as,

$$d(\sigma_{ij}\varepsilon_{ij}) = \left(\frac{\partial(\sigma_{ij}\varepsilon_{ij})}{\partial \sigma_{ij}}\right)_\varepsilon d\sigma_{ij} + \left(\frac{\partial(\sigma_{ij}\varepsilon_{ij})}{\partial \varepsilon_{ij}}\right)_\sigma d\varepsilon_{ij} \ .$$
(3.84)

Reformulating Eq. (3.84) gives,

$$d(\sigma_{ij}\varepsilon_{ij}) = \varepsilon_{ij}d\sigma_{ij} + \sigma_{ij}d\varepsilon_{ij} \ .$$
(3.85)

The exact differential quasi-elastic energy can be formulated as,

$$d(E_i D_i) = \left(\frac{\partial(E_i D_i)}{\partial E_i}\right)_D dE_i + \left(\frac{\partial(E_i D_i)}{\partial D_i}\right)_E dD_i \ .$$
(3.86)

Reformulating Eq. (3.86) gives,

$$d(E_i D_i) = D_i dE_i + E_i dD_i \ .$$
(3.87)

The exact differential entropy form can also be formulated as,

$$d(TS) = \left(\frac{\partial(TS)}{\partial T}\right)_S dT + \left(\frac{\partial(TS)}{\partial S}\right)_T dS \quad . \tag{3.88}$$

or, $$d(TS) = SdT + TdS \quad . \tag{3.89}$$

3.6. Elastic-Electrical Gibbs Free Energy (Type $-\sigma, E, T$)

The concept of Gibbs free energy can be further explored to investigate the intensive and extensive properties in order to give the thermodynamic, Gibbs equation of state of type- σ, E, T which can be derived using Legendre transform and Maxwell's relations. The independent variables of elastic-electrical Gibbs free energy can be obtained using Legendre's transform where equation (3.81) can be used to replace independent variables from Eq. (3.80) of entropy S with $\left(\frac{\partial U}{\partial S}\right)_{\varepsilon,D} = T$, strain ε_{ij} with $\left(\frac{\partial U}{\partial \varepsilon_{ij}}\right)_{S,D_i} = \sigma_{ij}$ and electric displacement D_i with $\left(\frac{\partial U}{\partial D_i}\right)_{S,\varepsilon} = E_i$. At this point, elastic-electrical Gibbs free energy can be stated as the characteristic thermodynamics potential with a function of differential terms of T, σ_{ij} and E_i in the macroscopic state using Legendre's transform as,

$$G = \left(U - \sigma_{ij}\varepsilon_{ij} - E_i D_i - TS\right) \quad . \tag{3.90}$$

Corresponding with Eqs. (3.85), (3.87) and (3.89), equation (3.90) can be stated as,

$$dG = d\left(U - \sigma_{ij}\varepsilon_{ij} - E_i D_i - TS\right) = TdS + \sigma_{ij}d\varepsilon_{ij} + E_i dD_i - \varepsilon_{ij}d\sigma_{ij}$$

$$-\sigma_{ij}d\varepsilon_{ij} - D_i dE_i - E_i dD_i - SdT - TdS \quad . \tag{3.91}$$

Simplifying Eq. (3.91) gives,

$$dG = -SdT - \varepsilon_{ij}d\sigma_{ij} - D_i dE_i \quad . \tag{3.92}$$

Electro-Elasticity Gibbs free energy can be stated as the exact partial differential form as,

$$dG = \left(\frac{\partial G}{\partial T}\right)_{\sigma,E} dT + \left(\frac{\partial G}{\partial \sigma_{ij}}\right)_{T,E} d\sigma_{ij} + \left(\frac{\partial G}{\partial E_i}\right)_{T,\sigma} dE_i \quad . \tag{3.93}$$

The intensive properties from Eq. (3.93) can be obtained as,

$$\left(\frac{\partial G}{\partial T}\right)_{\sigma,E} = -S \quad , \qquad \left(\frac{\partial G}{\partial \sigma_{ij}}\right)_{T,E} = -\varepsilon_{ij} \quad , \qquad \left(\frac{\partial G}{\partial E_i}\right)_{T,\sigma} = -D_i \quad . \qquad (3.94)$$

Using Maxwell's relations to obtain other interrelation of differential partial terms, gives,

$$\left(\frac{\partial S}{\partial E_i}\right)_{T,\sigma} = \left(\frac{\partial D_i}{\partial T}\right)_{\sigma,E} , \left(\frac{\partial S}{\partial \sigma_{ij}}\right)_{T,E} = \left(\frac{\partial \varepsilon_{ij}}{\partial T}\right)_{\sigma,E} , \left(\frac{\partial \varepsilon_{ij}}{\partial E_i}\right)_{T,\sigma} = \left(\frac{\partial D_i}{\partial \sigma_{ij}}\right)_{T,E} . (3.95)$$

Corresponding with Eq. (3.93), equation (3.95) is reflected as the conceptual quantity where the characteristic measurable properties from Eq. (3.95) are mostly unknown. This equation is in exact differential form as indicated in the Maxwell's relations. In this case, the intensive properties D_i, ε_{ij}, and S can be further considered as extensive properties in order to formulate the Gibbs thermodynamics equation of state to obtain the measurable quantities, where these properties are function of differential terms of extensive properties of T, σ_{kl} and E_k as,

$$dD_i = \left(\frac{\partial D_i}{\partial \sigma_{kl}}\right)_{E,T} d\sigma_{kl} + \left(\frac{\partial D_i}{\partial E_k}\right)_{\sigma,T} dE_k + \left(\frac{\partial D_i}{\partial T}\right)_{\sigma,E} dT \quad , \qquad (3.96)$$

$$d\varepsilon_{ij} = \left(\frac{\partial \varepsilon_{ij}}{\partial \sigma_{kl}}\right)_{E,T} d\sigma_{kl} + \left(\frac{\partial \varepsilon_{ij}}{\partial E_k}\right)_{\sigma,T} dE_k + \left(\frac{\partial \varepsilon_{ij}}{\partial T}\right)_{\sigma,E} dT \quad , \qquad (3.97)$$

and

$$dS = \left(\frac{\partial S}{\partial \sigma_{kl}}\right)_{E,T} d\sigma_{kl} + \left(\frac{\partial S}{\partial E_k}\right)_{\sigma,T} dE_k + \left(\frac{\partial S}{\partial T}\right)_{\sigma,E} dT \quad . \qquad (3.98)$$

Corresponding with Eqs. (3.96), (3.97) and (3.98), Maxwell's relations and the previous sections, the following intensive properties can be expressed as,

$$\left(\frac{\partial D_i}{\partial E_k}\right)_{\sigma,T} = \epsilon_{ik}^{\sigma,T} \quad , \quad \left(\frac{\partial D_i}{\partial \sigma_{kl}}\right)_{E,T} = d_{ikl}^{T} \quad , \qquad \left(\frac{\partial D_i}{\partial T}\right)_{\sigma,E} = P_i^{\sigma} \quad , \qquad (3.99)$$

$$\left(\frac{\partial \varepsilon_{ij}}{\partial E_k}\right)_{\sigma,T} = d_{ijk}^{T} \quad , \quad \left(\frac{\partial \varepsilon_{ij}}{\partial \sigma_{kl}}\right)_{E,T} = s_{ijkl}^{E,T} \quad , \quad \left(\frac{\partial \varepsilon_{ij}}{\partial T}\right)_{\sigma,E} = \alpha_{ij}^{E} \quad , \qquad (3.100)$$

$$\left(\frac{\partial S}{\partial E_k}\right)_{\sigma,T} = P_k^{\sigma} \quad , \left(\frac{\partial S}{\partial \sigma_{kl}}\right)_{E,T} = \alpha_{kl}^{E} \quad , \qquad (3.101)$$

$$TdS = dH \quad \rightarrow \quad T\left(\frac{\partial S}{\partial T}\right)_{\sigma,E} = \frac{dH}{dT} = C^{\sigma,E} \rightarrow \left(\frac{\partial S}{\partial T}\right)_{\sigma,E} = \frac{C^{\sigma,E}}{T} \quad . \qquad (3.102)$$

It should be noted that the relation given in Figure (3.5) can be used to explain Eqs. (3.99) to (3.102). $\left(\frac{\partial \varepsilon_{ij}}{\partial T}\right)_{\sigma,E} = \left(\frac{\partial S}{\partial \sigma_{kl}}\right)_{E,T}$ indicates the relationships between $T \rightarrow \varepsilon_{ij}$ and $\sigma_{kl} \rightarrow S$ to give the same value where the coefficient of thermal expansion is the same as the piezocaloric effect. Moreover, $\left(\frac{\partial D_i}{\partial T}\right)_{\sigma,E} = \left(\frac{\partial S}{\partial E_k}\right)_{\sigma,T}$ indicates the relationships between $T \rightarrow D_i$ and $E_i \rightarrow S$ to give similarity between the coefficient of the pyroelectric and the electrocaloric effect and $\left(\frac{\partial \varepsilon_{ij}}{\partial E_k}\right)_{\sigma,T} = \left(\frac{\partial D_i}{\partial \sigma_{kl}}\right)_{E,T}$ indicates the equal value between the converse piezoelectric effect and the direct piezoelectric effect relating the stress-voltage function as shown in the relationship $E_k \rightarrow \varepsilon_{ij}$ and $\sigma_{kl} \rightarrow D_i$ from Figure (3.5). Equations (3.99) to (3.102) were sometimes called the thermopiezoelectric coefficients in terms of elastic-electrical Gibbs free energy. Each coefficient was reflected as Maxwell's relations of the measurable partial differential form. It should be noted that the coefficients are in tensor form where the coefficients $\epsilon_{ik}^{\sigma,T}, d_{ikl}^T, P_i^\sigma, s_{ijkl}^{E,T}, \alpha_{kl}^E$ and $C^{\sigma,E}$ indicated permittivity, piezoelectric constant, pyroelectric constant, elastic compliance, thermal expansion and specific heat, respectively. Superscripts $\sigma, T,$ and E indicated the quantities to be kept constant, referring to the stress, temperature and electric field. As can be seen, the coefficient of thermal expansion at constant electric field α_{ij}^E and heat capacity at constant stress $C^{\sigma,E}$ were analogous with coefficient of volume expansion α_{ij} and heat capacity at constant pressure C_p, respectively from classical thermodynamics.

Corresponding with Eqs. (3.99) to (3.102), equations (3.96) to (3.98) can be reformulated to obtain the direct and converse effects of the piezoelectric expression including the entropy as,

$$D_i = d_{ikl}^T \sigma_{kl} + \epsilon_{ik}^{\sigma,T} E_k + P_i^\sigma \Delta T$$

$$\varepsilon_{ij} = s_{ijkl}^{E,T} \sigma_{kl} + d_{ijk}^T E_k + \alpha_{ij}^E \Delta T \qquad . \quad (3.103)$$

$$\Delta S = \alpha_{kl}^E \sigma_{kl} + P_k^\sigma E_k + \frac{C^{\sigma,E}}{T} \Delta T$$
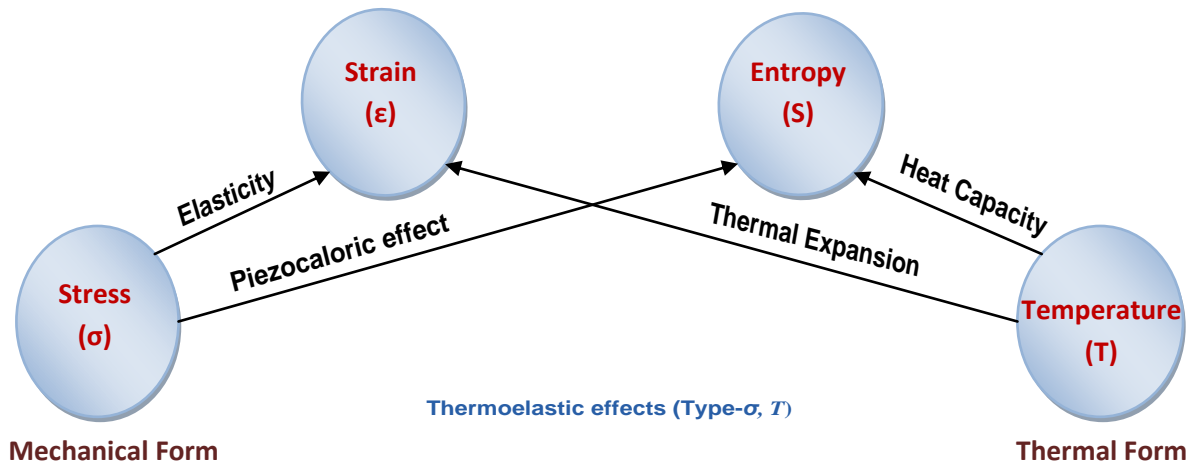
Figure 3.6 The Relations Between Mechanical and Thermal Effects of
the Thermoelastic Material (Type $-\sigma, T$)

As can be seen, the complete thermopiezoelectric equation of state corresponding with elastic-electrical Gibbs free energy has been formulated. This equation considered the piezoelectric materials with the effect of temperature in terms of Figure (3.5). The non-piezoelectric system and pyroelectric effect under temperature effect can be separated from the previous equation and this is known as the thermoelastic behaviour. From Figure (3.6), the thermoelastic behaviour can be written using the relations of strain and entropy as the extensive properties (Type $-\sigma$, T), formulated in terms of Eq. (3.103) as,

$$\varepsilon_{ij} = s^T_{ijkl}\sigma_{kl} + \alpha_{ij}\,\Delta T \quad, \qquad (3.104)$$

and

$$\Delta S = \alpha_{kl}\sigma_{kl} + \frac{C^\sigma}{T}\Delta T$$

It is noted that there are only four coefficients relating the thermoelastic properties (Type $- \sigma$, T). As we can see from Figure (3.6), the relation $\sigma_{kl} \to \varepsilon_{ij}$ produces the elastic compliance (s^T_{ijkl}) and the relation $T \to \varepsilon_{ij}$ and $\sigma_{kl} \to S$ produces the thermal expansion at constant stress (α_{ij}) and the piezocaloric coefficient (α_{kl}) respectively, and both of these relations have the same value. The final relation $T \to S$ gives the specific heat at constant stress (C^σ). Other relationships, specifically the thermoelastic type (Type $- \varepsilon$, T) can be proved using the electrical Helmholtz free energy for thermoelasticity as given in the next section.

Furthermore, another relation between adiabatic and isothermal elastic compliances with constant electric field can also be obtained where equations (3.97) and (3.98) can be used in terms of the thermoelastic condition given in Eq. (3.104). In this case, the adiabatic process $dS = 0$ can be applied to Eq. (3.98) and then the differential temperature dT can be eliminated in Eq. (3.104a) using Eq. (3.104b) to give,

$$d\varepsilon_{ij} = \left(\frac{\partial \varepsilon_{ij}}{\partial \sigma_{kl}}\right)_T d\sigma_{kl} - \frac{\left(\frac{\partial \varepsilon_{ij}}{\partial T}\right)_\sigma \left(\frac{\partial S}{\partial \sigma_{kl}}\right)_T d\sigma_{kl}}{\left(\frac{\partial S}{\partial T}\right)_\sigma} \qquad . \qquad (3.105)$$

Modifying Eq. (3.105) in terms of the elastic compliances gives,

$$\left(\frac{\partial \varepsilon_{ij}}{\partial \sigma_{kl}}\right)_S = \left(\frac{\partial \varepsilon_{ij}}{\partial \sigma_{kl}}\right)_T - \frac{\left(\frac{\partial \varepsilon_{ij}}{\partial T}\right)_\sigma \left(\frac{\partial S}{\partial \sigma_{kl}}\right)_T}{\left(\frac{\partial S}{\partial T}\right)_\sigma} \qquad . \qquad (3.106)$$

Simplifying, equation (3.106) can be written as,

$$\left(\frac{\partial \varepsilon_{ij}}{\partial \sigma_{kl}}\right)_S - \left(\frac{\partial \varepsilon_{ij}}{\partial \sigma_{kl}}\right)_T = -\left(\frac{\partial \varepsilon_{ij}}{\partial T}\right)_\sigma \left(\frac{\partial S}{\partial \sigma_{kl}}\right)_T \left(\frac{\partial T}{\partial S}\right)_\sigma . \qquad (3.107)$$

Corresponding to the thermodynamic coefficients given from Eqs. (3.99b-c), (3.100b) and (3.102), equation (3.107) can be formulated as,

$$s_{ijkl}^{S} - s_{ijkl}^{T} = -\alpha_{ij}\alpha_{kl}\left(T/C_\sigma\right) \qquad . \qquad (3.108)$$

This indicates that the relations between adiabatic and isothermal elastic compliances can be obtained from the left side in Eq. (3.108) where the thermal expansion and heat capacity have positive values of coefficients. This indicates that the left side of Eq. (3.108) results in a negative value indicating that the elastic compliance due to the adiabatic effect has a smaller value than the elastic compliance for the isothermal process, Nye [73]. Assuming the thermoelastic property for constant strain field, the relations between heat capacity at constant strain and stress can be obtained from Eqs. (3.97) and (3.98) in terms of Eq. (3.104) to give,

$$dS = \left(\frac{\partial S}{\partial T}\right)_{\sigma,E} dT - \frac{\left(\frac{\partial S}{\partial \sigma_{kl}}\right)_{E,T} \left(\frac{\partial \varepsilon_{ij}}{\partial T}\right)_{\sigma,E}}{\left(\frac{\partial \varepsilon_{ij}}{\partial \sigma_{kl}}\right)_{E,T}} dT \qquad . \qquad (3.109)$$

Modifying Eq. (3.109) can give,

$$\left(\frac{\partial S}{\partial T}\right)_{\varepsilon} - \left(\frac{\partial S}{\partial T}\right)_{\sigma} = -\frac{\left(\frac{\partial S}{\partial \sigma_{kl}}\right)_{T}\left(\frac{\partial \varepsilon_{ij}}{\partial T}\right)_{\sigma}}{\left(\frac{\partial \varepsilon_{ij}}{\partial \sigma_{kl}}\right)_{T}} \ . \tag{3.110}$$

Corresponding to the thermodynamic coefficients given from Eqs. (3.100b-c), (3.101b) and (3.102), equation (3.110) can then be formulated as,

$$C^{\varepsilon} - C^{\sigma} = -\frac{\alpha_{ij}\alpha_{kl}T}{s^{T}_{ijkl}} \ . \tag{3.111}$$

This indicates that the relations between heat capacity at constant strain and stress can be obtained from the left side of Eq. (3.111) where the thermal expansion and elastic compliances always gave positive coefficient values. The right side of Eq. (3.111) always gives a negative value indicating that the heat capacity at constant strain has a smaller value than the heat capacity at constant stress and constant strain.

3.7. Elastic Gibbs Free Energy (Type $-\sigma, D, T$)

In this section, the elastic Gibbs free energy will be further discussed according to the independent properties of stress σ, electric displacement D and temperature T where this implies that the elastic Gibbs free energy was a function of the independent properties because these properties can be used to investigate the thermodynamic equation of state or measurable equation of state. The difference between elastic Gibbs free energy (type-σ, D,T) and electric Gibbs free energy (type-σ,E,T) is the fundamental property of electrical terms (D and E) but both of these theorems show the interrelationship that can be expressed using matrix algebra. This indicates that Maxwell's relations of the thermodynamic equations of state gave exact differential forms. Independent variables of elastic Gibbs free energy can be obtained using Legendre's transform where equation (3.81) can be used to replace independent variables from Eq. (3.80) of entropy S with $\left(\frac{\partial U}{\partial S}\right)_{\varepsilon,D} = T$ and strain ε_{ij} with $\left(\frac{\partial U}{\partial \varepsilon_{ij}}\right)_{S,D} = \sigma_{ij}$. At this point, elastic Gibbs free energy can be stated in

terms of the characteristic thermodynamic potential with a function of differential terms T, σ_{ij} and D_i in the macroscopic state,

$$G = G(\sigma_{ij}, D_i, T) \qquad . \tag{3.112}$$

Equation (3.112) needs to be proved by applying Legendre's transform as,

$$dG = d(U - \sigma_{ij}\varepsilon_{ij} - TS) \qquad . \tag{3.113}$$

Expanding Eq. (3.113) in differential form gives,

$$dG = dU - \varepsilon_{ij}d\sigma_{ij} - \sigma_{ij}d\varepsilon_{ij} - SdT - TdS \quad . \tag{3.114}$$

Substituting Eq. (3.82) into Eq. (3.114) gives,

$$dG = TdS + \sigma_{ij}d\varepsilon_{ij} + E_i dD_i - \varepsilon_{ij}d\sigma_{ij} - \sigma_{ij}d\varepsilon_{ij} - SdT - TdS \quad . \tag{3.115}$$

Simplifying, equation (3.115) obtains,

$$dG = E_i dD_i - \varepsilon_{ij}d\sigma_{ij} - SdT \qquad . \tag{3.116}$$

Corresponding with Eq. (3.116), the exact partial differential for Gibbs free energy of elasticity can be stated as,

$$dG = \left(\frac{\partial G}{\partial D_i}\right)_{\sigma,T} dD_i + \left(\frac{\partial G}{\partial \sigma_{ij}}\right)_{D,T} d\sigma_{ij} + \left(\frac{\partial G}{\partial T}\right)_{D,\sigma} dT \quad . \tag{3.117}$$

The intensive properties for Gibbs free energy of elasticity can also be obtained as,

$$\left(\frac{\partial G}{\partial D}\right)_{\sigma,T} = E_i \ , \qquad \left(\frac{\partial G}{\partial \sigma_{ij}}\right)_{D,T} = -\varepsilon_{ij} \ , \qquad \left(\frac{\partial G}{\partial T}\right)_{D,\sigma} = -S \quad . \tag{3.118}$$

Maxwell's relations can be used to give,

$$-\left(\frac{\partial S}{\partial D_i}\right)_{\sigma,T} = \left(\frac{\partial E_i}{\partial T}\right)_{D,\sigma}, \quad -\left(\frac{\partial S}{\partial \sigma_{ij}}\right)_{D,T} = -\left(\frac{\partial \varepsilon_{ij}}{\partial T}\right)_{D,\sigma},$$
$$\left(\frac{\partial E_i}{\partial \sigma_{ij}}\right)_{D,T} = -\left(\frac{\partial \varepsilon_{ij}}{\partial D_i}\right)_{\sigma,T} . \tag{3.119}$$

Corresponding with Eq. (3.119), equation (3.117) reflected a conceptual quantity as indicated in the exact differential form from Maxwell's relations and the intensive properties E_i, ε_{ij} and S. These properties become extensive properties to further

develop the elastic Gibbs thermodynamics equations of state in order to obtain the measurable quantities. At this point, Gibbs thermodynamic equation of state can be formulated where the extensive properties of σ_{ij}, D_i, T are held as the independent properties as,

$$dE_i = \left(\frac{\partial E_i}{\partial \sigma_{kl}}\right)_{D,T} d\sigma_{kl} + \left(\frac{\partial E_i}{\partial D_j}\right)_{\sigma,T} dD_j + \left(\frac{\partial E_i}{\partial T}\right)_{\sigma,D} dT \quad , \quad (3.120)$$

$$d\varepsilon_{ij} = \left(\frac{\partial \varepsilon_{ij}}{\partial \sigma_{kl}}\right)_{D,T} d\sigma_{kl} + \left(\frac{\partial \varepsilon_{ij}}{\partial D_k}\right)_{\sigma,T} dD_k + \left(\frac{\partial \varepsilon_{ij}}{\partial T}\right)_{\sigma,D} dT \quad , \quad (3.121)$$

$$dS = \left(\frac{\partial S}{\partial \sigma_{kl}}\right)_{D,T} d\sigma_{kl} + \left(\frac{\partial S}{\partial D_j}\right)_{\sigma,T} dD_j + \left(\frac{\partial S}{\partial T}\right)_{\sigma,D} dT \quad . \quad (3.122)$$

The measurable quantities can be obtained from the intensive properties from Eqs. (3.120) to (3.122) to give,

$$\left(\frac{\partial E_i}{\partial D_j}\right)_{\sigma,T} = \frac{1}{\epsilon_{ij}^{\sigma,T}} \quad , \quad \left(\frac{\partial \varepsilon_{ij}}{\partial D_k}\right)_{\sigma,T} = \frac{1}{e_{ijk}^{T}} = g_{ijk}^{T} \quad , \quad (3.123)$$

$$\left(\frac{\partial E_i}{\partial T}\right)_{D,\sigma} = -\left(\frac{\partial E_i}{\partial D_j}\right)_{\sigma,T}\left(\frac{\partial D_j}{\partial T}\right)_{\sigma,D} = -\frac{P_j^{\sigma}}{\epsilon_{ij}^{\sigma,T}} = -f_i^{\sigma} \quad , \quad (3.124)$$

$$\left(\frac{\partial E_i}{\partial \sigma_{kl}}\right)_{D,T} = \left(\frac{\partial D_j}{\partial \sigma_{kl}}\right)_{E,T}\left(\frac{\partial E_i}{\partial D_j}\right)_{\sigma,T} = -\frac{d_{jkl}^{T}}{\epsilon_{ij}^{\sigma,T}} = -g_{ikl}^{T} \quad , \quad (3.125)$$

$$\left(\frac{\partial \varepsilon_{ij}}{\partial \sigma_{kl}}\right)_{D,T} = s_{ijkl}^{E,T} \quad , \quad \left(\frac{\partial \varepsilon_{ij}}{\partial T}\right)_{\sigma,D} = \alpha_{ij}^{D} \quad , \quad (3.126)$$

$$\left(\frac{\partial S}{\partial D_j}\right)_{\sigma,T} = \left(\frac{\partial E_i}{\partial D_j}\right)_{\sigma,T}\left(\frac{\partial S}{\partial E_i}\right)_{\sigma,T} = \frac{P_i^{\sigma}}{\epsilon_{ij}^{\sigma,T}} = f_j^{\sigma} \quad , \quad \left(\frac{\partial S}{\partial \sigma_{kl}}\right)_{D,T} = \alpha_{kl}^{D} \quad , \quad (3.127)$$

$$T\left(\frac{\partial S}{\partial T}\right)_{\sigma,D} = \frac{dH}{dT} = C^{\sigma,D} \rightarrow \left(\frac{\partial S}{\partial T}\right)_{\sigma,D} = \frac{C^{\sigma,D}}{T} \quad . \quad (3.128)$$

Equations (3.123) to (3.128) are sometimes called the thermopiezoelectric coefficients in terms of elastic Gibbs free energy (type-σ,D,T) or also the inverse of the thermopiezoelectric coefficients of elastic-electrical Gibbs free energy (type-σ,E,T). It should be noted that equations (3.124), (3.125) and (3.127a) were obtained

due to the combinations or products of two partial differential forms from Maxwell's relations. Moreover, from Figure (3.5), the relations of $\sigma_{kl} \to E_i$ and $D_k \to \varepsilon_{ij}$ indicate the direct and converse piezoelectric effects per unit permittivity (secondary terms of direct and converse piezoelectric effect), respectively, where this also shows similar physical meaning with $\left(\frac{\partial E_i}{\partial \sigma_{kl}}\right)_{E,T} = \left(\frac{\partial \varepsilon_{ij}}{\partial D_k}\right)_{\sigma,T}$ indicating the same numerical values between the secondary terms of direct and converse piezoelectric effects in terms of the stress-charge effect. The coefficient of thermal expansion $\left(\frac{\partial \varepsilon_{ij}}{\partial T}\right)_{\sigma,E}$ is the same as the piezocaloric effect $\left(\frac{\partial S}{\partial \sigma_{kl}}\right)_{E,T}$ where this indicates the relations $T \to \varepsilon_{ij}$ and $\sigma_{kl} \to S$. Moreover, the relation $T \to E_i$ with physical terms $\left(\frac{\partial E_i}{\partial T}\right)_{D,\sigma}$ indicates the coefficient of the pyroelectric effect at constant stress per unit permittivity (electrothermal) which is the same as the electrocaloric effect at constant stress per unit permittivity (heat of polarization) $\left(\frac{\partial S}{\partial D_j}\right)_{\sigma,T}$ with the relation $D_j \to S$. Each coefficient reflects Maxwell's relations of the measurable partial differential form. It should be noted that the coefficients in the tensor form $\epsilon_{ik}^{\sigma,T}, g_{ikl}^{T}, f_i^{\sigma}, s_{ijkl}^{E,T}, \alpha_{kl}^{E}$ and $C^{\sigma,D}$ indicate permittivity at constant stress, piezoelectric constant per unit permittivity in terms of stress-charge, pyroelectric per unit permittivity in terms of stress-charge, elastic compliance at constant electric field, strain-temperature thermal expansion and specific heat at constant stress. Corresponding with Eqs. (3.123) to (3.128), equations (3.120) to (3.122) can be reformulated to obtain the direct and converse effects of piezoelectric including the entropy as,

$$E_i = -g_{ikl}^{T} \sigma_{kl} + \frac{1}{\epsilon_{ij}^{\sigma,T}} D_j - f_i^{\sigma} \Delta T \ ,$$

$$\varepsilon_{ij} = s_{ijkl}^{E,T} \sigma_{kl} + g_{ijk}^{T} D_k + \alpha_{ij}^{D} \Delta T \ , \tag{3.129}$$

$$\Delta S = \alpha_{kl}^{D} \sigma_{kl} + f_j^{\sigma} D_j + \frac{C^{\sigma,D}}{T} \Delta T \ .$$

3.8. Electrical Helmholtz Free Energy (Type-ε,E,T)

In this section, the thermodynamics potential from the electrical Helmholtz free energy can be further discussed where each independent property is used in

order to develop the intensive variables using the thermodynamic equation of state based on Maxwell's relation. In terms of the Legendre's transform, the independent properties of electrical Helmholtz free energy can be stated using Eq. (3.81) by replacing independent variables from internal energy in Eq. (3.80) of the electric displacement D_i with $\left(\frac{\partial U}{\partial D_i}\right)_{S,\varepsilon} = E_i$ and entropy S with $\left(\frac{\partial U}{\partial S}\right)_{\varepsilon,D} = T$ which is formulated as,

$$dF = d(U - E_i D_i - TS) \qquad . \tag{3.130}$$

Expanding Eq. (3.130) into exact differential form gives,

$$d(U - E_i D_i - TS) = dU - E_i dD_i - D_i dE_i - TdS - SdT . \tag{3.131}$$

Substituting Eq. (3.82) into Eq. (3.131) obtains,

$$dF = TdS + \sigma_{ij} d\varepsilon_{ij} + E_i dD_i - E_i dD_i - D_i dE_i - TdS - SdT . \tag{3.132}$$

Equation (3.132) can be simplified as,

$$dF = \sigma_{ij} d\varepsilon_{ij} - D_i dE_i - SdT . \tag{3.133}$$

At this stage, equation (3.133) reflects the electrical Helmholtz free energy which can be stated in a more compact exact differential form as,

$$dF = \left(\frac{\partial F}{\partial \varepsilon_{ij}}\right)_{E,T} d\varepsilon_{ij} + \left(\frac{\partial F}{\partial E_i}\right)_{\varepsilon,T} dE_i + \left(\frac{\partial F}{\partial T}\right)_{\varepsilon,E} dT \qquad . \tag{3.134}$$

The intensive properties from Eq. (3.134) can be extracted into the dependent variables as,

$$\left(\frac{\partial F}{\partial \varepsilon_{ij}}\right)_{E,T} = \sigma_{ij} \ , \quad \left(\frac{\partial F}{\partial E_i}\right)_{E,T} = -D_i \ , \quad \left(\frac{\partial F}{\partial T}\right)_{\varepsilon,E} = -S . \tag{3.135}$$

Maxwell's relations can be applied to Eq. (3.135) resulting in,

$$\left(\frac{\partial \sigma_{ij}}{\partial E_i}\right) = -\left(\frac{\partial D_i}{\partial \varepsilon_{ij}}\right) \ , \quad \left(\frac{\partial \sigma_{ij}}{\partial T}\right) = -\left(\frac{\partial S}{\partial \varepsilon_{ij}}\right) \ , \quad -\left(\frac{\partial D_i}{\partial T}\right) = -\left(\frac{\partial S}{\partial E_i}\right) . \tag{3.136}$$

The intensive variables from the electrical Helmholtz free energy provide conceptual properties as these variables imply unknown functional measurable properties. Since the thermodynamic equations of state need to be established in terms of the

differentiable functions of the independent variables and Maxwell's relations, the intensive variables from Eq. (3.135) become extensive variables. Therefore, the electrical Helmholtz equations of state can be formulated as,

$$d\sigma_{ij} = \left(\frac{\partial \sigma_{ij}}{\partial \varepsilon_{kl}}\right)_{E,T} d\varepsilon_{kl} + \left(\frac{\partial \sigma_{ij}}{\partial E_k}\right)_{\varepsilon,T} dE_k + \left(\frac{\partial \sigma_{ij}}{\partial T}\right)_{\varepsilon,E} dT \ , \qquad (3.137)$$

$$dD_i = \left(\frac{\partial D_i}{\partial \varepsilon_{kl}}\right)_{E,T} d\varepsilon_{kl} + \left(\frac{\partial D_i}{\partial E_k}\right)_{\varepsilon,T} dE_k + \left(\frac{\partial D_i}{\partial T}\right)_{\varepsilon,E} dT \ , \qquad (3.138)$$

$$dS = \left(\frac{\partial S}{\partial \varepsilon_{kl}}\right)_{E,T} d\varepsilon_{kl} + \left(\frac{\partial S}{\partial E_k}\right)_{\varepsilon,T} dE_k + \left(\frac{\partial S}{\partial T}\right)_{\varepsilon,E} dT \ . \qquad (3.139)$$

Equations (3.137) to (3.139) are known as the thermodynamic equation of state from the electrical Helmholtz free energy which represents as the measurable equation of state because the new intensive properties from Eqs. (3.137) to (3.139) give the coefficient of thermopiezoelectricity based on the exact differential form of Maxwell's relation relating to the electrical Helmholtz free energy. The coefficients of thermopiezoelectricity can be formulated as,

$$\left(\frac{\partial \sigma_{ij}}{\partial \varepsilon_{kl}}\right)_{E,T} = C_{ijkl}^{E,T} \quad , \quad \left(\frac{\partial \sigma_{ij}}{\partial E_k}\right)_{\varepsilon,T} = -e_{ijk}^T \ , \qquad (3.140)$$

$$\left(\frac{\partial \sigma_{ij}}{\partial T}\right)_{\varepsilon,E} = -\left(\frac{\partial \sigma_{ij}}{\partial \varepsilon_{kl}}\right)_{E,T}\left(\frac{\partial \varepsilon_{kl}}{\partial T}\right)_{\sigma,E} = -C_{ijkl}^{E,T}\ \alpha_{kl}^E = -\beta_{ij} \quad , \quad (3.141)$$

$$\left(\frac{\partial D_i}{\partial \varepsilon_{kl}}\right)_{E,T} = e_{ikl}^T \quad , \qquad \left(\frac{\partial D_i}{\partial E_k}\right)_{\varepsilon,T} = \epsilon_{ik}^{\varepsilon,T} \quad , \qquad (3.142)$$

$$\left(\frac{\partial D_i}{\partial T}\right)_{\varepsilon,E} = P_i^\varepsilon \ , \qquad \left(\frac{\partial S}{\partial E_k}\right)_{\varepsilon,T} = P_k^\varepsilon \ , \qquad (3.143)$$

$$\left(\frac{\partial S}{\partial \varepsilon_{kl}}\right)_{E,T} = \left(\frac{\partial \sigma_{ij}}{\partial \varepsilon_{kl}}\right)_{E,T}\left(\frac{\partial S}{\partial \sigma_{ij}}\right)_{E,T} = C_{ijkl}^{E,T}\alpha_{ij}^E = \beta_{kl}, \qquad (3.144)$$

$$\left(\frac{\partial S}{\partial T}\right)_{\varepsilon,E} = \frac{T\partial S}{T\partial T} = \frac{C^{\varepsilon,E}}{T} \quad . \qquad (3.145)$$

Equations (3.140) to (3.145) represent the thermodynamic coefficients of the electrical Helmholtz free energy. It should be noted that equations (3.141) and

(3.144) were obtained due to the product of partial differential forms from Maxwell's relations. Moreover, $\left(\frac{\partial \sigma_{ij}}{\partial E_k}\right)_{\varepsilon,T} = \left(\frac{\partial D_i}{\partial \varepsilon_{kl}}\right)_{E,T}$ indicates that the second term of the converse piezoelectric effect is numerically equal to the second term of the direct piezoelectric effect in terms of the strain-voltage effect where this is indicated in Figure (3.5) for the relations $E_k \rightarrow \sigma_{ij}$ and $\varepsilon_{kl} \rightarrow D_i$, respectively. The relation T $\rightarrow \sigma_{ij}$ indicates the product of coefficient of thermal expansion with elastic stiffness constant to give thermal pressure $\left(\frac{\partial \sigma_{ij}}{\partial T}\right)_{\varepsilon,E}$ which is the same as the product of piezocaloric effect and the elastic stiffness constant with relation $\varepsilon_{kl} \rightarrow S$ to give the heat of deformation $\left(\frac{\partial S}{\partial \varepsilon_{kl}}\right)_{E,T}$. Moreover, the relations $T \rightarrow D_i$ and $E_k \rightarrow S$ indicate the pyroelectric effect at constant strain and the electrocaloric effect at constant strain which shows the physical meaning that $\left(\frac{\partial D_i}{\partial T}\right)_{\varepsilon,E}$ has the same value as $\left(\frac{\partial S}{\partial E_k}\right)_{\varepsilon,T}$. Each thermodynamic coefficient was reflected as Maxwell's relations of the measurable partial differential form. It should be noted that the coefficients are given in tensor form where $\epsilon_{ik}^{\sigma,T}, e_{ikl}^{T}, P_i^{\varepsilon}, C_{ijkl}^{E,T}, \beta_{ij}, \beta_{kl}$ and $C^{\varepsilon,E}$ indicate permittivity, piezoelectric constant in terms of strain-voltage, pyroelectric constant in terms of strain-voltage, elastic stiffness at constant electric field, stress-temperature thermal expansion (thermal pressure), heat of deformation and specific heat at constant strain.

The equations (3.137) to (3.139) can be reformulated in terms of Eqs. (3.140) to (3.145) as,

$$\sigma_{ij} = C_{ijkl}^{E,T}\varepsilon_{kl} - e_{ijk}^{T}E_k - \beta_{ij}\Delta T$$

$$D_i = e_{ikl}^{T}\varepsilon_{kl} + \epsilon_{ik}^{\varepsilon,T}E_k + P_i^{\varepsilon}\Delta T \qquad . \qquad (3.146)$$

$$\Delta S = \beta_{kl}\varepsilon_{kl} + P_k^{\varepsilon}E_k + \frac{C^{\varepsilon,E}}{T}\Delta T$$

The complete thermopiezoelectric equations of state corresponding with electrical Helmholtz free energy has been formulated. This equation considered the piezoelectric materials with the effect of entropy in terms of Figure (3.5). The previous equation can be reduced in terms of thermoelasticity with the non-piezoelectric system and pyroelectric effect. At this point, thermoelastic (Type $-\varepsilon,T$)

behaviour can be established. From Figure (3.7), the thermoelastic behaviour can be considered using the relations of strain and entropy as the dependent properties (Type $-\varepsilon, T$) and can be formulated in terms of Eq. (3.146) as,

$$\sigma_{ij} = C_{ijkl}^{T}\varepsilon_{kl} - \beta_{ij}\Delta T \quad , \qquad (3.147)$$

$$\Delta S = \beta_{kl}\varepsilon_{ij} + \frac{C^{\varepsilon}}{T}\Delta T \quad .$$

It is noted that there are only four coefficients relevant to thermoelasticity (Type $-\varepsilon, T$). As can be seen from Figure (3.7), the relation $\varepsilon_{kl} \rightarrow \sigma_{ij}$ produced the stiffness elastic coefficient (C_{ijkl}^{T}) and the relation $T \rightarrow \sigma_{ij}$ and $\varepsilon_{kl} \rightarrow S$ produced the thermal pressure (β_{ij}) and heat of deformation (β_{kl}), respectively and both of these relations show the same value. The final relation $T \rightarrow S$ gives the specific heat at constant strain $(C^{\varepsilon,E})$. It should be noted that the thermoelastic equation (Type $-\varepsilon, T$) can also be stated as the inverse thermoelastic equation (Type $-\sigma, T$).
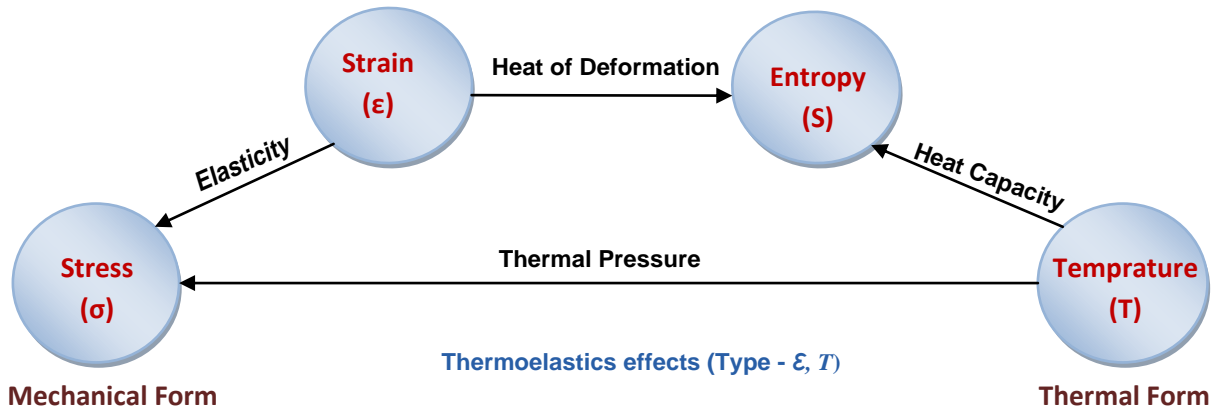
Figure 3.7 The Relations Between Mechanical and Thermal of
the Thermoelastic Material (Type-ε, T)

Another relationship between the adiabatic and isothermal elastic stiffness can be obtained where equations (3.137) and (3.139) can be used in terms of the thermoelastic condition given in Eq. (3.147). In this case, for an adiabatic process, dS=0, that can be applied to Eq. (3.137) and then the differential temperature dT can be eliminated in Eq. (3.139) using Eq. (3.137) to give,

$$d\sigma_{ij} = \left(\frac{\partial \sigma_{ij}}{\partial \varepsilon_{kl}}\right)_{T} d\varepsilon_{kl} - \frac{\left(\frac{\partial \sigma_{ij}}{\partial T}\right)_{\varepsilon}\left(\frac{\partial S}{\partial \varepsilon_{kl}}\right)_{T} d\varepsilon_{kl}}{\left(\frac{\partial S}{\partial T}\right)_{\varepsilon}} \quad . \qquad (3.148)$$

Modifying Eq. (3.148) in terms of the elastic compliances results in,

$$\left(\frac{\partial \sigma_{ij}}{\partial \varepsilon_{kl}}\right)_S = \left(\frac{\partial \sigma_{ij}}{\partial \varepsilon_{kl}}\right)_T - \frac{\left(\frac{\partial \sigma_{ij}}{\partial T}\right)_\varepsilon \left(\frac{\partial S}{\partial \varepsilon_{kl}}\right)_T}{\left(\frac{\partial S}{\partial T}\right)_\varepsilon} \quad . \tag{3.149}$$

Simplifying Eq. (3.149) gives,

$$\left(\frac{\partial \sigma_{ij}}{\partial \varepsilon_{kl}}\right)_S - \left(\frac{\partial \sigma_{ij}}{\partial \varepsilon_{kl}}\right)_T = -\left(\frac{\partial \sigma_{ij}}{\partial T}\right)_\varepsilon \left(\frac{\partial S}{\partial \varepsilon_{kl}}\right)_T \left(\frac{\partial T}{\partial S}\right)_\varepsilon \quad . \tag{3.150}$$

Corresponding with the thermodynamic coefficients given from Eqs. (3.140a), (3.141b), (3.144) and (3.145), equation (3.150) can be formulated as,

$$C_{ijkl}^S - C_{ijkl}^T = \beta_{ij}\beta_{kl}\left(T/C^\varepsilon\right) \quad . \tag{3.151}$$

This indicates that the relations between adiabatic and isothermal elastic stiffness can be obtained from the left side in Eq. (3.151) where the thermal pressure and heat capacity always have positive value of coefficients. This indicates that the left side in Eq. (3.151) always has positive value indicating that the elastic stiffness for the adiabatic effect has a larger value than the elastic stiffness for the isothermal effect.

3.9. Elastic Helmholtz Free Energy (Type- ε, D, T)

In this section, the elastic Helmholtz Free Energy will be further discussed according to the independent properties of strain ε, electric displacement D and temperature T. This implied that the elastic Helmholtz Free Energy was a function of independent properties as it indicated the fundamental functions for thermodynamic equation of state. Independent variables of Elastic Helmholtz Free Energy can be obtained using Legendre's transform where equation (3.81) can be used to replace independent variable of Eq. (3.80) of entropy S with $\left(\frac{\partial U}{\partial S}\right)_{\varepsilon,D} = T$. At this point, the elastic Helmholtz Free Energy can be stated as the characteristic thermodynamic potential with a function of differential terms ε, D and T in the macroscopic state. Elastic Helmholtz Free Energy can be stated as,

$$dF = d(U - TS) \quad . \tag{3.152}$$

Expanding Eq. (3.152) into differential form results in,

$$dF = dU - TdS - SdT \quad . \tag{3.153}$$

Substituting Eq. (3.82) into Eq. (3.153) provides,

$$dF = TdS + \sigma_{ij}d\varepsilon + E_i dD_i - TdS - SdT \quad . \tag{3.154}$$

Simplifying Eq. (3.154) gives,

$$dF = \sigma_{ij}d\varepsilon_{ij} + E_i dD_i - SdT \quad . \tag{3.155}$$

Equation (3.155) can be stated as an exact partial differential for elastic Helmholtz energy as,

$$dF = \left(\frac{\partial F}{\partial \varepsilon_{ij}}\right)_{D,T} d\varepsilon_{ij} + \left(\frac{\partial F}{\partial D_i}\right)_{\varepsilon,T} dD_i + \left(\frac{\partial F}{\partial T}\right)_{\varepsilon,D} dT \quad . \tag{3.156}$$

The intensive properties for Helmholtz energy can be stated as,

$$\left(\frac{\partial F}{\partial \varepsilon_{ij}}\right)_{D,T} = \sigma_{ij} \quad ; \quad \left(\frac{\partial F}{\partial D_i}\right)_{\varepsilon,T} = E_i \quad ; \quad \left(\frac{\partial F}{\partial T}\right)_{\varepsilon,D} = -S \quad . \tag{3.157}$$

Using Maxwell's relations gives,

$$\left(\frac{\partial \sigma_{ij}}{\partial D_i}\right)_{\varepsilon,T} = \left(\frac{\partial E_i}{\partial \varepsilon_{ij}}\right)_{D,T}, \left(\frac{\partial \sigma_{ij}}{\partial T}\right)_{\varepsilon,D} = -\left(\frac{\partial S}{\partial \varepsilon_{ij}}\right)_{T,D}, \left(\frac{\partial E_i}{\partial T}\right)_{D,\varepsilon} = -\left(\frac{\partial S}{\partial D_i}\right)_{T,\varepsilon}. \tag{3.158}$$

At this point, the intensive properties for σ_{ij}, E_i, and S become extensive properties when the thermodynamic equation of state is formulated in terms of the Maxwell's relations where the extensive properties of ε_{kl}, D_j and T were kept constant as,

$$dE_i = \left(\frac{\partial E_i}{\partial \varepsilon_{kl}}\right)_{D,T} d\varepsilon_{kl} + \left(\frac{\partial E_i}{\partial D_j}\right)_{\varepsilon,T} dD_j + \left(\frac{\partial E_i}{\partial T}\right)_{\varepsilon,D} dT \quad , \tag{3.159}$$

$$d\sigma_{ij} = \left(\frac{\partial \sigma_{ij}}{\partial \varepsilon_{kl}}\right)_{D,T} d\varepsilon_{kl} + \left(\frac{\partial \sigma_{ij}}{\partial D_k}\right)_{\varepsilon,T} dD_k + \left(\frac{\partial \sigma_{ij}}{\partial T}\right)_{\varepsilon,D} dT \quad , \tag{3.160}$$

$$dS = \left(\frac{\partial S}{\partial \varepsilon_{kl}}\right)_{D,T} d\varepsilon_{kl} + \left(\frac{\partial S}{\partial D_j}\right)_{\varepsilon,T} dD_j + \left(\frac{\partial S}{\partial T}\right)_{\varepsilon,D} dT \quad . \tag{3.161}$$

Corresponding with Eqs. (3.159), (3.160) and (3.161), the thermodynamic coefficients in terms of Maxwell's relations can be obtained as,

$$\left(\frac{\partial E_i}{\partial D_j}\right)_{\varepsilon,T} = \frac{1}{\epsilon_{ij}^{\varepsilon,T}} \quad , \quad \left(\frac{\partial \sigma_{ij}}{\partial D_k}\right)_{\varepsilon,T} = \frac{1}{d_{ijk}^T} = h_{ijk}^T \quad , \tag{3.162}$$

$$\left(\frac{\partial E_i}{\partial T}\right)_{\varepsilon,D} = -\left(\frac{\partial E_i}{\partial D_j}\right)_{\varepsilon,T}\left(\frac{\partial D_j}{\partial T}\right)_{\varepsilon,E} = -\frac{P_j^\varepsilon}{\epsilon_{ij}^{\varepsilon,T}} = -f_i^\varepsilon \quad , \tag{3.163}$$

$$\left(\frac{\partial E_i}{\partial \varepsilon_{kl}}\right)_{D,T} = \left(\frac{\partial E_i}{\partial D_j}\right)_{\varepsilon,T}\left(\frac{\partial D_j}{\partial \varepsilon_{kl}}\right)_{E,T} = \frac{e_{jkl}^T}{\epsilon_{ij}^{\varepsilon,T}} = h_{ikl}^T \quad ,\left(\frac{\partial \sigma_{ij}}{\partial \varepsilon_{kl}}\right)_{D,T} = C_{ijkl}^{D,T} \quad , \tag{3.164}$$

$$\left(\frac{\partial \sigma_{ij}}{\partial T}\right)_{\varepsilon,D} = -\left(\frac{\partial \sigma_{ij}}{\partial \varepsilon_{kl}}\right)_{D,T}\left(\frac{\partial \varepsilon_{kl}}{\partial T}\right)_{\sigma,E} = -C_{ijkl}^{D,T}\alpha_{kl}^E = -\beta_{ij} \quad , \tag{3.165}$$

$$\left(\frac{\partial S}{\partial D_j}\right)_{\varepsilon,T} = \left(\frac{\partial E_i}{\partial D_j}\right)_{\varepsilon,T}\left(\frac{\partial S}{\partial E_i}\right)_{\varepsilon,T} = \frac{P_i^\varepsilon}{\epsilon_{ij}^{\varepsilon,T}} = f_j^\varepsilon \quad , \tag{3.166}$$

$$\left(\frac{\partial S}{\partial \varepsilon_{kl}}\right)_{D,T} = \left(\frac{\partial \sigma_{ij}}{\partial \varepsilon_{kl}}\right)_{D,T}\left(\frac{\partial S}{\partial \sigma_{ij}}\right)_{E,T} = C_{ijkl}^{D,T}\alpha_{ij}^E = \beta_{kl} \quad , \tag{3.167}$$

$$TdS = dH \rightarrow T\left(\frac{\partial S}{\partial T}\right)_{\varepsilon,D} = \frac{dH}{dT} = C^{\varepsilon,D} \rightarrow \left(\frac{\partial S}{\partial T}\right)_{\varepsilon,D} = \frac{C^{\varepsilon,D}}{T} \quad . \tag{3.168}$$

The thermodynamics coefficients $\left(\frac{\partial E_i}{\partial \varepsilon_{kl}}\right)_{D,T} = \left(\frac{\partial \sigma_{ij}}{\partial D_k}\right)_{\varepsilon,T}$ indicate that the converse piezoelectric effect is numerically equal to the direct piezoelectric effect per unit permittivity in terms of the strain-charge effect with the relations $\varepsilon_{kl} \rightarrow E_i$ and $D_k \rightarrow \sigma_{ij}$. The product of coefficient of thermal expansion with elastic stiffness constant $\left(\frac{\partial \sigma_{ij}}{\partial T}\right)_{\varepsilon,E}$ is known as the thermal pressure with relation $T \rightarrow \sigma_{ij}$ and the product of the piezocaloric effect with elastic stiffness constant $\left(\frac{\partial S}{\partial \varepsilon_{kl}}\right)_{E,T}$ is known as the heat of deformation with relation $\varepsilon_{kl} \rightarrow S$. Both of the physical properties have the same value $\left(\frac{\partial \sigma_{ij}}{\partial T}\right)_{\varepsilon,E} = \left(\frac{\partial S}{\partial \varepsilon_{kl}}\right)_{E,T}$. Moreover, the relations $T \rightarrow E_i$ and $D_j \rightarrow S$ indicate the electrothermal and heat of polarisation, respectively and both of these relations show the same physical property values where $\left(\frac{\partial E_i}{\partial T}\right)_{\varepsilon,D}$ indicate the coefficient of pyroelectric effect at constant strain per unit permittivity (electrothermal) which is the same as the electrocaloric effect at constant strain per unit permittivity (heat of polarization) $\left(\frac{\partial S}{\partial D_j}\right)_{\varepsilon,T}$. Each thermodynamic coefficient was written using Maxwell's relations in measurable partial differential form. Moreover, the thermopiezoelectric coefficients are written in tensor form where the coefficients $\epsilon_{im}^{\varepsilon,T}, d_{ijk}^T , f_i^\varepsilon, C_{ijkl}^{D,T}, \beta_{kl}$ and $C^{\varepsilon,D}$ indicate permittivity at constant strain, piezoelectric constant, pyroelectric constant per unit permittivity, elastic

stiffness at constant charge, stress-temperature thermal expansion and specific heat at constant strain. Corresponding with Eqs. (3.162) to (3.168), equations (3.159) to (3.161) can be reformulated to obtain the constitutive equations of elastic Helmholtz Free Energy of piezoelectricity as,

$$E_i = h_{ikl}^T \varepsilon_{kl} + \frac{1}{\epsilon_{ij}^{\varepsilon,T}} D_j - f_i^\varepsilon \Delta T \,,$$

$$\sigma_{ij} = C_{ijkl}^{D,T} \varepsilon_{kl} + h_{ijk}^T D_k - \beta_{ij} \Delta T \quad, \tag{3.169}$$

and

$$\Delta S = \beta_{kl} \varepsilon_{kl} + f_j^\varepsilon D_j + \frac{C^{\varepsilon,D}}{T_o} \Delta T \,.$$

The previous thermopiezoelectric potentials represents the interrelationship of electromechanical, thermoelectric and electrothermal components with the various applicable intensive and extensive properties based on electrical Gibbs free energy, elastic Gibbs free energy, elastic Helmholtz free energy and electric Helmholtz free energy. The difference between Gibbs and Helmholtz is the use of the extensive and intensive properties. In the next section, the elastic enthalpy and electrical enthalpy with adiabatic and isothermal processes will be discussed. The electrical enthalpy is commonly used for formulating the constitutive equations of piezoelectric plate, shell and beam, Tiersten [75], Mindlin [88], and Tanaka [90].

3.10. Elastic-Electrical Enthalpy (Type – σ, E)

The nature of conservation of energy from the piezoelectric element is discussed here according to the independent properties of stress and electric field. The formalised energy can be called the elastic-electrical enthalpy which depends on the internal energy, potential energy due to the change of strain and elastic-electrical energy without considering the changes of temperature and entropy. However, the formalised internal energy in the system purely follows the first law of thermodynamics and the transformation of heat with the reversible process from the second law of thermodynamics. At this point, the elastic-electrical enthalpy implies a dependent energy process on the material nature of piezoelectricity and its surrounding. The formalised elastic-electrical enthalpy can be formulated as a function of stress σ, electric field E and entropy S. However, as presumed here, the system was under isothermal and adiabatic processes implying the temperature

change $\Delta T = 0$ and the entropy change $\Delta S = 0$. The remaining properties were assumed to have functions of stress and electric field where this can be stated as $H = (\sigma, E)$. For the adiabatic and isothermal processes, the elastic-electrical Gibbs free energy becomes the elastic-electrical enthalpy to give,

$$dH = d(U - \sigma_{ij}\varepsilon_{ij} - E_i D_i) \quad . \tag{3.170}$$

Expanding Eq. (3.170) using the differential form gives,

$$dH = dU - \varepsilon_{ij}d\sigma_{ij} - \sigma_{ij}d\varepsilon_{ij} - E_i dD_i - D_i dE_i \quad . \tag{3.171}$$

Substituting Eq. (3.82) into (3.171) provides,

$$dH = \sigma_{ij}d\varepsilon_{ij} + E_i dD_i - \varepsilon_{ij}d\sigma_{ij} - \sigma_{ij}d\varepsilon_{ij} - E_i dD_i - D_i dE_i \quad . \tag{3.172}$$

Simplifying Eq. (3.172) obtains,

$$dH = -\varepsilon_{ij}d\sigma_{ij} - D_i dE_i \quad . \tag{3.173}$$

Equation (3.173) can be modified into the exact differential form to give,

$$dH = \left(\frac{\partial H}{\partial \sigma_{ij}}\right)_E d\sigma_{ij} + \left(\frac{\partial H}{\partial E_i}\right)_\sigma dE_i \quad . \tag{3.174}$$

The intensive properties can be obtained separately from Eq. (3.174) as,

$$\left(\frac{\partial H}{\partial \sigma_{ij}}\right)_E = -\varepsilon_{ij} \;\; ; \;\; \left(\frac{\partial H}{\partial E_i}\right)_\sigma = -D_i \quad , \tag{3.175}$$

where the Maxwell's relation can be obtained as,

$$\left(\frac{\partial \varepsilon_{ij}}{\partial E_k}\right) = \left(\frac{\partial D_i}{\partial \sigma_{kl}}\right) \quad . \tag{3.176}$$

The intensive properties in Eq. (3.175) become extensive properties in order to formulate the enthalpy equation of state which are function of independent properties of σ_{kl} and E_k to give,

$$dD_i = \left(\frac{\partial D_i}{\partial E_k}\right)_\sigma dE_k + \left(\frac{\partial D_i}{\partial \sigma_{kl}}\right)_E d\sigma_{kl} \quad , \tag{3.177}$$

$$d\varepsilon_{ij} = \left(\frac{\partial \varepsilon_{ij}}{\partial E_k}\right)_\sigma dE_k + \left(\frac{\partial \varepsilon_{ij}}{\partial \sigma_{kl}}\right)_E d\sigma_{kl} \quad . \tag{3.178}$$

The enthalpy coefficients in terms of Maxwell's relations can be obtained from Eqs. (3.177) and (3.178) to give,

$$\left(\frac{\partial D_i}{\partial E_k}\right)_\sigma = \epsilon_{ik}^\sigma \quad , \quad \left(\frac{\partial D_i}{\partial \sigma_{kl}}\right)_E = d_{ikl}^E \quad , \tag{3.179}$$

$$\left(\frac{\partial \varepsilon_{ij}}{\partial E_k} \right)_{\sigma} = d_{ijk}^{\sigma} \quad , \quad \left(\frac{\partial \varepsilon_{ij}}{\partial \sigma_{kl}} \right)_{E} = s_{ijkl}^{E} \ . \tag{3.180}$$

It should be noted that Maxwell's relations implied four coefficients relating the elastic-electrical enthalpy. As we can see from Figure (3.8), the relation $\sigma_{kl} \rightarrow \varepsilon_{ij}$ produced the elastic compliance (s_{ijkl}^{E}) and the relation $\sigma_{kl} \rightarrow D_i$ and $E_k \rightarrow \varepsilon_{ij}$ produced the direct and converse piezoelectric constants, respectively and both of these relations show the same value. The final relation $E_k \rightarrow D_i$ gives the permittivity at constant stress. Equations (3.179) and (3.180) are sometimes known as the thermodynamic coefficients. Each coefficient denotes the measurable quantities in terms of the partial differential forms. It should be noted that the tensor coefficients $\epsilon_{ik}^{\sigma}, d_{ikl}^{E}$ and s_{ijkl}^{E} indicate permittivity, piezoelectric constant and elastic compliance. Superscripts σ, and E indicate the quantities at constant stress and electric field. Corresponding with Eqs. (3.179) and (3.180), equations (3.177) to (3.178) can be reformulated to obtain the direct and converse effects of piezoelectricity as,

$$D_i = \epsilon_{ik}^{\sigma} E_k + d_{ikl}^{E} \sigma_{kl} \quad , \tag{3.181}$$

$$\varepsilon_{ij} = d_{ijk}^{\sigma} E_k + s_{ijkl}^{E} \sigma_{kl} \ .$$
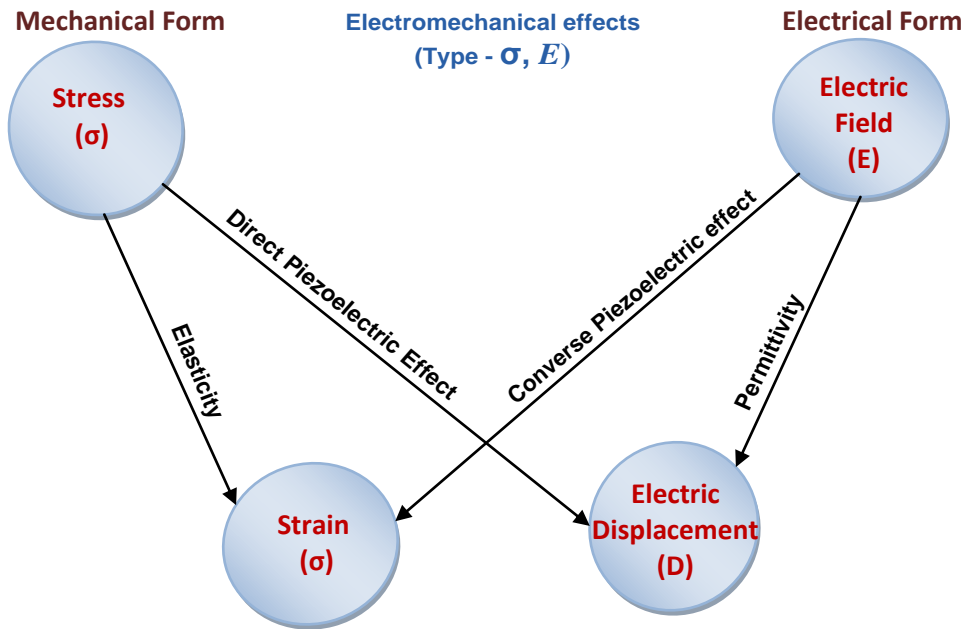
Figure 3.8 The Relations Between Mechanical and Electrical Effects of Piezoelectricity (Type $- \sigma, E$)

Furthermore, the relation between electrically clamped and free elastic compliances under isothermal condition can be further obtained, where equations (3.177) and (3.178) can be used in terms of the enthalpy of electro-elasticity condition given in Eq. (3.181). In this case, the electrical displacement $dD_i = 0$ can be applied in Eq. (3.177) and then the differential electric field dE_k can be eliminated in Eq. (3.178) by using Eq. (3.177) to give,

$$d\varepsilon_{ij} = \left(\frac{\partial \varepsilon_{ij}}{\partial \sigma_{kl}}\right)_E d\sigma_{kl} - \frac{\left(\frac{\partial \varepsilon_{ij}}{\partial E_k}\right)_\sigma \left(\frac{\partial D_i}{\partial \sigma_{kl}}\right)_E d\sigma_{kl}}{\left(\frac{\partial D_i}{\partial E_k}\right)_\sigma} . \qquad (3.182)$$

Modifying Eq. (3.182) in terms of the elastic compliances results in,

$$\left(\frac{\partial \varepsilon_{ij}}{\partial \sigma_{kl}}\right)_D - \left(\frac{\partial \varepsilon_{ij}}{\partial \sigma_{kl}}\right)_E = - \frac{\left(\frac{\partial \varepsilon_{ij}}{\partial E_k}\right)_\sigma \left(\frac{\partial D_i}{\partial \sigma_{kl}}\right)_E}{\left(\frac{\partial D_i}{\partial E_k}\right)_\sigma} . \qquad (3.183)$$

Corresponding with the thermodynamic coefficients given from Eqs. (3.179) and (3.180), equation (3.183) can be formulated as,

$$s^D_{ijkl} - s^E_{ijkl} = - \frac{d^\sigma_{ijk} d^E_{ikl}}{\epsilon^\sigma_{ik}} . \qquad (3.184)$$

This indicates that electrically clamped and free elastic compliances under isothermal effect can be obtained from the left side in Eq. (3.184) where the multiplication between piezoelectric constants always gives the positive value although the value of the piezoelectric constant is negative and the permittivity also has positive value. This shows that the left side of Eq. (3.184) always has negative value indicating that the elastic compliance at constant electric displacement has a smaller value than the elastic compliance at electric field because the tensile stress due to constant electrical charge creates the polarization and can reduce the strain dramatically compared with the tensile stress with constant electric field which can change the material shape to create high strain. Another relation in terms of the elastic-electrical enthalpy includes the clamped and free isothermal permittivities. Setting $d\varepsilon_{ij} = 0$ in Eq. (3.178) and then eliminating $d\sigma_{kl}$ from Eq. (3.177) results in,

$$dD_i = \left(\frac{\partial D_i}{\partial E_k}\right)_\sigma dE_k - \frac{\left(\frac{\partial D_i}{\partial \sigma_{kl}}\right)_E \left(\frac{\partial \varepsilon_{ij}}{\partial E_k}\right)_\sigma dE_k}{\left(\frac{\partial \varepsilon_{ij}}{\partial \sigma_{kl}}\right)_E} \qquad . \qquad (3.185)$$

Modifying Eq. (3.185) in terms of the permittivity provides,

$$\left(\frac{\partial D_i}{\partial E_k}\right)_\varepsilon - \left(\frac{\partial D_i}{\partial E_k}\right)_\sigma = - \frac{\left(\frac{\partial D_i}{\partial \sigma_{kl}}\right)_E \left(\frac{\partial \varepsilon_{ij}}{\partial E_k}\right)_\sigma}{\left(\frac{\partial \varepsilon_{ij}}{\partial \sigma_{kl}}\right)_E} \qquad . \qquad (3.186)$$

Corresponding with the thermodynamic coefficients given from Eqs. (3.179) and (3.180), equation (3.186) can also be formulated as,

$$\epsilon_{ik}^\varepsilon - \epsilon_{ik}^\sigma = - \frac{d_{ikl}^E d_{ijk}^\sigma}{s_{ijkl}^E} \qquad . \qquad (3.187)$$

This indicates that electrically clamped and free permittivities under isothermal effect can be obtained from the left side of Eq. (3.187) where the product between the piezoelectric constants always has positive value although the value of the piezoelectric constant is negative and the elastic stiffness gives the positive value of coefficients. This indicates that the left side of Eq. (3.187) is negative and that the permittivity at constant stress has a larger value than the permittivity at constant strain.

3.11. Electrical Enthalpy ($Type - \varepsilon, E$)

The electrical enthalpy depends on the internal energy and electrical energy where this represents the most common use of the piezoelectric energy for a wide range of applications for plates, shells, and beams. Earlier researchers, Tiersten [75], Mindlin [88], D'Ottavio *et al* [89], Tanaka [90], and Yang [91] developed mathematical models of the electrical enthalpy in terms of Hamiltonian's principle where the piezoelectric system was presumed as an adiabatic and isothermal processes. The transformation of energy in terms of the electrical enthalpy can be achieved by using Legendre's transform in terms of Eq. (3.81) where the independent variable from Eq. (3.80) of electrical displacement D_i can be replaced with $\left(\frac{\partial U}{\partial D}\right)_{S,\varepsilon} = E_i$. The electrical enthalpy can be formulated as,

$$dH = d(U - E_i D_i) \qquad . \qquad (3.188)$$

Expanding Eq. (3.188) using the differential form gives,

$$\mathrm{d}H = \mathrm{d}U - E_i \mathrm{d}D_i - D_i \mathrm{d}E_i \ . \tag{3.189}$$

Substituting Eq. (3.82) into (3.189) results in,

$$H = \sigma_{ij} \mathrm{d}\varepsilon_{ij} + E_i \mathrm{d}D_i - E_i \mathrm{d}D_i - D_i \mathrm{d}E_i \ . \tag{3.190}$$

Simplifying Eq. (3.190) provides,

$$\mathrm{d}H = \sigma_{ij} \mathrm{d}\varepsilon_{ij} - D_i \mathrm{d}E_i \ . \tag{3.191}$$

Equation (3.191) can be modified into the exact differential form to give,

$$\mathrm{d}H = \left(\frac{\partial H}{\partial \varepsilon_{ij}}\right)_E \mathrm{d}\varepsilon_{ij} + \left(\frac{\partial H}{\partial E_i}\right)_\varepsilon \mathrm{d}E_i \ . \tag{3.192}$$

The intensive properties can be obtained separately from Eq. (3.192) as,

$$\left(\frac{\partial H}{\partial \varepsilon_{ij}}\right)_E = \sigma_{ij} \quad , \qquad \left(\frac{\partial H}{\partial E_i}\right)_\varepsilon = -D_i \quad , \tag{3.193}$$

where Maxwell's relation can be obtained as,

$$\left(\frac{\partial \sigma_{ij}}{\partial E_i}\right)_\varepsilon = -\left(\frac{\partial D_i}{\partial \varepsilon_{ij}}\right)_E \ . \tag{3.194}$$

The enthalpy equation of state can be formulated according to extensive properties reduced from intensive properties in Eq. (3.193) where the independent properties ε_{kl} and E_k are held constant as,

$$\mathrm{d}D_i = \left(\frac{\partial D_i}{\partial \varepsilon_{kl}}\right)_E \mathrm{d}\varepsilon_{kl} + \left(\frac{\partial D_i}{\partial E_k}\right)_\varepsilon \mathrm{d}E_k \ , \tag{3.195}$$

$$\mathrm{d}\sigma_{ij} = \left(\frac{\partial \sigma_{ij}}{\partial \varepsilon_{kl}}\right)_E \mathrm{d}\varepsilon_{kl} + \left(\frac{\partial \sigma_{ij}}{\partial E_k}\right)_\varepsilon \mathrm{d}E_k \ . \tag{3.196}$$

The electrical enthalpy coefficients can be obtained from Eqs. (3.195) and (3.196) to give,

$$\left(\frac{\partial \sigma_{ij}}{\partial \varepsilon_{kl}}\right)_E = C_{ijkl}^E \quad , \qquad \left(\frac{\partial \sigma_{ij}}{\partial E_k}\right)_\varepsilon = -e_{ijk}^\varepsilon \quad , \tag{3.197}$$

$$\left(\frac{\partial D_i}{\partial \varepsilon_{kl}}\right)_E = e_{ikl}^E \quad , \qquad \left(\frac{\partial D_i}{\partial E_k}\right)_\varepsilon = \epsilon_{ik}^\varepsilon \quad . \tag{3.198}$$

It should be noted that Maxwell's relations have four coefficients relating the enthalpy of electro-elasticity. As can be seen from Figure (3.9), the relation $\varepsilon_{kl} \rightarrow \sigma_{ij}$ produced the elastic stiffness and the relation $\varepsilon_{kl} \rightarrow D_i$ and $E_k \rightarrow \sigma_{ij}$ produced the second direct and second converse piezoelectric constants relating the strain-

voltage, respectively and both of these relations show the same value. The final relation $E_k \rightarrow D_i$ gives the permittivity at constant strain. The thermodynamic coefficients of the electrical enthalpy reflect the measurable quantities in terms of the exact differential forms. The tensor form of coefficients $\epsilon_{ik}^{\varepsilon}, e_{ikl}^{E}$ and C_{ijkl}^{E} indicate permittivity at constant strain, piezoelectric constant at constant electric field and elastic stiffness at constant electric field. Superscripts ε and E indicate the quantities at constant strain and electric field. Corresponding with Eqs. (3.197) and (3.198), equations (3.195) and (3.196) can be reformulated to obtain the direct and converse effects of piezoelectricity as,

$$\sigma_{ij} = C_{ijkl}^{E} \varepsilon_{kl} - e_{ijk}^{\varepsilon} E_k \quad , \qquad (3.199)$$
$$D_i = e_{ikl}^{E} \varepsilon_{kl} + \epsilon_{ik}^{\varepsilon} E_k .$$
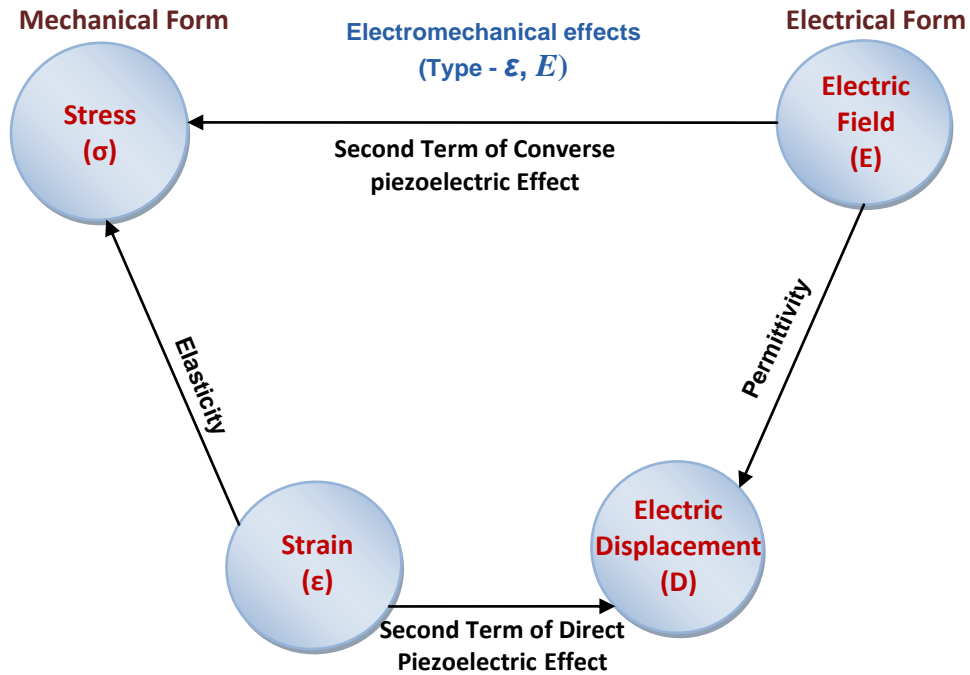
Figure 3.9 The Relations Between Mechanical and Electrical Effects of
Piezoelectric (Type $- \varepsilon, E$)

Another relation between the clamped and free permittivities at constant stress can be further formulated, where equations (3.195) and (3.196) can be used in terms of the electrical enthalpy condition given in Eq. (3.199). In this case, the stress constant condition $d\sigma_{ij} = 0$, can be applied in Eq. (3.196) and then the differential strain $d\varepsilon$ can be eliminated in Eq. (3.195) using Eq. (3.196) to give,

$$\left(\frac{\partial D_i}{\partial E_k}\right)_\sigma - \left(\frac{\partial D_i}{\partial E_k}\right)_\varepsilon = -\frac{\left(\frac{\partial D_i}{\partial \varepsilon_{kl}}\right)_E \left(\frac{\partial \sigma_{ij}}{\partial E_k}\right)_\varepsilon}{\left(\frac{\partial \sigma_{ij}}{\partial \varepsilon_{kl}}\right)_E} \qquad . \qquad (3.200)$$

Corresponding with the thermodynamic coefficients given from Eqs. (3.197) and (3.198), equation (3.200) can be formulated as,

$$\epsilon_{ik}^\sigma - \epsilon_{ik}^\varepsilon = \frac{e_{ikl}^E e_{ijk}^\varepsilon}{C_{ijkl}^E} \qquad . \qquad (3.201)$$

This indicates that electrically clamped and free permittivities under isothermal conditions can be obtained from the left side of Eq. (3.201) where the product between the second term of the piezoelectric constants always gives a positive value although the value of the second term of piezoelectric constant is negative and the elastic stiffness also gives a positive value. This means that the left side of Eq. (3.201) always gives positive value indicating that the permittivity at constant stress has larger value than the permittivity at constant strain under the isothermal effect.

The thermopiezoelectric energy function forms can be formulated in terms of the thermopiezoelectric equations of states, Legendre's transform and Maxwell's relations as given in the previous section. The first thermopiezoelectric energy form is from the Elastic-Electrical Gibbs Free Energy (Type $-\sigma, E, T$) as,

$$G(\sigma_{ij}, E_i, T) = -\frac{1}{2} s_{ijkl}^{E,T} \sigma_{ij}\sigma_{kl} - d_{ikl}^T \sigma_{kl}E_i - \sigma_{ij}\alpha_{ij}^E \Delta T - \frac{1}{2}\epsilon_{ik}^{\sigma,T} E_k E_i$$
$$- E_k P_k^\sigma \Delta T - \frac{C^{\sigma,E}}{2T}\Delta T^2 \qquad . \qquad (3.202)$$

The Elastic Gibbs Free Energy (Type $-\sigma, D, T$) can also be formulated as

$$G(\sigma_{ij}, D_i, T) = -\frac{1}{2} s_{ijkl}^{E,T} \sigma_{ij}\sigma_{kl} - g_{ijk}^T \sigma_{ij}D_k - \alpha_{kl}^D \sigma_{kl}\Delta T + \frac{1}{2\epsilon_{ij}^{\sigma,T}} D_j D_i$$
$$- f_j^\sigma D_j \Delta T - \frac{C^{\sigma,D}}{2T}\Delta T^2 \qquad . \qquad (3.203)$$

The Electrical Helmholtz Free Energy (Type $-\varepsilon, E, T$) can be formulated as,

$$F(\varepsilon_{ij}, E_i, T) = \frac{1}{2} C_{ijkl}^{E,T} \varepsilon_{kl}\varepsilon_{ij} - e_{ijk}^T E_k \varepsilon_{ij} - \beta_{ij} \varepsilon_{ij}\Delta T - \frac{1}{2}\epsilon_{ik}^{\varepsilon,T} E_k E_i$$
$$- P_i^\varepsilon E_i \Delta T - \frac{C^{\varepsilon,E}}{2T}\Delta T^2 \qquad . \qquad (3.204)$$

The Elastic Helmholtz Free Energy (Type $-\varepsilon, D, T$) can be formulated as,

$$F(\varepsilon_{ij}, D_i, T) \;=\; \frac{1}{2} C^{D,T}_{ijkl}\varepsilon_{ij}\varepsilon_{kl} + h^{T}_{ijk}D_k\,\varepsilon_{ij} - \beta_{ij}\varepsilon_{ij}\Delta T \;+\; \frac{1}{2\epsilon^{\varepsilon,T}_{ij}}\,D_j\,D_i$$

$$- f^{\varepsilon}_i\,D_i\,\Delta T \;-\; \frac{C^{\varepsilon,E}}{2T}\Delta T^2 \;. \tag{3.205}$$

The Elastic-Electrical Enthalpy (Type $-\sigma$, E) can be formulated as,

$$H(\sigma_{ij}, E_i) = \; -\frac{1}{2} s^{E}_{ijkl}\sigma_{ij}\sigma_{kl} - E_i\,d_{ikl}\sigma_{kl} - \frac{1}{2}\epsilon^{\sigma}_{ik}E_i\,E_k \;. \tag{3.206}$$

The Electrical Enthalpy (Type $-\varepsilon$, E) can be formulated as,

$$H(\varepsilon_{ij}, E_i) = \; \frac{1}{2} C^{E}_{ijkl}\varepsilon_{ij}\varepsilon_{kl} \; - e_{ijk}E_k\,\varepsilon_{ij} \; -\frac{1}{2}\epsilon^{\varepsilon}_{ik}E_k\,E_i \;. \tag{3.207}$$

The previous thermopiezoelectric energy function forms showed different physical equations indicating the physical relations of each property. This indicates that the chosen thermopiezoelectric energy form can be used in the applications of smart material and structures. In this case, the conditions of the system depend upon the plane strain or plane stress of the elasticity, boundary conditions, applied mechanical, electrical and thermal loads, and geometry of structure. The constitutive equations can be further analysed using the variational principle or Hamiltonian theorem, Tiersten [75], Mindlin [88] and Dokmeci [92]. In this dissertation, the Electrical Enthalpy or Electrical Helmholtz Free Energy under adiabatic and isothermal processes along with the energy potential of substructure and kinetic energy will be discussed for further mathematical development of the piezoelectric bimorph beam with tip mass under two input base excitations for power harvesting as discussed in chapter 4. The tensor notations can be condensed using Voigt's notation to give the matrix forms which can be further applied into the piezoelectric material properties using Einstein's summation convention as given in appendix A.

In this chapter, the thermopiezoelectric relations in terms of Elastic-Electrical Gibbs Free Energy, Elastic Gibbs Free Energy, Electrical Helmholtz Free Energy and Elastic Helmholtz Free Energy are summarised in Table 1. It should be noted that the enthalpy will not be included in Table 1 because the enthalpy coefficients which were formulated previously, have covered the Elastic-electrical Gibbs Free Energy and Electrical Helmholtz Free Energy under adiabatic and isothermal processes.

Table 3.1 Gibbs and Helmholtz's Thermopiezoelectric Relations

W	X	Y	Z	$\left(\dfrac{\partial Y}{\partial X}\right)_{W,Z}$	W	X	Y	Z	$\left(\dfrac{\partial Y}{\partial X}\right)_{W,Z}$
σ	E	D_i	T	ϵ_{ik}	E	ε_{kl}	σ_{ij}	T	C_{ijkl}
E	σ_{kl}	D_i	T	d_{ikl}	ε	E_k	σ_{ij}	T	$-e_{ijk}$
σ	T	D_i	E	P_i	ε	T	σ_{ij}	E	$-C_{ijkl}\,\alpha_{kl} = -\beta_{ij}$
σ	E_k	ε_{ij}	T	d_{ijk}	E	ε_{kl}	D_i	T	e_{ikl}
E	σ_{kl}	ε_{ij}	T	s_{ijkl}	ε	E_k	D_i	T	ϵ_{ik}
σ	T	ε_{ij}	E	α_{ij}	ε	T	D_i	E	P_i
σ	E_k	S	T	P_k	ε	E_k	S	T	P_k
E	σ_{kl}	S	T	α_{kl}	E	ε_{kl}	S	T	$C_{ijkl}\alpha_{ij} = \beta_{kl},$
σ	T	S	E	$\dfrac{C}{T}$	ε	T	S	E	$\dfrac{C}{T}$
σ	D_j	E_i	T	$\dfrac{1}{\epsilon_{ij}^{\sigma,T}}$	ε	D_j	E_i	T	$\dfrac{1}{\epsilon_{ij}^{\varepsilon,T}}$
σ	D_k	ε_{ij}	T	$\dfrac{1}{e_{ijk}} = g_{ijk}$	ε	D_k	σ_{ij}	T	$\dfrac{1}{d_{ijk}} = h_{ijk}$
D	T	E_i	σ	$-\dfrac{P_j}{\epsilon_{ij}} = -f_i$	ε	T	E_i	D	$-\dfrac{P_j^{\varepsilon}}{\epsilon_{ij}} = -f_i$
D	σ_{kl}	E_i	T	$-\dfrac{d_{jkl}}{\epsilon_{ij}} = -g_{ikl}$	D	ε_{kl}	E_i	T	$\dfrac{e_{jkl}}{\epsilon_{ij}} = h_{ikl}$
D	σ_{kl}	ε_{ij}	T	s_{ijkl}	D	ε_{kl}	σ_{ij}	T	C_{ijkl}
D	T	ε_{ij}	D	α_{ij}	ε	T	σ_{ij}	D	$-C_{ijkl}\alpha_{kl} = -\beta_{ij}$
σ	D_j	S	T	$\dfrac{P_i}{\epsilon_{ij}} = f_j$	ε	D_j	S	T	$\dfrac{P_i}{\epsilon_{ij}} = f_j$
D	σ_{kl}	S	T	α_{kl}	D	ε_{kl}	S	T	$C_{ijkl}\alpha_{ij} = \beta_{kl}$
σ	T	S	E	$\dfrac{C}{T}$	ε	T	S	D	$\dfrac{C}{T}$

3.12. Closing remark

The main focus of this chapter has been the development of the continuum thermopiezoelectric equations of state with the entities of extensive and intensive properties using Legendre's transform and Maxwell's relations. Each of the properties of thermopiezoelectricity have interrelationships with other properties in order to find out the potential measurable properties which were known as the thermopiezoelectric coefficients based on the laws of thermodynamics and Gibbs and Helmholtz's free energy and enthalpy. As considered here, the derivations of the mathematical thermodynamic expression can give the understanding of the physical behaviour of the piezoelectric material and its relations between the physical properties. As Einstein [93] said, "A theory is more impressive the greater the simplicity of its premises is, the more different kinds of things it relates, and the more extended its area of applicability. Therefore, the deep impression which classical thermodynamics made upon me. It is the only physical theory of universal content concerning which I am conceived that, within the framework of the applicability of the basic concepts, it will never be overthrown."

Einstein's note has given the inspiration and ideas to develop the comprehensive derivations of the thermodynamic potentials especially the piezoelectric material in this chapter that was not discussed and presented previously in detail for many scientists. The constitutive thermodynamic potentials of the piezoelectric system can be used to explore further applications of areas of smart materials and structures. In the next chapter, the application of thermopiezoelectricity can be narrowed to the application of vibration power harvesters where the novel constitutive models of electromechanical dynamic equations of piezoelectric bimorph beam for power harvesting will be introduced.

CHAPTER
4

Constitutive Dynamic Equations of the Electromechanical Piezoelectric Bimorph Beam under Two input Base Excitations

This chapter outlines the development of novel mathematical methods for modelling the cantilevered piezoelectric bimorph beams with tip mass under two input base longitudinal and transverse motions. The piezoelectric bimorph beams were based on the Euler-Bernoulli and Rayleigh models coupled with polarity-electric field effects for low power harvesting. The Euler-Bernoulli and Rayleigh piezoelectric beams considered transverse bending by including the extensional longitudinal form of interlayer elements. The typical thin beam is suitable for the design of the vibration piezoelectric beam power harvester. It should be noted that the Rayleigh piezoelectric beam specifically only considered the rotary inertia of the structure element whereas the Euler-Bernoulli piezoelectric beam excluded it. Henceforth, the Rayleigh piezoelectric bimorph beam will be presented in the mathematical derivations. Once the equations are established, the Euler-Bernoulli piezoelectric beam models will be considered for neglecting the rotary inertia of the bimorph. The existences of input base excitations on the cantilevered piezoelectric beam not only affect the strain field of the interlayer elements but also affect the electrical behaviour of the coupled polarity-electric field. The mathematical derivations of the electromechanical system will be developed in the next section. The piezoelectric bimorph system will be analysed according to the electrical enthalpy or electrical Helmholtz free energy under adiabatic and isothermal processes of the piezoelectric layers, potential energy of substructure and kinetic energy, external energies due to input base excitations and electrical charge using the variational method of Hamiltonian's principle. At this stage, strong form analytical method, weak form analytical approaches and closed-form boundary value methods will be discussed in detail. The weak form analytical approach derived from the strong form solution was

further derived using the Ritz method by introducing an eigenvector function (Ritz coefficient) and space- and time-dependent Ritz eigenfunction series which were further formulated using orthonormalisation. The closed-form boundary value method derived from the strong-form method was further formulated using a direct analytical solution with orthonormalisation by introducing the space- and time-dependent eigenfunction series into boundary conditions. The closed-form solution was shown to provide accurate results over the frequency response domain because of its convergence at any particular mode of interest whereas the weak form can give similar results with the closed form provided that the typical mode shapes and number of modes are chosen correctly in order to meet the convergence criteria. Moreover, the broadband electromechanical piezoelectric beam (multi-beam) for the multi-frequency situation is also discussed in this chapter. As the previous chapter mentioned, the electromechanical system using piezoelectric material has unique reversible effects to create both direct and converse modes where the charge material moves a certain distance to create a net dipole moment. The resulting polarity aligns the electric field generating the electric voltage. When the strain field was applied to the material element, the direct piezoelectric effect or polarity will be formed due to the mechanical field. The sensitivity of the piezoelectric material described by Maxwell's relations underlies the interaction between the electrical and mechanical energies. The constitutive equations of the cantilevered piezoelectric bimorph with two input base motions along with the frequency analysis of Laplace transform will be analysed in this section.

4.1. Mathematical Analysis

The linear electrical enthalpy of the piezoelectric material in the tensor notation as discussed in chapter 3 was based on the continuum thermodynamics which can be condensed using Voigt's notation and then further reduced using Einstein's summation convention, Nye [73], Tiersten [75] and Tanaka [90] as,

$$\hat{H}(\varepsilon_1, E_3) = \frac{1}{2}\overline{Q}_{11}^E \varepsilon_1^2 - e_{31}E_3\varepsilon_1 - \frac{1}{2}\varsigma_{33}^\varepsilon E_3^2 , \tag{4.1}$$

$$\sigma_1 = \frac{\partial \hat{H}}{\partial \varepsilon_1} \quad , \quad D_3 = -\frac{\partial \hat{H}}{\partial E_3} , \tag{4.2}$$

$$\sigma_1 = \overline{Q}_{11}^E \varepsilon_1 - e_{31}E_3 \quad , \quad D_3 = e_{31}\varepsilon_1 + \varsigma_{33}^\varepsilon E_3 . \tag{4.3}$$

The above formulations assume the adiabatic and isothermal processes. Here $\overline{Q}_{11}^{E}$, e_{31}, $\varsigma_{33}^{\varepsilon}$, E_3, σ_1, ε_1 and D_3 represent the elastic coefficient at constant electric field, piezoelectric coefficient, permittivity under constant strain, electric field, stress, strain and electric displacement, respectively. Some notations from Eqs. (4.1)-(4.3) have been adapted in this thesis for further mathematical derivations.

In this section, the piezoelectric bimorph beams under two input base motions are discussed. There are a number of researchers dealing with input base motion of the cantilevered beam. Mostly they discussed one input transverse base motion of the piezoelectric beams for predicting power harvesting from single mode [6,7,8,41] and multi-mode [9,10] frequency responses. At this point, as considered; the physical, mathematical and outcome benefits of these researches which are not found from other previous works are as follows:

1. The coupling effects between mechanical and electrical behaviours under dynamic response are considered comprehensively to indicate the important issues either theoretical and mathematically.

2. The strain and polarity-electric field which obviously depends not only on the physical characteristics of the material and its geometry but also on the understanding of the sign conventions (where the new coupling superposition methods for series and parallel electrical connections will be introduced) to determine the clear mathematical concepts and theories of forward and backward piezoelectric coupling coefficients under input dynamic excitations (longitudinal and transverse motions).

3. The novel mathematical methods develop the electromechanical piezoelectric power harvester response where the comprehensive analytical models have been introduced both mathematically and physically.

4. The electromechanical weak and closed form analytical methods provide deep insight into the physical system behaviours including convergence criteria strategy.

5. The series and parallel multi-electromechanical piezoelectric bimorph beams are derived to provide the broadband multi-frequency response behaviour for optimisation study of electrical outputs.

Furthermore, the kinematic equations of the infinitesimal piezoelectric beam with two input base motions were developed to formulate the energies of the structure element. The effect of two input base motions of the structure not only affects the strain fields of each layer of the piezoelectric bimorph but also affects the piezoelectric couplings to create the electrical force and moment of the piezoelectric layers when the series and parallel connections are chosen for the bimorph. This also affects the prediction of power harvesting as discussed and analysed later in chapter.

In Figure 4.1, let point P be an arbitrary point on the undeformed beam structure with positions x and z in the fixed frame of reference oXZ as defined by $\mathbf{R^{op}} = x\mathbf{e_1} + z\mathbf{e_3}$. Let the base support at point o move to point o' in vector $\mathbf{R_{base}}$ where point p also moves to point p' for the frame of reference of $o'xz$ as indicated. The position vector $\mathbf{R_{base}}$ has the same magnitude as vector $\mathbf{R^{pp'}}$ by defining $\mathbf{R_{base}} = u_{base}\mathbf{e_1} + w_{base}\mathbf{e_3}$. Because the base support undergoes motions, point p' undergoes deformation in the longitudinal extension and transverse bending forms as indicated by moving to point p''. Let the present position at point p'' have a condition of absolute displacement with respect to frame of reference oXZ defined by $\mathbf{w_{abs}}$ and $\mathbf{u_{abs}}$, where $\mathbf{w_{abs}} = (w_{base} + w_{rel})\mathbf{e_3}$ and $\mathbf{u_{abs}} = (u_{base} + u_{rel})\mathbf{e_1}$.
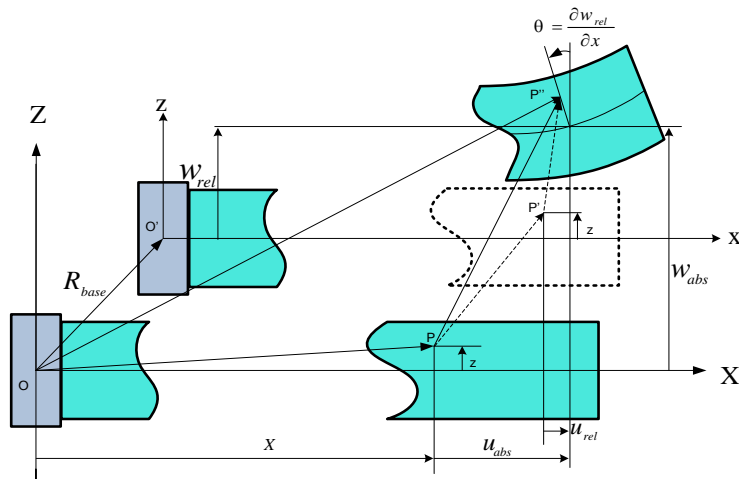
Figure 4.1 Kinematic of Piezoelectric Bimorph Beam

To obtain position vector $\mathbf{R^{pp''}}$, $\mathbf{R^{op''}}$ needs to be defined as,

$$\mathbf{R^{op''}} = \left(x + u_{abs} - z\frac{\partial w_{rel}(x,t)}{\partial x} \right)\mathbf{e_1} + (w_{abs} + z)\mathbf{e_3}. \qquad (4.4)$$

As the position vector $\mathbf{R}^{op}$ is defined, the position vector $\mathbf{R}^{pp''}$ can be obtained and differentiated with respect to time to give,

$$\dot{\mathbf{R}}^{pp''}(x,z,t) = \dot{\mathbf{R}}^{op''} - \dot{\mathbf{R}}^{op} ,$$

$$\dot{\mathbf{R}}^{pp''}(x,z,t) = \left(\dot{u}_{rel}(x,t)+\dot{u}_{base}(t)\right)\mathbf{e_1} - \frac{\partial \dot{w}_{rel}(x,t)}{\partial x}\mathbf{e_2}\times z\,\mathbf{e_3} + \left(\dot{w}_{base}(t)+\dot{w}_{rel}(x,t)\right)\mathbf{e_3} . \quad (4.5)$$

$\dot{\mathbf{R}}^{pp''}$ is defined as the absolute velocity of point p'' with respect to the fixed frame of reference oXZ. The geometrical position of the tip mass from the bimorph can be measured from the fixed frame of reference oXZ to the deformation point and this vector can be differentiated with respect to time to give the absolute velocity of the tip mass in terms of the moving base support as,

$$\dot{\mathbf{R}}^m\left(L,r_{gm}\in\{x_{gm},z_{gm}\},t\right) = \left(\dot{u}_{rel}(L,t)+\dot{u}_{base}(t)\right)\mathbf{e_1} - \frac{\partial \dot{w}_{rel}(L,t)}{\partial x}\mathbf{e_2}\times\left(x_{gm}\,\mathbf{e_1}+z_{gm}\,\mathbf{e_3}\right)$$

$$+ \left(\dot{w}_{base}(t)+\dot{w}_{rel}(L,t)\right)\mathbf{e_3} . \quad (4.6)$$

In this case, the centre of gravity of the tip mass was assumed to coincide with the end of the piezoelectric bimorph L where x_{gm} and z_{gm} are distances from arbitrary elemental mass $dm = \rho\,d\Gamma$ to the centre of gravity of the tip mass. The position vector $\mathbf{R}^{p'p''}$ specifies as the relative displacement due to moving base support at fixed frame oXZ,

$$\mathbf{R}^{p'p''}(x,z,t) = \mathbf{R}^{pp''} - \mathbf{R}^{pp'} = \left(u_{rel} - z\frac{\partial w_{rel}}{\partial x}\right)\mathbf{e_1} + w_{rel}(x,t)\mathbf{e_3} . \quad (4.7)$$

We note that, $\mathbf{R}^{p'p''}$ can be further differentiated with respect to x to give the strain field of the element structure,

$$\varepsilon_{xx} = \varepsilon_1 = \frac{\partial\left(\mathbf{R}^{p'p''}\cdot\mathbf{e_1}\right)}{\partial x} = \frac{\partial u_{rel}}{\partial x} - z\frac{\partial^2 w_{rel}}{\partial x^2} = \varepsilon_1^{(0)} - z\varepsilon_1^{(1)} . \quad (4.8)$$

It should be noted that displacement fields are defined as relative displacement fields for the infinitesimal bimorph beam element. Similar methods can be used to formulate the relative displacement fields with initial relative longitudinal displacement field using the Euler-Bernoulli's beam as,

$$u(x,z,t)_{rel} = u_{rel}(x,t) - z\theta_{rel} , \quad (4.9)$$

$$w(x,z,t)_{rel} = w_{rel}(x,t) . \quad (4.10)$$

Lagrangian strain tensor for linear component, Reddy [94] can be applied to formulate the piezoelectric bimorph beam as,

$$L_{ij} = \frac{1}{2}\left(u_{i,j} + u_{j,i}\right) \quad . \tag{4.11}$$

Applying relative displacement fields from Eq. (4.9) into Eq. (4.11) gives,

$$L_{xx} = \left(\frac{\partial u_{rel}}{\partial x} - z\frac{\partial \theta_{rel}}{\partial x}\right) \quad . \tag{4.12}$$

Transverse shear deformation of the material element is not considered for Euler-Bernoulli's bimorph beam giving the relation,

$$L_{xz} = \frac{1}{2}\left(-\theta_{rel} + \frac{\partial w_{rel}}{\partial x}\right) = 0 . \tag{4.13}$$

Thus, $\theta_{rel} = \partial w_{rel}/\partial x$ represents the gradient transverse deformation or rotation that is substituted into Eq. (4.12) to give the resulting strain field in the x direction as,

$$\varepsilon_1 = L_{xx} = \left(\frac{\partial u_{rel}}{\partial x} - z\frac{\partial^2 w_{rel}}{\partial x^2}\right) = \varepsilon_1^{(0)} - z\varepsilon_1^{(1)}. \tag{4.14}$$

As expected, equations (4.8) and (4.14) indicated the same result. The general constitutive equation of the piezoelectric element can be obtained by using Hamiltonian form, Tiersten [75] and Reddy [95],

$$\int_{t_1}^{t_2} \delta\left(L_a + W_f\right)dt = \int_{t_1}^{t_2}\left(\delta KE - \delta PE + \delta WE + \delta W_f\right)dt = 0 . \tag{4.15}$$

Essentially, the functional forms from Hamiltonian's principle can be extended using the Lagrangian theorem L_a incorporated with the external mechanical and electrical works W_f due to the input base motions. Each variable categorised in the functional forms L_a and W_f in terms of the mathematical model can be stated as,

$$L_a = L_a\left(\dot{w}_{rel}, \dot{u}_{rel}, \dot{w}_{rel}(L), \dot{u}_{rel}(L), \frac{\partial \dot{w}_{rel}}{\partial x}(L), \frac{\partial^2 w_{rel}}{\partial x^2}, \frac{\partial u_{rel}}{\partial x}, E\right), \tag{4.16}$$

$$W_f = W_f\left(w_{rel}, u_{rel}, w_{rel}(L), u_{rel}(L), v\right). \tag{4.17}$$

Equations (4.16) and (4.17) can be further formulated using total differential equations as,

$$\delta L_a = \frac{\partial L_a}{\partial \dot{w}_{rel}}\delta\dot{w}_{rel} + \frac{\partial L_a}{\partial \dot{u}_{rel}}\delta\dot{u}_{rel} + \frac{\partial L_a}{\partial\left(\frac{\partial \dot{w}_{rel}}{\partial x}\right)}\delta\left(\frac{\partial \dot{w}_{rel}}{\partial x}\right) + \frac{\partial L_a}{\partial \dot{w}_{rel}(L)}\delta\dot{w}_{rel}(L) + \frac{\partial L_a}{\partial \dot{u}_{rel}(L)}\delta\dot{u}_{rel}(L)$$

$$+\frac{\partial L_a}{\partial\left(\frac{\partial \dot{w}_{rel}}{\partial x}(L)\right)}\delta\left(\frac{\partial \dot{w}_{rel}}{\partial x}(L)\right)+\frac{\partial L_a}{\partial\left(\frac{\partial^2 w_{rel}}{\partial x^2}\right)}\delta\left(\frac{\partial^2 w_{rel}}{\partial x^2}\right)+\frac{\partial L_a}{\partial\left(\frac{\partial u_{rel}}{\partial x}\right)}\delta\left(\frac{\partial u_{rel}}{\partial x}\right)+\frac{\partial L_a}{\partial E}\delta E, \quad (4.18)$$

$$\delta W_f = \frac{\partial W_f}{\partial w_{rel}}\delta w_{rel} + \frac{\partial W_f}{\partial u_{rel}}\delta u_{rel} + \frac{\partial W_f}{\partial w_{rel}(L)}\delta w_{rel}(L) + \frac{\partial W_f}{\partial u_{rel}(L)}\delta u_{rel}(L) + \frac{\partial W_f}{\partial v}\delta v. \quad (4.19)$$

Here Hamiltonian's principle from Eq. (4.15) can be restricted into the particular form of the constitutive electromechanical dynamic equation of the piezoelectric bimorph beam with substructure of brass shim and tip mass giving,

$$\int_{t_1}^{t_2}\delta\left(L_a + W_f\right)dt = \int_{t_1}^{t_2}\left(\sum_{k\in m}\delta KE^{(k)} + \delta KE_{tip} - \sum_{k\in p}\delta\hat{H}^{(k)} - \delta PE^{subs} + \sum_{i=1}^{n}\delta W_f^{(i)}\right)dt = 0$$

$$\forall m\in\{1,2,3\},\, p\in\{1,3\}\subset d\Gamma \quad . \quad (4.20)$$

Each term from Eq. (4.20) can be stated as kinetic energy KE for every layer including tip mass, potential energy PE from centre brass shim or substructure, electrical enthalpy energy $\hat{H}$ from piezoelectric material at the lower and upper layers and applied mechanical and output electrical works W_f due to the input base motions. Superscripts k and i indicated the layers of bimorph and input inertia mechanical forces (input base excitations). It is noted that the electrical enthalpy can be stated as, $\delta\hat{H} = \delta PE^p - \delta WE^p$ which implies the potential energy and electrical energy from the piezoelectric layers as also implied from Eqs. (4.1) to (4.3).

It should be noted that the parameter potential energies of the piezoelectric and substructure, kinetic energy of bimorph and tip mass, electrical energy of the bimorph, external mechanical energy and external electrical energy are presented and derived separately for the next stage in order to arrange convenient formulations. After that, the constitutive electromechanical dynamic equations using Eq. (4.20) will be applied to model the strong and weak forms. The geometry of the piezoelectric bimorph beam with the tip mass can be modelled as shown in Figure 4.2. Variables L, h_s and h_p indicate the bimorph length, substructure thickness and piezoelectric thickness (same thickness between bottom and top layers), respectively. Other geometry parameters of tip mass will be given in the forthcoming section.
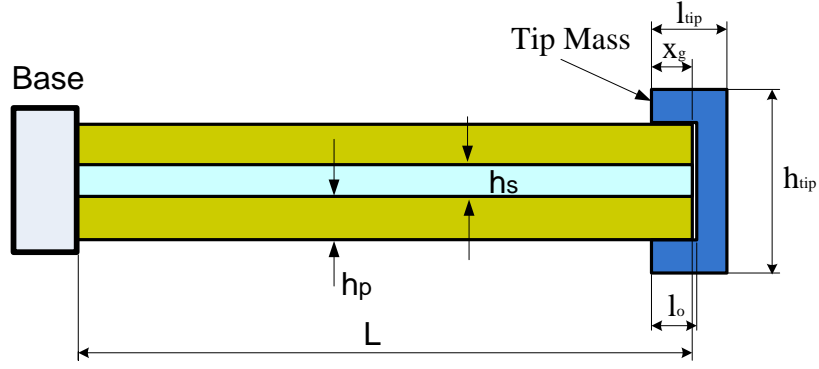
Figure 4.2 Piezoelectric Bimorph Beam with a Tip Mass

The general stress field terms and displacement fields from the infinitesimal beam element can be stated as functions with respect to the x direction on the face of an infinitesimal element as,

$$\sigma_A = \sigma(x) \qquad u_A = u(x) \ . \qquad (4.21)$$

Each element face has a stress vector term. Thus terms, $\sigma_A = \sigma(x)$ and $u_A = u(x)$, applied to the element face on the x direction and allowing for the deformed infinitesimal element results in $\sigma = \sigma(x + dx/2)$ and $\sigma = \sigma(x - dx/2)$ in the opposite direction. Introducing the change of displacement vector $u = u(x + dx/2)$ and $u = u(x - dx/2)$ into the element face on the x direction will result in a stress field. Taylor's series can be used to consider the change of stress field and vector displacement,

$$\sigma_A = \sigma_{xx} + \frac{d\sigma_{xx}}{dx}\frac{dx}{2} \qquad u_A = u_x + \frac{du_x}{dx}\frac{dx}{2} \ , \qquad (4.22)$$

$$\sigma_B = \sigma_{xx} - \frac{d\sigma_{xx}}{dx}\frac{dx}{2} \qquad u_B = u_x - \frac{du_x}{dx}\frac{dx}{2} \ . \qquad (4.23)$$

The changes of stress field and displacement vector for each face of the infinitesimal element in x direction are further formulated by applying Hamiltonian's theorem for potential energy to give,

$$\int_{t_1}^{t_2} \delta PE dt = \int_{t_1}^{t_2} \sigma_A dydz\delta u_A dt - \int_{t_1}^{t_2} \sigma_B dydz\delta u_B dt \ . \qquad (4.24)$$

Corresponding to Eqs. (4.22) and (4.23), equation (4.24) can be reformulated as,

$$\int_{t_1}^{t_2} \delta PE dt = \int_{t_1}^{t_2}\int_{\Gamma}\left(\sigma_{xx} + \frac{d\sigma_x}{dx}\frac{dx}{2}\right)\delta\left(u_x + \frac{u_x}{dx}\frac{dx}{2}\right)dydzdt$$

$$-\int\limits_{t_1}^{t_2}\int\limits_{\Gamma}\left(\sigma_{xx}-\frac{\mathrm{d}\sigma_x}{\mathrm{d}x}\frac{\mathrm{d}x}{2}\right)\delta\left(u_x-\frac{\mathrm{d}u_x}{\mathrm{d}x}\frac{\mathrm{d}x}{2}\right)\mathrm{d}y\mathrm{d}z\mathrm{d}t \ . \tag{4.25}$$

Modifying the differential displacement vector from Eq. (4.25) using the total partial differential, gives,

$$\delta u_A \to \delta u_A = \delta\left(u_x+\frac{\mathrm{d}u_x}{\mathrm{d}x}\frac{\mathrm{d}x}{2}\right) = \delta u_x+\frac{1}{2}\delta\left(\frac{\mathrm{d}u_x}{\mathrm{d}x}\right)\mathrm{d}x+\frac{1}{2}\mathrm{d}u_x\delta(\mathrm{d}x) \ ,$$

If $\delta(\mathrm{d}x)$ is too small, differential displacement vector terms can be restated as,

$$\delta u_A = \delta u_x+\frac{1}{2}\delta\left(\frac{\mathrm{d}u_x}{\mathrm{d}x}\right)\mathrm{d}x \ . \tag{4.26}$$

Performing the same operation on δu_B gives,

$$\delta u_B = \delta u_x-\frac{1}{2}\delta\left(\frac{\mathrm{d}u_x}{\mathrm{d}x}\right)\mathrm{d}x \ . \tag{4.27}$$

Modifying the differential displacement vector from Eq. (4.25) using Eqs. (4.26) and (4.27) gives,

$$\int\limits_{t_1}^{t_2}\delta PE\mathrm{d}t = \int\limits_{t_1}^{t_2}\int\limits_{\Gamma}\left(\sigma_{xx}+\frac{\mathrm{d}\sigma_{xx}}{\mathrm{d}x}\frac{\mathrm{d}x}{2}\right)\left(\delta u_x+\frac{1}{2}\delta\left(\frac{\mathrm{d}u_x}{\mathrm{d}x}\right)\mathrm{d}x\right)\mathrm{d}y\mathrm{d}z\mathrm{d}t$$

$$-\int\limits_{t_1}^{t_2}\int\limits_{\Gamma}\left(\sigma_{xx}-\frac{\mathrm{d}\sigma_x}{\mathrm{d}x}\frac{\mathrm{d}x}{2}\right)\left(\delta u_x-\frac{1}{2}\delta\left(\frac{\mathrm{d}u_x}{\mathrm{d}x}\right)\mathrm{d}x\right)\mathrm{d}y\mathrm{d}z\mathrm{d}t \ . \tag{4.28}$$

Manipulating Eq. (4.28) provides

$$\int\limits_{t_1}^{t_2}\delta PE\mathrm{d}t = \int\limits_{t_1}^{t_2}\int\limits_{\Gamma}\left(\sigma_{xx}.\delta\varepsilon_{xx}+\frac{\mathrm{d}\sigma_{xx}}{\mathrm{d}x}.\delta u_x\right)\mathrm{d}x\,\mathrm{d}y\mathrm{d}z\mathrm{d}t \ . \tag{4.29}$$

It should be noted that $\mathrm{d}\sigma_{xx}/\mathrm{d}x = 0$ using the first Newton' Law, giving,

$$\left(\sigma_{xx}+\frac{\mathrm{d}\sigma_{xx}}{\mathrm{d}x}\frac{\mathrm{d}x}{2}\right)\mathrm{d}y\mathrm{d}z-\left(\sigma_{xx}-\frac{\mathrm{d}\sigma_{xx}}{\mathrm{d}x}\frac{\mathrm{d}x}{2}\right)\mathrm{d}y\mathrm{d}z = 0 \ . \tag{4.30}$$

As expected, $\mathrm{d}\sigma_{xx}/\mathrm{d}x = 0$ after manipulating Eq. (4.30). As a result, equation (4.29) represents the energy field in stress form multiplied by the differential (virtual) strain field to give the potential energy form with time based on the Hamiltonian theorem as follows,

$$\int\limits_{t_1}^{t_2}\delta PE\mathrm{d}t = \int\limits_{t_t}^{t_2}\int\limits_{\Gamma}\sigma_{xx}\delta\varepsilon_{xx}\mathrm{d}\Gamma\mathrm{d}t \ ,$$

where,
$$\int_{t_1}^{t_2} \delta PE \mathrm{d}t = \int_{t_1}^{t_2} \left(\delta PE^{subs} + \delta PE^{p} \right) \mathrm{d}t . \tag{4.31}$$

It should be noted that the piezoelectric bimorph has three layers, the upper and lower layers consisting of piezoelectric material with a centre brass shim. The three stress fields operate within these layers. Thus, equation (4.31) can be modified as,

$$\int_{t_1}^{t_2} \delta PE \mathrm{d}t = \int_{t_1}^{t_2} \int_{\Omega} \left(N_{xx} \delta \varepsilon_1^{(0)} - M_{xx} \delta \varepsilon_1^{(1)} - P_{xx}^{(0)} \delta \varepsilon_1^{(0)} + P_{xx}^{(1)} \delta \varepsilon_1^{(1)} \right) \mathrm{d}x \mathrm{d}y \mathrm{d}t . \tag{4.32}$$

Applying Eq. (4.14) into Eq. (4.32) to obtain the differential strain field, gives,

$$\int_{t_1}^{t_2} \delta PE \mathrm{d}t = \int_{t_1}^{t_2} \int_{\Omega} \left[N_{xx} \delta \left(\frac{\partial u_{rel}}{\partial x} \right) - M_{xx} \delta \left(\frac{\partial^2 w_{rel}}{\partial x^2} \right) - P_{xx}^{(o)} \delta \left(\frac{\partial u_{rel}}{\partial x} \right) + P_{xx}^{(1)} \delta \left(\frac{\partial^2 w_{rel}}{\partial x^2} \right) \right] \mathrm{d}x \mathrm{d}y \mathrm{d}t . \tag{4.33}$$

The in-plane force resultants per unit width for each layer are formulated as,

$$N_{xx} = \int_{-h_p - \frac{h_s}{2}}^{-\frac{h_s}{2}} \sigma_{xx}^{(pl)} \mathrm{d}z + \int_{-\frac{h_s}{2}}^{\frac{h_s}{2}} \sigma_{xx}^{(sm)} \mathrm{d}z + \int_{\frac{h_s}{2}}^{h_p + \frac{hs}{2}} \sigma_{xx}^{(pt)} \mathrm{d}z . \tag{4.34}$$

The in-plane moment resultants per unit width for each layer are formulated as,

$$M_{xx} = \int_{-h_p - \frac{h_s}{2}}^{-\frac{h_s}{2}} z \sigma_{xx}^{(pl)} \mathrm{d}z + \int_{-\frac{h_s}{2}}^{\frac{h_s}{2}} z \sigma_{xx}^{(sm)} \mathrm{d}z + \int_{\frac{h_s}{2}}^{h_p + \frac{hs}{2}} z \sigma_{xx}^{(pt)} \mathrm{d}z . \tag{4.35}$$

The in-plane force and moment resultants represent the longitudinal extension field and transverse bending field respectively of the piezoelectric bimorph. Superscripts *pl, sm* and *pt* indicate the lower layer of piezoelectric, brass centre shim and upper layer of piezoelectric element respectively. Moreover, the in-plane force resultants due to the electric component of the piezoelectric bimorph are invoked as,

$$P_{xx}^{(o)} = \int_{-h_p - \frac{h_s}{2}}^{-\frac{h_s}{2}} e_{31}^{(pl)} E_z^{(pl)} \mathrm{d}z + \int_{\frac{h_s}{2}}^{hp + \frac{h_s}{2}} e_{31}^{(pt)} E_z^{(pt)} \mathrm{d}z . \tag{4.36}$$

The in-plane moment resultant due to the electric component of the piezoelectric bimorph can be formulated as,

$$P_{xx}^{(1)} = \int_{-h_p - \frac{h_s}{2}}^{-\frac{h_s}{2}} z e_{31}^{(pl)} E_z^{(pl)} \mathrm{d}z + \int_{\frac{h_s}{2}}^{hp + \frac{h_s}{2}} z e_{31}^{(pt)} E_z^{(pt)} \mathrm{d}z . \tag{4.37}$$

Since the piezoelectric bimorph couples the mechanical and electrical terms, equation (4.33) is the integro-differential equations with base elastic-electric field. By considering Eq. (4.33), each term inside the bracket can be formulated separately as follows,

$$N_{xx} = C_{11}^{(D,k)}\varepsilon_1^{(0)} - C_{11}^{(E,k)}\varepsilon_1^{(1)} \ , \ M_{xx} = C_{11}^{(E,k)}\varepsilon_1^{(0)} - C_{11}^{(F,k)}\varepsilon_1^{(1)} \ , \ P_{xx}^{(0)} = R_{31}^{(G,k)}v(t) \ , \ P_{xx}^{(1)} = R_{31}^{(H,k)}v(t).\text{(4.38)}$$

Corresponding to Eq. (4.38), equation (4.33) can be reformulated as,

$$\int_{t_1}^{t_2}\delta PE\mathrm{d}t = \int_{t_1}^{t_2}\int_{\Omega}\left[\left(C_{11}^{(D,k)}\varepsilon_{xx}^{(0)} - C_{11}^{(E,k)}\varepsilon_{xx}^{(1)}\right)\delta\left(\frac{\partial u_{rel}}{\partial x}\right) - \left(C_{11}^{(E,k)}\varepsilon_{xx}^{(0)} - C_{11}^{(F,k)}\varepsilon_{xx}^{(1)}\right)\delta\left(\frac{\partial^2 w_{rel}}{\partial x^2}\right)\right.$$
$$\left. - R_{31}^{(G,k)}v(t)\delta\left(\frac{\partial u_{rel}}{\partial x}\right) + R_{31}^{(H,k)}v(t)\delta\left(\frac{\partial^2 w_{rel}}{\partial x^2}\right)\right]\mathrm{d}x\mathrm{d}y\mathrm{d}t . \qquad (4.39)$$

Superscripts *D, E, F, G* and *H* indicate the properties of stiffness coefficients for longitudinal extension, extensional-bending stiffness and transverse bending, backward piezoelectric couplings for longitudinal extension and transverse bending respectively. The coefficients C_{11} and R_{31} indicate the stiffness coefficients and backward piezoelectric couplings, respectively and superscript *k* indicates layers of the bimorph. It is noted that these coefficients will be further discussed in the next stage.

The potential energy from Eq. (4.39) for Hamiltonian's theorem can be manipulated as,

$$\int_{t_1}^{t_2}\delta PE\mathrm{d}t = \int_{t_1}^{t_2}\left[\int_{\Omega}\left\{C_{11}^{(D,k)}\varepsilon_1^{(0)}\frac{\partial\delta u_{rel}}{\partial x} + C_{11}^{(F,k)}\varepsilon_1^{(1)}\frac{\partial^2\delta w_{rel}}{\partial x^2} - R_{31}^{(G,k)}v(t)\frac{\partial\delta u_{rel}}{\partial x} + R_{31}^{(H,k)}v(t)\frac{\partial^2\delta w_{rel}}{\partial x^2}\right\}\mathrm{d}\Omega\right]\mathrm{d}t .\text{(4.40)}$$

Modifying Eq. (4.40) by applying the variational lemma and divergence theorem gives,

$$\int_{t_2}^{t_2}\delta PE\mathrm{d}t = \int_{t_2}^{t_2}\left[\int_{\Omega}\left\{-C_{11}^{(D,k)}\frac{\partial\varepsilon_1^{(0)}}{\partial x}\delta u_{rel} + C_{11}^{(F,k)}\frac{\partial^2\varepsilon_1^{(1)}}{\partial x^2}\delta w_{rel} + R_{31}^{(G,k)}\frac{\partial v}{\partial x}\delta u_{rel} + R_{31}^{(H,k)}\frac{\partial^2 v}{\partial x^2}\delta w_{rel}\right\}\mathrm{d}x\mathrm{d}y\right.$$
$$+ \oint_S n_x N_{xx}^{(D,k)}\delta u_{rel}\mathrm{d}S - \oint_S n_x\frac{\partial M_{xx}^{(F,k)}}{\partial x}\delta w_{rel}\mathrm{d}S + \oint_s n_x M_{xx}^{(F,k)}\frac{\partial\delta w_{rel}}{\partial x}\mathrm{d}S - \oint_s n_x R_{31}^{(G,k)}v\delta u_{rel}\mathrm{d}S$$
$$\left. - \oint_S n_x R_{31}^{(H,k)}\frac{\partial v}{\partial x}\delta w_{rel}\mathrm{d}S + \oint_S n_x R_{31}^{(H,k)}v\frac{\partial\delta w_{rel}}{\partial x}\mathrm{d}S\right]\mathrm{d}t . \qquad (4.41)$$

The elastic stiffness coefficients of the piezoelectric bimorph C_{11} are formulated according to the characteristic material properties and the cross section of each layer of bimorph to give,

$$\forall C_{11}^{(n,k)} \in \left[\sum_{k=1}^{3} \int_{h_k}^{h_{k+1}} \overline{Q}_{11}^{(D,k)} \mathrm{d}z \ , \ \sum_{k=1}^{3} \int_{h_k}^{h_{k+1}} z\overline{Q}_{11}^{(E,k)} \mathrm{d}z \ , \ \sum_{k=1}^{3} \int_{h_k}^{h_{k+1}} z^2 \overline{Q}_{11}^{(F,k)} \mathrm{d}z \right] \ , \ \forall k \subset n \in \{D,E,F\}. \quad (4.42)$$

Parameter $\overline{Q}_{11}$ represents the plane stress-based elastic stiffness of the bimorph beam. Each stiffness coefficient can be expanded through the boundary value dimensions of the bimorph. In this case, each layer has three different stiffness coefficients depending on the thickness and material, $k \subset n \in \mathrm{R}^3 \to \mathrm{R}$ for each layer in differential volume domain $\mathrm{d}\Gamma \subset \mathrm{R}^3$ because the thickness is a subset of $\mathrm{d}\Gamma$. The piezoelectric bimorph considered here has symmetrical geometry with the same material used for the upper and lower layers with a centre brass shim. The extensional stiffness coefficient of the interlayer of the piezoelectric bimorph can then be written as,

$$C_{11}^{(D,k)} = h_p \overline{Q}_{11}^{(D,1)} + h_s \overline{Q}_{11}^{(D,2)} + h_p \overline{Q}_{11}^{(D,3)} \quad . \quad (4.43)$$

As $\overline{Q}_{11}^{(D,1)} = \overline{Q}_{11}^{(D,3)}$, the extensional stiffness coefficient from Eq. (4.42) can be reformulated as,

$$C_{11}^{(D,k)} = 2h_p \overline{Q}_{11}^{(D,1)} + h_s \overline{Q}_{11}^{(D,2)} \quad , \quad (4.44)$$

The extensional-bending stiffness coefficient from Eq. (4.42) can also be formulated as,

$$C_{11}^{(E,k)} = -\left(\frac{h_p^2}{2} + \frac{h_p h_s}{2} \right) \overline{Q}_{11}^{(E,1)} + \left(\frac{h_p^2}{2} + \frac{h_p h_s}{2} \right) \overline{Q}_{11}^{(E,3)} \quad . \quad (4.45)$$

It is found that the extensional-bending stiffness coefficient $C_{11}^{(E,k)}$ tends to be zero due to the symmetrical geometry and material of the bimorph element structure. This gives,

$$\overline{Q}_{11}^{(E,1)} = \overline{Q}_{11}^{(E,3)} \quad .$$

Because the upper layer of the piezoelectric element has the same material and properties as the lower layer, the extensional-bending coefficient can be stated as,

$$C_{11}^{(E,k)} = 0 \quad . \quad (4.46)$$

Therefore, the coefficient $C_{11}^{(E,k)}$ is not shown from Eq. (4.40). Furthermore, the bending stiffness coefficient can be formulated as,

$$C_{11}^{(F,k)} = \left(-\frac{h_s^3}{24} - \frac{1}{3}\left(-h_p - \frac{h_s}{2}\right)^3\right)\overline{Q}_{11}^{(F,1)} + \frac{h_s^3}{4}\overline{Q}_{11}^{(F,2)} + \left(\frac{1}{3}\left(h_p + \frac{h_s}{2}\right)^3 - \frac{h_s^3}{24}\right)\overline{Q}_{11}^{(F,3)} .\text{(4.47)}$$

$\overline{Q}_{11}^{(F,1)}$ and $\overline{Q}_{11}^{(F,3)}$ have the same material located in the lower and upper piezoelectric layers, respectively, thus $\overline{Q}_{11}^{(F,1)} = \overline{Q}_{11}^{(F,3)}$. Equation (4.47) can then be reformulated as,

$$C_{11}^{(F,k)} = \left(\frac{2}{3}\left(h_p + \frac{h_s}{2}\right)^3 - \frac{h_s^3}{12}\right)\overline{Q}_{11}^{(F,1)} + \frac{h_s^3}{4}\overline{Q}_{11}^{(F,2)} . \tag{4.48}$$

It should be noted that $\overline{Q}_{11}^{(D,1)} = \overline{Q}_{11}^{(D,3)} = \overline{Q}_{11}^{(F,1)} = \overline{Q}_{11}^{(F,3)}$ and $\overline{Q}_{11}^{(D,2)} = \overline{Q}_{11}^{(F,2)}$ indicate the plane stress-based elastic stiffness at constant electric field for piezoelectric material and plane stress-based elastic stiffness for brass material, respectively.

Moreover, the second coefficient R_{31} from Eq. (4.41), known as the backward piezoelectric coupling, will be discussed in terms of series and parallel connections of the piezoelectric bimorph. *It is noted that the direct effect of the piezoelectric element, developed in potential form, indicates the backward piezoelectric coupling whereas the converse effect of the piezoelectric element gives the forward piezoelectric coupling which develops electrical energy as discussed in the forthcoming section. As the piezoelectric behaviour is reversible, the forward piezoelectric couplings have the same values as the backward piezoelectric couplings.* This indicates that the piezoelectric couplings are affected by the electrical force and moment of the piezoelectric layers which depend on the strain fields and the polarity-electric field. Many researchers only showed the effects of transverse strain and polarity-electric field based on one input transverse base motion in terms of series and parallel connections, [4,6,7,8,9,41]. However, they still did not give detailed information and formulation of the piezoelectric coupling of the dynamic system. It should be noted that this affects all formulations of the constitutive dynamics equations. The focus here is with the piezoelectric bimorph beam with two input base transverse and longitudinal motions. In this section, the piezoelectric coupling associated with series and parallel connections will be

discussed in detail and new techniques of formulating the piezoelectric coupling will also be given. The electric field of the piezoelectric bimorph depends on the positive and negative terminals located at the lower and upper surfaces of the piezoelectric element, respectively. Each connection (the series and parallel connections) can be arranged into two types of poled configurations i.e. X-poled and Y-Poled which depends on the direction of polarities and strain effect between the piezoelectric benders $k \in \{1,3\}$ (upper element and lower element). As considered previously, the piezoelectric bimorph is not only assumed to undergo pure transverse bending but it also undergoes additional deformation i.e. longitudinal extension form, which is reflected in the strain fields of the Euler-Bernoulli's beam expression. Therefore, such situation will affect the polarisation of the piezoelectric bimorph which depends on strain at the lower and upper layers due to input mechanical vibration and also the chosen type of connections. At this point, when the piezoelectric element was *initially* undefomed, the polarisation direction, for example, was in the z-axis called the initial polarized state. When the tensile stress acts perpendicular to the z-axis on the element, the polarisation will behave in the opposite direction to the z-axis as shown in Figure 4.3. Conversely, when the piezoelectric element was under compressive stress perpendicular with the z-axis, the polarisation will be in the same direction with the z-axis, [96]. This means that the change of stress from tensile to compressive or vice versa in the piezoelectric element will result in a *reversal* of the direction of polarisation, [73]. This situation is known as the direct piezoelectric effect where the polarisation is proportional to the stress field and the stress field is also proportional to the strain field or it can be stated in terms of the Einstein's summation convention as $P_i = d_{ij}\sigma_j$. This has been reflected in the electrical enthalpy of the piezoelectric formulation, [75,76]. Based on this case, the piezoelectric bimorph under series and parallel connections can be further considered. For example, in series connection in Figure 4.4, when the piezoelectric element undergoes transverse input base motion, by assumption here, the upper and lower layers of piezoelectric bimorph will respectively deform with the tension and compressive strains and polarisation of the upper layer will create opposite directions compared with the lower layer (X-poled). It should be noted that the polarisation directions affect mathematically the piezoelectric coefficients due to the stress field on the element structure whilst the electric field generates electrical voltage.

Consequently, the electrical moments at both lower and upper layers will be formed. This process occurs continuously when the piezoelectric bimorph beam is under continuous vibration. With the same connection, when the piezoelectric bimorph was under input longitudinal base motion, the upper and lower layers of the bimorph have the same deformation, for example, compressive strain and then the polarisation at the upper and lower layers have the same direction (Y-poled), while the electric field will be generating electric voltage to create the electrical force at both the lower and upper layers. This situation exists when the piezoelectric bimorph beam operates under two input base motions which was considered here mathematically by backward coupling superposition of the elastic-polarity field. Smits and Choi [4] and Smits *et al* [97] discussed the sign conventions of electric field and piezoelectric coefficient for the series and parallel connections. However, their formulations of transverse bending bimorph beam only considered static condition. In this section, the complete piezoelectric couplings due to the effect of electric field and polarity directions are discussed here when the bimorph undergoes two input base motions.
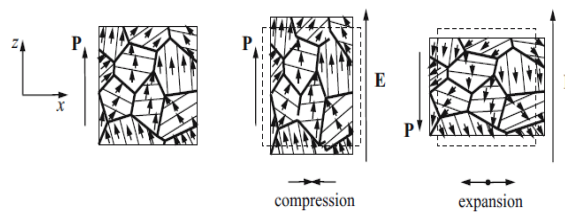
Figure 4.3 The effect of polarisation of Piezoelectric Element, [96]
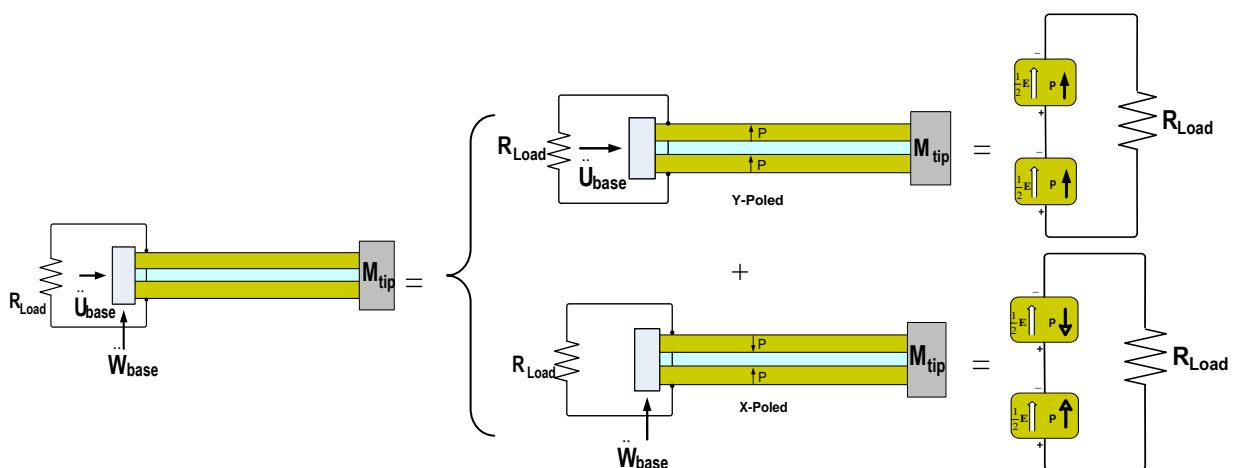
Figure 4.4 Cantilevered piezoelectric bimorph beam with two input base longitudinal and transverse excitations under series connections
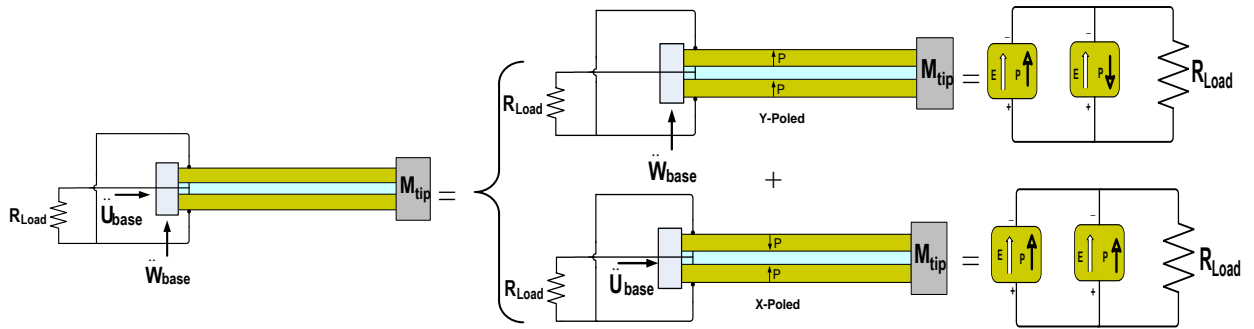
Figure 4.5 Cantilevered piezoelectric bimorph beam with two input base longitudinal and transverse excitations under parallel connections

As shown in Figure 4.5, the piezoelectric bimorph under parallel connection also depends on the input base motions and direction of polarity. The strain fields between the upper and lower layers have similar behaviour with series connection when the piezoelectric bimorph has two input base motions. The difference lies with the polarisation and electric field directions due to the chosen parallel connection of the piezoelectric bimorph. This is achieved at the upper layer of the piezoelectric bimorph under X-poled series connection by applying a strong electric field to direct initial polarisation in the same direction with the lower layer or it can be provided according to the manufacturing company in such a way that the parallel connection can be arranged as shown in Figure 4.5. In this case, the polarisation tends to show the same directions each other when the strains are opposite between the lower and upper layers due to the input transverse base motion. On the other hand, when the piezoelectric bimorph, with same materials, was treated to the input base longitudinal motion as shown in Figure 4.5, two polarisations at the upper and lower layers tend to give opposite directions due to the compressive strains in the piezoelectric elements, respectively.

In this case, the sign conventions of electric field and piezoelectric coefficient needs to be considered for the series and parallel connections under two input base motions. As assumed here, the polarisation indicates the opposite direction with respect to electric field, with the piezoelectric constant having a resulting negative sign and vice versa. Series connection normally has two wires where one wire attaches to the electrode of the lower layer and one wire attaches to the electrode of the upper layer whereas parallel connection normally has three wires where one wire

connects to the centre shim and two wires are located at the electrodes of the lower and upper layers. It is noted that the common piezoelectric constant produced from the manufacturing company is in the form d_{31} but this can be modified by multiplying the plane stress-based elastic stiffness at constant electric field to give $e_{31} = d_{31}\overline{Q}_{11}^E = d_{31}C_{11}^E$. The complete form can be found in appendix A.

Furthermore, the series connection of the piezoelectric bimorph results in the positive sign of electric field at both the lower and upper layers with the same direction as the positive z axis because the piezoelectric bimorph for series connection has a positive terminal at the electrode of the lower layer and a negative terminal at the upper layer. However, the parallel connection indicates a positive sign of the electric field for the lower layer and a negative sign for the upper layer because the piezoelectric bimorph for the parallel connection has a positive terminal at the electrodes of the lower and upper layers and a negative terminal between the centre brass shim. The electric field can be formulated as,

$$E_3^{(n,k)} = -\nabla\varphi(z,t) = \Xi(z)^{(n,k)}v(t) \quad , \tag{4.49}$$

where $\varphi(z,t) = -(-1)^r \Phi(z)v(t)$, $\Xi(z)^{(n,k)} = -(-1)^r \nabla\Phi(z)$.

It is considered here that $\Phi(z)$ represents the shape function of the electric voltage $v(t)$ and it applies to each layer of the piezoelectric bimorph. $\Xi(z)^{(n,k)}$ is the gradient operator of the electric voltage shape function and subscript r refers to 1 or 2 to be used for sign convention. This indicates the change of sign of the electric field due to the terminal connections of the upper and lower electrodes of the piezoelectric bimorph containing the charges normally flowing from positive to negative terminals. The modified piezoelectric constant can be formulated as,

$$\Psi_{31}^{(n,k)} = (-1)^s e_{31}^{(n,k)} \quad . \tag{4.50}$$

As previously discussed for series and parallel connections, the backward piezoelectric coupling will be further discussed including the relationship between the shape function of electric fields and piezoelectric coefficients for each layer.

Superscript s refers to the change of sign of piezoelectric coefficient due to change of polarisation. The equation (4.41) for piezoelectric couplings $R_{31}^{(n,k)}$ can be formulated at each outside layers as,

$$\forall R_{31}^{(n,k)} \in \left[\sum_{k \in p} \int_{h_k}^{h_{k+1}} \Psi_{31}^{(G,k)} \Xi(z)^{(G,k)} dz \quad , \quad \sum_{k \in p} \int_{h_k}^{h_{k+1}} z \Psi_{31}^{(H,k)} \Xi(z)^{(H,k)} dz \right], \forall k \in \{1,3\} \subset n \in \{G,H\}. \quad (4.51)$$

$R_{31}^{(G,k)}$ represents the backward piezoelectric coupling for the longitudinal extension term and $R_{31}^{(H,k)}$ represents the backward piezoelectric coupling for the transverse bending term. As mentioned previously, the backward piezoelectric couplings indicate equal form with the forward piezoelectric couplings where these properties can be shown at forthcoming section for electrical energy form. When the piezoelectric bimorph beam is arranged for series connection, two poled vector configurations apply in the piezoelectric material in the series connection, which is X-poled (opposite direction of polarisation) due to the transverse bending term and Y-poled (same direction of polarisation) due to the extensional term. On the other hand, the parallel connection with the same material can also have two poled effects, Y-poled due to the transverse bending term and X-poled due to the extension term. In this case, a cantilever piezoelectric bimorph with two input excitations was taken into consideration for two connection types i.e. series connection and parallel connection.

Case 1. Series connection. Corresponding to Eq. (4.49), the electric voltage $v(t)$ for series connection is considered to provide half the voltage between the electrodes of the piezoelectric bimorph. This means that the shape function of electric potential will be divided by the factor of two. Therefore, the shape function of the electric potential can be formulated based on the thickness of each layer of the piezoelectric bimorph to give,

$$\Phi(z)_s^{(n,1)} = \frac{-z - \dfrac{h_s}{2}}{2h_p} \quad , \quad -\frac{h_s}{2} - h_p \le z \le -\frac{h_s}{2} \quad ; \quad \Phi(z)_s^{(n,3)} = \frac{z - \dfrac{h_s}{2}}{2h_p} \quad , \quad \frac{h_s}{2} \le z \le \frac{h_s}{2} + h_p. \quad (4.52)$$

a. X-poled due to transverse bending form undergoes the change of sign of the piezoelectric constant where the polarisations in both layers have opposite direction each other. It is noted that only polarisation at bottom layer has the same direction as the electric field in the z direction. Equation (4.51) for transverse effect meets the function of polarisation for each layer $k \in \{1,3\}$ due to the conditions of Eqs. (4.49), (4.50) and (4.52),

$$\left(R_{31}^{(H,k)} \right)_{series} = \left\{ \Psi_{31}^{(H,k)} \Xi(z)^{(H,k)} \middle| \; s = 2, \, r = 2, \forall \, k = 1 \subset n \in H \subset \Omega \times \left[-\frac{h_s}{2} - h_p, -\frac{h_s}{2} \right] \subset \Gamma \right\}, \quad (4.53)$$

$$\left(R_{31}^{(H,k)}\right)_{\text{series}} = \left\{ \Psi_{31}^{(H,k)} \Xi(z)^{(H,k)} \middle| \, s=1, \, r=1, \forall \, k=3 \subset n \in H \subset \Omega \times \left[\frac{h_s}{2}, \frac{h_s}{2}+h_p\right] \subset \Gamma \right\}. \quad (4.54)$$

Backward piezoelectric couplings of the X-poled transverse bending form can be formulated using Eq. (4.51) resulting in,

$$R_{31(\text{series})}^{(H,k)} = -\frac{e_{31}^{(H,1)}}{2h_p}\left(\frac{h_p^{\,2}}{2}+\frac{h_p h_s}{2}\right) - \frac{e_{31}^{(H,3)}}{2h_p}\left(\frac{h_p^{\,2}}{2}+\frac{h_p h_s}{2}\right) = -\frac{e_{31}}{h_p}\left(\frac{h_p^{\,2}}{2}+\frac{h_p h_s}{2}\right). \quad (4.55)$$

b. Y-poled due to longitudinal extension form does not undergo the change of sign of piezoelectric constant because the polarisations in both layers have the same direction as the electric field. Equation (4.51) for longitudinal effect meets the function of polarisation for each layer due to the condition of Eqs. (4.49), (4.50) and (4.52),

$$\left(R_{31}^{(G,k)}\right)_{\text{series}} = \left\{ \Psi_{31}^{(G,k)} \Xi(z)^{(G,k)} \middle| \, s=2, r=2, \forall \, k=1 \subset n \in G \subset \Omega \times \left[-\frac{h_s}{2}-h_p, -\frac{h_s}{2}\right] \subset \Gamma \right\}, \quad (4.56)$$

$$\left(R_{31}^{(G,k)}\right)_{\text{series}} = \left\{ \Psi_{31}^{(G,k)} \Xi(z)^{(G,k)} \middle| \, s=2, \, r=1, \forall \, k=3 \subset n \in G \subset \Omega \times \left[\frac{h_s}{2}, \frac{h_s}{2}+h_p\right] \subset \Gamma \right\}. \quad (4.57)$$

Backward piezoelectric couplings of the Y-poled longitudinal extension can be formulated using Eq. (4.51) resulting in,

$$R_{31(\text{series})}^{(G,k)} = \frac{h_p e_{31}^{(G,1)}}{2h_p} + \frac{h_p e_{31}^{(G,3)}}{2h_p} = e_{31} \qquad . \qquad (4.58)$$

Case 2. Parallel connection. The electric voltage $v(t)$ for parallel connection is considered to give one voltage between the electrodes of the piezoelectric bimorph. This means that the shape function of the electric potential is divided by a factor of one. Therefore, the shape function of electric potential can be formulated based on the thickness of each layer of the piezoelectric bimorph, to give,

$$\Phi(z)_p^{(n,1)} = \frac{-z-\dfrac{h_s}{2}}{h_p} \quad, \quad -\frac{h_s}{2}-h_p \leq z \leq -\frac{h_s}{2} \; ; \; \Phi(z)_p^{(n,3)} = \frac{z-\dfrac{h_s}{2}}{h_p} \quad, \quad \frac{h_s}{2} \leq z \leq \frac{h_s}{2}+h_p. \quad (4.59)$$

a. X-poled due to longitudinal extension form undergoes the change of sign of the piezoelectric constant where the polarisations has opposite direction. The polarisation in the lower layer is in the same direction as the electric field in the z direction which gives a positive sign of the piezoelectric coefficient. However, the upper layer has the electric field in the opposite sign with global direction of electric field in the z direction, thus resulting in a negative sign of the piezoelectric

coefficient. Equation (4.51) for longitudinal effect meets the function of polarisation for each layer due to the condition of Eqs. (4.49), (4.50) and (4.59),

$$\left(R_{31}^{(G,k)}\right)_{\text{parallel}} = \left\{ \Psi_{31}^{(G,k)} \Xi(z)^{(G,k)} \mid s = 2,\ r = 2, \forall\ k = 1 \subset n \in G \subset \Omega \times \left[-\frac{h_s}{2} - h_p, -\frac{h_s}{2} \right] \subset \Gamma \right\}, \quad (4.60)$$

$$\left(R_{31}^{(G,k)}\right)_{\text{parallel}} = \left\{ \Psi_{31}^{(G,k)} \Xi(z)^{(G,k)} \mid s = 1,\ r = 2, \forall\ k = 3 \subset n \in G \subset \Omega \times \left[\frac{h_s}{2}, \frac{h_s}{2} + h_p \right] \subset \Gamma \right\}. \quad (4.61)$$

Backward piezoelectric coupling of the X-poled longitudinal extension can be formulated using Eq. (4.51) resulting in,

$$R_{31(\text{parallel})}^{(G,k)} = e_{31}^{(G,1)} + e_{31}^{(G,3)} = 2e_{31}. \quad (4.62)$$

b. Y-poled due to transverse bending form does not undergo the change of sign of piezoelectric constant where the polarisations in both layers have the same direction as the global direction of the electric field in the z direction. It should be noted that the electric field at the upper layer has opposite sign with the global direction of the electric field in the z direction, therefore; a negative electric field at upper layer is applied. The backward piezoelectric coefficients in both layers have conditions as,

$$\left(R_{31}^{(H,k)}\right)_{\text{parallel}} = \left\{ \Psi_{31}^{(H,k)} \Xi(z)^{(H,k)} \mid s = 2,\ r = 2, \forall\ k = 1 \subset n \in H \subset \Omega \times \left[-\frac{h_s}{2} - h_p, -\frac{h_s}{2} \right] \subset \Gamma \right\}, \quad (4.63)$$

$$\left(R_{31}^{(H,k)}\right)_{\text{parallel}} = \left\{ \Psi_{31}^{(H,k)} \Xi(z)^{(H,k)} \mid s = 2,\ r = 2, \forall\ k = 3 \subset n \in H \subset \Omega \times \left[\frac{h_s}{2}, \frac{h_s}{2} + h_p \right] \subset \Gamma \right\}. \quad (4.64)$$

Backward piezoelectric coupling of the Y-poled transverse bending form can be formulated using Eq. (4.51) resulting in,

$$R_{31(\text{parallel})}^{(H,k)} = -\frac{e_{31}^{(H,1)}}{h_p}\left(\frac{h_p^2}{2} + \frac{h_p h_s}{2} \right) - \frac{e_{31}^{(H,3)}}{h_p}\left(\frac{h_p^2}{2} + \frac{h_p h_s}{2} \right) = -\frac{2e_{31}}{h_p}\left(\frac{h_p^2}{2} + \frac{h_p h_s}{2} \right). \quad (4.65)$$

Furthermore, kinetic energy of the piezoelectric bimorph is considered according to the displacement vectors from Eqs. (4.5) and (4.6) and the density of the piezoelectric bimorph. This concept is further expanded using the Hamiltonian's principle. It should be noted that the kinetic energy term of the piezoelectric bimorph not only represents the initial kinetic energies due to the zero-th mass moment of inertia but also rotary kinetic energy due to the second mass moment of inertia (rotary inertia). In addition, kinetic energy from the tip mass is also considered by two types of energies i.e. initial kinetic energy due to zero-th mass moment of inertia and rotary kinetic energy due to rotary inertia. Two rotary inertias exist in the

piezoelectric bimorph with a tip mass. As mentioned previously, the piezoelectric bimorph was under two base excitations, therefore; the potential energies present due to existing relative displacement $(u_{rel}),(w_{rel})$ which is prescribed as the absolute displacement, $(u_{abs}),(w_{abs})$ relative to base displacement $(u_{base}),(w_{base})$. Therefore, the strain field can be expressed in terms of the relative field motion. The kinetic energy can be written in terms of the absolute displacements, $(u_{abs}),(w_{abs})$ because absolute displacement of beam element moves from its static condition to form the characteristic motion over the time interval t. Therefore, the constitutive kinetic energy equations needs to be defined in terms of the relative velocity $(\dot{u}_{rel})$ and $(\dot{w}_{rel})$ and base velocity $(\dot{u}_{base})$ and $(\dot{w}_{base})$. At this point, the absolute velocity for longitudinal motion is $\dot{u}_{rel} + \dot{u}_{base}$ and absolute velocity for transverse motion is $\dot{w}_{rel} + \dot{w}_{base}$ as depicted in Figure 4.1. Corresponding with Eqs. (4.5) and (4.6), the kinetic energy can be formulated based on the mass density of piezoelectric bimorph and density of tip mass as,

$$
\begin{aligned}
\int_{t_1}^{t_2} \delta KE \mathrm{d}t = \int_{t_1}^{t_2} & \left[\int_{\Gamma} \left\{ \rho \left(\dot{u}_{rel}\mathbf{e_1} + \dot{u}_{base}\mathbf{e_1} - \frac{\partial \dot{w}_{rel}}{\partial x}\mathbf{e_2} \times z\,\mathbf{e_3} \right) \bullet \delta \left(\dot{u}_{rel}e_1 + \dot{u}_{base}\mathbf{e_1} - \frac{\partial \dot{w}_{rel}}{\partial x}\mathbf{e_2} \times z\,\mathbf{e_3} \right) \right. \right. \\
& + \rho(\dot{w}_{base}+\dot{w}_{rel})\mathbf{e_3} \bullet \delta(\dot{w}_{base}+\dot{w}_{rel})\mathbf{e_3} + \rho_{tip}\left(\dot{u}_{rel}(L)\mathbf{e_1} + \dot{u}_{base}\mathbf{e_1} - z\frac{\partial \dot{w}_{rel}}{\partial x}(L)\mathbf{e_2} \times \left(x_{gm}\mathbf{e_1}+z_{gm}\mathbf{e_3}\right) \right) \\
& \bullet \delta \left(\dot{u}_{rel}(L)\mathbf{e_1} + \dot{u}_{base}\mathbf{e_1} - \frac{\partial \dot{w}_{rel}}{\partial x}(L)\mathbf{e_2} \times \left(x_{gm}\mathbf{e_1}+z_{gm}\mathbf{e_3}\right) \right) \\
& \left. \left. + \rho_{tip}(\dot{w}_{base}(L)\mathbf{e_1}+\delta\dot{w}_{rel}(L)\mathbf{e_1}) \bullet \delta(\dot{w}_{base}(L)\mathbf{e_1}+\delta\dot{w}_{rel}(L)\mathbf{e_1}) \right\} \mathrm{d}\Gamma \right] \mathrm{d}t .
\end{aligned}
\tag{4.66}
$$

It should be noted that symbol ($\bullet$) indicates dot product. In terms of Eq. (4.18), the parameter of virtual relative velocity from Eq. (4.66) will meet the conditions of continuity and differentiability over the length of the bimorph. Each energy term from Hamiltonian's principle will be arranged in the next section. Modifying Eq. (4.66) by multiplying each term in the parenthesis and integrating with respect to z gives,

$$
\begin{aligned}
\int_{t_1}^{t_2} \delta KE \mathrm{d}t = \int_{t_1}^{t_2} & \left[\int_{\Omega} \left\{ I^{(A,k)}\dot{u}_{rel}\delta\dot{u}_{rel} + I^{(C,k)}\left(\frac{\partial \dot{w}_{rel}}{\partial x}\right)\delta\left(\frac{\partial \dot{w}_{rel}}{\partial x}\right) + I^{(A,k)}\dot{u}_{base}\delta\dot{u}_{rel} - I^{(B,k)}\dot{u}_{rel}\delta\left(\frac{\partial \dot{w}_{rel}}{\partial x}\right) \right. \right. \\
& \left. - I^{(B,k)}\dot{u}_{base}\delta\left(\frac{\partial \dot{w}_{rel}}{\partial x}\right) - I^{(B,k)}\frac{\partial \dot{w}_{rel}}{\partial x}\delta\dot{u}_{rel} + I^{(A,k)}\dot{w}_{rel}\delta\dot{w}_{rel} + I^{(A,k)}\dot{w}_{base}\delta\dot{w}_{rel} \right\} \mathrm{d}x\mathrm{d}y
\end{aligned}
$$

$$+ I_{tip}^{(A)} \ddot{u}_{rel}(L) \delta \dot{u}_{rel}(L) + I_{tip}^{(C)} \left(\frac{\partial \dot{w}_{rel}(L)}{\partial x} \right) \delta \left(\frac{\partial \dot{w}_{rel}(L)}{\partial x} \right) + I_{tip}^{(A)} \ddot{u}_{base}(L) \delta \dot{u}_{rel}(L)$$

$$- I_{tip}^{(B)} \frac{\partial \dot{w}_{rel}}{\partial x}(L) \delta \ddot{u}_{rel}(L) - I_{tip}^{(B)} \ddot{u}_{rel}(L) \delta \left(\frac{\partial \dot{w}_{rel}}{\partial x}(L) \right) - I_{tip}^{(B)} \ddot{u}_{base}(L) \delta \left(\frac{\partial \dot{w}_{rel}}{\partial x}(L) \right)$$

$$+ I_{tip}^{(A)} \ddot{w}_{rel}(L) \delta \dot{w}_{rel}(L) + I_{tip}^{(A)} \ddot{w}_{base}(L) \delta \dot{w}_{rel}(L) \Big] dt \quad . \tag{4.67}$$

The inertia mass per unit area is formulated according with the characteristic materials and the cross sectional of each layer of bimorph,

$$\forall I^{(n,k)} \in \left[\sum_{k=1}^{3} \int_{h_k}^{h_{k+1}} \rho^{(A,k)} dz \ , \ \sum_{k=1}^{3} \int_{h_k}^{h_{k+1}} z \rho^{(B,k)} dz \ , \ \sum_{k=1}^{3} \int_{h_k}^{h_{k+1}} z^2 \rho^{(C,k)} dz \right], \ \forall k \subset n \in \{A,B,C\}. \tag{4.68}$$

Each inertia mass can be expanded through the boundary values of dimensions of the bimorph. Superscript n and k indicate the mass density and layer, respectively. In this case, each layer has three different terms of inertia mass depending on the thickness and material, $k \subset n \in \mathbb{R}^3 \to \mathbb{R}$ for each layer in the domain $d\Gamma \in \mathbb{R}^3$ where the thickness is a subset of $d\Gamma$. However, the piezoelectric bimorph has the symmetrical geometry with the same material and thickness in the upper and lower layers with the centre brass shim. The zero-th mass moment of inertia per unit area gives the relationship of the interlayer piezoelectric bimorph as,

$$I^{(A,k)} = h_p \rho^{(A,1)} + h_s \rho^{(A,2)} + h_p \rho^{(A,3)} \quad . \tag{4.69}$$

or it can be simplified to be,

$$I^{(A,k)} = 2h_p \rho^{(A,1)} + h_s \rho^{(A,2)} \quad . \tag{4.70}$$

The densities $\rho^{(A,1)}$ and $\rho^{(A,3)}$ represent the material located within the upper and lower piezoelectric layers respectively which have the same piezoelectric material. The first mass moment of inertia per unit area from Eq. (4.68) can also be formulated as,

$$I^{(B,k)} = -\left(\frac{h_p^{\ 2}}{2} + \frac{h_p h_s}{2} \right) \rho^{(B,1)} + \left(\frac{h_p^{\ 2}}{2} + \frac{h_p h_s}{2} \right) \rho^{(B,3)} \quad . \tag{4.71}$$

The first mass moment of inertia per unit area $I^{(B,k)}$ tends to be zero, since the centroid of the section is located at the neutral axis of the bimorph which has

symmetrical geometry and the same material of the bimorph element structure. It becomes,

$$\rho^{(B,1)} = \rho^{(B,3)} \,, \tag{4.72}$$

The upper layer of the piezoelectric element is assumed to have the same materials as the lower layer, giving the extensional-bending inertia mass resulting as,

$$I^{(B,k)} = 0 \,. \tag{4.73}$$

Furthermore, the second mass moment inertia is formulated as,

$$I^{(C,k)} = \left(-\frac{h_s^3}{24} - \frac{1}{3}\left(-h_p - \frac{h_s}{2} \right)^3 \right)\rho^{C,1} + \frac{h_s^3}{4}\rho^{C,2} + \left(\frac{1}{3}\left(h_p + \frac{h_s}{2} \right)^3 - \frac{h_s^3}{24} \right)\rho^{C,3} \,. \tag{4.74}$$

It should be noted that the third term of mass moment inertia is also known as the rotary inertia. The mass densities $\rho^{(C,1)}$ and $\rho^{(C,3)}$ are assumed to have the same material located on the lower and upper piezoelectric layers, respectively, thus $\rho^{(C,1)} = \rho^{(C,3)}$ for which equation (4.74) is reformulated as,

$$I^{(C,k)} = \left(\frac{2}{3}\left(h_p + \frac{h_s}{2} \right)^3 - \frac{h_s^3}{12} \right)\rho^{(C,1)} + \frac{h_s^3}{4}\rho^{(C,2)} \,. \tag{4.75}$$

Superscripts A and C indicate properties of mass moment of inertia for zero-th and second terms, respectively. In this case, the lower and upper layers indicate the piezoelectric structures for $k = 1$ and $k = 3$, respectively whereas the middle layer for $k = 2$ represents the brass shim of the substructure. It should be noted that $\rho^{(A,1)} = \rho^{(A,3)} = \rho^{(C,1)} = \rho^{(C,3)}$ and $\rho^{(A,2)} = \rho^{(C,2)}$.

A tip mass moment of inertia is also formulated as,

$$\forall I_{tip}^{(m)} \in \left[\int_{\Gamma} \rho_{tip}^{(A)} dxdydz \,, \int_{\Gamma} z\rho_{tip}^{(B)} dxdydz \,, \int_{\Gamma} \left(x_{gm}^2 + z_{gm}^2 \right)\rho_{tip}^{(C)} dxdydz \right] \,, \forall m \in \{A,B,C\}. \tag{4.76}$$

It is noted that the third integral term implies the second mass moment of inertia for the arbitrary geometric shapes where further detail can be found in Beer and Johnston [98]. Figure 4.2 indicated an example geometric shape of the tip mass where the zero-th tip mass moment of inertia is formulated,

$$I_{tip}^{(A)} = \left(h_{tip}l_{tip} - \left(2h_p + h_s \right)l_b \right)s_{tip}\rho_{tip}^{(A)} \,. \tag{4.77}$$

The first mass moment of inertia $I_{tip}^{(B)}$ tends to be zero because the geometric shape only has one centre of gravity where each moment with respect to the centroid has equal magnitude. The second tip mass moment of inertia is known as rotary inertia at the centre of gravity of the tip mass which is assumed to coincide with the end length of the piezoelectric bimorph beam. This results in,

$$I_{tip}^{(C)} = \left\{ \left(\frac{\left(l_{tip}^2 + h_{tip}^2\right)}{12} + \bar{x}_1^2 - \frac{\left(\left(2h_p + h_s\right)^2 + l_b^2\right)}{12} - \bar{x}_2^2 \right) \left(l_{tip}h_{tip} - \left(2h_p + h_s\right)l_b\right) \right\} s_{tip} \rho_{tip}^{(C)} , \quad (4.78)$$

where $\bar{x}_1 = x_g - l_{tip}/2$, $\bar{x}_2 = x_g - l_b/2$ and x_g is centre of gravity of geometry of tip mass. The Hamiltonian's kinetic energy can be reformulated by modifying Eq. (4.67) and integrating with respect to time and applying the divergence theorem to relieve the virtual displacement fields to give,

$$\int_{t_1}^{t_2} \delta KE\mathrm{d}t = \int_{t_1}^{t_2} \left[\int_\Omega \left\{ -I^{(A,k)}\ddot{u}_{rel}\delta u_{rel} + I^{(C,k)}\frac{\partial^2 \ddot{w}_{rel}}{\partial x^2}\delta w_{rel} - I^{(A,k)}\ddot{w}_{rel}\delta w_{rel} \right. \right.$$

$$\left. -I^{(A,k)}\ddot{u}_{base}\delta u_{rel} - I^{(A,k)}\ddot{w}_{base}\delta w_{rel} \right\}\mathrm{d}x\mathrm{d}y - I_{tip}^{(A)}\ddot{u}_{rel}(L)\delta u_{rel}(L)$$

$$- I_{tip}^{(C)}\frac{\partial \ddot{w}_{rel}}{\partial x}(L)\frac{\partial \delta w_{rel}(L)}{\partial c} - I_{tip}^{(A)}\ddot{w}_{rel}(L)\delta w_{rel}(L) - I_{tip}^{(A)}\ddot{u}_{base}(L)\delta u_{rel}(L)$$

$$\left. - I_{tip}^{(A)}\ddot{w}_{base}(L)\delta w_{rel}(L) - \oint_S I^{(C,k)}n_x \frac{\partial \ddot{w}_{rel}}{\partial x}\delta w_{rel}\mathrm{d}S \right]\mathrm{d}t \quad . \quad (4.79)$$

Each of the equation components which have subscript "*base*" at $I^{(A,k)}\ddot{u}_{base}$ and $I^{(A,k)}\ddot{w}_{base}$ can be separated from Eq. (4.79) in order to consider as non-conservative virtual work of the distributed inertia input loads into the base support of the cantilevered piezoelectric bimorph beam. Since the bimorph does not have other external forces except for the input base excitation, the general equation for non-conservative virtual work due to the input excitation and the applied charge can be written as,

$$\delta W_f = -F\delta r - \sum_{i=1} q_i \delta\varphi(t). \quad (4.80)$$

It should be noted that the last term of Eq. (4.80) is considered as the applied charge on the top and bottom electrodes (*i* layers) of the piezoelectric bimorph which depends on the series and parallel connections where the minus sign indicates the electrical work done into the system. Since the bimorph generates the electrical

charge output, the parameter $-\sum_{i=1} q_i \delta\varphi(z,t)$ should indicate positive sign by

modifying $\varphi(z,t)$ with $v(t)$. In this case, the electrical work parameter needs to be proved. As mentioned previously, the electrical boundary condition of the bimorph electric voltage shape function can be used here to identify the electrical work. The electric charge output from the parallel connection can be simply formulated as $q_1 + q_2 = q$ where the bottom and top electrodes are denoted q_1 and q_2, respectively. The generalised electric voltage in Eq. (4.49) can be restated as $\varphi(z,t) = -(-1)^r \Phi(z)v(t)$ and the shape function $\Phi(z)$ corresponding to the electrical boundary conditions of the piezoelectric element is given from Eq. (4.59). In this case, the parameter $-q_i \delta\varphi(z,t)$ in the parallel connection can be modified to give $(\Phi(z)q_1 + \Phi(z)q_2)\delta v(t) = (q/2 + q/2)\delta v(t) = q\delta v(t)$. By doing the same thing for the series connection, the electric charge output $q_1 = q_2 = q$ associated with the electrical boundary condition in Eq. (4.52) can give $\Phi(z)q_1\delta v(t) = \Phi(z)q_2\delta v(t) = q\delta v(t)$ for the bottom and top electrodes. As can be seen, the electrical work for the series and parallel connections of the bimorph have the same parameter with the negative sign but when the piezoelectric bimorph electromechanical dynamic responses with variable load resistance will be formulated, the electrical voltage for both electrical connections will differ. Corresponding with Eq. (4.80) from the last term, the electrical work due to the charge output from the system can be proved as $+q\delta v(t)$. At this point, the non-conservative virtual work from Eq. (4.80) can be modified as,

$$\int_{t_1}^{t_2} \delta W_f \, dt = \int_{t_1}^{t_2} \left[\int_\Omega \left\{ -I^{(A,k)} \ddot{u}_{base} \delta u_{rel} - I^{(A,k)} \ddot{w}_{base} \delta w_{rel} \right\} dxdy \right.$$

$$\left. - I_{tip}^{(A)} \ddot{u}_{base}(L)\delta u_{rel}(L) - I_{tip}^{(A)} \ddot{w}_{base}(L)\delta w_{rel}(L) + q\delta v(t) \right] dt \quad . \tag{4.81}$$

The electrical energy of the piezoelectric element represents the coupling effect of the constitutive equations that can be developed using the Hamiltonian theorem. As formulated previously, the backward piezoelectric couplings for series and parallel connections were developed in potential energy form, because it can have a profound effect on the coupled elastic-electric field. In this case, the corresponding electric field and permittivity of the piezoelectric component can be used to formulate the internal capacitance of the piezoelectric layers and forward piezoelectric couplings

for both series and parallel connections. The electrical energy of the piezoelectric in the Hamiltonian form is stated as,

$$\int_{t_1}^{t_2} \delta WE^P \mathrm{d}t = \int_{t_1}^{t_2}\int_{\Gamma} D_3 \delta(E_3) \mathrm{d}\Gamma \mathrm{d}t .$$

(4.82)

The electric displacement field of the piezoelectric element D_3 is also known as the converse effect which is obtained from electrical enthalpy energy. Using Eq. (4.3), equation (4.80) can be written as,

$$\int_{t_1}^{t_2} \delta WE^P \mathrm{d}t = \int_{t_1}^{t_2}\int_{\Gamma} \left[e_{31}\varepsilon_1 \delta(E_3) + \varsigma_{33}^{\varepsilon} E_3 \delta(E_3) \right] \mathrm{d}\Gamma \mathrm{d}t .$$

(4.83)

The electrical energy term can be reformulated as,

$$\int_{t_1}^{t_2} \delta WE^P \mathrm{d}t = \int_{t_1}^{t_2}\left[\int_{\Omega}\left(R_{31}^{(G,k)}\frac{\partial u_{rel}}{\partial x} - R_{31}^{(H,k)}\frac{\partial^2 w_{rel}}{\partial x^2} + S_{33}^{(k)}v \right)\delta v \mathrm{d}\Omega \right] \mathrm{d}t .$$

(4.84)

The first and second terms of Eq. (4.84) represents the forward piezoelectric couplings and can also be formulated to give the similar form as shown from the backward piezoelectric couplings from Eq. (4.51). The third term from Eq. (4.84) can be used to obtain the capacitance of the piezoelectric element.

The third term in Eq. (4.84) is prescribed as capacitance and it can be solved as,

$$\forall S_{33}^{(k)} = \left[\sum_{k \in p}\int_{h_k}^{h_{k+1}} \Xi(z)^{(k)}\varsigma_{33}^{(k)}\Xi(z)^{(k)}\mathrm{d}z \right], \ \forall k \in \{1,3\}.$$

(4.85)

The series and parallel connections can now be considered in the next part.

Case 1. Series connection. The capacitance of the piezoelectric element was formulated in Eq. (4.85). The summation of capacitances between the upper and lower layers of the piezoelectric bimorph has a factor of 1/2. It is found that the piezoelectric bimorph under longitudinal and transverse motion fields did not affect the computation of piezoelectric capacitance itself but the result of the capacitance must be considered by the constitutive equation of the piezoelectric field due to the coupled electromechanical system. Equation (4.85) for series connection can be used to formulate the capacitance as,

$$S_{33}^{(k)} = \frac{h_p\varsigma_{33}^{(1)}}{4h_p^{2}} + \frac{h_p\varsigma_{33}^{(3)}}{4h_p^{2}} = \frac{\varsigma_{33}}{2h_p} .$$

(4.86)

It should be noted that the upper and lower layers of the piezoelectric bimorph have the same material and geometrical structure, thus the permittivity of the piezoelectric component gives $\varsigma_{33}^{(1)} = \varsigma_{33}^{(3)} = \varsigma_{33}$.

Case 2. Parallel connection. With the same formulation of Eq. (4.85), the parallel capacitance can be considered. The summation of capacitances between the upper and lower layers of the piezoelectric bimorph has a factor of 2. At this point, the capacitance of the piezoelectric element for parallel connection can be formulated as,

$$S_{33}^{(k)} = \frac{h_p \varsigma_{33}^{(1)}}{h_p{}^2} + \frac{h_p \varsigma_{33}^{(3)}}{h_p{}^2} = \frac{2\varsigma_{33}}{h_p} \qquad . \tag{4.87}$$

The forward piezoelectric coupling and capacitance can affect the electric displacement as a converse effect where it depends on the geometrical structure of the piezoelectric element and the electric voltage.

The constitutive electromechanical dynamic equations of the piezoelectric bimorph can be obtained by considering Eqs. (4.41) (4.79), (4.81) and (4.84) into the Hamiltonian's principle from Eq. (4.20). The constitutive electromechanical dynamic equation for the piezoelectric bimorph beam can be formulated in terms of virtual relative and base displacement forms as,

$$
\begin{aligned}
\int_{t_1}^{t_2} & \left[\int_\Omega \left\{ -I^{(A,k)}\ddot{u}_{rel}\delta u_{rel} + I^{(C,k)}\frac{\partial^2 \ddot{w}_{rel}}{\partial x^2}\delta w_{rel} - I^{(A,k)}\ddot{w}_{rel}\delta w_{rel} - I^{(A,k)}\ddot{u}_{base}\delta u_{rel} - I^{(A,k)}\ddot{w}_{base}\delta w_{rel} \right. \right. \\
& + C_{11}^{(D,k)}\frac{\partial \varepsilon_1^{(0)}}{\partial x}\delta u_{rel} - C_{11}^{(F,k)}\frac{\partial^2 \varepsilon_1^{(1)}}{\partial x^2}\delta w_{rel} - R_{31}^{(G,k)}\frac{\partial v}{\partial x}\delta u_{rel} - R_{31}^{(H,k)}\frac{\partial^2 v}{\partial x^2}\delta w_{rel} + R_{31}^{(G,k)}\frac{\partial u_{rel}}{\partial x}\delta v \\
& \left. - R_{31}^{(H,k)}\frac{\partial^2 w_{rel}}{\partial x^2}\delta v + S_{33}^{(k)}v\delta v \right\} dx dy + q\delta v - I_{tip}^{(A)}\ddot{u}_{rel}(L)\delta u_{rel}(L) - I_{tip}^{(C)}\frac{\partial \ddot{w}_{rel}}{\partial x}(L)\delta\frac{\partial w_{rel}}{\partial x}(L) \\
& - I_{tip}^{(A)}\ddot{w}_{rel}(L)\delta w_{rel}(L) - I_{tip}^{(A)}\ddot{u}_{base}(L)\delta u_{rel}(L) - I_{tip}^{(A)}\ddot{w}_{base}(L)\delta w_{rel}(L) \\
& - \oint_S n_x N_{xx}^{(D,k)}\delta u_{rel}dS + \oint_S n_x \frac{\partial M_{xx}^{(F,k)}}{\partial x}\delta w_{rel}dS - \oint_S n_x M_{xx}^{(F,k)}\frac{\partial \delta w_{rel}}{\partial x}dS + \oint_S n_x R_{31}^{(G,k)}v\delta u_{rel}dS \\
& \left. + \oint_S n_x R_{31}^{(H,k)}\frac{\partial v}{\partial x}\delta w_{rel}dS - \oint_S n_x R_{31}^{(H,k)}v\frac{\partial \delta w_{rel}}{\partial x}dS - \oint_S I^{(C,k)}n_x \frac{\partial \ddot{w}_{rel}}{\partial x}\delta w_{rel}dS \right] dt = 0. \tag{4.88}
\end{aligned}
$$

It can be seen that the strong form of electromechanical dynamic equation from Eq. (4.88) was derived according to the variational method of Hamiltonian's principle. Equation (4.88) reduced from the extremum of functional form with integration by

two instants of time t_1 and t_2 for all domains in L_a and W_f implied space of continuous differentiable function for all independent variables of relative longitudinal $u_{rel}(x,t) \in C^2[0,L] \subset \Omega \subset R^3$ and relative transverse displacements $w_{rel}(x,t) \in C^4[0,L] \subset \Omega \subset R^3$ associated with electric potential $\varphi(z,t) = \Phi(z)v(t)$
$\in E_3 \in \left\{ C^1\left[-\dfrac{h_s}{2} - h_p, -\dfrac{h_s}{2}\right] \cup C^1\left[\dfrac{h_s}{2}, \dfrac{h_s}{2} + h_p\right] \right\} \subset \Omega \subset R^3$ in terms of actual forces and moments of the mechanical and electrical fields for the piezoelectric element as prescribed in the partial differential electromechanical dynamic equations in domain $d\Omega$ including the boundary conditions on the vector surface dS in terms of the divergence theorem. In this case, the reduced equation must fulfill the mathematical lemma of the variational method of duBois-Reymond's theorem for each virtual displacement field.

4.2. The Strong Form of Electromechanical Dynamic Equation

As prescribed in Eq. (4.88), parameters of virtual relative base displacements and electrical potential forms can be separated in terms of partial differential dynamic equations for extensional, transverse and electrical fields. In this case, there are three constitutive electromechanical equations of the cantilevered piezoelectric bimorph beam associated with moving virtual displacement fields of δu_{rel}, δw_{rel}, $\delta u_{rel}(L)$, $\partial w_{rel}(L)/\partial x$ and δv.

The first constitutive electromechanical dynamic equation in extensional form in terms of virtual relative longitudinal displacement field δu_{rel} can be formulated as,

$$\int_{t_1}^{t_2}\left[\int_{\Omega}\left\{ -I^{(A,k)}\ddot{u}_{rel}\delta u_{rel} - I^{(A,k)}\ddot{u}_{base}\delta u_{rel} + C_{11}^{(D,k)}\frac{\partial \varepsilon_1^{(0)}}{\partial x}\delta u_{rel} - R_{31}^{(G,k)}\frac{\partial v}{\partial x}\delta u_{rel} \right\}dx\,dy - I_{tip}^{(A)}\ddot{u}_{base}\delta u_{rel}(L) \right.$$
$$\left. -I_{tip}^{(A)}\ddot{u}_{rel}(L)\delta u_{rel}(L) - \oint_S n_x N_{xx}^{(D,k)}\delta u_{rel}dS + \oint_S n_x R_{31}^{(G,k)}v\delta u_{rel}dS \right]dt = 0 \quad . \tag{4.89}$$

The electromechanical dynamic equation in extensional form can be written as,

$$\delta u_{rel}(x,t) \quad : \quad -\hat{I}^{(A,k)}\ddot{u}_{rel} - \hat{I}^{(A,k)}\ddot{u}_{base} + \hat{C}_{11}^{(D,k)}\frac{\partial \varepsilon_1^{(0)}}{\partial x} - R_{31}^{(G,k)}\frac{\partial v}{\partial x} = 0 \quad , \tag{4.90}$$

It is noted that the symbol ^ indicates the modified parameter after integrating with respect to y and the divergence theorem from sixth and seventh terms in Eq. (4.89)

can also be modified. The variable n_x indicates the unit vector normal in the x axis where the boundary condition can be stated as,

$$\delta u_{rel}(L,t) \quad : \quad -I_{tip}^{(A)}\ddot{u}_{base} - I_{tip}^{(A)}\ddot{u}_{rel}(L) - \hat{C}_{11}^{(D,k)}\frac{\partial u_{rel}}{\partial x} + \hat{R}_{31}^{(G,k)}v = 0$$

and $\quad u_{rel}(0,t)=0$. $\hspace{4cm}$ (4.91)

It should be noted that the fourth term of Eq. (4.90) is zero because the electric voltage is only a function of time. However, equation (4.99) can be used to formulate the weak form of the Hamiltonian constitutive electromechanical dynamic equation. The second constitutive electromechanical dynamic equation for transverse bending form in terms of the virtual relative transverse displacement field δw_{rel} reduced from Eq. (4.88) can be formulated as,

$$\int_{t_1}^{t_2}\left[\int_\Omega\left\{I^{(C,k)}\frac{\partial^2\ddot{w}_{rel}}{\partial x^2}\delta w_{rel} - I^{(A,k)}\ddot{w}_{rel}\delta w_{rel} - I^{(A,k)}\ddot{w}_{base}\,\delta w_{rel}\right.\right.$$

$$-C_{11}^{(F,k)}\frac{\partial^2\varepsilon_1^{(1)}}{\partial x^2}\delta w_{rel} - R_{31}^{(H,k)}\frac{\partial^2 v}{\partial x^2}\Bigg\}dxdy - I_{tip}^{(C)}\frac{\partial\ddot{w}_{rel}}{\partial x}(L)\frac{\partial\delta w_{rel}}{\partial x}(L)$$

$$- I_{tip}^{(A)}\ddot{w}_{rel}(L)\delta w_{rel}(L) - I_{tip}^{(A)}\ddot{w}_{base}\delta w_{rel}(L) + \left\{\oint_S n_x\frac{\partial M_{xx}^{(F,k)}}{\partial x}\delta w_{rel} - \oint_S n_x M_{xx}^{(F,k)}\frac{\partial\delta w_{rel}}{\partial x}\right.$$

$$\left.\left.- \oint_S n_x R_{31}^{(H,k)}v\frac{\partial\delta w_{rel}}{\partial x} + \oint_S n_x R_{31}^{(H,k)}\frac{\partial v}{\partial x}\delta w_{rel} - \oint_S I^{(C,k)}n_x\frac{\partial\ddot{w}_{rel}}{\partial x}\delta w_{rel}\right\}dS\right]dt = 0. \hspace{1cm} (4.92)$$

The electromechanical dynamic equation for transverse bending can be written as,

$$\delta w_{rel}(x,t): \hat{I}^{(C,k)}\frac{\partial^2\ddot{w}_{rel}}{\partial x^2} - \hat{I}^{(A,k)}\ddot{w}_{rel} - \hat{I}^{(A,k)}\ddot{w}_{base} - \hat{C}_{11}^{(F,k)}\frac{\partial^2\varepsilon_1^{(1)}}{\partial x^2} - \hat{R}_{31}^{(H,k)}\frac{\partial^2 v}{\partial x^2}\delta w_{rel} = 0. \hspace{0.3cm} (4.93)$$

The symbol ^ indicates the modified parameter after integrating with respect to y. The boundary condition can be stated after modifying the divergence theorem from sixth and seventh terms in Eq. (4.92) as,

$$\delta w_{rel}(L,t) : -I_{tip}^{(A)}\ddot{w}_{base} - I_{tip}^{(A)}\ddot{w}_{rel}(L) - \hat{I}^{(C,k)}\frac{\partial\ddot{w}}{\partial x}(L) + \hat{C}_{11}^{(F,k)}\frac{\partial}{\partial x}\left(\frac{\partial^2 w_{rel}}{\partial x^2}\right)(L) + \hat{R}_{31}^{(H,k)}\frac{\partial v}{\partial x} = 0,$$

$$\frac{\partial\delta w_{rel}}{\partial x}(L,t) : -I_{tip}^{(C)}\frac{\partial\ddot{w}_{rel}}{\partial x}(L) - \hat{C}_{11}^{(F,k)}\frac{\partial^2 w_{rel}}{\partial x^2}(L) - \hat{R}_{31}^{(H,k)}v = 0, \hspace{1cm} (4.94)$$

$$w_{rel}(0,t)=0 \quad , \quad \frac{\partial w_{rel}}{\partial x}(0,t)=0.$$

It should be noted that the fifth term of Eq. (4.93) is zero because the electric voltage is a function of time. However, equation (4.93) can be modified to formulate the weak form of the Hamiltonian constitutive electromechanical dynamic equation. The third constitutive dynamic equation for electrical potential in terms of the virtual electrical potential field $\delta v(t)$ can be formulated as,

$$\delta v \; : \quad \int_0^L \left(\hat{R}_{31}^{(G,k)} \frac{\partial u_{rel}}{\partial x} - \hat{R}_{31}^{(H,k)} \frac{\partial^2 w_{rel}}{\partial x^2} + \hat{S}_{33}^{(k)} v \right) \mathrm{d}x + q = 0 \,. \qquad (4.95)$$

The equation (4.90) represents the electromechanical dynamic equation in terms of relative displacement u_{rel} based on the moving virtual relative displacement δu_{rel}. The similar dynamic equation can also be found from Eq. (4.92) based on virtual relative δw_{rel} transverse displacement fields. Equation (4.91) indicates the essential boundary conditions and the natural boundary conditions. The similar model can also be found from Eq. (4.94) which contains the essential boundary conditions and the natural boundary conditions. It should be noted that essential boundary conditions are sometimes called static boundary conditions which depend on support conditions whereas the natural boundary conditions are sometimes called dynamic boundary conditions depending on the external loading conditions due to the inertia loads from the base and internal loading conditions from internal forces and moments at the piezoelectric beam element. In this case, the electromechanical dynamic equations of the cantilevered piezoelectric beam must fulfill the mathematical lemma of the variational method of duBois-Reymond's theorem for each virtual displacement field.

4.3. The Weak Solution form of Electromechanical Dynamic Equation

As prescribed by Eq. (4.88), the form of the electromechanical dynamic equation represents the strong form (classical method) of Hamiltonian's theorem. In this case, the weak form of Hamiltonian theorem can also be formulated by concerning only virtual relative extensional δu_{rel} and transverse δw_{rel} displacement fields to give the analytical integro-partial differential dynamic equation over the length of the piezoelectric bimorph beam. The weak form of Hamiltonian theorem includes the virtual displacements into the calculations of the constitutive electromechanical dynamic equation. In other words, the virtual displacements are assumed to be the

non-zero terms. Therefore, the solutions of the dynamic equation in terms of variables fields (u_{rel} , w_{rel} , v) and virtual variables fields (δu_{rel} , δw_{rel} , δv) must be assumed as eigenfunction forms. At this point, the weak form of the Hamiltonian theorem can be formulated in terms of Eq. (4.88) as,

$$
\begin{aligned}
\int_{t_1}^{t_2} &\left[\int_{\Omega} \left(C_{11}^{(D,k)} \varepsilon_1^{(0)} \frac{\partial \delta u_{rel}}{\partial x} + C_{11}^{(F,k)} \varepsilon_1^{(1)} \frac{\partial^2 \delta w_{rel}}{\partial x^2} - R_{31}^{(G,k)} v(t) \frac{\partial \delta u_{rel}}{\partial x} \right. \right. \\
&+ R_{31}^{(H,k)} v(t) \frac{\partial^2 \delta w_{rel}}{\partial x^2} + I^{(A,k)} \ddot{u}_{rel} \delta u_{rel} - S_{33}^{(k)} v(t) \delta v(t) \\
&+ I^{(C,k)} \frac{\partial \ddot{w}_{rel}}{\partial x} \frac{\partial \delta(w_{rel})}{\partial x} + I^{(A,k)} \ddot{w}_{rel} \delta w_{rel} - R_{31}^{(G,k)} \frac{\partial u_{rel}}{\partial x} \delta v(t) \\
&\left. + R_{31}^{(H,k)} \frac{\partial^2 w_{rel}}{\partial x^2} \delta v(t) + I^{(A,k)} \ddot{u}_{base} \delta u_{rel} + I^{(A,k)} \ddot{w}_{base} \delta w_{rel} \right) \mathrm{d}x \mathrm{d}y \\
&- q \delta v(t) + I_{tip}^{(A)} \ddot{u}_{rel}(L) \delta u_{rel}(L) + I_{tip}^{(C)} \frac{\partial \ddot{w}_{rel}}{\partial x}(L) \frac{\partial \delta w_{rel}}{\partial x}(L) \\
&+ I_{tip}^{(A)} \ddot{u}_{base} \delta u_{rel}(L) + I_{tip}^{(A)} \ddot{w}_{base} \delta w_{rel}(L) + I_{tip}^{(A)} \ddot{w}_{rel}(L) \delta w_{rel}(L) \\
&\left. + \oint_S \left(- n_x N_{xx}^{(D,k)} \delta u_{rel} + n_x \frac{\partial M_{xx}^{(F,k)}}{\partial x} \delta w_{rel} - n_x M_{xx}^{(F,k)} \frac{\partial \delta w_{rel}}{\partial x} - I^{(C,k)} n_x \frac{\partial \ddot{w}_{rel}}{\partial x} \delta w_{rel} \right) \mathrm{d}S \right] \mathrm{d}t = 0 . \quad (4.96)
\end{aligned}
$$

The weak form of Hamiltonian's principle can also be obtained alternatively in terms of Eqs. (4.90), (4.91), (4.93), (4.94) and (4.95) by applying the variational principle. It should be noted that respective parameters in the second parenthesis from Eq. (4.96) are in-plane force due to internal extensional force, in-plane shear force and moment due to internal transverse moment and in-plane shear force due to rotary of bimorph on the portion of differential vector surface $\mathrm{d}S$ in order to fulfill the divergence theorem of the natural boundary conditions with respect to differential surface area $\mathrm{d}\Omega$. Equation (4.96) is called the weak form of electromechanical dynamic equation based on the continuity requirement of transverse bending with the transformation from fourth to second continuous derivative function $w_{rel}(x,t) \in \mathrm{C}^4[0,L] \rightarrow \mathrm{C}^2[0,L] \subset \Omega \subset \mathrm{R}^3$ and the continuity requirement of longitudinal extension transformed from second to first continuous derivative function $u_{rel}(x,t) \in \mathrm{C}^2[0,L] \rightarrow \mathrm{C}^1[0,L] \subset \Omega \subset \mathrm{R}^3$ while the electric field is a gradient function of electric potential of each thickness of piezoelectric layer $\varphi(z,t) = \Phi(z) v(t) \in E_3 \in \left\{ \mathrm{C}^1 \left[-\frac{h_s}{2} - h_p, -\frac{h_s}{2} \right] \cup \mathrm{C}^1 \left[\frac{h_s}{2}, \frac{h_s}{2} + h_p \right] \right\} \subset \Omega \subset \mathrm{R}^3$.

It should be noted that equations (4.88) and (4.96) can be used to formulate the Rayleigh and Euler-Bernoulli piezoelectric bimorph beams. The Rayleigh beam only considered the rotary inertias of the piezoelectric bimorph. The Euler-Bernoulli piezoelectric bimorph beam can also be formulated using the same equation by ignoring the rotary inertia of the piezoelectric bimorph. In forthcoming mathematical derivations, this equation will use the rotary inertia of the piezoelectric bimorph where this will be easier to neglect once the orthonormality property of electromechanical dynamic equations will be established. It should be noted that the second integral represents the divergence theorem reflecting the boundary conditions on the surface S of the bimorph element in the direction n_x of the unit vector normal to the x-axis. The second integral is sometimes called the generalised internal force and moment for every element discretisation and these become necessary when the element boundary S coincides with boundary of domain Ω. The second integral can be a crucial part to be included in Eq. (4.96) when using finite element analysis where their existence depends on external loads on certain nodes of the structure. In terms of the analytical approach that is proposed here, the second integral can be ignored because the displacement fields (u_{rel}, w_{rel}) and virtual displacement fields ($\delta u_{rel}, \delta w_{rel}$) reflected from Eq. (4.96) were assumed as eigenfunction forms which meet the continuity of mechanical form or strain field and boundary conditions.

4.3.1. The Weak Form of Coupled Electromechanical Dynamic Response of Transverse-Longitudinal Form (Weak-CEDRTL)

In this section, we discuss the solution form of Eq. (4.96) by using the convergent eigenfunction series forms. The solutions must meet continuity and also boundary conditions of the piezoelectric bimorph beam under longitudinal extension and transverse bending effects in order to give reasonable solutions. In the next section, the solution forms due to the effects of combinations of input longitudinal and transverse base motions, independent input longitudinal base motion and independent transverse base motion of the bimorph will be discussed comprehensively. It should be noted that equation (4.96) represents the dynamic equation of the electromechanical system under two input base motions. This equation can be formulated separately from the longitudinal and transverse forms as discuss further in the next section. As previously mentioned, the effects of input base

motions on the bimorph not only affects the mechanical domain (stress and strain fields) but also the electrical domain (electric field and polarity). The solution forms can be prescribed using the space- and time-dependent eigenfunction forms as,

$$w_{rel}(x,t) = \sum_{r=1}^{m} w_r(t)\Psi_r(x) \quad , \quad u_{rel}(x,t) = \sum_{r=1}^{m} u_r(t)\Theta_r(x) \quad . \quad (4.97)$$

Parameters $\Psi(x)$ and $\Theta(x)$ indicate the mode shapes or normal modes of the eigenfunction series which can be determined using analytical solution forms for the cantilevered piezoelectric beam with a tip mass where the mode shape of the Euler-Bernoulli and Rayleigh beams will be formulated in appendix B. Two solution forms can be derived in the next section. It should be noted that parameters, $\Psi_r(x)$ and $\Theta_r(x)$ are defined as the independent mode shapes of relative motions to meet the continuity requirements of the mechanical strain field.

Corresponding to Eq. (4.97), equation (4.96) can be formulated according to the eigenfunction series forms. Setting virtual displacement forms $\delta u_{rel}(t)$, $\delta w_{rel}(t)$, $\delta v(t)$ separately can be used to obtain three independent dynamic equations. Parameters of virtual displacements meet the duBois-Reymond's lemma to indicate that only dynamic equations have solutions. At this point, three dynamic equations from the piezoelectric bimorph beam can be formulated.

The first dynamic equation represents the electromechanical piezoelectric bimorph under longitudinal extension. Here it is written as,

$$\sum_{q=1}^{m}\left\{\sum_{r=1}^{m}\left[\int_{\Omega} I^{(A,k)}\Theta_q(x)\Theta_r(x)\ddot{u}_r(t)dxdy + I_{tip}^{(A)}\Theta_q(L)\Theta_r(L)\ddot{u}_r(t) + \int_{\Omega} C_{11}^{(D,k)}\frac{d\Theta_q(x)}{dx}\frac{d\Theta_r(x)}{dx}u_r(t)dxdy\right] \right.$$
$$\left. - \int_{\Omega} R_{31}^{(G,k)}\frac{d\Theta_q(x)}{dx}v(t)dxdy + \int_{\Omega} I^{(A,k)}\Theta_q(x)\ddot{u}_{base}(t)dxdy + I_{tip}^{(A)}\Theta_q(L)\ddot{u}_{base}(t)\right\}\delta u_q(t) = 0. \quad (4.98)$$

The second dynamic equation represents the electromechanical piezoelectric bimorph under transverse bending. It can be stated as,

$$\sum_{q=1}^{m}\sum_{r=1}^{m}\left[\int_{\Omega}I^{(A,k)}\Psi_q(x)\Psi_r(x)\ddot{w}_r(t)dxdy + \int_{\Omega}I^{(C,k)}\frac{d\Psi_q(x)}{dx}\frac{d\Psi_r(x)}{dx}\ddot{w}_r(t)dxdy + I_{tip}^{(A)}\Psi_q(L)\Psi_r(L)\ddot{w}_r(t)\right.$$

$$\left. + I_{tip}^{(C)}\frac{d\Psi_q(L)}{dx}\frac{d\Psi_r(L)}{dx}\ddot{w}_r(t) + \int_{\Omega}C_{11}^{(F,k)}\frac{d^2\Psi_q(x)}{dx^2}\frac{d^2\Psi_r(x)}{dx^2}w_r(t)dxdy\right] + \int_{\Omega}R_{31}^{(H,k)}\frac{d^2\Psi_q}{dx^2}v(t)dxdy$$

$$\left. + \int_{\Omega}I^{(A,k)}\Psi_q(x)\ddot{w}_{base}(t)dxdy + I_{tip}^{(A)}\Psi_q(L)\ddot{w}_{base}(t)\right\}\delta w_q(t) = 0. \qquad (4.99)$$

The third dynamic equation represents the electromechanical piezoelectric bimorph under electrical form. It can be written as,

$$\sum_{r=1}^{m}\int_{\Omega}\left[-R_{31}^{(G,k)}\frac{d\Theta_r(x)}{dx}u_r(t) + R_{31}^{(H,k)}\frac{d^2\Psi_r(x)}{dx^2}w_r(t)\right]dxdy\,\delta v(t)$$

$$-\int_{\Omega}S_{33}^{(k)}v(t)\delta v(t)dxdy - q(t)\delta v(t) = 0\,, \qquad (4.100)$$

or it can be differentiated with respect to time to obtain current function giving,

$$-\sum_{r=1}^{m}\int_{\Omega}R_{31}^{(G,k)}\frac{d\Theta_r(x)}{dx}\dot{u}_r(t)dxdy + \sum_{r=1}^{m}\int_{\Omega}R_{31}^{(H,k)}\frac{d^2\Psi_r(x)}{dx^2}\dot{w}_r(t)dxdy$$

$$-\int_{\Omega}S_{33}^{(k)}\dot{v}(t)dxdy - \frac{1}{R_{load}}v(t) = 0\,. \qquad (4.101)$$

The constitutive electromechanical dynamic equations from Eqs. (4.98), (4.99) and (4.101) can be reformulated in matrix form by including the damping coefficients after integration with respect to y to give,

$$\begin{bmatrix} M_{qr}^{(u)} & 0 & 0 \\ 0 & M_{qr}^{(w)} & 0 \\ 0 & 0 & 0 \end{bmatrix}\begin{Bmatrix} \ddot{u}_r \\ \ddot{w}_r \\ \ddot{v} \end{Bmatrix} + \begin{bmatrix} C_{qr}^{(u)} & 0 & 0 \\ 0 & C_{qr}^{(w)} & 0 \\ P_r^{(u)} & P_r^{(w)} & P_D \end{bmatrix}\begin{Bmatrix} \dot{u}_r \\ \dot{w}_r \\ \dot{v} \end{Bmatrix} + \begin{bmatrix} K_{qr}^{(u)} & 0 & P_q^{(u)} \\ 0 & K_{qr}^{(w)} & P_q^{(w)} \\ 0 & 0 & R_L \end{bmatrix}\begin{Bmatrix} u_r \\ w_r \\ v \end{Bmatrix} = \begin{bmatrix} -Q_q^{(u)} & 0 & 0 \\ 0 & -Q_q^{(w)} & 0 \\ 0 & 0 & 0 \end{bmatrix}\begin{Bmatrix} \ddot{u}_{base} \\ \ddot{w}_{base} \\ \ddot{v}_{base} \end{Bmatrix}. (4.102)$$

where:

$$M_{qr}^{(u)} = \int_0^L \hat{I}^{(A,k)}\Theta_q(x)\Theta_r(x)dx + I_{tip}^{(A)}\Theta_q(L)\Theta_r(L)\,,$$

$$M_{qr}^{(w)} = \int_0^L \hat{I}^{(A,k)}\Psi_q(x)\Psi_r(x)dx + \int_0^L \hat{I}^{(C,k)}\frac{d\Psi_q(x)}{dx}\frac{d\Psi_r(x)}{dx}dx + I_{tip}^{(A)}\Psi_q(L)\Psi_r(L) + I_{tip}^{(C)}\frac{d\Psi_q}{dx}(L)\frac{d\Psi_r}{dx}(L),$$

$$K_{qr}^{(u)} = \int_0^L \hat{C}_{11}^{(D,k)}\frac{d\Theta_q(x)}{dx}\frac{d\Theta_r(x)}{dx}dx \quad,\quad K_{qr}^{(w)} = \int_0^L \hat{C}_{11}^{(F,k)}\frac{d^2\Psi_q(x)}{dx^2}\frac{d^2\Psi_r(x)}{dx^2}dx \quad,$$

$$P_r^{(u)} = -\int_0^L \hat{R}_{31}^{(G,k)}\frac{d\Theta_r(x)}{dx}dx \quad,\quad P_r^{(w)} = \int_0^L \hat{R}_{31}^{(H,k)}\frac{d^2\Psi_r(x)}{dx^2}dx \quad,$$

$$R_L = -\frac{1}{R_{load}} \quad,\quad P_D = -\int_0^L \hat{S}_{33}^{(k)}dx, \quad Q_q^{(u)} = \int_0^L \hat{I}^{(A,k)}\Theta_q(x)dx + I_{tip}^{(A,k)}\Theta_q(L) \quad, (4.103)$$

$$Q_q^{(w)} = \int_0^L \hat{I}^{(A,k)} \Psi_q(x) dx + I_{tip}^{(A)} \Psi_q(L) \quad , \quad C_{qr}^{(u)} = \alpha_u M_{qr}^{(u)} + \beta_u K_{qr}^{(u)} \quad ,$$

$$C_{qr}^{(w)} = \alpha_w M_{qr}^{(w)} + \beta_w K_{qr}^{(u)} , \quad \hat{I}^{(A,k)} = bI^{(A,k)} , \quad \hat{I}^{(C,k)} = bI^{(C,k)} , \quad \hat{C}_{11}^{(D,k)} = bC_{11}^{(D,k)} ,$$

$$\hat{C}_{11}^{(F,k)} = bC_{11}^{(F,k)} , \quad \hat{R}_{31}^{(G,k)} = bR_{31}^{(G,k)} \quad , \quad \hat{R}_{31}^{(H,k)} = bR_{31}^{(H,k)} \quad , \quad \hat{S}_{33}^{(k)} = bS_{33}^{(k)} .$$

It should be noted that the ^ symbol refers to the modified variables after multiplying with the width b of the bimorph. Equation (4.102) is a non homogeneous differential dynamic equation of the piezoelectric bimorph beam with two input base-excitation. This equation can be used for modelling the piezoelectric bimorph with either series connection or parallel connection. The connections just depend on the chosen piezoelectric couplings from Eqs. (4.55), (4.58), (4.62) and (4.65) and also the chosen internal capacitance from Eqs. (4.86) and (4.87). In addition to that, other parameters from this research such as mass moment of inertia, stiffness coefficients, piezoelectric constant and permittivity are viewed as constant values. The geometry of the piezoelectric bimorph beam must also be considered where it will affect all aspects of power harvesting performance. It was previously stated that each connection has two different poled configurations under two input base excitations, where these have been invoked mathematically. This represents a significant difference from other researchers in which most of their studies of the piezoelectric bimorph only considered the pure bending (transverse bending) where each connection has one different poled configuration i.e. X-Poled for series connection or Y-Poled for Parallel connection.

Corresponding with the eigenfunction series from Eq. (4.97), the results of mode shapes due to longitudinal and transverse form from appendix B can be substituted into Eqs. (4.98), (4.99) and (4.101) to obtain solutions of the piezoelectric bimorph under two input base motions. Equation (4.102) can be solved using Laplace transforms. In this case, the dynamic equation of the piezoelectric bimorph can be modified to give,

$$\begin{bmatrix} M_{qr}^{(u)} s^2 + C_{qr}^{(u)} s + K_{qr}^{(u)} & 0 & P_q^{(u)} \\ 0 & M_{qr}^{(w)} s^2 + C_{qr}^{(w)} s + K_{qr}^{(w)} & P_q^{(w)} \\ P_r^{(u)} s & P_r^{(w)} s & P_D s + R_L \end{bmatrix} \begin{Bmatrix} u_r(s) \\ w_r(s) \\ v_r(s) \end{Bmatrix} = \begin{Bmatrix} -Q_q^{(u)} s^2 u_{base}(s) \\ -Q_q^{(w)} s^2 w_{base}(s) \\ 0 \end{Bmatrix} . (4.104)$$

The longitudinal motion can be formulated using Cramer's method as,

$$u_r(s) = \frac{1}{Z(s)} \begin{vmatrix} -Q_q^{(u)}s^2 u_{base}(s) & 0 & P_q^{(u)} \\ -Q_q^{(w)}s^2 w_{base}(s) & M_{qr}^{(w)}s^2 + C_{qr}^{(w)}s + K_{qr}^{(w)} & P_q^{(w)} \\ 0 & P_r^{(w)}s & P_D s + R_L \end{vmatrix}. \quad (4.105)$$

Equation (4.105) can be manipulated as,

$$u_r(s) = \frac{1}{Z(s)} \left[-\left\{ \left(M_{qr}^{(w)}s^2 + C_{qr}^{(w)}s + K_{qr}^{(w)} \right)\left(P_D s + R_L \right) - sP_r^{(w)}P_q^{(w)} \right\} Q_r^{(u)}s^2 u_{base}(s) - sP_r^{(w)}P_q^{(u)}Q_q^{(w)}s^2 w_{base}(s) \right]. \quad (4.106)$$

Equation (4.104) can be further modified to obtain the transverse motion using Laplace transforms and then applying Cramer's method to give,

$$w_r(s) = \frac{1}{Z(s)} \begin{vmatrix} M_{qr}^{(u)}s^2 + C_{qr}^{(u)}s + K_{qr}^{(u)} & -Q_q^{(u)}s^2 u_{base}(s) & P_q^{(u)} \\ 0 & -Q_q^{(w)}s^2 w_{base}(s) & P_q^{(w)} \\ P_r^{(u)}s & 0 & P_D s + R_L \end{vmatrix}. \quad (4.107)$$

Equation (4.107) can be further extended using the determinant, resulting in the equation,

$$w_r(s) = \frac{1}{Z(s)} \left[-sP_r^{(u)}P_q^{(w)}Q_q^{(u)}s^2 u_{base}(s) - \left\{ \left(M_{qr}^{(u)}s^2 + C_{qr}^{(u)}s + K_{qr}^{(u)} \right)\left(P_D s + R_L \right) - sP_r^{(u)}P_q^{(u)} \right\} Q_q^{(w)}s^2 w_{base}(s) \right]. \quad (4.108)$$

Electric voltage from Eq. (4.104) can also be formulated as,

$$v(s) = \frac{1}{Z(s)} \begin{vmatrix} M_{qr}^{(u)}s^2 + C_{qr}^{(u)}s + K_{qr}^{(u)} & 0 & -Q_q^{(u)}s^2 u_{base}(s) \\ 0 & M_{qr}^{(w)}s^2 + C_{qr}^{(w)}s + K_{qr}^{(w)} & -Q_q^{(w)}s^2 w_{base}(s) \\ P_r^{(u)}s & P_r^{(w)}s & 0 \end{vmatrix}. \quad (4.109)$$

Simplifying, equation (4.109) can be written to obtain,

$$v(s) = \frac{1}{Z(s)} \left[sP_r^{(u)}\left(M_{qr}^{(w)}s^2 + C_{qr}^{(w)}s + K_{qr}^{(w)} \right)Q_q^{(w)}s^2 u_{base}(s) + sP_r^{(w)}\left(M_{qr}^{(u)}s^2 + C_{qr}^{(u)}s + K_{qr}^{(u)} \right)Q_q^{(w)}s^2 w_{base}(s) \right]. \quad (4.110)$$

As formulated the determinant of the homogenous dynamic form from Eq. (4.104) can be expressed as,

$$Z(s) = \begin{vmatrix} M_{qr}^{(u)}s^2 + C_{qr}^{(u)}s + K_{qr}^{(u)} & 0 & P_q^{(u)} \\ 0 & M_{qr}^{(w)}s^2 + C_{qr}^{(w)}s + K_{qr}^{(w)} & P_q^{(w)} \\ P_r^{(u)}s & P_r^{(w)}s & P_D s + R_L \end{vmatrix}. \quad (4.111)$$

Expanding Eq. (4.111) and rearranging, the characteristic polynomial form can be written as,

$$\begin{aligned} Z(s) = &\ s^5 P_D M_{qr}^{(u)}M_{qr}^{(w)} + s^4\left(P_D M_{qr}^{(u)}C_{qr}^{(w)} + P_D C_{qr}^{(u)}M_{qr}^{(w)} + R_L M_{qr}^{(u)}M_{qr}^{(w)} \right) \\ &+ s^3\left(P_D C_{qr}^{(u)}C_{qr}^{(w)} + R_L M_{qr}^{(u)}C_{qr}^{(w)} + R_L C_{qr}^{(u)}M_{qr}^{(w)} - P_r^{(u)}P_q^{(u)}M_{qr}^{(w)} \right. \\ &\left. - P_r^{(w)}P_q^{(w)}M_{qr}^{(u)} + K_{qr}^{(w)}P_D M_{qr}^{(u)} + K_{qr}^{(u)}P_D M_{qr}^{(w)} \right) + s^2\left(R_L C_{qr}^{(u)}C_{qr}^{(w)} \right. \\ &\left. - P_r^{(u)}P_q^{(u)}C_{qr}^{(w)} - P_r^{(w)}P_q^{(w)}C_{qr}^{(u)} + K_{qr}^{(w)}P_D C_{qr}^{(u)} + K_{qr}^{(w)}R_L M_{qr}^{(u)} + K_{qr}^{(u)}P_D C_{qr}^{(w)} \right. \end{aligned}$$

$$+ K_{qr}^{(u)} R_L M_{qr}^{(w)} \Big) + s \Big(K_{qr}^{(w)} R_L C_{qr}^{(u)} - K_{qr}^{(w)} P_r^{(u)} P_q^{(u)} + K_{qr}^{(u)} R_L C_{qr}^{(w)}$$

$$- K_{qr}^{(u)} P_r^{(w)} P_q^{(w)} + K_{qr}^{(u)} K_{qr}^{(w)} P_D \Big) + K_{qr}^{(u)} K_{qr}^{(w)} R_L . \qquad (4.112)$$

The transfer function relating the input base-longitudinal acceleration to output longitudinal displacement can be obtained, if input transverse motion was not applied as,

$$H_{11}(s) = \frac{u_r(s)}{s^2 u_{base}(s)} \bigg|_{s^2 w_{base}(s) = 0} = \frac{- \Big\{ \Big(M_{qr}^{(w)} s^2 + C_{qr}^{(w)} s + K_{qr}^{(w)} \Big)(P_D s + R_L) - s P_r^{(w)} P_q^{(w)} \Big\} Q_q^{(u)}}{Z(s)} . (4.113)$$

The relative transfer function between the input base-transverse acceleration and output longitudinal displacement can be obtained as,

$$H_{12}(s) = \frac{u_r(s)}{s^2 w_{base}(s)} \bigg|_{s^2 u_{base}(s) = 0} = - \frac{s P_r^{(w)} P_q^{(u)} Q_q^{(w)}}{Z(s)} . \qquad (4.114)$$

The transfer function between the input base-longitudinal acceleration and transverse displacement can be obtained as,

$$H_{21}(s) = \frac{w_r(s)}{s^2 u_{base}(s)} \bigg|_{s^2 w_{base}(s) = 0} = - \frac{s P_r^{(u)} P_q^{(w)} Q_q^{(u)}}{Z(s)} . \qquad (4.115)$$

Corresponding to Eq. (4.108), the relative transfer functions of the input base-transverse acceleration with respect to output transverse displacement can be obtained if longitudinal motion was not applied, which becomes,

$$H_{22}(s) = \frac{w_r(s)}{s^2 w_{base}(s)} \bigg|_{s^2 u_{base}(s) = 0} = \frac{- \Big\{ \Big(M_{qr}^{(u)} s^2 + C_{qr}^{(u)} s + K_{qr}^{(u)} \Big)(P_D s + R_L) - s P_r^{(u)} P_q^{(u)} \Big\} Q_q^{(w)}}{Z(s)} . \qquad (4.116)$$

With the same method, the transfer function between the input base-longitudinal acceleration and electric voltage can be obtained as,

$$H_{31}(s) = \frac{v(s)}{s^2 u_{base}(s)} \bigg|_{s^2 w_{base}(s) = 0} = \frac{s P_r^{(u)} \Big(M_{qr}^{(w)} s^2 + C_{qr}^{(w)} s + K_{qr}^{(w)} \Big) Q_q^{(u)}}{Z(s)} . \qquad (4.117)$$

The relative transfer function of the input base-transverse acceleration with respect to output electric voltage can be obtained if longitudinal motion was not applied. This gives,

$$H_{32}(s) = \frac{v(s)}{s^2 w_{base}(s)} \bigg|_{s^2 u_{base}(s) = 0} = \frac{s P_r^{(w)} \Big(M_{qr}^{(u)} s^2 + C_{qr}^{(u)} s + K_{qr}^{(u)} \Big) Q_q^{(w)}}{Z(s)} . \qquad (4.118)$$

The transfer function relating power harvesting to input transverse acceleration can be derived as,

$$\left.\frac{P(s)}{\left(s^2 w_{base}(s)\right)^2}\right|_{\omega^2 u_{base}(s)=0} = \frac{\left(s^3 M_{qr}^{(u)}P_r^{(w)} + s^2 C_{qr}^{(u)}P_r^{(w)} + sK_{qr}^{(u)}P_r^{(w)}\right)^2 Q_q^{(w)2}}{R_{load}Z(s)^2}. \quad (4.119)$$

The transfer function of power harvesting due to input longitudinal acceleration can be derived as,

$$\left.\frac{P(s)}{\left(s^2 u_{base}(s)\right)^2}\right|_{\omega^2 w_{base}(s)=0} = \frac{\left(s^3 M_{qr}^{(w)}P_r^{(u)} + s^2 C_{qr}^{(w)}P_r^{(u)} + sK_{qr}^{(w)}P_r^{(u)}\right)^2 Q_q^{(u)2}}{R_{load}Z(s)^2}. \quad (4.120)$$

Manipulating Eqs. (4.113) to (4.118) gives another relationship of transfer functions as formulated in Eqs. (4.121) to (4.126),

$$\left.\frac{w_r(s)}{u_r(s)}\right|_{s^2 w_{base}(s)=0} = \frac{sP_r^{(u)}P_q^{(w)}}{\left(M_{qr}^{(w)}s^2 + C_{qr}^{(w)}s + K_{qr}^{(w)}\right)\left(P_D s + R_L\right) - sP_r^{(w)}P_q^{(w)}}, \quad (4.121)$$

$$\left.\frac{u_r(s)}{w_r(s)}\right|_{s^2 u_{base}(s)=0} = \frac{sP_r^{(w)}P_q^{(u)}}{\left(\left(M_{qr}^{(u)}s^2 + C_{qr}^{(u)}s + K_{qr}^{(u)}\right)\left(P_D s + R_L\right) - sP_r^{(u)}P_q^{(u)}\right)}, \quad (4.122)$$

$$\left.\frac{u_r(s)}{v(s)}\right|_{s^2 w_{base}(s)=0} = \frac{-\left(M_{qr}^{(w)}s^2 + C_{qr}^{(w)}s + K_{qr}^{(w)}\right)\left(P_D s + R_L\right) + sP_r^{(w)}P_q^{(w)}}{sP_r^{(u)}\left(M_{qr}^{(w)}s^2 + C_{qr}^{(w)}s + K_{qr}^{(w)}\right)}, \quad (4.123)$$

$$\left.\frac{u_r(s)}{v(s)}\right|_{s^2 u_{base}(s)=0} = \frac{-P_q^{(u)}}{M_{qr}^{(u)}s^2 + C_{qr}^{(u)}s + K_{qr}^{(u)}}, \quad (4.124)$$

$$\left.\frac{w_r(s)}{v(s)}\right|_{s^2 w_{base}(s)=0} = \frac{-P_q^{(w)}}{M_{qr}^{(w)}s^2 + C_{qr}^{(w)}s + K_{qr}^{(w)}}, \quad (4.125)$$

$$\left.\frac{w_r(s)}{v(s)}\right|_{s^2 u_{base}(s)=0} = \frac{-\left(M_{qr}^{(u)}s^2 + C_{qr}^{(u)}s + K_{qr}^{(u)}\right)\left(P_D s + R_L\right) + sP_r^{(u)}P_q^{(u)}}{sP_r^{(w)}\left(M_{qr}^{(u)}s^2 + C_{qr}^{(u)}s + K_{qr}^{(u)}\right)}. \quad (4.126)$$

Corresponding with Eqs. (4.113) to (4.120), the frequency response function (FRF) can be formulated. The first FRF represents longitudinal motion with respect to input excitations. In the case where the input transverse acceleration is ignored, the FRF can be obtained from base-input longitudinal motion as it was formulated,

$$H_{11}(j\omega) = \left.\frac{u_r(j\omega)}{-\omega^2 u_{base}e^{(j\omega t)}}\right|_{s=j\omega} = \frac{1}{Z(j\omega)}\left[\left(M_{qr}^{(w)}R_L\omega^2 + \omega^2 P_D C_{qr}^{(w)} - K_{qr}^{(w)}R_L\right)\right.$$

$$\left. + j\left(P_D M_{qr}^{(w)}\omega^3 - \omega C_{qr}^{(w)}R_L - \omega P_D K_{qr}^{(w)} + \omega P_r^{(w)}P_q^{(w)}\right)\right]Q_q^{(u)}. \quad (4.127)$$

It is noted that $-\omega^2 u_{base}e^{(j\omega t)}$ is input acceleration. Equation (4.127) can be modified to obtain the FRF as a function of position of the piezoelectric element (x) and frequency $(j\omega)$ by transforming it back into the eigenfunction. This then yields,

$$H_{11}(x,j\omega) = \frac{1}{Z(j\omega)} \left[\left(M_{qr}^{(w)} R_L \omega^2 + \omega^2 P_D C_{qr}^{(w)} - K_{qr}^{(w)} R_L \right) \right.$$

$$\left. + j \left(P_D M_{qr}^{(w)} \omega^3 - \omega C_{qr}^{(w)} R_L - \omega P_D K_{qr}^{(w)} + \omega P_r^{(w)} P_q^{(w)} \right) \right] Q_q^{(u)} \Theta_r(x). \quad (4.128)$$

If base-input longitudinal motion was not applied, the FRF of base-input transverse motion can be obtained as,

$$H_{12}(j\omega) = \left. \frac{u_r(j\omega)}{-\omega^2 w_{base} e^{j\omega t}} \right|_{s=j\omega} = -\frac{j\omega P_r^{(w)} P_q^{(u)} Q_q^{(w)}}{Z(j\omega)} \quad . \quad (4.129)$$

Equation (4.129) can be modified in terms of the FRF as a function of position in the piezoelectric element (x) and frequency $(j\omega)$ as,

$$H_{12}(x,j\omega) = -\frac{j\omega P_r^{(w)} P_q^{(u)} Q_q^{(w)} \Theta_r(x)}{Z(j\omega)} \quad . \quad (4.130)$$

The second FRF represents transverse motion with respect to input motions. If base-input transverse motion is ignored, the FRF of base-input longitudinal motion can be obtained as,

$$H_{21}(j\omega) = \left. \frac{w_r(j\omega)}{-\omega^2 u_{base} e^{j\omega t}} \right|_{s=j\omega} = -\frac{j\omega P_r^{(u)} P_q^{(w)} Q_q^{(u)}}{Z(j\omega)} \quad . \quad (4.131)$$

Equation (4.131) can be modified in terms of the FRF as a function of piezoelectric position (x) and frequency $(j\omega)$ as,

$$H_{21}(x, j\omega) = -\frac{j\omega P_r^{(u)} P_q^{(w)} Q_q^{(u)} \Psi_r(x)}{Z(j\omega)}. \quad (4.132)$$

The FRF of transverse displacement with respect to base-input transverse acceleration can be obtained as,

$$H_{22}(j\omega) = \left. \frac{w_r(j\omega)}{-\omega^2 w_{base} e^{j\omega t}} \right|_{s=j\omega} = \frac{1}{Z(j\omega)} \left[\left(M_{qr}^{(u)} R_L \omega^2 + \omega^2 P_D C_{qr}^{(u)} - K_{qr}^{(u)} R_L \right) \right.$$

$$\left. + j \left(P_D M_{qr}^{(u)} \omega^3 - \omega C_{qr}^{(u)} R_L - \omega P_D K_{qr}^{(u)} + \omega P_r^{(u)} P_q^{(u)} \right) \right] Q_q^{(w)}. \quad (4.133)$$

By using the corresponding eigenfunction from Eq. (4.97) and the FRF from Eq. (4.133), the FRF as a function of piezoelectric element position (x) and frequency $(j\omega)$ can formulated as,

$$H_{22}(x, j\omega) = \frac{1}{Z(j\omega)} \left[\left(M_{qr}^{(u)} R_L \omega^2 + \omega^2 P_D C_{qr}^{(u)} - K_{qr}^{(u)} R_L \right) \right.$$

$$\left. + j \left(P_D M_{qr}^{(u)} \omega^3 - \omega C_{qr}^{(u)} R_L - \omega P_D K_{qr}^{(u)} + \omega P_r^{(u)} P_q^{(u)} \right) \right] Q_q^{(w)} \Psi_r(x). \quad (4.134)$$

The FRF between output electric voltage and the input base-longitudinal acceleration can be obtained as,

$$H_{31}(j\omega) = \frac{v(j\omega)}{-\omega^2 u_{base} e^{j\omega t}}\bigg|_{s=j\omega} = \frac{\left(-j\omega^3 M_{qr}^{(w)} P_r^{(u)} - \omega^2 C_{qr}^{(w)} P_r^{(u)} + j\omega K_{qr}^{(w)} P_r^{(u)}\right) Q_q^{(u)}}{Z(j\omega)}. \quad (4.135)$$

The FRF of the output electric voltage with respect to the input base-transverse acceleration can be derived as base-input longitudinal acceleration is omitted. This can be written as,

$$H_{32}(j\omega) = \frac{v(j\omega)}{-\omega^2 w_{base} e^{j\omega t}}\bigg|_{s=j\omega} = \frac{\left(-j\omega^3 M_{qr}^{(u)} P_r^{(w)} - \omega^2 C_{qr}^{(u)} P_r^{(w)} + j\omega K_{qr}^{(u)} P_r^{(w)}\right) Q_q^{(w)}}{Z(j\omega)}. \quad (4.136)$$

The FRF of power harvesting related to the transverse acceleration can be derived as,

$$\frac{P(j\omega)}{\left(-\omega^2 w_{base} e^{j\omega t}\right)^2}\bigg|_{s=j\omega} = \frac{\left(-j\omega^3 M_{qr}^{(u)} P_r^{(w)} - \omega^2 C_{qr}^{(u)} P_r^{(w)} + j\omega K_{qr}^{(u)} P_r^{(w)}\right)^2 Q_q^{(w)2}}{R_{load} Z(j\omega)^2}. \quad (4.137)$$

The FRF of power harvesting related to the longitudinal acceleration can be derived as,

$$\frac{P(j\omega)}{\left(-\omega^2 u_{base} e^{j\omega t}\right)^2}\bigg|_{s=j\omega} = \frac{\left(-j\omega^3 M_{qr}^{(w)} P_r^{(u)} - \omega^2 C_{qr}^{(w)} P_r^{(u)} + j\omega K_{qr}^{(w)} P_r^{(u)}\right)^2 Q_q^{(u)2}}{R_{load} Z(j\omega)^2}. \quad (4.138)$$

where:

$$
\begin{aligned}
Z(j\omega) = {}& \omega^4\left(P_D M_{qr}^{(u)} C_{qr}^{(w)} + P_D C_{qr}^{(u)} M_{qr}^{(w)} + R_L M_{qr}^{(u)} M_{qr}^{(w)}\right) \\
& - \omega^2\left(R_L C_{qr}^{(u)} C_{qr}^{(w)} - P_r^{(u)} P_q^{(u)} C_{qr}^{(w)} - P_r^{(w)} P_q^{(w)} C_{qr}^{(u)} + K_{qr}^{(w)} P_D C_{qr}^{(u)} + K_{qr}^{(w)} R_L M_{qr}^{(u)}\right. \\
& \left. + K_{qr}^{(u)} P_D C_{qr}^{(w)} + K_{qr}^{(u)} R_L M_{qr}^{(w)}\right) + K_{qr}^{(u)} K_{qr}^{(w)} R_L + j\left[\omega^5 P_D M_{qr}^{(u)} M_{qr}^{(w)}\right. \\
& - \omega^3\left(P_D C_{qr}^{(u)} C_{qr}^{(w)} + R_L M_{qr}^{(u)} C_{qr}^{(w)} + R_L C_{qr}^{(u)} M_{qr}^{(w)} - P_r^{(u)} P_q^{(u)} M_{qr}^{(w)}\right. \\
& \left.\left. - P_r^{(w)} P_q^{(w)} M_{qr}^{(u)} + K_{qr}^{(w)} P_D M_{qr}^{(u)} + K_{qr}^{(u)} P_D M_{qr}^{(w)}\right)\right]
\end{aligned}
\qquad (4.139)
$$

4.3.2. The Weak Form of Coupled Electromechanical Dynamic Response of Transverse form (Weak-CEDRT)

This section focuses on the constitutive electromechanical dynamic equation of the piezoelectric bimorph with tip mass due to the strain field from transverse bending and electric field under input transverse base excitation. The equation (4.96) can be reduced to formulate the coupled dynamic equation of bending transverse mechanical and electrical forms and other variables of Eq. (4.96) can be ignored.

The constitutive electromechanical dynamic equation of the piezoelectric bimorph under input base transverse motion can be formulated as,

$$\int_{t_1}^{t_2}\left[\int_{\Omega}\left\{C_{11}^{(F,k)}\varepsilon_1^{(1)}\frac{\partial^2\delta w_{rel}}{\partial x^2}+R_{31}^{(H,k)}v(t)\frac{\partial^2\delta w_{rel}}{\partial x^2}+I^{(C,k)}\frac{\partial\ddot{w}_{rel}}{\partial x}\frac{\partial\delta(w_{rel})}{\partial x}+I^{(A,k)}\ddot{w}_{rel}\delta w_{rel}\right.\right.$$
$$\left.+R_{31}^{(H,k)}\frac{\partial^2 w_{rel}}{\partial x^2}\delta v(t)-S_{33}^{(k)}v(t)\delta v(t)+I^{(A,k)}\ddot{w}_{base}\delta w_{rel}\right\}dxdy-q(t)\delta v(t)$$
$$\left.+I_{tip}^{(C)}\frac{\partial\ddot{w}_{rel}}{\partial x}(L)\frac{\partial\delta(w_{rel})}{\partial x}(L)+I_{tip}^{(A)}\ddot{w}_{rel}(L)\delta w_{rel}(L)+I_{tip}^{(A)}\ddot{w}_{base}(L)\delta w_{rel}(L)\right]dt=0\,.(4.140)$$

The solution form can be obtained using eigenfunction series and the solutions must meet continuity and also boundary conditions of the piezoelectric bimorph beam under transverse bending effects. The solution form can be prescribed as,

$$w_{rel}(x,t)=\sum_{r=1}^{m}w_r(t)\Psi_r(x)\quad.\tag{4.141}$$

At this point, two dynamic equations of the piezoelectric bimorph beam can be formulated. The first dynamic equation represents the electromechanical piezoelectric bimorph under transverse bending form. It can be stated as,

$$\sum_{q=1}^{m}\left\{\sum_{r=1}^{m}\left[\int_{\Omega}I^{(A,k)}\Psi_q(x)\Psi_r(x)\ddot{w}_r(t)dxdy+\int_{\Omega}I^{(C,k)}\frac{d\Psi_q(x)}{dx}\frac{d\Psi_r(x)}{dx}\ddot{w}_r(t)dxdy+I_{tip}^{(A)}\Psi_q(L)\Psi_r(L)\ddot{w}_r(t)\right.\right.$$
$$\left.+I_{tip}^{(C)}\frac{d\Psi_q(L)}{dx}\frac{d\Psi_r(L)}{dx}\ddot{w}_r(t)+\int_{\Omega}C^{(F,k)}\frac{d^2\Psi_q(x)}{dx^2}\frac{d^2\Psi_r(x)}{dx^2}w_r(t)dxdy\right]+\int_{\Omega}R_{31}^{(H,k)}\frac{d^2\Psi_q}{dx^2}v(t)dxdy$$
$$\left.+\int_{\Omega}I^{(A,k)}\Psi_q(x)\ddot{w}_{base}(t)dxdy+I_{tip}^{(A)}\Psi_q(L)\ddot{w}_{base}(t)\right\}\delta w_q(t)=0\,.\tag{4.142}$$

The second dynamic equation represents the electromechanical piezoelectric bimorph under electrical form. It can be stated as,

$$\sum_{r=1}^{m}\int_{\Omega}R_{31}^{(H,k)}\frac{d^2\Psi_r(x)}{dx^2}\dot{w}_r(t)dxdy-\int_{\Omega}S_{33}^{(k)}\dot{v}(t)dxdy-\frac{1}{R_{load}}v(t)=0\,.\tag{4.143}$$

Two dynamic equations can be formulated in matrix form as,

$$\begin{bmatrix}M_{qr}^{(w)}&0\\0&0\end{bmatrix}\begin{Bmatrix}\ddot{w}_r\\\ddot{v}\end{Bmatrix}+\begin{bmatrix}C_{qr}^{(w)}&0\\P_r^{(w)}&P_D\end{bmatrix}\begin{Bmatrix}\dot{w}_r\\\dot{v}\end{Bmatrix}+\begin{bmatrix}K_{qr}^{(w)}&P_q^{(w)}\\0&R_L\end{bmatrix}\begin{Bmatrix}w_r\\v\end{Bmatrix}=\begin{bmatrix}-Q_q^{(w)}&0\\0&0\end{bmatrix}\begin{Bmatrix}\ddot{w}_{base}\\\ddot{v}_{base}\end{Bmatrix}.(4.144)$$

It should be noted that the each parameter in Eq. (4.144) can be obtained from Eq. (4.103). Laplace transforms can then be used to formulate the matrix equation as,

$$\begin{bmatrix}M_{qr}^{(w)}s^2+C_{qr}^{(w)}s+K_{qr}^{(w)}&P_q^{(w)}\\P_r^{(w)}s&P_D s+R_L\end{bmatrix}\begin{Bmatrix}w_r(s)\\v(s)\end{Bmatrix}=\begin{Bmatrix}-s^2 Q_q^{(w)}w_{base}(s)\\0\end{Bmatrix}.\tag{4.145}$$

The transfer function due to the input transverse acceleration related to the transverse displacement can be formulated as,

$$\frac{w_r(s)}{s^2 w_{base}(s)} = \frac{-(P_D s + R_L)s Q_q^{(w)}}{Z(s)} \quad . \tag{4.146}$$

The electrical potential can be expressed as,

$$\frac{v(s)}{s^2 w_{base}(s)} = \frac{s P_r^{(w)} Q_q^{(w)}}{Z(s)} \quad . \tag{4.147}$$

where :

$$Z(s) = M_{qr}^{(w)} P_D s^3 + M_{qr}^{(w)} R_L s^2 + C_{qr}^{(w)} P_D s^2 + C_{qr}^{(w)} R_L s + K_{qr}^{(w)} P_D s + K_{qr}^{(w)} R_L - P_q^{(w)} P_r^{(w)} s$$

Corresponding to Eq. (4.146), the frequency response function (FRF) of the transverse displacement related to the input transverse acceleration based on the bimorph element position (x) and frequency $(j\omega)$ can be formulated as,

$$H_1(x, j\omega) = \frac{w_{rel}(x, j\omega)}{-\omega^2 w_{base} e^{j\omega t}} = \frac{-(j\omega P_D + R_L) Q_q^{(w)} \Psi_r(x)}{Z(j\omega)} \quad . \tag{4.148}$$

The FRF of electrical potential related to the input transverse acceleration can be obtained as,

$$H_2(j\omega) = \frac{v(j\omega)}{-\omega^2 w_{base} e^{j\omega t}} = \frac{j\omega P_r^{(w)} Q_q^{(w)}}{Z(j\omega)} \quad . \tag{4.149}$$

The time dependent relative transverse displacement can be formulated in terms of the FRF as,

$$w_{rel}(t) = H_1(j\omega) \omega^2 w_{base} e^{j\omega t} \quad . \tag{4.150}$$

Corresponding with Eq. (4.141), equation (4.150) can be modified to give the time dependant relative transverse displacement as a function of position in the piezoelectric element (x) and frequency $(j\omega)$ as,

$$w_{rel}(x,t) = H_1(x, j\omega)\left(-\omega^2 w_{base} e^{j\omega t}\right). \tag{4.151}$$

Corresponding with the kinematic diagram from Figure (4.1), the absolute transverse displacement can be reduced as,

$$w_{abs}(x,t) = w_{base} e^{j\omega t} + H_1(x, j\omega)\left(-\omega^2 w_{base} e^{j\omega t}\right). \tag{4.152}$$

The generalized time dependant electrical potential can be formulated as,

$$v(t) = H_2(j\omega)\left(-\omega^2 w_{base} e^{j\omega t}\right) \quad . \tag{4.153}$$

It should be noted that w_{base} represents the input base transverse displacement excitations on the bimorph. Corresponding to Eq. (4.152), equation (4.148) can be modified in terms of the FRF of absolute displacement and velocity relating the input transverse displacement at any position along the bimorph respectively to give,

$$\hat{H}_1^{(disp)}(x,j\omega) = \frac{w_{base}e^{j\omega t} + w_{rel}(x,t)}{-\omega^2 w_{base}e^{j\omega t}} = -\frac{1}{\omega^2} + H_1(x,j\omega), \tag{4.154}$$

$$\hat{H}_1^{(vel)}(x,j\omega) = \frac{\dfrac{d}{dt}\left[w_{base}e^{j\omega t} + w_{rel}(x,t)\right]}{-\omega^2 w_{base}e^{j\omega t}} = \frac{1}{j\omega} + jH_1(x,j\omega) . \tag{4.155}$$

where :

$$Z(j\omega) = -j\omega^3 M_{qr}^{(w)}P_D - \omega^2 M_{qr}^{(w)}R_L - \omega^2 C_{qr}^{(w)}P_D + j\omega C_{qr}^{(w)}R_L + j\omega K_{qr}^{(w)}P_D - j\omega P_r^{(w)}P_q^{(w)} + K_{qr}^{(w)}R_L .$$

4.3.3. The Weak Form of the Coupled Electromechanical Dynamic Response of Longitudinal Form (Weak-CEDRL)

This section focuses on the constitutive electromechanical dynamic response based on the coupled longitudinal strain and polarity-electric field of the bimorph under input base longitudinal motion. The equation (4.96) can be reduced to formulate the coupled dynamic equation of longitudinal extension mechanical and electrical forms and other variables of Eq. (4.96) can be ignored.

The constitutive electromechanical dynamic equation can be written as

$$\int_{t_1}^{t_2}\left[\iint_\Omega\left(I^{(A,k)}\ddot{u}_{rel}\delta u_{rel} + I^{(A,k)}\ddot{u}_{base}\delta u_{rel} + C_{11}^{(D,k)}\varepsilon_1^{(0)}\frac{\partial\delta u_{rel}}{\partial x} - R_{31}^{(G,k)}v(t)\frac{\partial\delta u_{rel}}{\partial x} - S_{33}^{(k)}v(t)\delta v(t)\right.\right.$$
$$\left.\left. - R_{31}^{(G,k)}\frac{\partial u_{rel}}{\partial x}\delta v(t)\right)dxdy - q\delta v(t) + I_{tip}^{(A)}\ddot{u}_{rel}(L)\delta u_{rel}(L) + I_{tip}^{(A)}\ddot{u}_{base}\delta u_{rel}(L)\right]dt . \tag{4.156}$$

The solution form can be obtained using eigenfunction series and the solutions must meet continuity and also boundary conditions of the piezoelectric bimorph beam under longitudinal extension bending effects. The solution form can be prescribed as,

$$u_{rel}(x,t) = \sum_{r=1}^m u_r(t)\Theta_r(x) . \tag{4.157}$$

At this point, two dynamic equations of the piezoelectric bimorph beam can be formulated. The first dynamic equation represents the electromechanical piezoelectric bimorph under longitudinal form. It can be stated as,

$$\sum_{q=1}^{m}\left\{\sum_{r=1}^{m}\left[\int_{\Omega}I^{(A,k)}\Theta_q(x)\Theta_r(x)\ddot{u}_r(t)dxdy + I_{tip}^{(A)}\Theta_q(L)\Theta_r(L)\ddot{u}_r(t) + \int_{\Omega}C_{11}^{(D,k)}\frac{d\Theta_q(x)}{dx}\frac{d\Theta_r(x)}{dx}u_r(t)dxdy\right]\right.$$

$$\left.-\int_{\Omega}R_{31}^{(G,k)}\frac{d\Theta_q(x)}{dx}v(t)dxdy + \int_{\Omega}I^{(A,k)}\Theta_q(x)\ddot{u}_{base}(t)dxdy + I_{tip}^{(A)}\Theta_q(L)\ddot{u}_{base}(t)\right\}\delta u_q(t) = 0. \quad (4.158)$$

The second equation represents the electromechanical piezoelectric bimorph under electrical form. It can be stated as,

$$-\sum_{r=1}^{m}\int_{\Omega}R_{31}^{(H,k)}\frac{d^2\Psi_r(x)}{dx^2}\dot{w}_r(t)dxdy - \int_{\Omega}S_{33}^{(k)}\dot{v}(t)dxdy - \frac{1}{R_{load}}v(t) = 0 \quad . \quad (4.159)$$

The two dynamic equations can be formulated in matrix form as,

$$\begin{bmatrix} M_{qr}^{(u)} & 0 \\ 0 & 0 \end{bmatrix}\begin{Bmatrix} \ddot{u}_r \\ \ddot{v} \end{Bmatrix} + \begin{bmatrix} C_{qr}^{(u)} & 0 \\ P_r^{(u)} & P_D \end{bmatrix}\begin{Bmatrix} \dot{u}_r \\ \dot{v} \end{Bmatrix} + \begin{bmatrix} K_{qr}^{(u)} & P_q^{(u)} \\ 0 & R_L \end{bmatrix}\begin{Bmatrix} u_r \\ v \end{Bmatrix} = \begin{bmatrix} -Q_q^{(u)} & 0 \\ 0 & 0 \end{bmatrix}\begin{Bmatrix} \ddot{u}_{base} \\ \ddot{v}_{base} \end{Bmatrix} .(4.160)$$

The Laplace transform can be used to formulate the transfer function as,

$$\begin{bmatrix} M_{qr}^{(u)}s^2 + C_{qr}^{(u)}s + K_{qr}^{(u)} & P_q^{(u)} \\ P_r^{(w)}s & P_D s + R_L \end{bmatrix}\begin{Bmatrix} u_r(s) \\ v(s) \end{Bmatrix} = \begin{Bmatrix} -s^2 Q_q^{(u)}u_{base}(s) \\ 0 \end{Bmatrix} . \quad (4.161)$$

The transfer function due to the longitudinal displacement related to the input base longitudinal acceleration can be formulated as,

$$\frac{u_r(s)}{s^2 u_{base}(s)} = \frac{-(P_D s + R_L)Q_q^{(u)}}{Z(s)} \quad . \quad (4.162)$$

The voltage transfer function can be written as,

$$\frac{v(s)}{s^2 u_{base}(s)} = \frac{sP_r^{(u)}Q_q^{(u)}}{Z(s)} \quad , \quad (4.163)$$

where,

$$Z(s) = M_{qr}^{(u)}P_D s^3 + M_{qr}^{(u)}R_L s^2 + C_{qr}^{(u)}P_D s^2 + C_{qr}^{(u)}R_L s + K_{qr}^{(u)}P_D s + K_{qr}^{(u)}R_L - P_q^{(u)}P_r^{(u)}s \quad .$$

Corresponding to Eq. (4.157), the frequency response function (FRF) of the longitudinal displacement related to the input longitudinal acceleration based on the bimorph element position (x) and frequency $(j\omega)$ can be formulated as,

$$H_1(x, j\omega) = \frac{u_{rel}(x, j\omega)}{-\omega^2 u_{base}e^{j\omega t}} = \frac{-(j\omega P_D + R_L)Q_q^{(u)}\Psi_r(x)}{Z(j\omega)} \quad . \quad (4.164)$$

The frequency response function of electrical potential related to the input longitudinal acceleration can be expressed as,

$$H_2(j\omega) = \frac{v(j\omega)}{-\omega^2 u_{base} e^{j\omega t}} = -\frac{j\omega P_r^{(u)} Q_q^{(u)}}{Z(j\omega)} , \tag{4.165}$$

where,

$$Z(j\omega) = -j\omega^3 M_{qr}^{(u)} P_D - \omega^2 M_{qr}^{(u)} R_L - \omega^2 C_{qr}^{(u)} P_D + j\omega C_{qr}^{(u)} R_L + j\omega K_{qr}^{(u)} P_D - j\omega P_r^{(u)} P_q^{(u)} + K_{qr}^{(u)} R_L .$$

The time dependent relative longitudinal displacement can be formulated in terms of the FRF as,

$$u_{rel}(t) = H_1(j\omega)\omega^2 u_{base} e^{j\omega t} . \tag{4.166}$$

Equation (4.166) can be modified to give the relative longitudinal displacement as a function of position in the piezoelectric element (x) and frequency $(j\omega)$ as,

$$u_{rel}(x,t) = H_1(x, j\omega)(-\omega^2 u_{base} e^{j\omega t}) . \tag{4.167}$$

Corresponding with Eq. (4.167), the absolute longitudinal displacement can be reduced as,

$$u_{abs}(x,t) = u_{base} e^{j\omega t} + H_1(x, j\omega)(-\omega^2 u_{base} e^{j\omega t}). \tag{4.168}$$

The generalised electrical potential can be formulated as,

$$v(t) = H_2(j\omega)(-\omega^2 u_{base} e^{j\omega t}) . \tag{4.169}$$

Corresponding to Eq. (4.168), equation (4.164) can be modified in terms of the FRF of absolute displacement and velocity relating the input longitudinal displacement at any position along the bimorph respectively to give,

$$\hat{H}_1^{(disp)}(x, j\omega) = \frac{u_{base} e^{j\omega t} + u_{rel}(x,t)}{-\omega^2 u_{base} e^{j\omega t}} = -\frac{1}{\omega^2} + H_1(x, j\omega), \tag{4.170}$$

$$\hat{H}_1^{(vel)}(x, j\omega) = \frac{\dfrac{d}{dt}[u_{base} e^{j\omega t} + u_{rel}(x,t)]}{-\omega^2 u_{base} e^{j\omega t}} = \frac{1}{j\omega} + j H_1(x, j\omega). \tag{4.171}$$

4.4. Multi-mode Frequency Analysis of the Normalised Coupled Electromechanical Dynamic Response of Longitudinal Form (Weak-CEDRL)

The multi-mode frequency analysis of the electromechanical dynamic equations can be extended using Eq. (4.165). The solution form complies the generalised longitudinal function of the Ritz eigenfunction series, which can be further formulated using the orthonormality, Ritz [99], Courant and Hilbert [100]. In this case, the extended convergent Ritz eigenfunction series can be stated as,

$$u_{rel}(x,t) = \sum_{r=1}^{m} c_r^{(u)} \Theta_r(x) e^{i\omega t} \qquad . \qquad (4.172)$$

Substituting Eq. (4.172) into Eq. (4.156) by considering only the mechanical equations to give independent algebraic equations of the eigenvalues corresponding to the longitudinal form as,

$$\sum_{r=1}^{m} \left[K_{qr}^{(u)} - \omega^{(u)} M_{qr}^{(u)} \right] c_r^{(u)} = 0, \qquad q = 1,2,....,m \ . \qquad (4.173)$$

The unknown Ritz coefficient $c_r^{(u)}$ is sometimes called the eigenvectors which need to be identified along with the natural frequencies. Therefore, the generalised Ritz mode shapes in terms of the *r*-degree of freedom can be formulated as,

$$\Theta_r(x) = \sum_{k=1}^{m} c_{kr}^{(u)} \Theta_k(x) \qquad r = 1,2,....,m \qquad . \qquad (4.174)$$

The normalised Ritz mode shapes can be formulated with respect to the generalised mass as,

$$\hat{\Theta}_r(x) = \frac{\Theta_r(x)}{\left(\int_0^L \hat{I}^{(A,k)} \Theta_r(x)^2 dx + I_{tip}^{(A)} \Theta_r(L)^2 \right)^{1/2}} \qquad r = 1,2,....,m \ . \qquad (4.175)$$

The normalised eigenfunction series associated with the generalised time dependent function can now be stated as,

$$u_{rel}(x,t) = \sum_{r=1}^{m} \hat{\Theta}_r(x) u_r(t) \qquad . \qquad (4.176)$$

Corresponding to Eq. (4.156), the orthonormalisations can be provided by using Eq. (4.175) and applying the orthogonality property of the mechanical dynamic equation as,

$$\int_0^L \hat{I}^{(A,k)} \hat{\Theta}_r(x) \hat{\Theta}_q(x) dx + I_{tip}^{(A)} \hat{\Theta}_r(L) \hat{\Theta}_q(L) = \delta_{rq}, \qquad (4.177)$$

$$\int_0^L \hat{C}_{11}^{(D,k)} \frac{d\hat{\Theta}_r(x)}{dx} \frac{d\hat{\Theta}_q(x)}{dx} dx = \omega_r^{(u)2} \delta_{rq} \qquad . \qquad (4.178)$$

where δ_{rq} is the Kronecker delta, defined as unity for $q = r$ and zero for $q \neq r$. The mechanical damping can be reduced in terms of the orthonormalisation as,

$$C_{rq}^{(u)} = \alpha^{(u)} \delta_{rq} + \beta^{(u)} \omega_r^{(u)2} \delta_{rq} = 2\zeta_r^{(u)} \omega_r^{(u)} \delta_{rq}. \qquad (4.179)$$

Applying the orthonormalisations from Eqs. (4.177) and (4.178) into the electromechanical piezoelectric bimorph beam from Eq. (4.156) gives,

$$\ddot{u}_r(t) + 2\zeta_r^{(u)}\omega_r^{(u)}\dot{u}_r(t) + \omega_r^{(u)2}u_r(t) + P_r^{(u)}v(t) = -Q_r^{(u)}\ddot{u}_{base}(t) \qquad (4.180)$$

$$\hat{P}_r^{(u)}\dot{u}_r(t) + P_D\dot{v}(t) + R_L v(t) = 0$$

Because equation (4.180) has been normalised by using Eq. (4.176) in terms of Eqs. (4.177) and (4.178), the parameters $P_r^{(u)}$, $\hat{P}_r^{(u)}$, R_L, P_D and $Q_r^{(u)}$ can be reduced as,

$$P_r^{(u)} = -\int_0^L \hat{R}_{31}^{(G,k)}\frac{d\hat{\Theta}_r(x)}{dx}dx \qquad , \hat{P}_r^{(u)} = \sum_{r=0}^m P_r^{(u)} \quad , \qquad R_L = -\frac{1}{R_{load}} \quad ,$$

$$P_D = -\int_0^L \hat{S}_{33}^{(k)}dx, \qquad Q_r^{(u)} = \int_0^L \hat{I}^{(A,k)}\hat{\Theta}_r(x)dx + I_{tip}^{(A)}\hat{\Theta}_r(L) \quad .$$

The Laplace transforms can be applied in Eq. (4.180) to give the transfer functions. The multi-mode transfer function between the input base longitudinal acceleration and relative longitudinal displacement can be obtained as,

$$H_1(s) = \frac{u_r(s)}{s^2 u_{base}(s)} = -\frac{1}{s^2 + 2\zeta_r^{(u)}\omega_r^{(u)}s + \omega_r^{(u)2}}\left(\frac{(sP_D + R_L)Q_r^{(u)}}{j\omega P_D + R_L - \sum_{r=1}^m \frac{sP_r^{(u)2}}{s^2 + 2\zeta_r^{(u)}\omega_r^{(u)}s + \omega_r^{(u)2}}}\right). \qquad (4.181)$$

The multi-mode transfer function of the input base longitudinal acceleration relating to the longitudinal displacement output in terms of the bimorph element position (x) and subsidiary variable (s) can be formulated after simplifying to give,

$$H_1(x,s) = \frac{u_{rel}(x,s)}{s^2 u_{base}(s)} = -\sum_{r=1}^m\left[\frac{\hat{\Theta}_r(x)}{s^2 + 2\zeta_r^{(u)}\omega_r^{(u)}s + \omega_r^{(u)2}}\left(\frac{(sP_D + R_L)Q_r^{(u)}}{j\omega P_D + R_L - \sum_{r=1}^m \frac{sP_r^{(u)2}}{s^2 + 2\zeta_r^{(u)}\omega_r^{(u)}s + \omega_r^{(u)2}}}\right)\right]. \qquad (4.182)$$

With the same method, the multi-mode transfer function between the input base longitudinal acceleration and the electric voltage can be obtained as,

$$H_2(s) = \frac{v(s)}{s^2 u_{base}(s)} = \frac{\sum_{r=1}^m \frac{sP_r^{(u)}Q_r^{(u)}}{s^2 + 2\zeta_r^{(u)}\omega_r^{(u)}s + \omega_r^{(u)2}}}{sP_D + R_L - \sum_{r=1}^m \frac{sP_r^{(u)2}}{s^2 + 2\zeta_r^{(u)}\omega_r^{(u)}s + \omega_r^{(u)2}}}. \qquad (4.183)$$

The multi-mode transfer function related to power harvesting with respect to the input base longitudinal acceleration can be derived as,

$$\frac{P(s)}{\left(s^2 u_{base}(s)\right)^2} = \left[\frac{\dfrac{1}{\sqrt{R_{load}}} \displaystyle\sum_{r=1}^{m} \dfrac{sP_r^{(u)}Q_r^{(u)}}{s^2 + 2\zeta_r^{(u)}\omega_r^{(u)}s + \omega_r^{(u)2}}}{sP_D + R_L - \displaystyle\sum_{r=1}^{m} \dfrac{sP_r^{(u)2}}{s^2 + 2\zeta_r^{(u)}\omega_r^{(u)}s + \omega_r^{(u)2}}}\right]^2 . \tag{4.184}$$

Corresponding to Eqs. (4.181) – (4.184), the frequency response functions (FRFs) can be formulated by substituting variable (s) with $(j\omega)$. The multi-mode FRF of the generalised time dependent function of the longitudinal displacement with respect to the input base longitudinal acceleration can be obtained as,

$$H_1(j\omega) = \frac{u_r(j\omega)}{-\omega^2 u_{base}e^{j\omega t}} = -\frac{1}{\omega_r^{(u)2} - \omega^2 + j2\zeta_r^{(u)}\omega_r^{(u)}\omega}\left(\frac{\left(j\omega P_D + R_L\right)Q_r^{(u)}}{j\omega P_D + R_L - \displaystyle\sum_{r=1}^{m} \dfrac{j\omega P_r^{(u)2}}{\omega_r^{(u)2} - \omega^2 + j2\zeta_r^{(u)}\omega_r^{(u)}\omega}}\right), \tag{4.185}$$

Equation (4.185) can be modified to obtain the FRF as a function of position of the piezoelectric element (x) and frequency $(j\omega)$ by transforming it back into the Ritz eigenfunction form to give,

$$H_1(x, j\omega) = \frac{u_{rel}(x, j\omega)}{-\omega^2 u_{base}e^{j\omega t}} = -\sum_{r=1}^{m}\left[\frac{\hat{\Theta}_r(x)}{\omega_r^{(u)2} - \omega^2 + j2\zeta_r^{(u)}\omega_r^{(u)}\omega}\left(\frac{\left(j\omega P_D + R_L\right)Q_r^{(u)}}{j\omega P_D + R_L - \displaystyle\sum_{r=1}^{m} \dfrac{j\omega P_r^{(w)2}}{\omega_r^{(u)2} - \omega^2 + j2\zeta_r^{(u)}\omega_r^{(u)}\omega}}\right)\right]. \tag{4.186}$$

The multi-mode FRF of the electric voltage related to the input base longitudinal acceleration can be derived as,

$$H_2(j\omega) = \frac{v(j\omega)}{-\omega^2 u_{base}e^{j\omega t}} = \frac{\displaystyle\sum_{r=1}^{m} \dfrac{j\omega P_r^{(u)}Q_r^{(u)}}{\omega_r^{(u)2} - \omega^2 + j2\zeta_r^{(u)}\omega_r^{(u)}\omega}}{j\omega P_D + R_L - \displaystyle\sum_{r=1}^{m} \dfrac{j\omega P_r^{(u)2}}{\omega_r^{(u)2} - \omega^2 + j2\zeta_r^{(u)}\omega_r^{(u)}\omega}} . \tag{4.187}$$

The multi-mode FRF of power harvesting related to the input longitudinal acceleration can be derived as,

$$\frac{P(j\omega)}{\left(\omega^2 u_{base}e^{j\omega t}\right)^2} = \left[\frac{\dfrac{1}{\sqrt{R_{load}}} \displaystyle\sum_{r=1}^{m} \dfrac{j\omega P_r^{(u)}Q_r^{(u)}}{\omega_r^{(u)2} - \omega^2 + j2\zeta_r^{(u)}\omega_r^{(u)}\omega}}{j\omega P_D + R_L - \displaystyle\sum_{r=1}^{m} \dfrac{j\omega P_r^{(u)2}}{\omega_r^{(u)2} - \omega^2 + j2\zeta_r^{(u)}\omega_r^{(u)}\omega}}\right]^2 . \tag{4.188}$$

The generalised time dependent function of relative transverse displacement can be reformulated in terms of Eqs. (4.176) and (4.185) as,

$$u_{rel}(x,t) = H_1(x, j\omega)\left(-\omega^2 u_{base}e^{j\omega t}\right). \tag{4.189}$$

Corresponding to Eq. (4.189), the absolute transverse displacement can be reduced as,

$$u_{abs}(x,t) = u_{base}e^{j\omega t} + H_1(x,j\omega)(-\omega^2 u_{base}e^{j\omega t}).$$
(4.190)

The generalised electrical voltage can be formulated as,

$$v(t) = H_2(j\omega)\ddot{u}_{base} = H_2(j\omega)(-\omega^2 u_{base}e^{j\omega t}) \quad .$$
(4.191)

Corresponding to Eq. (4.190), the equation (4.186) can be modified in terms of the multi-mode FRF of the absolute displacement and velocity relating the input longitudinal displacement at any position along the bimorph respectively as,

$$\hat{H}_1^{(disp)}(x,j\omega) = \frac{-\omega^2 u_{base}e^{j\omega t} + u_{rel}(x,t)}{-\omega^2 u_{base}e^{j\omega t}} = -\frac{1}{\omega^2} + H_1(x,j\omega),$$

$$\hat{H}_1^{(vel)}(x,j\omega) = \frac{\dfrac{d}{dt}\left[u_{base}e^{j\omega t} + u_{rel}(x,t)\right]}{-\omega^2 u_{base}e^{j\omega t}} = \frac{1}{j\omega} + j\omega H_1(x,j\omega) \quad . \quad (4.192)$$

4.5. Multi-mode Frequency Analysis of the Normalised Coupled Electromechanical Dynamic Response of Transverse Form (Weak-CEDRT)

This section focuses on the multi-mode FRFs of the electromechanical dynamic equation of transverse bending form with input transverse base motion. The solution form of Eq. (4.140) can be stated as the Ritz eigenfunction series for identifying eigenvectors which can be further used to formulate the normalised Ritz eigenfunction form, Ritz [99], Courant and Hilbert [100]. The extended convergent Ritz eigenfunction series can be used as the solution form to give,

$$w_{rel}(x,t) = \sum_{r=1}^{m} c_r^{(w)} \Psi_r(x) e^{i\omega t} \quad . \quad (4.193)$$

Substituting Eq. (4.193) into Eq. (4.140) where the mechanical equation is considered to give the independent algebraic expressions of the eigenvalues corresponding to the transverse bending form as,

$$\sum_{r=1}^{m} \left[K_{qr}^{(w)} - \omega^{(w)} M_{qr}^{(w)}\right] c_r^{(w)} = 0, \quad q = 1,2,\dots,m \quad . \quad (4.194)$$

It should be noted that $c_r^{(w)}$ is called the unknown Ritz coefficients for the transverse bending form also referred to as the eigenvectors. Once the Ritz coefficients associated with the natural frequencies are determined, the generalized Ritz mode shapes in terms of the r-degrees of freedom can be formulated as,

$$\Psi_r(x) = \sum_{k=1}^{m} c_{kr}^{(w)} \Psi_k(x) \qquad\qquad r = 1,2,...., m \quad . \quad (4.195)$$

The generalised Ritz eigenfunction form can be normalised with respect to mass as,

$$\hat{\Psi}_r(x) = \frac{\Psi_r(x)}{\left(\int_0^L \hat{I}^{(C,k)} \left(\frac{d\Psi_r(x)}{dx} \right)^2 dx + \int_0^L \hat{I}^{(A,k)} \Psi_r(x)^2 dx + I_{tip}^{(A)} \Psi_r(L)^2 + I_{tip}^{(C)} \left(\frac{d\Psi_r}{dx}(L) \right)^2 \right)^{1/2}} \quad r=1,2,....,m \quad , (4.196)$$

The normalised eigenfunction series forms associated with the generalised time dependent variable can now be stated as,

$$w_{rel}(x,t) = \sum_{r=1}^{m} \hat{\Psi}_r(x) w_r(t) \quad . \tag{4.197}$$

As mentioned previously, the derivation of the electromechanical dynamic equations in this section were based on the Rayleigh and Euler-Bernoulli beam assumptions. The Euler-Bernoulli beam assumption can be formulated by ignoring the rotary inertia of the bimorph beam at the third term from Eq. (4.140) and the first term from Eq. (4.196) or (4.198). Corresponding to Eq. (4.196), the orthonormalisations can be proved by using Eq. (4.197) and applying the orthogonality property of the mechanical dynamic equations as,

$$\int_0^L \hat{I}^{(C,k)} \frac{d\hat{\Psi}_r(x)}{dx} \frac{d\hat{\Psi}_q(x)}{dx} dx + \int_0^L \hat{I}^{(A,k)} \hat{\Psi}_r(x) \hat{\Psi}_q(x) dx + I_{tip}^{(A)} \hat{\Psi}_r(L) \hat{\Psi}_q(L) + I_{tip}^{(C)} \frac{d\hat{\Psi}_r(L)}{dx} \frac{d\hat{\Psi}_q(L)}{dx} = \delta_{rq}, \quad (4.198)$$

$$\int_0^L \hat{C}_{11}^{(F,k)} \frac{d^2\hat{\Psi}_r(x)}{dx^2} \frac{d^2\hat{\Psi}_q(x)}{dx^2} dx = \omega_r^{(w)2} \delta_{rq} \quad , \tag{4.199}$$

where δ_{rq} is the Kronecker delta, defined as unity for $q = r$ and zero for $q \neq r$. The mechanical damping can be reduced in terms of orthonormalisation as,

$$C_{rq}^{(w)} = \alpha^{(w)} \delta_{rq} + \beta^{(w)} \omega_r^{(w)2} \delta_{rq} = 2\zeta_r^{(w)} \omega_r^{(w)} \delta_{rq}. \tag{4.200}$$

In this case, although the modal mechanical damping ratios can be determined mathematically, the estimation of modal mechanical damping ratios from experiment preferable to give accurate results. Applying the orthonormalisations from Eqs. (4.198) and (4.199) into the electromechanical piezoelectric bimorph beam from Eq. (4.140) gives,

$$\ddot{w}_r(t) + 2\zeta_r^{(w)} \omega_r^{(w)} \dot{w}_r(t) + \omega_r^{(w)2} w(t) + P_r^{(w)} v(t) = -Q_r^{(w)} \ddot{w}_{base}(t) , \tag{4.201}$$

$$\hat{P}_r^{(w)} \dot{w}_r(t) + P_D \dot{v}(t) + R_L v(t) = 0 .$$

It is noted that equation (4.201) has been normalised due to Eq. (4.197). The parameters $P_r^{(w)}$, $\hat{P}_r^{(w)}$ and $Q_r^{(w)}$ can then be reduced as,

$$P_r^{(w)} = \int_0^L \hat{R}_{31}^{(H,k)} \frac{d^2\hat{\Psi}_r(x)}{dx^2}dx \;, \quad \hat{P}^{(w)} = \sum_{r=0}^m P_r^{(w)} \;, \quad R_L = -\frac{1}{R_{load}} \;,$$

$$P_D = -\int_0^L \hat{S}_{33}^{(k)}dx \;, \quad Q_r^{(w)} = \int_0^L \hat{I}^{(A,k)}\hat{\Psi}_r(x)dx + I_{tip}^{(A)}\hat{\Psi}_r(L) \;.$$

Equation (4.201) can be solved using Laplace transforms. The multi-mode transfer function of the relative transverse displacement related to the base input transverse acceleration can be obtained as,

$$H_1(s) = \frac{w_r(s)}{s^2 w_{base}(s)} = -\frac{1}{s^2 + 2\zeta_r^{(w)}\omega_r^{(w)}s + \omega_r^{(w)2}} \left(\frac{(sP_D + R_L)Q_r^{(w)}}{j\omega P_D + R_L - \sum_{r=1}^m \frac{sP_r^{(w)2}}{s^2 + 2\zeta_r^{(w)}\omega_r^{(w)}s + \omega_r^{(w)2}}} \right). \quad (4.202)$$

In this case, the multi-mode transfer function of the relative transverse displacement related to the input transverse acceleration based on the bimorph element position (x) and subsidiary variable (s) in terms of frequency response can be formulated after simplifying some equations as,

$$H_1(x,s) = \frac{w_{rel}(x,s)}{s^2 w_{base}(s)} = -\sum_{r=1}^m \left[\frac{\hat{\Psi}_r(x)}{s^2 + 2\zeta_r^{(w)}\omega_r^{(w)}s + \omega_r^{(w)2}} \left(\frac{(sP_D + R_L)Q_r^{(w)}}{j\omega P_D + R_L - \sum_{r=1}^m \frac{sP_r^{(w)2}}{s^2 + 2\zeta_r^{(w)}\omega_r^{(w)}s + \omega_r^{(w)2}}} \right) \right]. \quad (4.203)$$

The multi-mode transfer function of the input base transverse acceleration with respect to the electric voltage output can be obtained as,

$$H_2(s) = \frac{v(s)}{s^2 w_{base}(s)} = \frac{\sum_{r=1}^m \frac{sP_r^{(w)}Q_r^{(w)}}{s^2 + 2\zeta_r^{(w)}\omega_r^{(w)}s + \omega_r^{(w)2}}}{sP_D + R_L - \sum_{r=1}^m \frac{sP_r^{(w)2}}{s^2 + 2\zeta_r^{(w)}\omega_r^{(w)}s + \omega_r^{(w)2}}}. \quad (4.204)$$

The multi-mode transfer function relating power harvesting to the input transverse acceleration can be derived as,

$$\frac{P(s)}{\left(s^2 w_{base}(s)\right)^2} = \left[\frac{\frac{1}{\sqrt{R_{load}}}\sum_{r=1}^m \frac{sP_r^{(w)}Q_r^{(w)}}{s^2 + 2\zeta_r^{(w)}\omega_r^{(w)}s + \omega_r^{(w)2}}}{sP_D + R_L - \sum_{r=1}^m \frac{sP_r^{(w)2}}{s^2 + 2\zeta_r^{(w)}\omega_r^{(w)}s + \omega_r^{(w)2}}} \right]^2. \quad (4.205)$$

Corresponding with Eqs. (4.202) to (4.205), the multi-mode FRFs of the electromechanical dynamic response can be obtained by substituting the subsidiary variable (s) with $(j\omega)$. The multi-mode FRF of transverse displacement with respect to input base transverse acceleration can be obtained as,

$$H_1(j\omega) = \frac{w_r(j\omega)}{-\omega^2 w_{base} e^{j\omega t}} = -\frac{1}{\omega_r^{(w)2} - \omega^2 + j2\zeta_r^{(w)}\omega_r^{(w)}\omega} \left(\frac{(j\omega P_D + R_L)Q_r^{(w)}}{j\omega P_D + R_L - \sum_{r=1}^{m} \frac{j\omega P_r^{(w)2}}{\omega_r^{(w)2} - \omega^2 + j2\zeta_r^{(w)}\omega_r^{(w)}\omega}} \right) .(4.206)$$

It should be noted that the input acceleration $-\omega^2 w_{base}(j\omega)$ is equivalent to $-\omega^2 w_{base} e^{j\omega t}$. Equation (4.206) can be modified to obtain the FRF as a function of position of the piezoelectric element (x) and frequency $(j\omega)$ by transforming it back into the Ritz eigenfunction form (Eq. 4.197) to give,

$$H_1(x,j\omega) = \frac{w_{rel}(x,j\omega)}{-\omega^2 w_{base} e^{j\omega t}} = -\sum_{r=1}^{m} \frac{\hat{\Psi}_r(x)}{\omega_r^{(w)2} - \omega^2 + j2\zeta_r^{(w)}\omega_r^{(w)}\omega} \left[\left(\frac{(j\omega P_D + R_L)Q_r^{(w)}}{j\omega P_D + R_L - \sum_{r=1}^{m} \frac{j\omega P_r^{(w)2}}{\omega_r^{(w)2} - \omega^2 + j2\zeta_r^{(w)}\omega_r^{(w)}\omega}} \right) \right] .(4.207)$$

The multi-mode FRF of the electric voltage output related to the input base transverse acceleration can be derived as,

$$H_2(j\omega) = \frac{v(j\omega)}{-\omega^2 w_{base} e^{j\omega t}} = \frac{\sum_{r=1}^{m} \frac{j\omega P_r^{(w)} Q_r^{(w)}}{\omega_r^{(w)2} - \omega^2 + j2\zeta_r^{(w)}\omega_r^{(w)}\omega}}{j\omega P_D + R_L - \sum_{r=1}^{m} \frac{j\omega P_r^{(w)2}}{\omega_r^{(w)2} - \omega^2 + j2\zeta_r^{(w)}\omega_r^{(w)}\omega}} . \quad (4.208)$$

The multi-mode FRF of the electric current output related to the input base transverse acceleration can be derived as,

$$H_3(j\omega) = \frac{I(j\omega)}{-\omega^2 w_{base} e^{j\omega t}} = \frac{\frac{1}{R_{load}} \sum_{r=1}^{m} \frac{j\omega P_r^{(w)} Q_r^{(w)}}{\omega_r^{(w)2} - \omega^2 + j2\zeta_r^{(w)}\omega_r^{(w)}\omega}}{j\omega P_D + R_L - \sum_{r=1}^{m} \frac{j\omega P_r^{(w)2}}{\omega_r^{(w)2} - \omega^2 + j2\zeta_r^{(w)}\omega_r^{(w)}\omega}} . \quad (4.209)$$

The multi-mode FRF of power harvesting related to the input transverse acceleration can be derived as,

$$\frac{P(j\omega)}{\left(-\omega^2 w_{base} e^{j\omega t}\right)^2} = \left[\frac{\dfrac{1}{\sqrt{R_{load}}}\displaystyle\sum_{r=1}^{m}\dfrac{j\omega P_r^{(w)}Q_r^{(w)}}{\omega_r^{(w)2} - \omega^2 + j2\zeta_r^{(w)}\omega_r^{(w)}\omega}}{j\omega P_D + R_L - \displaystyle\sum_{r=1}^{m}\dfrac{j\omega P_r^{(w)2}}{\omega_r^{(w)2} - \omega^2 + j2\zeta_r^{(w)}\omega_r^{(w)}\omega}}\right]^2. \quad (4.210)$$

To obtain the optimal multi-mode FRF power harvesting, equation (4.210) can be differentiated with respect to load resistance and the differentiable power function can be set to zero to give the optimal load resistance. It is noted that parameter R_L represents per-unit load resistance $-1/R_{load}$. Corresponding to Eq. (4.210), the optimal load resistance can be formulated as,

$$R_{load}^{opt} = \frac{\sqrt{X(\omega)^2 + Y(\omega)^2}}{X(\omega)^2 + Y(\omega)^2}, \quad (4.211)$$

where

$$X(\omega) = \omega P_D - \sum_{r=1}^{m}\frac{\omega P_r^{(w)2}\left(\omega_r^{(w)2} - \omega^2\right)}{\left(\omega_r^{(w)2} - \omega^2\right)^2 + \left(2\zeta_r^{(w)}\omega_r^{(w)}\omega\right)^2},$$

$$Y(\omega) = \sum_{r=1}^{m}\frac{\omega P_r^{(w)2}\left(2\zeta_r^{(w)}\omega_r^{(w)}\omega\right)}{\left(\omega_r^{(w)2} - \omega^2\right)^2 + \left(2\zeta_r^{(w)}\omega_r^{(w)}\omega\right)^2}.$$

It should be noted that the optimal load resistance can be substituted back into Eq. (4.211) to give the optimal power harvesting.

The time dependent function of relative transverse displacement can be obtained corresponding to Eq. (4.206) as,

$$w_r(t) = H_1(j\omega)\ddot{w}_{base} = H_1(j\omega)\left(-\omega^2 w_{base} e^{j\omega t}\right), \quad (4.212)$$

The generalised time dependent relative transverse displacement can be formulated in terms of any position along the piezoelectric beam in terms of Eq. (4.196) as,

$$w_{rel}(x,t) = H_1(x,j\omega)\left(-\omega^2 w_{base} e^{j\omega t}\right). \quad (4.213)$$

Corresponding to Eq. (4.211), the absolute transverse displacement can be reduced as,

$$w_{abs}(x,t) = w_{base} e^{j\omega t} + H_1(x, j\omega)\left(-\omega^2 w_{base} e^{j\omega t}\right). \quad (4.214)$$

The generalised electrical potential can be formulated as,

$$v(t) = H_2(j\omega)\ddot{w}_{base} = H_2(j\omega)\left(-\omega^2 w_b exp(j\omega t)\right). \quad (4.215)$$

Corresponding to Eq. (4.214), equation (4.207) can be modified in terms of the multi-mode FRF of the absolute displacements and velocities relating the input transverse acceleration at any position along the bimorph beam respectively as,

$$\hat{H}_1^{(disp)}(x, j\omega) = \frac{w_{base}e^{j\omega t} + w_{rel}(x,t)}{-\omega^2 w_{base}e^{j\omega t}} = -\frac{1}{\omega^2} + H_1(x, j\omega) \quad ,$$

$$\hat{H}_1^{(vel)}(x, j\omega) = \frac{\dfrac{d}{dt}\left[W_{base}e^{j\omega t} + w_{rel}(x,t)\right]}{-\omega^2 W_{base}e^{j\omega t}} = \frac{1}{j\omega} + j\omega H_1(x, j\omega). \quad (4.216)$$

4.6. Multi-mode Frequency Analysis of the Normalised Coupled Electromechanical Dynamic Response of Transverse-Longitudinal Form (Weak-CEDRTL)

This section focuses on the solution of the multi-mode electromechanical dynamic equations of the piezoelectric bimorph beam with tip mass based on the strain field due to the transverse bending and longitudinal extension under two input base excitations using Eq. (4.96). The solution presented here complies with the orthonormality of two independent Ritz eigenfunction forms. Corresponding with the convergent eigenfunction forms of Eq. (4.97), equations (4.98), (4.99) and (4.101) need to be modified in order to achieve the orthonormality conditions.

To normalise Eq. (4.97), the convergent Ritz eigenfunction forms can be stated as,

$$w_{rel}(x,t) = \sum_{r=1}^{m} c_r^{(w)}\Psi_r(x)e^{i\omega t} \quad , \quad u_{rel}(x,t) = \sum_{r=1}^{m} c_r^{(u)}\Theta_r(x)e^{i\omega t} \quad . \quad (4.217)$$

In terms of the only mechanical equation, equation (4.217) can be substituted into Eq. (4.96) to give the independent algebraic equations of the eigenvalues corresponding to the longitudinal and transverse bending form as,

$$\sum_{r=1}^{m}\left[K_{qr}^{(u)} - \omega^{(u)}M_{qr}^{(u)}\right]c_r^{(u)} = 0, \quad q = 1,2,.....,m, \quad (4.218)$$

$$\sum_{r=1}^{m}\left[K_{qr}^{(w)} - \omega^{(w)}M_{qr}^{(w)}\right]c_r^{(w)} = 0, \quad q = 1,2,.....,m. \quad (4.219)$$

It should be noted that $c_r^{(u)}$ and $c_r^{(w)}$ are called the unknown Ritz coefficients for the respective longitudinal and transverse bending forms which refer to the eigenvectors in the mechanical domain. Once the Ritz coefficients are determined associated with natural frequencies, the generalized Ritz mode shapes in terms of the r-degree of freedoms can be formulated as,

$$\Psi_r(x) = \sum_{k=1}^{m} c_{kr}^{(w)}\Psi_k(x) \quad , \quad \Theta_r(x) = \sum_{k=1}^{m} c_{kr}^{(u)}\Theta_k(x) \qquad r = 1,2,....,m \quad . \quad (4.220)$$

The generalised Ritz mode shapes can be normalised with respect to mass as,

$$\hat{\Psi}_r(x) = \frac{\Psi_r(x)}{\left(\int_0^L \hat{I}^{(C,k)}\left(\frac{d\Psi_r(x)}{dx}\right)^2 dx + \int_0^L \hat{I}^{(A,k)}\Psi_r(x)^2 dx + I_{tip}^{(A)}\Psi_r(L)^2 + I_{tip}^{(C)}\left(\frac{d\Psi_r}{dx}(L)\right)^2\right)^{1/2}} \quad r = 1,2,....,m \quad , \quad (4.221)$$

$$\hat{\Theta}_r(x) = \frac{\Theta_r(x)}{\left(\int_0^L \hat{I}^{(A,k)}\Theta_r(x)^2 dx + I_{tip}^{(A)}\Theta_r(L)^2\right)^{1/2}} \qquad r = 1,2,....,m \quad . \qquad (4.222)$$

The normalised eigenfunction series forms associated with the generalised time dependent function can now be stated as,

$$w_{rel}(x,t) = \sum_{r=1}^{m} \hat{\Psi}_r(x)w_r(t) \quad , \quad u_{rel}(x,t) = \sum_{r=1}^{m} \hat{\Theta}_r(x)u_r(t) \quad . \quad (4.223)$$

It is noted that this section is developed according to the Rayleigh piezoelectric bimorph beam. To formulate the Euler-Bernoulli piezoelectric bimorph beam, the rotary inertia of the bimorph beam in the second term from the Eq. (4.96) or the first term from Eq. (4.221) or (4.224) can be ignored. Corresponding to Eq. (4.96), the orthonormalisations can be proven by using Eq. (4.223) and applying the orthogonality property of the mechanical dynamic equations as,

$$\int_0^L \hat{I}^{(C,k)}\frac{d\hat{\Psi}_r(x)}{dx}\frac{d\hat{\Psi}_q(x)}{dx}dx + \int_0^L \hat{I}^{(A,k)}\hat{\Psi}_r(x)\hat{\Psi}_q(x)dx + I_{tip}^{(A)}\hat{\Psi}_r(L)\hat{\Psi}_q(L) + I_{tip}^{(C)}\frac{d\hat{\Psi}_r(L)}{dx}\frac{d\hat{\Psi}_q(L)}{dx} = \delta_{rq}, \quad (4.224)$$

$$\int_0^L \hat{I}^{(A,k)}\hat{\Theta}_r(x)\hat{\Theta}_q(x)dx + I_{tip}^{(A)}\hat{\Theta}_r(L)\hat{\Theta}_q(L) = \delta_{rq}, \quad \int_0^L \hat{C}_{11}^{(D,k)}\frac{d\hat{\Theta}_r(x)}{dx}\frac{d\hat{\Theta}_q(x)}{dx}dx = \omega_r^{(u)2}\delta_{rq}, \quad (4.225)$$

$$\int_0^L \hat{C}_{11}^{(F,k)}\frac{d^2\hat{\Psi}_r(x)}{dx^2}\frac{d^2\hat{\Psi}_q(x)}{dx^2}dx = \omega_r^{(w)2}\delta_{rq}. \qquad (4.226)$$

where δ_{rq} is the Kronecker delta, defined as unity for $q = r$ and zero for $q \neq r$. The Rayleigh mechanical damping can be reduced in terms of orthonormalisation as,

$$C_{rq}^{(u)} = \alpha^{(u)}\delta_{rq} + \beta^{(u)}\omega_r^{(u)2}\delta_{rq} = 2\zeta_r^{(u)}\omega_r^{(u)}\delta_{rq}, \qquad (4.227)$$

$$C_{rq}^{(w)} = \alpha^{(w)}\delta_{rq} + \beta^{(w)}\omega_r^{(w)2}\delta_{rq} = 2\zeta_r^{(w)}\omega_r^{(w)}\delta_{rq}. \qquad (4.228)$$

In this case, although the modal mechanical damping ratios can be determined mathematically, the chosen modal mechanical damping ratios $\zeta_r^{(u)}$ and $\zeta_r^{(w)}$ were obtained here by experiment to give accurate results at the resonance frequency

amplitude regions. Applying the orthonormalisations from Eqs. (4.224), (4.225) and (4.226) into the electromechanical piezoelectric bimorph beam equation from Eq. (4.96) gives,

$$\ddot{u}_r(t) + 2\zeta_r^{(u)}\omega_r^{(u)}\dot{u}_r(t) + \omega_r^{(u)2}u_r(t) + P_r^{(u)}v(t) = -Q_r^{(u)}\ddot{u}_{base}(t)$$

$$\ddot{w}_r(t) + 2\zeta_r^{(w)}\omega_r^{(w)}\dot{w}_r(t) + \omega_r^{(w)2}w(t) + P_r^{(w)}v(t) = -Q_r^{(w)}\ddot{w}_{base}(t). \quad (4.229)$$

$$\hat{P}_r^{(u)}\dot{u}_r(t) + \hat{P}_r^{(w)}\dot{w}_r(t) + P_D\dot{v}(t) + R_L v(t) = 0$$

It is noted that because equation (4.229) has been normalised due to Eq. (4.223), the parameters $P_r^{(u)}, P_r^{(w)}, \hat{P}_r^{(u)}, \hat{P}_r^{(w)}, R_L, P_D, Q_r^{(u)}$ and $Q_r^{(w)}$ can be reduced as,

$$P_r^{(u)} = -\int_0^L \hat{R}_{31}^{(G,k)}\frac{d\hat{\Theta}_r(x)}{dx}dx \; , \quad P_r^{(w)} = \int_0^L \hat{R}_{31}^{(H,k)}\frac{d^2\hat{\Psi}_r(x)}{dx^2}dx \; ,$$

$$\hat{P}_r^{(u)} = \sum_{r=0}^m P_r^{(u)} \; , \quad \hat{P}_r^{(w)} = \sum_{r=0}^m P_r^{(w)} \; , \quad R_L = -\frac{1}{R_{load}} \; , \quad P_D = -\int_0^L \hat{S}_{33}^{(k)}dx,$$

$$Q_r^{(u)} = \int_0^L \hat{I}^{(A,k)}\hat{\Theta}_r(x)dx + I_{tip}^{(A)}\hat{\Theta}_r(L) \; , \quad Q_r^{(w)} = \int_0^L \hat{I}^{(A,k)}\hat{\Psi}_r(x)dx + I_{tip}^{(A)}\hat{\Psi}_r(L) \; .$$

Equation (4.229) can be solved using Laplace transforms. In this case, the multi-mode electromechanical dynamic equations of the piezoelectric bimorph system can be reduced as,

$$u_{rel}(s) = -\frac{1}{Z(s)_r}\left[\left\{\left(s^2 + 2\zeta_r^{(w)}\omega_r^{(w)}s + \omega_r^{(w)2}\right)(sP_D + R_L) - \sum_{r=1}^m sP_r^{(w)2}\right\}Q_r^{(u)}\left(s^2 u_{base}(s)\right)\right.$$

$$\left. + \sum_{r=1}^m sP_r^{(w)}P_r^{(u)}Q_r^{(w)}\left(s^2 w_{base}(s)\right)\right], \quad (4.230)$$

$$w_r(s) = -\frac{1}{Z(s)_r}\left[\left\{\left(s^2 + 2\zeta_r^{(u)}\omega_r^{(u)}s + \omega_r^{(u)2}\right)(sP_D + R_L) - \sum_{r=1}^m sP_r^{(u)2}\right\}Q_r^{(w)}\left(s^2 w_{base}(s)\right)\right.$$

$$\left. + \sum_{r=1}^m sP_r^{(w)}P_r^{(u)}Q_r^{(u)}\left(s^2 u_{base}(s)\right)\right], \quad (4.231)$$

$$v(s) = \frac{1}{Z(s)_r}\left[\sum_{r=1}^m\left\{sP_r^{(w)}Q_r^{(w)}\left(s^2 + 2\zeta_r^{(u)}\omega_r^{(u)}s + \omega_r^{(u)2}\right)\left(s^2 w_{base}(s)\right)\right\}\right.$$

$$\left. + \sum_{r=1}^m\left\{sP_r^{(u)}Q_r^{(u)}\left(s^2 + 2\zeta_r^{(w)}\omega_r^{(w)}s + \omega_r^{(w)2}\right)\left(s^2 u_{base}(s)\right)\right\}\right]. \quad (4.232)$$

The characteristic polynomial form from Eq. (4.229) can be formulated as,

$$Z(s)_r = \left(s^2 + 2\zeta_r^{(u)}\omega_r^{(u)}s + \omega_r^{(u)2}\right)\left(s^2 + 2\zeta_r^{(w)}\omega_r^{(w)}s + \omega_r^{(w)2}\right)\left(sP_D + R_L\right)$$
$$- \sum_{r=1}^{m} sP_r^{(w)2}\left(s^2 + 2\zeta_r^{(u)}\omega_r^{(u)}s + \omega_r^{(u)2}\right) - \sum_{r=1}^{m} sP_r^{(u)2}\left(s^2 + 2\zeta_r^{(w)}\omega_r^{(w)}s + \omega_r^{(w)2}\right). \quad (4.233)$$

Corresponding to Eq. (4.230), the multi-mode transfer function of the longitudinal displacement related to the input base-longitudinal acceleration can be obtained after simplification, neglecting input transverse motion, to give,

$$H_{11}(s) = \left.\frac{u_r(s)}{\left(s^2 u_{base}(s)\right)}\right|_{s^2 w_{base}(s)=0}$$

$$= -\frac{1}{s^2 + 2\zeta_r^{(u)}\omega_r^{(u)}s + \omega_r^{(u)2}}\left(\frac{\left(sP_D + R_L\right)Q_r^{(u)} - \sum\limits_{r=1}^{m}\dfrac{sP_r^{(w)2}Q_r^{(u)}}{s^2 + 2\zeta_r^{(w)}\omega_r^{(w)}s + \omega_r^{(w)2}}}{sP_D + R_L - \sum\limits_{r=1}^{m}\dfrac{sP_r^{(w)2}}{s^2 + 2\zeta_r^{(w)}\omega_r^{(w)}s + \omega_r^{(w)2}} - \sum\limits_{r=1}^{m}\dfrac{sP_r^{(u)2}}{s^2 + 2\zeta_r^{(u)}\omega_r^{(u)}s + \omega_r^{(u)2}}}\right). \quad (4.234)$$

It is noted that equation (4.234) can be formulated in terms of the generalised relative longitudinal displacement on the bimorph element position (x) and subsidiary variable (s) in terms of applying Laplace transform to Eq. (4.221b) as,

$$H_{11}(x,s) = \left.\frac{u_{rel}(x,s)}{\left(s^2 u_{base}(s)\right)}\right|_{s^2 w_{base}(s)=0}$$

$$= -\sum_{r=1}^{m}\left[\frac{\hat{\Theta}_r(x)}{s^2 + 2\zeta_r^{(u)}\omega_r^{(u)}s + \omega_r^{(u)2}}\left(\frac{\left(sP_D + R_L\right)Q_r^{(u)} - \sum\limits_{r=1}^{m}\dfrac{sP_r^{(w)2}Q_r^{(u)}}{s^2 + 2\zeta_r^{(w)}\omega_r^{(w)}s + \omega_r^{(w)2}}}{sP_D + R_L - \sum\limits_{r=1}^{m}\dfrac{sP_r^{(w)2}}{s^2 + 2\zeta_r^{(w)}\omega_r^{(w)}s + \omega_r^{(w)2}} - \sum\limits_{r=1}^{m}\dfrac{sP_r^{(u)2}}{s^2 + 2\zeta_r^{(u)}\omega_r^{(u)}s + \omega_r^{(u)2}}}\right)\right]. \quad (4.235)$$

The multi-mode transfer function between the input base-transverse acceleration and output longitudinal displacement can be obtained as,

$$H_{12}(s) = \left.\frac{u_r(s)}{\left(s^2 w_{base}(s)\right)}\right|_{s^2 u_{base}(s)=0}$$

$$= -\frac{1}{s^2 + 2\zeta_r^{(u)}\omega_r^{(u)}s + \omega_r^{(u)2}}\left(\frac{\sum\limits_{r=1}^{m}\dfrac{sP_r^{(u)}P_r^{(w)}Q_r^{(w)}}{s^2 + 2\zeta_r^{(w)}\omega_r^{(w)}s + \omega_r^{(w)2}}}{sP_D + R_L - \sum\limits_{r=1}^{m}\dfrac{sP_r^{(w)2}}{s^2 + 2\zeta_r^{(w)}\omega_r^{(w)}s + \omega_r^{(w)2}} - \sum\limits_{r=1}^{m}\dfrac{sP_r^{(u)2}}{s^2 + 2\zeta_r^{(u)}\omega_r^{(u)}s + \omega_r^{(u)2}}}\right). \quad (4.236)$$

The multi-mode transfer function of the generalised longitudinal displacement function related to the input base-transverse acceleration can be obtained as,

$$H_{12}(x,s) = \left. \frac{u_{rel}(x,s)}{\left(s^2 w_{base}(s)\right)} \right|_{s^2 u_{base}(s)=0}$$

$$= -\sum_{r=1}^{m} \left[\frac{\hat{\Theta}_r(x)}{s^2 + 2\zeta_r^{(u)}\omega_r^{(u)}s + \omega_r^{(u)2}} \left(\frac{\sum_{r=1}^{m} \dfrac{sP_r^{(u)}P_r^{(w)}Q_r^{(w)}}{s^2 + 2\zeta_r^{(w)}\omega_r^{(w)}s + \omega_r^{(w)2}}}{sP_D + R_L - \sum_{r=1}^{m} \dfrac{sP_r^{(w)2}}{s^2 + 2\zeta_r^{(w)}\omega_r^{(w)}s + \omega_r^{(w)2}} - \sum_{r=1}^{m} \dfrac{sP_r^{(u)2}}{s^2 + 2\zeta_r^{(u)}\omega_r^{(u)}s + \omega_r^{(u)2}}} \right) \right] .(4.237)$$

The transfer function between the input base-longitudinal acceleration and transverse displacement can be obtained as,

$$H_{21}(s) = \left. \frac{w_r(s)}{\left(s^2 u_{base}(s)\right)} \right|_{s^2 w_{base}(s)=0}$$

$$= -\frac{1}{s^2 + 2\zeta_r^{(w)}\omega_r^{(w)}s + \omega_r^{(w)2}} \left(\frac{\sum_{r=1}^{m} \dfrac{sP_r^{(u)}P_r^{(w)}Q_r^{(u)}}{s^2 + 2\zeta_r^{(u)}\omega_r^{(u)}s + \omega_r^{(u)2}}}{sP_D + R_L - \sum_{r=1}^{m} \dfrac{sP_r^{(w)2}}{s^2 + 2\zeta_r^{(w)}\omega_r^{(w)}s + \omega_r^{(w)2}} - \sum_{r=1}^{m} \dfrac{sP_r^{(u)2}}{s^2 + 2\zeta_r^{(u)}\omega_r^{(u)}s + \omega_r^{(u)2}}} \right) .(4.238)$$

The multi-mode transfer function of the generalised transverse displacement field related to the input base-longitudinal acceleration can be obtained as,

$$H_{21}(x,s) = \left. \frac{w_{rel}(x,s)}{\left(s^2 u_{base}(s)\right)} \right|_{s^2 w_{base}(s)=0}$$

$$= -\sum_{r=1}^{m} \left[\frac{\hat{\Psi}_r(x)}{s^2 + 2\zeta_r^{(w)}\omega_r^{(w)}s + \omega_r^{(w)2}} \left(\frac{\sum_{r=1}^{m} \dfrac{sP_r^{(u)}P_r^{(w)}Q_r^{(u)}}{s^2 + 2\zeta_r^{(u)}\omega_r^{(u)}s + \omega_r^{(u)2}}}{sP_D + R_L - \sum_{r=1}^{m} \dfrac{sP_r^{(w)2}}{s^2 + 2\zeta_r^{(w)}\omega_r^{(w)}s + \omega_r^{(w)2}} - \sum_{r=1}^{m} \dfrac{sP_r^{(u)2}}{s^2 + 2\zeta_r^{(u)}\omega_r^{(u)}s + \omega_r^{(u)2}}} \right) \right] .(4.239)$$

Corresponding to Eq. (4.231), the multi-mode transfer function of the input base-transverse acceleration with respect to output transverse displacement can be obtained, neglecting longitudinal excitation to give,

$$H_{22}(s) = \left. \frac{w_r(s)}{s^2 w_{base}(s)} \right|_{s^2 u_{base}(s)=0}$$

$$= -\frac{1}{s^2 + 2\zeta_r^{(w)}\omega_r^{(w)}s + \omega_r^{(w)2}} \left(\frac{(sP_D + R_L)Q_r^{(w)} - \sum_{r=1}^{m} \dfrac{sP_r^{(u)2}Q_r^{(w)}}{s^2 + 2\zeta_r^{(u)}\omega_r^{(u)}s + \omega_r^{(u)2}}}{sP_D + R_L - \sum_{r=1}^{m} \dfrac{sP_r^{(w)2}}{s^2 + 2\zeta_r^{(w)}\omega_r^{(w)}s + \omega_r^{(w)2}} - \sum_{r=1}^{m} \dfrac{sP_r^{(u)2}}{s^2 + 2\zeta_r^{(u)}\omega_r^{(u)}s + \omega_r^{(u)2}}} \right) .(4.240)$$

By applying Laplace transform from Eq. (4.223a), the multi-mode transfer function of the generalised transverse displacement field related to the input transverse acceleration can be obtained as,

$$H_{22}(x,s) = \frac{w_{rel}(x,s)}{s^2 w_{base}(s)}\bigg|_{s^2 u_{base}(s)=0}$$

$$= -\sum_{r=1}^{m}\left[\frac{\hat{\Psi}_r(x)}{s^2 + 2\zeta_r^{(w)}\omega_r^{(w)}s + \omega_r^{(w)2}}\left(\frac{(sP_D+R_L)Q_r^{(w)} - \sum_{r=1}^{m}\dfrac{sP_r^{(u)2}Q_r^{(w)}}{s^2 + 2\zeta_r^{(u)}\omega_r^{(u)}s + \omega_r^{(u)2}}}{sP_D + R_L - \sum_{r=1}^{m}\dfrac{sP_r^{(w)2}}{s^2 + 2\zeta_r^{(w)}\omega_r^{(w)}s + \omega_r^{(w)2}} - \sum_{r=1}^{m}\dfrac{sP_r^{(u)2}}{s^2 + 2\zeta_r^{(u)}\omega_r^{(u)}s + \omega_r^{(u)2}}}\right)\right]. \quad (4.241)$$

With the same method, the multi-mode transfer function between the input base longitudinal acceleration and electric voltage can be obtained as,

$$H_{31}(s) = \frac{v(s)}{s^2 u_{base}(s)}\bigg|_{s^2 w_{base}(s)=0} = \frac{\sum_{r=1}^{m}\dfrac{sP_r^{(u)}Q_r^{(u)}}{s^2 + 2\zeta_r^{(u)}\omega_r^{(u)}s + \omega_r^{(u)2}}}{sP_D + R_L - \sum_{r=1}^{m}\dfrac{sP_r^{(w)2}}{s^2 + 2\zeta_r^{(w)}\omega_r^{(w)}s + \omega_r^{(w)2}} - \sum_{r=1}^{m}\dfrac{sP_r^{(u)2}}{s^2 + 2\zeta_r^{(u)}\omega_r^{(u)}s + \omega_r^{(u)2}}} \quad .(4.242)$$

The transfer function of the input base transverse acceleration with respect to output electric voltage can be obtained, neglecting longitudinal excitation to give,

$$H_{32}(s) = \frac{v(s)}{s^2 w_{base}(s)}\bigg|_{s^2 u_{base}(s)=0} = \frac{\sum_{r=1}^{m}\dfrac{sP_r^{(w)}Q_r^{(w)}}{s^2 + 2\zeta_r^{(w)}\omega_r^{(w)}s + \omega_r^{(w)2}}}{sP_D + R_L - \sum_{r=1}^{m}\dfrac{sP_r^{(w)2}}{s^2 + 2\zeta_r^{(w)}\omega_r^{(w)}s + \omega_r^{(w)2}} - \sum_{r=1}^{m}\dfrac{sP_r^{(u)2}}{s^2 + 2\zeta_r^{(u)}\omega_r^{(u)}s + \omega_r^{(u)2}}} \quad .(4.243)$$

The multi mode transfer function of the electric current related to the input base longitudinal acceleration can be stated as,

$$H_{41}(s) = \frac{I(s)}{s^2 u_{base}(s)}\bigg|_{s^2 w_{base}(s)=0} = \frac{\dfrac{1}{R_{load}}\sum_{r=1}^{m}\dfrac{sP_r^{(u)}Q_r^{(u)}}{s^2 + 2\zeta_r^{(u)}\omega_r^{(u)}s + \omega_r^{(u)2}}}{sP_D + R_L - \sum_{r=1}^{m}\dfrac{sP_r^{(w)2}}{s^2 + 2\zeta_r^{(w)}\omega_r^{(w)}s + \omega_r^{(w)2}} - \sum_{r=1}^{m}\dfrac{sP_r^{(u)2}}{s^2 + 2\zeta_r^{(u)}\omega_r^{(u)}s + \omega_r^{(u)2}}} \quad . \quad (4.244)$$

The multi-mode transfer function of the electric voltage output with respect to the input base transverse acceleration can be obtained, neglecting longitudinal excitation to give,

$$H_{42}(s) = \frac{I(s)}{s^2 w_{base}(s)}\bigg|_{s^2 u_{base}(s)=0} = \frac{\dfrac{1}{R_{load}}\sum_{r=1}^{m}\dfrac{sP_r^{(w)}Q_r^{(w)}}{s^2 + 2\zeta_r^{(w)}\omega_r^{(w)}s + \omega_r^{(w)2}}}{sP_D + R_L - \sum_{r=1}^{m}\dfrac{sP_r^{(w)2}}{s^2 + 2\zeta_r^{(w)}\omega_r^{(w)}s + \omega_r^{(w)2}} - \sum_{r=1}^{m}\dfrac{sP_r^{(u)2}}{s^2 + 2\zeta_r^{(u)}\omega_r^{(u)}s + \omega_r^{(u)2}}} \quad . \quad (4.245)$$

The multi-mode transfer function relating power harvesting to input transverse acceleration can be derived as,

$$\frac{P(s)}{\left(s^2 w_{base}(s)\right)^2}\bigg|_{s^2 w_{base}(s)=0} =$$

$$\left[\frac{\dfrac{1}{\sqrt{R_{load}}}\sum_{r=1}^{m}\dfrac{sP_r^{(w)}Q_r^{(w)}}{s^2+2\zeta_r^{(w)}\omega_r^{(w)}s+\omega_r^{(w)2}}}{sP_D+R_L-\sum_{r=1}^{m}\dfrac{sP_r^{(w)2}}{s^2+2\zeta_r^{(w)}\omega_r^{(w)}s+\omega_r^{(w)2}}-\sum_{r=1}^{m}\dfrac{sP_r^{(u)2}}{s^2+2\zeta_r^{(u)}\omega_r^{(u)}s+\omega_r^{(u)2}}} \right]^2 . \quad (4.246)$$

The multi-mode transfer function of power harvesting due to input longitudinal acceleration can be derived as,

$$\left. \frac{P(s)}{\left(s^2 u_{base}(s)\right)^2}\right|_{s^2 w_{base}(s)=0}$$

$$= \left[\frac{\dfrac{1}{\sqrt{R_{load}}}\sum_{r=1}^{m}\dfrac{sP_r^{(u)}Q_r^{(u)}}{s^2+2\zeta_r^{(u)}\omega_r^{(u)}s+\omega_r^{(u)2}}}{sP_D+R_L-\sum_{r=1}^{m}\dfrac{sP_r^{(w)2}}{s^2+2\zeta_r^{(w)}\omega_r^{(w)}s+\omega_r^{(w)2}}-\sum_{r=1}^{m}\dfrac{sP_r^{(u)2}}{s^2+2\zeta_r^{(u)}\omega_r^{(u)}s+\omega_r^{(u)2}}} \right]^2 . \quad (4.247)$$

Corresponding to Eqs. (4.234)-(4.247), the frequency response function (FRF) can be formulated. In this case, the electromechanical dynamic equation of the piezoelectric bimorph can be formulated in matrix FRF form as,

$$H(j\omega)=\begin{bmatrix} H_{11}(j\omega) & H_{12}(j\omega) \\ H_{21}(j\omega) & H_{22}(j\omega) \\ H_{31}(j\omega) & H_{32}(j\omega) \\ H_{41}(j\omega) & H_{42}(j\omega) \end{bmatrix}. \quad (4.248)$$

The first multi-mode FRF represents the generalised time dependent longitudinal function with respect to input motions. In the case when input transverse excitation is ignored, the FRF can be obtained from input base longitudinal excitation as,

$$H_{11}(j\omega)=\left.\frac{u_r(j\omega)}{-\omega^2 u_{base}e^{j\omega t}}\right|_{s=j\omega}$$

$$=-\frac{1}{\omega_r^{(u)2}-\omega^2+j2\zeta_r^{(u)}\omega_r^{(u)}\omega}\left(\frac{(j\omega P_D+R_L)Q_r^{(u)}-\sum_{r=1}^{m}\dfrac{j\omega P_r^{(w)2}Q_r^{(u)}}{\omega_r^{(w)2}-\omega^2+j2\zeta_r^{(w)}\omega_r^{(w)}\omega}}{j\omega P_D+R_L-\sum_{r=1}^{m}\dfrac{j\omega P_r^{(w)2}}{\omega_r^{(w)2}-\omega^2+j2\zeta_r^{(w)}\omega_r^{(w)}\omega}-\sum_{r=1}^{m}\dfrac{j\omega P_r^{(u)2}}{\omega_r^{(u)2}-\omega^2+j2\zeta_r^{(u)}\omega_r^{(u)}\omega}} \right). (4.249)$$

Equation (4.249) can be modified to obtain the FRF as a function of position of the piezoelectric element (x) and frequency $(j\omega)$ by transforming it back into the Ritz eigenfunction form as

$$H_{11}(x,j\omega)=\left.\frac{u_{rel}(x,j\omega)}{-\omega^2 u_{base}e^{j\omega t}}\right|_{s=j\omega}$$

$$= -\sum_{r=1}^{m} \left[\frac{\hat{\Theta}_r(x)}{\omega_r^{(u)2} - \omega^2 + j2\zeta_r^{(u)}\omega_r^{(u)}\omega} \left(\frac{(j\omega P_D + R_L)Q_r^{(u)} - \sum_{r=1}^{m}\dfrac{j\omega P_r^{(w)2}Q_r^{(u)}}{\omega_r^{(w)2} - \omega^2 + j2\zeta_r^{(w)}\omega_r^{(w)}\omega}}{j\omega P_D + R_L - \sum_{r=1}^{m}\dfrac{j\omega P_r^{(w)2}}{\omega_r^{(w)2} - \omega^2 + j2\zeta_r^{(w)}\omega_r^{(w)}\omega} - \sum_{r=1}^{m}\dfrac{j\omega P_r^{(u)2}}{\omega_r^{(u)2} - \omega^2 + j2\zeta_r^{(u)}\omega_r^{(u)}\omega}} \right) \right] \quad .(4.250)$$

The FRF of the relative transfer function between the input base transverse acceleration and output longitudinal displacement can be obtained as,

$$H_{12}(j\omega) = \left. \frac{u_r(j\omega)}{-\omega^2 w_{base}e^{j\omega t}} \right|_{s=j\omega}$$

$$= -\frac{1}{\omega_r^{(u)2} - \omega^2 + j2\zeta_r^{(u)}\omega_r^{(u)}\omega} \left(\frac{\sum_{r=1}^{m}\dfrac{j\omega P_r^{(u)}P_r^{(w)}Q_r^{(w)}}{\omega_r^{(w)2} - \omega^2 + j2\zeta_r^{(w)}\omega_r^{(w)}\omega}}{j\omega P_D + R_L - \sum_{r=1}^{m}\dfrac{j\omega P_r^{(w)2}}{\omega_r^{(w)2} - \omega^2 + j2\zeta_r^{(w)}\omega_r^{(w)}\omega} - \sum_{r=1}^{m}\dfrac{j\omega P_r^{(u)2}}{\omega_r^{(u)2} - \omega^2 + j2\zeta_r^{(u)}\omega_r^{(u)}\omega}} \right) \quad .(4.251)$$

Equation (4.251) can be modified as a function of position of the piezoelectric element (x) and frequency $(j\omega)$ by transforming it back into the Ritz eigenfunction form to give,

$$H_{12}(x, j\omega) = \left. \frac{u_{rel}(x, j\omega)}{-\omega^2 w_{base}e^{j\omega t}} \right|_{s=j\omega}$$

$$= -\sum_{r=1}^{m} \left[\frac{\hat{\Theta}_r(x)}{\omega_r^{(u)2} - \omega^2 + j2\zeta_r^{(u)}\omega_r^{(u)}\omega} \left(\frac{\sum_{r=1}^{m}\dfrac{j\omega P_r^{(u)}P_r^{(w)}Q_r^{(w)}}{\omega_r^{(w)2} - \omega^2 + j2\zeta_r^{(w)}\omega_r^{(w)}\omega}}{j\omega P_D + R_L - \sum_{r=1}^{m}\dfrac{j\omega P_r^{(w)2}}{\omega_r^{(w)2} - \omega^2 + j2\zeta_r^{(w)}\omega_r^{(w)}\omega} - \sum_{r=1}^{m}\dfrac{j\omega P_r^{(u)2}}{\omega_r^{(u)2} - \omega^2 + j2\zeta_r^{(u)}\omega_r^{(u)}\omega}} \right) \right] \quad .(4.252)$$

The second multi-mode FRF represents the transverse motion with respect to input motions. If base-input transverse motion is ignored, the FRF of transverse motion related to the base input longitudinal motion can be obtained as,

$$H_{21}(j\omega) = \left. \frac{w_r(j\omega)}{-\omega^2 u_{base}e^{j\omega t}} \right|_{s=j\omega}$$

$$= -\frac{1}{\omega_r^{(w)2} - \omega^2 + j2\zeta_r^{(w)}\omega_r^{(w)}\omega} \left(\frac{\sum_{r=1}^{m}\dfrac{j\omega P_r^{(u)}P_r^{(w)}Q_r^{(u)}}{\omega_r^{(u)2} - \omega^2 + j2\zeta_r^{(u)}\omega_r^{(u)}\omega}}{j\omega P_D + R_L - \sum_{r=1}^{m}\dfrac{j\omega P_r^{(w)2}}{\omega_r^{(w)2} - \omega^2 + j2\zeta_r^{(w)}\omega_r^{(w)}\omega} - \sum_{r=1}^{m}\dfrac{j\omega P_r^{(u)2}}{\omega_r^{(u)2} - \omega^2 + j2\zeta_r^{(u)}\omega_r^{(u)}\omega}} \right) \quad .(4.253)$$

Equation (4.253) can be modified to obtain the FRF as a function of position of the piezoelectric element (x) and frequency $(j\omega)$ by transforming it back into the Ritz eigenfunction form to give,

$$H_{21}(x, j\omega) = \left. \frac{w_{rel}(x, j\omega)}{-\omega^2 u_{base}e^{j\omega t}} \right|_{s=j\omega}$$

$$= -\sum_{r=1}^{m} \left[\frac{\hat{\Psi}_r(x)}{\omega_r^{(w)2} - \omega^2 + j2\zeta_r^{(w)}\omega_r^{(w)}\omega} \left(\frac{\displaystyle\sum_{r=1}^{m} \frac{j\omega P_r^{(u)} P_r^{(w)} Q_r^{(u)}}{\omega_r^{(u)2} - \omega^2 + j2\zeta_r^{(u)}\omega_r^{(u)}\omega}}{j\omega P_D + R_L - \displaystyle\sum_{r=1}^{m} \frac{j\omega P_r^{(w)2}}{\omega_r^{(w)2} - \omega^2 + j2\zeta_r^{(w)}\omega_r^{(w)}\omega} - \displaystyle\sum_{r=1}^{m} \frac{j\omega P_r^{(u)2}}{\omega_r^{(u)2} - \omega^2 + j2\zeta_r^{(u)}\omega_r^{(u)}\omega}} \right) \right] .(4.254)$$

The multi-mode FRF of transverse displacement with respect to input base transverse acceleration can be obtained as,

$$H_{22}(j\omega) = \frac{w_r(j\omega)}{-\omega^2 w_{base} e^{j\omega t}} \bigg|_{s=j\omega}$$

$$= -\frac{1}{\omega_r^{(w)2} - \omega^2 + j2\zeta_r^{(w)}\omega_r^{(w)}\omega} \left(\frac{(j\omega P_D + R_L)Q_r^{(w)} - \displaystyle\sum_{r=1}^{m} \frac{j\omega P_r^{(u)2} Q_r^{(w)}}{\omega_r^{(u)2} - \omega^2 + j2\zeta_r^{(u)}\omega_r^{(u)}\omega}}{j\omega P_D + R_L - \displaystyle\sum_{r=1}^{m} \frac{j\omega P_r^{(w)2}}{\omega_r^{(w)2} - \omega^2 + j2\zeta_r^{(w)}\omega_r^{(w)}\omega} - \displaystyle\sum_{r=1}^{m} \frac{j\omega P_r^{(u)2}}{\omega_r^{(u)2} - \omega^2 + j2\zeta_r^{(u)}\omega_r^{(u)}\omega}} \right) .(4.255)$$

Equation (4.255) can be modified to obtain the FRF as a function of position of the piezoelectric element (x) and frequency $(j\omega)$ by transforming it back into the Ritz eigenfunction form to give,

$$H_{22}(x, j\omega) = \frac{w_{rel}(x, j\omega)}{-\omega^2 w_{base} e^{j\omega t}} \bigg|_{s=j\omega}$$

$$= -\sum_{r=1}^{m} \left[\frac{\hat{\Psi}_r(x)}{\omega_r^{(w)2} - \omega^2 + j2\zeta_r^{(w)}\omega_r^{(w)}\omega} \left(\frac{(j\omega P_D + R_L)Q_r^{(w)} - \displaystyle\sum_{r=1}^{m} \frac{j\omega P_r^{(u)2} Q_r^{(w)}}{\omega_r^{(u)2} - \omega^2 + j2\zeta_r^{(u)}\omega_r^{(u)}\omega}}{j\omega P_D + R_L - \displaystyle\sum_{r=1}^{m} \frac{j\omega P_r^{(w)2}}{\omega_r^{(w)2} - \omega^2 + j2\zeta_r^{(w)}\omega_r^{(w)}\omega} - \displaystyle\sum_{r=1}^{m} \frac{j\omega P_r^{(u)2}}{\omega_r^{(u)2} - \omega^2 + j2\zeta_r^{(u)}\omega_r^{(u)}\omega}} \right) \right] .(4.256)$$

The FRF between output electric voltage and the input base longitudinal acceleration can be obtained as,

$$H_{31}(j\omega) = \frac{v(j\omega)}{-\omega^2 u_{base} e^{j\omega t}} \bigg|_{s=j\omega}$$

$$= \frac{\displaystyle\sum_{r=1}^{m} \frac{j\omega P_r^{(u)} Q_r^{(u)}}{\omega_r^{(u)2} - \omega^2 + j2\zeta_r^{(u)}\omega_r^{(u)}\omega}}{j\omega P_D + R_L - \displaystyle\sum_{r=1}^{m} \frac{j\omega P_r^{(w)2}}{\omega_r^{(w)2} - \omega^2 + j2\zeta_r^{(w)}\omega_r^{(w)}\omega} - \displaystyle\sum_{r=1}^{m} \frac{j\omega P_r^{(u)2}}{\omega_r^{(u)2} - \omega^2 + j2\zeta_r^{(u)}\omega_r^{(u)}\omega}} . \quad (4.257)$$

The multi-mode FRF of the electric voltage output with respect to the input base transverse excitation can be derived, omitting the input base longitudinal excitation to give,

$$H_{32}(j\omega) = \frac{v(j\omega)}{-\omega^2 w_{base} e^{j\omega t}}\bigg|_{s=j\omega}$$

$$= \frac{\displaystyle\sum_{r=1}^{m} \frac{j\omega P_r^{(w)} Q_r^{(w)}}{\omega_r^{(w)2} - \omega^2 + j2\zeta_r^{(w)}\omega_r^{(w)}\omega}}{j\omega P_D + R_L - \displaystyle\sum_{r=1}^{m} \frac{j\omega P_r^{(w)2}}{\omega_r^{(w)2} - \omega^2 + j2\zeta_r^{(w)}\omega_r^{(w)}\omega} - \displaystyle\sum_{r=1}^{m} \frac{j\omega P_r^{(u)2}}{\omega_r^{(u)2} - \omega^2 + j2\zeta_r^{(u)}\omega_r^{(u)}\omega}} \qquad .(4.258)$$

The multi-mode FRF of the electric voltage output related to the input base longitudinal acceleration can be obtained as,

$$H_{41}(j\omega) = \frac{I(j\omega)}{-\omega^2 u_{base} e^{j\omega t}}\bigg|_{s=j\omega}$$

$$= \frac{\dfrac{1}{R_{load}}\displaystyle\sum_{r=1}^{m} \frac{j\omega P_r^{(u)} Q_r^{(u)}}{\omega_r^{(u)2} - \omega^2 + j2\zeta_r^{(u)}\omega_r^{(u)}\omega}}{j\omega P_D + R_L - \displaystyle\sum_{r=1}^{m} \frac{j\omega P_r^{(w)2}}{\omega_r^{(w)2} - \omega^2 + j2\zeta_r^{(w)}\omega_r^{(w)}\omega} - \displaystyle\sum_{r=1}^{m} \frac{j\omega P_r^{(u)2}}{\omega_r^{(u)2} - \omega^2 + j2\zeta_r^{(u)}\omega_r^{(u)}\omega}} \qquad . \quad (4.259)$$

The FRF of the electric voltage output related to the input base transverse exciatation can be derived, omitting the input base longitudinal excitation to give,

$$H_{42}(j\omega) = \frac{I(j\omega)}{-\omega^2 w_{base} e^{j\omega t}}\bigg|_{s=j\omega}$$

$$= \frac{\dfrac{1}{R_{load}}\displaystyle\sum_{r=1}^{m} \frac{j\omega P_r^{(w)} Q_r^{(w)}}{\omega_r^{(w)2} - \omega^2 + j2\zeta_r^{(w)}\omega_r^{(w)}\omega}}{j\omega P_D + R_L - \displaystyle\sum_{r=1}^{m} \frac{j\omega P_r^{(w)2}}{\omega_r^{(w)2} - \omega^2 + j2\zeta_r^{(w)}\omega_r^{(w)}\omega} - \displaystyle\sum_{r=1}^{m} \frac{j\omega P_r^{(u)2}}{\omega_r^{(u)2} - \omega^2 + j2\zeta_r^{(u)}\omega_r^{(u)}\omega}} \qquad .(4.260)$$

The multi-mode FRF of power harvesting related to the longitudinal acceleration can be expressed as,

$$\frac{P(j\omega)}{\left(-\omega^2 u_{base} e^{j\omega t}\right)^2}\bigg|_{s=j\omega}$$

$$= \left[\frac{\dfrac{1}{\sqrt{R_{load}}}\displaystyle\sum_{r=1}^{m} \frac{j\omega P_r^{(u)} Q_r^{(u)}}{\omega_r^{(u)2} - \omega^2 + j2\zeta_r^{(u)}\omega_r^{(u)}\omega}}{j\omega P_D + R_L - \displaystyle\sum_{r=1}^{m} \frac{j\omega P_r^{(w)2}}{\omega_r^{(w)2} - \omega^2 + j2\zeta_r^{(w)}\omega_r^{(w)}\omega} - \displaystyle\sum_{r=1}^{m} \frac{j\omega P_r^{(u)2}}{\omega_r^{(u)2} - \omega^2 + j2\zeta_r^{(u)}\omega_r^{(u)}\omega}}\right]^2 \quad .(4.261)$$

The multi-mode FRF of power harvesting related the transverse acceleration can be derived as,

$$\frac{P(j\omega)}{\left(-\omega^2 w_{base} e^{j\omega t}\right)^2}\bigg|_{s=j\omega}$$

$$= \left[\frac{\dfrac{1}{\sqrt{R_{load}}} \displaystyle\sum_{r=1}^{m} \dfrac{j\omega P_r^{(w)} Q_r^{(w)}}{\omega_r^{(w)2} - \omega^2 + j2\zeta_r^{(w)}\omega_r^{(w)}\omega}}{j\omega P_D + R_L - \displaystyle\sum_{r=1}^{m} \dfrac{j\omega P_r^{(w)2}}{\omega_r^{(w)2} - \omega^2 + j2\zeta_r^{(w)}\omega_r^{(w)}\omega} - \displaystyle\sum_{r=1}^{m} \dfrac{j\omega P_r^{(u)2}}{\omega_r^{(u)2} - \omega^2 + j2\zeta_r^{(u)}\omega_r^{(u)}\omega}} \right]^2 \quad .(4.262)$$

The optimal multi-mode FRF power harvesting related to the transverse acceleration can be derived by differentiating with respect to load resistance and setting the differentiable power function to zero. It is noted that parameter R_L represents per-unit load resistance $-1/R_{load}$. Corresponding to Eq. (4.262), the optimal load resistance can be formulated as,

$$R_{load}^{opt} = \frac{\sqrt{X(\omega)^2 + Y(\omega)^2}}{X(\omega)^2 + Y(\omega)^2}, \qquad (4.263)$$

where

$$X(\omega) = \omega P_D - \sum_{r=1}^{m} \frac{\omega P_r^{(w)2}\left(\omega_r^{(w)2} - \omega^2\right)}{\left(\omega_r^{(w)2} - \omega^2\right)^2 + \left(2\zeta_r^{(w)}\omega_r^{(w)}\omega\right)^2} - \sum_{r=1}^{m} \frac{\omega P_r^{(u)2}\left(\omega_r^{(u)2} - \omega^2\right)}{\left(\omega_r^{(u)2} - \omega^2\right)^2 + \left(2\zeta_r^{(u)}\omega_r^{(u)}\omega\right)^2},$$

$$Y(\omega) = \sum_{r=1}^{m} \frac{\omega P_r^{(w)2}\left(2\zeta_r^{(w)}\omega_r^{(w)}\omega\right)}{\left(\omega_r^{(w)2} - \omega^2\right)^2 + \left(2\zeta_r^{(w)}\omega_r^{(w)}\omega\right)^2} - \sum_{r=1}^{m} \frac{\omega P_r^{(u)2}\left(2\zeta_r^{(u)}\omega_r^{(u)}\omega\right)}{\left(\omega_r^{(u)2} - \omega^2\right)^2 + \left(2\zeta_r^{(u)}\omega_r^{(u)}\omega\right)^2}.$$

It should be noted that the optimal load resistance can be substituted back into Eq. (4.262) to give the optimal power harvesting.

Corresponding to Eqs. (4.249) and (4.251), equation (4.230) can be reduced in terms of the generalised time dependent longitudinal function as,

$$u_r(t) = H_{11}(j\omega)\ddot{u}_{base} + H_{12}(j\omega)\ddot{w}_{base},$$

$$u_r(t) = H_{11}(j\omega)\left(-\omega^2 u_{base}e^{j\omega t}\right) + H_{12}(j\omega)\left(-\omega^2 w_{base}e^{j\omega t}\right). \qquad (4.264)$$

Corresponding to Eq. (4.223b), modifying Eq. (4.264) in terms of any position along the piezoelectric beam gives the steady state relative longitudinal displacement under two input base excitations as,

$$u_{rel}(x,t) = H_{11}(x,j\omega)\left(-\omega^2 u_{base}e^{j\omega t}\right) + H_{12}(x,j\omega)\left(-\omega^2 w_{base}e^{j\omega t}\right). \qquad (4.265)$$

The multi-mode absolute longitudinal displacement can be formulated in terms of Eq. (4.265) as,

$$u_{abs}(x,t) = u_{base}e^{j\omega t} + H_{11}(x,j\omega)\left(-\omega^2 u_{base}e^{j\omega t}\right) + H_{12}(x,j\omega)\left(-\omega^2 w_{base}e^{j\omega t}\right). \qquad (4.266)$$

It should be noted that the absolute displacement fields have been discussed at the beginning of this chapter in terms of kinematic diagram of beam where the equation (4.266) was formulated as $u_{abs}(x,t) = u_{base}(t) + u_{rel}(x,t)$. The generalised time dependent relative transverse displacement in Eq. (4.231) can be modified corresponding with Eqs. (4.253) and (4.255) as,

$$w_r(t) = H_{21}(j\omega)\ddot{u}_{base} + H_{22}(j\omega)\ddot{w}_{base} ,$$

$$w_r(t) = H_{21}(j\omega)\left(-\omega^2 u_{base} e^{j\omega t}\right) + H_{22}(j\omega)\left(-\omega^2 w_{base} e^{j\omega t}\right). \qquad (4.267)$$

The steady state relative transverse displacement can be reformulated in terms of any position on the piezoelectric beam as,

$$w_{rel}(x,t) = H_{21}(x, j\omega)\left(-\omega^2 u_{base} e^{j\omega t}\right) + H_{22}(x, j\omega)\left(-\omega^2 w_{base} e^{j\omega t}\right). \qquad (4.268)$$

Corresponding to Eq. (4.268), the multi-mode absolute transverse displacement can be reduced as,

$$w_{abs}(x,t) = w_{base} e^{j\omega t} + H_{21}(x, j\omega)\left(-\omega^2 u_{base} e^{j\omega t}\right) + H_{22}(x, j\omega)\left(-\omega^2 w_{base} e^{j\omega t}\right). \qquad (4.269)$$

It should be noted that equation (4.269) is formulated according to the kinematics of the bimorph beam as discussed previously to give $w_{abs}(x,t) = w_{base}(t) + w_{rel}(x,t)$. The equation (4.232) can be modified into the generalised electrical potential response in terms of Eqs. (4.257) and (4.258) to give,

$$v(t) = H_{31}(j\omega)\ddot{u}_{base} + H_{32}(j\omega)\ddot{w}_{base}, \qquad (4.270)$$

$$v(t) = H_{31}(j\omega)\left(-\omega^2 u_{base} e^{j\omega t}\right) + H_{32}(j\omega)\left(-\omega^2 w_{base} e^{j\omega t}\right) . \qquad (4.271)$$

It should be noted that u_{base} and w_{base} refer to the input base longitudinal and transverse displacement excitations on the bimorph. Corresponding to Eqs. (4.266) and (4.269), equations (4.250) and (4.256) can be modified to give the multi-mode FRF of the absolute displacements and velocities related to the base input longitudinal and transverse accelerations at any position along the bimorph respectively as,

$$\hat{H}_{11}^{(disp)}(x, j\omega) = \frac{u_{base} e^{j\omega t} + u_{rel}(x,t)}{-\omega^2 u_{base} e^{j\omega t}} = -\frac{1}{\omega^2} + H_{11}(x, j\omega)$$

$$\hat{H}_{11}^{(vel)}(x, j\omega) = \frac{\dfrac{d}{dt}\left[u_{base} e^{j\omega t} + u_{rel}(x,t)\right]}{-\omega^2 u_{base} e^{j\omega t}} = \frac{1}{j\omega} + j\omega H_{11}(x, j\omega)$$

$$\hat{H}_{22}^{(disp)}(x, j\omega) = \frac{w_{base} e^{j\omega t} + w_{rel}(x,t)}{-\omega^2 w_{base} e^{j\omega t}} = -\frac{1}{\omega^2} + H_{22}(x, j\omega) \qquad (4.272)$$

$$\hat{H}_{22}^{(vel)}(x, j\omega) = \frac{\dfrac{d}{dt}\left[w_{base}e^{j\omega t} + w_{rel}(x,t)\right]}{-\omega^2 w_{base}e^{j\omega t}} = \frac{1}{j\omega} + j\omega H_{22}(x, j\omega)$$

It should be noted that equations (4.266), (4.269) and (4.272) are applicable for analysing the absolute dynamic responses when comparing the results using the Laser Doppler Vibrometer (LDV) because the signal output from the Vibrometer can be transferred into a digital signal FFT Analyzer to display the results. The results obtained from measurements can be the time dependent absolute displacement, velocity, acceleration, Fourier spectrum and frequency response function located at any position along the piezoelectric bimorph.

4.7. Multi-mode Frequency Analysis of the Normalised Coupled Electromechanical Dynamic Response of Transverse-Longitudinal Form (Closed Form-CEDRTL)

This section focuses on the multi-mode frequency response using the closed form of the electromechanical dynamic equations under two input base excitations. The closed-form analytical method was formulated according to the strong form of the Hamiltonian principle which was formulated from Eq. (4.88). This included the electromechanical bimorph element with the boundary-value problem where the partial differential equations associated with the geometry and natural boundary conditions were formulated in section (4.2) from Eqs. (4.89) to (4.95). The solution form from this analytical method involves the convergent eigenfunction forms which can be formulated as

$$w_{rel}(x,t) = \sum_{r=1}^{\infty} \hat{\Psi}_r(x) w_r(t) \quad , \quad u_{rel}(x,t) = \sum_{r=1}^{\infty} \hat{\Theta}_r(x) u_r(t) \quad . \quad (4.273)$$

It should be noted that equation (4.280) is sometimes called the mode superposition theorem which utilizes the normalised mode shapes and generalised time dependent coordinates. At this point, the equation considering the coupling electromechanical longitudinal and transverse forms of the piezoelectric element can be further formulated in terms of frequency analysis. As formulated in Eqs. (4.90) and (4.93), the boundary-value problem formulated for the piezoelectric bimorph element can be expressed using the normalised eigenfunction series under two input base excitations.

The first representation of the electromechanical piezoelectric bimorph under transverse bending, can be formulated using the Eq. (4.93), corresponding to Eq. (4.273a) as,

$$\hat{I}^{(A,k)}\hat{\Psi}_r(x)\ddot{w}_r(t) + \hat{C}_{11}^{(F,k)}\frac{d^2}{dx^2}\left(\frac{d^2\hat{\Psi}_r(x)}{dx^2}\right)w_r(t) + \hat{I}^{(A,k)}\ddot{w}_{base} - \hat{I}^{(C,k)}\frac{d^2\hat{\Psi}_r(x)}{dx^2}\ddot{w}_r(t) = 0. \quad (4.274)$$

Multiplying Eq. (4.274) with $\hat{\Psi}_q(x)$ and integrating with respect to x gives,

$$\int_0^L \hat{I}^{(A,k)}\hat{\Psi}_r(x)\hat{\Psi}_q(x)\ddot{w}_r(t)dx - \int_0^L \hat{I}^{(C,k)}\frac{d^2\hat{\Psi}_r(x)}{dx^2}\hat{\Psi}_q(x)\ddot{w}_r(t)dx$$

$$+ \int_0^L \hat{C}_{11}^{(F,k)}\frac{d^2}{dx^2}\left(\frac{d^2\hat{\Psi}_r(x)}{dx^2}\right)\hat{\Psi}_q(x)w_r(t)dx + \int_0^L \hat{I}^{(A,k)}\hat{\Psi}_q(x)\ddot{w}_{base}dx = 0. \quad (4.275)$$

The boundary conditions from Eq. (4.94) can be further formulated by substituting Eq. (4.273a) as,

$$\hat{\Psi}_r(0,t) = 0 \quad , \quad \frac{d\hat{\Psi}_r(0,t)}{dx} = 0 \quad , \quad (4.276)$$

and two dynamic boundary conditions can be further formulated as,

$$-I_{tip}^{(A)}\ddot{w}_{base} - I_{tip}^{(A)}\hat{\Psi}_r(L)\ddot{w}_r(t) + \hat{C}_{11}^{(F,k)}\frac{d}{dx}\left(\frac{d^2\hat{\Psi}_r(L)}{dx^2}\right)w_r(t) - \hat{I}^{(C,k)}\frac{d\hat{\Psi}_r}{dx}(L)\ddot{w}_r(t) = 0, \quad (4.277)$$

$$-I_{tip}^{(C)}\frac{d\hat{\Psi}_r(L)}{dx}\ddot{w}_r(t) - \hat{C}_{11}^{(F,k)}\frac{d^2\hat{\Psi}_r(L)}{dx^2}w_r(t) - \hat{R}_{31}^{(H,k)}v(t) = 0. \quad (4.278)$$

In terms of conditions implied in Eqs. (4.277) and (4.278) and also using the orthogonality relations, the second and third terms of Eq. (4.275) can be further manipulated by using partial integration to give,

$$\int_0^L \hat{I}^{(C,k)}\frac{d^2\hat{\Psi}_r(x)}{dx^2}\hat{\Psi}_q(x)dx = \left. \hat{I}^{(C,k)}\frac{d\hat{\Psi}_r(x)}{dx}\hat{\Psi}_q(x)\right|_0^L - \int_0^L \hat{I}^{(C,k)}\frac{d\hat{\Psi}_r(x)}{dx}\frac{d\hat{\Psi}_q(x)}{dx}dx ,$$

$$\int_0^L \hat{C}_{11}^{(F,k)}\frac{d^2}{dx^2}\left(\frac{d^2\hat{\Psi}_r(x)}{dx^2}\right)\hat{\Psi}_q(x)dx = \left. \hat{C}_{11}^{(F,k)}\frac{d}{dx}\left(\frac{d^2\hat{\Psi}_r(x)}{dx^2}\right)\hat{\Psi}_q(x)\right|_0^L$$

$$- \left. \hat{C}_{11}^{(F,k)}\frac{d^2\hat{\Psi}_r(x)}{dx^2}\frac{d\hat{\Psi}_q(x)}{dx}\right|_0^L + \int_0^L \hat{C}_{11}^{(F,k)}\frac{d^2\hat{\Psi}_r(x)}{dx^2}\frac{d^2\hat{\Psi}_q(x)}{dx^2}dx . \quad (4.279)$$

Applying the boundary conditions from Eq. (4.276) into Eq. (4.279) and multiplying by $w_r(t)$, the dynamic equation of the geometry bimorph problem can be written as,

$$\int_0^L \hat{I}^{(C,k)}\frac{d^2\hat{\Psi}_r(x)}{dx^2}\hat{\Psi}_q(x)\ddot{w}_r(t)dx = \hat{I}^{(C,k)}\frac{d\hat{\Psi}_r(L)}{dx}\hat{\Psi}_q(L)\ddot{w}_r - \int_0^L \hat{I}^{(C,k)}\frac{d\hat{\Psi}_r(x)}{dx}\frac{d\hat{\Psi}_q(x)}{dx}\ddot{w}_r dx ,$$

$$\int_0^L \hat{C}_{11}^{(F,k)} \frac{d^2}{dx^2}\left(\frac{d^2\hat{\Psi}_r(x)}{dx^2}\right)\hat{\Psi}_q(x)w_r(t)\,dx = \hat{C}_{11}^{(F,k)} \frac{d}{dx}\left(\frac{d^2\hat{\Psi}_r(L)}{dx^2}\right)\hat{\Psi}_q(L)w_r(t)$$

$$- \hat{C}_{11}^{(F,k)} \frac{d^2\hat{\Psi}_r(L)}{dx^2}\frac{d\hat{\Psi}_q(L)}{dx}w_r(t) + \int_0^L \hat{C}_{11}^{(F,k)} \frac{d^2\hat{\Psi}_r(x)}{dx^2}\frac{d^2\hat{\Psi}_q(x)}{dx^2}w_r(t)\,dx. \qquad (4.280)$$

Substituting Eqs. (4.277) and (4.278) into Eq. (4.280b) gives,

$$\int_0^L \hat{C}_{11}^{(F,k)} \frac{d^2}{dx^2}\left(\frac{d^2\hat{\Psi}_r(x)}{dx^2}\right)\hat{\Psi}_q(x)w_r(t)\,dx = I_{tip}^{(A)}\hat{\Psi}_q(L)\ddot{w}_{base} + I_{tip}^{(A)}\hat{\Psi}_r(L)\hat{\Psi}_q(L)\ddot{w}_r(t) + I_{tip}^{(C)}\frac{d\hat{\Psi}_r(L)}{dx}\frac{d\hat{\Psi}_q(L)}{dx}\ddot{w}_r(t)$$

$$+ \hat{I}^{(C,k)}\frac{d\hat{\Psi}_r}{dx}(L)\hat{\Psi}_q(L)\ddot{w}_r(t) + \hat{R}_{31}^{(H,k)}\frac{d\hat{\Psi}_q(L)}{dx}v(t) + \int_0^L \hat{C}_{11}^{(F,k)}\frac{d^2\hat{\Psi}_r(x)}{dx^2}\frac{d^2\hat{\Psi}_q(x)}{dx^2}w_r(t)\,dx. \quad (4.281)$$

Corresponding to Eq. (4.281), equation (4.275) can be reformulated as,

$$\int_0^L \hat{I}^{(A,k)}\hat{\Psi}_r(x)\hat{\Psi}_q(x)\ddot{w}_r(t)\,dx - \int_0^L \hat{I}^{(C,k)}\frac{d^2\hat{\Psi}_r(x)}{dx^2}\hat{\Psi}_q(x)\ddot{w}_r(t)\,dx + I_{tip}^{(A)}\hat{\Psi}_q(L)\ddot{w}_{base}$$

$$+ I_{tip}^{(A)}\hat{\Psi}_r(L)\hat{\Psi}_q(L)\ddot{w}_r(t) + \hat{I}^{(C,k)}\frac{d\hat{\Psi}_r}{dx}(L)\hat{\Psi}_q(L)\ddot{w}_r(t) + I_{tip}^{(C)}\frac{d\hat{\Psi}_r(L)}{dx}\frac{d\hat{\Psi}_q(L)}{dx}\ddot{w}_r(t)$$

$$+ \int_0^L \hat{C}_{11}^{(F,k)}\frac{d^2\hat{\Psi}_r(x)}{dx^2}\frac{d^2\hat{\Psi}_q(x)}{dx^2}\,dx + \hat{R}_{31}^{(H,k)}v(t)\frac{d\hat{\Psi}_q(L)}{dx} + \int_0^L \hat{I}^{(A,k)}\hat{\Psi}_q(x)\ddot{w}_{base}\,dx = 0 \quad . \qquad (4.282)$$

Corresponding with Eq. (4.280a), equation (4.282) can be modified to give a more compact dynamic equation as,

$$\int_0^L \hat{I}^{(A,k)}\hat{\Psi}_r(x)\hat{\Psi}_q(x)\,dx\,\ddot{w}_r(t) + I_{tip}^{(A)}\hat{\Psi}_r(L)\hat{\Psi}_q(L)\ddot{w}_r(t) + I_{tip}^{(C)}\frac{d\hat{\Psi}_r(L)}{dx}\frac{d\hat{\Psi}_q(L)}{dx}\ddot{w}_r(t)$$

$$+ \int_0^L \hat{C}_{11}^{(F,k)}\frac{d^2\hat{\Psi}_r(x)}{dx^2}\frac{d^2\hat{\Psi}_q(x)}{dx^2}\,dx\,w_r(t) + \int_0^L \hat{I}^{(C,k)}\frac{d\hat{\Psi}_r(x)}{dx}\frac{d\hat{\Psi}_q(x)}{dx}\,dx\,\ddot{w}_r(t) + \hat{R}_{31}^{(H,k)}\frac{d\hat{\Psi}_q(L)}{dx}v(t)$$

$$= -\int_0^L \hat{I}^{(A,k)}\hat{\Psi}_q(x)\,dx\,\ddot{w}_{base} - I_{tip}^{(A)}\hat{\Psi}_q(L)\ddot{w}_{base} \quad . \qquad (4.283)$$

It should be noted that the normalised eigenfunction series in Eq. (4.273a) must meet the orthogonality relations to correctly represent the mode shapes. It is also noted that the mode shapes are given in appendix B. As mentioned previously, this section gives the piezoelectric bimorph beam equations based on Rayleigh's beam assumption as it considers the rotary inertia of the bimorph beam. The Euler-Bernoulli bimorph beam can be formulated by ignoring the rotary inertia of the bimorph beam. In this case, the normalised mass from Eq. (4.284) can be used to ignore the rotary inertia of the bimorph beam at the first integration to give the typical Euler-Bernoulli bimorph beam condition. The orthonormalisations can be

provided by using Eq. (4.273a) and applying the orthogonality property of the mechanical dynamic equations as,

$$\int_0^L \hat{I}^{(C,k)} \frac{\mathrm{d}\hat{\Psi}_r(x)}{\mathrm{d}x} \frac{\mathrm{d}\hat{\Psi}_q(x)}{\mathrm{d}x} \mathrm{d}x + \int_0^L \hat{I}^{(A,k)} \hat{\Psi}_r(x)\hat{\Psi}_q(x)\mathrm{d}x + I_{tip}^{(A)} \hat{\Psi}_r(L)\hat{\Psi}_q(L) + I_{tip}^{(C)} \frac{\mathrm{d}\hat{\Psi}_r(L)}{\mathrm{d}x} \frac{\mathrm{d}\hat{\Psi}_q(L)}{\mathrm{d}x} = \delta_{rq}, \quad (4.284)$$

$$\int_0^L \hat{C}_{11}^{(F,k)} \frac{\mathrm{d}^2\hat{\Psi}_r(x)}{\mathrm{d}x^2} \frac{\mathrm{d}^2\hat{\Psi}_q(x)}{\mathrm{d}x^2} \mathrm{d}x = \omega_r^{(w)2} \delta_{rq} \quad . \quad (4.285)$$

where δ_{rq} is the Kronecker delta, defined as unity for $q = r$ and zero for $q \neq r$. It should be noted that equations (4.284) and (4.285) represent specific orthogonality conditions based on the boundary conditions. The mechanical damping based on the Rayleigh's principle can be reduced in terms of orthonormality as,

$$C_{rq}^{(w)} = \alpha^{(w)} \delta_{rq} + \beta^{(w)} \omega_r^{(w)2} \delta_{rq} = 2\zeta_r^{(w)} \omega_r^{(w)} \delta_{rq}.$$

Equation (4.283) can now be reformulated by including Rayleigh's damping coefficient according to orthogonality conditions as,

$$\ddot{w}_r(t) + 2\zeta_r^{(w)}\omega_r^{(w)}\dot{w}_r(t) + \omega_r^{(w)2}w(t) + P_r^{(w)}v(t) = -Q_r^{(w)}\ddot{w}_{base}(t). \quad (4.286)$$

The second case of the electromechanical dynamic equation associated with boundary conditions represents the electromechanical piezoelectric bimorph under longitudinal extension. Here it is formulated using Eq. (4.90) corresponding to Eq. (4.273b) to give,

$$- \hat{I}^{(A,k)}\hat{\Theta}_r(x)\ddot{u}_r - \hat{I}^{(A,k)}\ddot{u}_{base}(t) + \hat{C}_{11}^{(D,k)} \frac{\mathrm{d}^2\hat{\Theta}_r(x)}{\mathrm{d}x^2} u_r = 0 \quad . \quad (4.287)$$

Multiplying Eq. (4.287) with $\hat{\Theta}_q(x)$ and integrating with respect to x gives,

$$- \int_0^L \hat{I}^{(A,k)}\hat{\Theta}_r(x)\hat{\Theta}_q(x)\ddot{u}_r\mathrm{d}x - \int_0^L \hat{I}^{(A,k)}\hat{\Theta}_q(x)\ddot{u}_{base}(t)\mathrm{d}x + \int_0^L \hat{C}_{11}^{(D,k)}\hat{\Theta}_q(x)\frac{\mathrm{d}^2\hat{\Theta}_r(x)}{\mathrm{d}x^2}u_r\mathrm{d}x = 0. \quad (4.288)$$

The boundary conditions from Eq. (4.91) can be further formulated by substituting Eq. (4.273b) as,

$$\Theta(0,t)=0, \quad - I_{tip}^{(A)}\ddot{u}_{base}(t) - I_{tip}^{(A)}\hat{\Theta}_r(L)\ddot{u}_r - \hat{C}_{11}^{(D,k)} \frac{\mathrm{d}\hat{\Theta}_r(L)}{\mathrm{d}x} u_r + \hat{R}_{31}^{(G,k)}v(t) = 0. \quad (4.289)$$

In terms of conditions implied the Eq. (4.289) and the orthogonality relations, the second term of Eq. (4.288) can be further manipulated by using the partial integral form as,

$$\int_0^L \hat{C}_{11}^{(D,k)}\hat{\Theta}_q(x)\frac{\mathrm{d}}{\mathrm{d}x}\left(\frac{\mathrm{d}\hat{\Theta}_r(x)}{\mathrm{d}x}\right)u_r\mathrm{d}x = \hat{C}_{11}^{(D,k)}\frac{\mathrm{d}\hat{\Theta}_r(L)}{\mathrm{d}x}\hat{\Theta}_q(L)u_r - \int_0^L \hat{C}_{11}^{(D,k)}\frac{\mathrm{d}\hat{\Theta}_r(x)}{\mathrm{d}x}\frac{\mathrm{d}\hat{\Theta}_q(x)}{\mathrm{d}x}u_r\mathrm{d}x. \quad (4.290)$$

Substituting the boundary conditions from Eq. (4.289) into (4.290) and multiplying by $u_r(t)$ in order to meet the dynamic equation of the geometry bimorph problem gives,

$$\int_0^L \hat{C}_{11}^{(A,k)} \hat{\Theta}_q(x) \frac{\mathrm{d}}{\mathrm{d}x}\left(\frac{\mathrm{d}\hat{\Theta}_r(x)}{\mathrm{d}x}\right) u_r \mathrm{d}x = -I_{tip}^{(A)} \hat{\Theta}_q(L) \ddot{u}_{base}(t) - I_{tip}^{(A)} \hat{\Theta}_r(L) \hat{\Theta}_q(L) \ddot{u}_r$$

$$-\int_0^L \hat{C}_{11}^{(D,k)} \frac{\mathrm{d}\hat{\Theta}_r(x)}{\mathrm{d}x} \frac{\mathrm{d}\hat{\Theta}_q(x)}{\mathrm{d}x} u_r\, \mathrm{d}x + \hat{R}_{31}^{(G,k)} \hat{\Theta}_q(L) v(t). \qquad (4.291)$$

Corresponding to Eq. (4.291), equation (4.288) can be reformulated as,

$$-\int_0^L \hat{I}^{(A,k)} \hat{\Theta}_r(x) \hat{\Theta}_q(x) \ddot{u}_r \mathrm{d}x \ -\int_0^L \hat{I}^{(A,k)} \hat{\Theta}_q(x) \ddot{u}_{base}(t) \mathrm{d}x - I_{tip}^{(A)} \hat{\Theta}_q(L) \ddot{u}_{base}(t)$$

$$-I_{tip}^{(A)} \hat{\Theta}_r(L) \hat{\Theta}_q(L) \ddot{u}_r - \int_0^L \hat{C}_{11}^{(D,k)} \frac{\mathrm{d}\hat{\Theta}_r(x)}{\mathrm{d}x} \frac{\mathrm{d}\hat{\Theta}_q(x)}{\mathrm{d}x} u_r\, \mathrm{d}x + \hat{R}_{31}^{(G,k)} \hat{\Theta}_q(L) v(t) = 0. (4.292)$$

Modifying Eq. (4.292) gives ,

$$\int_0^L \hat{I}^{(A,k)} \hat{\Theta}_r(x) \hat{\Theta}_q(x) \ddot{u}_r \mathrm{d}x \ + I_{tip}^{(A)} \hat{\Theta}_r(L) \hat{\Theta}_q(L) \ddot{u}_r + \int_0^L \hat{C}_{11}^{(D,k)} \frac{\mathrm{d}\hat{\Theta}_r(x)}{\mathrm{d}x} \frac{\mathrm{d}\hat{\Theta}_q(x)}{\mathrm{d}x} u_r\, \mathrm{d}x - \hat{R}_{31}^{(G,k)} \hat{\Theta}_q(L) v(t)$$

$$= -\int_0^L \hat{I}^{(A,k)} \hat{\Theta}_q(x) \ddot{u}_{base}(t) \mathrm{d}x - I_{tip}^{(A)} \hat{\Theta}_q(L) \ddot{u}_{base}(t). \qquad (4.293)$$

In this case, the second part of the normalised eigenfunction series in Eq. (4.273b) must meet the orthogonality relations in order to correctly specify the longitudinal mode shapes as formulated in appendix B. Furthermore, the specific orthogonality condition to Eq. (4.293) can be established as,

$$\int_0^L \hat{I}^{(A,k)} \hat{\Theta}_r(x) \hat{\Theta}_q(x) \mathrm{d}x \ + I_{tip}^{(A)} \hat{\Theta}_r(L) \hat{\Theta}_q(L) = \delta_{rq}, \qquad (4.294)$$

$$\int_0^L \hat{C}_{11}^{(D,k)} \frac{\mathrm{d}\hat{\Theta}_r(x)}{\mathrm{d}x} \frac{\mathrm{d}\hat{\Theta}_q(x)}{\mathrm{d}x} \mathrm{d}x = \omega_r^{(u)2} \delta_{rq} . \qquad (4.295)$$

where δ_{rq} is the Kronecker delta, defined as unity for $q = r$ and zero for $q \neq r$. The mechanical damping constant based on Rayleigh's principle can be reduced in terms of orthonormality as,

$$C_{rq}^{(u)} = \alpha^{(u)} \delta_{rq} + \beta^{(u)} \omega_r^{(u)2} \delta_{rq} = 2\zeta_r^{(u)} \omega_r^{(u)} \delta_{rq}. \qquad (4.296)$$

Equation (4.293) can now be reformulated by including the Rayleigh's damping coefficient based on the orthonormality conditions as,

$$\ddot{u}_r(t) + 2\zeta_r^{(u)} \omega_r^{(u)} \dot{w}_r(t) + \omega_r^{(u)2} w(t) + P_r^{(u)} v(t) = -Q_r^{(u)} \ddot{u}_{base}(t). \qquad (4.297)$$

The third case of the electromechanical dynamic equation represents the piezoelectric bimorph under electrical form. Here it is formulated as,

$$\int_0^L \left(\hat{R}_{31}^{(G,k)} \frac{\partial u_{rel}}{\partial x} - \hat{R}_{31}^{(H,k)} \frac{\partial^2 w_{rel}}{\partial x^2} + \hat{S}_{33}^{(k)} v(t) \right) dx + q(t) = 0 \; . \qquad (4.298)$$

Substituting Eq. (4.273) into Eq. (4.298) and differentiating it with respect to time to obtain the parameter velocity and electrical current gives,

$$\sum_{r=1}^{\infty} \int_0^L \hat{R}_{31}^{(G,k)} \frac{d\hat{\Theta}_r(x)}{dx} dx \dot{u}_r(t) - \sum_{r=1}^{\infty} \int_0^L \hat{R}_{31}^{(H,k)} \frac{d^2\hat{\Psi}_r(x)}{dx^2} dx \dot{w}_r(t) + \int_0^L \hat{S}_{33}^{(k)} dx \dot{v}(t) + \frac{1}{R_{load}} v(t) = 0 . (4.299)$$

The equation (4.299) can be reformulated as,

$$\sum_{r=1}^{\infty} \hat{P}_r^{(u)} \dot{u}_r(t) + \sum_{r=1}^{\infty} \hat{P}_r^{(w)} \dot{w}_r(t) + P_D \dot{v}(t) + R_L v(t) = 0 \; . \qquad (4.300)$$

In this case, the electromechanical piezoelectric bimorph beam based on Eqs. (4.286), (4.297) and (4.300) can be reformulated to give,

$$\ddot{u}_r(t) + 2\zeta_r^{(u)} \omega_r^{(u)} \dot{u}_r(t) + \omega_r^{(u)2} u_r(t) + P_r^{(u)} v(t) = -Q_r^{(u)} \ddot{u}_{base}(t)$$

$$\ddot{w}_r(t) + 2\zeta_r^{(w)} \omega_r^{(w)} \dot{w}_r(t) + \omega_r^{(w)2} w(t) + P_r^{(w)} v(t) = -Q_r^{(w)} \ddot{w}_{base}(t) \qquad (4.301)$$

$$\sum_{r=1}^{\infty} \hat{P}_r^{(u)} \dot{u}_r(t) + \sum_{r=1}^{\infty} \hat{P}_r^{(w)} \dot{w}_r(t) + P_D \dot{v}(t) + R_L v(t) = 0$$

It is clear that equation (4.299) provides the closed-form of electromechanical dynamic equations with two input base motions and this equation can be further formulated using Laplace transformations.

It is noted that because equation (4.301) has been normalised due to Eqs. (4.284), (4.285), (4.294) and (4.295), the parameters $P_r^{(u)}, P_r^{(w)}, \; \hat{P}_r^{(u)}, \hat{P}_r^{(w)}, P_D, R_L, \; Q_r^{(u)}$ and $Q_r^{(w)}$ can be reduced as,

$$P_r^{(u)} = -\hat{R}_{31}^{(G,k)} \hat{\Theta}_r(L), P_r^{(w)} = \hat{R}_{31}^{(H,k)} \frac{d\hat{\Psi}_r(L)}{dx}, P_D = \int_0^L \hat{S}_{33}^{(k)} dx \; ,$$

$$\sum_{r=1}^{\infty} \hat{P}_r^{(u)} = \sum_{r=1}^{\infty} \int_0^L \hat{R}_{31}^{(G,k)} \frac{d\hat{\Theta}_r(x)}{dx} dx \; , \; \sum_{r=1}^{\infty} \hat{P}_r^{(w)} = -\sum_{r=1}^{\infty} \int_0^L \hat{R}_{31}^{(H,k)} \frac{d^2\hat{\Psi}_r(x)}{dx^2} dx \; ,$$

$$R_L = \frac{1}{R_{load}} \; , \; Q_r^{(u)} = \int_0^L \hat{I}^{(A,k)} \hat{\Theta}_r(x) dx + I_{tip}^{(A)} \hat{\Theta}_r(L) \; , Q_r^{(w)} = \int_0^L \hat{I}^{(A,k)} \hat{\Psi}_r(x) dx + I_{tip}^{(A)} \hat{\Psi}_r(L) \; .$$

Equations (4.229) and (4.301) appear to be similar to each other but have different sign and operation for some parameters. Equation (4.301) can be solved using Laplace transformations. In this case, the multi-mode electromechanical dynamic equations of the piezoelectric bimorph can be reduced as,

$$u_r(s) = -\frac{1}{Z(s)_r}\left[\left\{\left(s^2 + 2\zeta_r^{(w)}\omega_r^{(w)}s + \omega_r^{(w)2}\right)(sP_D + R_L) - \sum_{r=1}^{\infty} s\hat{P}_r^{(w)}P_r^{(w)}\right\}Q_r^{(u)}s^2 u_{base}(s)\right.$$

$$\left. + \sum_{r=1}^{\infty} s\hat{P}_r^{(w)}P_r^{(u)}Q_r^{(w)}\left(s^2 w_{base}(s)\right)\right], \qquad (4.302)$$

$$w_r(s) = -\frac{1}{Z(s)_r}\left[\left\{\left(s^2 + 2\zeta_r^{(u)}\omega_r^{(u)}s + \omega_r^{(u)2}\right)(sP_D + R_L) - s\sum_{r=1}^{\infty} \hat{P}_r^{(u)}P_r^{(u)}\right\}Q_r^{(w)}s^2 w_{base}(s)\right.$$

$$\left. + \sum_{r=1}^{\infty} s\hat{P}_r^{(u)}P_r^{(w)}Q_r^{(u)}s^2 u_{base}(s)\right], \qquad (4.303)$$

$$v(s) = \frac{1}{Z(s)_r}\left[\sum_{r=1}^{\infty}\left\{s\hat{P}_r^{(w)}Q_r^{(w)}\left(s^2 + 2\zeta_r^{(u)}\omega_r^{(u)}s + \omega_r^{(u)2}\right)s^2 w_{base}(s)\right\}\right.$$

$$\left. + \sum_{r=1}^{\infty}\left\{-s\hat{P}_r^{(u)}Q_r^{(u)}\left(s^2 + 2\zeta_r^{(w)}\omega_r^{(w)}s + \omega_r^{(w)2}\right)s^2 u_{base}(s)\right\}\right]. \qquad (4.304)$$

The characteristic polynomial form from Eqs. (4.302) to (4.304) can be expressed as,

$$Z(s)_r = \left(s^2 + 2\zeta_r^{(u)}\omega_r^{(u)}s + \omega_r^{(u)2}\right)\left(s^2 + 2\zeta_r^{(w)}\omega_r^{(w)}s + \omega_r^{(w)2}\right)(sP_D + R_L)$$

$$- \sum_{r=1}^{\infty} s\hat{P}_r^{(w)}P_r^{(w)}\left(s^2 + 2\zeta_r^{(u)}\omega_r^{(u)}s + \omega_r^{(u)2}\right) + \sum_{r=1}^{\infty} s\hat{P}_r^{(u)}P_r^{(u)}\left(s^2 + 2\zeta_r^{(w)}\omega_r^{(w)}s + \omega_r^{(w)2}\right). \qquad (4.305)$$

Corresponding to Eqs. (4.302) to (4.304), the multi-mode transfer function of the longitudinal displacement related to the base input longitudinal acceleration can be obtained after simplifying as,

$$H_{11}(s) = \left.\frac{u_r(s)}{\left(s^2 u_{base}(s)\right)}\right|_{s^2 w_{base}(s)=0}$$

$$= -\frac{1}{s^2 + 2\zeta_r^{(u)}\omega_r^{(u)}s + \omega_r^{(u)2}}\left(\frac{(sP_D+R_L)Q_r^{(u)} - \sum\limits_{r=1}^{m}\dfrac{s\hat{P}_r^{(w)}P_r^{(w)}Q_r^{(u)}}{s^2 + 2\zeta_r^{(w)}\omega_r^{(w)}s + \omega_r^{(w)2}}}{sP_D + R_L - \sum\limits_{r=1}^{m}\dfrac{s\hat{P}_r^{(w)}P_r^{(w)}}{s^2 + 2\zeta_r^{(w)}\omega_r^{(w)}s + \omega_r^{(w)2}} - \sum\limits_{r=1}^{m}\dfrac{s\hat{P}_r^{(u)}P_r^{(u)}}{s^2 + 2\zeta_r^{(u)}\omega_r^{(u)}s + \omega_r^{(u)2}}}\right). \qquad (4.306)$$

The multi-mode transfer function of longitudinal displacement output related to the input base longitudinal acceleration based on the element position (x) and subsidiary variable (s) can be obtained after neglecting the input transverse excitation to give,

$$H_{11}(x,s) = \left.\frac{u_{rel}(x,s)}{\left(s^2 u_{base}(s)\right)}\right|_{s^2 w_{base}(s)=0}$$

$$= -\sum_{r=1}^{m}\left[\frac{\hat{\Theta}_r(x)}{s^2 + 2\zeta_r^{(u)}\omega_r^{(u)}s + \omega_r^{(u)2}}\left(\frac{\left(sP_D + R_L\right)Q_r^{(u)} - \sum_{r=1}^{m}\dfrac{s\hat{P}_r^{(w)}P_r^{(w)}Q_r^{(u)}}{s^2 + 2\zeta_r^{(w)}\omega_r^{(w)}s + \omega_r^{(w)2}}}{sP_D + R_L - \sum_{r=1}^{m}\dfrac{s\hat{P}_r^{(w)}P_r^{(w)}}{s^2 + 2\zeta_r^{(w)}\omega_r^{(w)}s + \omega_r^{(w)2}} - \sum_{r=1}^{m}\dfrac{s\hat{P}_r^{(u)}P_r^{(u)}}{s^2 + 2\zeta_r^{(u)}\omega_r^{(u)}s + \omega_r^{(u)2}}}\right)\right]. \quad (4.307)$$

The multi-mode transfer function of the longitudinal displacement related to the base input transverse acceleration can be formulated as,

$$H_{12}(s) = \left.\frac{u_r(s)}{\left(s^2 w_{base}(s)\right)}\right|_{s^2 u_{base}(s)=0}$$

$$= -\frac{1}{s^2 + 2\zeta_r^{(u)}\omega_r^{(u)}s + \omega_r^{(u)2}}\left(\frac{\sum_{r=1}^{m}\dfrac{s\hat{P}_r^{(w)}P_r^{(u)}Q_r^{(w)}}{s^2 + 2\zeta_r^{(w)}\omega_r^{(w)}s + \omega_r^{(w)2}}}{sP_D + R_L - \sum_{r=1}^{m}\dfrac{s\hat{P}_r^{(w)}P_r^{(w)}}{s^2 + 2\zeta_r^{(w)}\omega_r^{(w)}s + \omega_r^{(w)2}} - \sum_{r=1}^{m}\dfrac{s\hat{P}_r^{(u)}P_r^{(u)}}{s^2 + 2\zeta_r^{(u)}\omega_r^{(u)}s + \omega_r^{(u)2}}}\right). \quad (4.308)$$

The transfer function between the input base transverse acceleration and longitudinal displacement output based on the element position (x) and subsidiary variable (s) can be obtained as,

$$H_{12}(x,s) = \left.\frac{u_{rel}(x,s)}{\left(s^2 w_{base}(s)\right)}\right|_{s^2 u_{base}(s)=0}$$

$$= -\sum_{r=1}^{m}\left[\frac{\hat{\Theta}_r(x)}{s^2 + 2\zeta_r^{(u)}\omega_r^{(u)}s + \omega_r^{(u)2}}\left(\frac{\sum_{r=1}^{m}\dfrac{s\hat{P}_r^{(w)}P_r^{(u)}Q_r^{(w)}}{s^2 + 2\zeta_r^{(w)}\omega_r^{(w)}s + \omega_r^{(w)2}}}{sP_D + R_L - \sum_{r=1}^{m}\dfrac{s\hat{P}_r^{(w)}P_r^{(w)}}{s^2 + 2\zeta_r^{(w)}\omega_r^{(w)}s + \omega_r^{(w)2}} - \sum_{r=1}^{m}\dfrac{s\hat{P}_r^{(u)}P_r^{(u)}}{s^2 + 2\zeta_r^{(u)}\omega_r^{(u)}s + \omega_r^{(u)2}}}\right)\right]. \quad (4.309)$$

The multi-mode transfer function of the input base longitudinal acceleration related to the transverse displacement can be obtained as,

$$H_{21}(s) = \left.\frac{w_r(s)}{\left(s^2 u_{base}(s)\right)}\right|_{s^2 w_{base}(s)=0}$$

$$= -\frac{1}{s^2 + 2\zeta_r^{(w)}\omega_r^{(w)}s + \omega_r^{(w)2}}\left(\frac{\sum_{r=1}^{m}\dfrac{s\hat{P}_r^{(u)}P_r^{(w)}Q_r^{(u)}}{s^2 + 2\zeta_r^{(w)}\omega_r^{(w)}s + \omega_r^{(w)2}}}{sP_D + R_L - \sum_{r=1}^{m}\dfrac{s\hat{P}_r^{(w)}P_r^{(w)}}{s^2 + 2\zeta_r^{(w)}\omega_r^{(w)}s + \omega_r^{(w)2}} - \sum_{r=1}^{m}\dfrac{s\hat{P}_r^{(u)}P_r^{(u)}}{s^2 + 2\zeta_r^{(u)}\omega_r^{(u)}s + \omega_r^{(u)2}}}\right). \quad (4.310)$$

The transfer function of the generalised relative transverse displacement with respect to the input base longitudinal acceleration can be obtained in terms of the element position (x) and subsidiary variable (s) as,

$$H_{21}(x,s) = \left.\frac{w_{rel}(x,s)}{\left(s^2 u_{base}(s)\right)}\right|_{s^2 w_{base}(s)=0}$$

$$= -\sum_{r=1}^{m} \left[\frac{\hat{\Psi}_r(x)}{s^2 + 2\zeta_r^{(w)}\omega_r^{(w)}s + \omega_r^{(w)2}} \left(\frac{\sum_{r=1}^{m}\frac{s\hat{P}_r^{(u)}P_r^{(w)}Q_r^{(u)}}{s^2 + 2\zeta_r^{(w)}\omega_r^{(w)}s + \omega_r^{(w)2}}}{sP_D + R_L - \sum_{r=1}^{m}\frac{s\hat{P}_r^{(w)}P_r^{(w)}}{s^2 + 2\zeta_r^{(w)}\omega_r^{(w)}s + \omega_r^{(w)2}} - \sum_{r=1}^{m}\frac{s\hat{P}_r^{(u)}P_r^{(u)}}{s^2 + 2\zeta_r^{(u)}\omega_r^{(u)}s + \omega_r^{(u)2}}} \right) \right] .(4.311)$$

Corresponding to Eq. (4.303), the multi-mode transfer function representing the input base transverse acceleration with respect to transverse displacement output can be obtained, neglecting longitudinal excitation as,

$$H_{22}(s) = \frac{w_r(s)}{s^2 w_{base}(s)}\bigg|_{s^2 u_{base}(s)=0}$$

$$= -\frac{1}{s^2 + 2\zeta_r^{(w)}\omega_r^{(w)}s + \omega_r^{(w)2}} \left(\frac{(sP_D + R_L)Q_r^{(w)} - \sum_{r=1}^{m}\frac{s\hat{P}_r^{(u)}P_r^{(u)}Q_r^{(w)}}{s^2 + 2\zeta_r^{(u)}\omega_r^{(w)}s + \omega_r^{(u)2}}}{sP_D + R_L - \sum_{r=1}^{m}\frac{s\hat{P}_r^{(w)}P_r^{(w)}}{s^2 + 2\zeta_r^{(w)}\omega_r^{(w)}s + \omega_r^{(w)2}} - \sum_{r=1}^{m}\frac{s\hat{P}_r^{(u)}P_r^{(u)}}{s^2 + 2\zeta_r^{(u)}\omega_r^{(u)}s + \omega_r^{(u)2}}} \right). (4.312)$$

In terms of applying Laplace transforms to Eq. (4.273a), the multi-mode transfer function from Eq. (4.312) can be modified in terms of the position of the piezoelectric element (x) as,

$$H_{22}(x,s) = \frac{w_{rel}(x,s)}{s^2 w_{base}(s)}\bigg|_{s^2 u_{base}(s)=0}$$

$$= -\sum_{r=1}^{m} \left[\frac{\hat{\Psi}_r(x)}{s^2 + 2\zeta_r^{(w)}\omega_r^{(w)}s + \omega_r^{(w)2}} \left(\frac{(sP_D + R_L)Q_r^{(w)} - \sum_{r=1}^{m}\frac{s\hat{P}_r^{(u)}P_r^{(u)}Q_r^{(w)}}{s^2 + 2\zeta_r^{(u)}\omega_r^{(w)}s + \omega_r^{(u)2}}}{sP_D + R_L - \sum_{r=1}^{m}\frac{s\hat{P}_r^{(w)}P_r^{(w)}}{s^2 + 2\zeta_r^{(w)}\omega_r^{(w)}s + \omega_r^{(w)2}} - \sum_{r=1}^{m}\frac{s\hat{P}_r^{(u)}P_r^{(u)}}{s^2 + 2\zeta_r^{(u)}\omega_r^{(u)}s + \omega_r^{(u)2}}} \right) \right] .(4.313)$$

With the same method, the multi-mode transfer function between the input base longitudinal acceleration and electric voltage can be obtained as,

$$H_{31}(s) = \frac{v(s)}{s^2 u_{base}(s)}\bigg|_{s^2 w_{base}(s)=0} = \frac{\sum_{r=1}^{m}\frac{s\hat{P}_r^{(u)}Q_r^{(u)}}{s^2 + 2\zeta_r^{(u)}\omega_r^{(u)}s + \omega_r^{(u)2}}}{sP_D + R_L - \sum_{r=1}^{m}\frac{s\hat{P}_r^{(w)}\hat{P}_r^{(w)}}{s^2 + 2\zeta_r^{(w)}\omega_r^{(w)}s + \omega_r^{(w)2}} - \sum_{r=1}^{m}\frac{s\hat{P}_r^{(u)}P_r^{(u)}}{s^2 + 2\zeta_r^{(u)}\omega_r^{(u)}s + \omega_r^{(u)2}}} .(4.314)$$

The multi-mode transfer function of electric voltage output with respect to the input base transverse acceleration can be obtained, neglecting longitudinal excitation,

$$H_{32}(s) = \frac{v(s)}{s^2 w_{base}(s)}\bigg|_{s^2 u_{base}(s)=0} = \frac{\sum_{r=1}^{m}\frac{s\hat{P}_r^{(w)}Q_r^{(w)}}{s^2 + 2\zeta_r^{(w)}\omega_r^{(w)}s + \omega_r^{(w)2}}}{sP_D + R_L - \sum_{r=1}^{m}\frac{s\hat{P}_r^{(w)}P_r^{(w)}}{s^2 + 2\zeta_r^{(w)}\omega_r^{(w)}s + \omega_r^{(w)2}} - \sum_{r=1}^{m}\frac{s\hat{P}_r^{(u)}P_r^{(u)}}{s^2 + 2\zeta_r^{(u)}\omega_r^{(u)}s + \omega_r^{(u)2}}} . (4.315)$$

With the same method, the multi-mode transfer function between the input base longitudinal acceleration and electric voltage can be obtained as,

$$H_{41}(s) = \left.\frac{I(s)}{s^2 u_{base}(s)}\right|_{s^2 w_{base}(s)=0} = \frac{\dfrac{1}{R_{Load}}\sum\limits_{r=1}^{m}\dfrac{s\hat{P}_r^{(u)}Q_r^{(u)}}{s^2 + 2\zeta_r^{(u)}\omega_r^{(u)}s+\omega_r^{(u)2}}}{sP_D + R_L - \sum\limits_{r=1}^{m}\dfrac{s\hat{P}_r^{(w)}\hat{P}_r^{(w)}}{s^2 + 2\zeta_r^{(w)}\omega_r^{(w)}s+\omega_r^{(w)2}} - \sum\limits_{r=1}^{m}\dfrac{s\hat{P}_r^{(u)}P_r^{(u)}}{s^2 + 2\zeta_r^{(u)}\omega_r^{(u)}s+\omega_r^{(u)2}}} . \quad (4.316)$$

The multi-mode transfer function of electric voltage output with respect to the input base transverse acceleration can be obtained, neglecting longitudinal excitation as,

$$H_{42}(s)\frac{I(s)}{s^2 w_{base}(s)} = \frac{\dfrac{1}{R_{load}}\sum\limits_{r=1}^{m}\dfrac{s\hat{P}_r^{(w)}Q_r^{(w)}}{s^2 + 2\zeta_r^{(w)}\omega_r^{(w)}s+\omega_r^{(w)2}}}{sP_D + R_L - \sum\limits_{r=1}^{m}\dfrac{s\hat{P}_r^{(w)}P_r^{(w)}}{s^2 + 2\zeta_r^{(w)}\omega_r^{(w)}s+\omega_r^{(w)2}} - \sum\limits_{r=1}^{m}\dfrac{s\hat{P}_r^{(u)}P_r^{(u)}}{s^2 + 2\zeta_r^{(u)}\omega_r^{(u)}s+\omega_r^{(u)2}}} . \quad (4.317)$$

The multi-mode transfer function of power harvesting due to input longitudinal acceleration can be derived as,

$$\left.\frac{P(s)}{\left(s^2 u_{base}(s)\right)^2}\right|_{s^2 w_{base}(s)=0}$$

$$= \left[\frac{\dfrac{1}{\sqrt{R_{load}}}\sum\limits_{r=1}^{\infty}\dfrac{s\hat{P}_r^{(u)}Q_r^{(u)}}{s^2 + 2\zeta_r^{(u)}\omega_r^{(u)}s+\omega_r^{(u)2}}}{sP_D + R_L - \sum\limits_{r=1}^{\infty}\dfrac{s\hat{P}_r^{(w)}P_r^{(w)}}{s^2 + 2\zeta_r^{(w)}\omega_r^{(w)}s+\omega_r^{(w)2}} - \sum\limits_{r=1}^{\infty}\dfrac{s\hat{P}_r^{(u)}P_r^{(u)}}{s^2 + 2\zeta_r^{(u)}\omega_r^{(u)}s+\omega_r^{(u)2}}}\right]^2 . \quad (4.318)$$

The multi-mode transfer function relating power harvesting to input transverse excitation can be derived as,

$$\left.\frac{P(s)}{\left(s^2 w_{base}(s)\right)^2}\right|_{s^2 u_{base}(s)=0}$$

$$= \left[\frac{\dfrac{1}{\sqrt{R_{load}}}\sum\limits_{r=1}^{\infty}\dfrac{s\hat{P}_r^{(w)}Q_r^{(w)}}{s^2 + 2\zeta_r^{(w)}\omega_r^{(w)}s+\omega_r^{(w)2}}}{sP_D + R_L - \sum\limits_{r=1}^{\infty}\dfrac{s\hat{P}_r^{(w)}P_r^{(w)}}{s^2 + 2\zeta_r^{(w)}\omega_r^{(w)}s+\omega_r^{(w)2}} - \sum\limits_{r=1}^{\infty}\dfrac{s\hat{P}_r^{(u)}P_r^{(u)}}{s^2 + 2\zeta_r^{(u)}\omega_r^{(u)}s+\omega_r^{(u)2}}}\right]^2 . \quad (4.319)$$

Corresponding to Eqs. (4.306) to (4.319), the frequency response function (FRF) can be formulated. In this case, the electromechanical dynamic equation of the piezoelectric bimorph can be formulated in matrix form FRF as,

$$H(j\omega) = \begin{bmatrix} H_{11}(j\omega) & H_{12}(j\omega) \\ H_{21}(j\omega) & H_{22}(j\omega) \\ H_{31}(j\omega) & H_{32}(j\omega) \\ H_{41}(j\omega) & H_{42}(j\omega) \end{bmatrix} \qquad . \qquad (4.320)$$

The first multi-mode FRF represents longitudinal motion with respect to input motions. In the case where input transverse motion is ignored, FRF can be obtained from base-input longitudinal motion as it was formulated,

$$H_{11}(j\omega) = \frac{u_r(j\omega)}{-\omega^2 u_{base} e^{j\omega t}}\bigg|_{s=j\omega}$$

$$= -\frac{1}{\omega_r^{(u)2} - \omega^2 + j2\zeta_r^{(u)}\omega_r^{(u)}\omega}\left(\frac{\left(j\omega P_D + R_L\right)Q_r^{(u)} - \sum_{r=1}^{\infty}\dfrac{j\omega\hat{P}_r^{(w)}P_r^{(w)}Q_r^{(u)}}{\omega_r^{(w)2} - \omega^2 + j2\zeta_r^{(w)}\omega_r^{(w)}\omega}}{j\omega P_D + R_L - \sum_{r=1}^{\infty}\dfrac{j\omega\hat{P}_r^{(w)}P_r^{(w)}}{\omega_r^{(w)2} - \omega^2 + j2\zeta_r^{(w)}\omega_r^{(w)}\omega} - \sum_{r=1}^{\infty}\dfrac{j\omega\hat{P}_r^{(u)}P_r^{(u)}}{\omega_r^{(u)2} - \omega^2 + j2\zeta_r^{(u)}\omega_r^{(u)}\omega}} \right). \; (4.321)$$

Equation (4.321) can be modified to obtain the FRF as a function of position of the piezoelectric element (x) and frequency $(j\omega)$ by transforming it back into the Ritz eigenfunction form as

$$H_{11}(x, j\omega) = \frac{u_{rel}(x, j\omega)}{-\omega^2 u_{base} e^{j\omega t}}\bigg|_{s=j\omega}$$

$$= -\sum_{r=1}^{\infty}\left[\frac{\Theta_r(x)}{\omega_r^{(u)2} - \omega^2 + j2\zeta_r^{(u)}\omega_r^{(u)}\omega}\left(\frac{\left(j\omega P_D + R_L\right)Q_r^{(u)} - \sum_{r=1}^{\infty}\dfrac{j\omega\hat{P}_r^{(w)}P_r^{(w)}Q_r^{(u)}}{\omega_r^{(w)2} - \omega^2 + j2\zeta_r^{(w)}\omega_r^{(w)}\omega}}{j\omega P_D + R_L - \sum_{r=1}^{\infty}\dfrac{j\omega\hat{P}_r^{(w)}P_r^{(w)}}{\omega_r^{(w)2} - \omega^2 + j2\zeta_r^{(w)}\omega_r^{(w)}\omega} - \sum_{r=1}^{\infty}\dfrac{j\omega\hat{P}_r^{(u)}P_r^{(u)}}{\omega_r^{(u)2} - \omega^2 + j2\zeta_r^{(u)}\omega_r^{(u)}\omega}} \right) \right]. (4.322)$$

The multi-mode FRF of the relative transfer function between the input base transverse acceleration and output longitudinal displacement can be obtained as,

$$H_{12}(j\omega) = \frac{u_r(j\omega)}{-\omega^2 w_{base} e^{j\omega t}}\bigg|_{s=j\omega}$$

$$= -\frac{1}{\omega_r^{(u)2} - \omega^2 + j2\zeta_r^{(u)}\omega_r^{(u)}\omega}\left(\frac{\sum_{r=1}^{\infty}\dfrac{j\omega\hat{P}_r^{(w)}P_r^{(u)}Q_r^{(w)}}{\omega_r^{(w)2} - \omega^2 + j2\zeta_r^{(w)}\omega_r^{(w)}\omega}}{j\omega P_D + R_L - \sum_{r=1}^{\infty}\dfrac{j\omega\hat{P}_r^{(w)}P_r^{(w)}}{\omega_r^{(w)2} - \omega^2 + j2\zeta_r^{(w)}\omega_r^{(w)}\omega} + \sum_{r=1}^{\infty}\dfrac{j\omega\hat{P}_r^{(u)}P_r^{(u)}}{\omega_r^{(u)2} - \omega^2 + j2\zeta_r^{(u)}\omega_r^{(u)}\omega}} \right). (4.323)$$

Equation (4.323) can be modified as a function of position of the piezoelectric element (x) and frequency $(j\omega)$ by transforming it back into the Ritz eigenfunction form to give,

$$H_{12}(x, j\omega) = \left. \frac{u_{rel}(x, j\omega)}{-\omega^2 w_{base} e^{j\omega t}} \right|_{s=j\omega}$$

$$= -\sum_{r=1}^{\infty} \left[\frac{\hat{\Theta}_r(x)}{\omega_r^{(u)2} - \omega^2 + j2\zeta_r^{(u)}\omega_r^{(u)}\omega} \left(\frac{\sum_{r=1}^{\infty} \frac{j\omega \hat{P}_r^{(w)} P_r^{(u)} Q_r^{(w)}}{\omega_r^{(w)2} - \omega^2 + j2\zeta_r^{(w)}\omega_r^{(w)}\omega}}{j\omega P_D + R_L - \sum_{r=1}^{\infty} \frac{j\omega \hat{P}_r^{(w)} P_r^{(w)}}{\omega_r^{(w)2} - \omega^2 + j2\zeta_r^{(w)}\omega_r^{(w)}\omega} - \sum_{r=1}^{\infty} \frac{j\omega \hat{P}_r^{(u)} P_r^{(u)}}{\omega_r^{(u)2} - \omega^2 + j2\zeta_r^{(u)}\omega_r^{(u)}\omega}} \right) \right], (4.324)$$

The second multi-mode FRF is the transverse motion with respect to input motions. If base-input transverse motion is ignored, the FRF of transverse motion related to the base input longitudinal motion can be obtained as,

$$H_{21}(j\omega) = \left. \frac{w_r(j\omega)}{-\omega^2 u_{base} e^{j\omega t}} \right|_{s=j\omega}$$

$$= -\frac{1}{\omega_r^{(w)2} - \omega^2 + j2\zeta_r^{(w)}\omega_r^{(w)}\omega} \left(\frac{\sum_{r=1}^{\infty} \frac{j\omega \hat{P}_r^{(u)} P_r^{(w)} Q_r^{(u)}}{\omega_r^{(u)2} - \omega^2 + j2\zeta_r^{(u)}\omega_r^{(u)}\omega}}{j\omega P_D + R_L - \sum_{r=1}^{\infty} \frac{j\omega \hat{P}_r^{(w)} P_r^{(w)}}{\omega_r^{(w)2} - \omega^2 + j2\zeta_r^{(w)}\omega_r^{(w)}\omega} - \sum_{r=1}^{\infty} \frac{j\omega \hat{P}_r^{(u)} P_r^{(u)}}{\omega_r^{(u)2} - \omega^2 + j2\zeta_r^{(u)}\omega_r^{(u)}\omega}} \right). (4.325)$$

Equation (4.325) can be modified to obtain the FRF as a function of position of the piezoelectric element (x) and frequency $(j\omega)$ by transforming it back into the Ritz eigenfunction form to give,

$$H_{21}(x, j\omega) = \left. \frac{w_{rel}(x, j\omega)}{-\omega^2 u_{base} e^{j\omega t}} \right|_{s=j\omega}$$

$$= -\sum_{r=1}^{\infty} \left[\frac{\hat{\Psi}_r(x)}{\omega_r^{(w)2} - \omega^2 + j2\zeta_r^{(w)}\omega_r^{(w)}\omega} \left(\frac{-\sum_{r=1}^{\infty} \frac{j\omega \hat{P}_r^{(u)} P_r^{(w)} Q_r^{(u)}}{\omega_r^{(u)2} - \omega^2 + j2\zeta_r^{(u)}\omega_r^{(u)}\omega}}{j\omega P_D + R_L - \sum_{r=1}^{\infty} \frac{j\omega \hat{P}_r^{(w)} P_r^{(w)}}{\omega_r^{(w)2} - \omega^2 + j2\zeta_r^{(w)}\omega_r^{(w)}\omega} - \sum_{r=1}^{\infty} \frac{j\omega \hat{P}_r^{(u)} P_r^{(u)}}{\omega_r^{(u)2} - \omega^2 + j2\zeta_r^{(u)}\omega_r^{(u)}\omega}} \right) \right]. (4.326)$$

The multi-mode FRF of transverse displacement with respect to input base transverse acceleration can be obtained as,

$$H_{22}(j\omega) = \left. \frac{w_r(j\omega)}{-\omega^2 w_{base} e^{j\omega t}} \right|_{s=j\omega}$$

$$= -\frac{1}{\omega_r^{(w)2} - \omega^2 + j2\zeta_r^{(w)}\omega_r^{(w)}\omega} \left(\frac{(j\omega P_D + R_L)Q_r^{(w)} - \sum_{r=1}^{\infty} \frac{j\omega \hat{P}_r^{(u)} P_r^{(u)} Q_r^{(w)}}{\omega_r^{(u)2} - \omega^2 + j2\zeta_r^{(u)}\omega_r^{(u)}\omega}}{j\omega P_D + R_L - \sum_{r=1}^{\infty} \frac{j\omega \hat{P}_r^{(w)} P_r^{(w)}}{\omega_r^{(w)2} - \omega^2 + j2\zeta_r^{(w)}\omega_r^{(w)}\omega} - \sum_{r=1}^{\infty} \frac{j\omega \hat{P}_r^{(u)} P_r^{(u)}}{\omega_r^{(u)2} - \omega^2 + j2\zeta_r^{(u)}\omega_r^{(u)}\omega}} \right), (4.327)$$

Equation (4.327) can be modified to obtain the FRF as a function of position of the piezoelectric element (x) and frequency $(j\omega)$ by transforming it back into the Ritz eigenfunction form to give,

$$H_{22}(x, j\omega) = \frac{w_{rel}(x, j\omega)}{-\omega^2 w_{base} e^{j\omega t}}\Bigg|_{s=j\omega}$$

$$= -\sum_{r=1}^{\infty}\left[\frac{\hat{\Psi}_r(x)}{\omega_r^{(w)2} - \omega^2 + j2\zeta_r^{(w)}\omega_r^{(w)}\omega}\left(\frac{\left(j\omega P_D + R_L\right)Q_r^{(w)} - \sum_{r=1}^{\infty}\dfrac{j\omega\hat{P}_r^{(u)}P_r^{(u)}Q_r^{(w)}}{\omega_r^{(u)2} - \omega^2 + j2\zeta_r^{(u)}\omega_r^{(u)}\omega}}{j\omega P_D + R_L - \sum_{r=1}^{\infty}\dfrac{j\omega\hat{P}_r^{(w)}P_r^{(w)}}{\omega_r^{(w)2} - \omega^2 + j2\zeta_r^{(w)}\omega_r^{(w)}\omega} - \sum_{r=1}^{\infty}\dfrac{j\omega\hat{P}_r^{(u)}P_r^{(u)}}{\omega_r^{(u)2} - \omega^2 + j2\zeta_r^{(u)}\omega_r^{(u)}\omega}}\right)\right] .(4.328)$$

The multi-mode FRF between electric voltage output and the input base longitudinal acceleration can be obtained as,

$$H_{31}(j\omega) = \frac{v(j\omega)}{-\omega^2 u_{base} e^{j\omega t}}\Bigg|_{s=j\omega}$$

$$= \frac{\displaystyle\sum_{r=1}^{\infty}\frac{j\omega\hat{P}_r^{(u)}Q_r^{(u)}}{\omega_r^{(u)2} - \omega^2 + j2\zeta_r^{(u)}\omega_r^{(u)}\omega}}{j\omega P_D + R_L - \displaystyle\sum_{r=1}^{\infty}\frac{j\omega\hat{P}_r^{(w)}P_r^{(w)}}{\omega_r^{(w)2} - \omega^2 + j2\zeta_r^{(w)}\omega_r^{(w)}\omega} - \displaystyle\sum_{r=1}^{\infty}\frac{j\omega\hat{P}_r^{(u)}P_r^{(u)}}{\omega_r^{(u)2} - \omega^2 + j2\zeta_r^{(u)}\omega_r^{(u)}\omega}} . \quad (4.329)$$

The multi-mode FRF of electric voltage output related to the input base transverse acceleration can be derived, where the base input longitudinal acceleration is omitted to give,

$$H_{32}(j\omega) = \frac{v(j\omega)}{-\omega^2 w_{base} e^{j\omega t}}\Bigg|_{s=j\omega}$$

$$= \frac{\displaystyle\sum_{r=1}^{\infty}\frac{j\omega\hat{P}_r^{(w)}Q_r^{(w)}}{\omega_r^{(w)2} - \omega^2 + j2\zeta_r^{(w)}\omega_r^{(w)}\omega}}{j\omega P_D + R_L - \displaystyle\sum_{r=1}^{\infty}\frac{j\omega\hat{P}_r^{(w)}P_r^{(w)}}{\omega_r^{(w)2} - \omega^2 + j2\zeta_r^{(w)}\omega_r^{(w)}\omega} - \displaystyle\sum_{r=1}^{\infty}\frac{j\omega\hat{P}_r^{(u)}P_r^{(u)}}{\omega_r^{(u)2} - \omega^2 + j2\zeta_r^{(u)}\omega_r^{(u)}\omega}} . \quad (4.330)$$

The multi-mode FRF of electric current output related to the input base longitudinal excitation can be stated as,

$$H_{41}(j\omega) = \frac{I(j\omega)}{-\omega^2 u_{base} e^{j\omega t}}\Bigg|_{s=j\omega}$$

$$= \frac{\dfrac{1}{R_{load}}\displaystyle\sum_{r=1}^{\infty}\frac{j\omega\hat{P}_r^{(u)}Q_r^{(u)}}{\omega_r^{(u)2} - \omega^2 + j2\zeta_r^{(u)}\omega_r^{(u)}\omega}}{j\omega P_D + R_L - \displaystyle\sum_{r=1}^{\infty}\frac{j\omega\hat{P}_r^{(w)}P_r^{(w)}}{\omega_r^{(w)2} - \omega^2 + j2\zeta_r^{(w)}\omega_r^{(w)}\omega} - \displaystyle\sum_{r=1}^{\infty}\frac{j\omega\hat{P}_r^{(u)}P_r^{(u)}}{\omega_r^{(u)2} - \omega^2 + j2\zeta_r^{(u)}\omega_r^{(u)}\omega}} . \quad (4.331)$$

The multi-mode FRF of the electric current output related to the input base transverse acceleration can be derived, where the base input longitudinal acceleration is omitted to give,

$$H_{42}(j\omega) = \frac{I(j\omega)}{-\omega^2 w_{base} e^{j\omega t}}\Bigg|_{s=j\omega}$$

$$= \frac{\dfrac{1}{R_{load}} \displaystyle\sum_{r=1}^{\infty} \dfrac{j\omega \hat{P}_r^{(w)} Q_r^{(w)}}{\omega_r^{(w)2} - \omega^2 + j2\zeta_r^{(w)} \omega_r^{(w)} \omega}}{j\omega P_D + R_L - \displaystyle\sum_{r=1}^{\infty} \dfrac{j\omega \hat{P}_r^{(w)} P_r^{(w)}}{\omega_r^{(w)2} - \omega^2 + j\,2\zeta_r^{(w)} \omega_r^{(w)} \omega} - \displaystyle\sum_{r=1}^{\infty} \dfrac{j\omega \hat{P}_r^{(u)} P_r^{(u)}}{\omega_r^{(u)2} - \omega^2 + j\,2\zeta_r^{(u)} \omega_r^{(u)} \omega}} \quad.(4.332)$$

The multi-mode FRF of power harvesting related to the longitudinal acceleration can be derived as,

$$\frac{P(j\omega)}{\left(-\omega^2 u_{base} e^{j\omega t}\right)^2}\Bigg|_{s=j\omega}$$

$$= \left[\frac{\dfrac{1}{\sqrt{R_{load}}} \displaystyle\sum_{r=1}^{\infty} \dfrac{j\omega \hat{P}_r^{(u)} Q_r^{(u)}}{\omega_r^{(u)2} - \omega^2 + j2\zeta_r^{(u)} \omega_r^{(u)} \omega}}{j\omega P_D + R_L - \displaystyle\sum_{r=1}^{\infty} \dfrac{j\omega \hat{P}_r^{(w)} P_r^{(w)}}{\omega_r^{(w)2} - \omega^2 + j\,2\zeta_r^{(w)} \omega_r^{(w)} \omega} - \displaystyle\sum_{r=1}^{\infty} \dfrac{j\omega \hat{P}_r^{(u)} P_r^{(u)}}{\omega_r^{(u)2} - \omega^2 + j\,2\zeta_r^{(u)} \omega_r^{(u)} \omega}}\right]^2 \quad. (4.333)$$

The multi-mode FRF of power harvesting related to the transverse acceleration can be derived as,

$$\frac{P(j\omega)}{\left(-\omega^2 w_{base} e^{j\omega t}\right)^2}\Bigg|_{s=j\omega}$$

$$= \left[\frac{\dfrac{1}{\sqrt{R_{load}}} \displaystyle\sum_{r=1}^{\infty} \dfrac{j\omega \hat{P}_r^{(w)} Q_r^{(w)}}{\omega_r^{(w)2} - \omega^2 + j2\zeta_r^{(w)} \omega_r^{(w)} \omega}}{j\omega P_D + R_L - \displaystyle\sum_{r=1}^{\infty} \dfrac{j\omega \hat{P}_r^{(w)} P_r^{(w)}}{\omega_r^{(w)2} - \omega^2 + j\,2\zeta_r^{(w)} \omega_r^{(w)} \omega} - \displaystyle\sum_{r=1}^{\infty} \dfrac{j\omega \hat{P}_r^{(u)} P_r^{(u)}}{\omega_r^{(u)2} - \omega^2 + j\,2\zeta_r^{(u)} \omega_r^{(u)} \omega}}\right]^2 \quad.(4.334)$$

Differentiating Eq. (4.334) with respect to the load resistance and setting the differentiable power to zero gives the optimal load resistance. It is noted that the parameter R_L represents per-unit load resistance $-1/R_{load}$. The optimal resistance can be formulated as,

$$R_{load}^{opt} = \frac{\sqrt{X(\omega)^2 + Y(\omega)^2}}{X(\omega)^2 + Y(\omega)^2}, \quad (4.335)$$

where

$$X(\omega) = \omega P_D - \sum_{r=1}^{\infty} \frac{\omega \hat{P}_r^{(w)} P_r^{(w)} \left(\omega_r^{(w)2} - \omega^2\right)}{\left(\omega_r^{(w)2} - \omega^2\right)^2 + \left(2\zeta_r^{(w)} \omega_r^{(w)} \omega\right)^2} - \sum_{r=1}^{\infty} \frac{\omega \hat{P}_r^{(u)} P_r^{(u)} \left(\omega_r^{(u)2} - \omega^2\right)}{\left(\omega_r^{(u)2} - \omega^2\right)^2 + \left(2\zeta_r^{(u)} \omega_r^{(u)} \omega\right)^2},$$

$$Y(\omega) = \sum_{r=1}^{\infty} \frac{\omega \hat{P}_r^{(w)} P_r^{(w)} \left(2\zeta_r^{(w)} \omega_r^{(w)} \omega\right)}{\left(\omega_r^{(w)2} - \omega^2\right)^2 + \left(2\zeta_r^{(w)} \omega_r^{(w)} \omega\right)^2} - \sum_{r=1}^{\infty} \frac{\omega \hat{P}_r^{(u)} P_r^{(u)} \left(2\zeta_r^{(u)} \omega_r^{(u)} \omega\right)}{\left(\omega_r^{(u)2} - \omega^2\right)^2 + \left(2\zeta_r^{(u)} \omega_r^{(u)} \omega\right)^2} .$$

It is noted that the optimal multi-mode FRF of power harvesting related to the transverse acceleration can be obtained by substituting the optimal load resistance into Eq. (4.334).

Corresponding to Eqs. (4.321), (4.323), equation (4.302) can be reduced in terms of the FRF as,

$$u_r(t) = H_{11}(j\omega)\ddot{u}_{base} + H_{12}(j\omega)\ddot{w}_{base},$$

$$u_r(t) = H_{11}(j\omega)\left(-\omega^2 u_{base} e^{j\omega t}\right) + H_{12}(j\omega)\left(-\omega^2 w_{base} e^{j\omega t}\right). \tag{4.336}$$

Modifying Eq. (4.336) in terms of any position along the piezoelectric beam gives,

$$u_{rel}(x,t) = H_{11}(x, j\omega)\left(-\omega^2 u_{base} e^{j\omega t}\right) + H_{12}(x, j\omega)\left(-\omega^2 w_{base} e^{j\omega t}\right). \tag{4.337}$$

The multi-mode absolute longitudinal displacement can be formulated as,

$$u_{abs}(x,t) = -\omega^2 u_{base} e^{j\omega t} + H_{11}(x, j\omega)\left(-\omega^2 u_{base} e^{j\omega t}\right) + H_{12}(x, j\omega)\left(-\omega^2 w_{base} e^{j\omega t}\right). \tag{4.338}$$

The generalised time dependent relative transverse displacement in Eq. (4.303) can be modified corresponding to the Eqs. (4.325) and (4.327) as,

$$w_r(t) = H_{21}(j\omega)\ddot{u}_{base} + H_{22}(j\omega)\ddot{w}_{base} ,$$

$$w_r(t) = H_{21}(j\omega)\left(-\omega^2 u_{base} e^{j\omega t}\right) + H_{22}(j\omega)\left(-\omega^2 w_{base} e^{j\omega t}\right). \tag{4.339}$$

Corresponding to Eq. (4.273a), the relative transverse displacement can be reformulated in terms of any position along the piezoelectric beam as,

$$w_{rel}(x,t) = H_{21}(x, j\omega)\left(-\omega^2 u_{base} e^{j\omega t}\right) + H_{22}(x, j\omega)\left(-\omega^2 w_{base} e^{j\omega t}\right). \tag{4.340}$$

Corresponding to Eq. (4.340), the absolute transverse displacement can be reduced as,

$$w_{abs}(x,t) = -\omega^2 w_{base} e^{j\omega t} + H_{21}(x, j\omega)\left(-\omega^2 u_{base} e^{j\omega t}\right) + H_{22}(x, j\omega)\left(-\omega^2 w_{base} e^{j\omega t}\right). \tag{4.341}$$

The generalised electrical potential can be formulated as,

$$v(t) = H_{31}(j\omega)\ddot{u}_{base} + H_{32}(j\omega)\ddot{w}_{base}, \tag{4.342}$$

$$v(t) = H_{31}(j\omega)\left(-\omega^2 u_{base} e^{j\omega t}\right) + H_{32}(j\omega)\left(-\omega^2 w_{base} e^{j\omega t}\right). \tag{4.343}$$

It should be noted that u_{base} and w_{base} are input base longitudinal and transverse displacement excitations on the bimorph. Corresponding to Eqs. (4.338) and (4.341), the equations (4.322) and (4.328) can be modified in terms of the multi-mode FRF

of the absolute displacements and velocities relating the input longitudinal and transverse displacement at any position along the bimorph respectively as,

$$\hat{H}_{11}^{(disp)}(x, j\omega) = \frac{u_{base}e^{j\omega t} + u_{rel}(x,t)}{-\omega^2 u_{base}e^{j\omega t}} = -\frac{1}{\omega^2} + H_{11}(x, j\omega)$$

$$\hat{H}_{11}^{(vel)}(x, j\omega) = \frac{\frac{d}{dt}\left[u_{base}e^{j\omega t} + u_{rel}(x,t)\right]}{-\omega^2 u_{base}e^{j\omega t}} = \frac{1}{j\omega} + j\omega H_{11}(x, j\omega)$$

$$\hat{H}_{22}^{(disp)}(x, j\omega) = \frac{w_{base}e^{j\omega t} + w_{rel}(x,t)}{-\omega^2 w_{base}e^{j\omega t}} = -\frac{1}{\omega^2} + H_{22}(x, j\omega) \qquad (4.344)$$

$$\hat{H}_{22}^{(vel)}(x, j\omega) = \frac{\frac{d}{dt}\left[w_{base}e^{j\omega t} + w_{rel}(x,t)\right]}{-\omega^2 w_{base}e^{j\omega t}} = \frac{1}{j\omega} + j\omega H_{22}(x, j\omega)$$

It should be noted that equations (4.338), (4.341) and (4.344) are applicable for analysing the absolute dynamic responses and comparing the results measured using the Laser Doppler Vibrometer (LDV) at any position along the piezoelectric bimorph beam.

4.8. Effect of Broadband Multi-Electromechanical Piezoelectric Bimorph Beam with the Multi-Frequency

This section focuses on an array of piezoelectric bimorph beams with different geometries attached to the base structure under input excitation. The bimorph beams can be modelled using series and parallel connections as shown in Figure (4.6). The multi-bimorph beam can be modelled with different geometric structures (thickness, width and length) in order to widen the frequency resonance of each bimorph beam. This also depends on the connection types of the bimorph and various load resistances. The effect of the multi-bimorph beam underlies the optimization design throughout the frequency domain. To solve the broadband multi-frequency response for the multi-bimorph beam, the previous formulations can be extended into the generalised multi- electromechanical dynamic equations associated with the electrical form of the piezoelectric system.
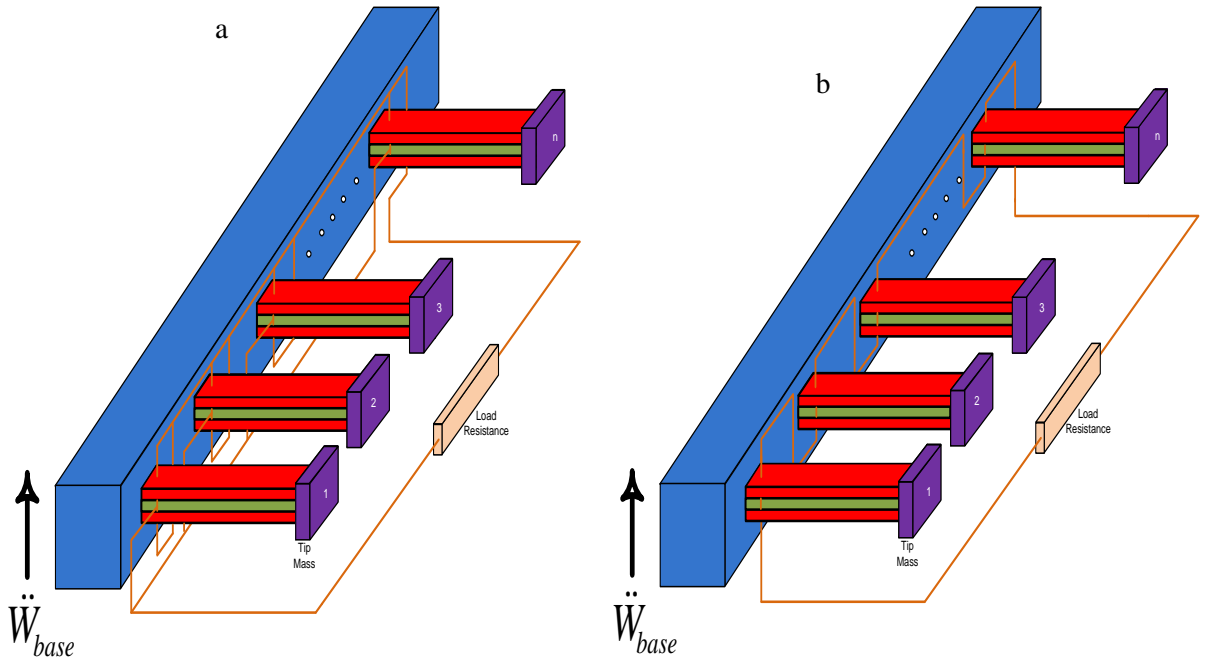
Figure 4.6 Multi-Electromechanical Piezoelectric Bimorph Beam with the Tip Masses : a) Parallel Connection, b) Series Connection

In this case, the previous equations from the normalised weak form of CEDRT in section 4.4 can be used as an example case to formulate the multi-mode frequency analysis of the broadband multi-frequency bimorph beam. The multi-mode equation can be reduced into the mathematical model of electromechanical differential equations for each bimorph beam. The generalised electromechanical piezoelectric dynamic equations can be formulated in the multi-mode system $r = 1,2,3....m$ in terms of the number of bimorph beam $i = 1,2,3....n$ (the broadband multi-frequency) as,

$$\ddot{w}_{r1}(t) + 2\zeta_{r1}^{(w)}\omega_{r1}^{(w)}\dot{w}_{r1}(t) + \omega_{r1}^{(w)2}w_{r1}(t) + P_{r1}^{(w)}v_1(t) = -Q_{r1}^{(w)}\ddot{w}_{base}(t)$$

$$\ddot{w}_{r2}(t) + 2\zeta_{r2}^{(w)}\omega_{r2}^{(w)}\dot{w}_{r2}(t) + \omega_{r2}^{(w)2}w_{r2}(t) + P_{r2}^{(w)}v_2(t) = -Q_{r2}^{(w)}\ddot{w}_{base}(t) \quad .(\,4.345)$$

$$.$$
$$.$$
$$.$$

$$\ddot{w}_{ri}(t) + 2\zeta_{ri}^{(w)}\omega_{ri}^{(w)}\dot{w}_i(t) + \omega_{ri}^{(w)2}w_{ri}(t) + P_{ri}^{(w)}v_i(t) = -Q_{ri}^{(w)}\ddot{w}_{base}(t)$$

Because the array of bimorph beams are clamped on the base structure with only one input excitation, the variable $\ddot{w}_{base}(t)$ will be the same for all electromechanical piezoelectric dynamic equations. The second form of the electromechanical piezoelectric dynamic equations can be formulated for the single mode system as,

$$\hat{P}_{r1}^{(w)}\dot{w}_{r1}(t) + P_{D2}\dot{v}_1(t) = \dot{q}_1(t)$$

$$\hat{P}_{r2}^{(w)}\dot{w}_{r2}(t) + P_{D2}\dot{v}_2(t) = \dot{q}_2(t)$$

$$\vdots \qquad \qquad \qquad \vdots \qquad \qquad (4.346)$$

$$\hat{P}_{ri}^{(w)}\dot{w}_r(t) + P_{Di}\dot{v}_i(t) = \dot{q}_i(t)$$

The equations (4.345) and (4.346) have been normalised in terms of the normalised Ritz eigenfunction series as given in previous derivations. The parameters $P_{ri}^{(w)}$, $\hat{P}_{ri}^{(w)}$, $Q_{ri}^{(w)}$, P_{Di} and R_{load} can then be stated as,

$$P_{ri}^{(w)} = \int\limits_0^{Li} \hat{R}_{31,i}^{(H,k)} \frac{d^2\hat{\Psi}_{ri}(x)}{dx^2}dx \;,\quad \hat{P}_{ri}^{(w)} = \sum_{i=1}^n\sum_{r=1}^m P_{ri}^{(w)} \;,\; R_L = -\frac{1}{R_{load}} \;,$$

$$P_{Di} = -\int\limits_0^{Li} \hat{S}_{33,i}^{(k)}\,dx \;\;,\quad Q_{ri}^{(w)} = \int\limits_0^{Li} \hat{I}_i^{(A,k)}\hat{\Psi}_{ri}(x)dx + I_{tip,i}^{(A)}\hat{\Psi}_{ri}(L) \cdot$$

It should be noted that each bimorph beam can be connected either using the parallel or series connections and the external load resistance can be an external circuit to connect all the bimorph beams in terms of the Kirchhoff's voltage law (KVL) and Kirchhoff's current law (KCL). The parallel connection of the multi-electromechanical bimorph beam can be stated as,

$$v_1(t) = v_2(t) = \ldots = v_i(t) = v(t) \qquad , \qquad \dot{q}_1(t) + \dot{q}_2(t) + \ldots + \dot{q}_i(t) = \dot{q}(t). \qquad (4.347)$$

The series connection of the multi-electromechanical bimorph beam can be stated as,

$$v_1(t) + v_2(t) + \ldots + v_i(t) = v(t) \qquad , \qquad \dot{q}_1(t) = \dot{q}_2(t) = \ldots = \dot{q}_i(t) = \dot{q}(t). \qquad (4.348)$$

The electrical voltage from the load resistance as shown in Figure (4.6) can be stated as

$$v(t) = \dot{q}(t)R_{load}. \qquad (4.349)$$

4.8.1.   The solution form of parallel connection

The multi-electromechanical piezoelectric bimorph beams can be modelled with parallel connection as shown in Figure (4.6a). In this case, three bimorph beams can be used to represent the broadband model sample having a single mode system. Once the single mode constitutive frequency equations are established, the multi-mode can simply be formulated in the forthcoming section because the mathematical derivations given in the previous section can be viewed as the frame of reference in representing the normalised multi-mode frequency analysis. Corresponding to Eq.

(4.347), the first form of the electromechanical piezoelectric dynamic equations from Eq. (4.345) can stated in terms of the three bimorphs under parallel connection as,

$$\ddot{w}_{11}(t) + 2\zeta_{11}^{(w)}\omega_{11}^{(w)}\dot{w}_{11}(t) + \omega_{11}^{(w)2}w_{11}(t) + P_{11}^{(w)}v(t) = -Q_{11}^{(w)}\ddot{w}_{base}(t)$$

$$\ddot{w}_{12}(t) + 2\zeta_{12}^{(w)}\omega_{12}^{(w)}\dot{w}_{2}(t) + \omega_{12}^{(w)2}w_{12}(t) + P_{12}^{(w)}v(t) = -Q_{12}^{(w)}\ddot{w}_{base}(t) . \quad (4.350)$$

$$\ddot{w}_{13}(t) + 2\zeta_{13}^{(w)}\omega_{13}^{(w)}\dot{w}_{13}(t) + \omega_{13}^{(w)2}w_{13}(t) + P_{13}^{(w)}v(t) = -Q_{13}^{(w)}\ddot{w}_{base}(t)$$

It is noted that the variable $v(t)$ must indicate the same form. The second form of the electromechanical piezoelectric dynamic equations can be formulated, where equation (4.347) can be applied to Eq. (4.346) to give,

$$\hat{P}_{11}^{(w)}\dot{w}_{1}(t) + P_{D1}\dot{v}(t) = \dot{q}_{1}(t)$$

$$\hat{P}_{12}^{(w)}\dot{w}_{2}(t) + P_{D2}\dot{v}(t) = \dot{q}_{2}(t) \quad . \quad (4.351)$$

$$\hat{P}_{13}^{(w)}\dot{w}_{3}(t) + P_{D3}\dot{v}(t) = \dot{q}_{3}(t)$$

As shown in Eqs. (4.348) and (4.349), each equation indicates identical variable $\dot{v}(t)$. Corresponding to Eq. (4.349), Equations (4.350) and (4.351) can be algebraically solved using Laplace transforms, reduced into matrix form giving the linear superposition of equations. The single mode of electrical voltage transfer function of the three broadband piezoelectric bimorph beams can be expressed as,

$$\frac{V(s)}{s^2 w_{base}(s)} = \frac{\displaystyle\sum_{i=1}^{3}\frac{sP_{1i}^{(w)}Q_{1i}^{(w)}}{s^2 + 2\zeta_{1i}^{(w)}\omega_{1i}^{(w)}s + \omega_{1i}^{(w)2}}}{s\displaystyle\sum_{i=1}^{3}P_{Di} + R_L - \left(\displaystyle\sum_{i=1}^{3}\frac{sP_{1i}^{(w)2}}{s^2 + 2\zeta_{1i}^{(w)}\omega_{1i}^{(w)}s + \omega_{1i}^{(w)2}}\right)} . \quad (4.352)$$

The transfer function of electrical current can also be formulated as,

$$\frac{I(s)}{s^2 w_{base}(s)} = \frac{\dfrac{1}{R_{load}}\displaystyle\sum_{i=1}^{3}\frac{sP_{1i}^{(w)}Q_{1i}^{(w)}}{s^2 + 2\zeta_{i}^{(w)}\omega_{i}^{(w)}s + \omega_{i}^{(w)2}}}{s\displaystyle\sum_{i=1}^{3}P_{Di} + R_L - \left(\displaystyle\sum_{i=1}^{3}\frac{sP_{1i}^{(w)2}}{s^2 + 2\zeta_{1i}^{(w)}\omega_{1i}^{(w)}s + \omega_{1i}^{(w)2}}\right)} . \quad (4.353)$$

The single mode electrical power transfer function related to the input transverse acceleration can be obtained as,

$$\frac{P(s)}{s^2 w_{base}(s)} = \left[\frac{\dfrac{1}{\sqrt{R_{load}}} \displaystyle\sum_{i=1}^{3} \dfrac{s P_{1i}^{(w)} Q_{1i}^{(w)}}{s^2 + 2\zeta_{1i}^{(w)}\omega_{1i}^{(w)}s + \omega_{1i}^{(w)2}}}{s\displaystyle\sum_{i=1}^{3} P_{Di} + R_L - \left(\displaystyle\sum_{i=1}^{3} \dfrac{s P_{1i}^{(w)2}}{s^2 + 2\zeta_{1i}^{(w)}\omega_{1i}^{(w)}s + \omega_{1i}^{(w)2}} \right)} \right]^2 . \quad (4.354)$$

The single mode frequency response function (FRF) of electrical voltage can be formulated as,

$$\frac{v(j\omega)}{-\omega^2 w_{base} e^{j\omega t}} = \frac{\displaystyle\sum_{i=1}^{3} \dfrac{j\omega P_{1i}^{(w)} Q_{ri}^{(w)}}{\omega_{1i}^{(w)2} - \omega^2 + j2\zeta_{1i}^{(w)}\omega_{1i}^{(w)}\omega}}{\displaystyle\sum_{i=1}^{3} j\omega P_{Di} + R_L - \left(\displaystyle\sum_{i=1}^{3} \dfrac{s P_{1i}^{(w)2}}{\omega_{1i}^{(w)2} - \omega^2 + j2\zeta_{1i}^{(w)}\omega_{1i}^{(w)}\omega} \right)} . \quad (4.355)$$

The single mode FRF of electrical current related to the input acceleration can be obtained to give,

$$\frac{I(j\omega)}{-\omega^2 w_{base} e^{j\omega t}} = \frac{\dfrac{1}{R_{load}} \displaystyle\sum_{i=1}^{3} \dfrac{j\omega P_{1i}^{(w)} Q_{1i}^{(w)}}{\omega_{1i}^{(w)2} - \omega^2 + j2\zeta_{1i}^{(w)}\omega_{1i}^{(w)}\omega}}{\displaystyle\sum_{i=1}^{3} j\omega P_{Di} + R_L - \left(\displaystyle\sum_{i=1}^{3} \dfrac{s P_{1i}^{(w)2}}{\omega_{1i}^{(w)2} - \omega^2 + j2\zeta_{1i}^{(w)}\omega_{1i}^{(w)}\omega} \right)} . \quad (4.356)$$

The single mode FRF of electrical power can be formulated as,

$$\frac{P(j\omega)}{-\omega^2 w_{base} e^{j\omega t}} = \left[\frac{\dfrac{1}{\sqrt{R_{load}}} \displaystyle\sum_{i=1}^{3} \dfrac{j\omega P_{1i}^{(w)} Q_{1i}^{(w)}}{\omega_{1i}^{(w)2} - \omega^2 + j2\zeta_{1i}^{(w)}\omega_{1i}^{(w)}\omega}}{\displaystyle\sum_{i=1}^{3} j\omega P_{Di} + R_L - \left(\displaystyle\sum_{i=1}^{3} \dfrac{s P_{1i}^{(w)2}}{\omega_{1i}^{(w)2} - \omega^2 + j2\zeta_{1i}^{(w)}\omega_{1i}^{(w)}\omega} \right)} \right]^2 . \quad (4.357)$$

In terms of the multi-mode system reduced from Eqs. (4.352) to (4.357), these equations can be extended into the generalised multi-mode frequency response functions of the broadband piezoelectric bimorph beams to give the electrical voltage. Coefficient r indicates the first mode until the mth mode and coefficient i indicates the first bimorph beam until the nth bimorph, which is formulated as,

$$\frac{v(j\omega)}{-\omega^2 w_{base} e^{j\omega t}} = \frac{\displaystyle\sum_{i=1}^{n}\sum_{r=1}^{m} \dfrac{j\omega P_{ri}^{(w)} Q_{ri}^{(w)}}{\omega_{ri}^{(w)2} - \omega^2 + j2\zeta_{ri}^{(w)}\omega_{ri}^{(w)}\omega}}{\displaystyle\sum_{i=1}^{n} j\omega P_{Di} + R_L - \left(\displaystyle\sum_{i=1}^{n}\sum_{r=1}^{m} \dfrac{s P_{ri}^{(w)2}}{\omega_{ri}^{(w)2} - \omega^2 + j2\zeta_{ri}^{(w)}\omega_{ri}^{(w)}\omega} \right)} . \quad (4.358)$$

The multi-mode FRF of electrical current related to the input transverse acceleration can be obtained as,

$$\frac{I(j\omega)}{-\omega^2 w_{base} e^{j\omega t}} = \frac{\dfrac{1}{R_{load}} \displaystyle\sum_{i=1}^{n}\sum_{r=1}^{m} \dfrac{j\omega P_{ri}^{(w)} Q_{ri}^{(w)}}{\omega_{ri}^{(w)2} - \omega^2 + j2\zeta_{ri}^{(w)}\omega_{ri}^{(w)}\omega}}{\displaystyle\sum_{i=1}^{n} j\omega P_{Di} + R_L - \left(\displaystyle\sum_{i=1}^{n}\sum_{r=1}^{m} \dfrac{sP_{ri}^{(w)2}}{\omega_{ri}^{(w)2} - \omega^2 + j2\zeta_{ri}^{(w)}\omega_{ri}^{(w)}\omega} \right)} . \quad (4.359)$$

The multi-mode FRF of electrical power can also be formulated to give,

$$\frac{P(j\omega)}{-\omega^2 w_{base} e^{j\omega t}} = \left[\frac{\dfrac{1}{\sqrt{R_{load}}} \displaystyle\sum_{i=1}^{n}\sum_{r=1}^{m} \dfrac{j\omega P_{ri}^{(w)} Q_{ri}^{(w)}}{\omega_{ri}^{(w)2} - \omega^2 + j2\zeta_{ri}^{(w)}\omega_{ri}^{(w)}\omega}}{\displaystyle\sum_{i=1}^{n} j\omega P_{Di} + R_L - \left(\displaystyle\sum_{i=1}^{n}\sum_{r=1}^{m} \dfrac{sP_{ri}^{(w)2}}{\omega_{ri}^{(w)2} - \omega^2 + j2\zeta_{ri}^{(w)}\omega_{ri}^{(w)}\omega} \right)} \right]^2 . \quad (4.360)$$

4.8.2. The solution form of series connection

In this section, the multi-electromechanical piezoelectric bimorph beam under series connection is discussed. Three piezoelectric bimorph beams under input transverse acceleration can be used to model the single mode frequency analysis of electrical voltage, current and power. Corresponding to Eq. (4.348), the first generalised electromechanical dynamic equation for the single mode can be formulated from Eq. (4.345) to give,

$$\ddot{w}_{11}(t) + 2\zeta_{11}^{(w)}\omega_{11}^{(w)}\dot{w}_{11}(t) + \omega_{11}^{(w)2}w_{11}(t) + P_{11}^{(w)}v_1(t) = -Q_{11}^{(w)}\ddot{w}_{base}(t)$$

$$\ddot{w}_{12}(t) + 2\zeta_{12}^{(w)}\omega_{12}^{(w)}\dot{w}_{12}(t) + \omega_{12}^{(w)2}w_{12}(t) + P_{12}^{(w)}v_2(t) = -Q_{12}^{(w)}\ddot{w}_{base}(t) \quad . (4.361)$$

$$\ddot{w}_{13}(t) + 2\zeta_{13}^{(w)}\omega_{13}^{(w)}\dot{w}_{13}(t) + \omega_{13}^{(w)2}w_{13}(t) + P_{13}^{(w)}v_3(t) = -Q_{13}^{(w)}\ddot{w}_{base}(t)$$

The second generalised electromechanical dynamic equations for the single mode can also be formulated in terms of Eq. (4.346) to give,

$$\hat{P}_{11}^{(w)}\dot{w}_{11}(t) + P_{D1}\dot{v}_1(t) = \dot{q}(t)$$

$$\hat{P}_{12}^{(w)}\dot{w}_{12}(t) + P_{D2}\dot{v}_2(t) = \dot{q}(t)$$

$$\hat{P}_{13}^{(w)}\dot{w}_{13}(t) + P_{D3}\dot{v}_3(t) = \dot{q}(t) \qquad (4.362)$$

Corresponding to Eq. (4.349), equations (4.361) and (4.362) can be further manipulated in terms of Laplace transforms to give the matrix electromechanical dynamic equations. The multi-output electrical voltage related to the input transverse acceleration can be stated into the transfer function based on a linear superposition of equations as,

$$\frac{V(s)}{s^2 w_{base}(s)} = \frac{\displaystyle\sum_{i=1}^{3} \frac{\dfrac{P_{1i}^{(w)}}{P_{Di}} Q_{1i}^{(w)}}{s^2 + 2\zeta_{1i}^{(w)}\omega_{1i}^{(w)}s + \omega_{1i}^{(w)2} - \dfrac{P_{1i}^{(w)2}}{P_{Di}}}}{\displaystyle\sum_{i=1}^{3}\frac{R_L}{sP_{Di}} + 1 + R_L\left(\displaystyle\sum_{i=1}^{3}\frac{\dfrac{P_{1i}^{(w)2}}{sP_{Di}^2}}{s^2 + 2\zeta_{1i}^{(w)}\omega_{1i}^{(w)}s + \omega_{1i}^{(w)2} - \dfrac{P_{1i}^{(w)2}}{P_{Di}}}\right)} . \qquad (4.363)$$

The single mode transfer function of electrical current can be formulated as,

$$\frac{I(s)}{s^2 w_{base}(s)} = \frac{\dfrac{1}{R_{load}}\displaystyle\sum_{i=1}^{3} \frac{\dfrac{P_{1i}^{(w)}}{P_{Di}} Q_{1i}^{(w)}}{s^2 + 2\zeta_{1i}^{(w)}\omega_{1i}^{(w)}s + \omega_{1i}^{(w)2} - \dfrac{P_{1i}^{(w)2}}{P_{Di}}}}{\displaystyle\sum_{i=1}^{3}\frac{R_L}{sP_{Di}} + 1 + R_L\left(\displaystyle\sum_{i=1}^{3}\frac{\dfrac{P_{1i}^{(w)2}}{sP_{Di}^2}}{s^2 + 2\zeta_{1i}^{(w)}\omega_{1i}^{(w)}s + \omega_{1i}^{(w)2} - \dfrac{P_{1i}^{(w)2}}{P_{Di}}}\right)} . \qquad (4.364)$$

The single mode electrical power transfer function can be formulated as,

$$\frac{P(s)}{s^2 w_{base}(s)} = \left[\frac{\dfrac{1}{\sqrt{R_{load}}}\displaystyle\sum_{i=1}^{3} \frac{\dfrac{P_{1i}^{(w)}}{P_{Di}} Q_{1i}^{(w)}}{s^2 + 2\zeta_{1i}^{(w)}\omega_{1i}^{(w)}s + \omega_{1i}^{(w)2} - \dfrac{P_{1i}^{(w)2}}{P_{Di}}}}{\displaystyle\sum_{i=1}^{3}\frac{R_L}{sP_{Di}} + 1 + R_L\left(\displaystyle\sum_{i=1}^{3}\frac{\dfrac{P_{1i}^{(w)2}}{sP_{Di}^2}}{s^2 + 2\zeta_{1i}^{(w)}\omega_{1i}^{(w)}s + \omega_{1i}^{(w)2} - \dfrac{P_{1i}^{(w)2}}{P_{Di}}}\right)}\right]^2 . \qquad (4.365)$$

The single mode frequency response function (FRF) of electrical voltage can be further formulated as,

$$\frac{v(t)}{-\omega^2 w_{base} e^{j\omega t}} = \frac{\displaystyle\sum_{i=1}^{3} \frac{\dfrac{P_{1i}^{(w)}}{P_{Di}} Q_{1i}^{(w)}}{\omega_{1i}^{(w)2} - \omega^2 + j\,2\zeta_{1i}^{(w)}\omega_{1i}^{(w)}\omega - \dfrac{P_{1i}^{(w)2}}{P_{Di}}}}{\displaystyle\sum_{i=1}^{3}\frac{R_L}{j\omega P_{Di}} + 1 + R_L\left(\displaystyle\sum_{i=1}^{3}\frac{\dfrac{P_{1i}^{(w)2}}{sP_{Di}^2}}{\omega_{1i}^{(w)2} - \omega^2 + j\,2\zeta_{1i}^{(w)}\omega_{1i}^{(w)}\omega - \dfrac{P_{1i}^{(w)2}}{P_{Di}}}\right)} . \qquad (4.366)$$

The single mode FRF of electrical current related to the input transverse acceleration can be obtained as,

$$\frac{I(t)}{-\omega^2 w_{base} e^{j\omega t}} = \frac{\dfrac{1}{R_{load}} \displaystyle\sum_{i=1}^{3} \dfrac{\dfrac{P_{1i}^{(w)}}{P_{Di}} Q_{1i}^{(w)}}{\omega_{1i}^{(w)2} - \omega^2 + j2\zeta_{1i}^{(w)}\omega_{1i}^{(w)}\omega - \dfrac{P_{1i}^{(w)2}}{P_{Di}}}}{\displaystyle\sum_{i=1}^{3} \dfrac{R_L}{j\omega P_{Di}} + 1 + R_L \left(\displaystyle\sum_{i=1}^{3} \dfrac{\dfrac{P_{1i}^{(w)2}}{sP_{Di}^{2}}}{\omega_{1i}^{(w)2} - \omega^2 + j2\zeta_{1i}^{(w)}\omega_{1i}^{(w)}\omega - \dfrac{P_{1i}^{(w)2}}{P_{Di}}} \right)} . \qquad (4.367)$$

The single mode FRF of electrical power can also be reduced as,

$$\frac{P(t)}{-\omega^2 w_{base} e^{j\omega t}} = \left[\frac{\dfrac{1}{\sqrt{R_{load}}} \displaystyle\sum_{i=1}^{3} \dfrac{\dfrac{P_{1i}^{(w)}}{P_{Di}} Q_{1i}^{(w)}}{\omega_{1i}^{(w)2} - \omega^2 + j2\zeta_{1i}^{(w)}\omega_{1i}^{(w)}\omega - \dfrac{P_{1i}^{(w)2}}{P_{Di}}}}{\displaystyle\sum_{i=1}^{3} \dfrac{R_L}{j\omega P_{Di}} + 1 + R_L \left(\displaystyle\sum_{i=1}^{3} \dfrac{\dfrac{P_{1i}^{(w)2}}{sP_{Di}^{2}}}{\omega_{1i}^{(w)2} - \omega^2 + j2\zeta_{1i}^{(w)}\omega_{1i}^{(w)}\omega - \dfrac{P_{1i}^{(w)2}}{P_{Di}}} \right)} \right]^2 . \qquad (4.368)$$

The previous equations represent the three electromechanical piezoelectric bimorph beams in terms of the single mode TFs and FRFs. In the next case, the broadband piezoelectric bimorph beams can be further formulated to give the generalised multi-mode FRFs of each beam. The multi-mode FRFs can also be found by further manipulating Eqs. (4.345) and (4.346) in terms of Eqs. (4.366), (4.367) and (4.368). The multi-mode FRF of the broadband electrical voltage can be formulated to give,

$$\frac{v(j\omega)}{-\omega^2 w_{base} e^{j\omega t}} = \frac{\displaystyle\sum_{i=1}^{n}\sum_{r=1}^{m} \dfrac{\dfrac{P_{ri}^{(w)}}{P_{Di}} Q_{ri}^{(w)}}{\omega_{ri}^{(w)2} - \omega^2 + j2\zeta_{ri}^{(w)}\omega_{ri}^{(w)}\omega - \dfrac{P_{ri}^{(w)2}}{P_{Di}}}}{\displaystyle\sum_{i=1}^{n} \dfrac{R_L}{j\omega P_{Di}} + 1 + R_L \left(\displaystyle\sum_{i=1}^{n}\sum_{r=1}^{m} \dfrac{\dfrac{P_{ri}^{(w)2}}{j\omega P_{Di}^{2}}}{\omega_{ri}^{(w)2} - \omega^2 + j2\zeta_{ri}^{(w)}\omega_{ri}^{(w)}\omega - \dfrac{P_{ri}^{(w)2}}{P_{Di}}} \right)} , \qquad (4.369)$$

where coefficient r indicates the first mode until the mth mode and coefficient i indicates the first bimorph beam until the nth bimorph. The multi-mode FRF of the broadband electrical current related to the input transverse acceleration can be formulated as,

$$\frac{I(j\omega)}{-\omega^2 w_{base}e^{j\omega t}} = \frac{\dfrac{1}{R_{load}}\displaystyle\sum_{i=1}^{n}\sum_{r=1}^{m}\dfrac{\dfrac{P_{ri}^{(w)}}{P_{Di}}Q_{ri}^{(w)}}{\omega_{ri}^{(w)2}-\omega^2+j2\zeta_{ri}^{(w)}\omega_{ri}^{(w)}\omega-\dfrac{P_{ri}^{(w)2}}{P_{Di}}}}{\displaystyle\sum_{i=1}^{n}\dfrac{R_L}{j\omega P_{Di}}+1+R_L\left(\displaystyle\sum_{i=1}^{n}\sum_{r=1}^{m}\dfrac{\dfrac{P_{ri}^{(w)2}}{j\omega P_{Di}^{2}}}{\omega_{ri}^{(w)2}-\omega^2+j2\zeta_{ri}^{(w)}\omega_{ri}^{(w)}\omega-\dfrac{P_{ri}^{(w)2}}{P_{Di}}}\right)} . \quad (4.370)$$

The multi-mode FRF of the broadband electrical power relating to the input transverse acceleration can be formulated as,

$$\frac{P(j\omega)}{-\omega^2 w_{base}e^{j\omega t}} = \left[\frac{\dfrac{1}{\sqrt{R_{load}}}\displaystyle\sum_{i=1}^{n}\sum_{r=1}^{m}\dfrac{\dfrac{P_{ri}^{(w)}}{P_{Di}}Q_{ri}^{(w)}}{\omega_{ri}^{(w)2}-\omega^2+j2\zeta_{ri}^{(w)}\omega_{ri}^{(w)}\omega-\dfrac{P_{ri}^{(w)2}}{P_{Di}}}}{\displaystyle\sum_{i=1}^{n}\dfrac{R_L}{j\omega P_{Di}}+1+R_L\left(\displaystyle\sum_{i=1}^{n}\sum_{r=1}^{m}\dfrac{\dfrac{P_{ri}^{(w)2}}{j\omega P_{Di}^{2}}}{\omega_{ri}^{(w)2}-\omega^2+j2\zeta_{ri}^{(w)}\omega_{ri}^{(w)}\omega-\dfrac{P_{ri}^{(w)2}}{P_{Di}}}\right)}\right]^2 . \quad (4.371)$$

4.9. Closing Remark

This chapter has considered novel analytical methods of modelling the electromechanical dynamic equations for one and two input base excitations of the piezoelectric bimorph beam with tip mass using the Rayleigh and Euler-Bernoulli's beam assumptions. As mentioned previously, the Rayleigh piezoelectric bimorph beam only considers the second mass moment of inertia (rotary) of the bimorph where this can also be reduced to the Euler-Bernoulli's piezoelectric bimorph beam by ignoring the rotary inertia of bimorph beam. Therefore, the electromechanical piezoelectric bimorph beam was formulated according to the Rayleigh beam assumption. Moreover, this chapter also discussed the strong form of electromechanical dynamic equations using Hamiltonian's principle under series and parallel connections. The weak form reduced from the strong form method represents the analytical approach developed using the Ritz method whereas the closed form boundary value method reduced from the strong form method can be further formulated using the direct analytical solution with orthonormalisation by

introducing the space- and time-dependent eigenfunction series into boundary conditions. Moreover, the electromechanical closed-form method can give accurate results because of its convergence for the chosen frequency response mode of interest. In comparison with the electromechanical weak form solution based on the Ritz analytical approach method, the typical mode shapes or space-independent eigenfunction forms and number of modes must be chosen correctly in order to meet convergence criteria and give results similar to the closed-form method. For example, some FRFs results from the analytical weak form of piezoelectric bimorph with tip mass as discussed at Chapter 6 plotted the first mode but were iterated using three modes of interest to give accurate results. In this case, the weak form was chosen, having the same typical space-independent eigenfunctions (appendices A and B) as for the closed-form to reduce computation time and number of iterations to meet the speedy convergence criteria. The effect of strain field due to transverse bending and longitudinal extension affects not only the mechanical moment and force of the interlayer (all layers of bimorph) but also the electrical moment and force of the piezoelectric layers (top and bottom layers of bimorph). Concerning the electrical moment and force, the backward and forward piezoelectric couplings due to the transverse and longitudinal forms can also be formulated, where these give the electromechanical coupling of the piezoelectric layers. Furthermore, the weak form of the electromechanical dynamic equations were formulated using the orthonormality conditions to obtain the coupled electromechanical dynamic response of transverse form (CEDRT), coupled electromechanical dynamic response of longitudinal form (CEDRL) and the coupled electromechanical dynamic response of transverse-longitudinal form (CEDRTL) to give the multi-mode transfer functions (TRs) and frequency response functions (FRFs). The closed form of the electromechanical dynamic equations in terms of orthonormality conditions is also formulated according to the CEDRTL. The broadband piezoelectric bimorph beam based on the CEDRT was also formulated to give the single- and multi-mode frequency analysis of the bimorph beams. At the same time, the multi-frequency broadband piezoelectric bimorph beam equations were also provided. In the next section, the parametric case study based on the electromechanical dynamic equation of the Euler-Bernoulli piezoelectric bimorph beam with the tip mass will be discussed.

CHAPTER
5

Parametric Case Study of the Electromechanical Piezoelectric Bimorph Beams

This chapter investigates parametric behaviour of the electromechanical piezoelectric bimorph beam with input base acceleration and variable load resistance, thickness and length. The electromechanical frequency responses of the bimorph utilized for the study include the tip displacement, tip velocity, electrical voltage and power. The normalised weak and closed forms of electromechanical dynamic response of the transverse-longitudinal equations (CEDRTL), which were derived in chapter 4, were applied in this chapter to analyse the series and parallel connections of the piezoelectric bimorph beam. The broadband multi-electromechanical piezoelectric bimorph beam using the weak form of CEDRT was also modelled to represent the optimised multi-frequency electrical voltage, current and power.

5.1. The Piezoelectric Bimorph Properties

The choice of material properties and geometrical structure were found to be essential aspects for optimising the response of the cantilevered piezoelectric bimorph beam. The list of properties of the bimorph can be found in Table 5.1 where the piezoelectric property was based on the PZT PSI-5A4E element with the centre brass shim from Piezo Systems, INC. The effect of rotary inertia of the bimorph was ignored because the Euler-Bernoulli beam model was considered in this chapter. A tip mass and its rotary inertia located on the tip of the bimorph were also considered in terms of its geometry and material properties. The geometry of the tip mass was very small as given in Figure 5.1. The zero-th mass moment of inertia and the second mass moment of inertia (rotary inertia) at the centre of tip end of bimorph can be formulated as,

$$I_{tip}^{(A)} = 2l_o h_a b_s \rho_{tip} \quad , \quad I_{tip}^{(C)} = 2l_o h_a b_s \rho_{tip} \left[\frac{\left(l_o^{\,2} + h_a^{\,2}\right)}{12} + \left(\frac{\left(h_a + h_s\right)}{2} + h_p \right)^2 \right] . \qquad 5.1$$

Table 5.1 Characteristic properties of the piezoelectric bimorph system.

Material properties	Piezoelectric	Brass	Geometry properties	Piezoelectric	Brass
Young's modulus , $\overline{Q}_{11}$ (GPa)	66	105	Length , L (mm)	30.1	30.1
Density, ρ (kg/m^3)	7800	9000	Thickness, h (mm)	0.15 (each)	0.13
Piezoelectric constant, d_{31} (pm/V)	-190	-	Width, b (mm)	6.4	6.4
Permittivity, ς_{33}^T (F/m)	$1800\,\varsigma_o$	-	First coefficient $I_{tip}^{(A)}$ (kg)[†]	7.9872×10^{-4}	
permittivity of free space, ς_o (pF/m)	8.854	-	Third coefficient $I_{tip}^{(C)}$ (kg m^2)[†]	2.5103×10^{-9}	

[†] Calculated according to the geometry and material properties of tip mass and the rotary inertia at centre of gravity of tip mass

coincident with the end of bimorph length as shown in Figure 5.1 where $l_o = 4$mm, $h_a = 2$mm and $b_a = 6.4$mm (width).

First and third coefficients refer to zeroth and second mass moment of inertias respectively.
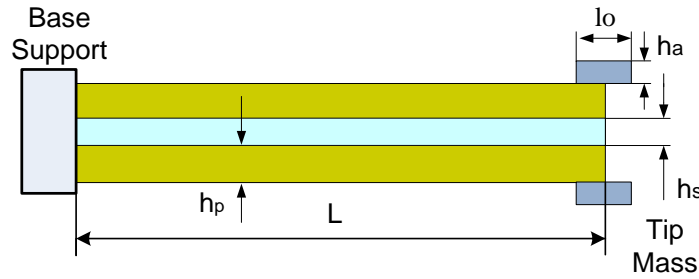
Figure 5.1. Geometry of the Bimorph and Tip Mass

It should be noted that variables h_p and h_s indicate the thickness of the layers of the piezoelectric bimorph and substructure (brass shim in the middle layer).

5.2. Electromechanical Dynamic Response of Piezoelectric Bimorph under Parallel Connection

In this section, the piezoelectric bimorph with a tip mass will be discussed using the multi-mode FRFs and variable geometry and load resistance. In the next section, the mechanical damping ratios and load resistances need to be determined. The analysis of the piezoelectric bimorph beams under parallel and series connections were based on the coupled electrical dynamic responses from the transverse bending and longitudinal forms with polarity-induced electrical fields and internal capacitance. The transverse base acceleration input was used to excite the bimorph providing multi-output electrical dynamic responses. It should be noted that all results in the forthcoming sections were plotted according to the suggested formulations given previously.

5.2.1. The Bimorph Multi-mode FRFs of Tip Absolute Dynamic Displacement

The trend of multi-mode FRFs of tip absolute dynamic displacement based on variable load resistance was simulated from 0 to 3000 Hz. In this case, the first three modes were shown with chosen resistor values of 500 Ω, 4 kΩ, 20 kΩ, 40 kΩ, 90 kΩ, 400 kΩ, 3 MΩ. The results of resonance frequencies and amplitudes were only calculated using these load resistor values. All results depended on the properties of the bimorph, boundary geometry, input base acceleration, tip mass and the type of circuit connection. It should be noted that the base input transverse acceleration onto the cantilevered piezoelectric beam can be considered as a moving static support base to create the dynamic load base due to the product of acceleration and generalized mass of the bimorph and tip mass. This implies that the effect of the base dynamic motion creates the relative displacement field with respect to the absolute dynamic displacement along the piezoelectric beam. In this section, the absolute tip dynamic displacement, which was considered as the total tip dynamic displacement was applied to plot the first three FRFs. It should be noted that the power harvesting results reported here represent meter per unit square of the input base transverse acceleration. The input base transverse acceleration on the bimorph was chosen as 9.81 m/s^2 which is equivalent to 1 g (1 g = gravitational acceleration 9.81 m/s^2). The multi-mode FRFs of tip relative dynamic displacement can be reformulated according to Eq. (4.213) in chapter 4 as,

$$H_{22}(x, j\omega) = \left. \frac{w_r(x, j\omega)}{\ddot{w}_{base}} \right|_{s=j\omega}$$

$$= -\sum_{r=1}^{3} \left[\frac{\hat{\Psi}_r(x)}{\omega_r^{(w)^2} - \omega^2 + j2\zeta_r^{(w)}\omega_r^{(w)}\omega} \left(\frac{(j\omega P_D + R_L)Q_r^{(w)} - \sum_{r=1}^{3} \dfrac{j\omega P_r^{(u)^2}Q_r^{(w)}}{\omega_r^{(u)^2} - \omega^2 + j2\zeta_r^{(u)}\omega_r^{(u)}\omega}}{j\omega P_D + R_L - \sum_{r=1}^{3} \dfrac{j\omega P_r^{(w)^2}}{\omega_r^{(w)^2} - \omega^2 + j2\zeta_r^{(w)}\omega_r^{(w)}\omega} - \sum_{r=1}^{3} \dfrac{j\omega P_r^{(u)^2}}{\omega_r^{(u)^2} - \omega^2 + j2\zeta_r^{(u)}\omega_r^{(u)}\omega}} \right) \right] \quad .(5.2)$$

The absolute dynamic displacement can then be reformulated as

$$\hat{H}_{22}^{(disp)}(x, j\omega) = -\frac{1}{\omega^2} + H_{22}(x, j\omega) \qquad . \tag{5.3}$$

It is noted that equation (5.3), reduced from the weak form of CERDTL, represents the sample formulation of the multi-mode FRFs which can be used to analyse any position (x) and frequency $(j\omega)$ along the piezoelectric beam. In this case, the tip absolute dynamic displacement can be modeled by substituting x with L. The closed

form of CERDTL was not shown here but was given in chapter 4. It is important to notice that the mechanical damping ratios need to be determined theoretically. It is convenient to determine the first two damping ratios based on the two specified frequencies around the first two modes and then determine the Rayleigh damping factors mathematically. The Rayleigh damping factors can be formulated, Clough and Penzien [101] as,

$$\begin{Bmatrix} a_1^n \\ a_2^n \end{Bmatrix} = \frac{2\omega_1\omega_2}{\omega_2^2 - \omega_1^2} \begin{bmatrix} \omega_2 & -\omega_1 \\ -1/\omega_2 & 1/\omega_1 \end{bmatrix} \begin{Bmatrix} \zeta_1^n \\ \zeta_2^n \end{Bmatrix} \quad , \quad n \in \{w,u\} \ . \tag{5.4}$$

Once equation (5.4) results were calculated, the mechanical damping ratio for higher modes can be stated as,

$$\zeta_r^n = \frac{a_1^n}{2\omega_r} + \frac{a_2^n \omega_r}{2} \ . \tag{5.5}$$

It should be noted that equations (5.2) and (5.3) require the FRFs of the coupled transverse and longitudinal response forms. This indicates that two initial mechanical damping ratios for transverse form need to be determined around two fundamental frequencies based on the transverse bending. In similar way, two initial mechanical damping ratios for longitudinal form can also be chosen around two fundamental frequencies. At this stage, two initial mechanical damping ratios for transverse form $\zeta_1^w = 0.0098$ and $\zeta_2^w = 0.011$ together with the first two modes of $\omega_1^w = 94.47\,\text{Hz}$ and $\omega_2^w = 967.56\,\text{Hz}$ can be substituted into Eq. (5.4) to give Rayleigh damping factors of $a_1^w = 1.6646$ $1/s$ and $a_2^w = 2.0959 \times 10^{-5}$ s, respectively. The third damping ratio for the third mode can be obtained automatically after substituting the damping factors into Eq. (5.4) to give $\zeta_3^w = 0.026$. In a similar way, the two initial damping ratios due to the longitudinal form can be specified as $\zeta_1^u = 0.02$ and $\zeta_2^u = 0.021$, resulting in the third damping ratio obtained from Eq. (5.5), $\zeta_3^u = 0.0213$. It should be noted that the damping ratios due to longitudinal form only gave small effect to modes around the fundamental bending modes. However, this effect cannot be ignored when analysing the experimental study. In this case, although only the input base transverse motion was applied to the cantilevered piezoelectric beam, the effect of electric-strain fields due to transverse bending and longitudinal forms and piezoelectric couplings still affected the bimorph. In such situation, equation (5.2) as derived in detail in chapter 4 can be applied to this chapter. Moreover, it is important

to notice here that the damping ratios were chosen according to the short circuit of the frequency modes by setting the load resistance around 500 Ω. It is convenient to investigate the mechanical damping ratios under frequency response with very low electrical voltage due to the low load resistance connected to the piezoelectric. This means that the piezoelectric bimorph tended to show a pure mechanical form where the mechanical damping ratios were determined. Once the mechanical damping ratios were determined, the multi-mode FRFs with varying load resistances can be modelled. Although, the mechanical damping ratios can be determined mathematically from Eq. (5.5) in terms of Eq. (5.4), these may not fit accurately when comparing the FRFs with the experimental study. In such a situation, it was more important to specify the mechanical damping ratios based on the experimental study.

As can be seen from Figure 5.2a, the FRF showing the first three modes of tip absolute dynamic displacement under varying load resistances was given as a result of the comparison between the weak and closed forms of CERDTL. The results of dynamic displacement amplitudes along the frequency domain seem to shift due to varying load resistances as shown in the enlarged view of the first mode in Figure 5.2b. The highest displacements referred to the short and open circuits of resonance frequencies at the first mode where the frequency of 94.47 Hz with the short circuit load resistance of 500 Ω shifted to the frequency of 98.60 Hz with the open circuit load resistance of 3 MΩ to yield the displacement magnitudes of 1.46 mm and 1.35 mm, respectively. The tip absolute transverse displacement at the free end of the cantilevered piezoelectric bimorph beam with the load resistances of 20 kΩ and 90 kΩ indicated amplitudes of 0.552 mm at the resonance of 92.25 Hz and 0.550 mm at the resonance of 97.88 Hz, respectively. Moreover, the second mode FRF seemed to give different trend compared with the first mode where the load resistances of 20 kΩ, 40 kΩ, 90 kΩ, 400 kΩ and 3 MΩ were located at the same resonance frequency of 978.5 Hz as shown in Figure 5.2c. The open circuit resonance frequency still showed the highest displacement amplitude compared with other load resistances. Moreover, the anti-resonances slightly shifted from between 2700 Hz and 2900 Hz after the third mode was formed. It should be noted that the higher resonances such as the third mode and so on tended to give very low displacement amplitude.

Another important aspect mentioned previously was that the chosen mechanical damping ratios also affected the resonance amplitude response.
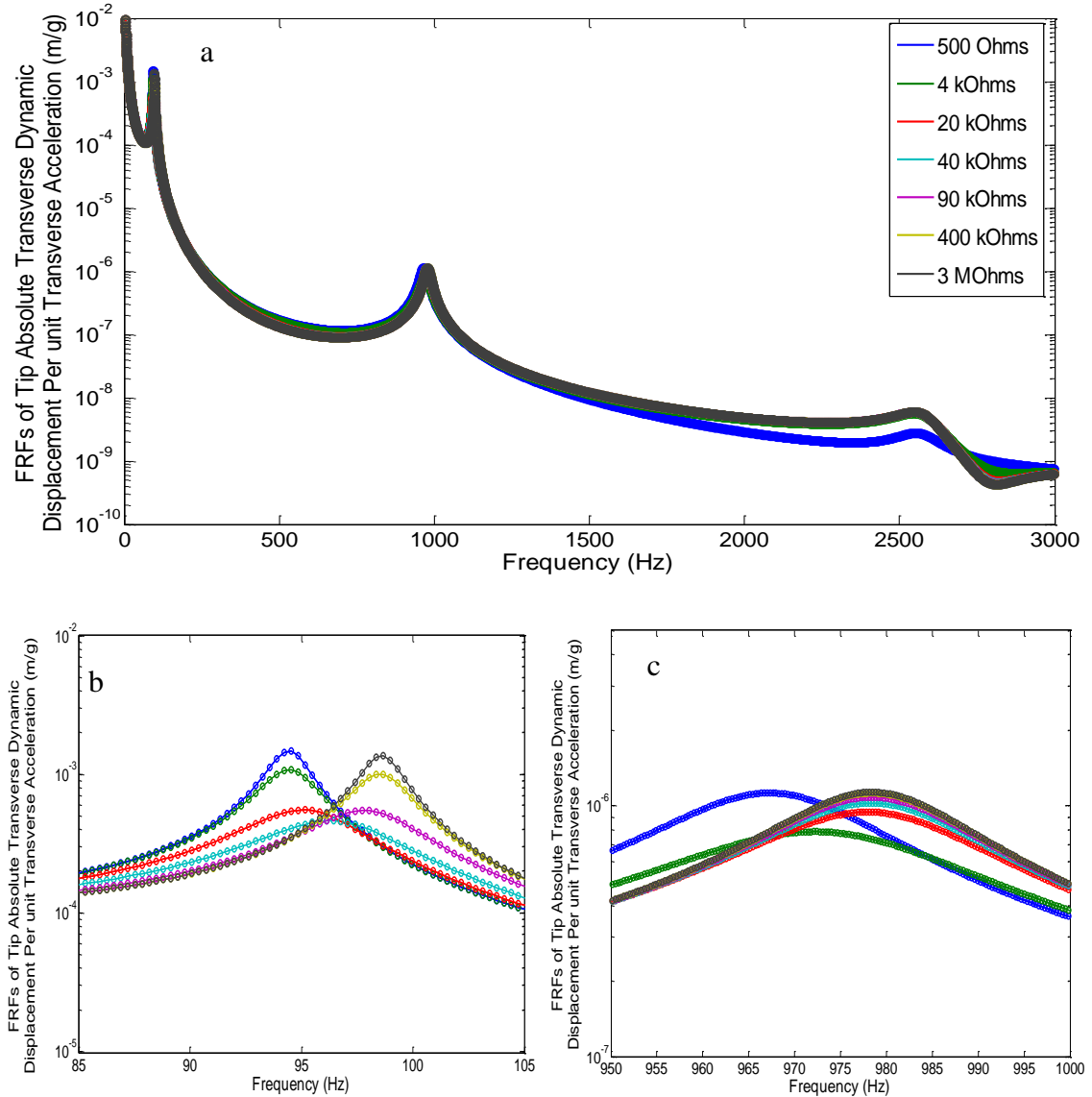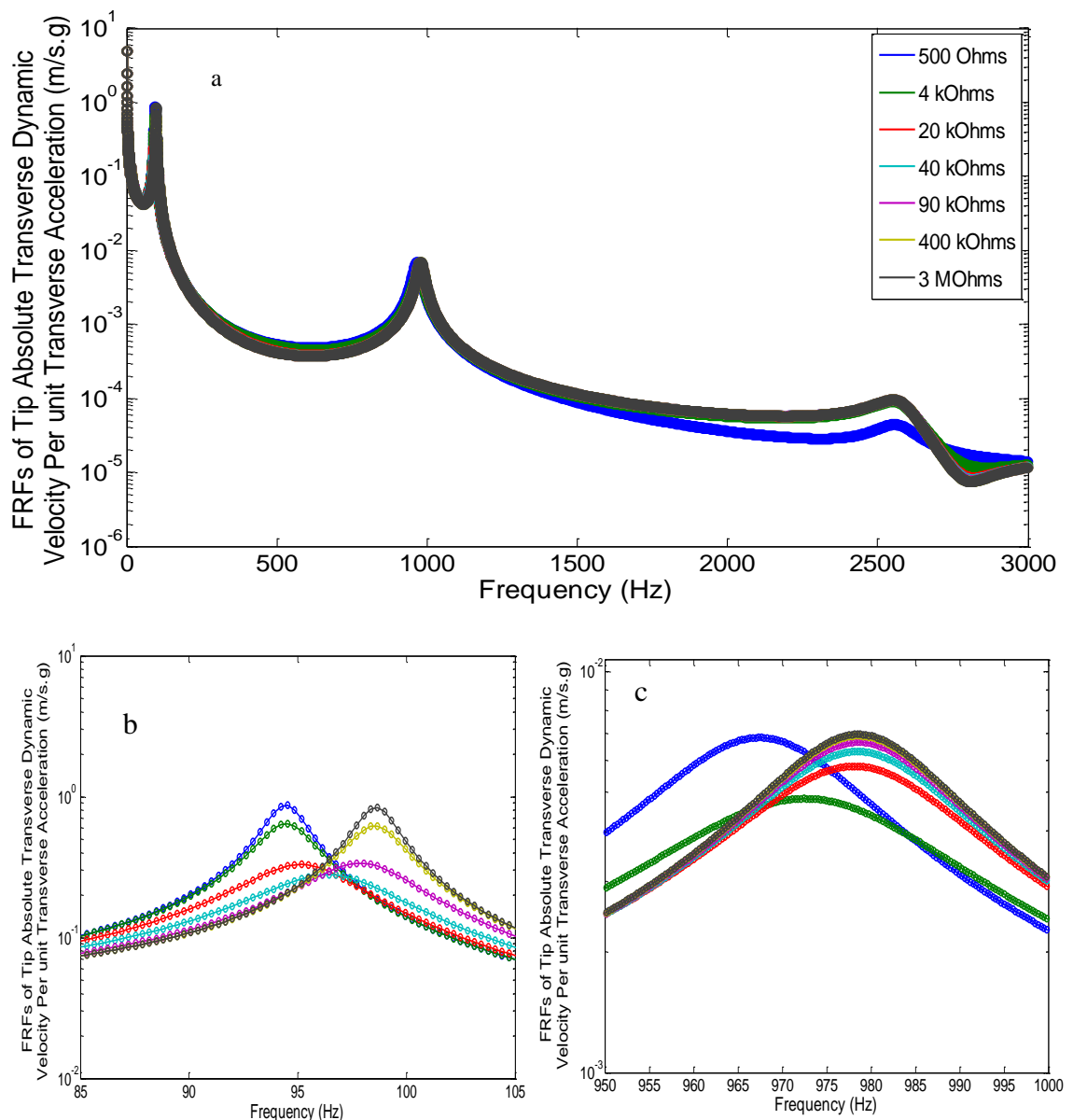

Figure 5.2. FRFs of tip absolute Dynamic Displacement with the Weak form (Solid line) and Closed form (Round dot) : a) The First three modes, b) First mode and c) Second Mode

5.2.2. The Bimorph Multi-mode FRFs of Tip Absolute Velocity

In this section, the first three FRFs of tip absolute velocity of the cantilevered piezoelectric bimorph were investigated under varying load resistances. As considered here, the tip absolute velocity was modelled due to the transverse velocity of the base support and relative velocity of the bimorph as formulated from Eq. (4.227) in chapter 4,

$$\hat{H}_{22}^{(vel)}(x, j\omega) = \frac{1}{j\omega} + j\omega H_{22}(x, j\omega) \,. \qquad (5.6)$$

The relative velocity of the bimorph varied from the base to tip. The relative velocity at the base was zero because the base support was the input excitation point for the bimorph, as shown in chapter 4. This indicates that the absolute velocity at the base support was equal with the input transverse base velocity. It should be noted that equation (5.6) needs to be multiplied with 9.81 m/s^2 as it indicates the input base acceleration onto the bimorph and substitute x with L and frequency from 0-3000 Hz to model the tip absolute velocity.

As can be seen in Figure 5.3a, the trend of the first three FRFs of tip velocity of the bimorph under varying load resistances tended to show consistency with each other where the first resonance frequency gave very high amplitude followed by the lower amplitude response of the second and third resonances. Figure 5.3a also showed the good agreement between the weak and closed forms of CERDTL. It is important to note here that the amplitude of the FRFs were affected not only due to the input transverse base acceleration and damping ratio but also due to the applied load resistances of the piezoelectric bimorph. The effect of load resistances on the electromechanical dynamic equations was viewed as resistive shunt damping behaviour. At this stage, the trend of the first mode can be seen on the enlarged view in Figure 5.3b where the frequency shift also occurred between the short and open circuits. The resonance frequencies of 94.47 Hz for short circuit and 98.60 Hz for open circuit around first mode gave high velocity amplitudes of 0.87 m/s.g and 0.84 m/s.g, respectively. Moreover, the absolute tip velocity with the load resistances of 20 kΩ and 90 kΩ indicated amplitudes of 0.33 m/s.g at the resonances of 92.25 Hz and 0.34 m/s.g at the resonance of 97.88 Hz, respectively as shown in the enlarged view of Figure 5.3a. The second mode results as given in Figure 5.3c appeared to give constant resonance frequency with different amplitudes at the load resistances of 20 kΩ, 40 kΩ, 90 kΩ, 400 kΩ and 3 MΩ. The only resonance shift occurred at the lower load resistances of 500 Ω and 4 kΩ. The FRFs of tip absolute velocity at the third mode tended to overlap each other with the predominant load resistances. The velocity response trends were observed to be similar in form with the results obtained from the tip absolute dynamic displacement. This was worthwhile to clarify as it is known that the velocity response obtained in Eq. (5.6) was simply obtained from the

first derivative of the FRF displacement field. However, when analyzing the dynamic time dependent displacement and velocity, the trend of velocity is 90° out of phase with respect to displacement. However this still implies the same natural frequency where this situation can be proved as,

$$\dot{w}_{abs}(x,t) = j\omega\{w_{abs}(x,t)\} \qquad , \qquad (5.7)$$

where

$$w_{abs}(x,t) = W_b \exp(j\omega t) + H_{21}(x, j\omega)\left(-\omega^2 U_b \exp(j\omega t)\right) + H_{22}(x, j\omega)\left(-\omega^2 W_b \exp(j\omega t)\right) \quad . (5.8)$$

Figure 5.3 FRFs of tip absolute Dynamic Velocity with the Weak form (Solid line) and Closed form (Round dot) : a) The First three modes , b) First mode and c) Second Mode

5.2.3. The Bimorph Multi-mode FRFs of Electrical Voltage

The first three mode FRFs of electrical voltage can be reformulated according with Eq. (4.215) in chapter 4 as,

$$
\frac{V(j\omega)}{\ddot{w}_{base}}\Bigg|_{\ddot{u}_{base}=0} = \frac{\displaystyle\sum_{r=1}^{3}\frac{j\omega P_r^{(w)}Q_r^{(w)}}{\omega_r^{(w)2}-\omega^2+j2\zeta_r^{(w)}\omega_r^{(w)}\omega}}{j\omega P_D + R_L - \displaystyle\sum_{r=1}^{3}\frac{j\omega P_r^{(w)2}}{\omega_r^{(w)2}-\omega^2+j2\zeta_r^{(w)}\omega_r^{(w)}\omega} - \displaystyle\sum_{r=1}^{3}\frac{j\omega P_r^{(u)2}}{\omega_r^{(u)2}-\omega^2+j2\zeta_r^{(u)}\omega_r^{(u)}\omega}} \quad . \text{(5.9)}
$$

As can be seen from Figure 5.4a, the first three mode FRFs of electrical voltage of the bimorph can be analysed with varying resistances as per the previous section. It is noted that when the resonance frequency approached the short circuit value, the load resistance approached zero $R_{load}\to 0$. Meanwhile, when the resonance frequency approached the open circuit value, the load resistance approached infinity $R_{load}\to\infty$. At this point, it was noted that the fundamental frequency of the first mode varied with the resistance values where the short circuit resistance gave the lowest resonance frequency and open circuit resistance gave the highest resonance frequency. With varying load resistance, the electrical voltage amplitude also varied as shown in Figures 5.4b. The FRFs under varying resistance tend to show an different pattern compared with previous trends from the FRFs of the tip displacement and velocity. Another important aspect can also be seen from Figure 5.4b where the electrical voltage increased with increasing load resistances around the first mode. Again, the FRFs of electrical voltage at the second mode as shown from Figure 5.4c tended to give the same resonance with different amplitudes for the majority of load resistances between 20 kΩ, 40 kΩ, 90 kΩ, 400 kΩ and 3 MΩ. Again, the trend of multi-mode FRFs under the weak and closed forms of CEDRTL indicated very good agreement. The third mode of electrical voltage also showed similar behaviour but the amplitudes under the majority of load resistances seemed to overlap each other.
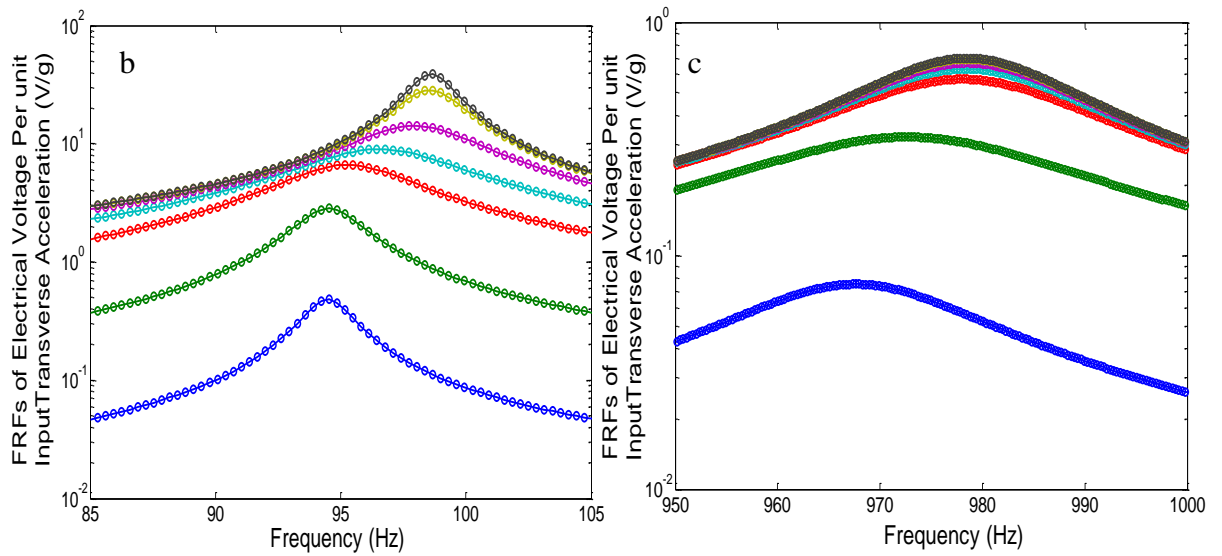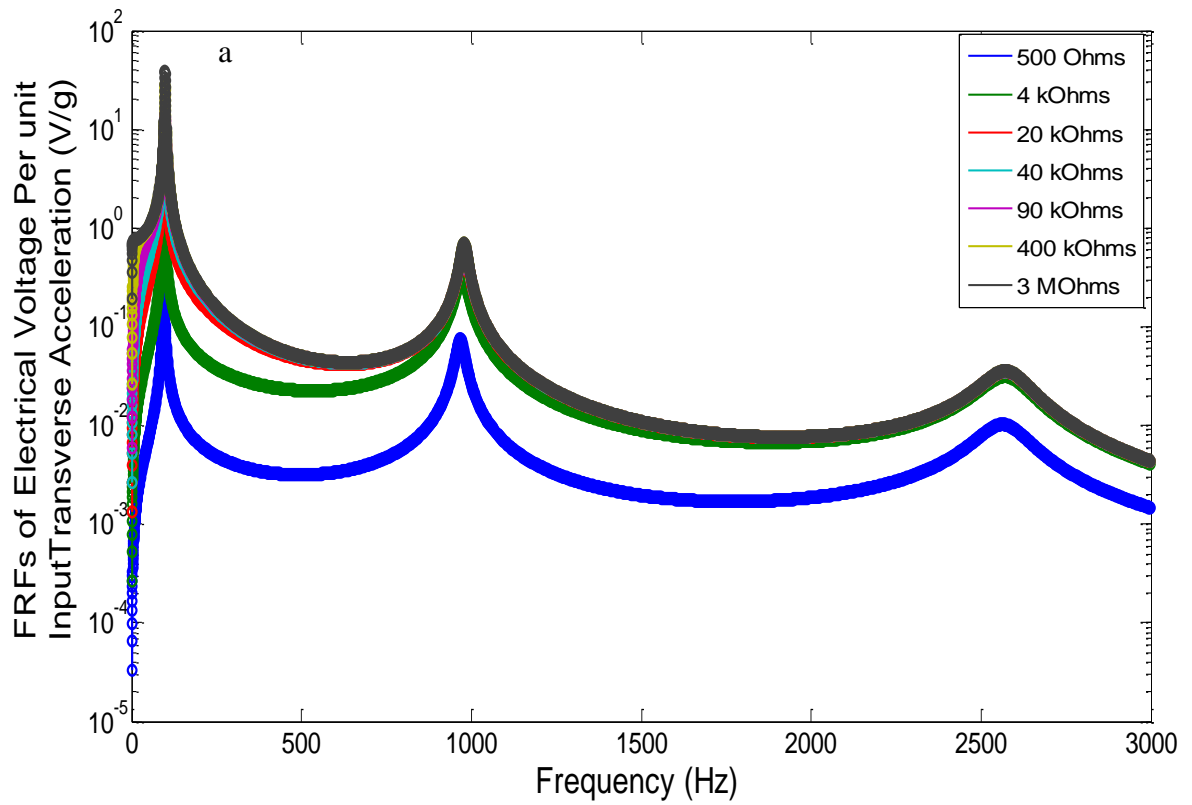
Figure 5.4. FRFs of Electrical Voltage with the Weak form (Solid line) and Closed form (Round dot) : a) The first three modes, b) First mode and c) Second mode

5.2.4. The Bimorph Multi-mode FRFs of Electrical Current

The first three mode FRFs of electrical current can be reformulated according to Eq. (4.216) in chapter 4 as,

$$\frac{I(j\omega)}{\ddot{w}_{base}}\bigg|_{\ddot{u}_{base}=0} = \frac{\dfrac{1}{R_{load}}\sum_{r=1}^{3}\dfrac{j\omega P_r^{(w)}Q_r^{(w)}}{\omega_r^{(w)2}-\omega^2+j2\zeta_r^{(w)}\omega_r^{(w)}\omega}}{j\omega P_D + R_L - \sum_{r=1}^{3}\dfrac{j\omega P_r^{(w)2}}{\omega_r^{(w)2}-\omega^2+j2\zeta_r^{(w)}\omega_r^{(w)}\omega} - \sum_{r=1}^{3}\dfrac{j\omega P_r^{(u)2}}{\omega_r^{(u)2}-\omega^2+j2\zeta_r^{(u)}\omega_r^{(u)}\omega}} \quad . \quad (5.10)$$

In this section, the first three mode FRFs of electrical current are shown in Figure 5.5 for the variable load resistance. The trend of the FRFs of electrical current seemed to give the opposite pattern with the FRFs of electrical voltage where the short and open circuits of load resistances seemed to give the highest and lowest amplitudes, respectively. For example, the electrical current at the first mode decreased with increasing load resistances followed by increasing resonance frequencies from the short to open circuits as shown in Figure 5.5b. Again, the FRFs of electrical current at the second mode with the load resistances of 20 kΩ, 40 kΩ, 20 kΩ, 90 kΩ, 400 kΩ and 3 MΩ indicated the same variations in resonance frequency with different amplitudes as shown in Figure 5.5c where the trend of amplitudes again showed the opposite behaviour with the electrical voltage. Similar behaviour was also found at the third mode. Again, the comparison between the multi-mode FRFs under the weak and closed forms of CEDRTL showed good agreement as seen from the enlarged view of Figure 5.5a.
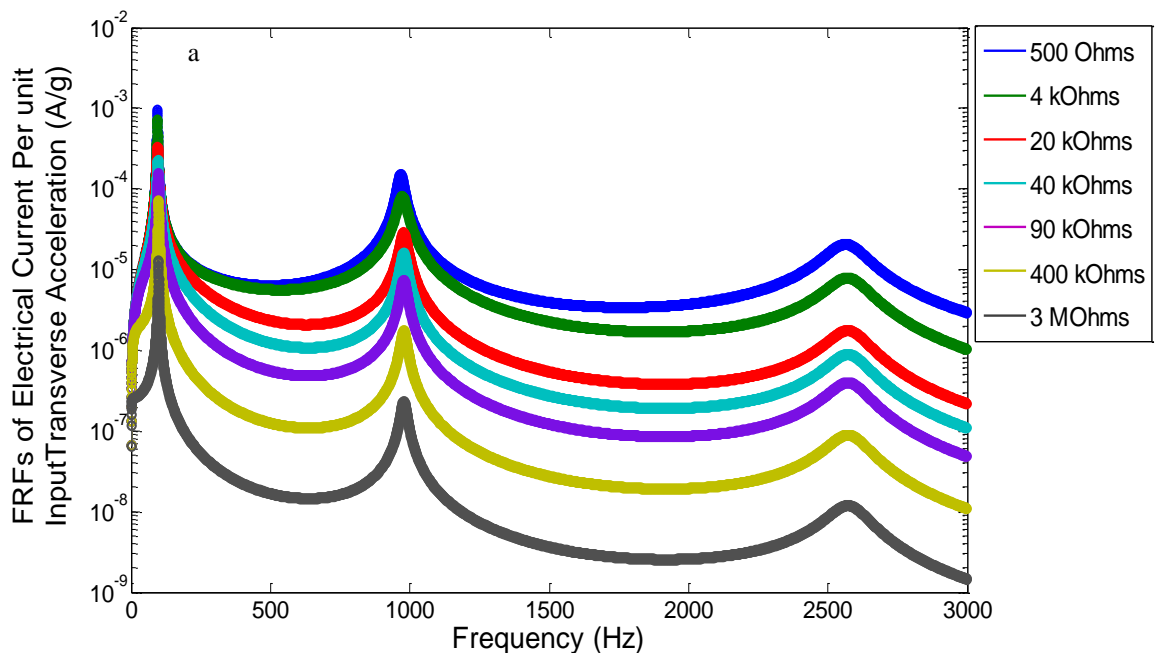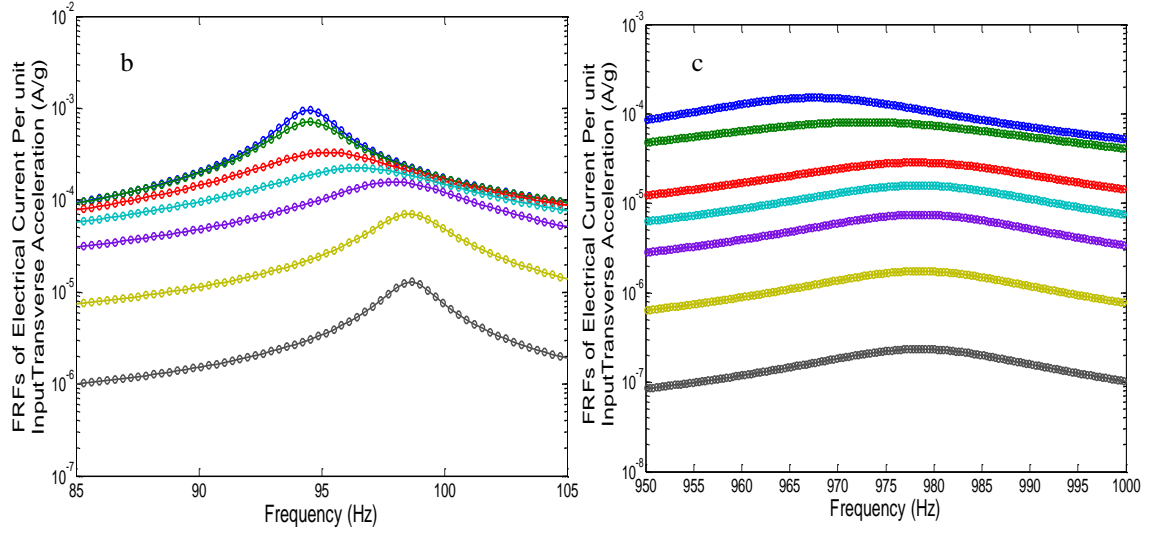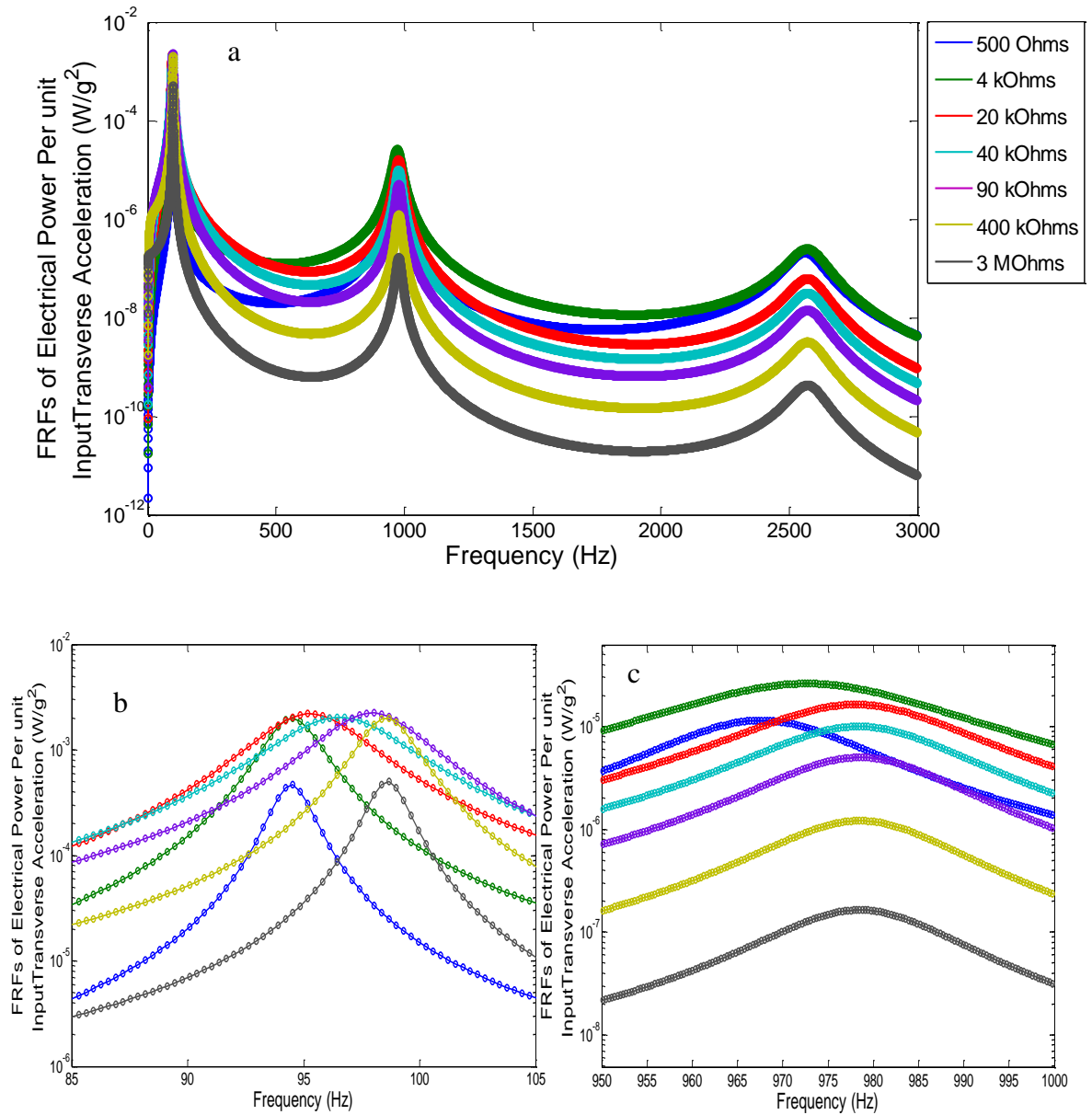
Figure 5.5 FRFs of Electrical Current with the Weak form (Solid line) and Closed form (Round dot) :
a) The First three modes, b) First mode and c) Second mode

5.2.5. The Bimorph Multi-mode FRFs of Electrical Power

In this section, the first three modes of FRFs for power harvesting under input base transverse acceleration can be formulated as,

$$
\frac{P(j\omega)}{\left(\ddot{w}_{base}\right)^2}\Bigg|_{\ddot{u}_{base}=0} = \left[\frac{\dfrac{1}{\sqrt{R_{load}}} \displaystyle\sum_{r=1}^{3} \dfrac{j\omega P_r^{(w)} Q_r^{(w)}}{\omega_r^{(w)2} - \omega^2 + j2\zeta_r^{(w)}\omega_r^{(w)}\omega}}{j\omega P_D + R_L - \displaystyle\sum_{r=1}^{3} \dfrac{j\omega P_r^{(w)2}}{\omega_r^{(w)2} - \omega^2 + j2\zeta_r^{(w)}\omega_r^{(w)}\omega} - \displaystyle\sum_{r=1}^{3} \dfrac{j\omega P_r^{(u)2}}{\omega_r^{(u)2} - \omega^2 + j2\zeta_r^{(u)}\omega_r^{(u)}\omega}} \right]^2 \quad .(5.11)
$$

The equation (5.11) has been derived from chapter 4 where this formulation was applied to analyse the trend of power harvesting with variable load resistance. Equation (5.11) represents the weak form of the CEDRTL. The closed form of the power harvesting was not given here but was formulated in chapter 4. The power harvesting result can be seen from Figure 5.6a, where the trend from the weak and closed forms tended to give very good agreement as shown from the enlarged view in Figures 5.6b and 5.6c. In this case, Figure 5.6a showed the influence of the transverse strain field and the piezoelectric coupling effects for the cantilevered piezoelectric bimorph beam. The cantilevered piezoelectric bimorph beam has a predominant transverse bending strain where the input transverse acceleration was exerted on the base structure of the piezoelectric bimorph to create the electric-strain field to give the power harvesting at the dominant resonance frequencies starting from 94.47Hz to 98.60 Hz. It should be noted that these resonance frequencies

indicated the short and open circuits with the load resistances of 500 Ω and 3 MΩ, respectively.

Moreover, the short and open circuit response indicated the lowest value of power amplitudes. The resonance frequencies shown in Figure 5.6b seem to shift as the load resistance changed. This indicates that the load resistance affects the power harvesting response as a function of frequency. The trend of power amplitudes gave the symmetrical pattern of response at the first mode. Another important aspect which can be noticed here is that the trend of power harvesting depends not only on varying resistances but also on the chosen properties of the piezoelectric beam and the geometry of the bimorph model. For example, even though the geometry of the bimorph was chosen here, changes in the system properties like permittivity and piezoelectric constants would give different power harvesting results. The chosen load resistances need to be investigated first to provide a symmetrical frequency response at the first mode. The reason to investigate the symmetrical power harvesting frequency response was to analyse the short and open circuits response as a function of load resistance and to optimise the amplitude. It was also noted that once the symmetrical pattern was obtained at the first mode, the second and third modes and so on would not necessarily give the monotonic symmetrical pattern, as the trend of the power harvesting at these modes tend to give the same resonance frequency with the higher load resistances approaching open circuit. This means that the resonance frequencies above the first resonance do not always shift. For example, the load resistances of 20 kΩ, 40 kΩ, 90 kΩ, 400 kΩ and 3 MΩ for the second and third modes predominantly indicated the same resonance frequency. The open circuit load resistance of 3 MΩ tended to give the lowest amplitude response for the first three modes whereas the amplitude of short circuit load resistance of 500 Ω gave the lowest first mode response that increased for the second and third modes as load resistance approached the open circuit.

Figure 5.6 FRFs of Electrical Power with the Weak form (Solid line) and Closed form (Round dot) : a) The first three modes, b) First mode and c) Second mode

5.2.6. Geometrical Parametric Analysis of the Bimorph for Generating Electrical Power

This section considers variable geometry of the bimorph and its affect on the response using parallel connection. The electrical power with varying load resistance was modelled around the first mode. The focus of the geometrical case study was based on changing the piezoelectric element thickness and length. The power harvesting amplitude around the first resonance frequency gave the trend based on the chosen varying resistances as shown from Figure 5.7. The power harvesting around the resonance frequency at the load resistance of 500 Ω tended to increase

with the increasing bimorph length and decreasing piezoelectric thickness as shown from Figure 5.7b. Although, the load resistance represents a very low value, the trend of power harvesting still increased slightly with the differences between maximum and minimum values being 49.4 $\mu W/g^2$. It should be noted that the minimum power of 0.326 mW/g^2 was located with the minimum bimorph length of 28.7 mm and the maximum piezoelectric thickness of 0.23 mm with the resonance frequency at 154.5 Hz whereas the maximum power of 0.611 mW/g^2 was located at the maximum bimorph length of 32.2 mm and the minimum piezoelectric thickness at 0.11 mm with the resonance frequency of 65.89 Hz. As expected, the resonance frequencies shifted with the change of geometrical bimorph parameters and also the variances of load resistance. It is noted that the effect of the change of geometrical parameters can affect the piezoelectric constants and internal capacitances as well as the inertia dynamic load onto the bimorph beam due to the product between the input base acceleration and the generalised inertia mass of bimorph including the tip mass. It should be noted that using the same input acceleration on the bimorph with different geometrical parameters, results in very different power amplitudes and also different resonance frequencies. The short and open circuit resonance frequencies, obviously, seemed to give the lowest value of power as shown in Figures 5.7b and 5.7d.

The overall results of power amplitudes with varying load resistance can also be seen in Figure 5.7o based on the variation of bimorph length and thickness. The short and open circuit resonance response still showed very low values of power amplitudes and also seemed to be close with each other. The power amplitudes from Figures 5.7p,q seemed to overlap each other for the coupled resistances, for example; the coupled power amplitudes with 4 kΩ and 400 kΩ , 20 kΩ and 90 kΩ were close to each other and also gave an identical power amplitude trend with the different resonance frequencies. It should be noticed that the FRFs of power amplitude from Figure 5.6 was based on the constant geometrical bimorph with 30.1 mm length and 0.15 mm thickness for the piezoelectric element. The results of power amplitudes from the constant geometrical bimorph also showed similar results as given from Figure 5.7. For example, as found at the bimorph length of 30.1 mm and piezoelectric thickness of 0.15 mm. The important aspect found here was that there were significant changes of the power amplitudes with the change of geometrical properties compared with the previous result. As shown in Figure 5.7, the power can

be increased by over 100 % by changing the thickness and length of the bimorph element. The trend of power amplitudes was affected not only from the load resistances but also from the variations of geometrical parameters of the bimorph. In this case, the optimal design of the bimorph represent an important aspect of the power harvesting.
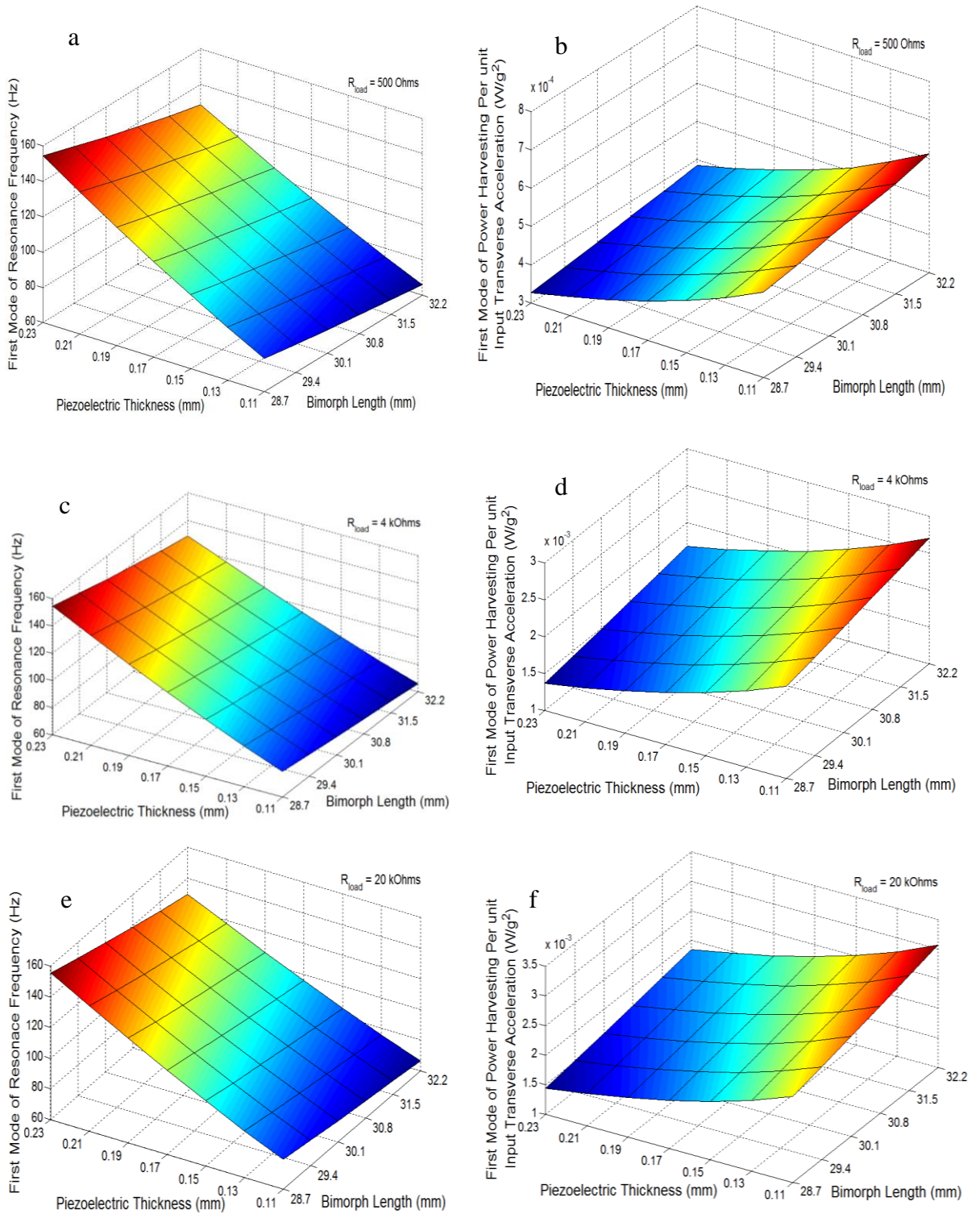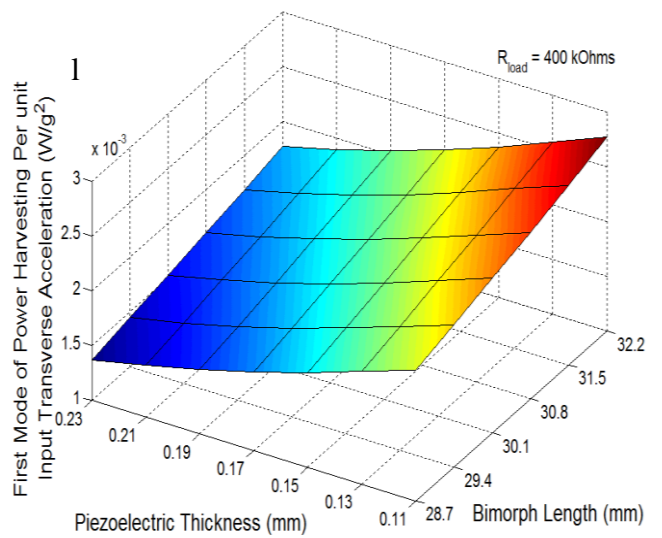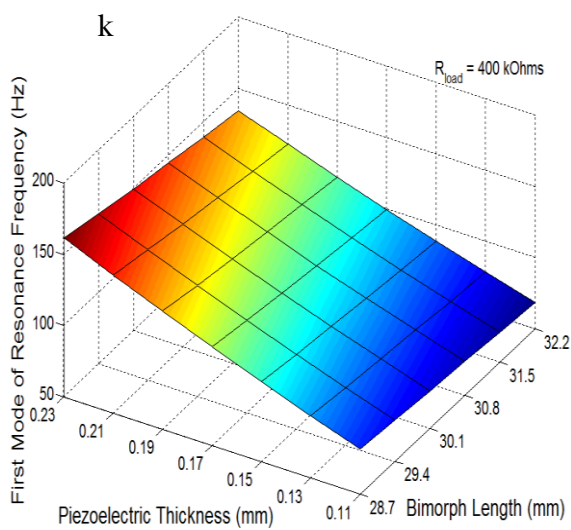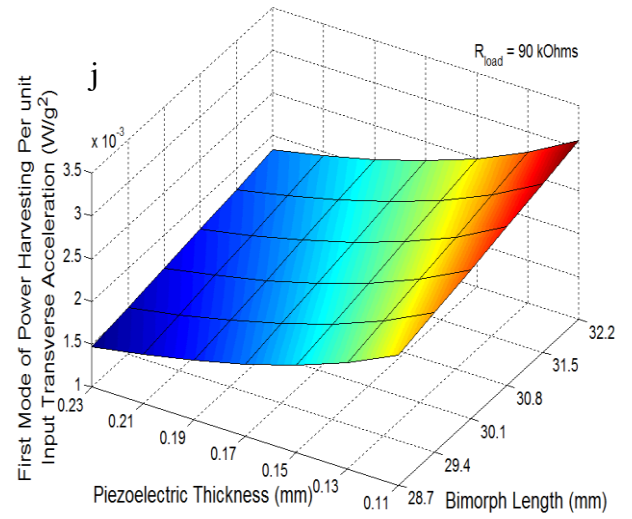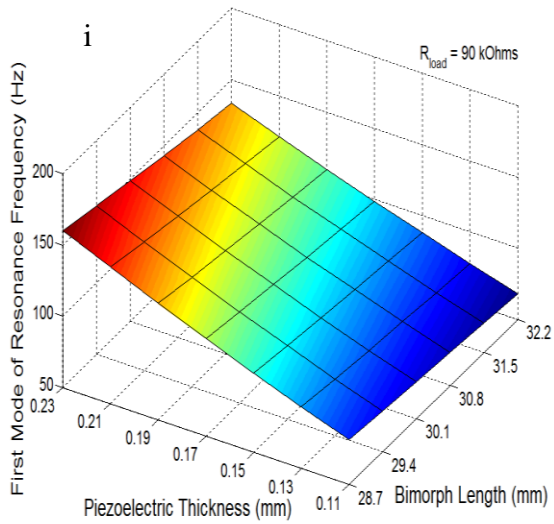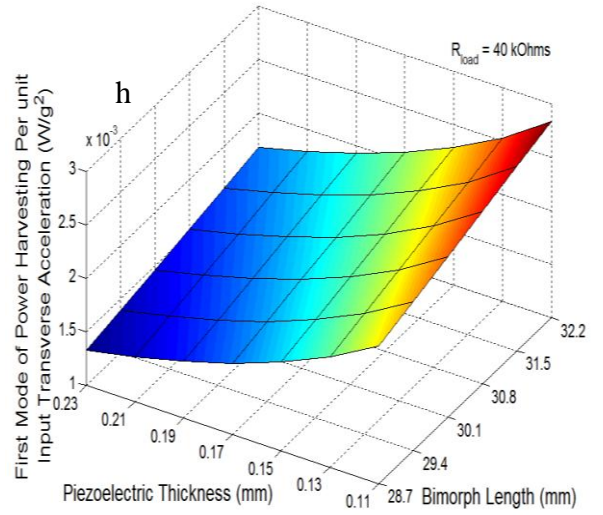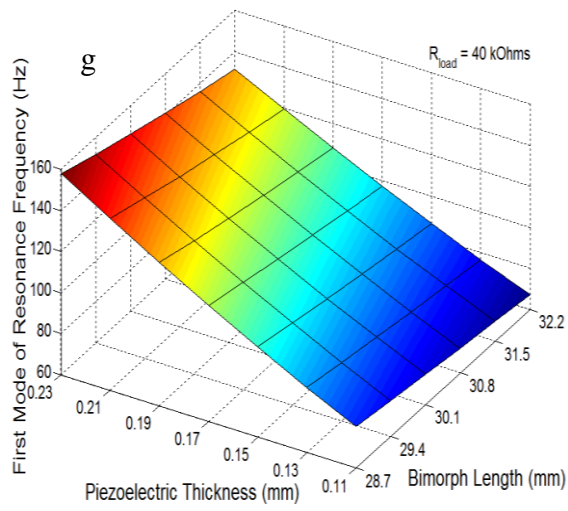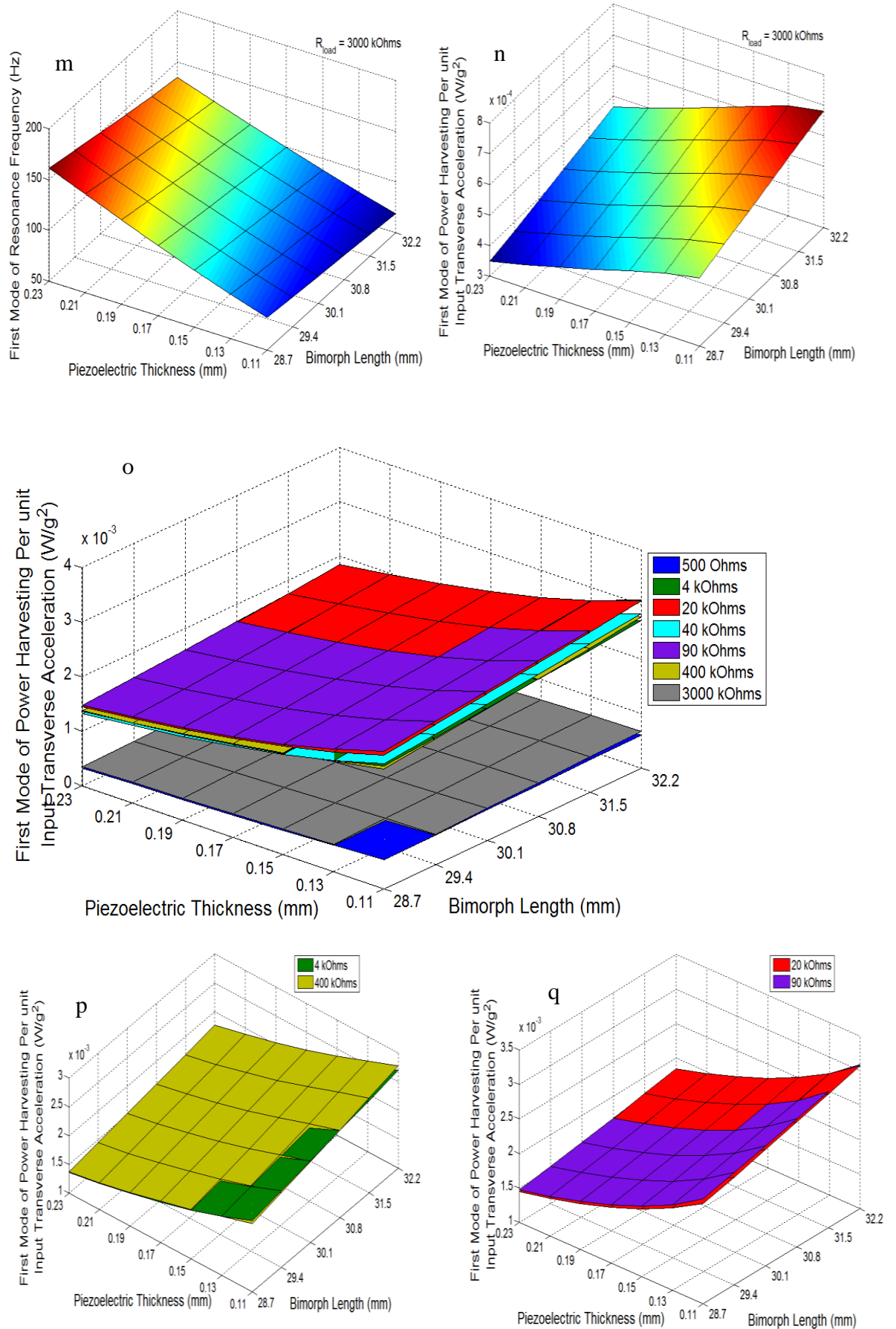
Figure 5.7. First Mode of power harvesting based on the geometrical parametric and Resonance frequency cases with the weak form : a, b) 500 Ω ; c,d) 4 kΩ ; e,f) 20 kΩ ; g,h) 40 kΩ ; i,j) 90 kΩ ; k,l) 400 kΩ ; m,n) 3 MΩ ; o) Variances of load resistance ; p) Combined between 4 kΩ and 400 kΩ ; q) combined between 20 kΩ and 90 kΩ

5.3. Electromechanical Dynamic Response of Piezoelectric Bimorph under Series Connection

In this section, the multi-mode FRFs and parametric case studies of the piezoelectric bimorph with a tip mass are discussed as a function of load resistance. The mechanical damping ratios and load resistance were chosen similar to the values used for the parallel connection. The analysis of the piezoelectric bimorph under series connection was based on the weak and closed forms of the coupling electromechanical dynamic responses of the transverse-longitudinal form (CEDRTL). The trends obtained in this section were based on the formulation given in the previous chapter where the parameters of the piezoelectric couplings and capacitances were different for each connection type on the bimorph as given in chapter 4. Moreover, the comparison between the series and parallel connections were discussed according to the multi-mode FRFs of the bimorph.

5.3.1. The Bimorph Multi-mode FRFs of Tip Absolute Dynamic Displacement

The trend of the first three FRFs of tip absolute dynamic displacement with varying load resistance was simulated according to the frequencies ranging from 0 to 3000 Hz. The load resistances of 500 Ω, 4 kΩ, 20 kΩ, 40kΩ, 90kΩ, 400kΩ, 3MΩ were the same values as used for the parallel connection. The tip absolute dynamic displacement can be considered to model the absolute tip transverse dynamic displacement as formulated previously. It should be noted that the results of the tip absolute dynamic displacement reported here represent meter per unit input base transverse acceleration where the input base transverse acceleration on the bimorph was 9.81 m/s^2 which is equivalent to 1 g (1 g = gravitational acceleration 9.81 m/s^2). As mentioned previously, the mechanical damping ratios were chosen according to the suggested formulations where the damping ratios should be based on the experimental study as discussed in chapter 6. Moreover, the mechanical damping ratios determined at the previous section were also used in this section where the results of FRFs of the electromechanical dynamic system can be used for comparison between the series and parallel connections.

As can be seen from Figure 5.8a, there has been a slight change of trend at the first mode series connection compared with the parallel connection based on the tip

absolute dynamic displacement under varying load resistances. The amplitudes around the range of resonance frequencies at the series connection with the lower load resistances of 500Ω, 4 kΩ, 20 kΩ and 40 kΩ showed a slight increase compared with the parallel connection as shown in Figure 5.2b. However, for the higher load resistances of 90 kΩ, 400 kΩ and 3 MΩ with the series connection, the amplitudes tended to give a slight decrease around the resonance frequencies compared with the parallel connection. In that case, Figures 5.9a,b clearly showed the different amplitude trends between the series and parallel connection short and open circuit resonance frequencies as the load resistance varies. The trend of displacement under the short circuit resonance frequency with the series connection gave a slightly higher result compared with the parallel connection whereas the trend of displacement under the open circuit resonance frequency with the parallel connection gave a slightly higher value compared with the series connection. The reason for this behaviour was that the effects of piezoelectric couplings due to the transverse and longitudinal forms contributed to change in the electromechanical damping and also stiffness. The internal capacitance of the piezoelectric material also contributed as electromechanical damping and the load resistance connecting to the bimorph was viewed as the resistive shunt damping. The electromechanical damping and stiffness and load resistance affects the pure mechanical behaviour of the bimorph resulting in the shift of the natural frequency and the amplitude response. It is important to note here that short or open circuit resonance frequency have different physical meaning with short or open circuit load resistance as discussed previous section. For example, the short circuit resonance frequency versus variable load resistance as given in Fig. 5.9a was plotted according to single resonance frequency of short circuit load resistance having off-resonances with different amplitudes for other load resistance.

The results of dynamic displacement amplitudes as a function of the frequency seemed to shift due to varying load resistances as shown in the enlarged view of the first mode in Figure 5.8b. It should be noticed here that with the same load resistances as used for the parallel connections, the series connection resonance frequencies shifted with different amounts. The lowest displacement amplitude at the first mode corresponded to the short circuit resonance frequency of 94.48 Hz with load resistance of 500 Ω and then shifted to the open circuit resonance frequency of 98.62 Hz with load resistance of 3 MΩ. As can be seen from the two Figures 5.8b

and 5.2b, both the resonance frequencies for the parallel and series connections tended to give very low amplitudes for both the short and open circuits. Moreover, the second mode of the FRF tended to indicate the dominant trend of frequency amplitudes as shown in Figure 5.8c where the majority of load resistances of 40 kΩ, 90 kΩ, 400 kΩ and 3 MΩ mostly tended to give the same resonance of 978.5 Hz with different amplitudes.
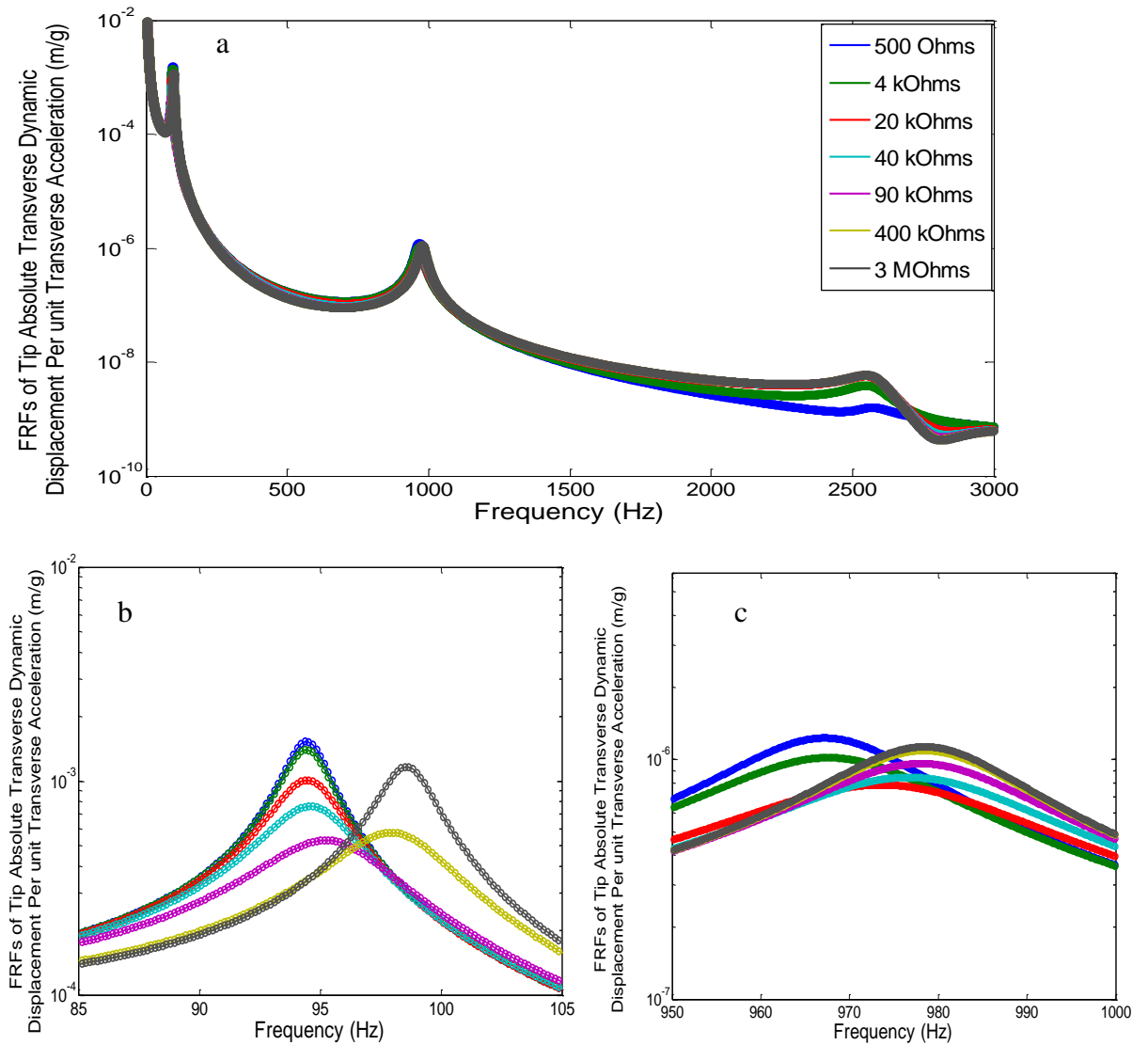
Figure 5.8 FRFs of tip absolute Dynamic Displacements with the Weak form (Solid line) and Closed form (Round dot): a) The first three modes, b) First mode and c) Second mode
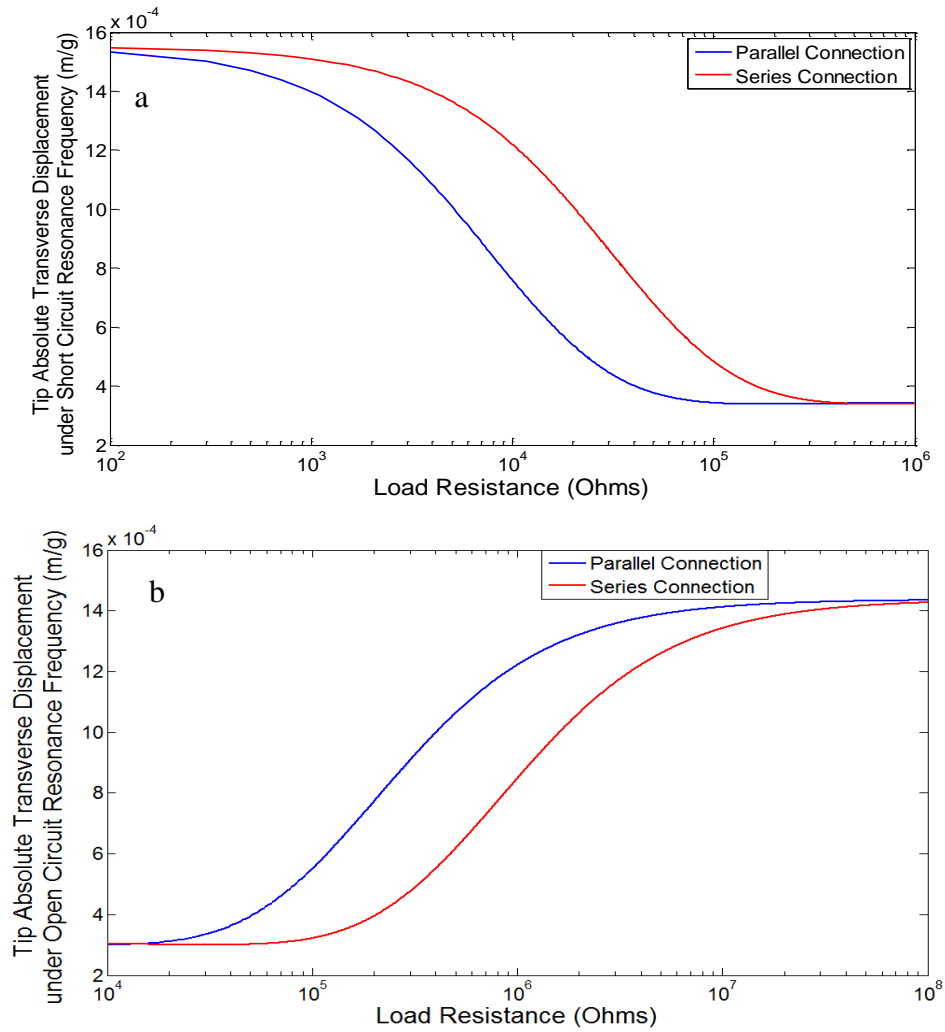
Figure 5.9 FRFs of tip absolute Dynamic Displacements under the series and parallel connections with the Weak form : a) Short Circuit, b) Open Circuit

5.3.2. The Bimorph Multi-mode FRFs of Tip Absolute Velocity

The first FRFs of tip absolute velocity of the cantilevered piezoelectric bimorph under series connection were calculated with variable load resistance. As considered previously, the FRFs of tip absolute velocity was still used according to the suggested formulation with the coefficients of piezoelectric coupling and capacitance having different values. The trend of the first three modes of tip velocity FRFs of the bimorph tended to give similar results with varying load resistances as shown in Figure 5.10a. The tip velocity at the fundamental resonance frequency for the series connection gave a slightly different trend compared with the parallel connection results as shown in Figures 5.10b and 5.3b, respectively. This indicates that with the same load resistances connected to the bimorph either under parallel or

series connection, the amplitudes of tip velocity on the bimorph would not necessarily give the same results and monotonic trends.

At this stage, the shifting resonance frequency at the first mode also occurred clearly from short to open circuit load resistance as shown in the enlarged view in Figure 5.10b. The resonance frequency of 94.47 Hz for short circuit and 98.60 Hz for open circuit gave very high velocity amplitudes of 0.91 m/s.*g* and 0.72 m/s.*g*, respectively. As shown in Figures 5.11a and 5.11b, the trend of velocity under the short circuit resonance frequency with the series connection gave a slightly higher result compared with the parallel connection whereas the trend of velocity under the open circuit resonance frequency with the parallel connection gave a slightly higher value compared with the series connection. Tip absolute velocity results for other frequencies can also be shown to have similar behaviour when comparing between the series and parallel connections.
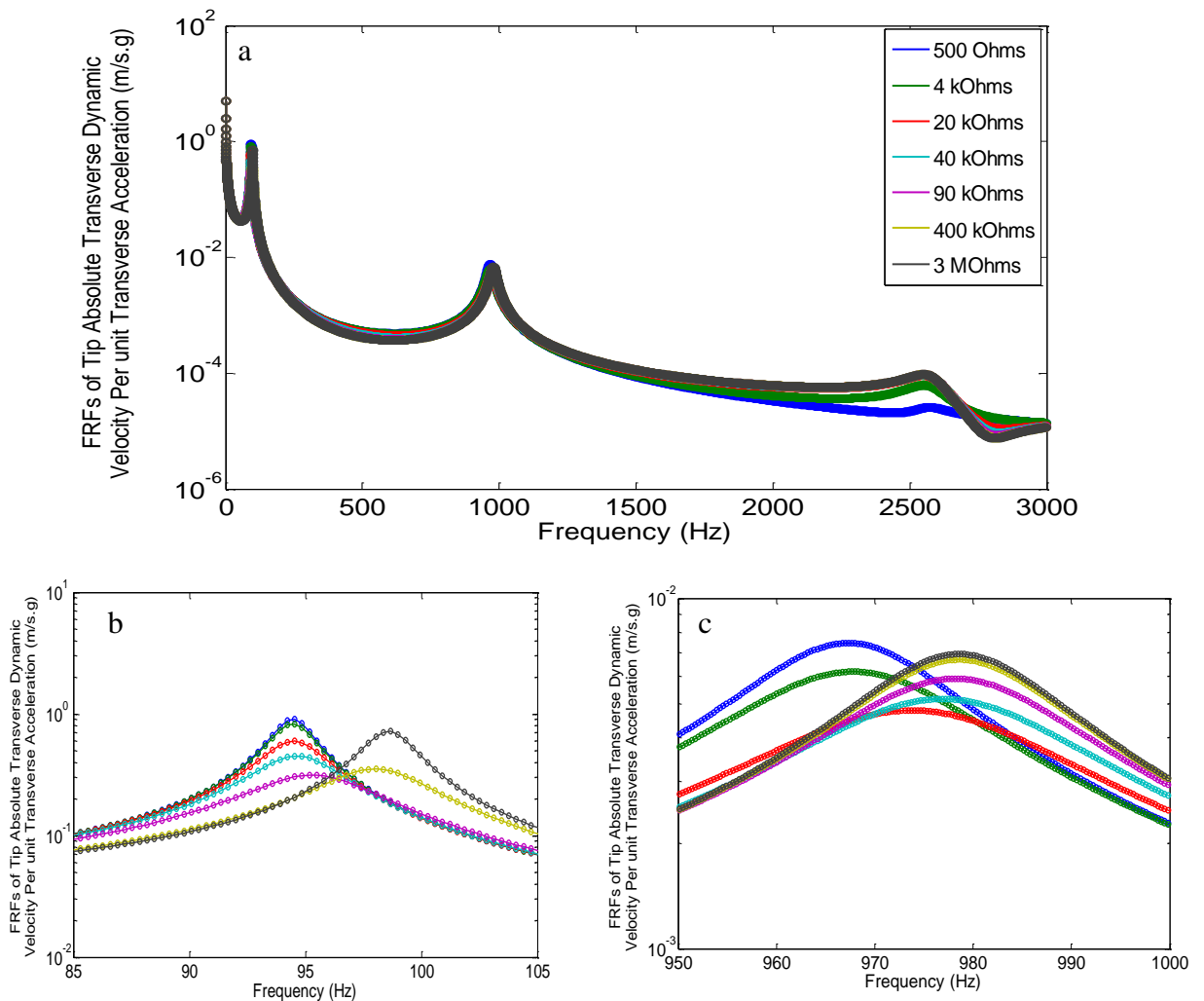
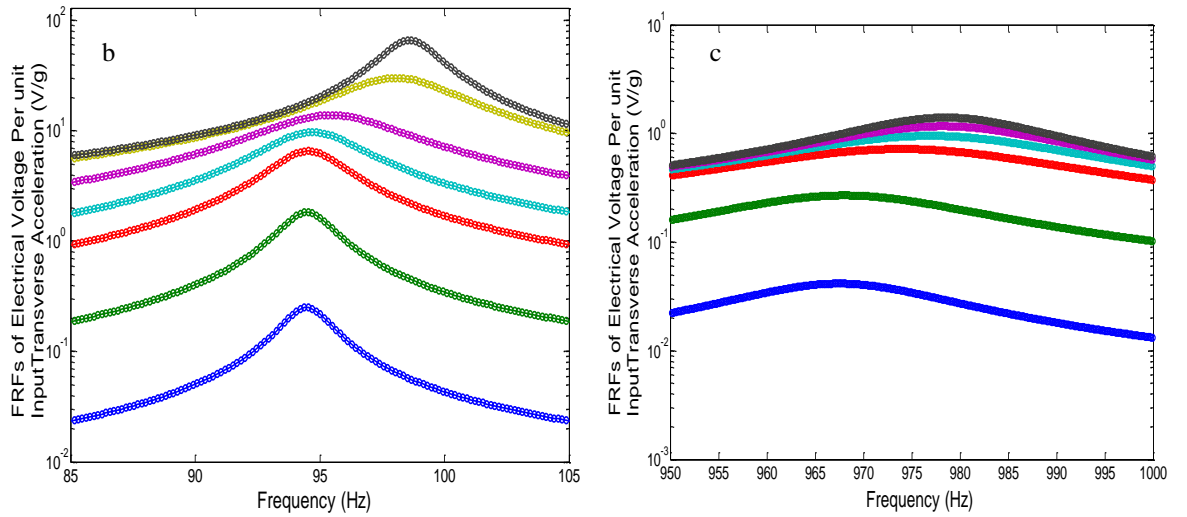Figure 5.10. FRFs of tip absolute Dynamic velocity with the Weak form (Solid line) and Closed form (Round dot): a) The First three modes, b) First mode and c) Second mode
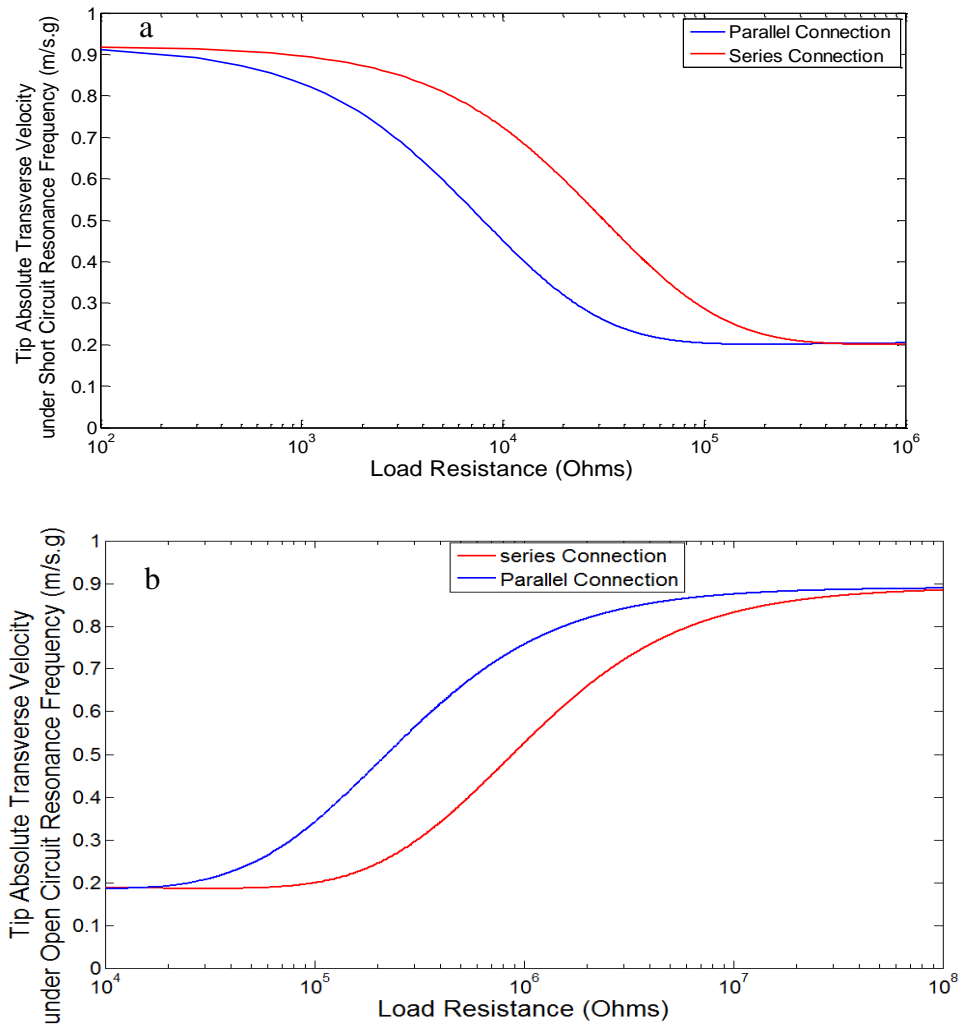
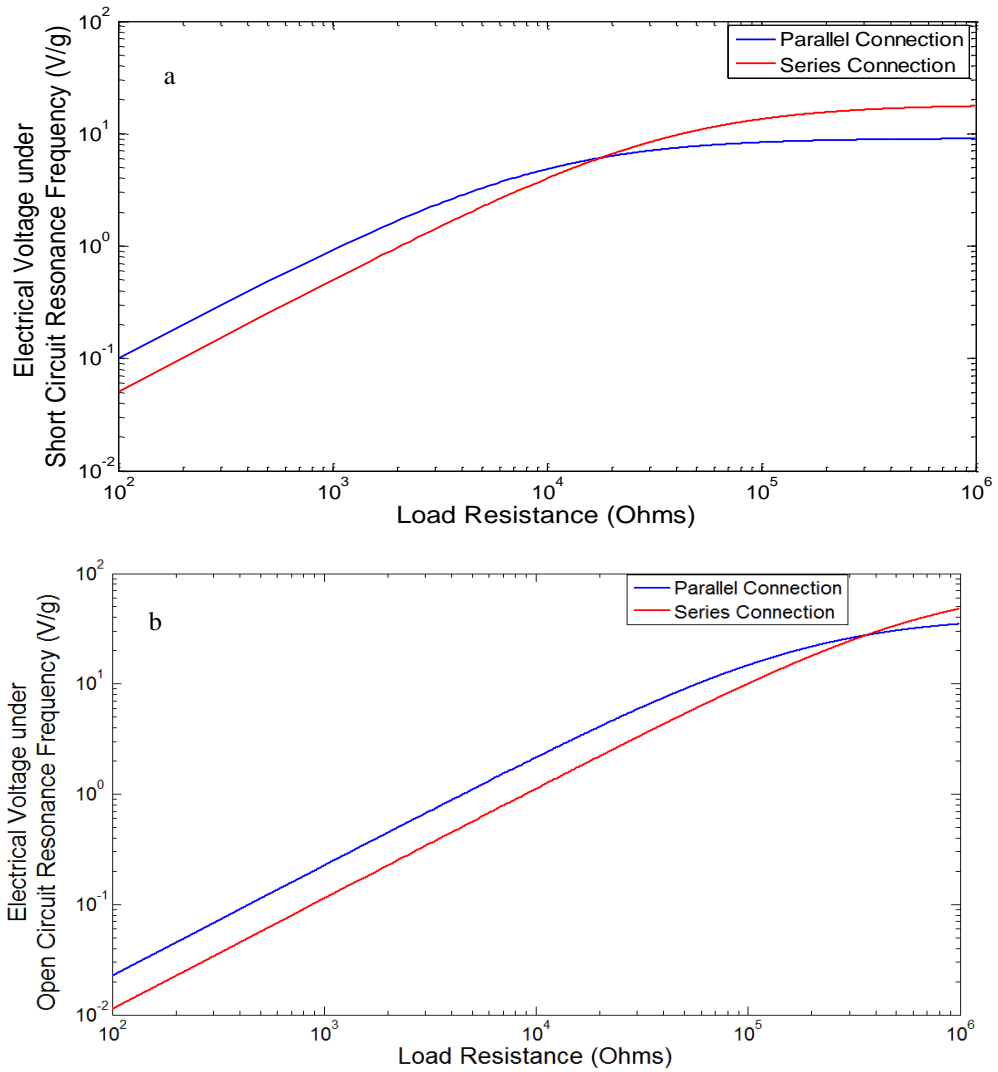Figure 5.11 FRFs of tip absolute Dynamic Velocity with the Weak form under the series and parallel connections : a) Short Circuit, b) Open Circuit

5.3.3. The Bimorph Multi-mode FRFs of Electrical Voltage

In this section, the first three modes of electrical voltage FRFs of the bimorph were analysed according to varying load resistances as shown in Figure 5.12a where the weak and closed forms of CEDRTL seemed to overlap each other as shown clearly from the enlarged view from Figures 5.12b,c. The amplitude of short circuit resonance frequency with the load resistance of 500 Ω gave the lowest voltage where the amplitude of open circuit resonance frequency with the load resistance of 3 MΩ indicated the highest voltage. With variation in the load resistance, the electrical voltage amplitude also varies where the electrical voltage increased with the increasing load resistances as shown in Figure 5.12b. The short circuit off-resonance response still indicated the lowest value of amplitude whereas the open circuit still

indicated the highest value of amplitude off-resonance. The second mode FRFs of electrical voltage also seemed to increase with the increasing load resistance indicating a similar trend with the first mode. By considering the velocity with the load resistance approaching to the short circuit, the amplitude increased where the voltage amplitude seemed to decrease. Conversely, when the load resistance approached open circuit, the velocity amplitude increased with increasing electrical voltage.

It should be noted that the chosen damping ratio in the FRFs can change the voltage amplitudes within the resonance regions. As shown in Figures 5.13a,b, when the load resistances under the short and open circuits resonance frequencies indicated over 17.9 kΩ and 358 kΩ, the electrical voltage with the series connection tended to give the higher amplitude compared with the parallel connection. It is noted that the short circuit resonance frequency with the load resistances of 17.9 kΩ indicated the transitional point of electrical voltage amplitudes between the series and parallel connections whereas the open circuit's resonance frequency with the load resistances of 358 kΩ also indicated the transitional point of electrical voltage amplitudes between the series and parallel connections. This transitional point of electrical voltage indicated the overlapped amplitudes between the series and parallel connections. The electrical voltage over the transitional point of resistance for the series connection always indicated the highest amplitude across the frequency domain.
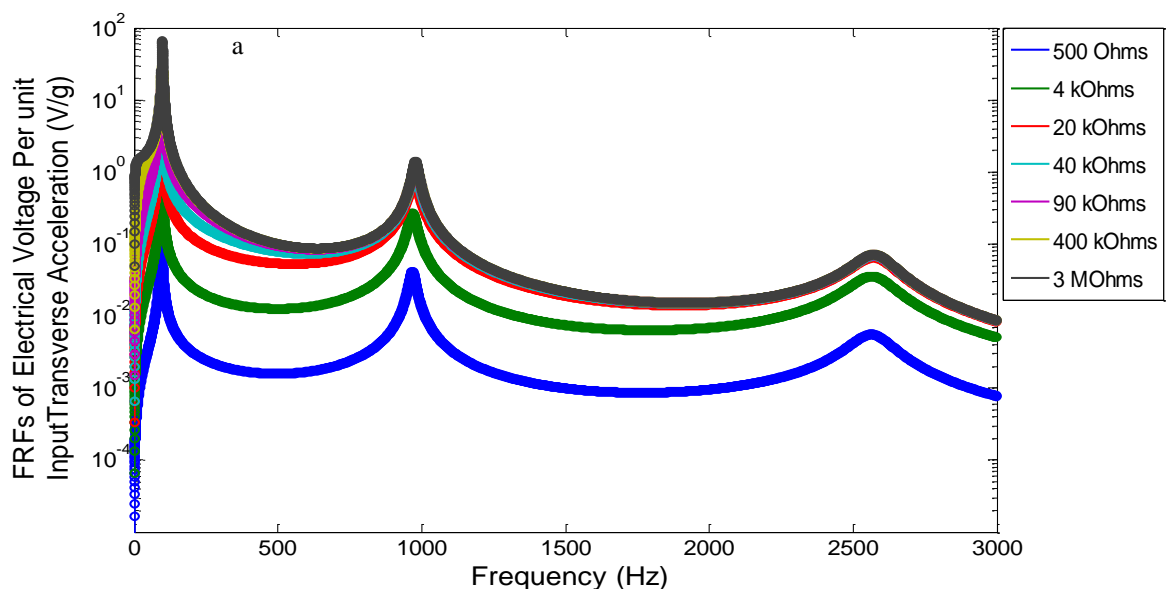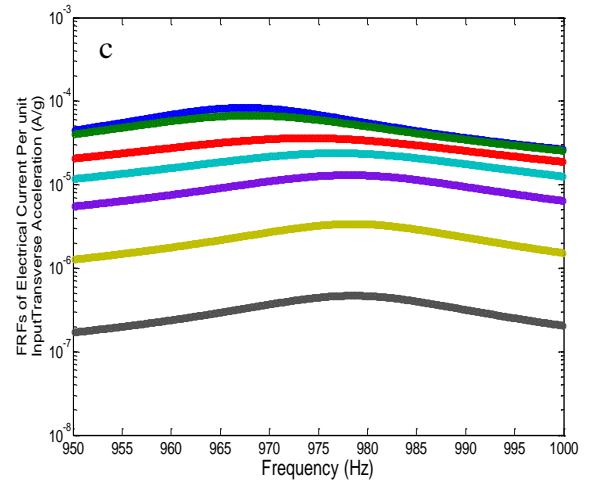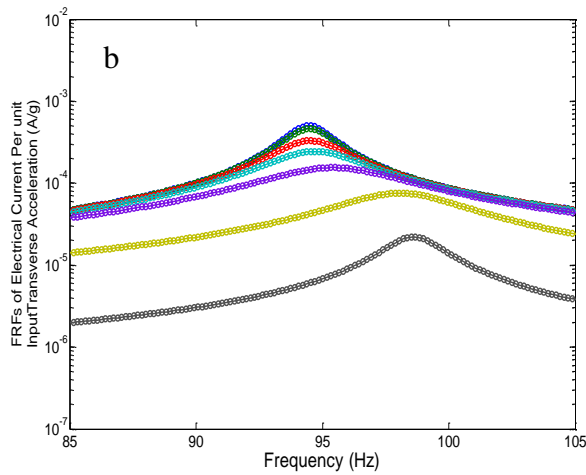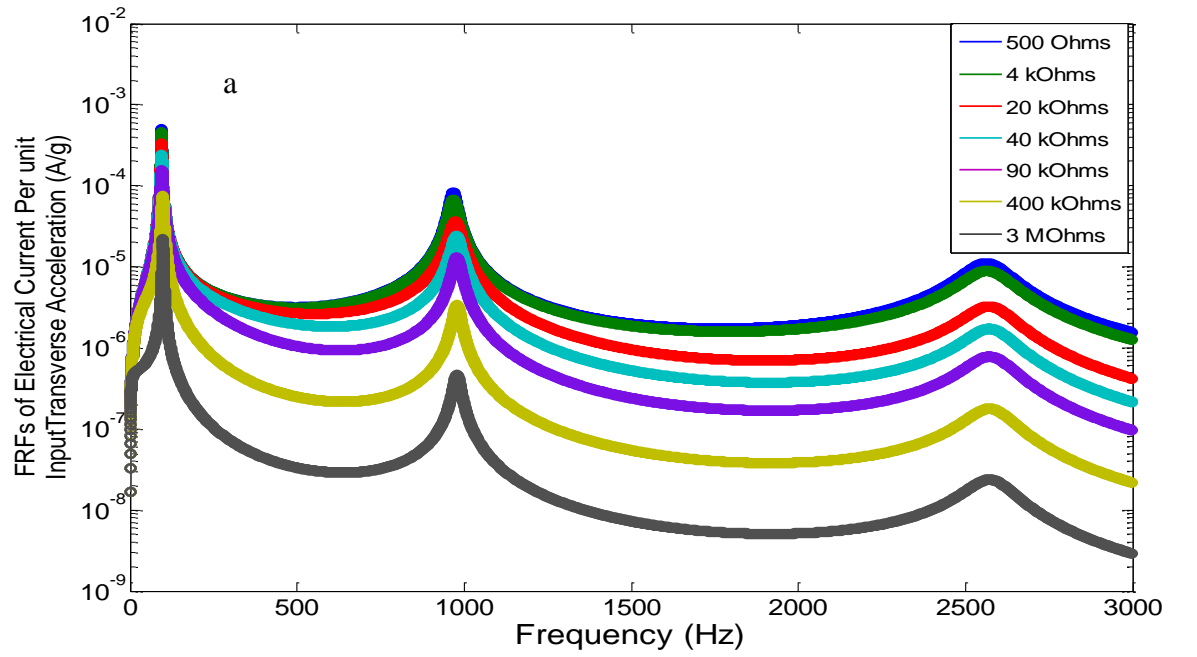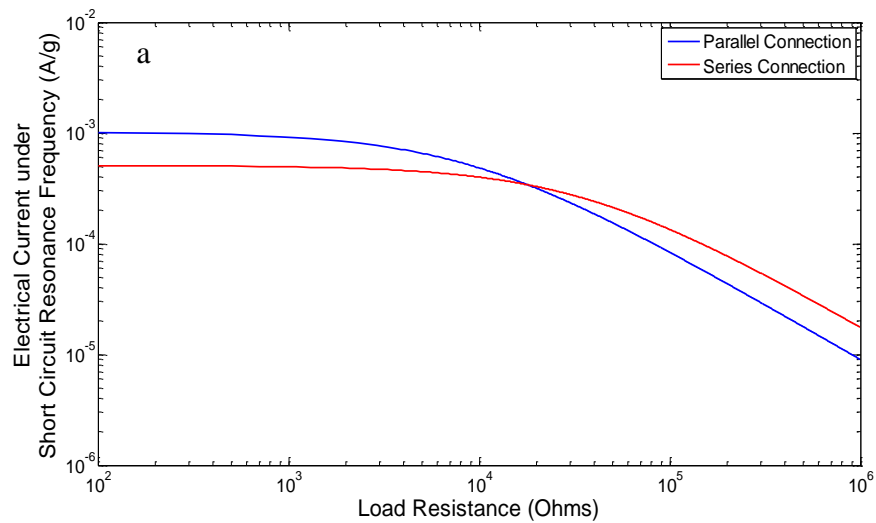
Figure 5.12 FRFs of electric voltages with the Weak form (Solid line) and Closed form (Round dot):
a) The first three modes, b) First mode and c) Second Mode

Figure 5.13 FRFs of Electrical Voltage under the series and parallel connections with the
Weak form : a) Short Circuit, b) Open Circuit

5.3.4. The Bimorph Multi-mode FRFs of Electrical Current

As can be seen from Figures 5.14a, the first three modes of electrical current under series connection was analysed according to varying resistances. As can be seen from the enlarged view in Figures 5.14b-c, the comparison between the weak and closed forms of the CEDRTL achieved good agreement. The trend of electrical current indicated the opposite pattern with the electrical voltage. The electrical current referred to the highest amplitude when the load resistance approached open circuit. The second mode of electrical current also seemed to have similar behaviour with the first mode where the electrical current amplitude increased with increasing load resistance. Another important aspect can also be considered to be the relationships between the dynamic velocity, displacement, electrical voltage and current. The velocity amplitude with the load resistance approaching short circuit seemed to increase, where the voltage amplitude decreased with the increasing electrical current for both connection types. Conversely, the velocity amplitude with the load resistance approaching open circuit tended to increase where the voltage amplitude increased with the decreasing electrical current.

By considering Figures 5.15a-b, the electrical current under the short circuit still indicated a higher amplitude compared with the open circuit as indicated for both connection types. However, the electrical current for the short and open circuits' frequency resonances with the parallel connection seemed to give the higher amplitudes with the load resistances below 17.9 kΩ and 358 kΩ, respectively compared with the electrical current with the series connection. It was noted that the short circuit resonance frequency with the load resistance of 17.9 kΩ indicated the transitional point of amplitude between the series and parallel connections whereas the open circuit resonance frequency with the load resistances of 358 kΩ also indicated the transitional point of amplitude between the series and parallel connections. The transitional point of amplitude indicated the same electrical current between the series and parallel connections. The region below the transitional point of resistance with the parallel connection always indicates the highest amplitude for every frequency domain. That indicates that the maximum electrical current would be compatible with the parallel connection whereas the maximum electrical voltage would be compatible with the series connection.

Figure 5.14 FRFs of electric Current with the Weak form (Solid line) and Closed form (Round dot):
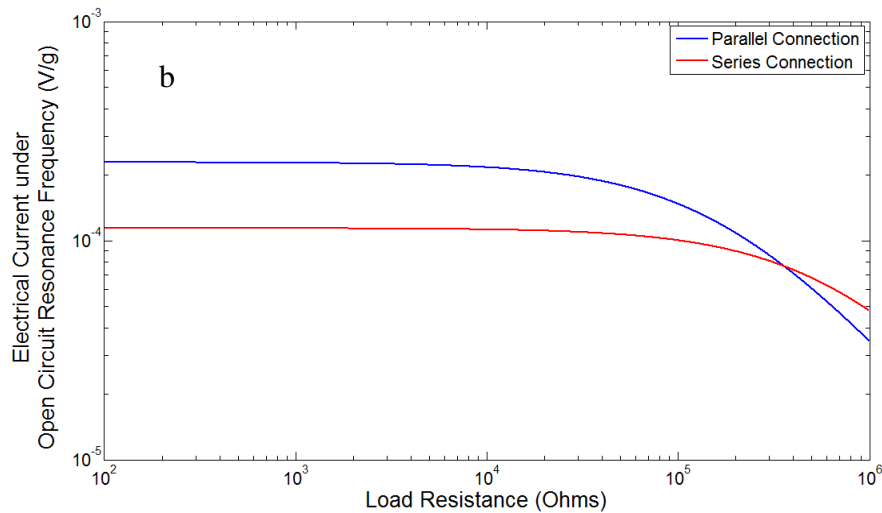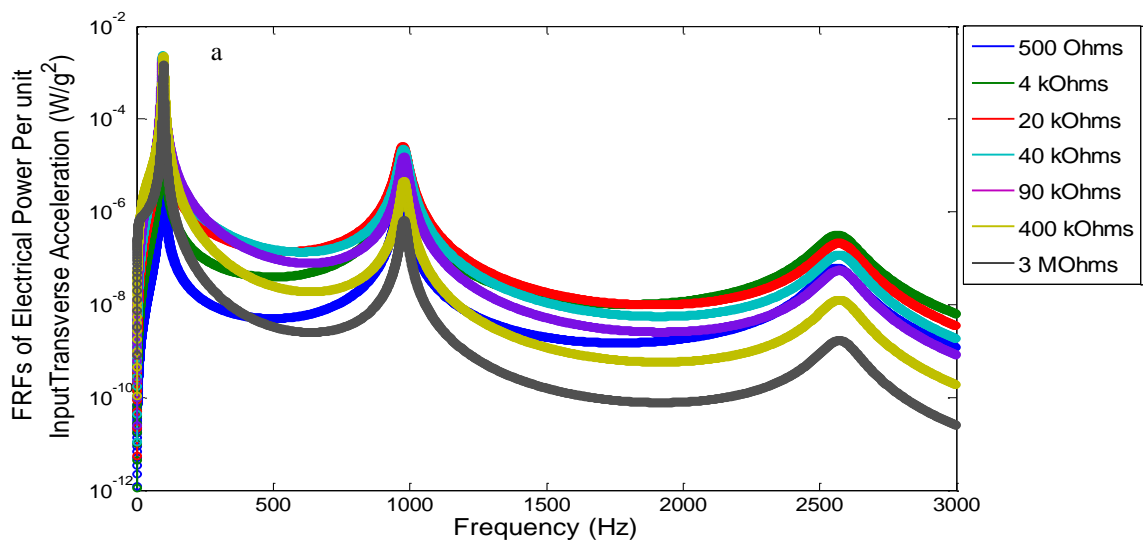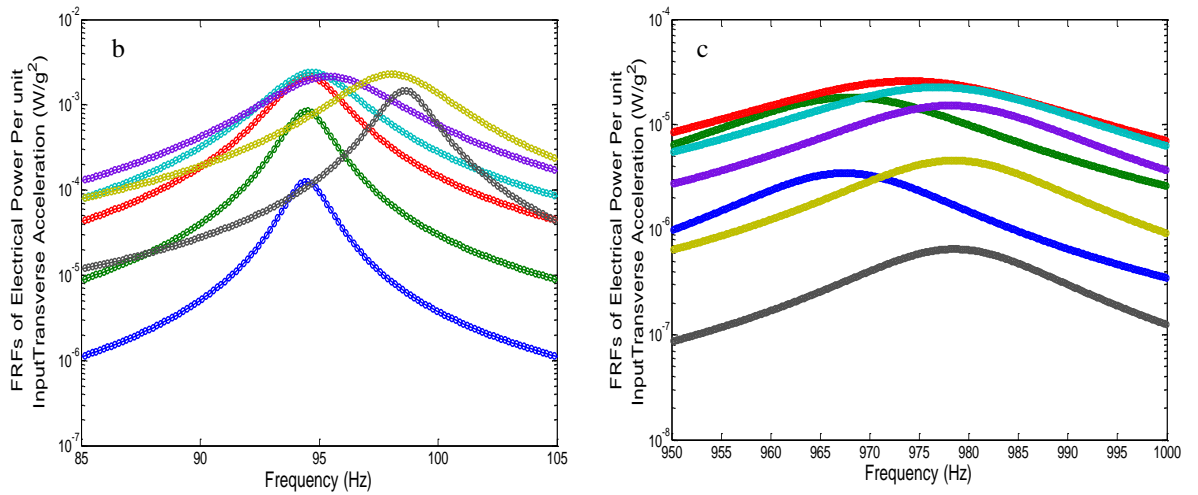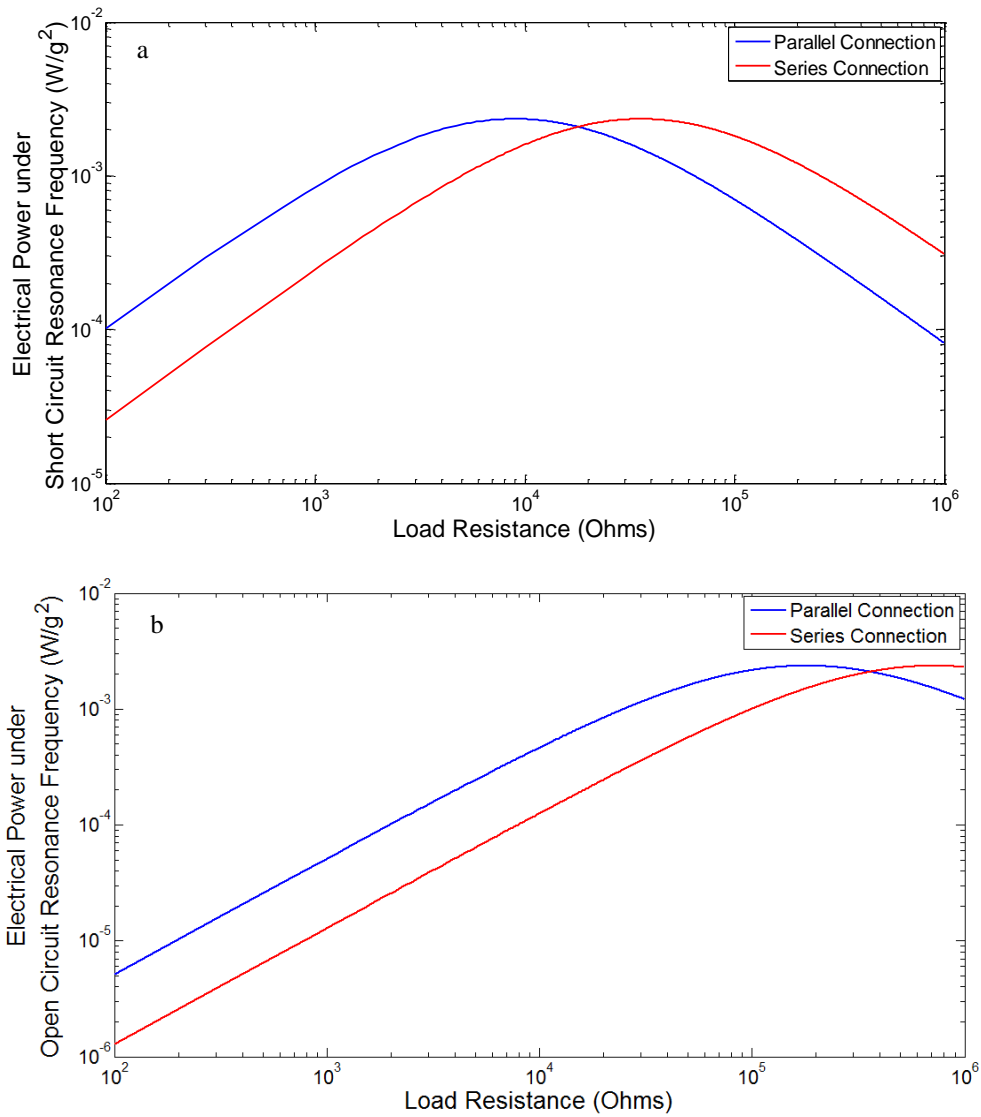a) The First three mode, b) First mode and c) Second Mode

Figure 5.15 FRFs of Electrical Current under the series and parallel connections with the Weak form : a) Short Circuit, b) Open Circuit

5.3.5. The Bimorph Multi-mode FRFs of Electrical Power

As can be seen from Figure 5.16a, the weak and closed forms of CEDRTL were compared according to the first three mode power harvesting FRFs with varying load resistances under the series connection. The shifting resonance frequencies under varying load resistances were mostly affected from the transverse bending form of the cantilevered piezoelectric bimorph beam due to the input base transverse acceleration. It should be noted that although the load resistances were the same values as for the parallel connection type of the piezoelectric bimorph, the resonance frequencies displayed slightly different trends compared with the parallel connection. As expected, the power amplitudes of the resonance frequencies at the series connection with the lower load resistances of 500Ω, 4 kΩ, 20 kΩ and 40 kΩ from Figure 5.16b indicated a slight decrease compared with the parallel connection as shown in Figure 5.4b. However, the amplitudes around the resonance frequencies under the higher load resistances of 90 kΩ, 400 kΩ and 3 MΩ with the series connection tended to give a slight increase compared with the parallel connection. This indicates that when the load resistances approach the open circuit at the resonance frequency under the series connection, the amplitude of power harvesting tends to give higher values compared with the parallel connection under the same load resistances. In this case, the effect of electromechanical damping and stiffness of the bimorph under the series connection with the higher load resistances approaching open circuit indicated higher amplitudes compared with the parallel

connection at the resonance frequency. On the other hand, when the load resistances approach the short circuit at the resonance frequency under series connection, the amplitude of power harvesting tends to give lower values compared with the parallel connection under the same load resistances. In this case, the electromechanical damping and stiffness of the bimorph under the parallel connection with the load resistances approaching the short circuit indicated higher amplitudes at the resonance frequency compared with the series connection.

Another important aspect shown from the frequency response was that the open circuit resonance frequency seemed to increase compared with the parallel connection from Figure 5.6b. However, the short circuit response still tended to give very low amplitude due to very low load resistance. It should be noted that if the symmetrical pattern of power trend around the first mode for both connections was preferable, the chosen load resistances for both connections would be different values. However, in this chapter; the purpose of using similar values of load resistances from the parallel connection is to display the different pattern of power harvesting trend under the series connection. As shown in Figures 5.17a-b, the electrical power under the short and open circuit resonance frequencies with the parallel connection seemed to give the highest amplitudes with the load resistances below the transitional points of 17.9 kΩ and 358 kΩ, respectively. Conversely, the electrical power with the load resistances over transitional points of 17.9 kΩ and 358 kΩ with the series connection indicated the highest amplitude under the short and open circuit resonance frequencies.

Figure 5.16 FRFs of Electric Power with the Weak form (Solid line) and Closed form (Round dot):
a) The First three mode, b) First mode and c) Second Mode

Figure 5.17 FRFs of Electrical Power under the series and parallel connections with the Weak
form : a) Short Circuit, b) Open Circuit

### 5.3.6. Geometrical Parametric Analysis of the Bimorph for Generating Electrical Power

The optimised electrical power with the variation in bimorph geometrical parameters was analysed for the series connection. The frequency domain around the first mode was the main focus to analyse the power harvesting under varying load resistances based on the variation of the piezoelectric element thickness and length. The trend of power harvesting with series connection gave similar response with respect to the parallel connection with the same chosen load resistances. In Figure 5.18a, the power harvesting around the resonance frequency at the load resistance of 500 Ω tended to increase with the increasing bimorph length followed by the decreasing piezoelectric thickness. It was assumed that the load resistance of 500 Ω tended to give the short circuit resonance frequency where the trend of power amplitudes still indicated the lowest values compared with other load resistances. The comparison between the amplitude of power under the series and parallel connections with the same load resistance also tended to give slightly different values. The trend of power harvesting under the series connection gave lower amplitude values compared with the parallel connection when the load resistances approached the short circuit. On the other hand, the trend of power harvesting with the load resistances approaching open circuit under series connection gave higher values of amplitudes compared with the parallel connection. The reason for this behaviour was as discussed in the previous section. Other shapes of power amplitude with load resistances of 4 kΩ, 20 kΩ, 40 kΩ, 90 kΩ and 400 kΩ can be shown from Figures 5.18b-n where the mode shapes of power seemed to form the same shape but tended to give slight changes in amplitudes and different resonance frequencies.

The results of all power amplitudes for varying load resistances is shown in Figure 5.18o based on the changes to bimorph length and thickness. It should be noted that the resulting power amplitudes for each load resistance indicated a slightly different trend with the parallel connection as given in section 5.2.6. The power amplitudes from Figure 5.18p with the different resonance frequencies seemed to be close to each other under the load resistances of 20 kΩ and 90 kΩ. The trend of power amplitude FRFs from Figure 5.16a also indicated the same results of the amplitudes and the resonance frequencies with the 30.1 mm long of bimorph and 0.15 mm thick of piezoelectric layer as shown from Figures 5.6a-n. At this point, the trend of power

amplitudes under the changes of load resistance with the different geometrical bimorphs showed similar results. Once again it should be noted that power can increase by up to 100 % with correct choice of bimorph element length and thickness.
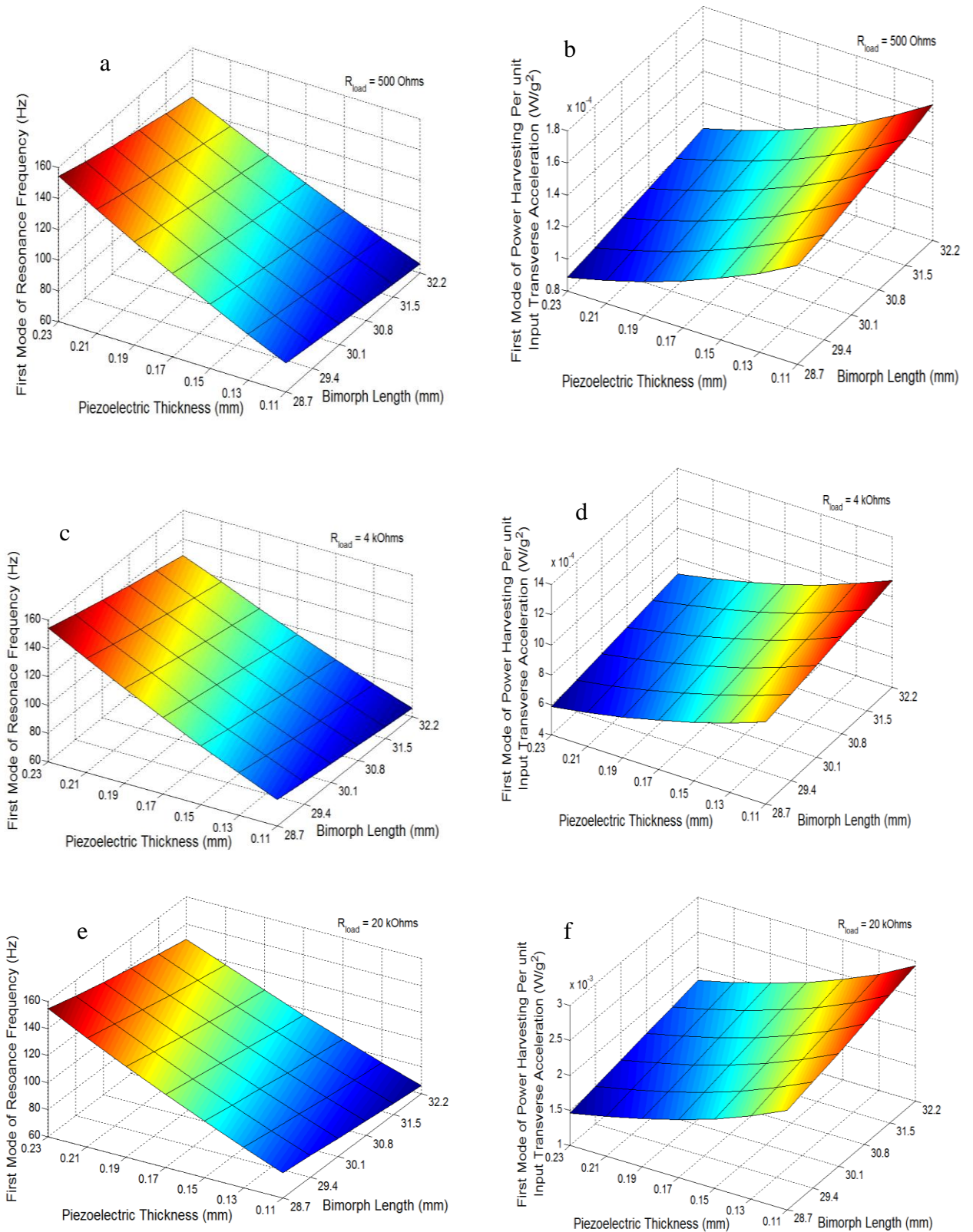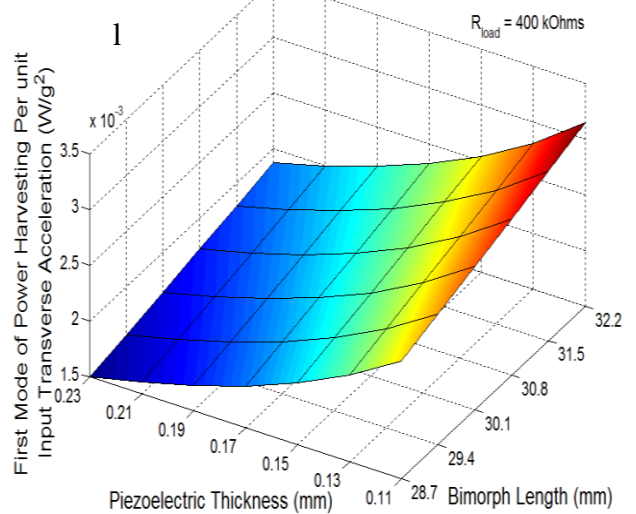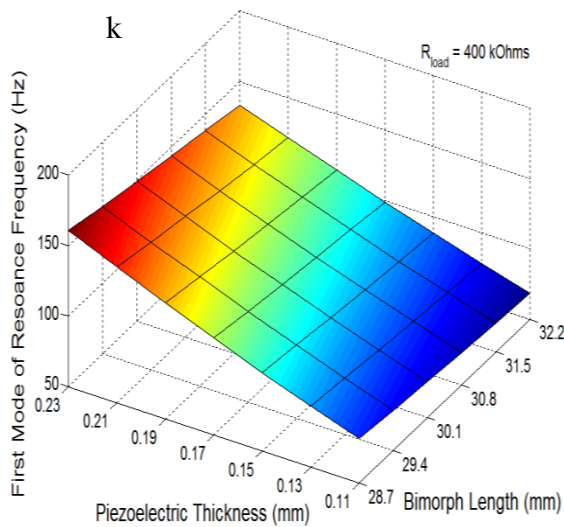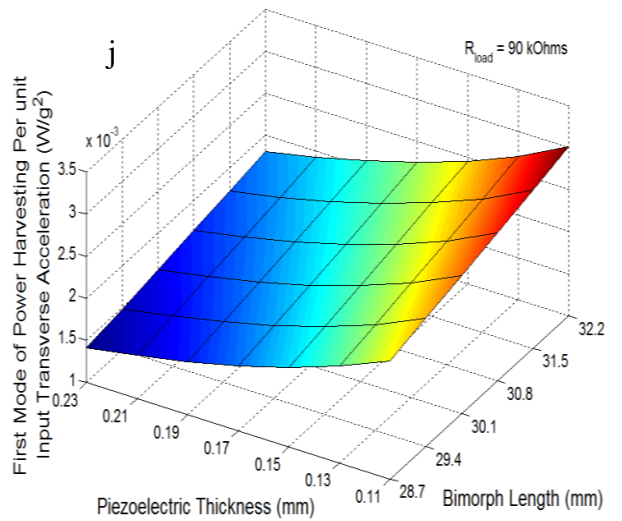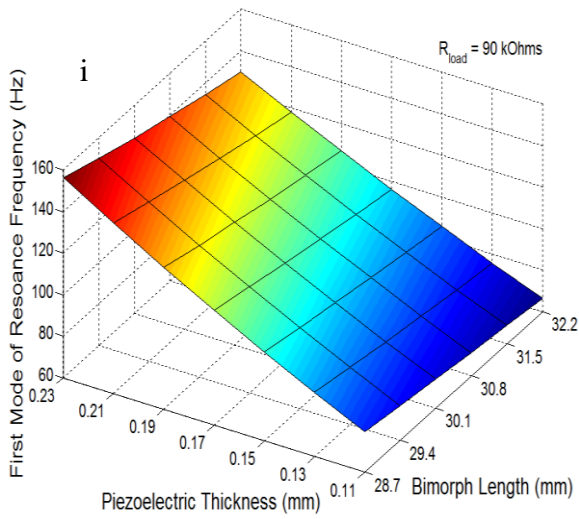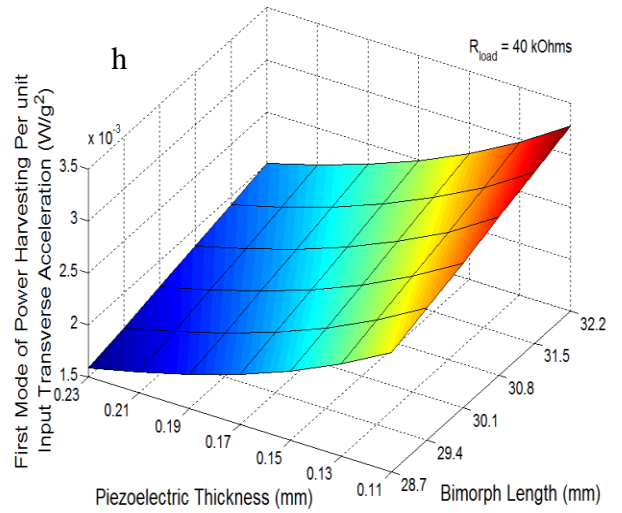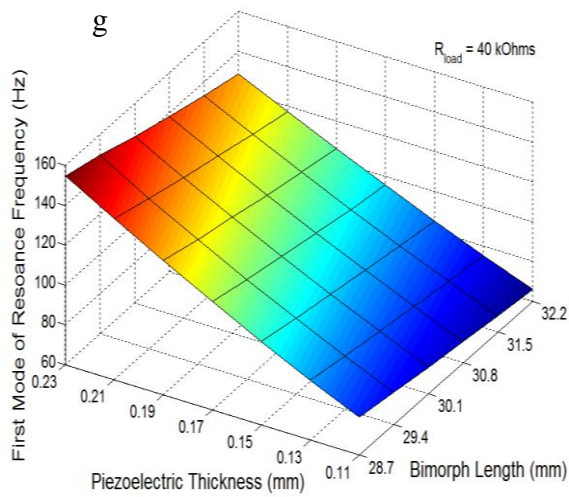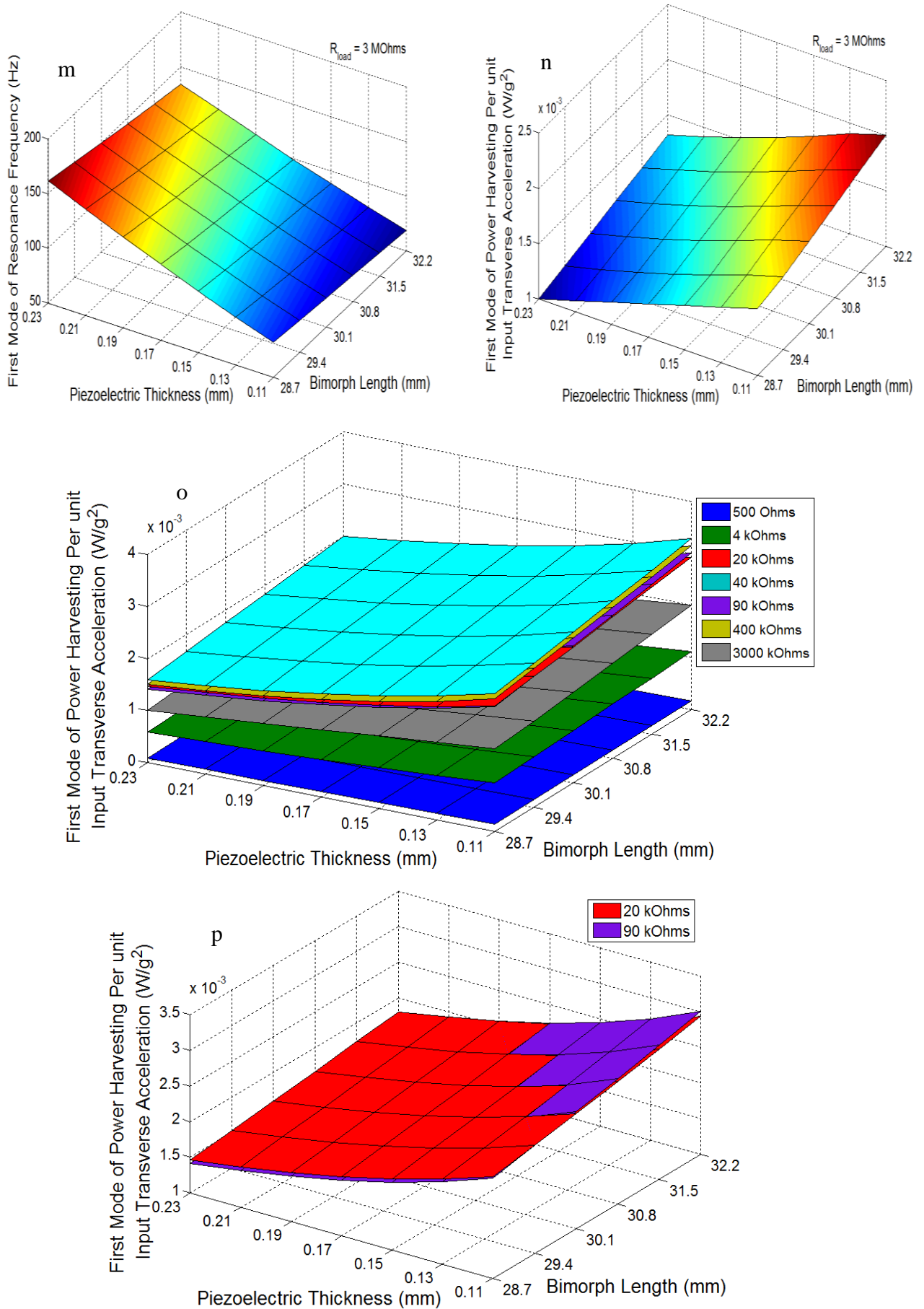
Figure 5.18 First Mode of power harvesting based on the geometrical parametric and Resonance frequency cases with the weak form: a, b) 500 Ω ; c,d) 4 kΩ ; e,f) 20 kΩ, g,h) 40 kΩ ; i, j) 90 kΩ ; k, l) 400 kΩ ; m,n) 3 MΩ ; o) Variances of load resistance ; p) combined between 20 kΩ and 90 kΩ

5.4. Multi-Electromechanical Piezoelectric Bimorph Beams

In this section, multiple bimorph beams with tip masses under series and parallel connections are discussed as a function of variable load resistance. The chosen bimorphs had varying length with constant thickness as given in Table 5.1. The example case based on CERDT model had three bimorphs with lengths of 30.1 mm, 30.8 mm and 31.5 mm to widen the frequency response at the first mode. It is noted that the results presented here were based on the formulation derived in chapter 4.7 and consist of the voltage, current and power behaviour.

5.4.1. Multi-Frequency Bimorph with Series Connection

As shown in Figure 5.19a, the first mode multi-frequency array of electrical voltage is illustrated with variable load resistance. The trend of electrical voltage amplitude varies as load resistance changes where the amplitude increases with increasing load resistance within the multi-frequency band both off-resonance and on-resonance. This behaviour showed similar trend with the single bimorph response as given previously. The maximum amplitude was dominated by bimorph one. Figure 5.19b shows the comparisons between different frequency trends for the triple, double and single bimorphs with load resistances of 500 Ω, 4 kΩ, 20 kΩ, 40 kΩ and 90 kΩ. The shifting resonance behaviour mostly occurred at bimorph one where the benefit of the triple bimorph response was the wider resonance frequency band.

Furthermore, the multi-frequency array of electrical current was also given as shown in Figure 5.20a. The amplitudes with higher load resistances tended to be close to each other where the electrical current amplitude increased with decreasing load resistance within the multi-frequency band. The electrical current with the short circuit load resistance gave the highest amplitude where the trend of electrical voltage with the short circuit load resistance conversely switched to the lowest amplitude. As can be seen from Figure 5.20b, the frequency response trends of the triple, double and single bimorphs indicated different amplitudes within the multi-frequency band. The first resonance amplitude from the single bimorph with load resistances of 500 Ω and 4 kΩ gave the higher amplitudes compared with the double and triple bimorphs. However, the first resonance frequency from the triple bimorph

with load resistances of 40 kΩ and 90 kΩ indicated the highest amplitudes. Overall, the triple bimorphs provided the expanded resonance frequency band.

Figure 5.21a shows the multi-frequency band of electrical power with variable load resistance. The resonance frequency of bimorph one with load resistance of 90 kΩ gave the highest power amplitude. However, bimorph two and three at the load resistances of 400 kΩ and 3 MΩ indicated higher amplitudes compared with load resistance of 90 kΩ. In Figure 5.21b, the trend of electrical power with single, double and triple bimorphs with load resistances of 500 Ω, 4 kΩ, 20 kΩ, 40 kΩ and 90 kΩ indicated the change of resonance amplitude power response. The single bimorph with load resistances of 500 Ω and 4 kΩ gave the highest amplitude among the double and triple bimorphs. However, the triple bimorphs not only gave an expanded resonance response frequency band but also provided the highest amplitudes with the correct chosen load resistance. For example the load resistance of 90 kΩ showed the highest amplitude as expected.
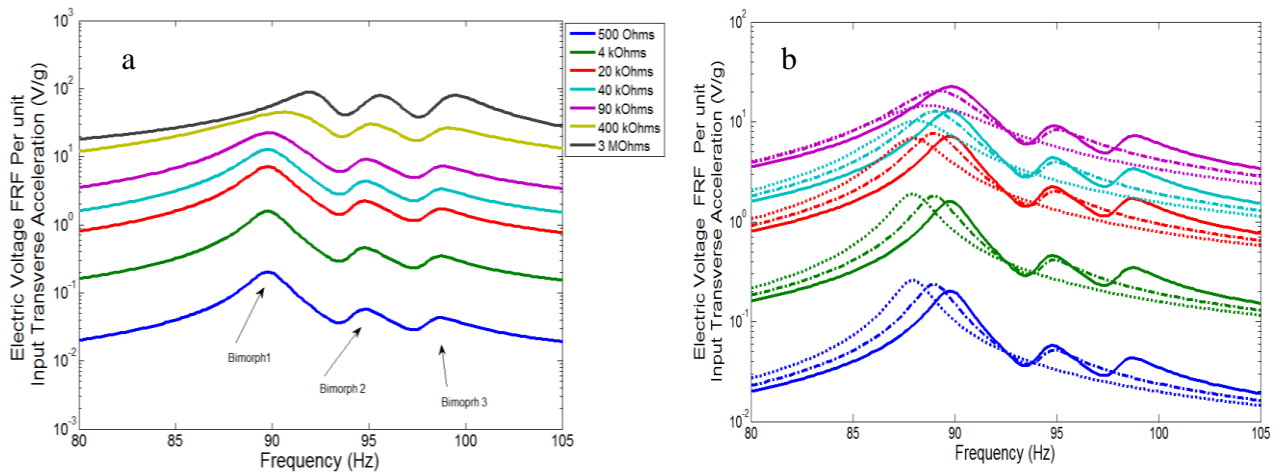

Figure 5.19 Electrical voltage FRFs : a) Three bimorphs b) Comparison with single (square dot), double (dash dot) and triple bimorphs (solid line)
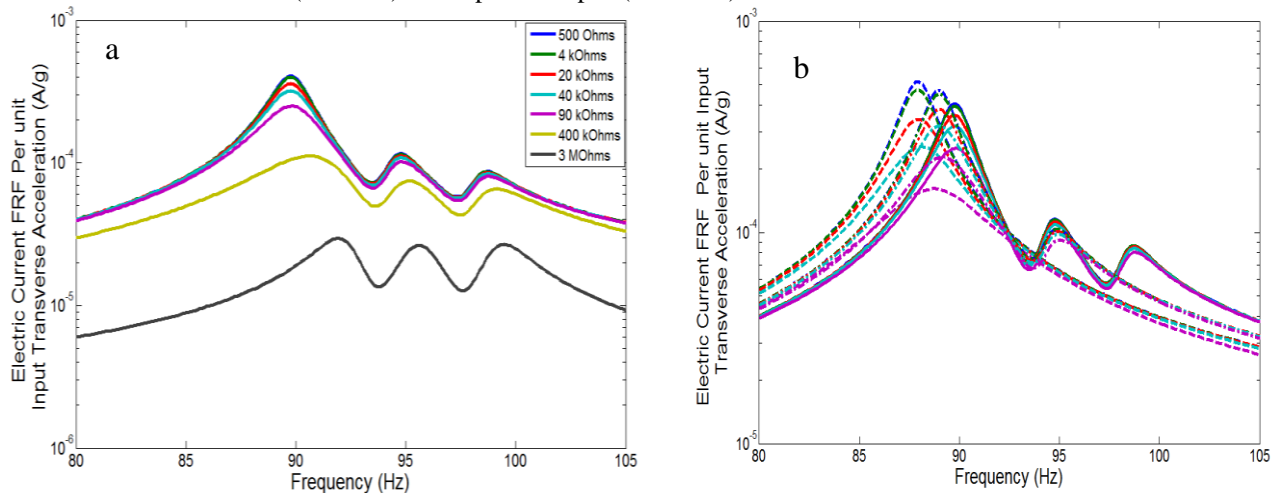

Figure 5.20 Electrical Current FRFs: a) Three bimorphs b) Comparison with single (square dot), double (dash dot) and triple bimorphs (solid line)
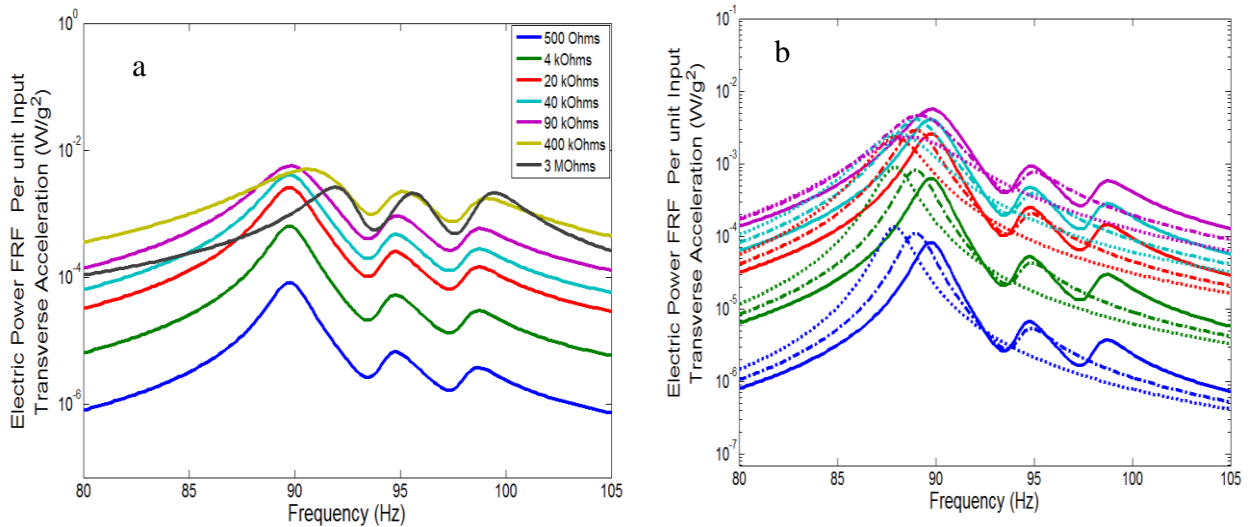
Figure 5.21 Electrical Power FRFs: a) Three bimorphs b) Comparison with single (square dot), double (dash dot) and triple bimorphs (solid line)

5.4.2. Multi-Frequency Bimorph with Parallel Connection

Figure 5.22a shows the multiple resonance frequency response of electrical voltage under variable load resistance with parallel connection. The trend of electrical voltage with parallel connection indicated a different pattern compared with the series connection where bimorph three with higher load resistances indicated the highest resonance frequency amplitude. The electrical voltage amplitude over the multi-frequency band still increased slightly with increasing load resistance. It was noted that when the load resistance was close to open circuit, the amplitude stayed constant. This behaviour was also shown for the previous case with the single bimorph. Comparison between single, double and triple bimorphs over the frequency band with the load resistances of 500 Ω, 4 kΩ, 20 kΩ, 40 kΩ and 90 kΩ are shown in Figure 5.22b. The resonance frequency of bimorph three provided the highest amplitudes of the single and double bimorphs. Overall, the voltage amplitudes from the triple bimorph gave a broadened multi-frequency band where the single bimorph just provided the single frequency at the first mode.

As shown in Figure 5.23a, the multi-frequency response of electrical current varied based on the varying load resistance. The trend of electrical current was different with that found with the electrical voltage. The electrical current amplitude for both parallel and series connections increased with increasing load resistance. However, the trend of electrical current between parallel and series connections indicated a

slight change. The bimorph three amplitude from parallel connection increased slightly, compared to that from bimorph one from series connection where a significant increase was observed. Figure 5.23b shows comparison between single, double and triple bimorphs over the frequency band with load resistances of 500 Ω, 4 kΩ, 20 kΩ, 40 kΩ and 90 kΩ. It was found that the triple bimorph seemed to indicate the highest amplitude and widened the resonance frequency band as expected.

As shown in Figure 5.24a the multi-frequency response of electrical power was modelled with variable load resistance. The resonance frequency of bimorph three with load resistance of 40 kΩ was close to that with 90 kΩ, where the highest amplitude was achieved with load resistance of 40 kΩ. However, by analysing the response from bimorph one and two, the resonance frequency amplitudes with load resistance of 40 kΩ seemed to drop slightly below that found with resistance of 20 kΩ where the resonance amplitude at load resistance of 4 kΩ gave the highest amplitude followed by the load resistance of 20 kΩ. Moreover, Figure 5.24b shows the trend of electrical power with single, double and triple bimorphs with load resistances of 500 Ω, 4 kΩ, 20 kΩ, 40 kΩ and 90 kΩ. It can be seen that the triple bimorphs indicated higher amplitudes over an expanded frequency band under variable load resistance compared with that obtained using only single and double bimorphs.
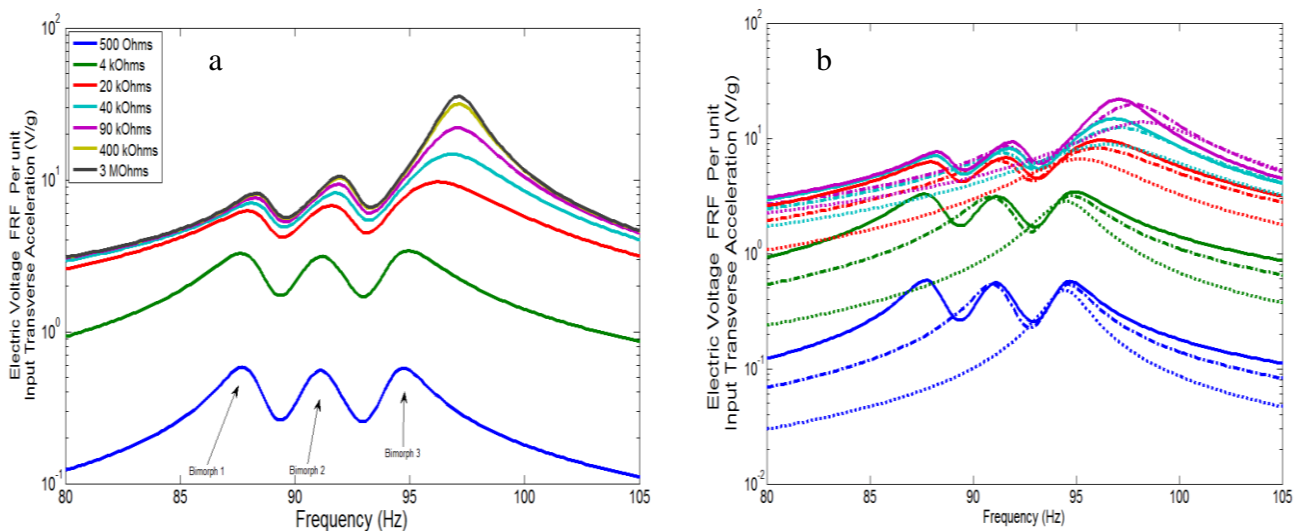

Figure 5.22 Electrical voltage FRFs: a) Three bimorphs b) Comparison with single (square dot), double (dash dot) and triple bimorphs (solid line)
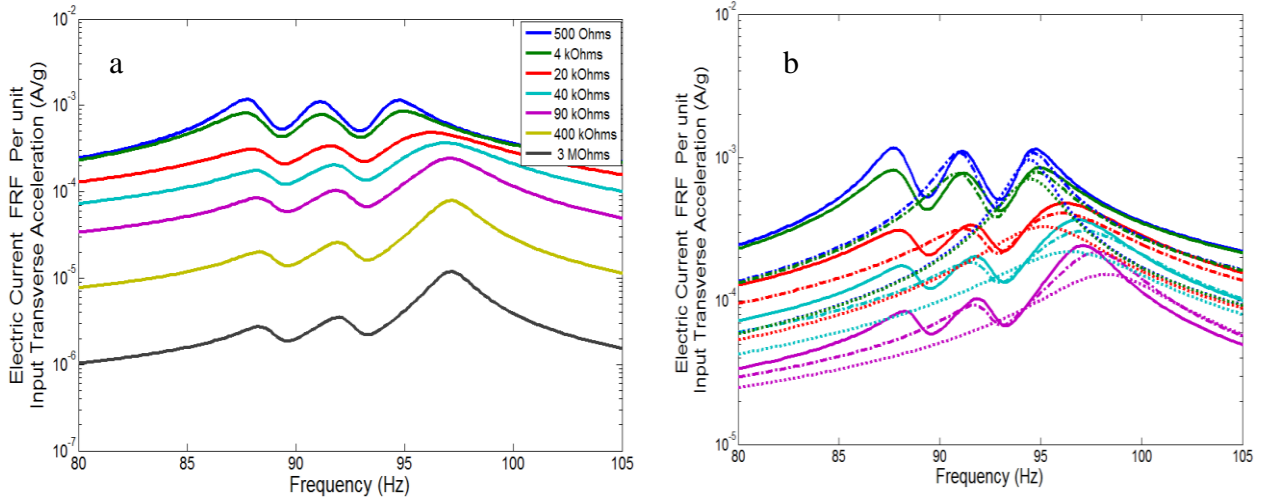
Figure 5.23 Electrical current FRFs : a) Three bimorphs b) Comparison with single (square dot), double (dash dot) and triple bimorphs (solid line)
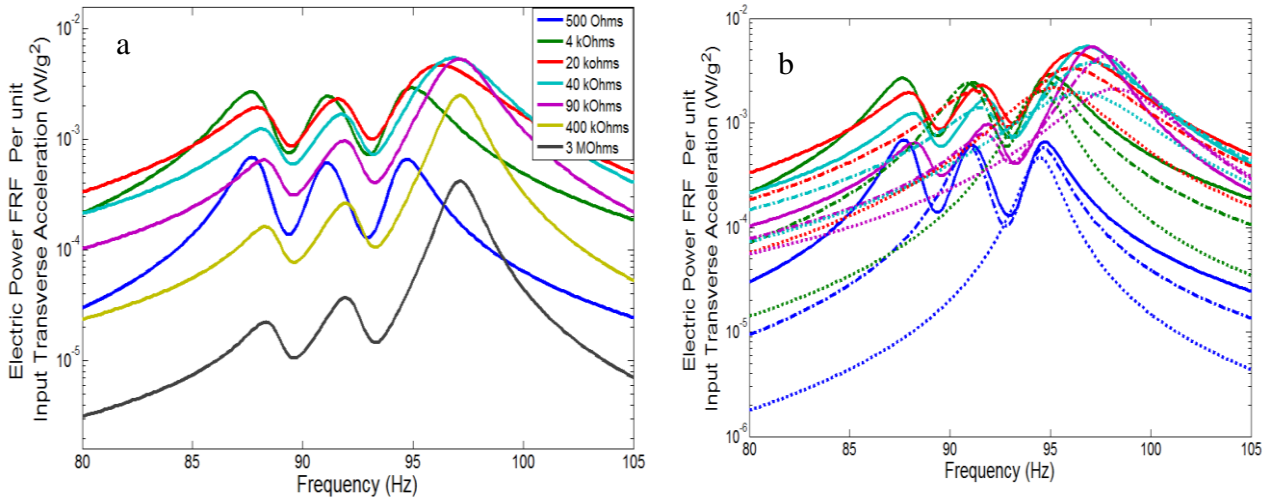

Figure 5.24 Electrical power FRFs : a) Three bimorphs b) Comparison with single (square dot), double (dash dot) and triple bimorphs (solid line)

5.5. Closing Remark

In this chapter, the multi-mode FRFs of the electromechanical dynamic responses under varying load resistances was discussed according to the weak and closed forms of the CEDRTL. The analysis of FRFs of the bimorph under the series and parallel connections consisted of the tip absolute dynamic displacement, tip absolute velocity, electrical current, electrical voltage, power harvesting and geometrical parametric bimorph analysis. The effect of changing load resistance was seen to shift the resonance frequencies from the short to open circuit for all of the FRFs of the bimorph. This indicated that the load resistance can be viewed as resistive shunt damping of the bimorph connection as it was clearly implied within

the electromechanical dynamic equation derived in chapter 4. The FRFs of the bimorph under parallel and series connections with the same load resistances did not necessary give monotonic trends. The trend of FRFs around the first mode for the dynamic displacement, velocity and electrical power displayed the symmetrical pattern with the chosen load resistances as indicated in the example from the parallel connection responses.

It was found that the chosen load resistances for the series and parallel connections would have different values if the symmetrical pattern of power frequency response for both connections was preferable. On the other hand, once the symmetrical pattern was given for one of the connection types of bimorph, the other connection with the same load resistance indicated an unsymmetrical frequency response. In this chapter, the load resistances under the series and parallel connections used the same values. Apart from that, the trend of velocity amplitude with the load resistance approaching short circuit seemed to increase where the voltage amplitude decreased with the increasing electrical current for both connection types. Conversely, the velocity amplitude with the load resistance approaching open circuit tended to increase where the voltage amplitude increased with the decreasing electrical current.

Moreover, when the load resistance went to the higher transitional point (approaching open circuit) under the series connection, the amplitudes of the electrical voltage, current and power tended to give higher amplitudes compared with the parallel connection under the same load resistances. This indicated that the effect of electromechanical damping and stiffness of the bimorph under the series connection with the higher load resistances approaching open circuit provided the highest amplitudes at the resonance frequency compared with the parallel connection. On the other hand, when the load resistances went to the lower transitional point (approaching short circuit) under the series connection, the FRF of the electrical voltage, current and power tended to give lower amplitudes compared with the parallel connection under the same load resistances. In this case, the effect of electromechanical damping and stiffness of the bimorph under parallel connection with the higher load resistances approaching short circuit provided the highest amplitude at the resonance frequency compared with the series connection. Moreover, by comparing the maximum levels of voltage and current amplitudes

versus varying load resistances, the maximum electrical current would be compatible with the parallel connection whereas the maximum electrical voltage would be compatible with the series connection. Finally, the results from changing the bimorph length and thickness indicated options for maximising the shape of the power response with variable load resistance. The results of power amplitudes FRFs from both connections with the same load resistances did not always give monotonic trends. The multi-electromechanical bimorph beam with the series and parallel connections was also given under variable load resistance. A three bimorph model was given as an example case, where the trend of electrical voltage, current and power for both electrical connections showed different pattern trends. The multi-bimorph system can widen the resonance frequency band and also increase the amplitude based on the correct chosen load resistance, compared with the single or double bimorphs, providing significantly more power.

CHAPTER

6

Piezoelectric Bimorph Analytical and Experimental Electromechanical Dynamic Responses

In this chapter, the analytical and experimental comparisons of the piezoelectric bimorph electromechanical dynamic responses are presented with and without the tip masses. The electromechanical dynamic response validation involved the CEDRT (coupling electromechanical dynamic response of the transverse form), CEDRTL (coupling electromechanical dynamic response of the transverse-longitudinal form) and experimental studies. The theoretical studies (CEDRT and CEDRTL) were based on the weak form of Hamiltonian's principle (electromechanical analytic approach with normalised Ritz method) for comparison with the experimental study. The closed form or distributed parameter method (electromechanical analytic method reduced from the strong form of Hamiltonian's principle) was not applied here because the validations between the weak and closed forms have been compared with very good agreement as discussed in the previous chapter. In the forthcoming sections, the frequency response functions (FRFs) of the bimorph under the input base transverse acceleration were validated using the tip absolute dynamic displacement, velocity, electrical voltage, current and power harvesting. In addition, the FRFs of the bimorph with the tip mass under the two input base accelerations of transverse and longitudinal are discussed to give the polar dynamic displacement, velocity, voltage, current and power harvesting.

6.1. The Properties of the Piezoelectric Bimorph and Experimental Setup

The material properties and geometrical structure are essential aspects for analysing the cantilevered piezoelectric bimorph beam. The list of properties of the bimorph used in this investigation is given in Table 6.1 where the piezoelectric bimorph properties were based on the PZT PSI-5A4E element from Piezo Systems,

INC. with the centre brass shim. The effect of rotary inertia of the bimorph was ignored because the Euler-Bernoulli beam model was considered in this chapter. A proof mass and its rotary inertia located on the tip of the bimorph were also considered, including its geometry and material properties which were made from steel. The Euler-Bernoulli beam was a typical thin structure model with the appropriate application for power harvesting. The geometry of the tip mass was relatively small as shown in Figure 6.1. The zero-th mass moment of inertia of the tip mass can be formulated as,

$$I_{tip}^{(A)} = \left(h_{tip} l_{tip} - \left(2h_p + h_s \right) l_o \right) s_{tip} \rho_{tip}^{(A)} \qquad . \tag{1}$$

The second mass moment of inertia, known as the rotary inertia at the centre of gravity of the tip mass coincident with the end of the piezoelectric bimorph beam can be formulated as,

$$I_{tip}^{(C)} = \left\{ \left(\frac{\left(l_{tip}^2 + h_{tip}^2 \right)}{12} + \bar{x}_1^2 - \frac{\left(\left(2h_p + h_s \right)^2 + l_o^2 \right)}{12} - \bar{x}_2^2 \right) \left(l_{tip} h_{tip} - \left(2h_p + h_s \right) l_o \right) \right\} s_{tip} \rho_{tip}^{(C)} , \tag{2}$$

where $\bar{x}_1 = x_g - l_{tip}/2$, $\bar{x}_2 = x_g - l_o/2$. Other coefficients x_g, s_{tip}, h_{tip} and l_{tip} indicate the centre of gravity, width, height and length of geometry of the tip mass. The cantilevered piezoelectric bimorph beam with the tip mass was clamped at the protractor base structure for input base excitation. The B & K impedance head type 8001, connected to the B & K Charge Amplifier Type 2635, was used to measure the input acceleration from the B & K exciter type 4809. Since the generating vibration signal amplitude needs to be regulated, the exciter was connected to B & K Power Amplifier Type 2706. Moreover, the wave function generator, connected to the Power Amplifier, was used to set specific harmonic input excitation. The vibration of the tip mass located at the end of the bimorph was measured using a laser digital vibrometer Polytec PDV 100 by attaching a small reflector tape onto the tip mass to measure the absolute dynamic displacement, velocity and frequency responses. All signal measurements from the charge amplifier, piezoelectric bimorph and vibrometer were connected to the B & K FFT pulse Analyzer 3560B. The processing signal through the Analyzer displayed the measurement results using the FFT pulse and MATLAB software. The complete experimental setup is shown in Figure 6.2.

Table 6.1 Characteristic properties of the piezoelectric bimorph system.

Material properties	Piezoelectric	Brass	Geometry properties	Piezoelectric	Brass
Young's modulus , $\overline{Q}_{11}$ (GPa)	66	105	Length , L (mm)	30.1	30.1
Density, ρ (kg/m^3)	7800	9000	Thickness, h (mm)	0.19 (each)	0.13
Piezoelectric constant, d_{31} (pm/V)	-190	-	Width, b (mm)	6.4	6.4
Permittivity, ς_{33}^{T} (F/m)	1800 ς_o	-	First coefficient $I_{tip}^{(A)}$ (kg)†	0.0022	
permittivity of free space, ς_o (pF/m)	8.854	-	Third coefficient $I_{tip}^{(C)}$ (kg m^2)†	7.3743×10^{-9}	

† Calculated according to the geometry and material properties of tip mass and the rotary inertia at centre of gravity of tip mass

coincident with the end of the bimorph length as shown in Figure 6.1 where $l_{tip} = 8.1\,mm, h_{tip} = 5.7\,mm$, $l_o = 5\,mm$ and $s_{tip} = 6.4\,mm$ (width). First

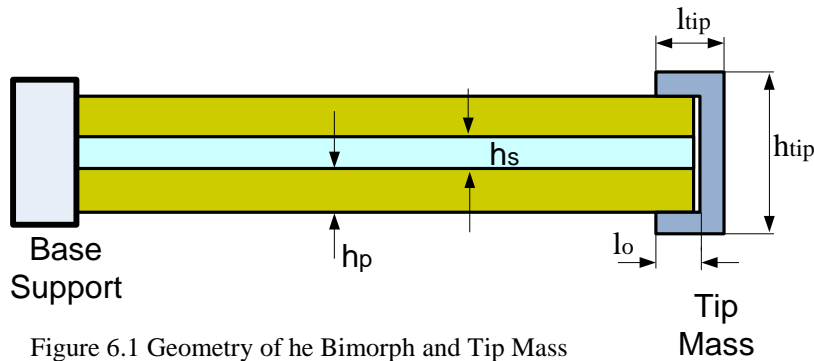and third coefficients refer to zeroth and second mass moment of inertias of tip mass respectively.
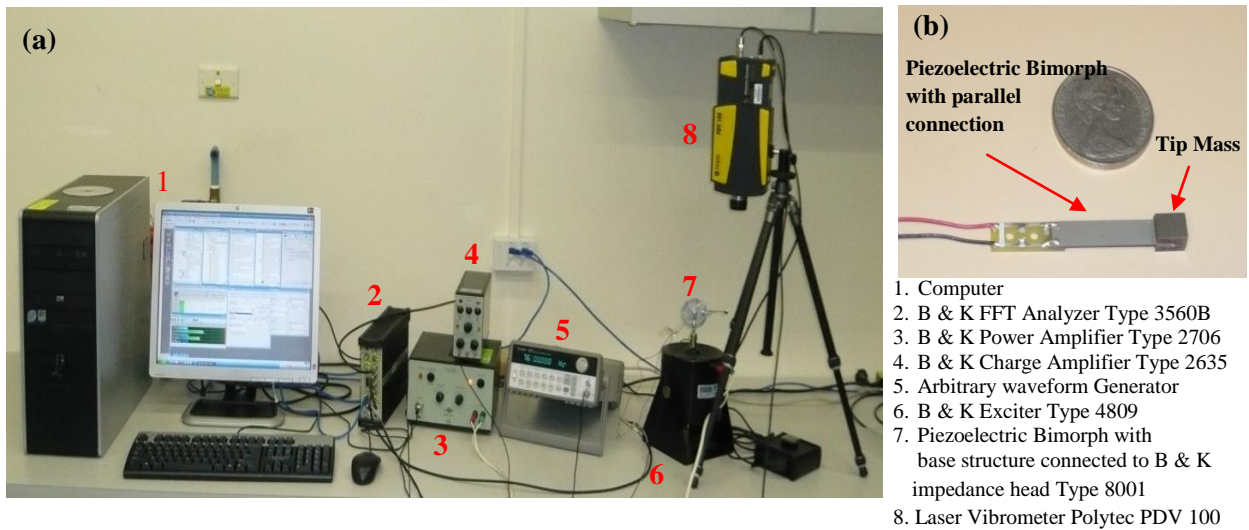

Figure 6.1 Geometry of he Bimorph and Tip Mass

1. Computer
2. B & K FFT Analyzer Type 3560B
3. B & K Power Amplifier Type 2706
4. B & K Charge Amplifier Type 2635
5. Arbitrary waveform Generator
6. B & K Exciter Type 4809
7. Piezoelectric Bimorph with base structure connected to B & K impedance head Type 8001
8. Laser Vibrometer Polytec PDV 100

Figure 6.2 (a) Experimental Setup and (b) Piezoelectric bimorph beam with tip mass under parallel connection

6.2. Electromechanical Dynamic Response of Piezoelectric Bimorph with a Tip Mass

In this section, the FRFs of the electromechanical piezoelectric bimorph with a tip mass will be discussed as the load resistance varies. In the next section, the analysis of the electromechanical dynamic response was based on the derivation of FRFs as provided in chapter 4. The numerical methods, (CEDRTL and CEDRT) were validated here against the experimental results. The piezoelectric bimorph beam

was modelled here using the parallel connection. The input transverse base acceleration of the bimorph was considered to give the multi-output electromechanical dynamic response. The properties of the bimorph and geometrical tip mass were also based on the characteristic data given in the previous section. At this point, the mechanical damping ratios and load resistances need to be determined.

6.2.1. FRFs of Bimorph Tip Absolute Dynamic Displacement

In this section, the trend of the first mode of the tip absolute dynamic displacement FRF was investigated with changing resistance of 560 Ω, 5.6 kΩ, 20 kΩ, 30 kΩ, 51 kΩ, 60 kΩ, 79 kΩ, 150 kΩ, 200 kΩ and 602 kΩ. As discussed previously, the effect of the input base transverse acceleration on the bimorph will result in dynamic inertia forces due to the products of generalised mode shape displacement fields with the bimorph mass, lumped tip mass and rotary inertia of the tip mass. This can be used to obtain the generalised time dependent dynamic response along the length of the bimorph to give the relative dynamic displacement. In this case, the absolute dynamic displacement (considered as the total dynamic displacement) can also be obtained due to the input base dynamic inertia force and the relative dynamic displacement. The bimorph input base transverse acceleration was chosen to be 3 m/s^2 which is equivalent to 306 mg (1 g = gravitational acceleration 9.81 m/s^2). To analyse the tip absolute dynamic displacement on the end of the bimorph, equation (4.279c) in chapter 4 can be used by inserting the variable x = L for the tip end of the bimorph. The results obtained were validated with an experimental study using a Laser Doppler Vibrometer (LDV) that measured the velocity of the centre of the tip mass coincident with the end of the bimorph as shown in Figure 6.2.

In the previous chapter, the mechanical damping ratios were chosen theoretically. At this stage, the mechanical damping ratios were determined experimentally using a short circuit load resistance of 560 Ω. The mechanical damping ratios were identified by matching the amplitude of experimental and theoretical tip absolute displacement or velocity FRF. The physical reason for choosing damping ratios under very low load resistance was to minimise the amplitude of electrical voltage FRF generated from the piezoelectric bimorph in order to approach a pure mechanical form, since mechanical damping itself was viewed as mechanical resistance behaviour due to

energy losses during vibration of piezoelectric bimorph. Theoretically, the energy losses can be from strain-rate (Kelvin-Voigt) and external air (viscous) damping effects. However, in the experimental study, only one damping ratio can be measured from the FRF without specifying the strain-rate and viscous damping effects. Moreover, once the mechanical damping ratios were determined, other FRF model with varying electrical load resistances can be plotted. The damping ratios for the transverse and longitudinal forms around the fundamental resonant frequency were found to be $\zeta_1^w = 0.0139$ and $\zeta_1^u = 0.030$. These values should not be confused with the electromechanical damping effect due to the piezoelectric coupling as discussed in the previous chapter. The transverse behaviour of the electromechanical system response was known to be dominant at the lower frequency domain (first resonance). The effect of the longitudinal system response was also considered here from the initial strain field, contributing to the frequency response, but only with small effect. Figure 6.3 shows the resulting frequency response with variable load resistance. At some cases, the effect of longitudinal extension at the frequency domain can be ignored with lower load resistances (500 Ω, 5.6 kΩ, 20 kΩ and 30 kΩ) because the CERDT and CERDTL tended to overlap each other. However, for higher load resistances (51 kΩ, 60 kΩ, 79 kΩ, 150 kΩ, 200 kΩ and 602 kΩ), the effect of longitudinal extension seemed to be more pronounced, especially at load resistance of 602 kΩ with the maximum percentage difference between the CEDRTL and CEDRT of 16.4 %. Moreover, the FRFs of tip absolute transverse dynamic displacement with variable load resistance under the CEDRTL model seemed to be close with the experimental results as given in Figure 6.4, where the longitudinal strain-polarity field for the electromechanical dynamic response was also included here for the low frequency domain. When the actual bimorph dynamic response is considered for industrial applications, these results show that the longitudinal response could be included in the strain-polarity field along with the bending response.

It should be noted from Figures 6.3 and 6.4 that the first resonance frequency shifts along the frequency domain with varying load resistances. When the load resistance tended toward short circuit at the frequency of 76.1 Hz, the amplitude tended to give the highest value. Similar behaviour was also found at the open circuit response at frequency of 79.6 Hz. This indicated that the effect of the lowest and highest load

resistances of 560 Ω and 602 kΩ on the bimorph tended to reduce the sensitivity of the electrical form around the resonance frequency region. This indicates that the system is dominated by the pure mechanical response of the bimorph with the electrical response for the short and open circuits showing the highest amplitudes as discussed in the forthcoming section. Obviously, the effect of mechanical damping ratio can be viewed as a constant value once the experimental result was taken and matched to the theoretical study. Moreover, the effect of piezoelectric coupling can further create electromechanical damping and these can also be viewed as constant values. In such situations, the damping effects encompassed both the mechanical and electrical forms from the electromechanical bimorph responses when the dimensional structure and material properties were kept constant. By considering the damping effect of the bimorph under dynamic response, the load resistance connected to the bimorph appeared to act as electromechanical attenuation and amplification of the amplitude across the frequency domain. In the next section, the electrical voltage frequency response with varying load resistances can be viewed, showing the dynamic amplification behaviour where the increase of load resistance can increase the amplitude of voltage with increasing resonance frequency. However, the electrical current frequency response with varying load resistances shows the electromechanical attenuation behaviour with increase of load resistance resulting in a decrease of current with the increase of resonance frequency. Again, the validations between the analytical and experimental results were achieved with good agreement. Four samples of the individual trend of tip absolute displacement were also given as shown in Figure 6.5. Moreover, the experimental findings show that the maximum tip absolute displacement tended to give the lowest and highest electrical voltage for the short and open circuits, respectively. Conversely, the maximum tip absolute displacement tended to give the highest and lowest electrical current for short and open circuits, respectively. This shows that the maximum dynamic displacement does not necessarily result in the highest current or voltage. Beside, both of these circuits (short and open) were found to give the lowest power harvesting. In many cases of vibration, the maximum dynamic displacement is generally avoided for most structures. It should be noted here that the power harvesting can be determined to give the best results without having the maximum displacement and minimum current or voltage. This situation can easily be shown at the intermediate point of displacement trend around 60 kΩ as shown in Figure 6.4 where the amplitude of

displacement at this load resistance showed the lowest value but also gave convenient amplitudes for the electrical current, voltage and optimal power harvesting across the frequency range as discussed in the forthcoming section. Figure 6.6 shows the tip transverse displacement of the experimental and CEDRTL model at the short and open circuit resonance frequencies of 76.1 and 79.6 Hz. The results show the tip displacement response at these two frequencies while the load resistance subsequently changes. In Figure 6.6, the tip displacement from the CEDRTL model indicated good agreement with the experimental results where the trend of the highest amplitudes under the short circuit was achieved at the lower load resistance, shown conversely with the open circuit result.
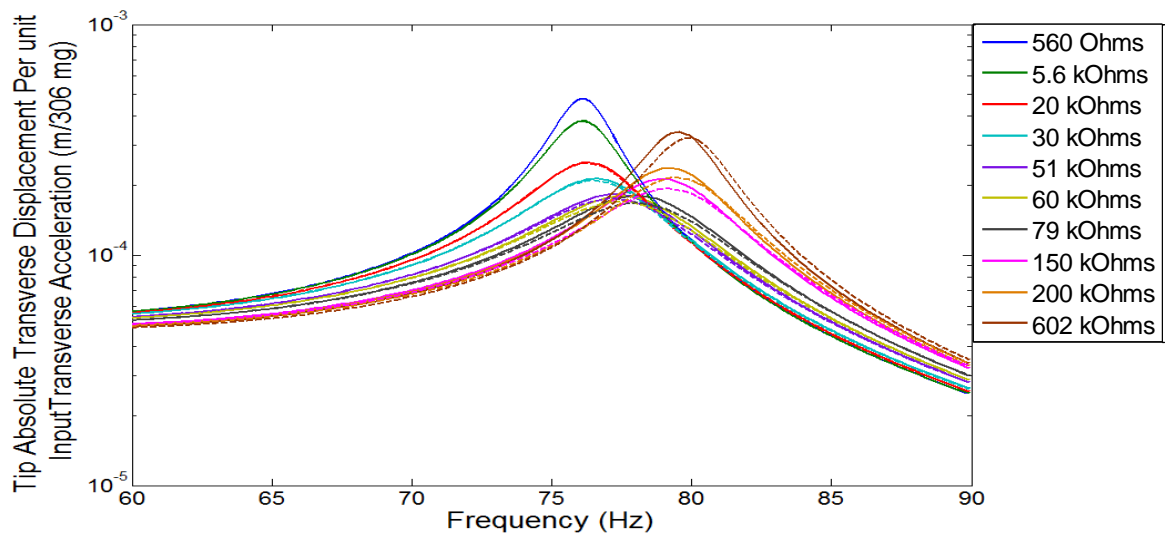
Figure 6.3 FRFs of tip absolute Dynamic Displacement with the CEDRTL (Solid line) and CEDRT (Dash line)
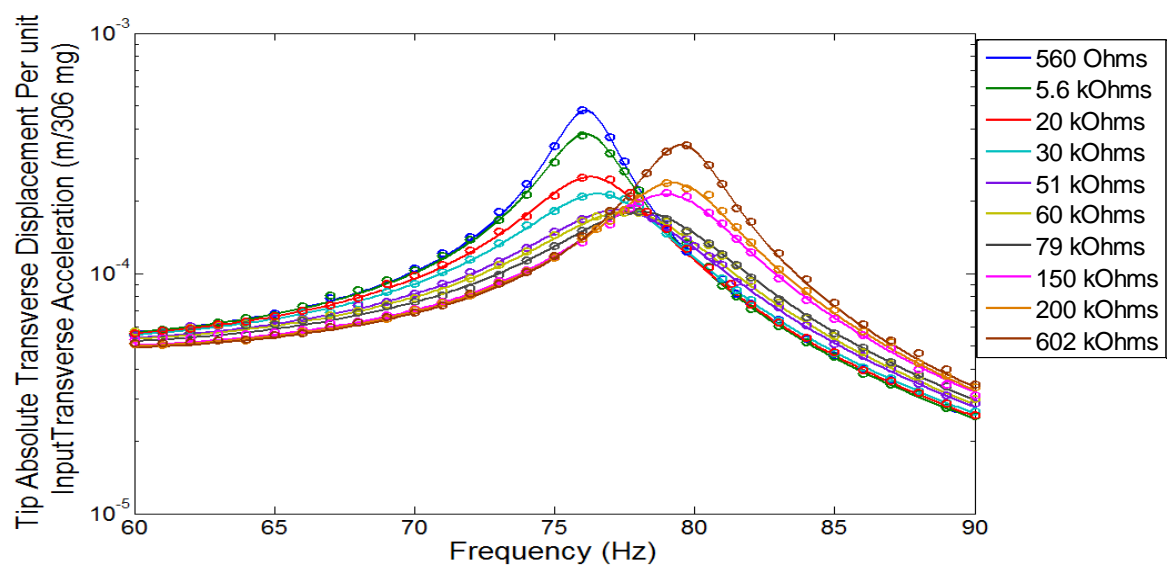
Figure 6.4 FRFs of tip absolute Dynamic Displacement with the CEDRTL (Solid line) and Experiment (Round dot)
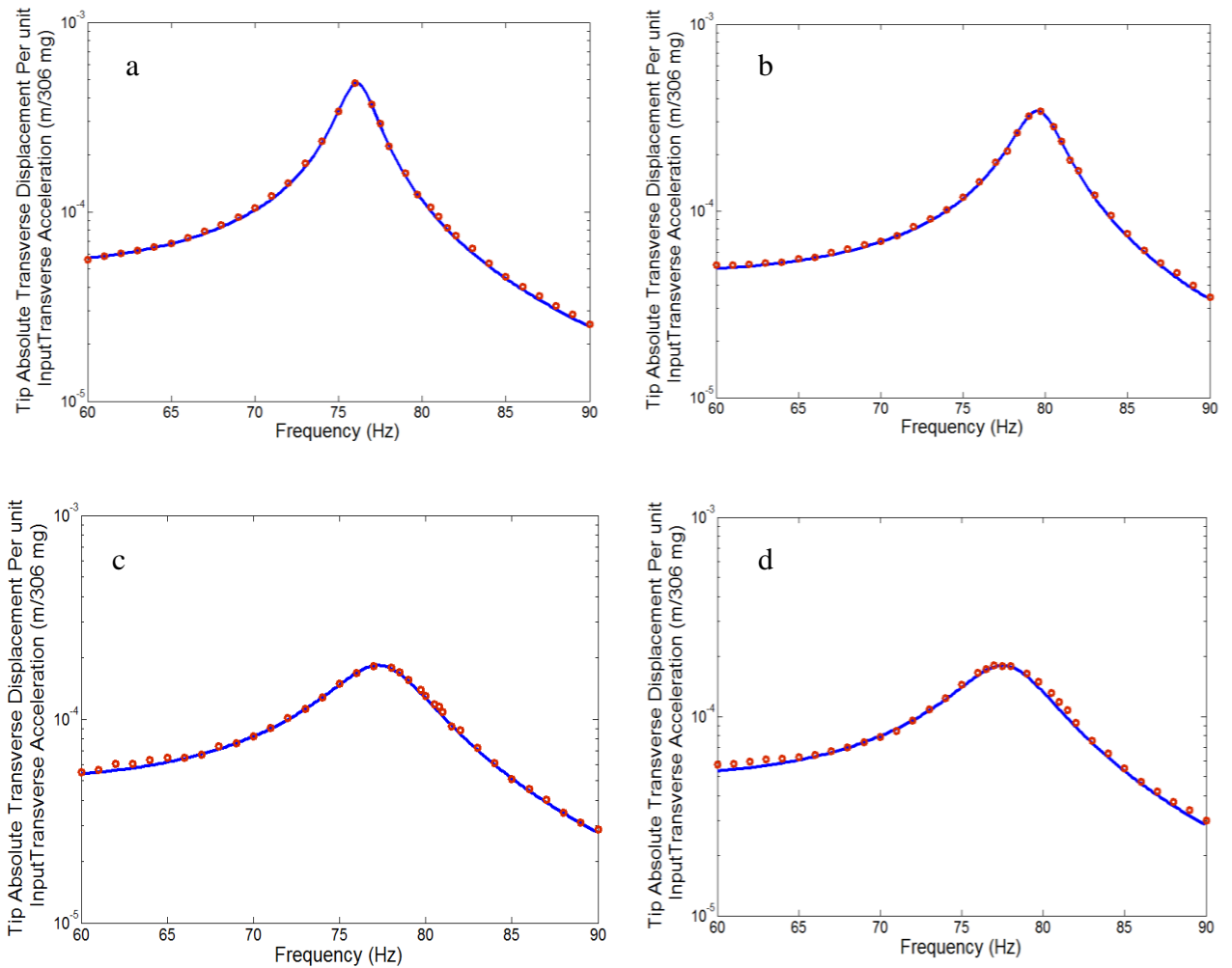
Figure 6.5 FRFs of tip absolute Dynamic Displacement with the CEDRTL (Solid line) and Experiment (Round dot) : 560 Ω , b) 602 kΩ , c) 51 kΩ and d) 60 kΩ
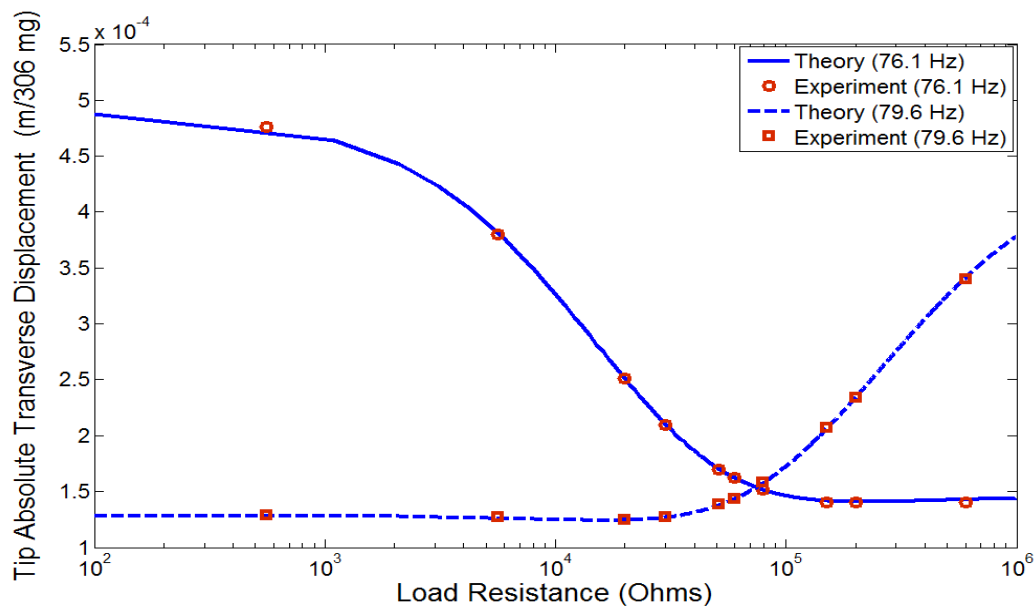

Figure 6.6 Tip absolute Dynamic Displacement with the CEDRTL versus Load Resistance under the Short circuit Resonance Frequency of 76.1 Hz and Open Circuit Resonance Frequency of 79.6 Hz

6.2.2. FRF of Bimorph Tip Absolute Dynamic Velocity

The first mode FRF of the tip absolute velocity of the cantilevered piezoelectric bimorph under parallel connection is shown here with varying load resistance. As can be seen in Figure 6.7, the trend of FRFs tip velocity using the CEDRTL and CEDRT models under varying load resistance is compared and the results showed good agreement except for the higher resistance results. The trends show the clear significance of incorporating the longitudinal form in the dynamic coupled behaviour. As mentioned previously, the contribution of longitudinal form not only affected the strain field but also the piezoelectric coupling. At this point, the use of the CEDRTL model was considered as the generalised base motion under multi-input vibration. The CEDRTL and CEDRT model results with the lower resistances seemed to overlap each other. However, the differences of the CEDRTL and CEDRT model results with the higher load resistances became more pronounced, especially at 602 kΩ with the maximum percentage difference of 16.7 %. Moreover, very good agreement between the CEDRTL and the experimental results was observed under varying load resistance as shown in Figure 6.8, with the individual trend of dynamic velocity also found in Figure 6.10. The result as shown in Figure 6.8 gave similar frequency response to that shown in Figure 6.4. It should be noted here that the effect of load resistance on the piezoelectric bimorph can be viewed as resistive shunt damping effect resulting in shifting of the resonant frequency with different amplitudes as shown clearly in Figure 6.9.

The contribution of load resistance into the electromechanical dynamic equations can also be viewed as the electrical stiffness equivalent. This provides one reason that the frequency trend increases from the short to open circuit result. The resonance frequency of 76.1 Hz for short circuit and 79.6 Hz for open circuit with the load resistances of 560 Ω and 602 kΩ, respectively gave high velocity amplitudes of 0.23 m/(s. 306 mg) and 0.17 m/(s. 306 mg), respectively. Moreover, the absolute velocity at the bimorph tip with the load resistances of 51 kΩ and 60 kΩ from Figure 6.10 indicated amplitudes of 0.089 m/(s.306 mg) at a resonance of 77.51 Hz and 0.087 m/(s.306 mg) at a resonance of 77.83 Hz, respectively. As shown in Figure 6.11, the tip absolute transverse velocity under the short and open circuit resonance frequencies seemed to have similar trend pattern with the transverse tip absolute displacement. The maximum amplitudes of the short circuit resonance was reached

with the load resistance approaching the lower load resistance whereas the open circuit resonance gave the maximum amplitude with the load resistance approaching the highest load resistance. Therefore, the short and open circuit resonances were found to give the higher velocity amplitude with the lower and higher load resistances (short and open circuit load resistances), respectively.
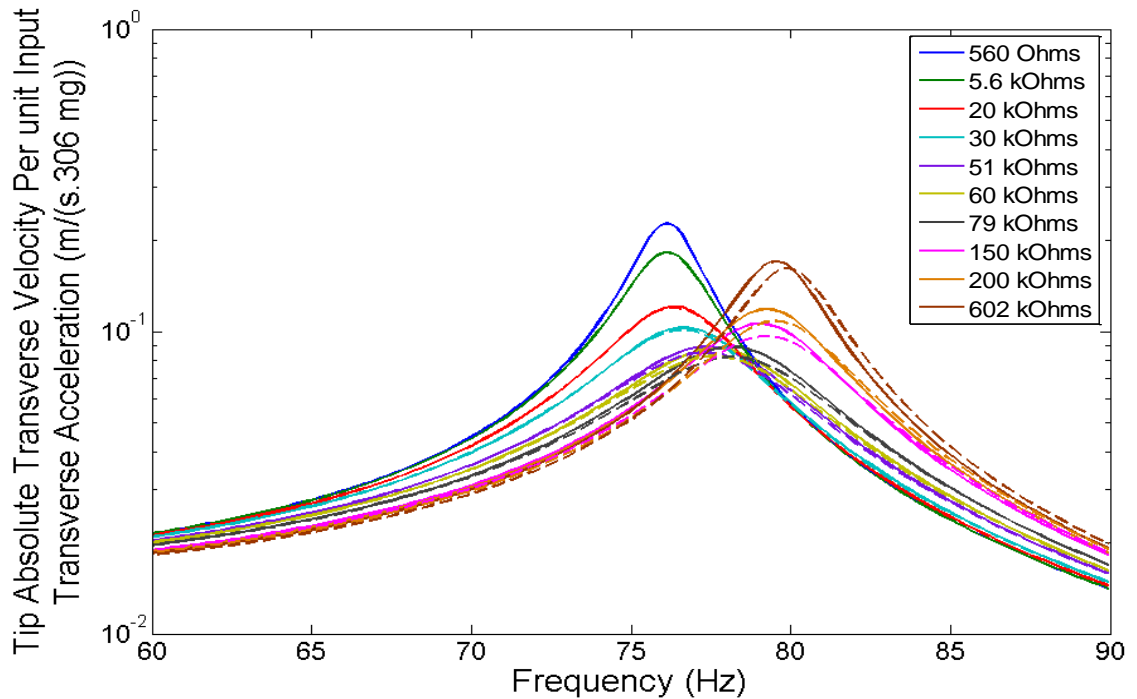

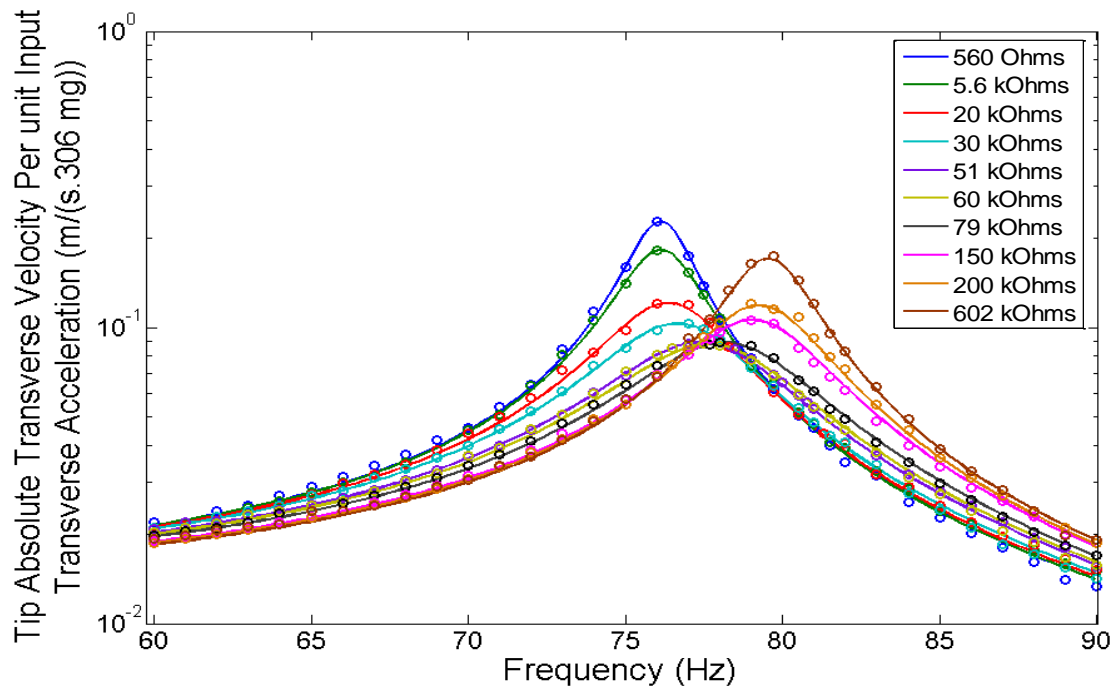Figure 6.7 FRFs of tip absolute Dynamic Velocity with the CEDRTL (Solid line) and CEDRT (Dash line)

Figure 6.8 FRFs of tip absolute Dynamic Velocity with the CEDRTL (Solid line) and Experiment (Round dot)
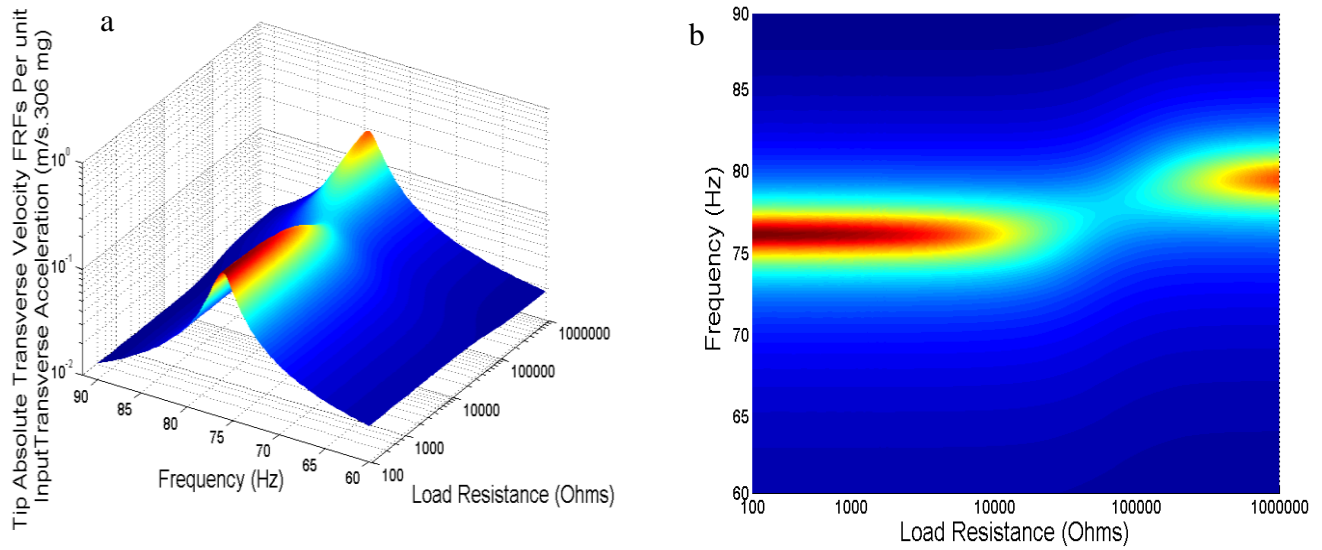
Figure 6.9 FRFs of tip absolute Dynamic Velocity: a) Amplitude Vs Frequency and Load resistance, b) Amplitude Pattern based on: Frequency Vs Load resistance
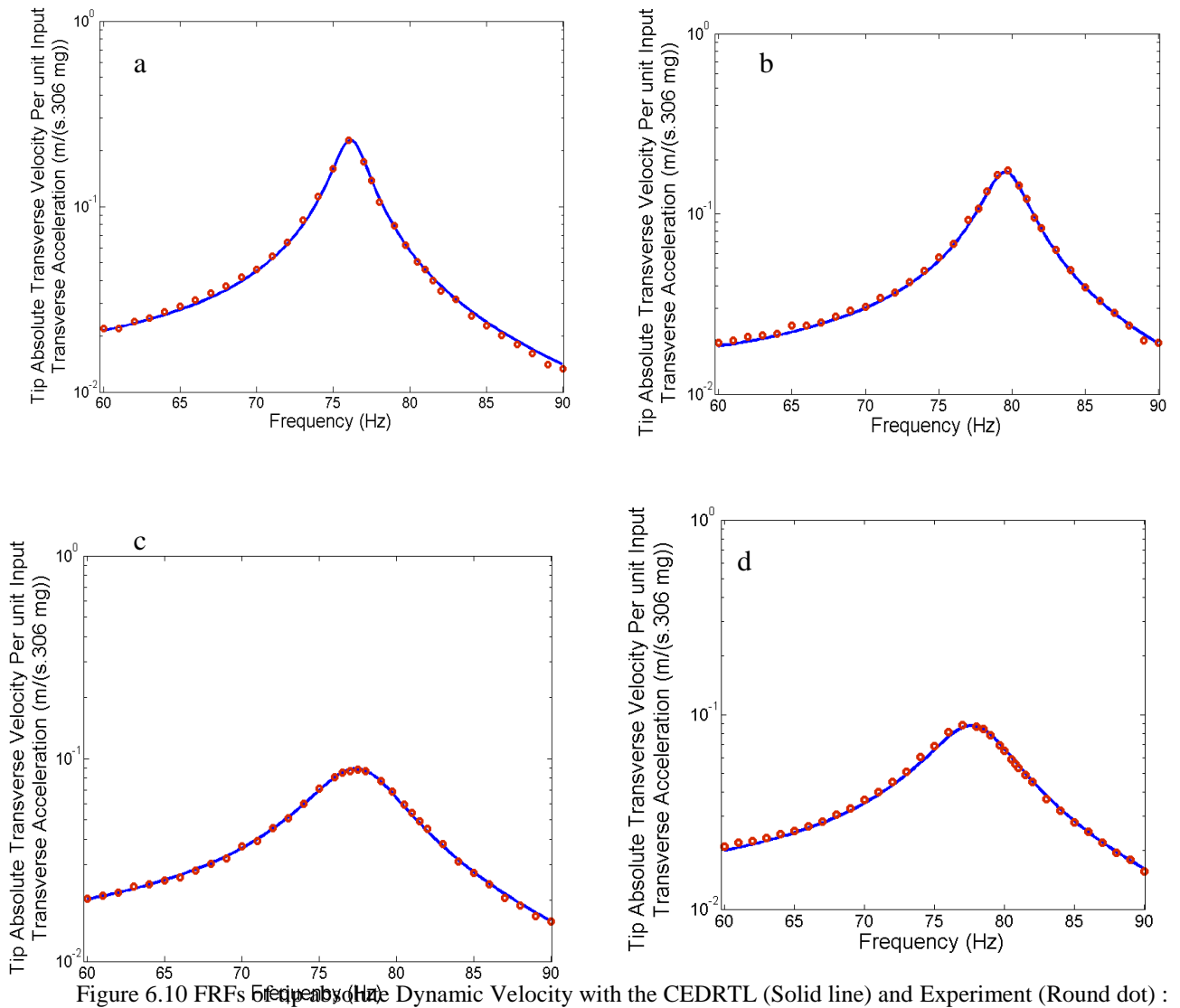

Figure 6.10 FRFs of tip absolute Dynamic Velocity with the CEDRTL (Solid line) and Experiment (Round dot) :
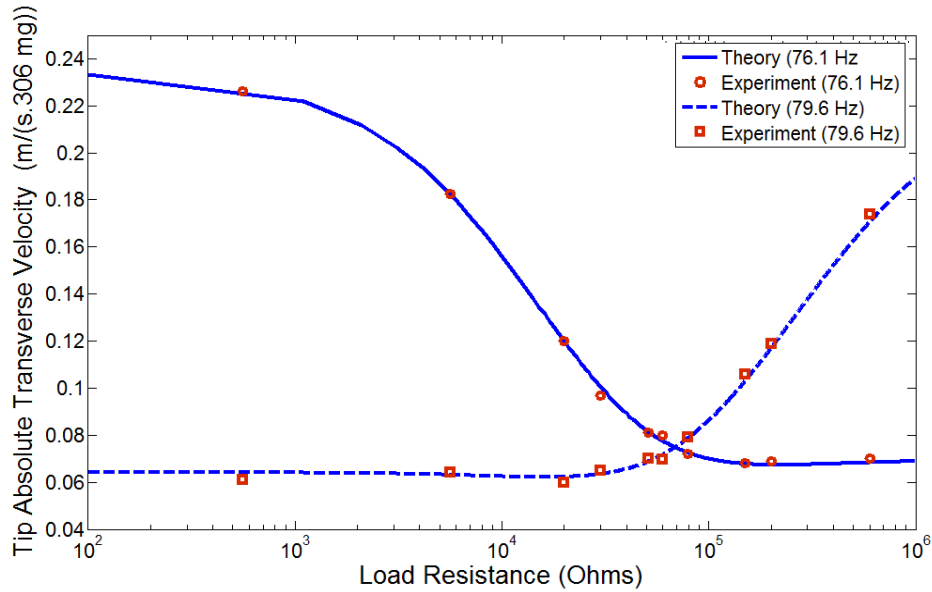a)   560 Ω , b) 602 kΩ , c) 51 kΩ and d) 60 kΩ

233

Figure 6.11 Tip absolute Dynamic Velocity with the CEDRTL versus Load Resistance under the Short circuit Resonance Frequency of 76.1 Hz and Open Circuit Resonance Frequency of 79.6 Hz

6.2.3. The FRF of Bimorph Electrical Voltage

As can be seen from Figure 6.12, the first mode FRF of electrical voltage is shown with varying resistance. As mentioned previously, the short circuit can be chosen with the lowest value of load resistance as $R_{load} \to 0$ and the open circuit can be set as the load resistance approaches infinity $R_{load} \to \infty$. The trend of electrical voltage for short circuit conditions tended to give the lowest amplitude whereas the open circuit gave the highest amplitude. In this case, the increase of load resistance resulted in an increasing amplitude followed by an increasing shift in the resonance frequency. In this situation, the electrical voltage frequency response with varying load resistance can be viewed as a dynamic amplification behaviour. The trend of electric voltage at the resonance frequency regions for each load resistance indicated a significant monotonic pattern from lowest to highest amplitudes. The off-resonance frequency regions also seemed to give the monotonic pattern with increasing resistance. The relationship between the trends of electrical voltage and tip absolute transverse displacement or velocity amplitudes were considered according to the load resistance where the short circuit electrical voltage at resonance indicated the lowest amplitude while the tip absolute dynamic displacement tended to give the highest amplitude. This shows that the electrical voltage under short circuit load resistance of

234

around 560 Ω might result in a reduction of bimorph fatigue life. A convenient electrical voltage frequency response can be predicted around the intermediate curve of 60 kΩ load resistance where this can be compared with the tip absolute dynamic displacement and velocity to give the lowest amplitude values as shown in Figures 6.4 and 6.8. Again, the CEDRTL response indicated a slight change when compared with the CEDRT response as shown in Figure 6.12. The comparison between CEDRTL and CEDRT results with the higher load resistances seemed to give maximum percentage difference of 22.2 % especially at 602 kΩ. Moreover, the comparison between the CEDRTL and experimental results were achieved with very good agreement for varying load resistance as shown in Figure 6.13. It should be noted that the inclusion of the longitudinal form into the electromechanical response resulted in an amplitude change compared with the CEDRT response. It is clearly seen from the three dimensional graph in Figure 6.14 that the region of maximum electrical voltage amplitude located at the open circuit load resistance gradually decreased to the minimum level at the short circuit load resistance followed by a shift in frequency. Although the bimorph structure was considered to have small dimensions with 30.1 mm length and 0.51 mm thickness, the bimorph tip mass with its rotary inertia has an important role to affect the CEDRTL dynamic response. As mentioned previously, the effect of tip mass under the input transverse base acceleration creates the inertia force onto the bimorph affecting the relative time dependent-displacement field function. The samples of electrical voltage trends shown in Figure 6.15 indicate very good agreement between the theoretical and experimental studies. Furthermore, Figure 6.16 also shows very good agreement between the short and open circuit resonance amplitudes versus load resistance. The maximum electrical voltage amplitudes with the short and open circuit resonances can be reached with increasing load resistance. However, the maximum level of open circuit resonance amplitude indicated a higher value compared with the short circuit when the short and open circuit amplitudes passed over the transitional point of 61.1 kΩ.
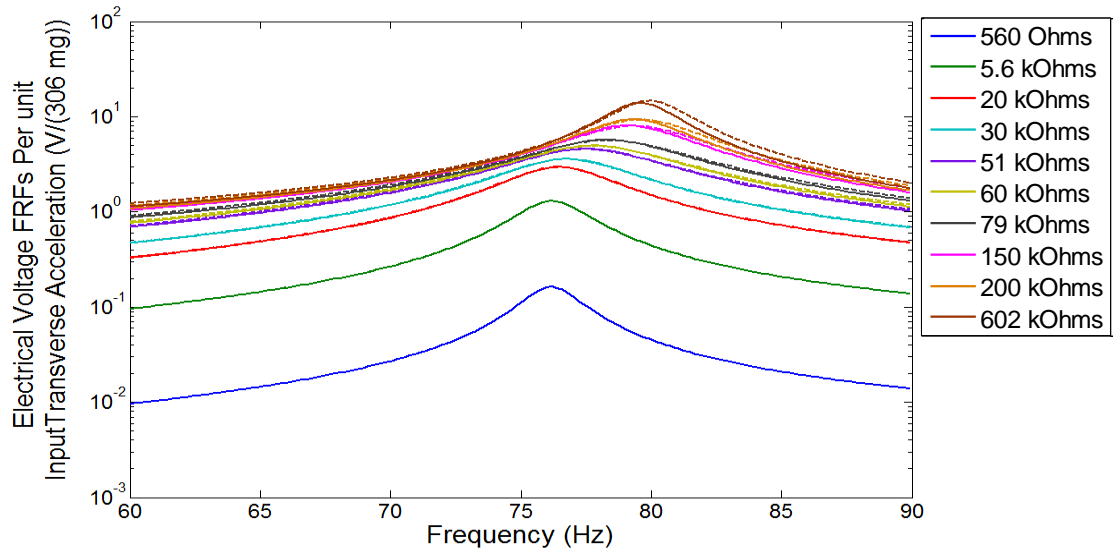
Figure 6.12 FRFs of Electrical Voltage with the CEDRTL (Solid line) and CEDRT (Dash line)
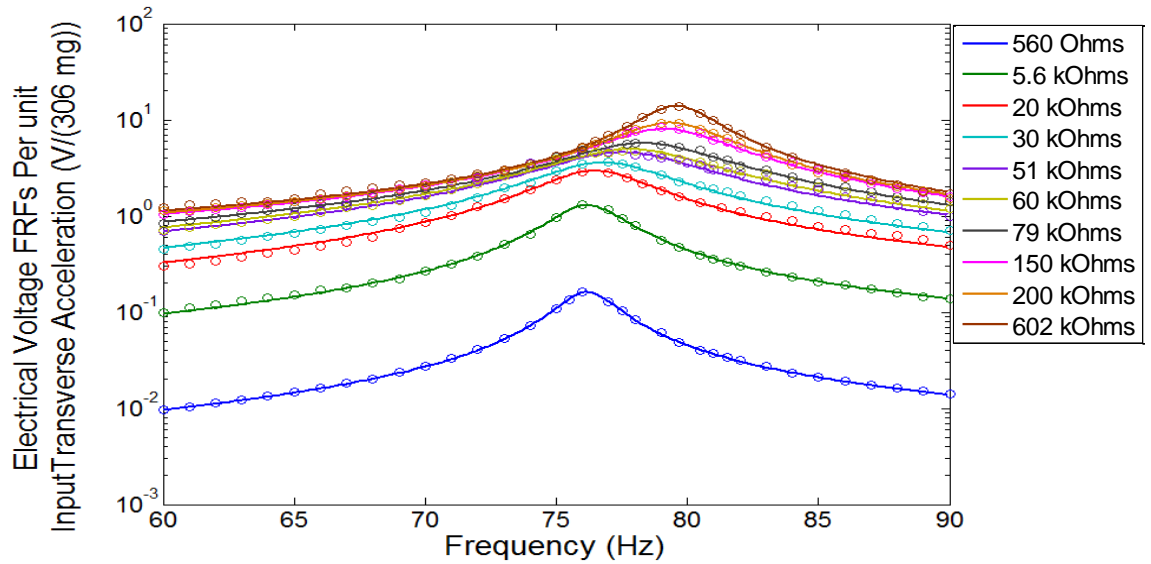

Figure 6.13 FRFs of Electrical Voltage with the CEDRTL (Solid line) and Experiment (Round dot)
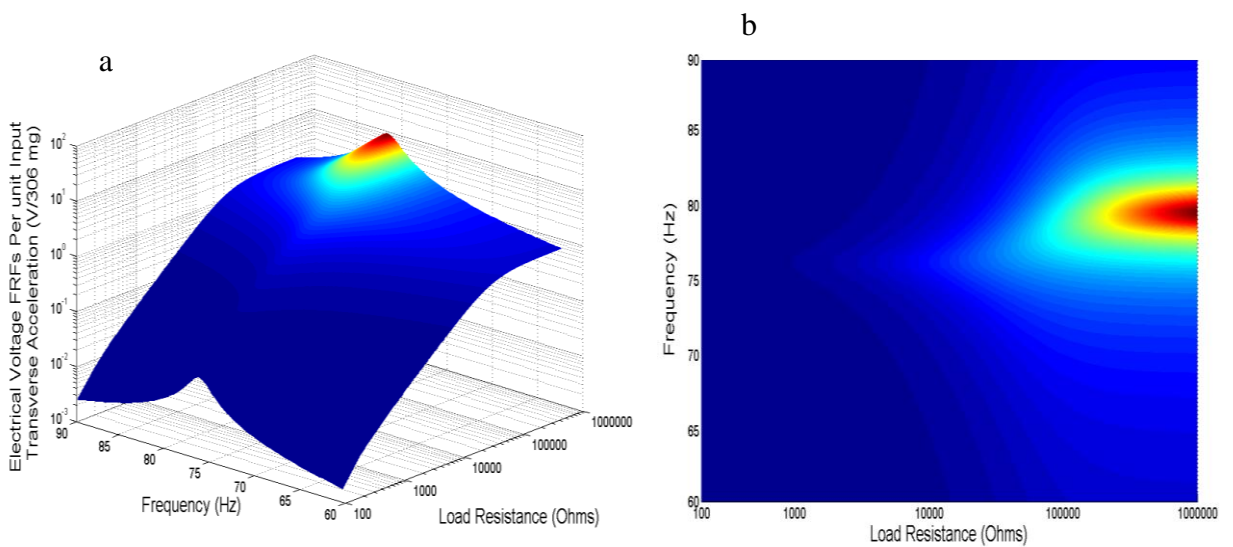

Figure 6.14 FRFs of Electrical Voltage : a) Amplitude Vs Frequency and Load resistance ,
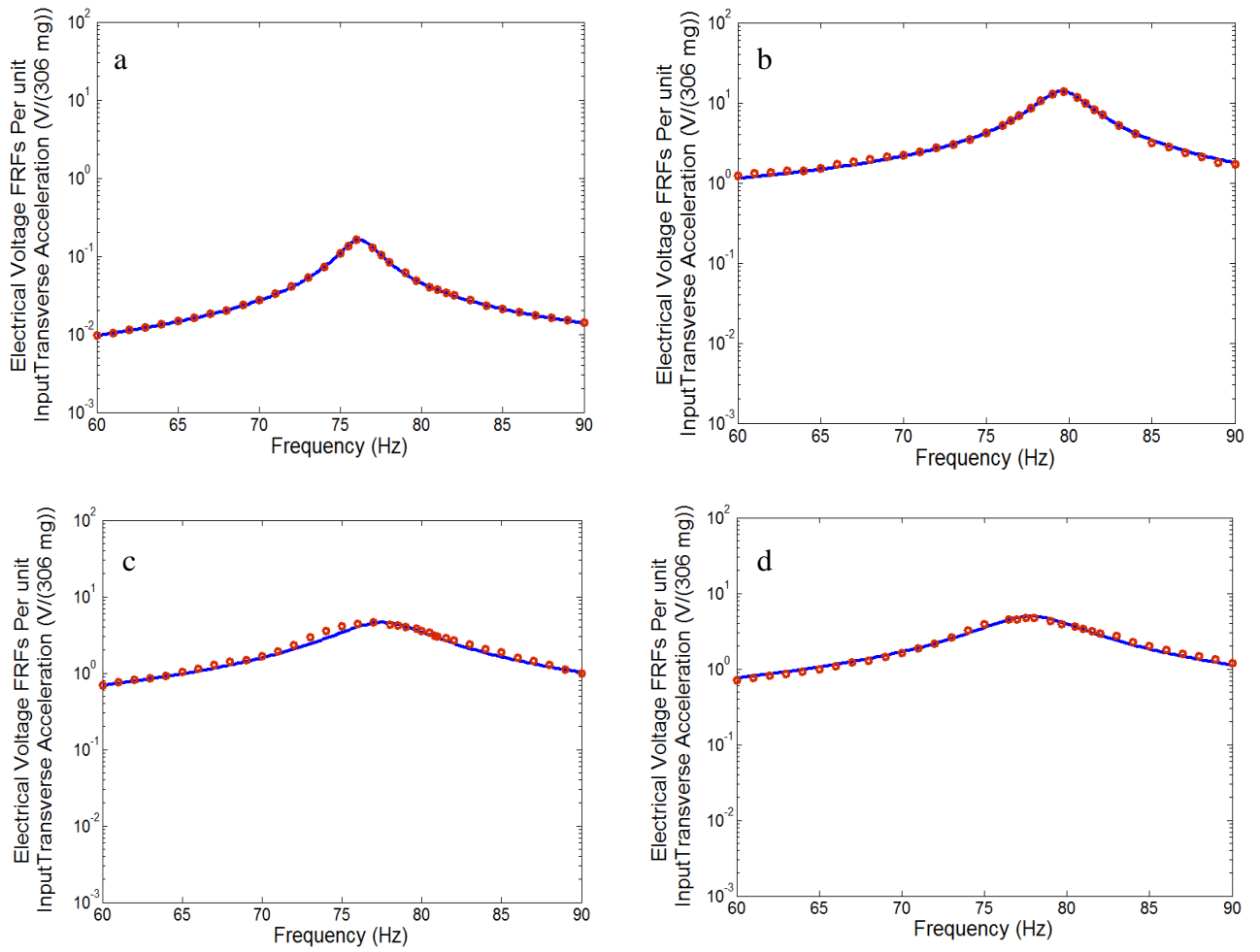b) Amplitude Pattern based on: Frequency Vs Load resistance

Figure 6.15 FRFs of Electrical Voltage with the CEDRTL (Solid line) and Experiment (Round dot) :
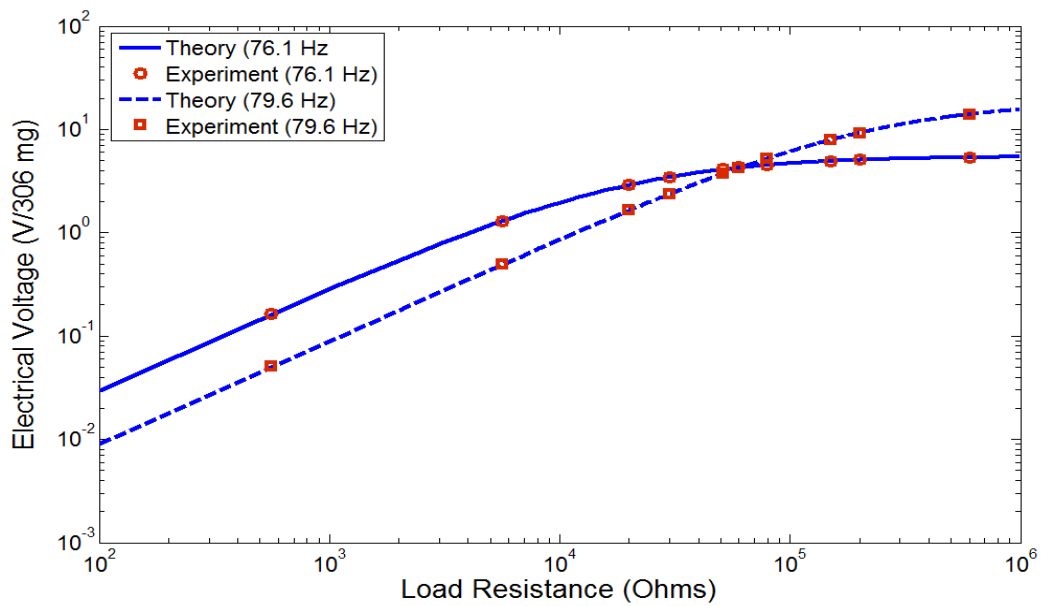a) 560 Ω , b) 602 kΩ , c) 51 kΩ and d) 60 kΩ

Figure 6.16 Electrical Voltage with the CEDRTL versus Load Resistance under the Short circuit
Resonance Frequency of 76.1 Hz and Open Circuit Resonance Frequency of 79.6 Hz

6.2.4. The FRF of Bimorph Electrical Current

In this section, the FRF of electrical current generated from the bimorph with input transverse acceleration is discussed under varying load resistance. The shifting frequency due to the change of load resistance indicates a different trend compared with that shown previously. Figure 6.17 shows that the comparison between the CEDRTL and CEDRT indicating a slight difference for some load resistances. When the load resistance approached short circuit, the CEDRTL and CEDRT results overlapped for the load resistances of 560 Ω, 5.6 kΩ and 20 kΩ. As shown in Figure 6.17, there was a slight increase of electrical current amplitude with decreasing load resistance followed by decreasing resonance frequencies. In this case, the electrical current frequency response with varying load resistance shows the electromechanical attenuation behaviour. The trend of electrical current shows a monotonic pattern opposite to that of the electric voltage response shown in Figure 6.12. The CEDRTL and experimental results gave very good agreement under varying load resistances as shown in Figure 6.18. The short circuit frequency response seemed to give the highest amplitude at load resistance of 560 Ω and resulted in the lowest resonance around 76.1 Hz compared to other load resistances. This was also clearly seen in Figure 6.19 where the maximum current amplitude dropped dramatically when the load resistance increased from short circuit. The load resistance of 5.6 kΩ still indicated short circuit behaviour although the amplitude obtained was a bit lower than the load resistance of 560 Ω, while the resonance frequency still indicated the same value. The open circuit load resistance of 602 kΩ seemed to give the lowest amplitude with the higher resonance frequency compared with other load resistances. Moreover, the trend of electric current response as a function of load resistance can be compared with the previous trends of tip absolute displacement, velocity and electric voltage. The minimum current amplitude at open circuit occurred with maximum amplitudes of tip absolute displacement and velocity. The electric voltage response had maximum amplitude at a resonance frequency of 79.6 Hz. Conversely, the maximum current amplitude at short circuit indicated the maximum amplitude of tip absolute displacement or velocity with decreasing voltage amplitude at the resonance frequency of 76.1 Hz. This shows that the electrical current increased when the load resistance approached short circuit, but the tip absolute displacement and velocity of the bimorph tended to give the highest amplitude. This indicates that

this situation would be unsuitable for power harvester optimisation as the highest tip absolute displacement or velocity amplitude did not result in the highest power harvesting under the short circuit resistance. Moreover, the electrical current FRF for the short circuit load resistance gave the highest amplitude whereas the electric voltage response also indicated the highest amplitude for open circuit load resistance. The sensitivity of the bimorph to generate the optimal power harvesting shows the importance of understanding the underlying strain-polarity field on the piezoelectric element from the bimorph under variable load resistance as discussed in the next section. The convenient electrical current amplitude would be from an intermediate curve of load resistance 60 kΩ where this value indicated the lowest tip absolute displacement or velocity amplitude around the resonance frequency but showed convenient values for voltage, current and optimal power harvesting. Furthermore, there was a slightly different trend in the specific current amplitude under the higher load resistances between the CEDRTL and the CEDRT response with the maximum percentage difference of 22.2 % observed within the non-resonance regions. The strain field model used here included the transverse form with initial longitudinal strain where this affected the internal force and moment due to the transverse bending and extensional longitudinal response at each bimorph interlayer resulting in the electrical force and moment response due to the coupling effects of the piezoelectric element. Finally, some examples of the individual trends of current with different load resistances were found from Figure 6.20 where good agreement between the theoretical and experimental studies was achieved. Moreover, the maximum amplitudes of electrical current for both short and open circuit resonance frequencies under varying load resistance was achieved with decreasing load resistance as shown in Figure 6.21. The level of maximum current amplitudes from short and open circuit resonances was shown to be different. Moreover, the short circuit resonance amplitude below the transitional point of 61.1 kΩ gave higher current value compared with the open circuit resonance amplitude. By looking over the transitional point, the open circuit current amplitude otherwise indicated higher values compared with the short circuit current amplitude.
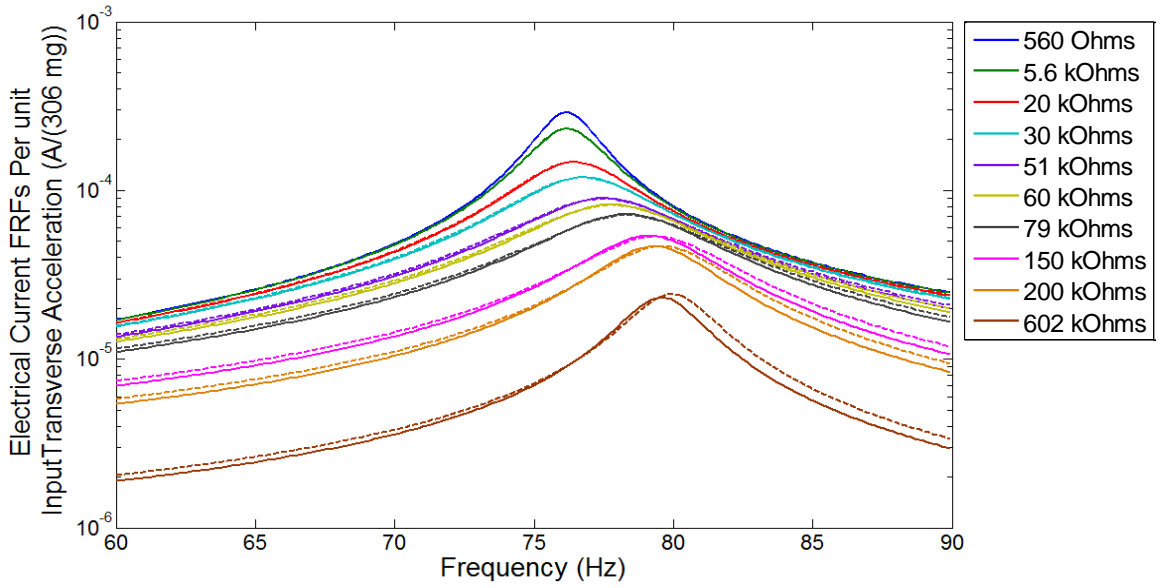
Figure 6.17 FRFs of Electrical Current with the CEDRTL (Solid line) and CEDRT (Dash line)
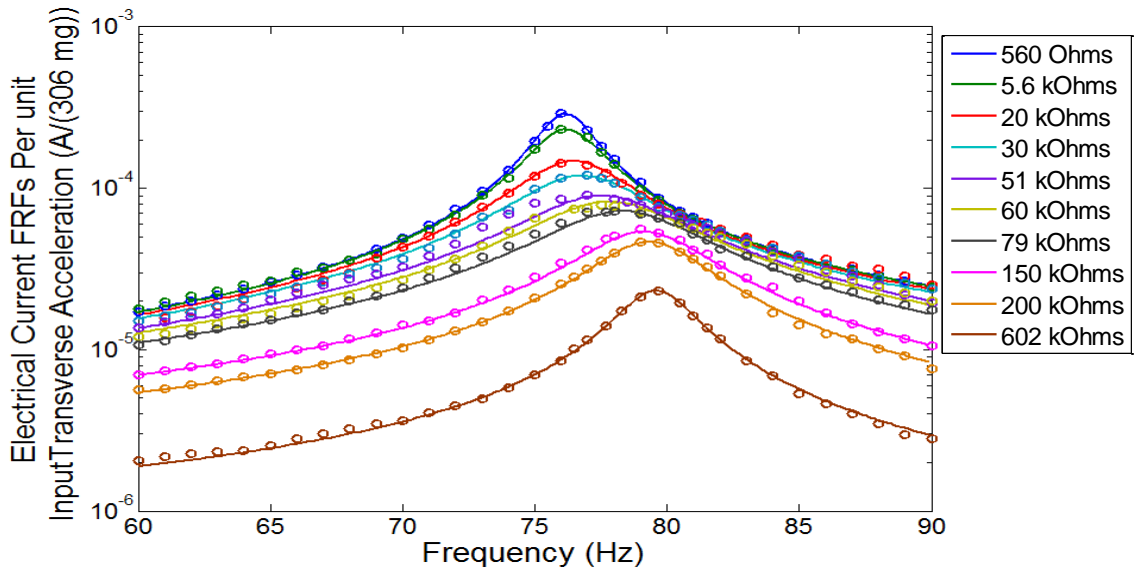

Figure 6.18 FRFs of Electrical Current with the CEDRTL (Solid line) and Experiment (Round dot)
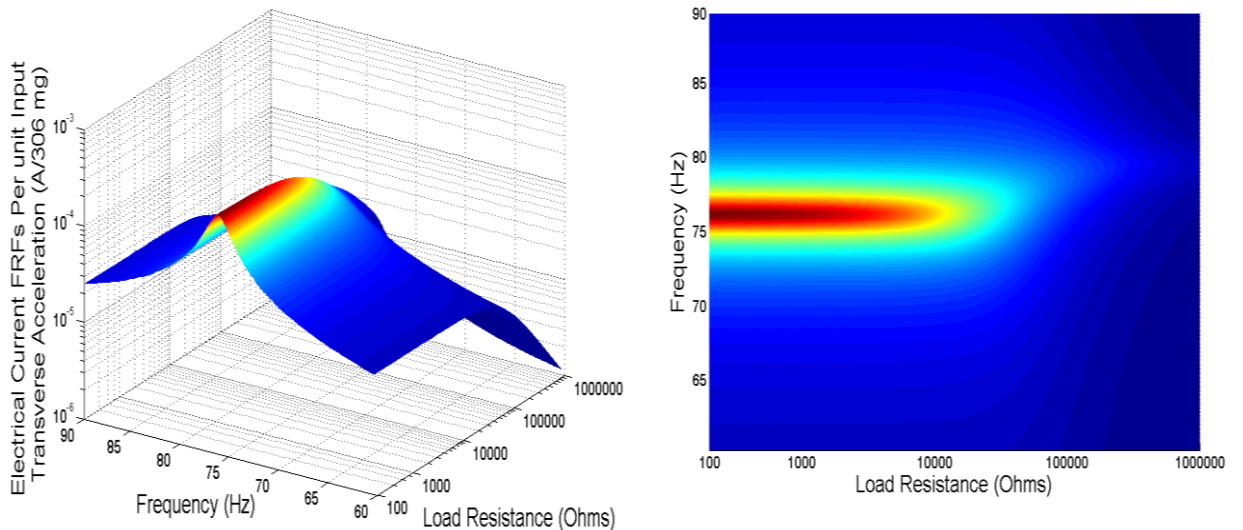

Figure 6.19 FRFs of Electrical Current : a) Amplitude Vs Frequency and Load resistance ,
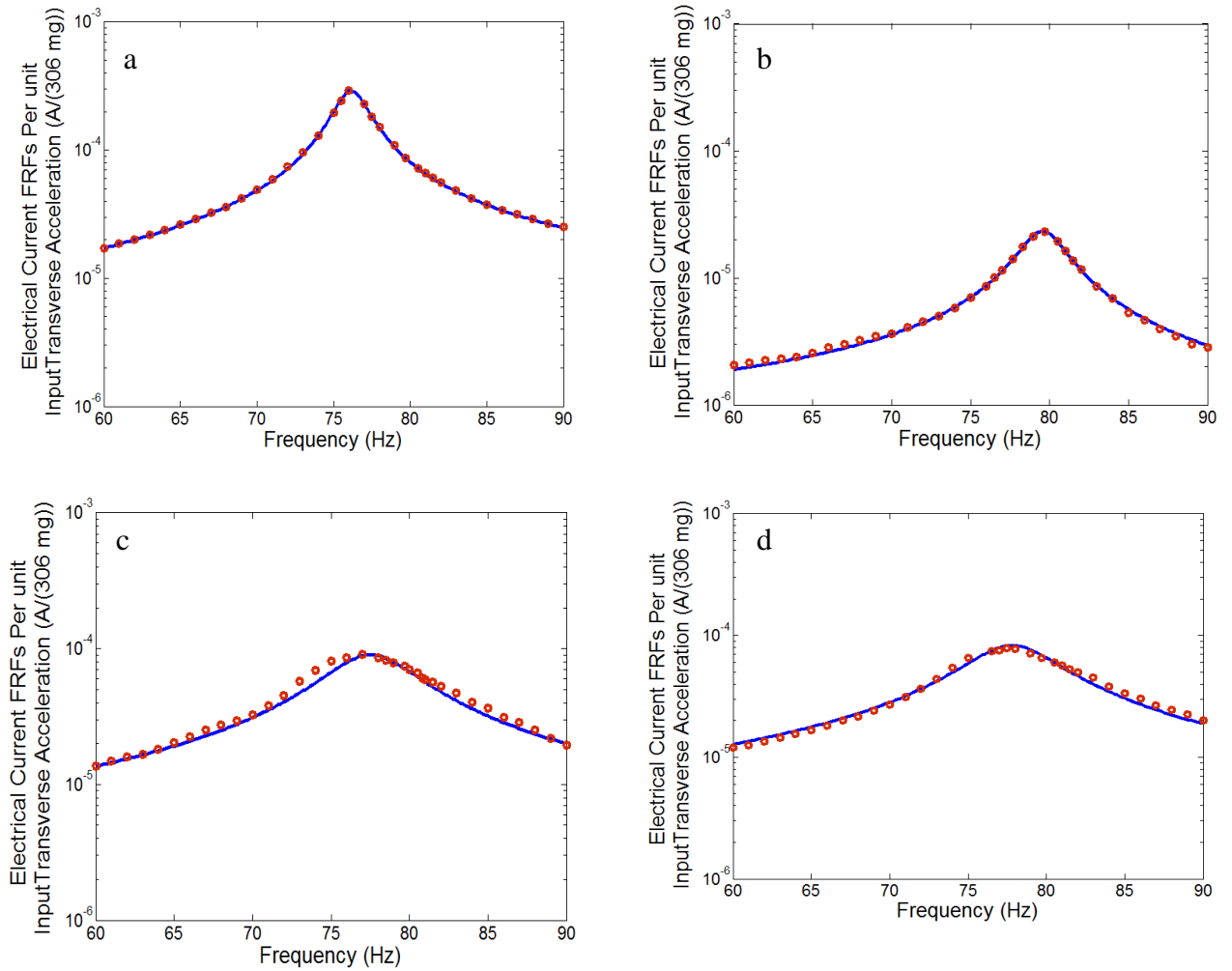b) Amplitude Pattern based on: Frequency Vs Load resistance

Figure 6.20 FRFs of Electrical Current with the CEDRTL (Solid line) and Experiment (Round dot) :
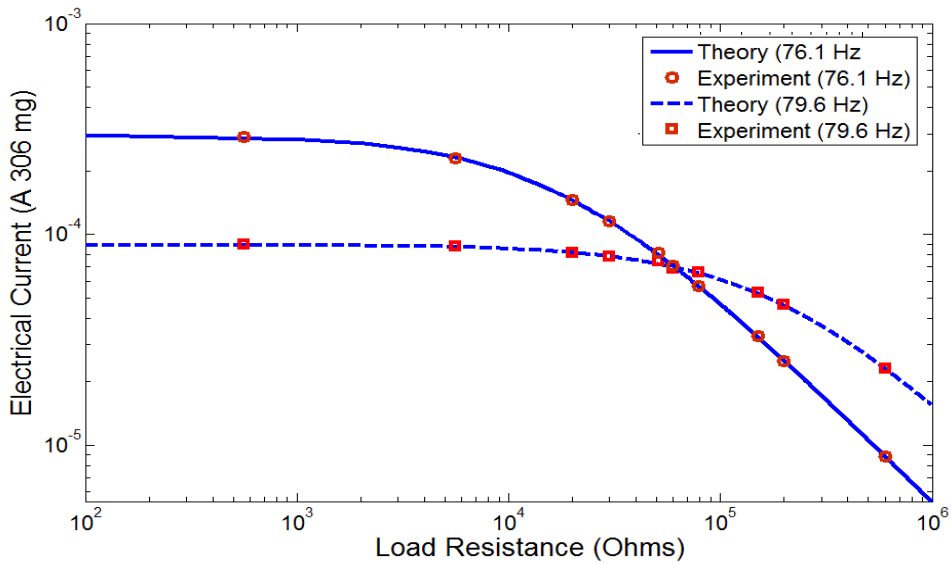b) 560 Ω (short circuit), b) 602 kΩ (open circuit), c) 51 kΩ and d) 60 kΩ

Figure 6.21 Electrical Current with the CEDRTL versus Load Resistance under the Short circuit
Resonance Frequency of 76.1 Hz and Open Circuit Resonance Frequency of 79.6 Hz

6.2.5. The FRF of Bimorph Electrical Power

In this section, the electrical power harvesting frequency response of the bimorph is presented for varying load resistance. As can be seen from Figure 6.22, the comparison between the CEDRTL and the CEDRT response was shown to yield slightly different amplitudes with a maximum percentage difference being 49.11 % for the off-resonance regions with the higher load resistance approaching open circuit. The existence of the longitudinal effect on the electromechanical bimorph response should not be ignored especially under two input base motion as discussed in the forthcoming section of polar FRFs. The addition of the tip mass on the bimorph might also create coupling of the extensional mechanical and electrical forces in the piezoelectric layers. In other words, the effect of a lumped mass can create additional longitudinal strains in the interlayers of the bimorph as shown in chapter 4. Moreover, the trend of the power harvesting FRF tended to give different results when compared with previous cases. Another important aspect which can be reported here is that the trend of power harvesting depends not only on the varying load resistances but also on the chosen properties of the piezoelectric layers and the geometry of the bimorph model. For example; even though, the geometry of the bimorph was chosen with the same parameters, it can still have different physical properties like capacitance and piezoelectric coupling resulting in different power harvesting values. This indicates that the chosen load resistances need to be investigated first to show the symmetrical pattern of frequency response around the first mode. It was observed that the power harvesting resonance frequency seemed to shift as the load resistance changed and formed the symmetrical pattern as a function of frequency. Both the short and open circuit resonance frequencies indicated the lowest value of power amplitudes. By comparing the different cases of FRFs like the tip absolute velocity, electrical current and voltage amplitudes; the short and open circuits resonance frequencies seemed to give different trends. For example, the FRF of voltage under the short circuit gave the lowest amplitude but the FRF of electrical current seemed to give the highest amplitude with the same resonance frequency. The FRF of velocity also showed the different trend referring to the highest amplitude. This indicates that the power harvesting under short and open circuit conditions might not be optimal because the tip absolute displacement or velocity indicated the maximum value while the electrical current and voltage amplitude

results appeared to have opposite trends to each other. As expected, on one hand the current with the short circuit had the maximum value while on the other hand the voltage with the open circuit had the maximum value or vice verse. Moreover, power harvesting under those circuits seemed to give the lowest amplitudes as shown in Figure 6.25a,b indicating that the short or open circuit is not the preferred system for power harvesting. The optimal power harvesting amplitude occurred with the load resistance of 60 kΩ at the resonance frequency region as this gave the lowest level of tip absolute dynamic displacement or velocity amplitude and was located at the intermediate curves from the dynamic displacement, velocity, electrical current and voltage. It should be noted that the optimal load resistance with local minimum point as shown in the black square curve from Figure 6.23 was coincidently overlapped with the load resistance of 60 kΩ. Two absolute maximum points from the optimal load resistance curve were also coincidently overlapped with the load resistances of 20 kΩ and 200 kΩ, respectively. It is also noted that both local minimum and absolute maximum points indicated the optimal power harvesting. Moreover, the absolute maximum points indicated the higher transverse displacement and velocity amplitudes and also gave higher power harvesting results compared with the local minimum point. This can be seen clearly from Figure 6.24 where the maximum power amplitude region was achieved at the load resistance away from short and open circuits. Therefore, the power harvesting with the load resistance of 60 kΩ showed the most convenient value for the optimization with the lowest velocity or displacement amplitude. The four samples of individual power harvesting trends under the load resistances of 560 Ω, 602 kΩ, 51 kΩ and 60 kΩ are shown in Figure 6.25 where the results obtained indicated good agreement between the theoretical and experimental studies. The short and open circuit resonance frequency power results are shown in Figure 6.26 under various load resistances. Both the short and open circuit resonance amplitudes can appear to reach the maximum level with different load resistances. However, when the short circuit resonance amplitude moved to the lower transitional point of 61.1 kΩ, the amplitude showed higher values compared with the open circuit. This conversely occurs when the open circuit resonance amplitude moved to the higher transitional point to give the higher value compared with the short circuit.

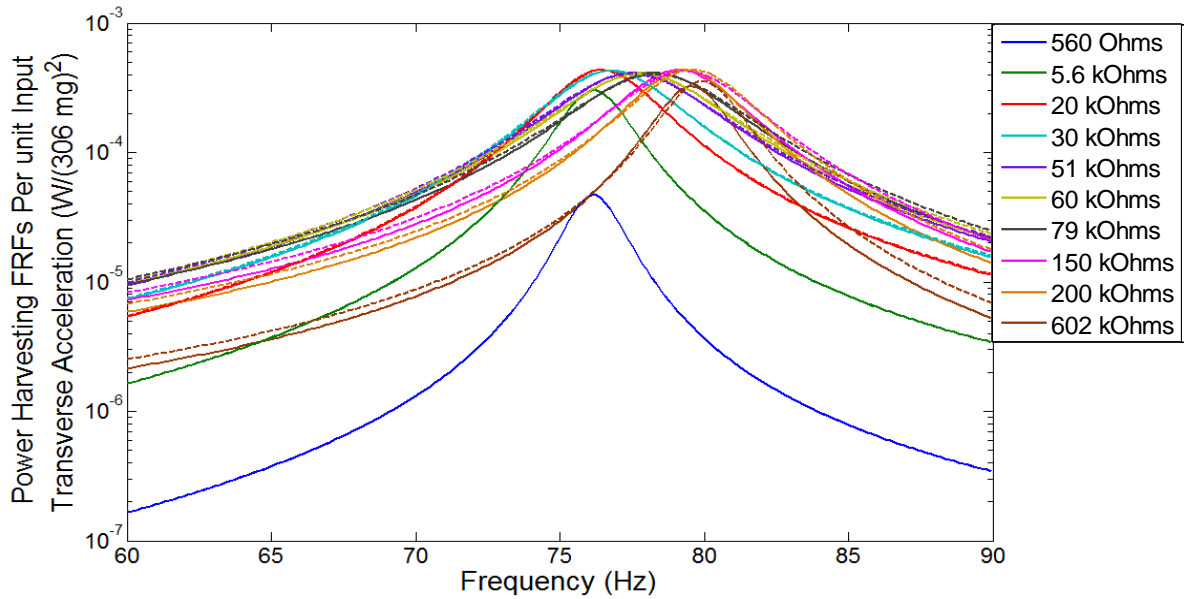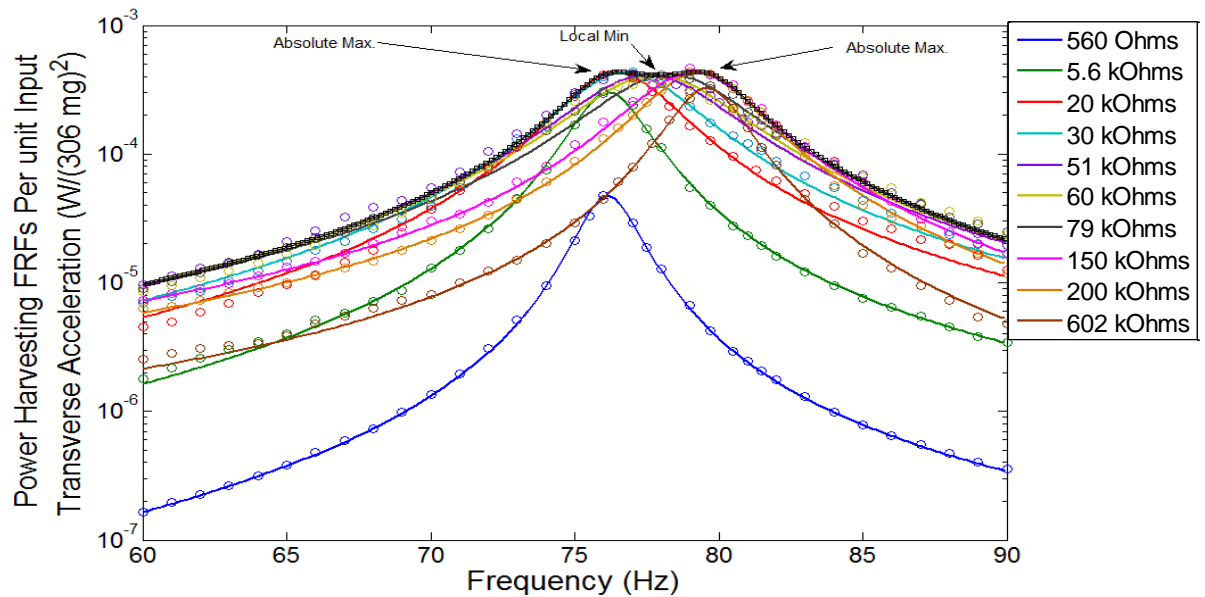Figure 6.22 FRFs of Power Harvesting with the CEDRTL (Solid line) and CEDRT (Dash line)

Figure 6.23 FRFs of Power Harvesting with the CEDRTL (Solid line) and Experiment (Round dot)
Including Optimal Values From Local Minimum to Absolute Maximum (Black Square)
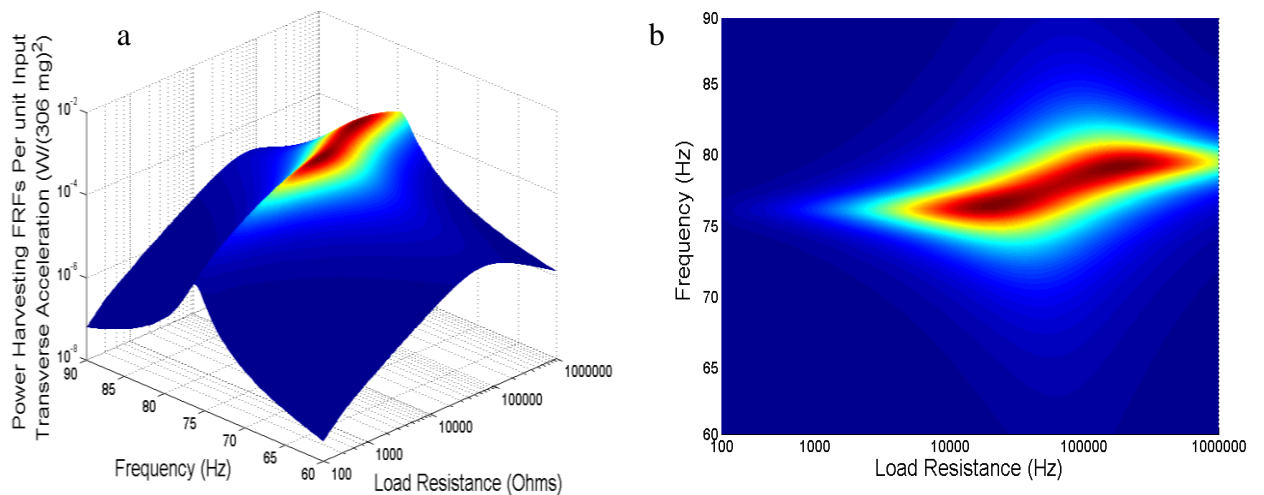
Figure 6.24 FRFs of Electrical Power: a) Amplitude Vs Frequency and Load resistance,
b) Amplitude Pattern based on: Frequency Vs Load resistance
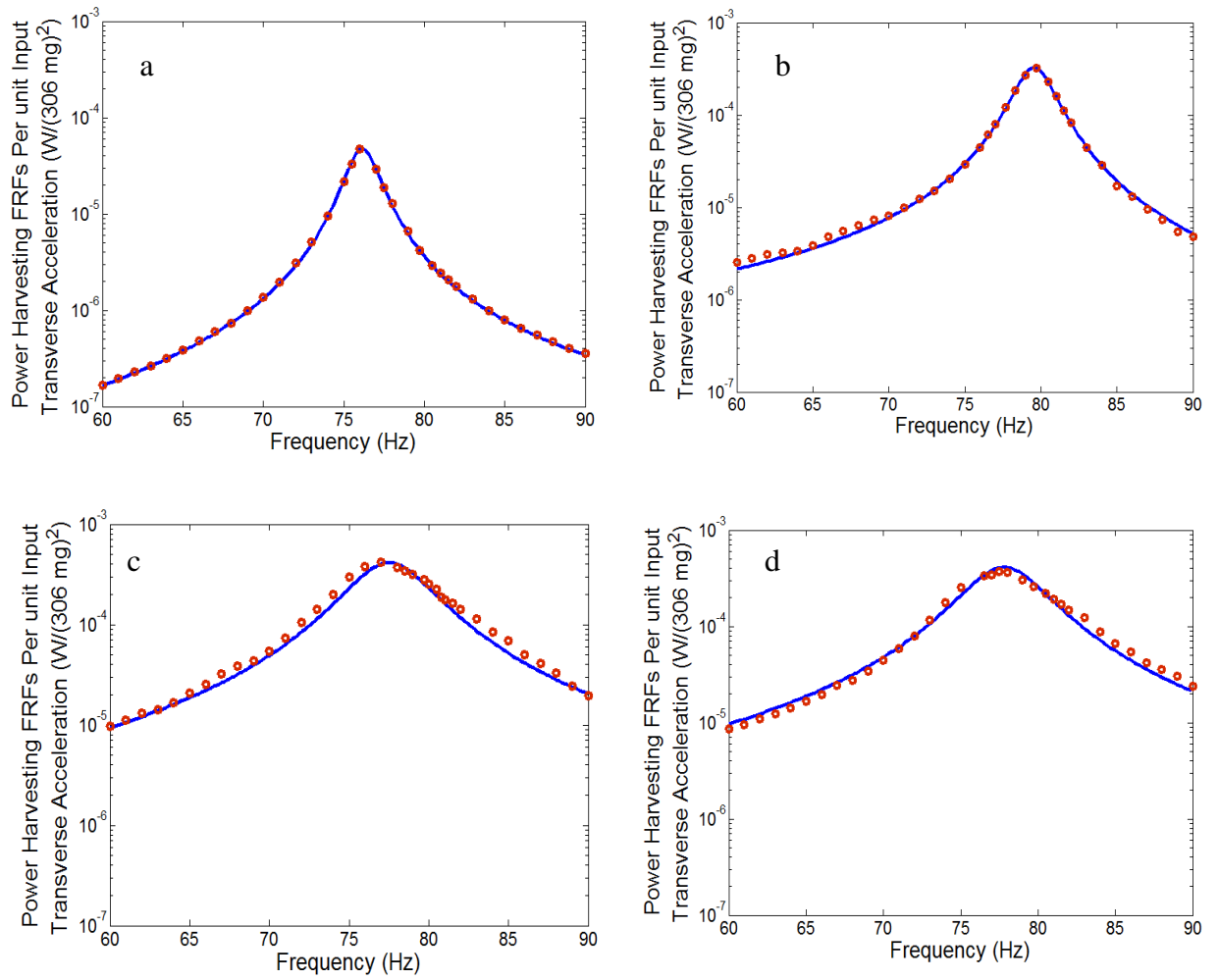
Figure 6.25 FRFs of Power Harvesting with the CEDRTL (Solid line) and Experiment (Round dot) :
c) 560 Ω (Short Circuit) , b) 602 kΩ (Open Circuit), c) 51 kΩ and d) 60 kΩ

Figure 6.26 Power Harvesting with the CEDRTL versus Load Resistance under the Short circuit
Resonance Frequency of 76.1 Hz and Open Circuit Resonance Frequency of 79.6 Hz

6.3. Electromechanical Dynamic Response of the Piezoelectric Bimorph without Tip Mass

This section presents the electromechanical piezoelectric bimorph response without the tip mass using multi-mode FRFs with varying load resistance. The properties of the bimorph were the same as used previou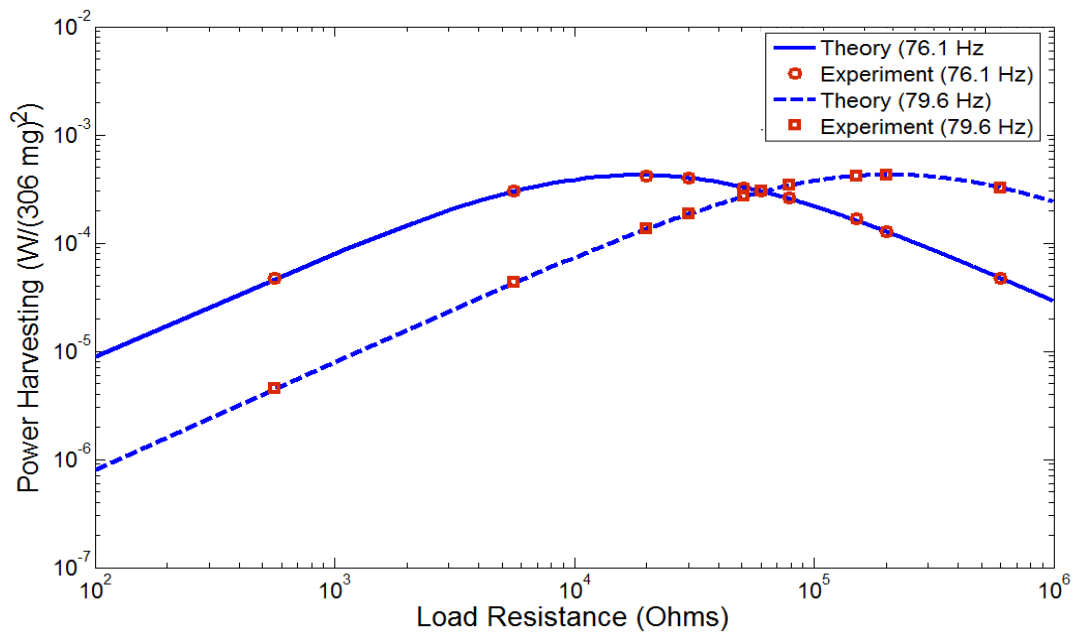sly. The mechanical damping ratios were used according to the experimental results. Moreover, the values of load resistances from the previous section were still used to analyse the multi-mode electromechanical dynamic response based on the theoretical and experimental studies. The bimorph response with and without the tip mass are also discussed.

6.3.1. The Multi-mode Bimorph FRFs Tip Absolute Dynamic Displacement

The multi-mode tip absolute dynamic displacement FRFs was simulated from 0 to 2000 Hz with varying load resistance. In this case, the first two modes were plotted with the same variation of load resistance as chosen previously. The input base transverse acceleration to the cantilevered piezoelectric beam was kept constant with the value of 3 m/s^2 which is equivalent to 306 mg (1 g = gravitational acceleration 9.81 m/s^2). With the same procedure for measuring the dynamic displacement using the Laser Doppler Vibrometer (LDV) as given in the previous study, equation (4.279c) in chapter 4 can be used for comparison by replacing variable x with the tip end of the bimorph L. The results obtained can also be compared with the CEDRTL and CEDRT response including the results of the experimental study. It can be seen in Figures 6.29-6.30 that the comparison between the theoretical and experimental studies for the first two modes with load resistance of 560 Ω appeared to give very close results to each other. As the load resistance of 560 Ω approached short circuit, the results were used to determine the mechanical damping ratios based on the experimental results, matched with the theoretical results as shown in Figure 6.30a. The mechanical damping ratios from the first and second modes were calculated to be $\zeta_1^w = 0.016$ and $\zeta_2^w = 0.0172$.

In the previous study, the tip absolute dynamic displacement was analysed according to the comparisons between the experimental study, the CEDRTL and the CEDRT results. In the present study, the CEDRTL was still applied but the trend of the CEDRT model seemed to be closer to the experimental results compared with the

CEDRTL with the maximum percentage difference of 11.42 %. In this case, the noticeable difference between the CEDRTL and CEDRT response predominantly occurred around the off-resonance region with the higher load resistances as shown from Figure 6.27 with the enlarged view from Figure 6.28. This indicates that the existence of longitudinal effect at the bimorph interlayer element without the tip mass could reasonably be ignored. For obvious reasons, the bimorph without the tip mass cannot give the extra tip inertia dynamic loading due to the additional effects of extensional strain field and extensional kinetic energy. In other words, the inclusion of the tip mass onto the bimorph can create the strong effects of bending and electrical moments with the additional effects of the longitudinal extensional and electrical forces into the interlayer bimorph element under dynamic response conditions.

It can be seen from Figure 6.29 with enlarged view from Figure 6.30a that the first mode of the FRFs of tip absolute dynamic displacement shifted as the load resistance changed. The short circuit resonance frequency of 267.4 Hz tended to give the highest amplitude of 48.5 μm and the open circuit frequency of 278.5 Hz also showed similar behaviour with an amplitude of 44.4 μm. Moreover, as mentioned previously, the effect of the maximum tip absolute displacement tended to give the lowest and highest electrical voltage for the short and open circuits, respectively. Conversely, the maximum tip absolute displacement tended to give the highest and lowest electrical current for short and open circuits, respectively. This indicates that the maximum dynamic displacement does not provide the highest current or voltage. Beside, both of these circuit conditions result in low power harvesting. Another important aspect reported here is that the trend of the tip absolute dynamic displacement without tip mass tended to give a slightly different pattern compared with the results including the tip mass because the effect of tip mass can change the frequency response amplitude. This indicates that the tip mass tuned not only the mechanical system but also the electrical system. For example, this case can be found specifically at the load resistances of 20 kΩ, 30 kΩ, 51 kΩ, 60 kΩ and 79 kΩ where the resonance frequencies without the tip mass created the unsymmetrical pattern whereas the bimorph system with the tip mass tended to give the symmetrical response. Good agreement was again observed between the theoretical and experimental studies as shown in Figure 6.30. It should be noted that the effect of tip

mass on the bimorph system resulted in higher amplitudes compared to that without the tip mass especially at the first mode. The advantage of including the tip mass onto the bimorph was the higher voltage and power harvesting amplitudes at the first mode and also the lower resonance frequency as given in the previous study.

An irregular mode from Figure 6.29 occurred between the frequencies of 571.7 Hz and 773.9 Hz in the experimental results due to the imperfection of the clamped support of the bimorph onto the base protractor structure. The irregular mode was still away from the first and second modes, so its impact was thought to be insignificant. Close agreement between the theoretical and experimental studies from the first two modes was achieved. By looking especially at the second mode of the FRF, the tip absolute displacement tended to indicate different trends compared with the first mode. The same resonance frequency of 1697 Hz was obtained with the changing load resistances of 20 kΩ, 30 kΩ, 51 kΩ, 79 kΩ, 150 kΩ, 200 kΩ and 602 kΩ.
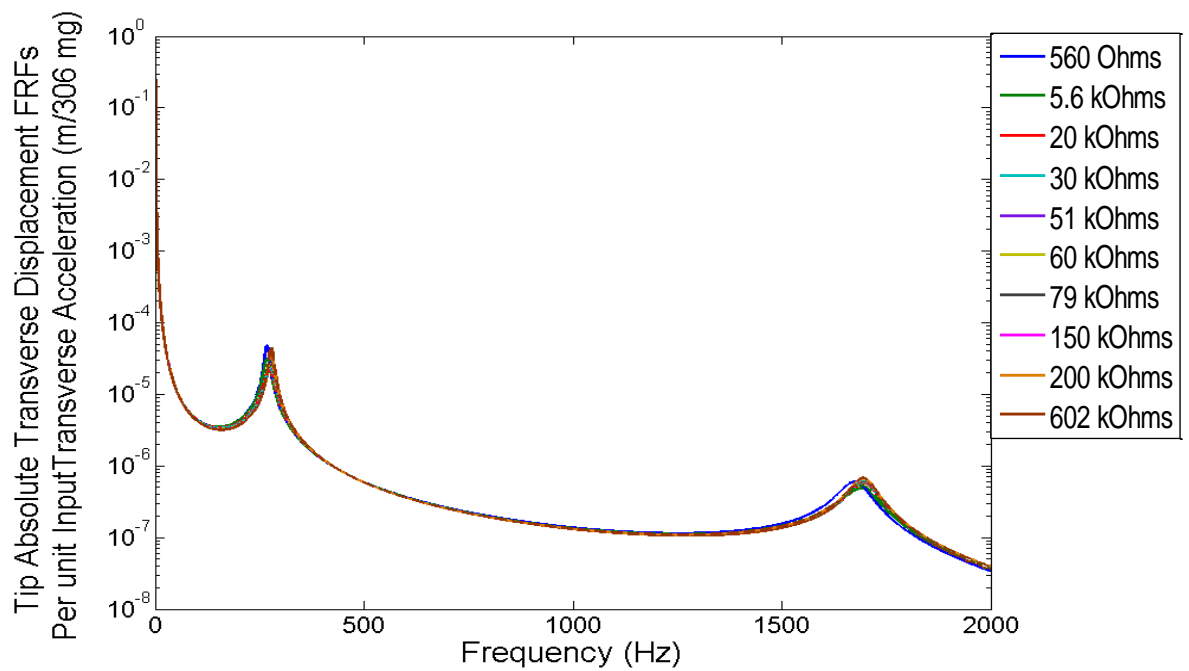
Figure 6.27 First two modes FRFs of tip absolute Dynamic Displacement with the CEDRT (Solid line) and CEDRTL (Dash line)
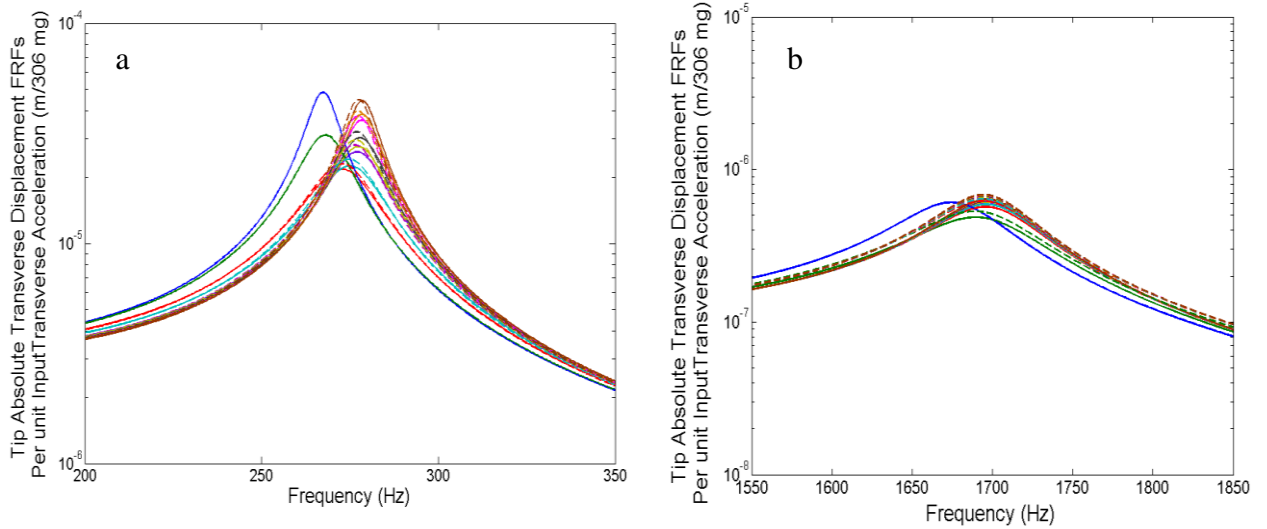
Figure 6.28 FRFs of tip absolute Dynamic Displacement with the CEDRT (Solid line)
and CEDRTL (Dash line) : a) First Mode and b) Second Mode

Figure 6.29 FRFs of Tip Absolute Displacement with the CEDRT (Solid line) and Experiment (Round dot)

Figure 6.30 FRFs of Tip Absolute Displacement with the CEDRT (Solid line)
and Experiment (Round dot) : a) First Mode and b) Second Mode

249

Figure 6.31 FRFs of Tip Absolute Displacement with the CEDRT (Solid line) and Experiment (Round dot)
: a) 560 Ω (Short Circuit) and b) 602 kΩ (Open Circuit)

6.3.2. The Multi-mode Bimorph FRFs of Tip Absolute Dynamic Velocity

In this section, the trend of the first two modes of tip absolute velocity of the cantilevered piezoelectric bimorph with varying load resistance is shown using the CEDRTL and CEDRT models indicating very close-fitting. As can be seen from Figure 6.32, with the enlarged view of Figure 6.33, the resonance frequencies with the CEDRT for the short and open circuits of 267.4 Hz and 278.5 Hz appeared to give the highest tip absolute velocity with amplitudes of 0.081 m/(s.306 mg) and 0.078 m/(s.306 mg), respectively. Moreover, the resonance frequency with the CEDRT for varying load resistance closely agreed with the experimental study. The

trend of tip absolute velocity seemed to have the similar pattern to that with the FRF from the tip absolute displacement. Individual trends of electromechanical tip absolute velocity response with different load resistances also showed good agreement between the CEDRT and experimental results as given in Figure 6.34 as clearly seen from the enlarged view from Figure 6.35.

The effect of the maximum tip absolute velocity tended to give the lowest and highest electrical voltage for short and open circuits, respectively. Conversely, the maximum tip absolute velocity tended to give the highest and lowest electrical current for short and open circuits, respectively. This indicates that the maximum dynamic velocity does not necessarily provide the highest current or voltage. In such situations, both of these circuits provided low power harvesting as shown further in the next section. Moreover, the irregular mode between the first and second modes as shown in Figure 6.34 still occurred due to the imperfect clamped support of the bimorph. However, this did not appear to affect the resonance frequency region amplitudes. Two examples of velocity FRFs with the short and open circuit load resistances as shown in Figure 6.36 still indicated very good agreement between the theoretical and experimental results except for the irregular response from the frequency range between 571.7 Hz and 773.9 Hz.
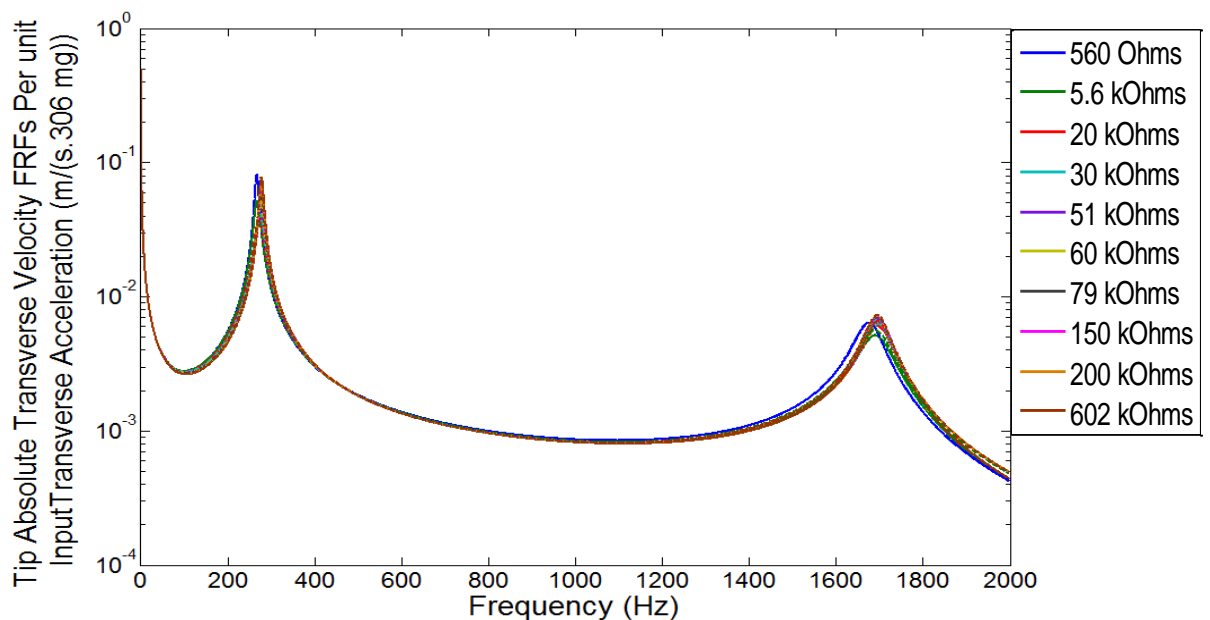
Figure 6.32 First two modes FRFs of tip absolute Dynamic Velocity with the CEDRT (Solid line) and CEDRTL (Dash line)

Figure 6.33 FRFs of tip absolute Dynamic Velocity with the CEDRT (Solid line) and CEDRTL (Dash line) :
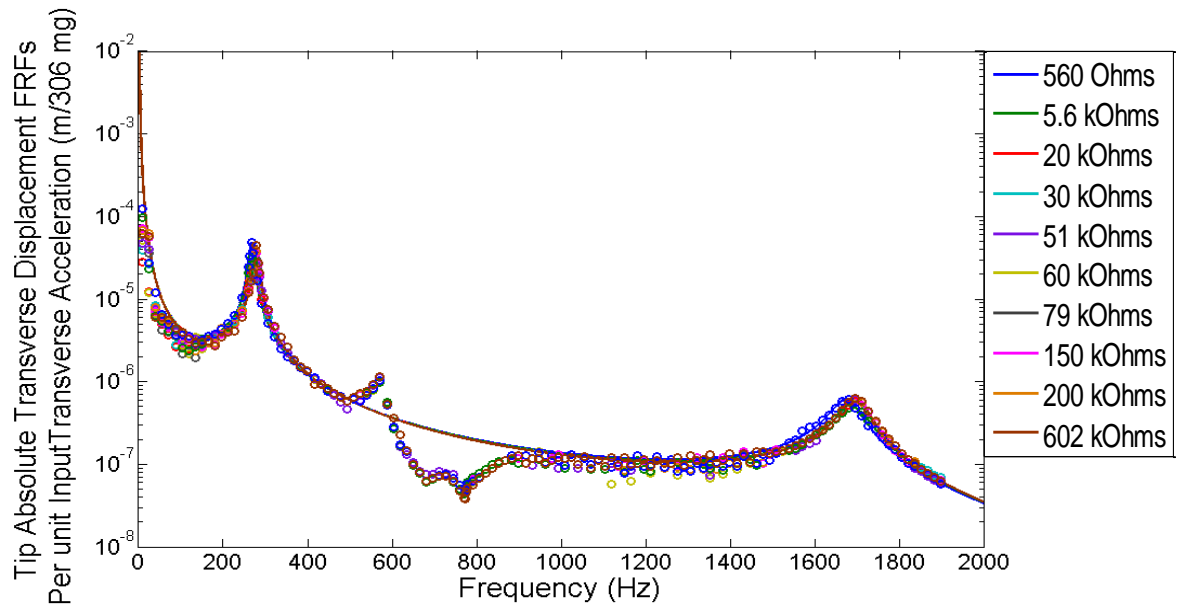a) First Mode and b) Second Mode

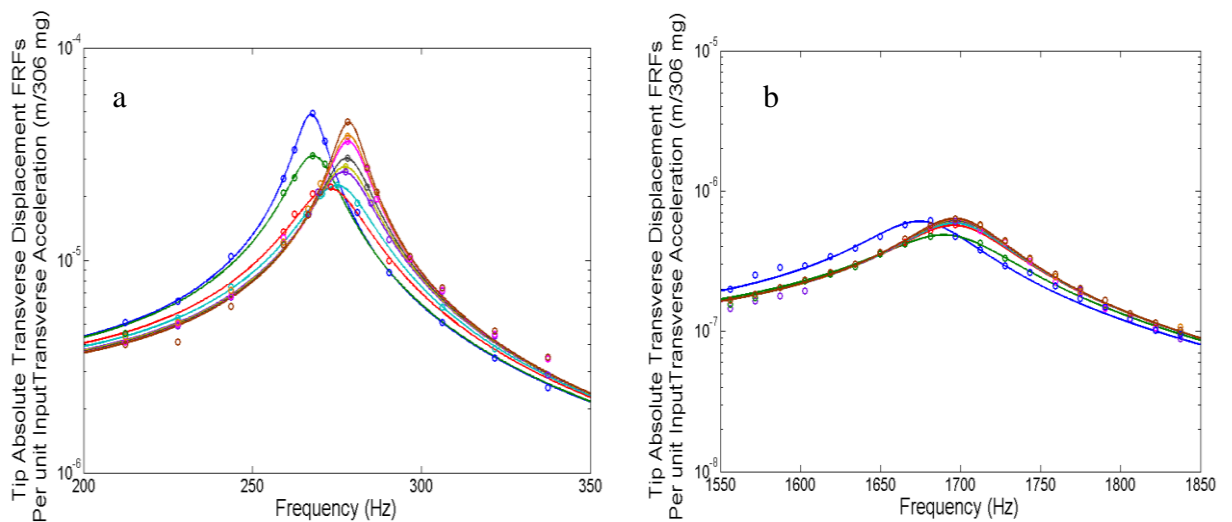Figure 6.34 FRFs of Tip Absolute Velocity with the CEDRT (Solid line) and Experiment (Round dot)

Figure 6.35 FRFs of Tip Absolute Velocity with the CEDRT (Solid line) and Experiment (Round dot)
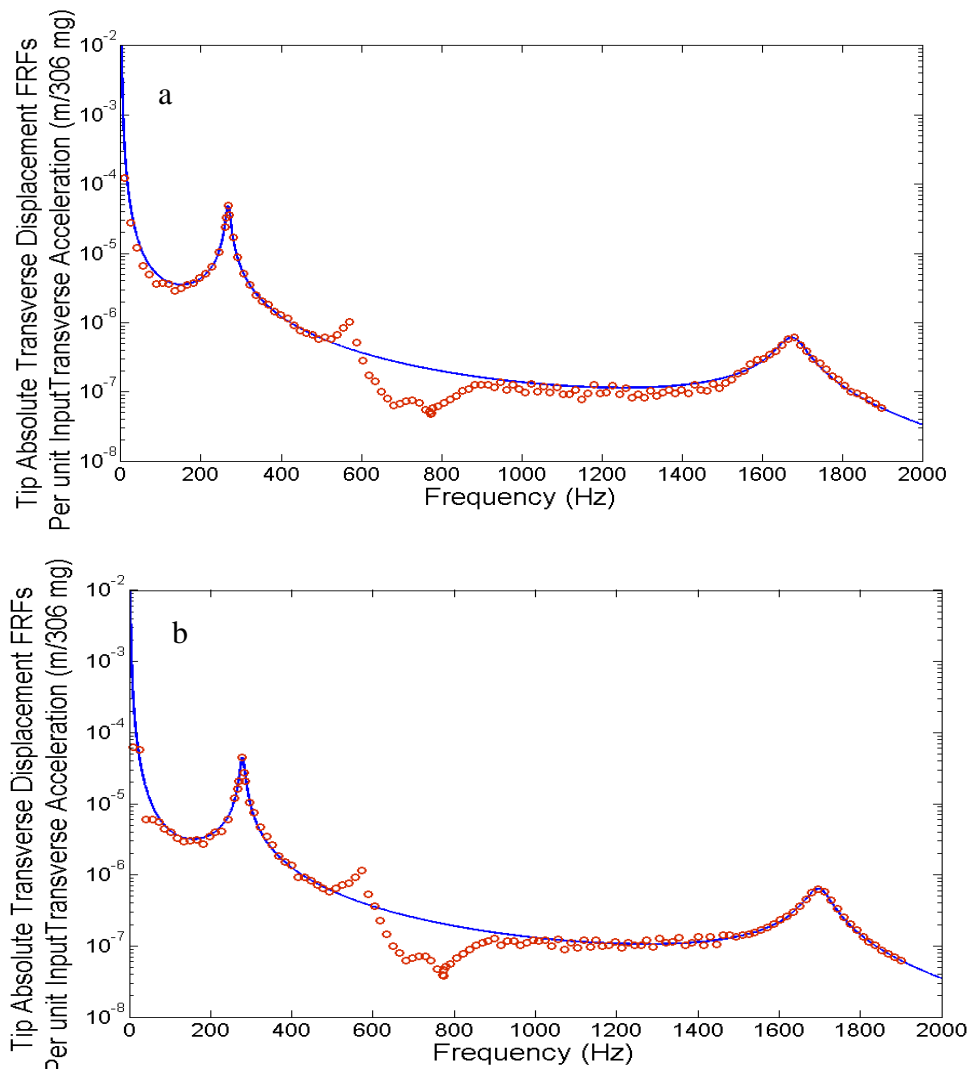a) First Mode and b) Second Mode

Figure 6.36 FRFs of Tip Absolute Velocity with the CEDRT (Solid line) and Experiment (Round dot) : a) 560 Ω (Short Circuit) and b) 602 kΩ (Open Circuit)

6.3.3. The Multi-mode Bimorph FRFs of Electrical Voltage

As can be seen from Figure 6.37, the first two FRFs modes of electrical voltage are shown with variable load resistances based on the CEDRT and CEDRTL models. The resonance frequency of the first mode tended to increase from the short to open circuit load resistance along with the voltage amplitude. The CEDRT and CEDRTL models gave a maximum percentage difference of amplitude around 22.96 % across the higher load resistances at the off-resonances as shown in the enlarged view from Figure 6.38. The CEDRT results for the first mode under the short and open circuits indicated a response of 0.053 V/306 mg and 1.88 V/306 mg with the

resonance frequencies of 267.4 Hz and 278.5 Hz, respectively as shown in Figures 6.39, 6.40 and 6.41. The CEDRT results indicated closer agreement with the experimental result than that compared with the CEDRTL as shown in Figure 6.39. This can also be seen clearly from the enlarged view from Figure 6.40. The second FRF mode also showed good agreement between the CEDRT and experimental studies. Moreover, the second mode amplitudes with the higher load resistances tended to give close-fitting values at the same resonance frequency of 1698 Hz. Two individual samples of the electrical voltage FRFs with short and open circuit load resistance were also shown in Figure 6.41.

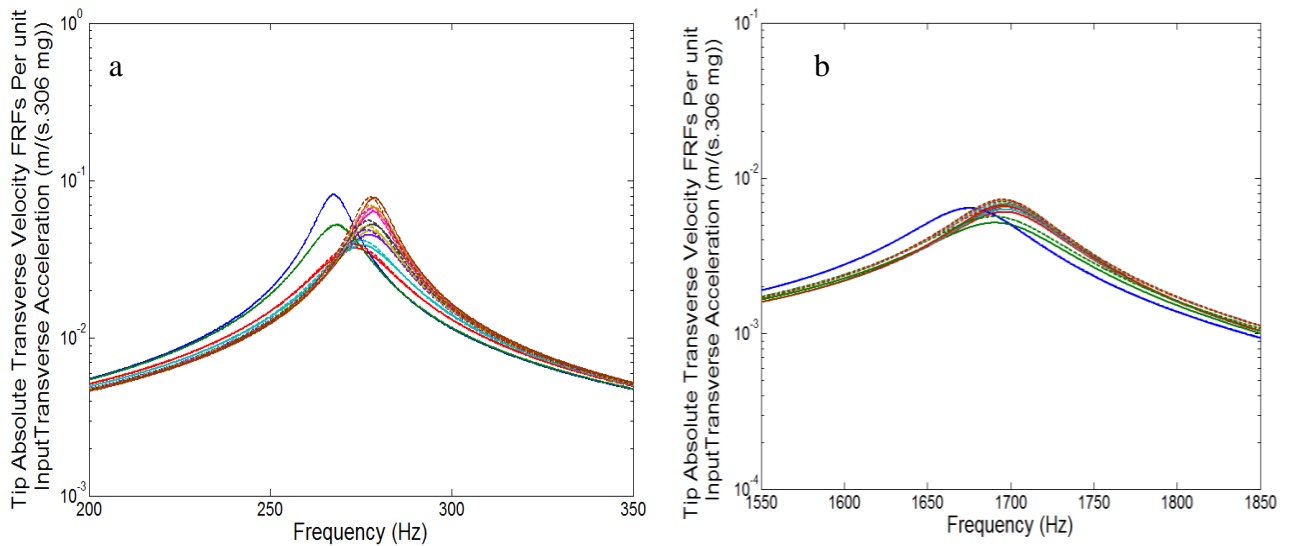Figure 6.37 First two modes FRFs of Electric Voltage with the CEDRT (Solid line) and CEDRTL (Dash line)

Figure 6.38 FRFs of Electric Voltage with the CEDRT (Solid line) and CEDRTL (Dash line)
: a) First Mode and b) Second Mode

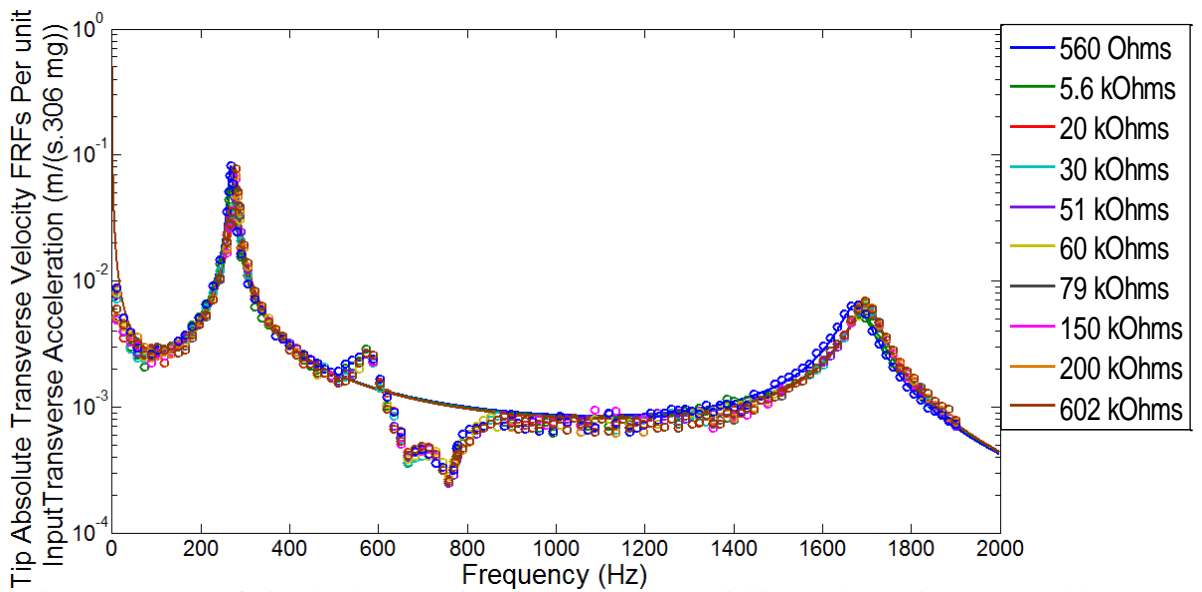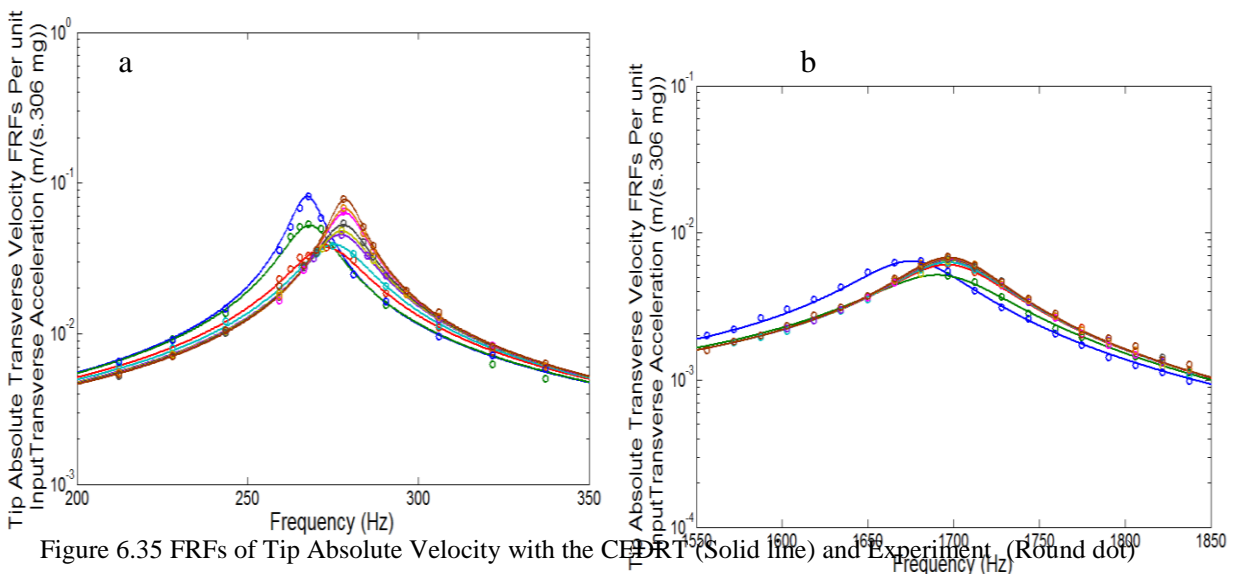Figure 6.39 FRFs of Electrical Voltage with the CEDRT (Solid line) and Experiment (Round dot)

Figure 6.40 FRFs of Electrical Voltage with the CEDRT (Solid line) and Experiment (Round dot) :
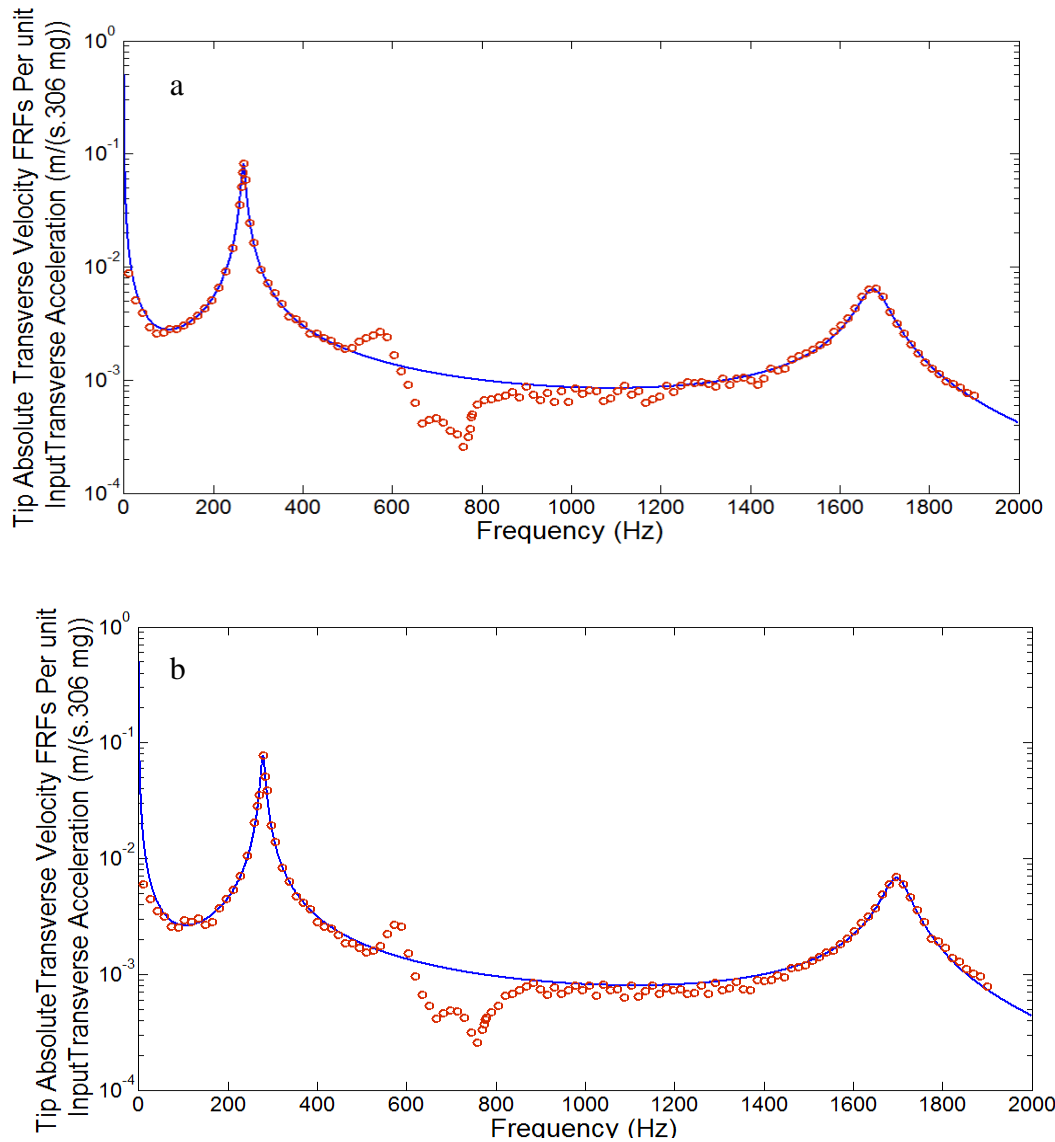a) First Mode and b) Second Mode

Figure 6.41 FRFs of Electrical Voltage with the CEDRT (Solid line) and Experiment (Round dot)
: a) 560 Ω (Short Circuit) and b) 602 kΩ (Open Circuit)

6.3.4. The Multi-mode Bimorph FRFs of Electrical Current

Figure 6.42 showed the first two FRF modes of electrical current based on the CEDRT and CEDRTL models for variable load resistance. The first mode of electrical current showed the opposite trend with the electrical voltage as shown in the enlarged view of Figures 6.43a and 6.38a. The resonance frequencies of electrical current decreased from the short to open circuits whereas the electrical voltage (from short and open circuits) gave increasing resonance frequency followed by increasing amplitude. The second resonant mode of electric current seemed to consistently have the resonance frequency of 1698 Hz as the load resistance varied from 20 kΩ to 602 kΩ with decreasing amplitude from 4.25 µA/306 mg until 0.16 µA/306 mg. Although the percentage difference between the CEDRT and CEDRTL models indicated around 23 %, the CEDRT model appeared to be closer with the experimental results compared with CEDRTL as shown in Figure 6.44. The second mode amplitude with the dominant higher resistances tended to approach constant resonance as shown in Figure 6.45b. Since two examples of current FRFs with the short and open circuit load resistances as shown in Figure 6.46 indicated very good agreement between the theoretical and experimental results, both of which clearly showed the highest and lowest amplitudes, respectively. Moreover, the FRFs of electrical current of the bimorph without tip mass seemed to give lower amplitudes and higher resonance frequencies for each load resistance compared with the bimorph system with the tip mass. The effect of the tip mass on the bimorph appeared to result in a significant increase of system amplitudes and a reduction of the resonance frequency especially at the first mode. However, the bimorph without

the tip mass resulted in smaller amplitude differences between the first, second and higher resonance frequency responses.
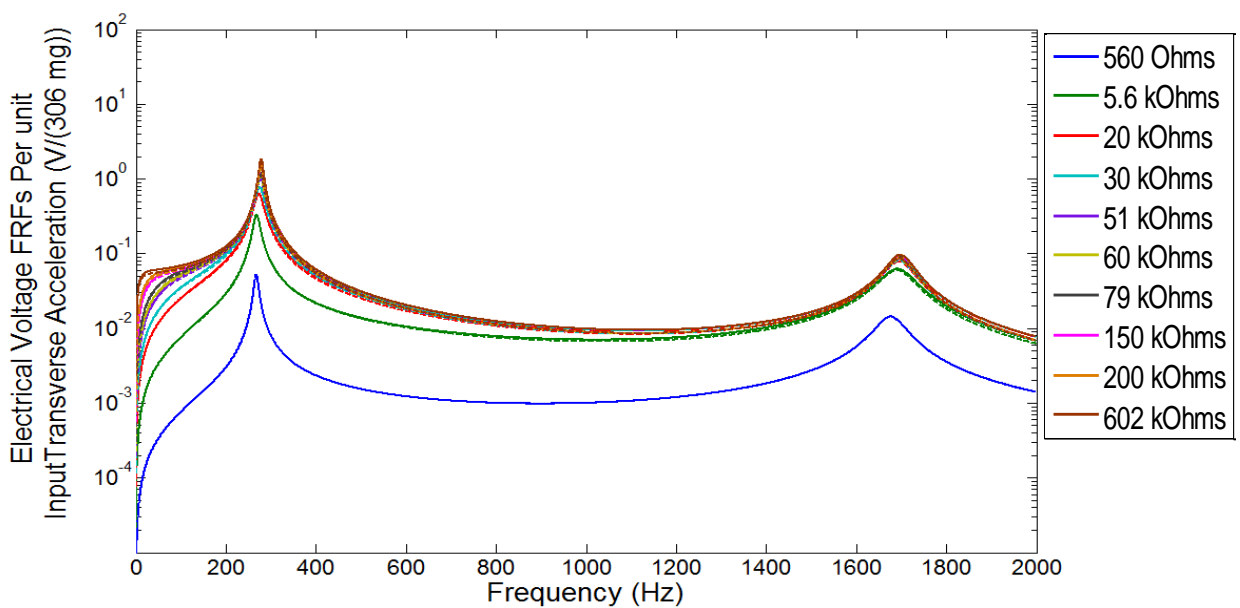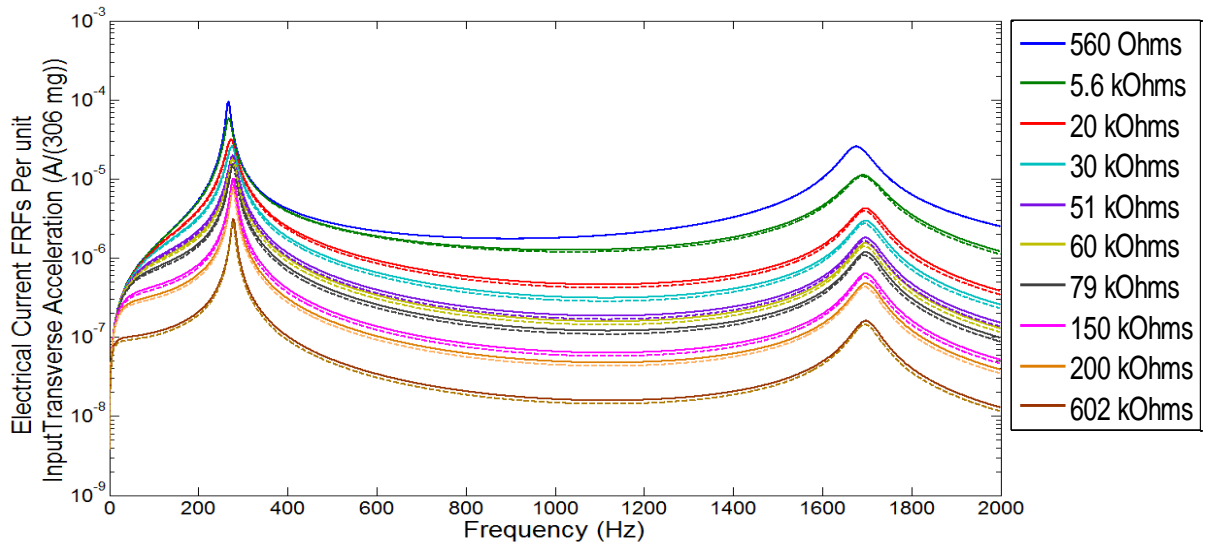

Figure 6.42 First two modes FRFs of Electric Current with the CEDRT (Solid line) and CEDRTL (Dash line)
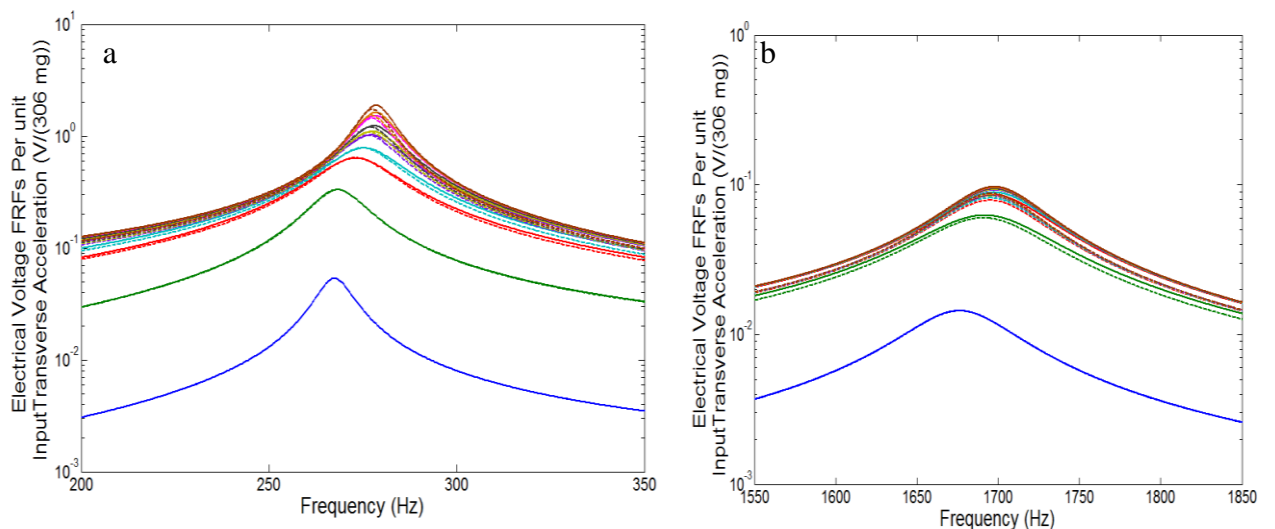

Figure 6.43 FRFs of Electrical Current with the CEDRT (Solid line) and CEDRTL (Dash line) :
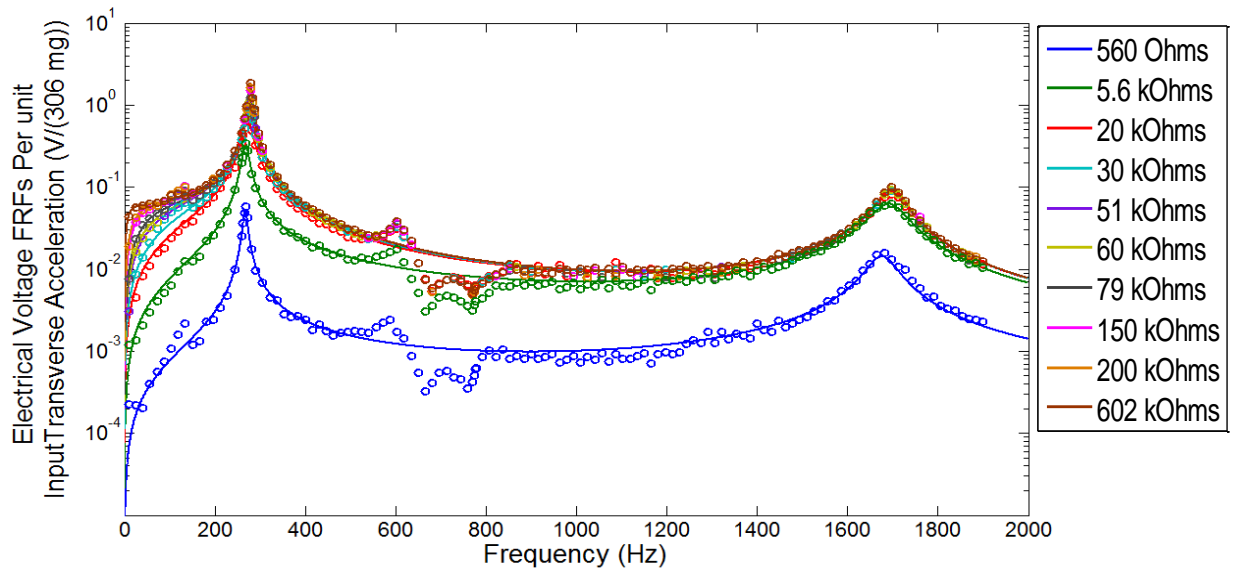a) First Mode and b) Second Mode
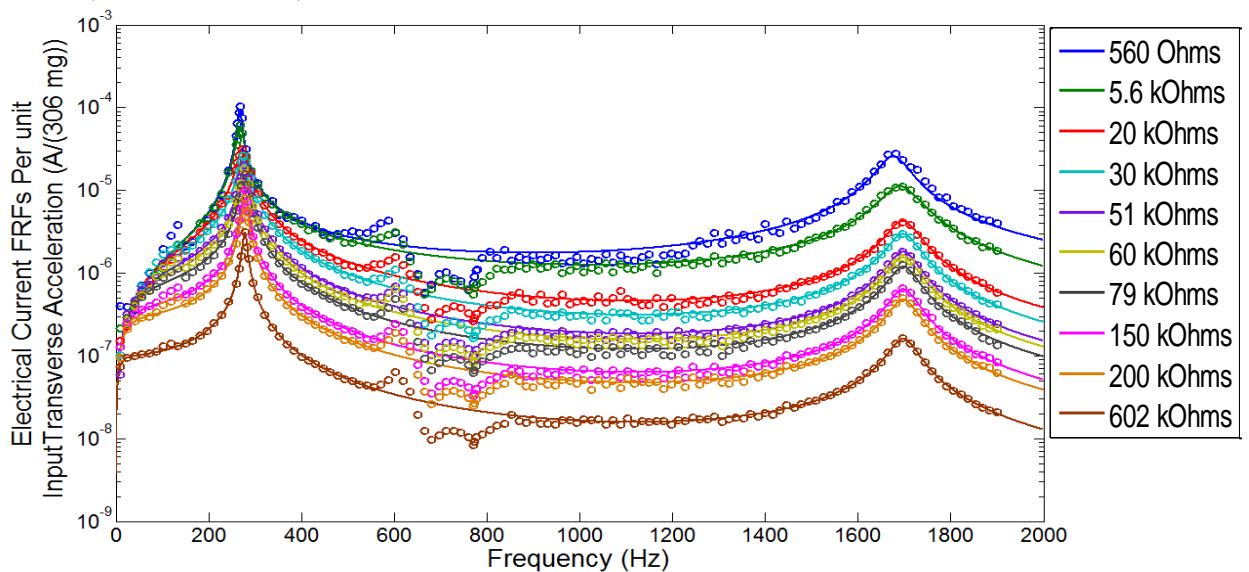
Figure 6.44 FRFs of Electrical Current with the CEDRT (Solid line) and Experiment (Round dot)
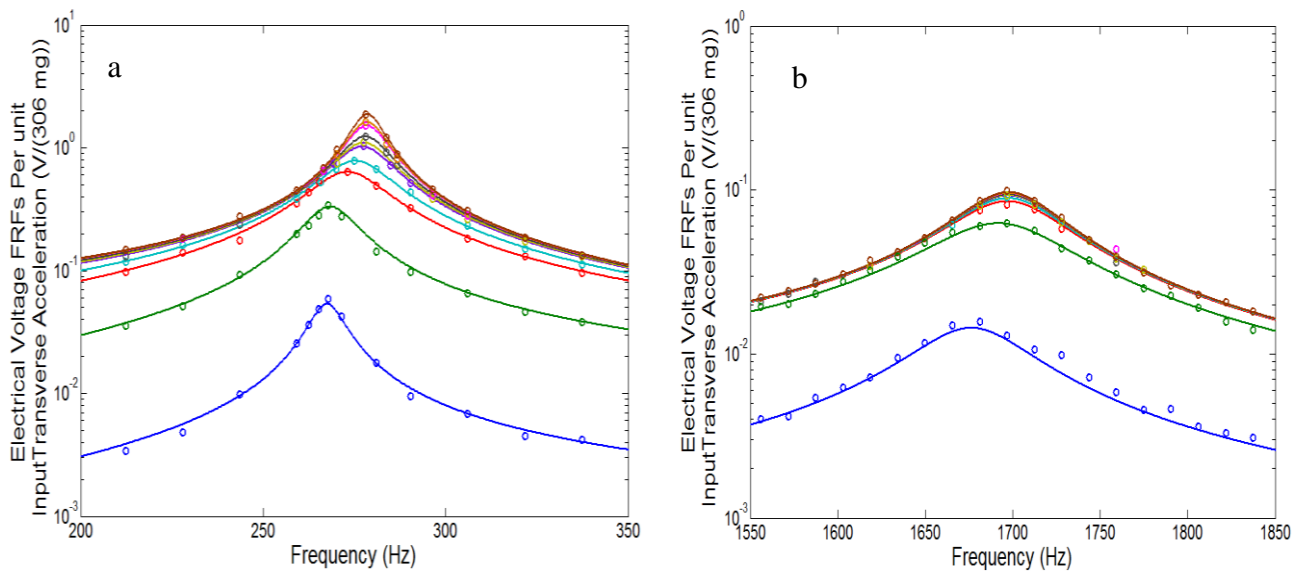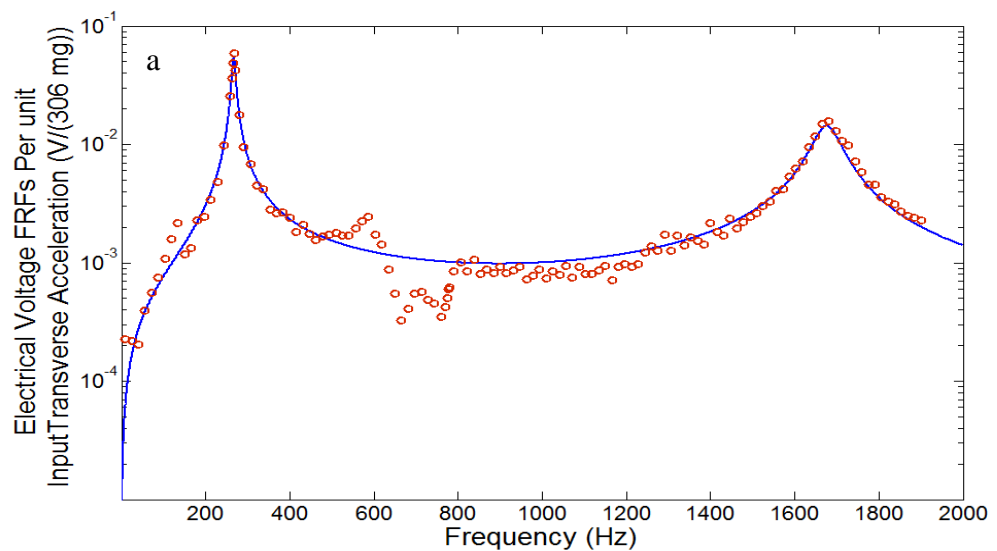
Figure 6.45 FRFs of Electrical Current with the CEDRT (Solid line) and Experiment (Round dot) :
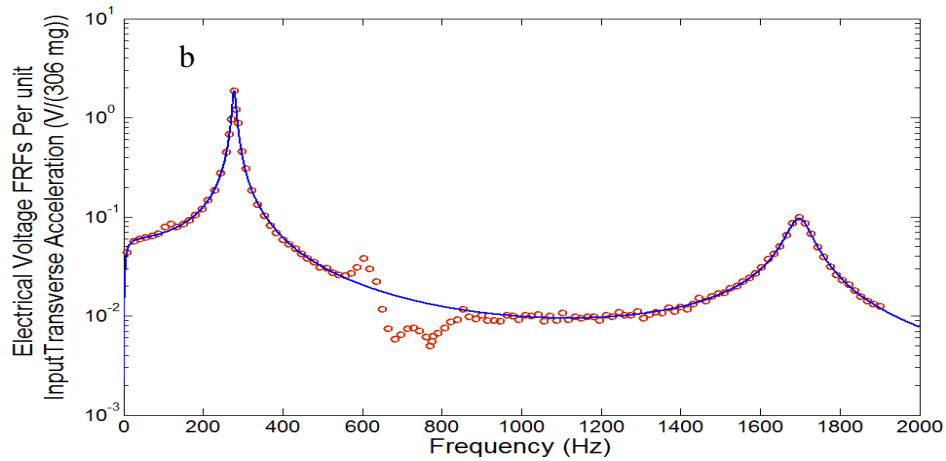a) First Mode and b) Second Mode

Figure 6.46 FRFs of Electrical Current with the CEDRT (Solid line) and Experiment (Round dot)
: a) 560 Ω (Short Circuit) and b) 602 kΩ (Open Circuit)

6.3.5. The Multi-mode Bimorph FRFs of Power Harvesting

As can be seen from Figure 6.47, the first two FRFs power harvesting modes based on the CEDRTL and CEDRT models are shown with variable load resistance. The power harvesting FRFs without tip mass gave lower amplitudes than that with the addition of the tip mass. The contribution of the tip mass onto the bimorph also affected the change of the symmetrical pattern of the FRF amplitudes for the various load resistances. The change in resonance frequency of the first mode tended to change the amplitude response as the load resistance changed as shown from Figure 6.48a. The second mode of power harvesting still showed the predominantly consistent resonance frequency of 1698 Hz as shown in Figure 6.48b. Good agreement of the FRFs between the CEDRT and experimental studies was achieved as shown in Figure 6.49 with the enlarged view from Figure 6.50. As mentioned previously, the irregular mode located between the first and second resonance frequencies occurred naturally under the measurement due to the imperfectly rigid clamped support from the base protractor structure. However this did not appear to affect the results from the first two FRFs modes. The short and open circuit power harvesting results for the first mode from Figure 6.51 still showed the lowest amplitudes, even though these circuits gave the highest amplitudes of tip absolute velocity and displacement. Moreover, by relating this with the FRFs electrical voltage results as given previously, the short and open circuits appeared to give the lowest and highest voltage amplitudes respectively with the increasing resonance frequencies. This trend was opposite to that given from the FRFs of electrical current. The chosen load resistances, viewed as resistive shunt damping, affects the electromechanical behaviour of the piezoelectric element resulting in the power harvesting behaviour, where the resonance frequency shifted as the load resistances changed. In addition, the piezoelectric bimorph itself, having the physical behaviour of the coupled electromechanical system, also involved piezoelectric couplings and internal capacitance, giving rise to electromechanical damping as well as electromechanical stiffness. This case has also been proven mathematically in chapter 4, and has given the results from the parametric case study shown in chapter 5 and validated with the experimental study in this chapter.
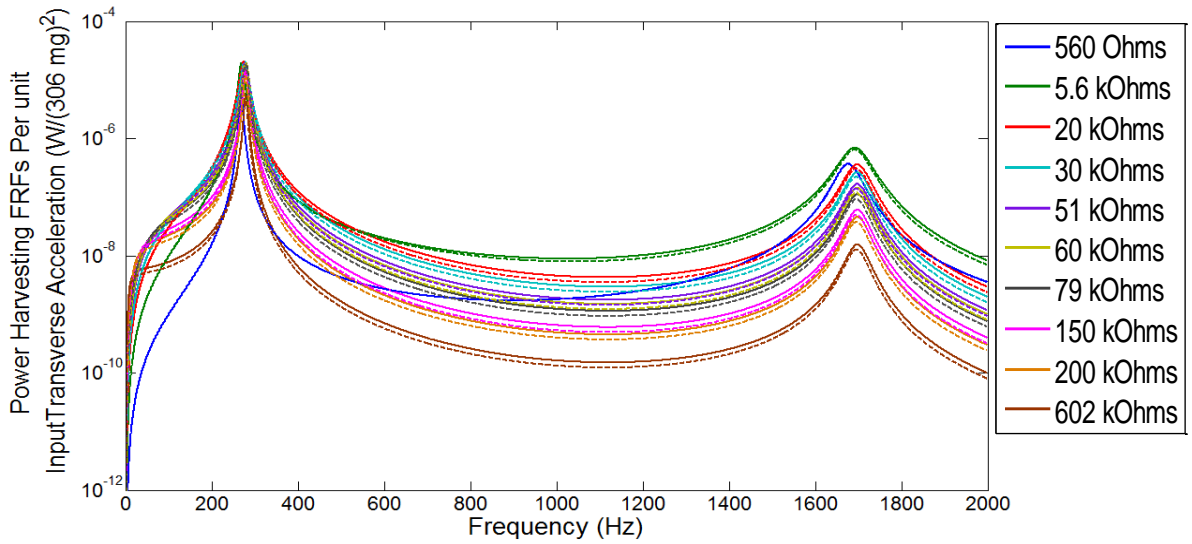
Figure 6.47 First two modes FRFs of Power Harvesting with the CEDRT (Solid line) and CEDRTL (Dash line)
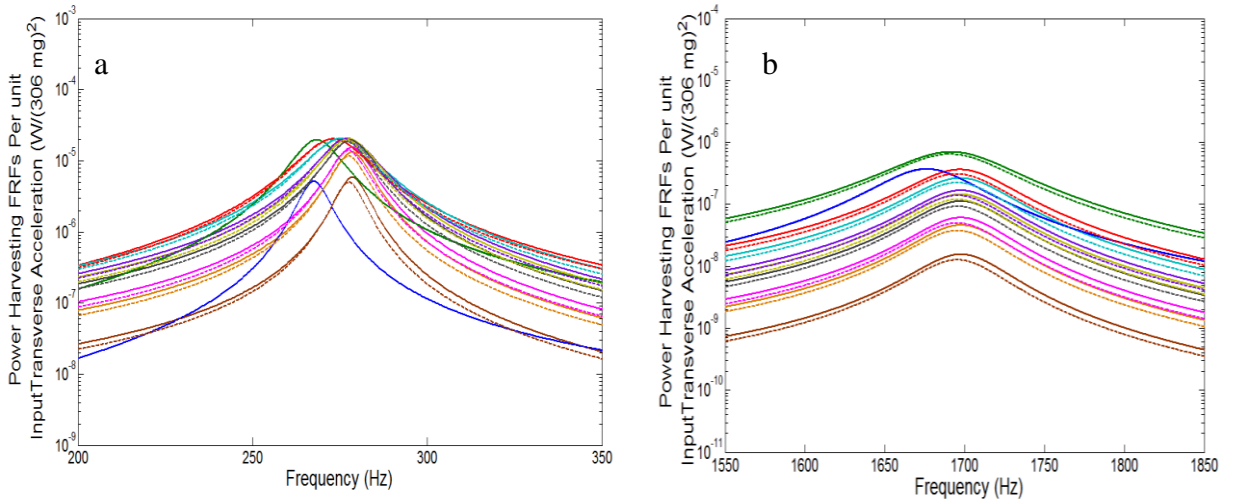
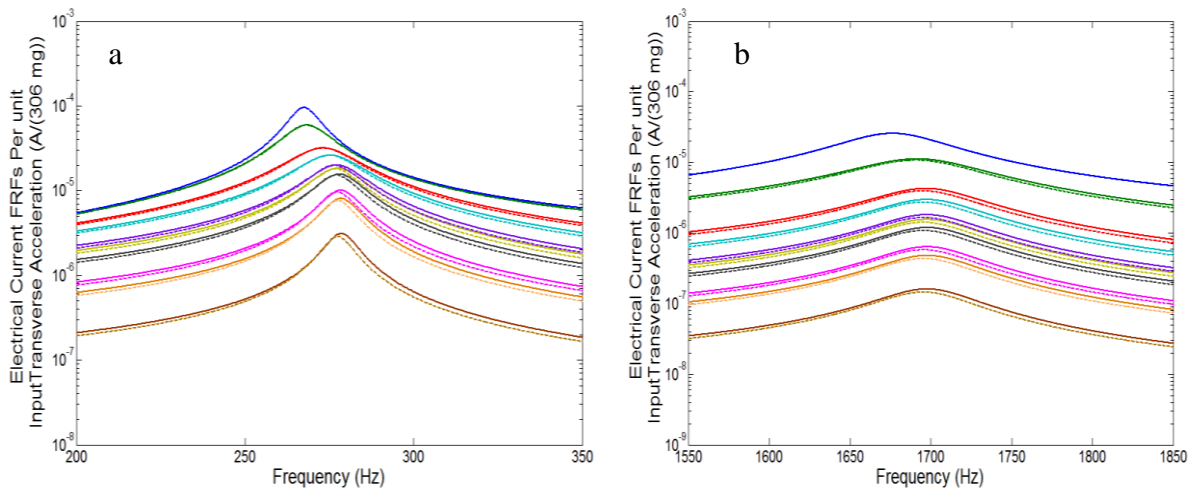Figure 6.48 FRFs of Power Harvesting with the CEDRT (Solid line) and CEDRTL (Dash line) :
a) First Mode and b) Second Mode
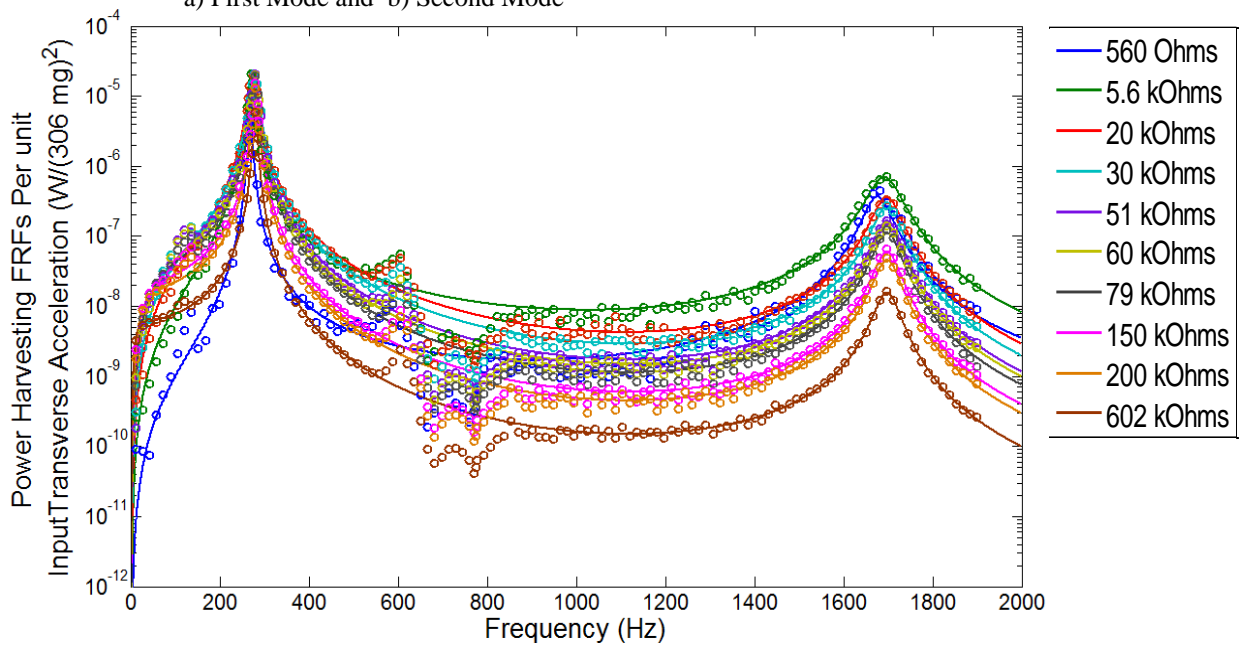
Figure 6.49 FRFs of Power Harvesting with the CEDRT (Solid line) and Experiment (Round dot)
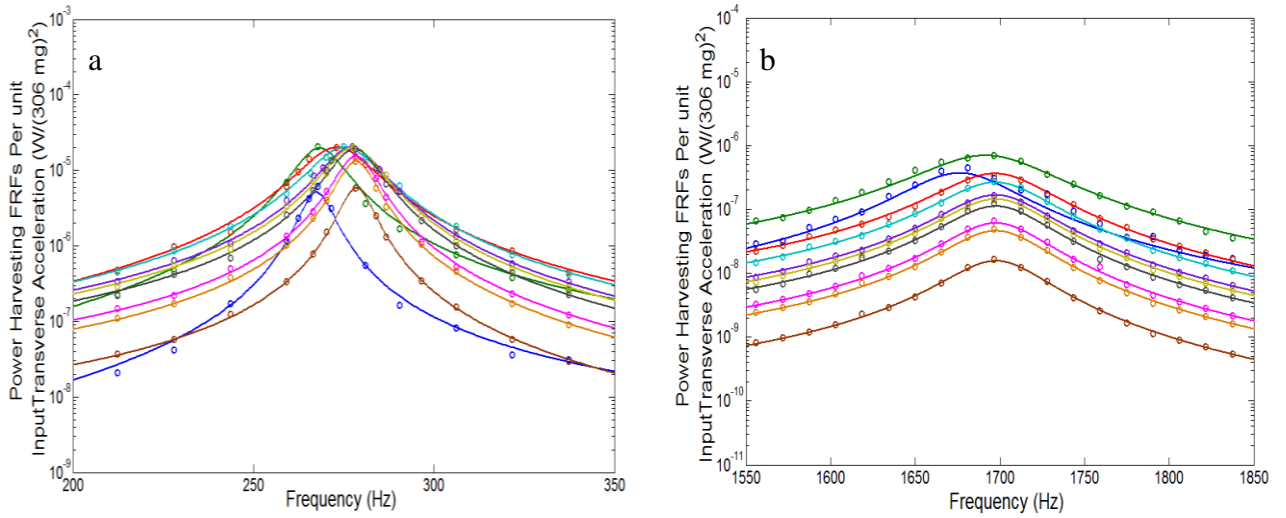
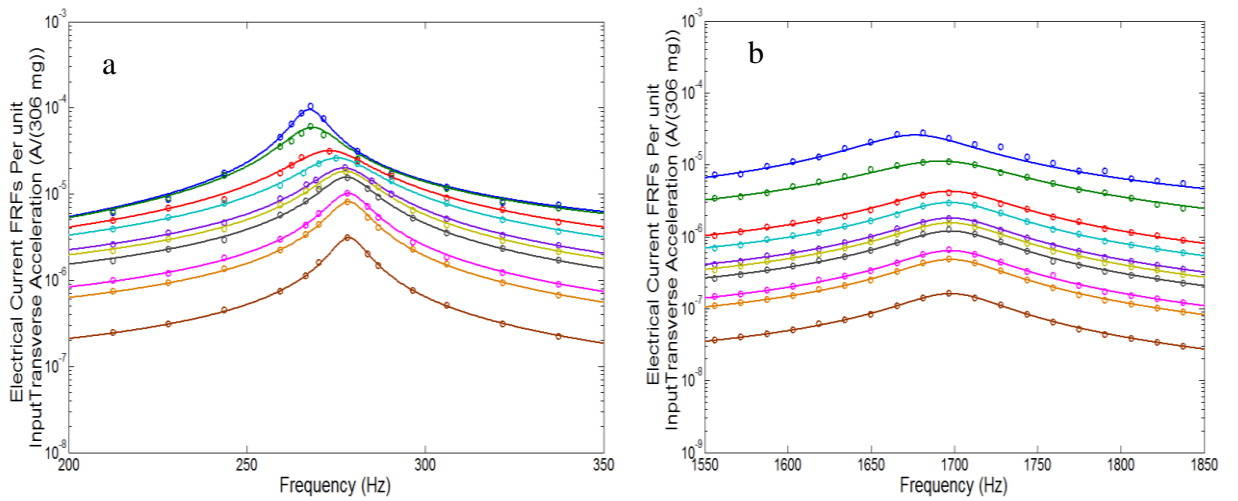Figure 6.50 FRFs of Power Harvesting with the CEDRT (Solid line) and Experiment (Round dot) :
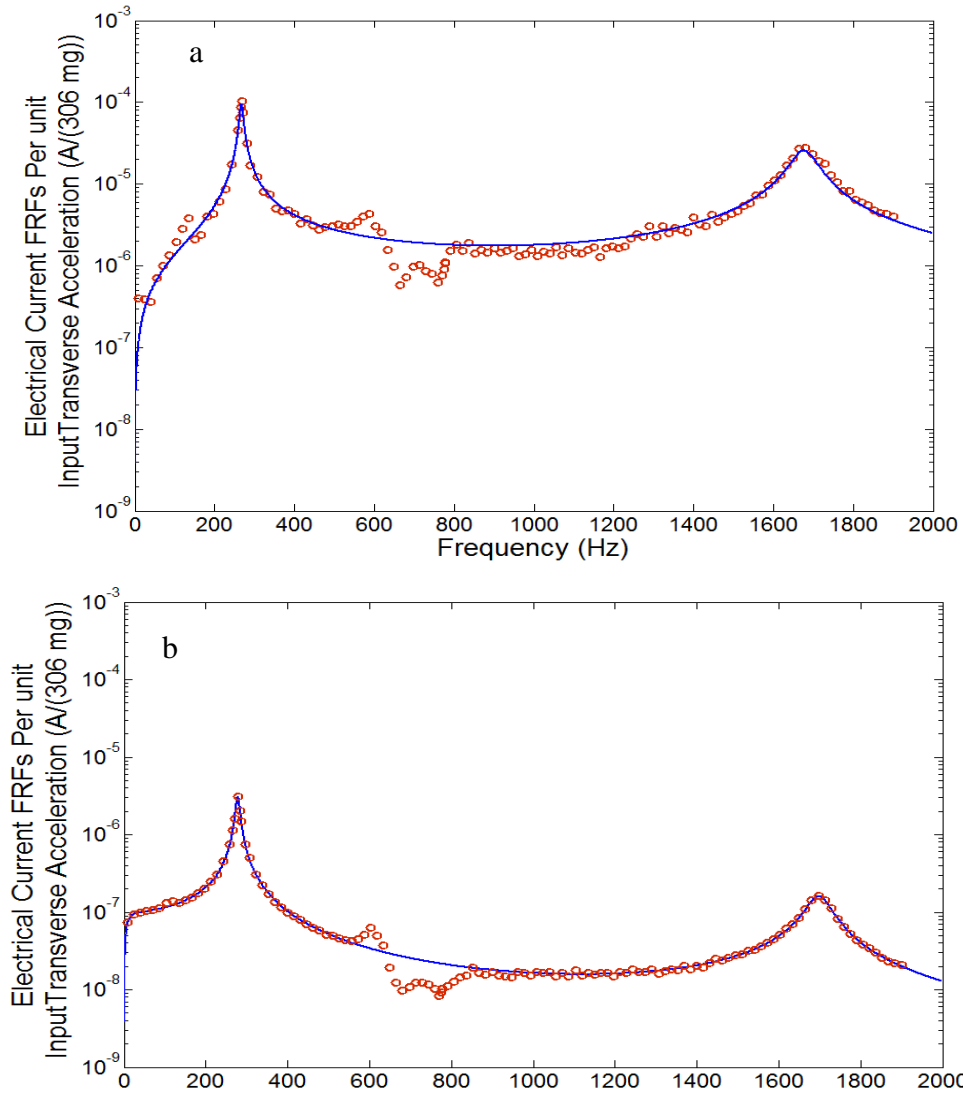a) First Mode and b) Second Mode
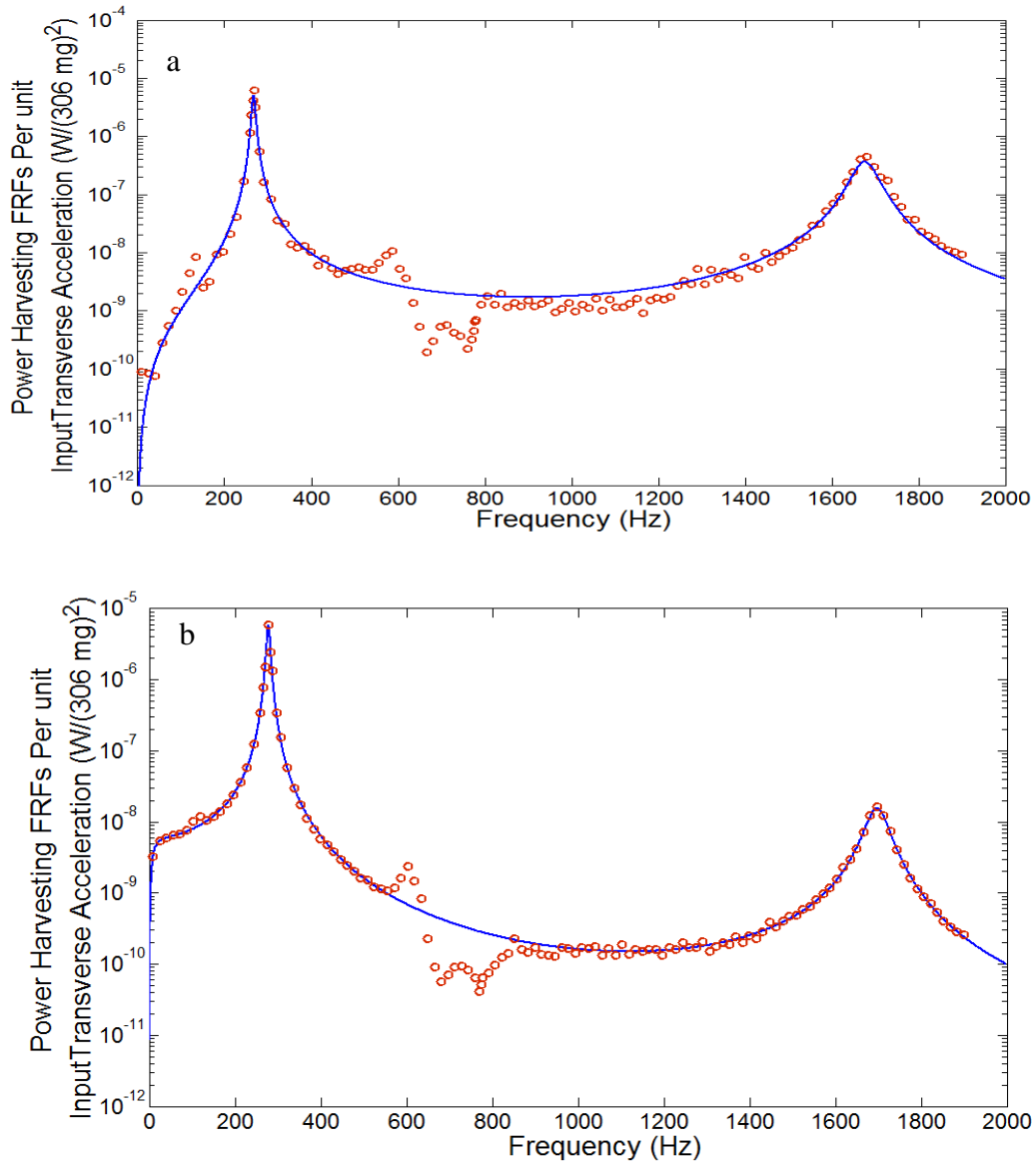
Figure 6.51 FRFs of Power Harvesting with the CEDRT (Solid line) and Experiment (Round dot) :
a) 560 Ω (Short Circuit) and b) 602 kΩ (Open Circuit)

6.4. Polar Electromechanical Dynamic Response due to Varying Base Input Accelerations

In this section, the piezoelectric bimorph with a tip mass under varying base input acceleration direction was studied with variable load resistance. The piezoelectric bimorph was clamped to a base protractor structure capable of being setup with different angles as shown in Figure 6.52. Only one input acceleration from the head impedance went to the base protractor structure. However, this protractor structure can be aligned with angles from $0^o – 180^o$ with incremental angles of 22.5^o in order to vary the direction of the base input motion from transverse to longitudinal. In the theoretical study, the investigation of the effects of the bimorph electromechanical dynamic responses with CEDRTL model in the polar coordinate system with incremental angles of 1° was discussed using the input base accelerations. The results were also compared and validated with the experimental results.
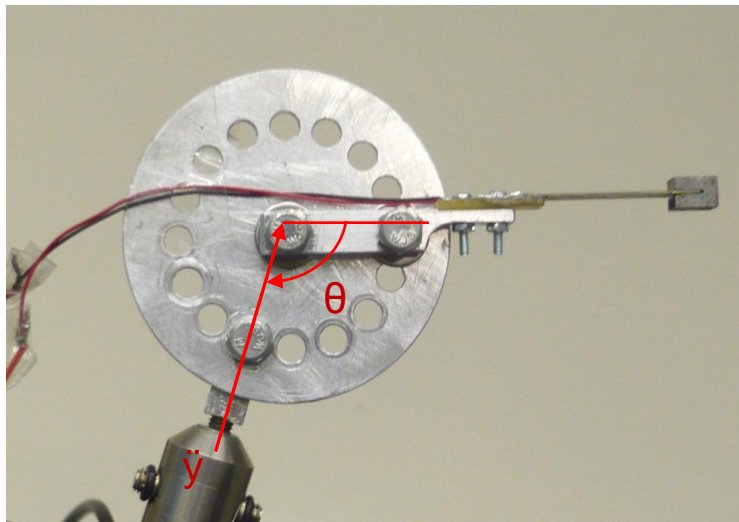
Figure 6.52 Input base acceleration with the bimorph beam protractor mounting structure

6.4.1. Bimorph Polar Dynamic Displacement Response

The electromechanical dynamic displacements of the beam were investigated using the mounting protractor with angles from $0^o – 180^o$ across the chosen frequency and load resistance ranges. As can be seen from Figure 6.53, the polar electromechanical tip absolute dynamic displacement was measured at frequencies of 72.67 Hz, 77.71 Hz, 75 Hz, 80 Hz. It should be noted that there were identical trends

of tip absolute displacement with the angles from 0°-90° and 90°-180° as indicated by the symmetrical pattern due to the base input acceleration level of 3 m/s^2. It should be noted that the base input acceleration level was kept at the constant value by varying the angle incrementally by 22.5^o for experimental result and by 1° for the numerical result. Moreover, the trends of the polar electromechanical tip absolute displacement gave very good agreement between the analytical and experimental results. As can be seen from Figure 6.53c, the maximum tip absolute displacement of the frequency of 75 Hz with the load resistances of 20 kΩ, 60 kΩ and 150 kΩ was reached at the angle of 90° with the amplitudes of 0.22 mm/(306 mg)^2, 0.14 mm/(306 mg)^2 and 0.12 mm/(306 mg)^2, respectively. This case represents the situation with the dominant transverse bending form of the bimorph where the results obtained are similar to the amplitudes shown from the FRFs of the tip absolute displacement as given in Figure 6.4. The lowest tip absolute displacement can be found at the angles of 0° and 180° due to the dominant longitudinal response form at this condition. The effect of input base acceleration with the interval angles between $0^o < \theta < 90^o$ and $90^o < \theta < 180^o$ can produce both transverse and longitudinal response forms due to the electromechanical response forms as formulated in equation (4.276). The other frequencies of 72.67 Hz, 77.71 Hz and 80 Hz also showed good agreement between the analytical and experimental results with the chosen load resistances. It should be noted that the FRF of the tip absolute dynamic displacement at the frequency of 77.71 Hz under the load resistances of 60 kΩ and 150 kΩ as shown in Figure 6.4 tended to be quite closed together. This can be compared to the result shown in Figure 6.53b, indicating the similar result.
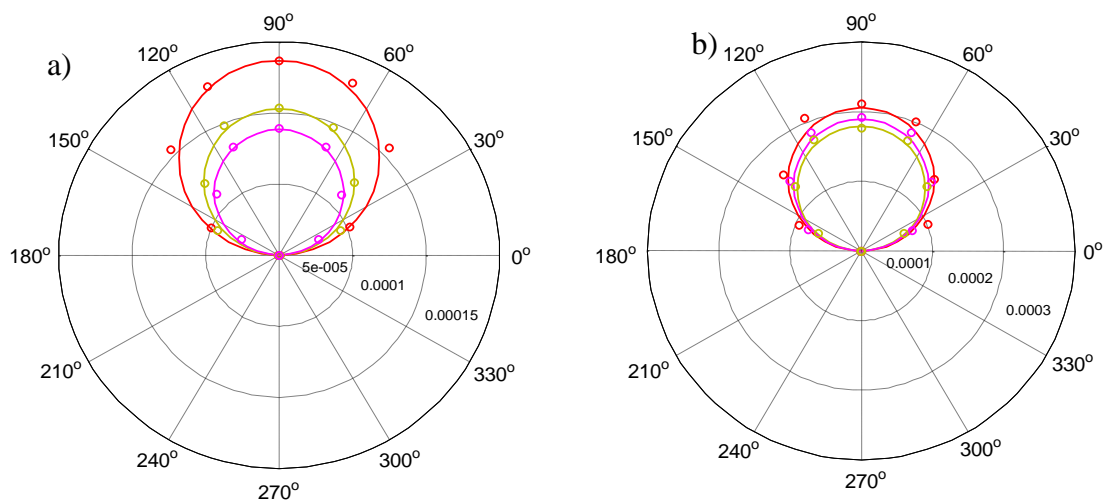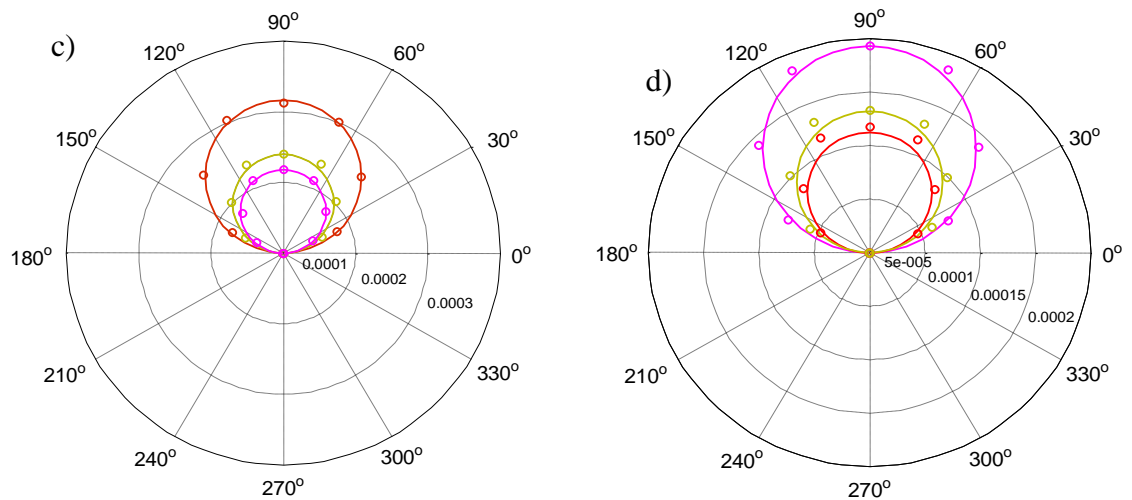
Figure 6.53 FRFs of Polar Tip Absolute Transverse Displacement from measurement (m/306 m*g*) at 20 kΩ, ⬤ at 60 kΩ, ⬤ at 150 kΩ ⬤ and from theoretical at 20 kΩ, ▬▬ at 60 kΩ, ▬▬ at 150 kΩ ▬▬ : (a) 72.67 Hz (b) 77.71 Hz (c) 75 Hz and (d) 80 Hz

6.4.2. Bimorph Polar Dynamic Velocity Response

In this section, the polar electromechanical dynamic velocities are shown in Figure 6.54 with frequencies of 72.67 Hz, 77.71 Hz, 75 Hz and 80 Hz at the load resistances of 20 kΩ, 60 kΩ and 150 kΩ. The resulting trend shows similar behaviour with the polar tip absolute displacement. The tip absolute displacement and velocity again showed similar results to those from the previous discussion on the FRF results shown in Figures 6.4 and 6.8. The maximum amplitude for the polar coordinate system velocity response shown in Figure 6.54 occurred at the angle of 90° as expected. The response at the frequency of 72.67 Hz resulted in amplitudes of 0.0624 m/(s.306 m*g*), 0.0469 m/(s.306 m*g*) and 0.0402 m/(s.306 m*g*) with the load resistances of 20 kΩ, 60 kΩ and 150 kΩ respectively. This was also similar to the results shown in the FRF from Figure 6.8. The other angles with the same frequencies still indicated good agreement between the analytical and experimental results as shown in Figure 6.54. The transverse response again dominates the polar tip velocity, as seen from the angle of 90° due to the base input transverse acceleration onto the bimorph. The response at angles between $0^o < \theta < 90^o$ and $90^o < \theta < 180^o$ again contains the coupled electromechanical transverse and longitudinal forms with the dominant polar tip response coming from the transverse base motion.
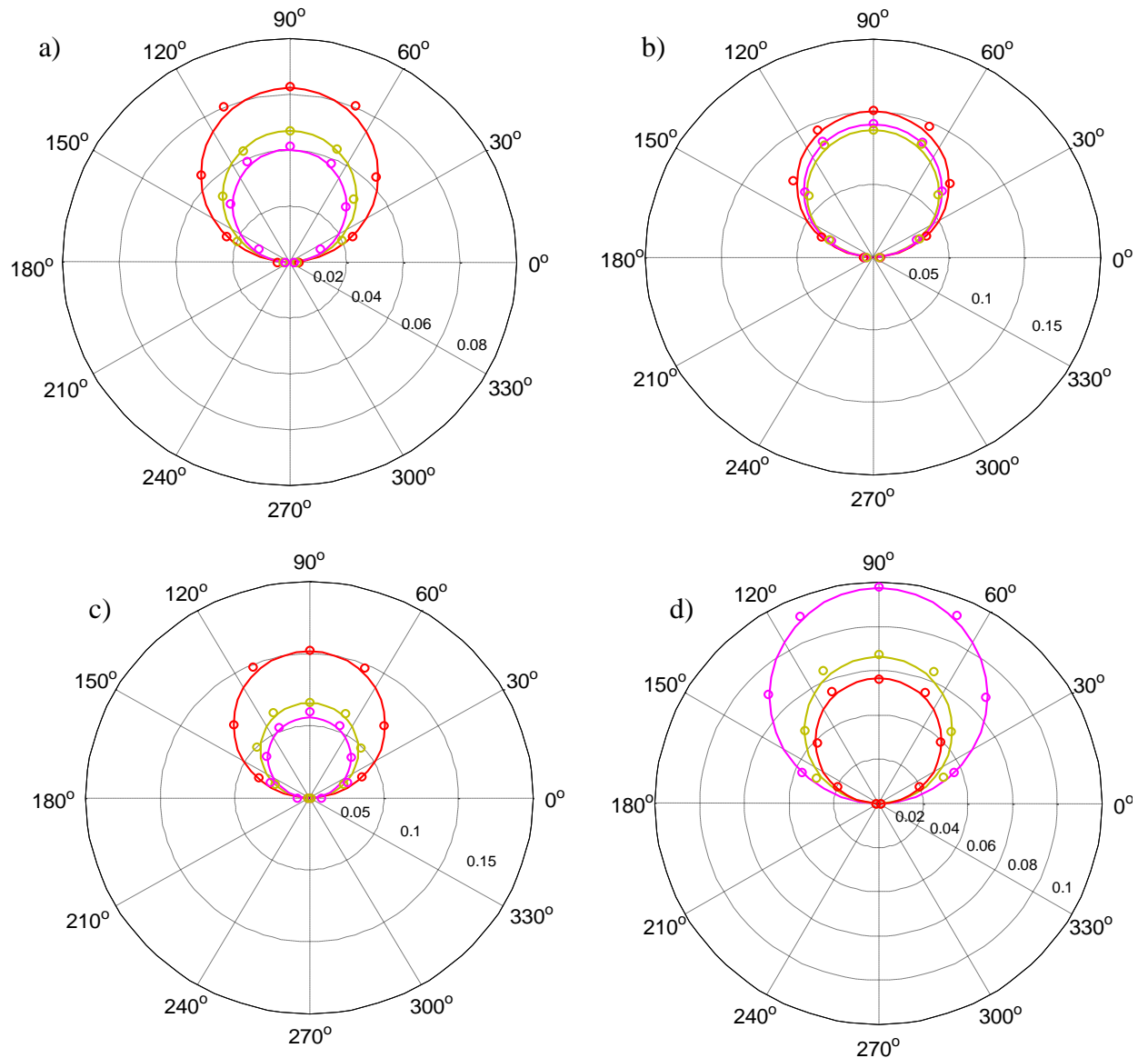
Figure 6.54 FRFs of Polar Tip Absolute Transverse Velocity from measurement (m/s.306 m*g*) at 20 kΩ, ⬤ at 60 kΩ, ⬤ at 150 kΩ, ⬤ and from theoretical at 20 kΩ, ▬▬ at 60 kΩ, ▬▬ at 150 kΩ ▬▬ :
(a) 72.67 Hz (b) 77.71 Hz (c) 75 Hz and (d) 80 Hz

6.4.3. Bimorph Polar Electrical Voltage Response

The polar electrical voltage response at frequencies of 75 Hz, 80 Hz, 77.71 Hz and 72.67 Hz are shown in Figure 6.55 with the load resistances of 20 kΩ, 60 kΩ and 150 kΩ as used previously. The maximum electrical voltage response was observed to occur at the protractor angles of 90° as expected. The response at the frequency of 72.67 Hz resulted in amplitudes of 1.38 V/(306 m*g*), 2.4 V/(306 m*g*) and 2.8 V/(306 m*g*), for the different load resistances respectively. The polar electrical voltage response presented reasonable comparison between the numerical

and experimental results. Consistency of increasing amplitudes at the polar electrical voltage responses increased at each frequency with increasing load resistances of 20 kΩ, 60 kΩ and 150 kΩ. This situation shows similar trends as observed previously as the electrical resistance goes from short circuit to open circuit.
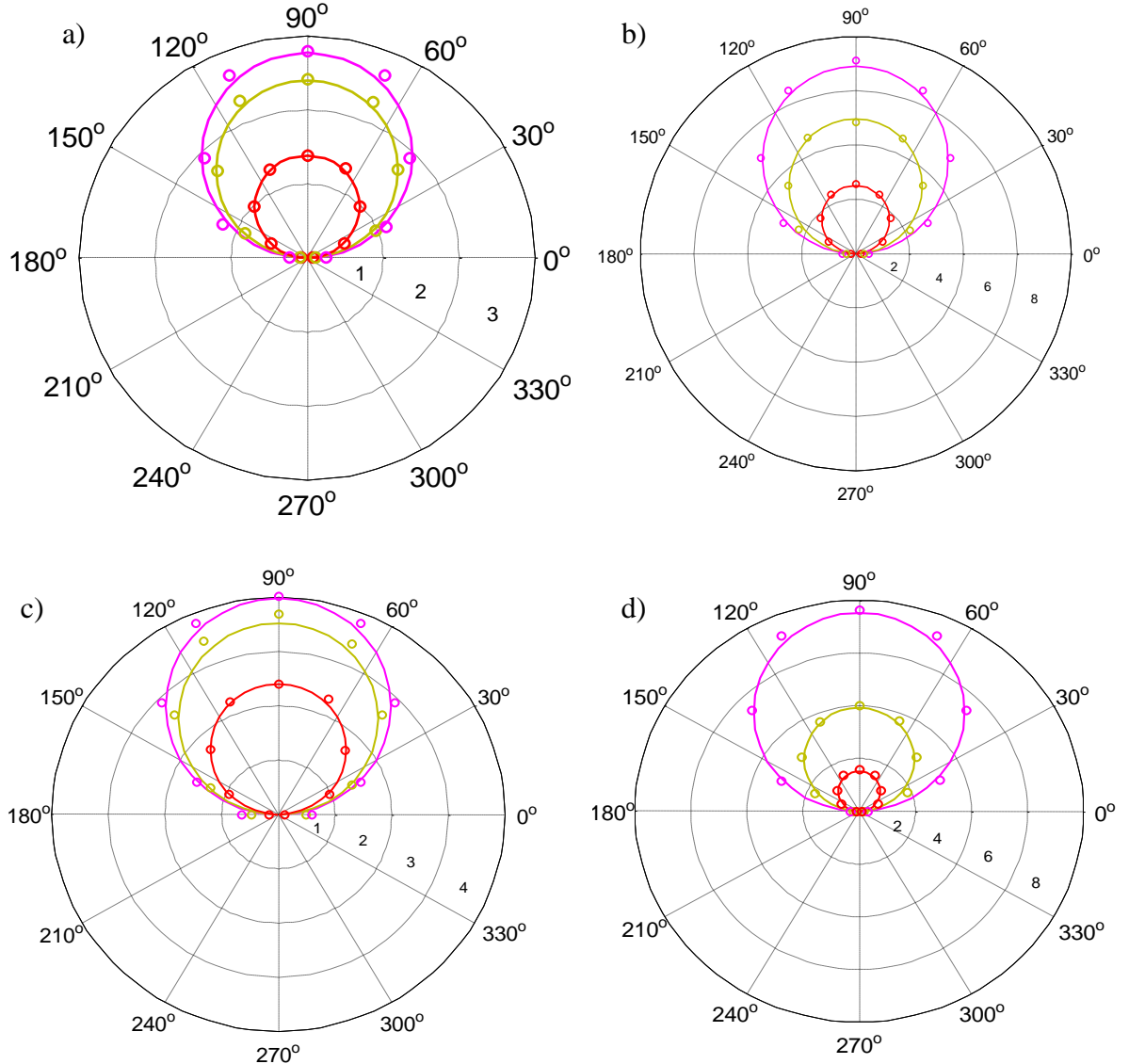
Figure 6.55 FRFs of Polar Electrical Voltage from measurement (V/306 m*g*) at 20 kΩ, ⬡ at 60 kΩ, ⬡ at 150 kΩ, ⬡ and from theoretical at 20 kΩ, ▬ at 60 kΩ, ▬ at 150 kΩ ▬ : (a) 72.67 Hz (b) 77.71 Hz (c) 75 Hz and (d) 80 Hz

6.4.4. Bimorph Polar Electrical Current Response

The polar electrical current response with the chosen frequencies still showed good agreement between the numerical and experimental results as shown in Figure 6.56. The consistency of increasing polar electric current amplitudes occurred for decreasing load resistances of 150 kΩ, 60 kΩ and 20 kΩ for each frequency as

expected. This trend was opposite to that obtained for the electrical voltage as shown previously. Similar behaviour was also found with the FRFs of electrical current and voltage shown previously. The results for the protractor angle of 90° again showed the maximum polar electrical amplitudes for each load resistance due to the input transverse acceleration. The results indicate the dominant effect of the transverse bending response of the bimorph, although the effect of the longitudinal response should not be ignored, especially at the higher load resistance as discussed previously with the comparisons between the CEDRT and CEDRTL.
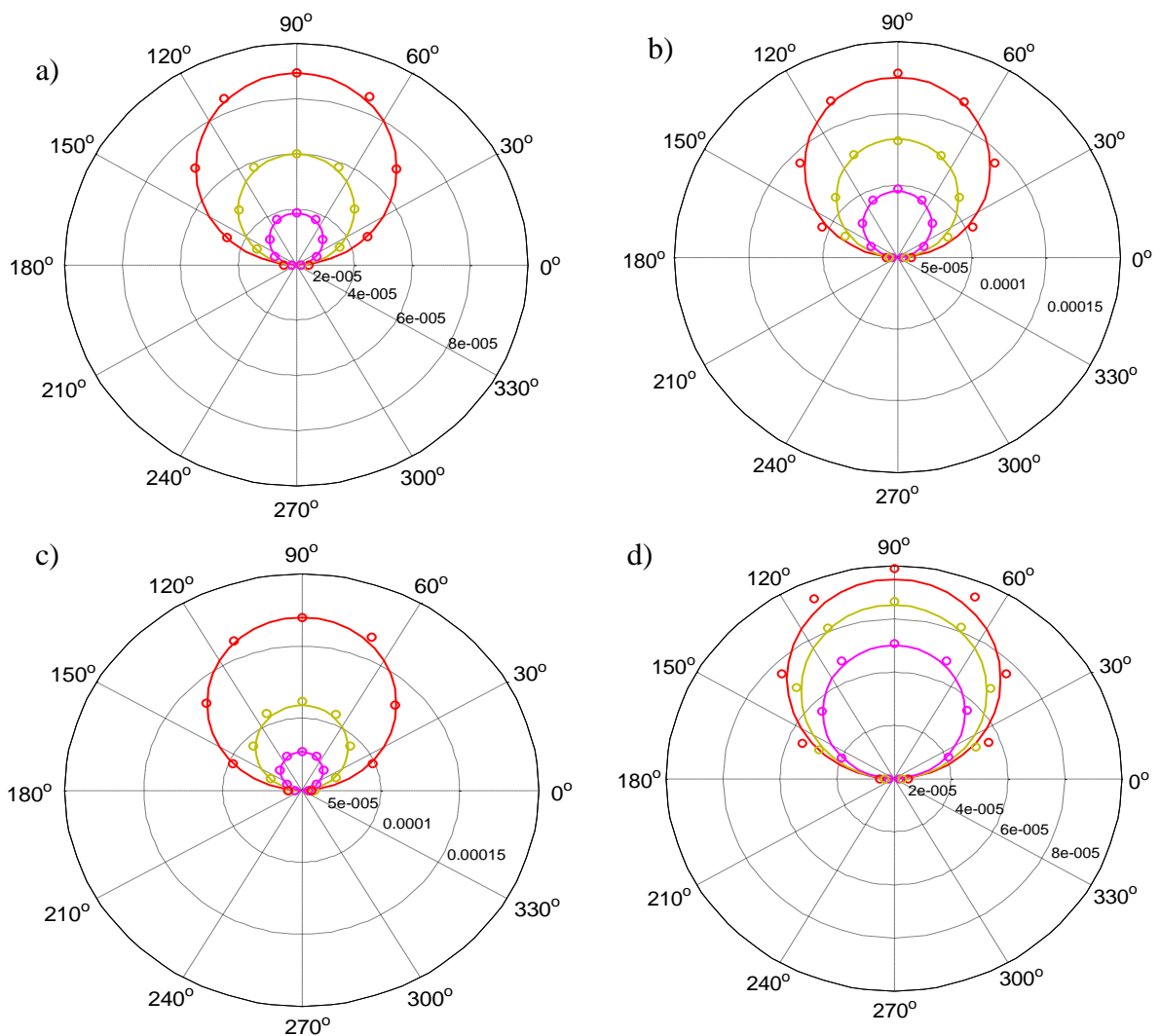
Figure 6.56 FRFs of Polar Electrical Current from measurement (A/306 *mg*) at 20 kΩ, ⬤ at 60 kΩ, ⬤ at 150 kΩ, ⬤ and from theoretical at 20 kΩ, ▬▬ at 60 kΩ, ▬▬ at 150 kΩ ▬▬ : (a) 72.67 Hz (b) 77.71 Hz (c) 75 Hz and (d) 80 Hz

6.4.5. Bimorph Polar Electrical Power Response

Figure 6.57 shows the power harvesting amplitudes with variable load resistance in polar form for frequencies of 72.67 Hz, 77.71 Hz, 75 Hz and 80 Hz, respectively. The polar results of power show the symmetrical response for the angles from 0°-90° and 90°-180° due to the base input acceleration. The polar power harvesting amplitudes also showed very close agreement between the analytical and experimental results. The maximum power was measured at the angle of 90° due to the dominant transverse bending form of the bimorph as expected from the CEDRTL analysis model. The lowest power can be found at the angles of 0° and 180° where this indicates the dominant longitudinal motion as again predicted by the CEDRTL model. The polar power harvesting results shown in Figures 6.57a and 6.57b for the load resistances of 20 KΩ and 150 kΩ tended to overlap each other. This situation can also be found from Figure 6.23 where the two lines of power amplitudes from the load resistances of 20 kΩ and 150 kΩ coincide for the frequencies of 77.71 Hz and 72.67 Hz. The comparisons between the analytical and experimental results still showed reasonable agreement. The polar power harvesting should be seen to be a result of the combination of both the transverse and longitudinal system response. Similar behaviour of power was also found from the protractor angles of 180°-270° and 270°-360°. It is noted that the dominant effect of transverse form of the bimorph was showed in the majority of angles resulting higher power compared with longitudinal form since the strain-polarity-electric field due to bending form predominantly affected to the bimorph under input base excitations creating mechanical and electrical moments. It is noted that the backward and forward piezoelectric couplings for transverse form were developed due to the electrical moments as discussed at chapter 4. Moreover, the longitudinal response at the load resistance approaching short circuit can be ignored as discussed in section 6.2.5, where the CERDTL and CEDRT models seemed to overlap each other.
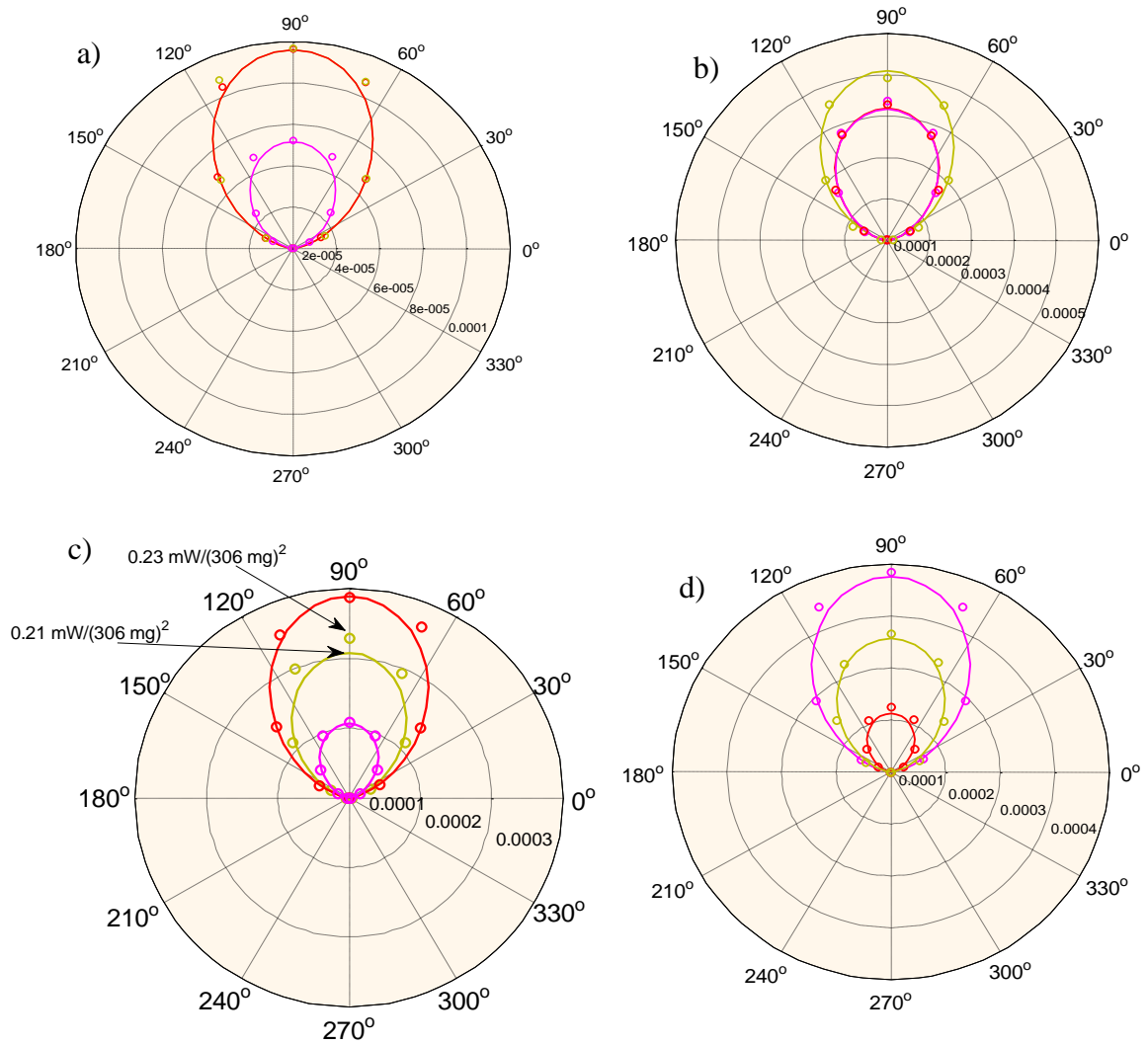
Figure 6.57 FRFs of Polar Power Harvesting from measurement (W/(306 m*g*)²) at 20 kΩ, ⬤ at 60 kΩ, ⬤ at 150 kΩ, ⬤ and from theoretical at 20 kΩ, ▬▬▬ at 60 kΩ, ▬▬▬ at 150 kΩ ▬▬▬ : (a) 72.67 Hz (b) 77.71 Hz (c) 75 Hz and (d) 80 Hz

6.5. Closing Remark

This chapter has presented the results from analytical study and experimental measurements of the electromechanical dynamic response of the piezoelectric bimorph beam with and without a tip mass. The analytical studies of the CEDRTL and CEDRT analysis models were also plotted under various load resistance values from short circuit to open circuit. The effect of the CEDRTL model demonstrates the electromechanical principle where the strain field includes the coupling between the transverse bending and longitudinal extension forms, where the CEDRT model ignored the longitudinal effect. Both the CEDRTL and CEDRT models have been derived from the energy fields using the principle of continuum piezoelectric

thermodynamics with the assumptions of isothermal and adiabatic processes as further derived using Hamiltonian's principle. The mechanical damping ratios were determined by matching the frequency amplitudes at the short circuit load resistance from the experimental results with the theoretical studies. The shifting of the resonance frequencies occurred as the load resistances changed where this case mostly occurred at the first mode. Moreover, the CEDRTL and CEDRT model comparisons gave slight changes of power amplitude trends especially where the load resistances approached the open circuit condition with the maximum difference percentage of 49.11 %. However, when the load resistance approached the short circuit, the frequency amplitudes given from CEDRTL and CEDRT model seemed to overlap each other. The FRFs from the CEDRTL model and the experimental results of the bimorph with the tip mass have been compared with good agreement. The effect of tip mass on the bimorph is known to create additional bending and electrical moment effects with the coupling effect of the longitudinal extension and electrical forces in the interlayer bimorph element. The tip mass provides extra dynamic inertia loading due to the additional effects of extensional kinetic energy. Apart from that, the tip absolute displacement or velocity with the load resistance approaching short and open circuits indicated the highest amplitudes. However, the voltage amplitude increased from short to open circuit resistance whereas increasing electrical current amplitude otherwise occurred from the open to short circuits. Therefore, the highest velocity or displacement is not the substantial basis for providing the maximum current and maximum voltage. In this case, the optimal power harvesting with the absolute maximum values achieved 0.43 mW/(306 mg)^2 at the load resistances of 20 kΩ and 200 kΩ. The optimal power at the absolute maximum value provided higher velocity or displacement amplitude compared with the optimal power at the local minimum value, with the load resistance of 60 kΩ giving the convenient value of power of 0.41 mW/(306 mg)^2. The optimal power density at the local minimum value achieved 4.17 mW/(cm^3.(306 mg)^2). It is noted that the standard volume was based on the geometry of the piezoelectric bimorph. Furthermore, the multi-mode FRFs of the bimorph without the tip mass was modelled with the CEDRT and the comparison with experimental results indicated that the CEDRT model was closer to the measurement compared with the CEDRTL. The maximum difference percentage of CEDRTL and CEDRT for power amplitude occurred at the load resistance approaching open circuit giving around 46 % difference. The effect of tip mass on

the piezoelectric bimorph with variable load resistance was found to increase power at the resonance region with the average increase of 96 % with decreasing resonance frequency of 72 %. The effect of longitudinal response under lower load resistance can be ignored, when the CEDRTL and CEDRT models overlap each other. However, the longitudinal response on the bimorph with the higher load resistance should not be ignored, especially when the tip mass is included for the two input base excitations. The bimorph system, when used in vibration environment with rotating equipment, will be subject to multidirectional input excitations. This will normally result in coupled bending and longitudinal input and subsequently coupled piezoelectric response. Finally, the polar electromechanical dynamic responses of the bimorph with the tip mass under two input base transverse and longitudinal accelerations has also been discussed, showing close agreement between the analytical and experimental results. The maximum power was achieved from the bimorph beam under input transverse excitation.

CHAPTER

7

Summary and Conclusions

This dissertation has presented various mathematical dynamic formulations of piezoelectric-based power harvester schemes. The impact benefit of piezoelectric transduction includes the ease of scalability, compact configuration, high energy density and high sensitivity which can be applied for future applications of self-powered smart sensor devices for health condition monitoring and defence communication technology. The main focus of this research work has been the development of novel analytical methods for modelling the behaviour of the piezoelectric bimorph beam vibration power harvester. This included the electromechanical dynamic system behaviour using the electrical enthalpy of piezoelectric layers under adiabatic and isothermal processes associated with the mechanical fields of elasticity and dynamical systems. The physical aspect of the piezoelectric system as discussed in Chapter 3 has also been considered to draw clear insight of the physical properties of continuum thermopiezoelectricity in order to explore the interrelationships between the mechanical, electrical and thermal forms as there appear to be no research publications that present the detail of the theoretical development of the continuum thermopiezoelectricity.

The continuum thermopiezoelectric equations of state with extensive and intensive properties using the laws of thermodynamics, Legendre transformation and Maxwell's relations have been derived comprehensively to establish equations that can be reduced in terms of Elastic-Electrical Gibbs Free Energy, Elastic Gibbs Free Energy, Electrical Helmholtz Free Energy, Elastic Helmholtz Free Energy, the Elastic-Electrical Enthalpy and the Electrical Enthalpy.

The application of continuum thermopiezoelectricity can be extended into areas of smart materials and structures. In this dissertation, the continuum thermopiezoelectricity associated with the extended Hamiltonian principle has been

narrowed to consider novel analytical methods of the electromechanical piezoelectric power harvesters as discussed in Chapter 4. Two analytical methods representing the weak and closed forms of the Rayleigh and Euler-Bernoulli piezoelectric bimorph beams under the action of two input base excitations have been established according to the electrical enthalpy of the piezoelectric layers (bimorph top and bottom layers), potential energy of substructure material (middle layer), kinetic energy of bimorph including the tip mass with their rotary inertias and the non-conservative external works due to the input mechanical inertia force and electrical charge. It should be noted that the external work of inertia forces was derived according to the input base excitation in terms of the product of the generalised mode shape of displacement fields with the zero-th mass moment of inertia of the bimorph and tip mass. The Rayleigh piezoelectric beam only considers the rotary inertia of the bimorph in the resulting electromechanical dynamic equations. This can also be further reduced to give the electromechanical dynamic equations of the Euler-Bernoulli piezoelectric beam by ignoring the rotary inertia of the bimorph from the Rayleigh piezoelectric beam. The constitutive electromechanical dynamic equations of the piezoelectric bimorph beam according to the weak form have been formulated into three categories represented by the coupled electromechanical dynamic response of the transverse-longitudinal form (CEDRTL), coupled electromechanical dynamic response of the longitudinal form (CEDRL) and coupled electromechanical dynamic response of the transverse form (CEDRTL).

All constitutive electromechanical dynamic equations as shown in Chapter 4 have been extended to derive the solutions using the Laplace transformation and Ritz eigenfunction series based on orthonormality. The extended solution forms give the multi-mode transfer functions, frequency response functions, optimal power functions and the generalised time-dependent amplitude functions which represent the relative and absolute dynamic displacement including velocity, electrical voltage, current and power. Moreover, the closed form reduced from the strong form of Hamiltonian's principle has been formulated using the CEDRTL model which can also be further extended using Laplace transformation associated with the convergent eigenfunction series under the orthonormality condition. The broadband multi-electromechanical piezoelectric bimorph beam with the multi-frequency response has also been formulated using the weak form of the CEDRT model to give the single-

and multi-mode transfer functions and frequency response system behaviour. Considering the analytical derivation of piezoelectric power harvesters, no research publications have been found focusing on the mathematical derivation of equations of the constitutive electromechanical dynamic behaviour represented by the CEDRTL, CEDRL and CEDRTL models.

Furthermore, the parametric case study of the Euler-Bernoulli piezoelectric bimorph beam with the tip mass under input transverse excitation using the weak and closed forms of the CEDRTL model have been compared to give very good agreement with the multi-mode frequency response functions as given in chapter 5. Since the typical piezoelectric bimorph beam is a thin structure, the Euler-Bernoulli formulation represents an accurate formulation for applications of vibration power harvesting. The results of the parametric case study with series and parallel connections have been discussed using the multi-mode FRFs of the tip absolute dynamic displacement, velocity, electrical voltage, current and power relating to the input transverse base excitation with variable load resistance. In addition, the short to open circuit resonance frequency response for variable load resistance have been discussed for series and parallel connections. Since the load resistance behaves as resistive shunt damping, the shifting resonance frequency from short to open circuits affects the mechanical stiffness of the bimorph and electromechanical stiffness of the piezoelectric layers (backward and forward electromechanical piezoelectric couplings).

It is noted that the electromechanical piezoelectric couplings have been formulated according to the electrical moment and force of the piezoelectric layers due to the piezoelectric direct mode and the piezoelectric converse mode of the electrical energy which implies backward and forward piezoelectric couplings, respectively, due to the transverse and longitudinal extension forms as given in chapter 4. Moreover, it was found that the short and open circuit load resistances gave the highest amplitudes of the first mode tip absolute dynamic displacement and velocity as shown in the FRFs. The use of the short and open circuit load resistance here was not the most important factor for increasing the electrical voltage, current and even power. This situation, in fact, has been proved, where the electrical voltage amplitudes increased from the short to open circuit load resistances with increasing resonance frequency. Conversely, the electrical current amplitude increased from the

open to short circuit load resistances with decreasing resonance frequency. Moreover, the FRFs of electrical power indicated the lowest amplitudes for both short and open circuit load resistance conditions. The parametric geometrical bimorph with varying piezoelectric thickness and length was discussed to see the resulting effect on the resonance frequencies as a function of load resistance. The broadband multi-electromechanical piezoelectric bimorph beam with variable load resistance has also been discussed by comparing the single-frequency and multi-frequency models of the beams as it has potential benefit for tuning or widening the resonance frequency band for electrical voltage, current and power.

In chapter 6, the validations of the theoretical and experimental results have been achieved with very good agreement. The mechanical damping ratios played an important role influencing the resonance peak amplitudes where the mechanical damping ratios have been given by matching the short circuit resonance frequency response from the theoretical studies with the experimental results. The piezoelectric bimorph beams with the tip mass under the input base transverse excitation using the weak form of the CEDRTL and CEDRT models have been compared to show the agreement with the experimental results. All results showed the frequency response functions of tip absolute dynamic displacement, velocity, electrical voltage, current and power. Since the piezoelectric bimorph with the tip mass using the CEDRTL model considered the effect of strain fields associated with the electromechanical piezoelectric couplings due to the transverse bending and longitudinal extension forms, the inclusion of tip mass also affected the input inertia forces due to the base transverse acceleration onto the bimorph. This creates coupling effects with mechanical bending and electrical moments with the additional effects of mechanical longitudinal extension and electrical forces into the interlayer bimorph element under the dynamic response. Therefore, the single mode frequency response results of the CEDRTL modelling with variable load resistance seemed to approach the experimental results closer as compared with the CEDRT results. The results indicated that for lower load resistances approaching short circuit, the CEDRTL and CEDRT tended to overlap whereas for higher load resistances approaching open circuit, the CERDTL and CEDRT models provided different results. Moreover, the multi-mode frequency response functions of the piezoelectric bimorph beam without tip mass has also been given by comparing the two theoretical methods (CEDRTL

and CEDRT) with the results of the experiment. The resulting experimental frequency response functions seemed closer with the CEDRT compared with the CEDRTL model.

Finally, the piezoelectric bimorph beam with the tip mass under the two input base transverse and longitudinal excitations using the CEDRTL model have been validated with the experimental results to give very good agreement. It is noted that the results were based on the input base excitation of 3 m/s^2 (306 mg) for the base protractor structure and attached piezoelectric bimorph beam. The protractor base structure was adjusted with incremental angle of 22.5$^\text{o}$ from 0$^\text{o}$ to 180$^\text{o}$. For the theoretical model, the iteration of input base excitation was given with incremental angle of 1$^\text{o}$. As a result, the bimorph beam would be considered to have one and two input excitations. The input base transverse excitation was achieved with an angle of 90$^\text{o}$ and the input base longitudinal excitation was achieved with the setup angles of 0$^\text{o}$ and 180$^\text{o}$. The angles between 0$^\text{o}$ and 180$^\text{o}$ (excluding 90$^\text{o}$) created combinations of input base excitations. The results shown in this case gave the polar tip absolute dynamic displacement, velocity, electrical voltage, current and power under the chosen frequencies and load resistances. It was found that the input excitation with angle of 90$^\text{o}$ on the bimorph seemed to give maximum amplitude under the dynamic response and load resistance, where that situation provided the predominant bending transverse response of the bimorph. In addition, the effect of input excitation with the angles of 0$^\text{o}$ and 180$^\text{o}$ attained the lowest amplitudes where this case implied the predominant longitudinal extension of the bimorph. Moreover, although the input excitation with the angles between 0$^\text{o}$ and 180$^\text{o}$ affected the transverse bending and longitudinal extension effects on the bimorph, the transverse bending still provided the dominant effect on the bimorph. It was also noted that the symmetrical trend of polar amplitude response was achieved at the angles from 0$^\text{o}$ to 90$^\text{o}$ and 90$^\text{o}$ to 180$^\text{o}$.

Piezoelectric materials can be applied across a wide range of applications for the future development of self-powering smart wireless sensor devices. The extracted mechanical energy from the wasted or unused vibration environment can be used to obtain the electrical energy using piezoelectric elements for powering embedded batteries of smart wireless sensor devices in order to monitor the health condition of rotating machines located in remote area. The formulations provided previously can be applied into different aspects of material properties and micro-scale structures

where the purpose is the optimisation of the electromechanical dynamic power harvesters.

Future Work and Recommendation

As discussed in several cases in this dissertation, the vibration power harvester can be further investigated for future developments as stated in the following issues:

1. The future research study can address the mathematical study with analytical and perturbation methods of the non-linear electromechanical piezoelectric bimorph beam behaviour under high amplitudes of input base excitation.

2. Mathematical methods of topological piezoelectric design with/without the temperature effect for understanding the optimal power harvesting under input mechanical excitations.

3. The broadband multi-electromechanical piezoelectric beam coupled with multi-electromagnetic transduction for multi-resonance behaviour can be investigated for multi-purpose applications of smart sensor devices.

4. The design management electronic circuit with embedded battery and wireless sensor node can be the focus of investigation.

References

[1] Anton, S.R. and Sodano, H.A., 2007, "A review of power harvesting from vibration using piezoelectric materials (2003-2006)," Smart Materials and Structures, **16**, pp. R1-R21

[2] Priya, S., 2007, "Advances in energy harvesting using low profile piezoelectric transducers," Journal of Electroceramic, **19**, pp.167-184

[3] Roundy, S., Wright, P. and Rabaey, J., 2003, "A study of low level vibrations as a power source for wireless sensor nodes," Computer Communications **26**, pp. 1131–1144

[4] Smits, J.G. and Choi, W.-S., 1991, "The constituent equations of piezoelectric heterogeneous bimorphs," IEEE Transactions on Ultrasonics, Ferroelectrics, and Frequency Control, **46**, pp. 256–269

[5] Wang, Q.-M., Du, X.-H., Xu, B. and Eric Cross, L.E., 1999, "Theoretical analysis of the sensor effect of cantilever piezoelectric benders," AIP Journal of Applied Physics, **85**, pp. 1702-1712

[6] Roundy, S. and Wright, P.K., 2004, "A piezoelectric vibration based generator for wireless electronics," Smart Materials and Structures, **18**, pp. 1131–1142

[7] duToit, N.E, Wardle, B.L. and Kim, S-G., 2005, "Design considerations for MEMS-scale piezoelectric mechanical vibration energy harvesters," Journal of Integrated Ferroelectrics, **71**, pp. 121-160

[8] Shu, Y.C. and Lien, I.C., 2006, "Analysis of power output for piezoelectric energy harvesting systems" Smart Materials and Structures, **15**, pp. 1499-1512

[9] Erturk, A. and Inman, D.J., 2009, "An experimentally validated bimorph cantilevered model for Piezoelectric energy harvesting from base excitations," Smart Materials and Structures, **18**, 1-18

[10] Goldschmidtboeing, F. and Woias, P., 2008 "Characterization of different beam shapes for piezoelectric energy harvesting," Journal of Micromechanics and Microengineering, **18,** pp, 104013

[11] Vullers, R.J.M, van Schijk, R., Doms, I., van Hoof, C. and Meterns, R., 2009 "Micropower energy harvesting," Solid-State Electronics, **53**, pp. 684-693

[12] Sodano, H.A., Inman, D.J. and Park G., 2005, "Comparison of Piezoelectric Energy Harvesting Devices for Recharging Batteries," Journal of Intelligent Material Systems and Structures, **16**, pp. 799-807

[13] Sodano, H.A., Lloyd, J. and Inman, D.J., 2006, "An experimental comparison between several active composite actuators for power generation," Smart Materials and Structures, **15**, pp. 1211-1216

[14] Sodano, H.A., Inman, D.J. and Park, G., 2005, "Generation and Storage of Electricity from Power Harvesting Devices." Journal of Intelligent Material Systems and Structures, **16**, pp. 67-75.

[15] Kymissis, J., Kendall, C., Paradiso, J. and Gershenfeld, N., 1998, "Parasitic power harvesting in shoes," Proceeding of 2nd IEEE International Symposium on Wearable Computer., Pittsburg, PA, October, pp. 132-139

[16] Shenck, N.S. and Paradiso, J.A., 2001, "Energy scavenging with shoe-mounted piezoelectrics," IEEE Micro, **21,** pp. 30–42

[17] Starner, T. and Paradiso, J.A., 2004, "Human generated power for mobile electronic," in Piguet, C.(ed), Low-Power Electronic Design, CRC Press, Chapter 45

[18] Paradiso, J.A., 2006, "System for human-powered mobile computing," 43rd ACM/IEEE Design Automation Conference, pp. 645 – 650

[19] Mateu, L. and Moll, F., 2005, "Optimum piezoelectric bending beam structures for energy harvesting using shoe inserts," Journal of Intelligent Material Systems and Structures, **16**, pp. 835-845

[20] Mateu, L. and Moll, F., 2006, "Appropriate charge of the storage capacitor in a piezoelectric energy harvesting device for discontinuous load operation," Sensors and Actuators A : Physical, **132**, pp. 302-310

[21] Ferrari, M. Ferrari, V., Marioli, D. and Taroni, A., 2005, "Modelling, fabrication and performance measurements of a piezoelectric energy converter for power harvesting in autonomous Microsystems," Proceeding on Instrumentation and Measurement Technology Conference, Ottawa, ON, Canada, May, pp. 1862-1866

[22] Arms, S.W., Townsend, C.P., Churchill, D.L., Galbreath, J.H. and Mundell, S. W., 2005, "Power management for energy harvesting wireless sensors, Proceeding of Smart Structures and Materials Conf.; Proceeding of SPIE **57, 63**, pp. 267–275

[23] Lin, J.H, Wu, X.M., Ren, T.L. and Liu, L.T., 2007, "Design considerations for MEMS-scale piezoelectric mechanical vibration energy harvesters," Journal of Integrated Ferroelectrics, **95**, pp. 128–141

[24] Chen, S.-N., Wang, G.-J. and Chien, M.-C, 2006, "Analytical modeling of piezoelectric vibration-induced micro power generator," Mechatronics, **16**, pp. 379-387

[25] dutoit, N.E. and Wardle, B.L., 2006, "Performance of micro fabricated piezoelectric vibration energy harvesters," Integrated Ferroelectrics, **83**, pp.13-32

[26] Kim, M., Hoegen, M., Dugundji, J. and Wardle, B. L., 2010, "Modeling and experimental verification of proof mass effects on vibration energy harvester performance," Smart Materials and Structures**, 19**, pp. 045023

[27] Ajitsaria, J., Choe, S.Y., Shen, D. and Kim, D.J., 2007, "Modeling and analysis of a bimorph piezoelectric cantilever beam for voltage generation," Smart Materials and Structures, **16**, pp. 447–54

[28] Jiang, S., Li, X., Guo, S., Hu, Y., Yang, J. and Jiang., 2005, "Performance of a piezoelectric bimorph for scavenging vibration energy," Smart Materials and Structures, **14**, pp. 769-774

[29] Yang, Z. and Yang, J., 2009, "Connected vibrating piezoelectric bimorph beams as a wide-band piezoelectric power harvester," Journal of Intelligent Material Systems and Structures, **20,** pp. 569-574

[30] Renaud, M., Fiorini, P. and Hoof, C.V., 2007, "Optimization of a Piezoelectric Unimorph for Shock and Impact Energy Harvesting," Smart Materials and Structures, **16**, pp. 1125-1135

[31] Kuehne, I., Marinkovic, D., Eckstein, G. and Seidal, H., 2008, "A new approach for MEMS power generation based on a piezoelectric diaphragm," Sensors and Actuators A : Physical, **142**, pp. 292-297

[32] Minazara E, Vasic D, Costa F, Poulin G 2006 Piezoelectric Diaphragm for Vibration Energy Harvesting, *Ultrasonics* **44** e699-e703.

[33] Lefeuvre, E., Badel, A., Richard, C., Petit, L. and Guyomar, D., 2006, "A Comparison Between Several Vibration-Powered Piezoelectric Generators for Standalone Systems," Sensors and Actuator A : Physical, **126**, pp. 405-416

[34] Chao, L., Tsui, C.-Y. and Ki, W.-H., 2007, "Vibration energy scavenging and management for ultra low power applications**,"** Proceeding of the international symposium on Low power electronics and design, USA, pp. 316-321

[35] Wang, D.-A. and Ko, H.H., 2010, "Piezoelectric energy harvesting from flow-induced vibration," Journal of Micromechanics and Microengineering, **20**, pp. 025019

[36] Feenstra, J., Granstrom, J. and Sodano, H.A., 2008, "Energy harvesting through a backpack employing a mechanically amplified piezoelectric stack," Mechanical System and Signal Processing, **22**, pp. 721–734

[37] Yang, Y. and Tang, L., 2009, "Equivalent circuit modeling of piezoelectric energy harvesters," Journal of Intelligent Material Systems and Structures, **20**, pp. 2223 -2235

[38] Lee, S., Youn, B.D. and Jung, B.C., 2009, **"**Robust segment-type energy harvester and its application to a wireless sensor," Smart Materials and Structures, **18**, pp. 095021

[39] Yang, Y., Tang, L. and Li., H., 2009, "Vibration energy harvesting using macro-fiber composites," Smart Materials and Structures, **18**, pp. 115025

[40] Mathers, A., Moon, K.S. and Yi, J., 2009, "A Vibration-Based PMN-PT energy harvester," IEEE Sensor Journal, **9** (7), pp. 731-739

[41] Song, H.J., Choi, Y.T., Wang, G. and Wereley, N.M., 2009, "Energy harvesting utilizing single crystal PMN-PT material and application to a self-powered accelerometer," Journal of Mechanical Design, **131**, pp. 091008

[42] Jeon, Y.B., Sood, R., Jeong, J.-h. and Kim, S.G., 2005, "MEMS power generator with transverse mode thin film PZT," Sensors and Actuators A : Physical, **122**, pp.16–22

[43] Song, H.J., Choi, Y.T., Wereley, N.M. and Purekar, A.S., 2010, "Energy harvesting devices using macro-fiber composite materials," Journal of Intelligent Material Systems and Structures, **21**, pp. 647-658

[44] Ferrari, M., Ferrari, V., Guizzetti, M., Marioli, D. and Taroni, A., 2008, "Piezoelectric multifrequency energy converter for power harvesting in autonomous Microsystems," Sensors and Actuators A : Physical, **142**, pp. 329–335

[45] Shahruz, S.M., 2006, "Design of mechanical band-pass filters for energy scavenging," Journal of Sound and Vibration, **292**, pp. 987-998

[46] Shahruz, S.M., 2008, "Performance of mechanical bandpass filters used in energy scavenging in the presence of fabrication errors and coupling," ASME Journal of Vibration and Acoustic, **130**, pp. 054505

[47] Song, H.J., Choi, Y.T., Purekar, A.S. and Wereley, N.M., 2009, "Performance evaluation of multi-tier energy harvesters using macro-fiber composite patches," Journal of Intelligent Material Systems and Structures, **20**, pp. 2077-2088

[48] Xue, H., Hu, Y. and Wang, Q.-M., 2008, "Broadband piezoelectric energy harvesting devices using multiple bimorphs with different operating frequencies," IEEE Transactions on Ultrasonics, Ferroelectrics, and Frequency Control, **55**, pp. 2104–2108

[49] Amirtharajah, R. and Chandrakasan, A.P., 1997, "Self-powered low power signal processing," Symposium on VLSI Circuits Digest of Technical Papers, pp. 25 - 26

[50] Amirtharajah, R. and Chandrakasan, A.P., 1998, "Self-powered signal processing using vibration-based power generation," IEEE Journal of Solid-State Circuits, **33**, pp. 687–95

[51] Beeby, S.P., Torah, R.N., Tudor, M.J., Glynne-Jones, P., O'Donnell, T., Saha, C.R. and Roy, S., 2007, "A micro electromagnetic generator for vibration energy harvesting," Journal of Micromechanics and Microengineering, **17**, pp. 1257–1265

[52] Glynne-Jones, P., Tudor, M.J., Beeby, S.P. and White, N.M., 2004, "An electromagnetic, vibration-powered generator for intelligent sensor systems, Sensors and Actuators A : Physical, **110,** pp. 344–349

[53] El-Hami, M., Glynne-Jones, P., White, N.M., Beeby, S.P., James, E., Brown, A.D. and Ross. J.N., 2001, "Design and fabrication of a new vibration-based electromechanical power generator," Sensors and Actuators A: Physical, **92**, pp. 335-342

[54] Zhu, D., Roberts, S., Tudor, M.J., Beeby, S.P., 2010, "Design and experimental characterization of a tunable vibration-based electromagnetic micro-generator," Sensors and Actuators A : Physical, **158**, pp. 284-293

[55] Sari, I., Balkan, T. and Kulah, H., 2009, **"**An electromagnetic micro energy harvester based on an array of parylene cantilevers," Journal of Micromechanics and Microengineering, **19**, pp. 105023

[56] Yang, B., Lee, C., Xiang, W., Xie, J., He, J.H., Kotlanka, R.K., Low, S.P. and Feng, H., 2009, "Electromagnetic energy harvesting from vibrations of multiple frequencies,"Journal of Micromechanics and Microengineering, **19**, pp. 035001

[57] Saha, C.R., O'Donnell, T., Wang, N. and McCloskey, P., 2008, "Electromagnetic generator for harvesting energy from human motion," Sensors and Actuators A : Physical, **147**, pp. 248–253

[58] Peters, C., Maurath, D., Schock, W. and Manoli, Y., 2008, **"**Novel electrically tunable mechanical resonator for energy harvesting," Proceedings of PowerMEMS 2008 and microEMS2008, Sendai, Japan, November 9-12, pp. 253-256

[59] Peters, C., Maurath, D., Schock, W. and Manoli, Y., Mezger, M. And Manoli Y, 2009, "A closed-loop wide-range tunable mechanical resonator for energy harvesting systems, Journal of Micromechanics and Microengeneering, **19,** pp. 094004

[60] Kim, S.-H., Ji, C.-H., Galle, P., Herrault, F., Wu, X., Lee, J.-H., Choi, C.-A. and Allen, M.G., 2009, **"**An electromagnetic energy scavenger from direct airflow," Journal of Micromechanics and Microengineering, **19,** pp. 094010

[61] Park, C.H, Bang, D.H and Park, J.Y, 2010, "Micro-fabricated electromagnetic power generator to scavenge low ambient vibration," IEEE Transactions on Magnetics, **46** (6), pp. 1937-1942

[62] Stephen, N.G., 2006, "On Energy Harvesting from Ambient Vibration, Journal of Sound and Vibration," **293,** pp. 409-425.

[63] Sterken, T., Fiorinil, P., Altena, G., Van Hoof, C. and Puers, R., 2007, "Harvesting energy from vibrations by a micromachined electret generator", Transducer and Eurosensors, 14th International Conference on Solid-State Sensors, Actuators and Microsystems, Lyon, France, June, pp. 129-132

[64] Tsutsumino, T., Suzuki, Y. and Kasagi, N, 2007, "Electromechanical modeling of micro electret generator for energy harvesting," 14th International Conference on Solid-State Sensors, Actuators and Microsystems, Lyon, France, June, pp. 863-866

[65] Naruse, Y., Matsubara, N., Mabuchi, K., Izumi, M. and Suzuki, S., 2009 "Electrostatic micro power generation from low-frequency vibration such as human motion," Journal of Micromechanics and Microengineering, **19**, pp. 094002

[66] Hoffmann, D., Folkmer, B. and Manoli, Y., 2009, "Fabrication, characterization and modelling of electrostatic micro-generators," Journal of Micromechanics and Microengineering, **19**, pp. 094001

[67] Tvedt, L.G.W., Blysta, L.-C. J. and Halvorsen, E., 2008, "Simulation of an electrostatic energy harvester at large amplitude narrow and wide band vibrations," Symposium on Design, Test, Integration and Packaging of MEMS/MOEMS, pp. 296 – 301

[68] Kiziroglou, M.E., He, C. and Yeatman, E.M., 2009, "Rolling rod electrostatic microgenerator," IEEE Transactions on Industrial Electronics, **56**, pp. 1101-1108

[69] Kiziroglou, M.E., He, C. and Yeatman, E.M., 2010, "Flexible substrate electrostatic energy harvester," Electronics Letters, **46**, pp. 166-167

[70] Desloge, E.A., 1968, *Thermal physics*, Holt, Rinehart and Winston, New York

[71] Hayt, W.H. and Jr., Buck, J.A., 2006, *Engineering electromagnetic*, McGraw-Hill Higher Education

[72] Stratton, J.A., 2007, *Electromagnetic Theory*, John Wiley & Sons, Inc., Hoboken, New Jersey

[73] Nye, J.F., 1985, *Physical properties of crystals : their representation by tensors and matrices*, Clarendon Press, Oxford, England

[74] Damjanovic, D., 1998, "Ferroelectric, dielectric and piezoelectric properties of ferroelectric thin films and ceramics," Report on Progress in Physics, **61**, pp. 1267–1324

[75] Tiersten, H.F., 1969, *Linear Piezoelectric Plate Vibrations*, Plenum Press

[76] Ikeda, T., 1990, *Fundamentals of piezoelectricity*, Oxford Science Publishing, New York

[77] Cady, W.G., 1946, *Piezoelectricity: An Introduction to the Theory and Applications of Electromechanical Phenomena in Crystals*, McGraw-Hill, New York

[78] Neumann, N., Es-Souni, M. and Luo, H., 2009, "Application of PMN-PT in pyroelectric detectors," 18th IEEE International Symposium on the Applications of Ferroelectrics

[79] Ploss, B., Ploss, B., Shin, F.G., Chan, H.L.W. and Choy, C.L., 2000, "Pyroelectric or piezoelectric compensated ferroelectric composites," Applied Physics Letters, **76** (19), pp. 2776-2778

[80] Porter, S.G., 1981, "A brief guide to pyroelectric detectors," Ferroelectrics, **33**, pp. 193-206

[81] Sears, F.W. and Salinger, G.L., 1986, *Thermodynamics, kinetic theory, and statistical thermodynamics*, Addison-Wesley Publishing Company

[82] Munn, R.W., 1973, "Thermodynamics and physical properties of solids in electric fields," Journal of Physics C : Solid State Physics, **6**, pp. 3213-3222

[83] Munn, R.W. and Newham, R.J., 1974, Thermodynamics of internal strain in perfect crystals : III. Piezoelectric and related properties," Journal of Physics C : Solid State Physics, **7**, pp. 848-863

[84] Kuiken, G. D. C., 1994, *Thermodynamics of irreversible processes applications to diffusion and rheology*, Wiley, New York

[85] Verhas, J., 1997, *Thermodynamics and rheology*, Kluwer Academic Publishers, Boston

[86] Kondepudi, D. and Prigogine, I., 1998, *Modern thermodynamics: from heat engines to dissipative structures*, John Wiley & Sons, New York

[87] Biot, M.A., 1955, "Thermoelasticity and Irreversible Thermodynamics," AIP Journal of Applied Physics, **27**, pp. 240-253

[88] Mindlin, R.D., 1972, "High Frequency Vibration of Piezoelectric Crystal Plate," International Journal of Solids and Structures, **8**, pp. 895-906

[89] D'Ottavio, M., Ballhause, D., Kroplin, B. and Carrera, E., 2006, "Closed-form solutions for the free-vibration problem of multilayered piezoelectric shells," Computers and Structures, **84**, pp. 1506–1518

[90] Tanaka, H., 1993, "Generalized basic equations for bending motions of piezoelectric bars formulated from Hamilton's principle," Journal of Acoustical Society of America, **4**, pp. 1764-1772

[91] Yang, J., 2006, *The Mechanics of Piezoelectric Structure*, World Scientific Publishing, Singapore
[92] Dokmeci, M.C., 1972, "On the higher order theories of piezoelectric crystal surfaces," AIP Journal of Mathematical Physics, **15**, pp. 2248-2252

[93] Einstein, A., 1970, *Autobiographical notes in Albert Einstein: Philosopher-Scientist*, P. A. Schilpp, ed., Library of Living Philosophers, Cambridge U.P., London, **7**, pp. 33

[94] Reddy, J.N., 2008, *An Introduction To Continuum Mechanics*, Cambridge University Press, USA

[95] Reddy, J.N., 2004, *Mechanics of Laminated Composite Plates and Shells*, 2nd edition, CRC Press

[96] Ballas, R.G., 2007, *Piezoelectric Multilayer Beam Bending Actuator*s, Springer-Verlag, Berlin

[97] Smits, J.G., Dalke, S.I. and Cooney, T.K., 1991, "The constituent equations of piezoelectric bimorphs," Sensors and Actuators A : Physical, **28,** 41–61

[98] Beer, F.P. and Johnston, E.R., 1977, *Vector Mechanics for Engineers: Statics and Dynamics*, McGraw-Hill, USA

[99] Ritz, W., 1909, "Über eine neue Methode zur Lösung gewisser Variationprobleme der Mathematischen Physik," Journal für die Reine und Angewandte Mathematik, **135**, pp. 1–61.

[100] Courant, R. And Hilbert, D., 1953, *Methods of Mathematical Physics, Vol. 1,* Interscience Publishers, New York

[101] Clough, R.W. and Penzien, J., 1993 *Dynamics of Structures*, Wiley, New York

Appendix A

A.1 Piezoelectric Constitutive Equations

The electrical enthalpy (H) as stated in chapter 3 can be reformulated as,

$$H\left(\varepsilon_{ij}, E_i\right) = \frac{1}{2} C^E_{ijkl} \varepsilon_{ij} \varepsilon_{kl} - e_{kij} E_k \varepsilon_{ij} - \frac{1}{2} \varsigma^\varepsilon_{ik} E_i E_k.$$ (A1)

In equation (A1), H is a function of ε_{kl} and E_k therefore deriving the partial differential of H with respect to ε_{ij} and E_i to give constitutive equations, yields

$$\sigma_{ij} = \frac{\partial H}{\partial \varepsilon_{ij}} \quad , \quad D_i = -\frac{\partial H}{\partial E_i}.$$ (A2)

This gives,

$$\sigma_{ij} = C^E_{ijkl} \varepsilon_{kl} - e_{ijk} E_k,$$ (A3)

$$D_i = e_{ikl} \varepsilon_{kl} + \varsigma^\varepsilon_{ik} E_k.$$ (A4)

The elastic-electrical enthalpy (H) as stated in chapter 3 can also be reformulated as,

$$H\left(\sigma_{ij}, E_i\right) = -\frac{1}{2} S^E_{ijkl} \sigma_{ij} \sigma_{kl} - d_{ikl} E_i \sigma_{kl} - \frac{1}{2} \varsigma^\sigma_{ik} E_i E_k.$$ (A5)

Equation (A5) is a function of ε_{kl} and E_k therefore deriving the partial differential of H with respect to σ_{ij} and E_i gives constitutive equations as,

$$\varepsilon_{ij} = -\frac{\partial H}{\partial \sigma_{ij}} \quad , \quad D_i = -\frac{\partial H}{\partial E_i}.$$ (A6)

This gives,

$$\varepsilon_{ij} = S^E_{ijkl} \sigma_{kl} + d_{ikl} E_k,$$ (A7)

$$D_i = d_{ikl} \sigma_{kl} + \varsigma^\sigma_{ik} E_k.$$ (A8)

Equations (A3), (A4), (A7) and (A8) have similar forms with the electrical enthalpy and elastic-electrical enthalpy given in chapter 3. It should be noted that the electrical enthalpy and elastic-electrical enthalpy have physical relationship in terms of

constitutive equations. In this case, it is important to condense tensor forms from Eqs. (A1) - (A8) to matrix form by using the Voigt's notation. It is also noted that double indices *ij* or *kl* can be replaced with single indices *p* or *q*. Tensor notations *i,j,k* and *l* take the values of 1,2 and 3 where *p* and *q* take the value of 1,2,3,4,5 and 6. The complete form of correlation between tensor double indices and the matrix form can be stated in terms of Voigt's notation as,

ij or *kl* : 11	22	33	23 or 32	31 or 13	12 or 21
p or *q* : 1	2	3	4	5	6

For example :

$$C_{ijkl} \rightarrow C_{pq} \quad , \quad e_{ikl} \rightarrow e_{iq} \quad , \quad \sigma_{ij} \rightarrow \sigma_p .$$

In terms of Voigt's notation, equations (A3) and (A4) from electrical enthalpy become,

$$\sigma_p = C^E_{pq} \varepsilon_q - e_{kp} E_k , \tag{A9}$$

$$D_i = e_{iq} \varepsilon_p + \varsigma^\varepsilon_{ik} E_k . \tag{A10}$$

Equations (A7) and (A8) from elastic-electrical enthalpy can also be stated as,

$$\varepsilon_p = S^E_{pq} \sigma_q + d_{iq} E_q , \tag{A11}$$

$$D_i = d_{iq} \sigma_q + \varsigma^\sigma_{ik} E_k . \tag{A12}$$

Equations (A9) and (A10) can then be written in matrix form as,

$$\{\sigma\}_{(6x1)} = \left[C^E\right]_{(6x6)} \{\varepsilon\}_{(6x1)} - \left[e\right]^T_{(6x3)} \{E\}_{(3x1)} , \tag{A13}$$

and,

$$\{D\}_{(3x1)} = \left[e\right]_{(3x6)} \{\varepsilon\}_{(6x1)} + \left[\varsigma^\varepsilon\right]_{(3x3)} \{E\}_{(3x1)} . \tag{A14}$$

Equation (A11) can also be proven by manipulating the constitutive equations from (A9) to give,

$$\{\varepsilon\}_{(6x1)} = \left[C^E\right]^{-1}_{(6x6)} \{\sigma\}_{(6x1)} + \left[C^E\right]^{-1}_{(6x6)} \left[e\right]^T_{(6x3)} \{E\}_{(3x1)} ,$$

or

$$\{\varepsilon\}_{(6x1)} = \left[S^E\right]_{(6x6)} \{\sigma\}_{(6x1)} + \left[d\right]^T_{(6x3)} \{E\}_{(3x1)} , \tag{A15}$$

where $\left[S^E\right]_{(6x6)}=\left[C^E\right]^{-1}_{(6x6)}$ represents the elastic material compliance by using the inverse

of stiffness coefficient and $\left[d\right]^T_{(6x3)}=\left[C\right]^{-1}_{(6x6)}\left[e\right]^T_{(6x3)}$ or $\left[d\right]_{(3x6)}=\left[e\right]_{(3x6)}\left[C\right]^{-1}_{(6x6)}$ and $\left[e\right]_{(3x6)}=\left[d\right]_{(3x6)}\left[C\right]_{(6x6)}$

or $\left[d\right]_{(3x6)}=\left[e\right]_{(3x6)}\left[S\right]_{(6x6)}$ to represent the relation form of the piezoelectric constants. It is

noted that equation (A15) has similar form with Eq. (A11). Moreover, equation
(A12) can also be proven by substituting equation [A15] into equation [A14]
yielding,

$$\{D\}_{(3x1)}=\left[e\right]_{(3x6)}\left[S^E\right]_{(6x6)}\{\sigma\}_{(6x1)}+\left[\left[e\right]_{(3x6)}\left[d\right]^T_{(6x3)}+\left[\varsigma^\varepsilon\right]_{(3x3)}\right]\{E\}_{(3x1)} \quad ,$$

or $$\{D\}_{(3x1)}=\left[d\right]_{(3x6)}\{\sigma\}_{(6x1)}+\left[\varsigma^\sigma\right]_{(3x3)}\{E\}_{(3x1)} \quad , \tag{A16}$$

where $\left[\varsigma^\sigma\right]_{(3x3)}=\left[\varsigma^\varepsilon\right]_{(3x3)}+\left[e\right]_{(3x6)}\left[d\right]^T_{(6x3)}$.

It is noted that equation (A16) has similar form with Eq. (A12).

A.2 PZT Material Coefficients

The Lead Zirconate Titanate (PZT) has characteristic piezoelectric coefficients in
terms of the plane-stress relationship as,

$$\begin{Bmatrix} \sigma_1 \\ \sigma_2 \\ \sigma_3 \\ \sigma_4 \\ \sigma_5 \\ \sigma_6 \\ D_1 \\ D_2 \\ D_3 \end{Bmatrix}=\begin{bmatrix} C_{11}^E & C_{12}^E & C_{13}^E & 0 & 0 & 0 & 0 & 0 & e_{31} \\ C_{12}^E & C_{11}^E & C_{13}^E & 0 & 0 & 0 & 0 & 0 & e_{31} \\ C_{13}^E & C_{13}^E & C_{33}^E & 0 & 0 & 0 & 0 & 0 & e_{33} \\ 0 & 0 & 0 & C_{44}^E & 0 & 0 & 0 & e_{15} & 0 \\ 0 & 0 & 0 & 0 & C_{44}^E & 0 & e_{15} & 0 & 0 \\ 0 & 0 & 0 & 0 & 0 & C_{66}^E & 0 & 0 & 0 \\ 0 & 0 & 0 & 0 & e_{15} & 0 & \varsigma_{11}^\varepsilon & 0 & 0 \\ 0 & 0 & 0 & e_{15} & 0 & 0 & 0 & \varsigma_{22}^\varepsilon & 0 \\ e_{31} & e_{31} & e_{33} & 0 & 0 & 0 & 0 & 0 & \varsigma_{33}^\varepsilon \end{bmatrix}\begin{Bmatrix} \varepsilon_1 \\ \varepsilon_2 \\ \varepsilon_3 \\ \varepsilon_4 \\ \varepsilon_5 \\ \varepsilon_6 \\ E_1 \\ E_1 \\ E_1 \end{Bmatrix}. \tag{A.17}$$

A.3 Piezoelectric Electrical Enthalpy Using Einstein's Summation Convention

Equation A1 can be restated in terms of Einstein's summation convention as,

$$H\left(\varepsilon_{ij},E_i\right)=\sum_{p=1}^{6}\sum_{q=1}^{6}\frac{1}{2}C_{pq}^E\varepsilon_p\varepsilon_q-\sum_{k=1}^{3}\sum_{p=1}^{6}e_{kp}E_k\varepsilon_p-\sum_{i=1}^{3}\sum_{k=1}^{3}\frac{1}{2}\varsigma_{ik}^\varepsilon E_iE_k. \tag{A18}$$

Corresponding to Eq. (A17), equation (A18) can be expanded to give,

$$H\left(\varepsilon_{ij}, E_i\right) = \frac{1}{2}C_{11}^E\varepsilon_1^{\ 2} + C_{12}^E\varepsilon_1\varepsilon_2 + C_{13}^E\varepsilon_1\varepsilon_3 + \frac{1}{2}C_{22}^E\varepsilon_2^{\ 2} + C_{23}^E\varepsilon_2\varepsilon_3$$

$$+ \frac{1}{2}C_{33}^E\varepsilon_3^{\ 2} + \frac{1}{2}C_{44}^E\varepsilon_4^{\ 2} + \frac{1}{2}C_{55}^E\varepsilon_5^{\ 2} + \frac{1}{2}C_{66}^E\varepsilon_6^{\ 2} - e_{31}E_3\varepsilon_1 - e_{32}E_3\varepsilon_2$$

$$- e_{33}E_3\varepsilon_3 - e_{24}E_2\varepsilon_4 - e_{15}E_1\varepsilon_5 - \frac{1}{2}\varsigma_{11}^\varepsilon E_1^{\ 2} - \frac{1}{2}\varsigma_{22}^\varepsilon E_2^{\ 2} - \frac{1}{2}\varsigma_{33}^\varepsilon E_3^{\ 2}. \qquad (A20)$$

where $C_{12}^E = C_{21}^E$, $C_{55}^E = C_{44}^E$, $C_{13}^E = C_{31}^E = C_{23}^E = C_{32}^E$, $e_{32} = e_{31}$ and $e_{24} = e_{15}$.

Since the electrical field induced from the piezoelectric element is in z-direction, the boundary condition for piezoelectric beams can be stated as

$$E_1 = E_2 = 0. \qquad (A21)$$

The strain field of the Euler-Bernoulli-Beam and Rayleigh beam can be stated as

$$\varepsilon_2 = \varepsilon_3 = \varepsilon_4 = \varepsilon_5 = \varepsilon_6 = 0. \qquad (A22)$$

It should be noted that Eq. (A22) does not mean plane-strain condition for material coefficient. It was only beam condition reduced from equation (A20) which was derived under the plane-stress material from Eq. (A17). The strain field of Timoshenko Beam can be stated as,

$$\varepsilon_2 = \varepsilon_3 = \varepsilon_4 = \varepsilon_6 = 0 . \qquad (A23)$$

The strain field of Kirchhoff plate can be stated as,

$$\varepsilon_3 = \varepsilon_4 = \varepsilon_5 = 0. \qquad (A.24)$$

In terms of Eqs. (A21) and (A22), equation (A20) for the Euler-Bernoulli beam and Rayleigh beam can be reduced as,

$$H\left(\varepsilon_{ij}, E_i\right) = \frac{1}{2}C_{11}^E\varepsilon_1^{\ 2} - e_{31}E_3\varepsilon_1 - \frac{1}{2}\varsigma_{33}^\varepsilon E_3^{\ 2}. \qquad (A25)$$

Corresponding to Eqs. (A9) and (A10), equation (A25) can be reduced in matrix form as,

$$\begin{Bmatrix} \sigma_1 \\ D_3 \end{Bmatrix} = \begin{bmatrix} C_{11}^E & -e_{31} \\ e_{31} & \varsigma_{33}^\varepsilon \end{bmatrix} \begin{Bmatrix} \varepsilon_1 \\ E_3 \end{Bmatrix} . \qquad (A26)$$

In terms of Eqs. (A21) and (A23), equation (A20) for Timoshenko Beam can be reduced as,

$$H\left(\varepsilon_{ij}, E_i\right) = \frac{1}{2}C_{11}^E\varepsilon_1^{\ 2} + \frac{1}{2}C_{55}^E\varepsilon_5^{\ 2} - e_{31}E_3\varepsilon_1 - \frac{1}{2}\varsigma_{33}^\varepsilon E_3^{\ 2} . \qquad (A27)$$

Corresponding to Eqs. (A9) and (A10), equation (A27) can be reduced in matrix form as,

$$\begin{Bmatrix} \sigma_1 \\ \sigma_5 \\ D_3 \end{Bmatrix} = \begin{bmatrix} C_{11}^E & 0 & -e_{31} \\ 0 & kC_{55}^E & 0 \\ e_{31} & 0 & \varsigma_{33}^\varepsilon \end{bmatrix} \begin{Bmatrix} \varepsilon_1 \\ \varepsilon_5 \\ E_3 \end{Bmatrix} .$$
(A28)

It is noted that shear correction factor k, which depends on the shape of the cross sectional beam, was included on the Timoshenko beam to give kC_{55}^E.

In terms of Eqs. (A21) and (A24), equation (A20) for Love-Kirchhoff plate can be reduced as,

$$H\left(\varepsilon_{ij}, E_i\right) = \frac{1}{2}C_{11}^E\varepsilon_1^2 + C_{12}^E\varepsilon_1\varepsilon_2 + \frac{1}{2}C_{22}^E\varepsilon_2^2 + \frac{1}{2}C_{66}^E\varepsilon_6^2 - e_{31}E_3\varepsilon_1 - e_{32}E_3\varepsilon_2 - \frac{1}{2}\varsigma_{33}^\varepsilon E_3^2 .$$ (A29)

Corresponding to Eqs. (A9) and (A10), equation (A29) can be reduced in matrix form as,

$$\begin{Bmatrix} \sigma_1 \\ \sigma_2 \\ \sigma_6 \\ D_3 \end{Bmatrix} = \begin{bmatrix} C_{11}^E & C_{12}^E & 0 & -e_{31} \\ C_{12}^E & C_{11}^E & 0 & -e_{31} \\ 0 & 0 & C_{66}^E & 0 \\ e_{31} & e_{31} & 0 & \varsigma_{33}^\varepsilon \end{bmatrix} \begin{Bmatrix} \varepsilon_1 \\ \varepsilon_2 \\ \varepsilon_6 \\ E_3 \end{Bmatrix} .$$
(A30)

Appendix B

To obtain eigenfunction forms, the solution forms of mechanical dynamic equations of transverse bending and longitudinal extension for the cantilevered piezoelectric bimorph beam with tip mass must be established independently. The mode shapes are solution forms of the eigenfunction series to be used in chapter 4. It should be noted that normal modes (normalised eigenfunctions) are not formulated here because the orthonormality equations based on the orthogonality property of mechanical equations, both weak and closed forms, can be found in detail in chapter 4.

B.1 Rayleigh piezoelectric bimorph beam with tip mass

The dynamic transverse bending equation for the Rayleigh cantilevered piezoelectric bimorph beam with tip mass can be formulated after simplification as,

$$\frac{d^4\Psi_r(x)}{dx^4} + a\frac{d^2\Psi_r(x)}{dx^2} - b\Psi_r(x) = 0. \tag{B1}$$

It should be noted that the second terms of Eq. (B1) represents the rotary inertia of the piezoelectric element. Four roots of solution can be obtained from Eq. (B1) as,

$$\lambda_1 = \pm\mu \quad , \quad \mu = \sqrt{\frac{1}{2}\left(-a + \sqrt{a^2 + 4b}\right)}, \tag{B2}$$

$$\lambda_2 = \pm i\upsilon \, , \, \upsilon = \sqrt{\frac{1}{2}\left(-a - \sqrt{a^2 + 4b}\right)} \, , \tag{B3}$$

where ;

$$a = \frac{\hat{I}^{(C,k)}\omega^2}{\hat{C}_{11}^{(F,k)}} \quad , \quad b = \frac{\hat{I}^{(A,k)}\omega^2}{\hat{C}_{11}^{(F,k)}} \, .$$

The boundary condition of the transverse bending equation can be formulated with tip mass and rotary inertias from the piezoelectric beam and tip mass as,

$$\hat{C}_{11}^{(F,k)}\frac{d^2\Psi}{dx^2}(L) - I_{tip}^{(C)}\omega^2\frac{d\Psi}{dx}(L) = 0 \, , \tag{B4}$$

$$\hat{C}_{11}^{(F,k)} \frac{\mathrm{d}^3 \Psi}{\mathrm{d}x^3}(L) + \hat{I}^{(C,k)} \omega^2 \frac{\mathrm{d}\Psi}{\mathrm{d}x}(L) + I_{tip}^{(A)} \omega^2 \Psi(L) = 0, \tag{B5}$$

$$\Psi(0) = 0 \quad , \quad \frac{\mathrm{d}\Psi}{\mathrm{d}x}(0) = 0. \tag{B6}$$

After manipulating some complex equations according to boundary conditions, the characteristic equation can be formulated in matrix form as,

$$\begin{bmatrix} A_{11} & A_{12} \\ A_{21} & A_{22} \end{bmatrix} \begin{Bmatrix} C_1 \\ C_4 \end{Bmatrix} = 0 . \tag{B7}$$

where,

$$A_{11} = -\hat{C}_{11}^{(F,k)} \mu^2 \cos(\mu L) + I_{tip}^{(C)} \mu\omega^2 \sin(\mu L) - \hat{C}_{11}^{(F,k)} \upsilon^2 \cosh(\upsilon L) + I_{tip}^{(C)} \upsilon\omega^2 \sinh(\upsilon L)$$

$$A_{12} = \hat{C}_{11}^{(F,k)} \upsilon^2 \sinh(\upsilon L) - I_{tip}^{(C)} \upsilon\omega^2 \cosh(\upsilon L) + \frac{\upsilon}{\mu} \left(\hat{C}_{11}^{(F,k)} \mu^2 \sin(\mu L) + I_{tip}^{(C)} \mu\omega^2 \cos(\mu L) \right)$$

$$A_{21} = \hat{C}_{11}^{(F,k)} \mu^3 \sin(\mu L) - \hat{I}^{(C,k)} \mu\omega^2 \sin(\mu L) + I_{tip}^{(A)} \omega^2 \cos(\mu L) -$$

$$\hat{C}_{11}^{(F,k)} \upsilon^3 \sinh(\upsilon L) - \hat{I}^{(C,k)} \upsilon\omega^2 \sinh(\upsilon L) - I_{tip}^{(A)} \omega^2 \cosh(\upsilon L)$$

$$A_{22} = \hat{C}_{11}^{(F,k)} \upsilon^3 \cosh(\upsilon L) + \hat{I}^{(C,k)} \upsilon\omega^2 \cosh(\upsilon L) + I_{tip}^{(A)} \omega^2 \sinh(\upsilon L) +$$

$$\frac{\upsilon}{\mu} \left(\hat{C}_{11}^{(F,k)} \mu^3 \cos(\mu L) - \hat{I}^{(C,k)} \mu\omega^2 \cos(\mu L) - I_{tip}^{(A)} \omega^2 \sin(\mu L) \right)$$

Frequency equation and eigenvalues are calculated by solving for the determinant from equation (B7). Trial and error methods can be used to obtain the eigenvalues. The best way to solve the frequency equation and eigenvalues was found by using MATLAB. The eigenfunction form can be formulated as,

$$\Psi_r(x) = C_1 \left((\cos \mu x) - \cosh(\upsilon x) - \frac{A_{21}}{A_{22}} \left(\sinh(\upsilon x) - \frac{\upsilon}{\mu} \sin(\mu x) \right) \right). \tag{B8}$$

B.2 Euler-Bernoulli piezoelectric bimorph beam with tip mass

The mechanical dynamic equation in transverse bending form can be simplified by ignoring the rotary inertia of the piezoelectric beam from Eq. (B1) to give,

$$\frac{\mathrm{d}^4 \Psi_r(x)}{\mathrm{d}x^4} - \mu^4 \Psi_r(x) = 0 \quad . \tag{B9}$$

Four distinct roots can be obtained as,

$$\lambda_{1,2} = \pm\mu \quad , \quad \lambda_{3,4} = \pm j\mu \quad . \tag{B10}$$

where $\mu^4 = \hat{I}^{(A,k)}\omega^2 / \hat{C}_{11}^{(F,k)}$. The boundary condition of the cantilevered piezoelectric beam with the tip mass and rotary moment of inertia from the tip mass can be formulated as,

$$\hat{C}_{11}^{(F,k)} \frac{d^2\Psi_r}{dx^2}(L) - I_{tip}^{(C)}\omega^2 \frac{d\Psi_r}{dx}(L) = 0, \tag{B11}$$

$$\hat{C}_{11}^{(F,k)} \frac{d^3\Psi_r}{dx^3}(L) + I_{tip}^{(A)}\omega^2\Psi_r(L) = 0, \tag{B12}$$

$$\Psi_r(0) = 0 \qquad , \qquad \frac{d\Psi_r}{dx}(0) = 0 \quad . \tag{B13}$$

The characteristic equation can be obtained after manipulating Eqs. (B9) - (B13) to give,

$$\begin{bmatrix} A_{11} & A_{12} \\ A_{21} & A_{22} \end{bmatrix} \begin{Bmatrix} c_1 \\ c_4 \end{Bmatrix} = 0 \quad , \tag{B14}$$

where,

$$A_{11} = -\left(\cos(\mu L) + \cosh(\mu L)\right) + \frac{I_{tip}^{(C)}\mu^3}{\hat{I}^{(A,k)}}\left(\sin(\mu L) + \sinh(\mu L)\right)$$

$$A_{12} = \left(\sin(\mu L) + \sinh(\mu L)\right) + \frac{I_{tip}^{(C)}\mu^3}{\hat{I}^{(A,k)}}\left(\cos(\mu L) - \cosh(\mu L)\right)$$

$$A_{21} = \left(\sin(\mu L) - \sinh(\mu L)\right) + \frac{I_{tip}^{(A)}\mu}{\hat{I}^{(A,k)}}\left(\cos(\mu L) - \cosh(\mu L)\right)$$

$$A_{22} = \left(\cos(\mu L) + \cosh(\mu L)\right) - \frac{I_{tip}^{(A)}\mu}{\hat{I}^{(A,k)}}\left(\sin(\mu L) - \sinh(\mu L)\right)$$

The frequency equation and eigenvalues can be calculated by analysing the determinant from Eq. (B14) to give,

$$\left(1 + \cos(\mu L)\cosh(\mu L)\right) - \frac{I_{tip}^{(C)}\mu^3}{\hat{I}^{(A,k)}}\left(\cos\mu L\sinh\mu L + \sin\mu L\cosh\mu L\right)$$

$$+ \frac{I_{tip}^{(A)}\mu}{\hat{I}^{(A,k)}}\left(\cos\mu L\sinh\mu L - \sin\mu L\cosh\mu L\right) + \frac{I_{tip}^{(A)}I_{tip}^{(C)}\mu^4}{\hat{I}^{(A,k)2}}\left(1 - \cos\mu L\cosh\mu L\right) = 0. \tag{B15}$$

After applying boundary conditions and some algebraic calculations, the eigenfunction can now be formulated as,

$$\Psi_r(x) = c_{1r}\left(\cos(\mu x) - \cosh(\mu x) + \frac{A_{21}}{A_{22}}\left(\sin(\mu x) - \sinh(\mu x)\right)\right) \quad . \tag{B16}$$

B.3 Longitudinal piezoelectric bimorph beam with tip mass

The dynamic equation of longitudinal motion for the cantilevered piezoelectric bimorph beam can be written as,

$$\frac{d^2\Theta(x)}{dx^2} + \gamma^2\Theta(x) = 0 \ . \tag{B17}$$

Equation (B17) can be modified into a characteristic equation and two roots from the characteristic equation can be obtained as,

$$\lambda_{1,2} = \pm j\gamma \ , \tag{B18}$$

where , $\quad \gamma^2 = \dfrac{\omega^2 \hat{I}^{(A,k)}}{\hat{C}_{11}^{(D,k)}} \quad .$

The boundary condition can be formulated as,

$$\hat{C}_{11}^{(D,k)}\frac{d\Theta}{dx}(L) - I_{tip}^{(A)}\omega^2\Theta(L) = 0 \quad , \quad \Theta(0) = 0 \ . \tag{B19}$$

The frequency equation and eigenvalues can be calculated by applying boundary conditions to give,

$$\tan\gamma L = \frac{\hat{C}_{11}^{(D,k)}\gamma}{I_{tip}^{(A)}\omega^2} \quad . \tag{B20}$$

After applying boundary conditions and some algebraic calculations, the mode shape can now be formulated as

$$\Theta_r(x) = b_{1r}\sin\gamma x \quad . \tag{B21}$$

Appendix C

```
%%%%%%%%%%%%%%%%%%%%%%%%%%%%%%%%%%%%%%%%%%%%%%%%%%%%%%%%%%%%%%%%%%
%%%%%    MATLAB Program of electromechanical Piezoelectric    %%%%
%%%%% Bimorph Beam with tip mass using CEDRTL and CEDRT models %%%%
%%%%%                      (Weak form)                        %%%%
%%%%%           Programmed by Mikail F. Lumentut              %%%%
%%%%%         Supervised by A/Prof. Ian M. Howard             %%%%
%%%%%          Department of Mechanical Engineering           %%%%
%%%%%            Curtin University of Technology              %%%%
%%%%%%%%%%%%%%%%%%%%%%%%%%%%%%%%%%%%%%%%%%%%%%%%%%%%%%%%%%%%%%%%%%%%

clc
clear
%%%%%%%%%%%%%%%%%%%%%%%%%%%%%%%%%%%%%%%%%%%%%%%%%%%%%%%%%%%%%%%%%%%%
%%%%%Input data of geometry and properties Piezoelectric bimorph%%%
%%%%%%%%%%%%%%%%%%%%%%%%%%%%%%%%%%%%%%%%%%%%%%%%%%%%%%%%%%%%%%%%%%%%
% Piezoelectric bimorph
hp=0.19e-3 ;        % Piezoelectric thickness
hs=0.13e-3 ;        % substructure thickness
bp=6.4e-3 ;         % Bimorph width
L=30.1e-3  ;        % Length of Bimorph
e31=-190e-12*Qp;    % Piezoelectric constant
beta=1540*8.9e-12;  % Permittivity of constant strain
% Tip mass
ha=5.7e-3 ;   % Mass thickness
lo=8.1e-3  ;  % Mass length 1
lb=5e-3  ;    % Mass length 2
bs=6.4e-3 ;   % Mass Width
% density
rhoa=7800 ;   % density of steel
rhop=7800 ;   % density of piezoelectric
rhos=9000 ;   % density of brass
% Piezoelectric constant
Rb=-2*(hp^2/2+(hp*hs)/2)*(b/hp)*e31;  % transverse form
Ra=2*b*e31;   % longitudinal form
% Internal capacitance of piezoelectric
Pd=-2*b*L*beta/(hp);
% elastic stiffness constants
Qp=66e9;    % Piezoelectric modulus of elastic constant
Qs=105e9;   % Brass modulus of elastic constant
Cc=b*(2/3*(hp+hs/2)^3-hs^3/12)*Qp+b*hs^3/4*Qs;  % transverse
                                     % stiffness coefficient
Ca=2*b*hp*Qp+b*hs*Qs;         % longitudinal stiffness coefficient
% Zero-th mass moment of inertia of tip mass
Ia=(ha*lo-(2*hp+hs)*lb)*bs*rhoa
% Second mass of inertia moment of tip mass
xg=(ha*lo*lo/2-(2*hp+hs)*lb*lb/2)/(ha*lo-(2*hp+hs)*lb);
x1=xg-lo/2;
x2=xg-lb/2;
Ic=(((lo^2+ha^2)/12+x1^2)-(((2*hp+hs)^2+lb^2)/12)-x2^2)*(lo*ha-
(2*hp+hs)*lb)*bs*rhoa ;
% Zero-th mass of inertia moment of bimorph
Im=2*bp*hp*rhop+bs*hs*rhos;
```

```matlab
%%%%%%%%%%%%%%%%%%%%%%%%%%%%%%%%%%%%%%%%%%%%%%%%%%%%%%%%%%%%%%%%%%%%%%%%%%%%%
%%%%% Calculating the eigenfunction forms, mass and stiffness %%%%%
%%%%% matrices, orthonormality and Piezoelectric coupling     %%%%%
%%%%%%%%%%%%%%%%%%%%%%%%%%%%%%%%%%%%%%%%%%%%%%%%%%%%%%%%%%%%%%%%%%%%%%%%%%%%%
% First eigenfunction of transverse form
syms x
vn1=33.2379 :
Aa1=(Ia*vn1)/Im;
Bb1=(Ic*vn1^3)/Im;
A11=-(cos(vn1*L)+cosh(vn1*L))+Bb1*(sin(vn1*L)+sinh(vn1*L));
A12=(sinh(vn1*L)+sin(vn1*L))+Bb1*(cos(vn1*L)-cosh(vn1*L));
A21=((sin(vn1*L)-sinh(vn1*L))+Aa1*(cos(vn1*L)-cosh(vn1*L)));
A22=((cos(vn1*L)+cosh(vn1*L))-Aa1*(sin(vn1*L)-sinh(vn1*L)));
zh1=(cos(vn1*x)-cosh(vn1*x)+(A21/A22)*(sin(vn1*x)-sinh(vn1*x)));
zhm1=(cos(vn1*L)-cosh(vn1*L)+(A21/A22)*(sin(vn1*L)-sinh(vn1*L)));
% Second eigenfunction of transverse form
vn2= 120.01682;
Aa2=(Ia*vn2)/Im;
Bb2=(Ic*vn2^3)/Im;
 An11=-(cos(vn2*L)+cosh(vn2*L))+Bb2*(sin(vn2*L)+sinh(vn2*L));
An12=(sinh(vn2*L)+sin(vn2*L))+Bb2*(cos(vn2*L)-cosh(vn2*L));
An21=((sin(vn2*L)-sinh(vn2*L))+Aa2*(cos(vn2*L)-cosh(vn2*L)));
An22=((cos(vn2*L)+cosh(vn2*L))-Aa2*(sin(vn2*L)-sinh(vn2*L)));
zh2=(cos(vn2*x)-cosh(vn2*x)+(An21/An22)*(sin(vn2*x)-sinh(vn2*x)));
zhm2=(cos(vn2*L)-cosh(vn2*L)+(An21/An22)*(sin(vn2*L)-sinh(vn2*L)));
% Third eigenfunction of transverse form
vn3=186.990149;
Aa3=(Ia*vn3)/Im;
Bb3=(Ic*vn3^3)/Im;
A311=-(cos(vn3*L)+cosh(vn3*L))+Bb3*(sin(vn3*L)+sinh(vn3*L));
A312=(sinh(vn3*L)+sin(vn3*L))+Bb3*(cos(vn3*L)-cosh(vn3*L));
A321=((sin(vn3*L)-sinh(vn3*L))+Aa3*(cos(vn3*L)-cosh(vn3*L)));
A322=((cos(vn3*L)+cosh(vn3*L))-Aa3*(sin(vn3*L)-sinh(vn3*L)));
zh3=(cos(vn3*x)-cosh(vn3*x)+(A321/A322)*(sin(vn3*x)-sinh(vn3*x)));
zhm3=(cos(vn3*L)-cosh(vn3*L)+(A321/A322)*(sin(vn3*L)-sinh(vn3*L)));
% Arranging the eigenfunction series into matrix forms
zh=[zh1 zh2 zh3];
zhl=[zhm1 zhm2 zhm3];
% Differential forms of the eigenfunction series
dzhx=diff(zh,x,2);
dzhy=diff(zh,x,1);
dzhz=diff(zh,x,1);
dzh1=subs(dzhy,L);
% initialisation of mechanical mass and stiffness matrices for
% transverse
Mbb=zeros(3,3);
Kbb=zeros(3,3);
% Calculating the mechanical mass and stiffness matrices for
% transverse form
for s=1:3
for n=1:3
Mbb(s,n)=Mbb(s,n)+(Im*int((zh(:,n)*zh(:,s)),x,0,L)+Ia*(zhl(:,n)*zhl(
:,s))+Ic*(dzh1(:,n)*dzh1(:,s)));
Kbb(s,n)=Kbb(s,n)+(Cc*int((dzhx(:,n)*dzhx(:,s)),x,0,L));
end
end
% Calculating the eigenvector and eigenvalues
invm=inv(Mbb);
kmmod=invm*Kbb;
[V,D]=eig(kmmod);
freq_nat=D;
```

```
% Calculating the Ritz transverse eigenfunction series
Zt1=vpa(V(1,1)*zh1+V(2,1)*zh2+V(3,1)*zh3);
Zt2=vpa(V(1,3)*zh1+V(2,3)*zh2+V(3,3)*zh3);
Zt3=vpa(V(1,2)*zh1+V(2,2)*zh2+V(3,2)*zh3);
% Arranging the Ritz transverse eigenfunction series into
% matrix forms
Nzh=[Zt1 Zt2 Zt3];
% Calculating transverse eigenfunction function series in terms of
% bimorph length
Nzhm1=subs(Zt1,x,L);
Nzhm2=subs(Zt2,x,L);
Nzhm3=subs(Zt3,x,L);
% Arranging transverse eigenfunction function series in terms of
% bimorph length
Nzhl=[Nzhm1 Nzhm2 Nzhm3];
% calculating differential forms of eigenfunction function series
dzhxn=diff(Nzh,x,2);
dzhyn=diff(Nzh,x,1);
dzhzn=diff(Nzh,x,1);
dzh1n=subs(dzhyn,x,L);
% Transverse mass normalisation
NMbb=sqrt(1/(simplify(Im*int(Nzh(1,1)*Nzh(1,1),x,0,L)+Ia*Nzhl(1,1)*N
zhl(1,1)+Ic*dzh1n(1,1)*dzh1n(1,1))));
NMbb2=sqrt(1/(simplify(Im*int(Nzh(1,2)*Nzh(1,2),x,0,L)+Ia*Nzhl(1,2)*
Nzhl(1,2)+Ic*dzh1n(1,2)*dzh1n(1,2))));
NMbb3=sqrt(1/(simplify(Im*int(Nzh(1,3)*Nzh(1,3),x,0,L)+Ia*Nzhl(1,3)*
Nzhl(1,3)+Ic*dzh1n(1,3)*dzh1n(1,3))));
% Normalised first Ritz eigenfunction forms
Nsh=vpa(simple(Nzh(1,1)*NMbb));
Nshm=subs(Nsh,x,L);
Ndzhyn=diff(Nsh,x,1);
Nshn=subs(Ndzhyn,x,L);
Ndzhxn=diff(Nsh,x,2);
% Checking whether normalisation is fulfilled and calculating the
% first inertia force
MbbN=vpa(Im*int(Nsh*Nsh,x,0,L)+Ia*Nshm*Nshm+Ic*Nshn*Nshn);
NKbb=vpa(Cc*int(Ndzhxn*Ndzhxn,x,0,L));
NQw1=vpa(Im*int(Nsh,x,0,L)+Ia*Nshm);
% Normalised second Ritz eigenfunction forms
Nsh2=vpa(simple(Nzh(1,2)*NMbb2));
Nshm2=subs(Nsh2,x,L);
Ndzhyn2=diff(Nsh2,x,1);
Nshn2=subs(Ndzhyn2,x,L);
Ndzhxn2=diff(Nsh2,x,2);
% Checking whether normalisation is fulfilled and calculating the
% second inertia force
MbbN2=vpa(Im*int(Nsh2*Nsh2,x,0,L)+Ia*Nshm2*Nshm2+Ic*Nshn2*Nshn2);
NKbb2=vpa(Cc*int(Ndzhxn2*Ndzhxn2,x,0,L));
NQw2=vpa(Im*int(Nsh2,x,0,L)+Ia*Nshm2);
% Normalised third Ritz eigenfunction forms
Nsh3=vpa(simple(Nzh(1,3)*NMbb3));
Nshm3=subs(Nsh3,x,L);
Ndzhyn3=diff(Nsh3,x,1);
Nshn3=subs(Ndzhyn3,x,L);
Ndzhxn3=diff(Nsh3,x,2);
% Checking whether normalisation is fulfilled is fulfilled and
% calculating the second inertia force
MbbN3=vpa(Im*int(Nsh3*Nsh3,x,0,L)+Ia*Nshm3*Nshm3+Ic*Nshn3*Nshn3);
NKbb3=vpa(Cc*int(Ndzhxn3*Ndzhxn3,x,0,L));
NQw3=vpa(Im*int(Nsh3,x,0,L)+Ia*Nshm3);
% transverse Piezoelectric coupling
```

```matlab
Pw1=vpa(Rb*int((Ndzhxn),x,0,L));
Pw2=vpa(Rb*int((Ndzhxn2),x,0,L));
Pw3=vpa(Rb*int((Ndzhxn3),x,0,L));
% First eigenfunction of longitudinal form
vv1=18.8287 ;
zhl1=(sin(vv1*x));
zhlm1=subs(zhl1,x,L);
% Second  eigenfunction of longitudinal form
vv2=108.073;
zhl2=(sin(vv2*x));
zhlm2=subs(zhl2,x,L);
% Third eigenfunction of longitudinal form
vv3=210.665;
zhl3=(sin(vv3*x));
zhlm3=subs(zhl3,x,L);
% arranging into matrix form
zhlo=[zhl1 zhl2 zhl3];
zhlom=[zhlm1 zhlm2 zhlm3];
% Differential form
dzhyo=diff(zhlo,x,1);
% Calculating eigenfunction function form in terms of bimorph length
dzho1=subs(dzhyo,L);
% Calculating the mechanical mass and stiffness matrices for
% longitudinal
Maa=zeros(3,3);
Kaa=zeros(3,3);
for s=1:3
for n=1:3
Maa(s,n)=Maa(s,n)+vpa(Im*int(zhlo(:,n)*zhlo(:,s),x,0,L)+Ia*zhlom(:,n
)*zhlom(:,s));
Kaa(s,n)=Kaa(s,n)+vpa(Ca*int(dzhyo(:,n)*dzhyo(:,s),x,0,L));
end
end
% Calculating the eigenvector and eigenvalues
invlo=inv(Maa);
    kmlo=invlo*Kaa;
    [V2,D2]=eig(kmlo);
    freq_nat2=D2;
% Calculating the Ritz longitudinal eigenfunction forms
Zto1=vpa(V2(1,1)*zhl1+V2(2,1)*zhl2+V2(3,1)*zhl3);
Zto2=vpa(V2(1,3)*zhl1+V2(2,3)*zhl2+V2(3,3)*zhl3);
Zto3=vpa(V2(1,2)*zhl1+V2(2,2)*zhl2+V2(3,2)*zhl3);
% Arranging the Ritz longitudinal eigenfunction forms into
% matrix forms
Nzho=[Zto1 Zto2 Zto3];
% Calculating longitudinal eigenfunction function form in terms of
% bimorph length
Nzho1=subs(Zto1,x,L);
Nzho2=subs(Zto2,x,L);
Nzho3=subs(Zto3,x,L);
% Arranging longitudinal eigenfunction function form in terms of
% bimorph length
Nzhmo=[Nzho1 Nzho2 Nzho3];
% calculating differential form
dzhxo=diff(Nzho,x,2);
dzhyo=diff(Nzho,x,1);
dzhzo=diff(Nzho,x,1);
dzh1o=subs(dzhyo,x,L);
% Longitudinal mass normalisation
NMaa1=sqrt(1/(simple(Im*int(Nzho(1,1)*Nzho(1,1),x,0,L)+Ia*Nzhmo(1,1)
*Nzhmo(1,1)))));
```

```
NMaa2=sqrt(1/(simple(Im*int(Nzho(1,2)*Nzho(1,2),x,0,L)+Ia*Nzhmo(1,2)
*Nzhmo(1,2)))));
NMaa3=sqrt(1/(simple(Im*int(Nzho(1,3)*Nzho(1,3),x,0,L)+Ia*Nzhmo(1,3)
*Nzhmo(1,3)))));
% Normalised first Ritz longitudinal eigenfunction forms
Nsho1=vpa(simple(Nzho(1,1)*NMaa1));
Nshmo1=subs(Nsho1,x,L);
Ndzhyno1=diff(Nsho1,x,1);
Nshno1=subs(Ndzhyno1,x,L);
Ndzhxno1=diff(Nsho1,x,2);
% Checking whether normalisation is fulfilled and calculating first
% generalised input inertia force due to input motion
MaaN1=vpa(Im*int(Nsho1*Nsho1,x,0,L)+Ia*Nshmo1*Nshmo1);
NKaa1=vpa((Ca*int(Ndzhyno1^2,x,0,L)));
NQu1=vpa(subs(Im*int(Nsho1,x,0,L)+Ia*Nshmo1));
% Normalised second Ritz longitudinal eigenfunction forms
Nsho2=vpa(simple(Nzho(1,2)*NMaa2));
Nshmo2=subs(Nsho2,x,L);
Ndzhyno2=diff(Nsho2,x,1);
Nshno2=subs(Ndzhyno2,x,L);
Ndzhxno2=diff(Nsho2,x,2);
% Checking whether normalisation is fulfilled and calculating second
% generalised input inertia force due to input motion
MaaN2=vpa(Im*int(Nsho2*Nsho2,x,0,L)+Ia*Nshmo2*Nshmo2);
NKaa2=vpa((Ca*int(Ndzhyno2^2,x,0,L)));
NQu2=vpa(subs(Im*int(Nsho2,x,0,L)+Ia*Nshmo2));
% Normalised third Ritz longitudinal eigenfunction forms
Nsho3=vpa(simple(Nzho(1,2)*NMaa3));
Nshmo3=subs(Nsho3,x,L);
Ndzhyno3=diff(Nsho3,x,1);
Nshno3=subs(Ndzhyno3,x,L);
Ndzhxno3=diff(Nsho3,x,2);
% Checking whether normalisation is fulfilled and calculating third
% generalised input inertia force due to input motion
MaaN3=vpa(Im*int(Nsho3*Nsho3,x,0,L)+Ia*Nshmo3*Nshmo3);
NKaa3=vpa((Ca*int(Ndzhyno3^2,x,0,L)));
NQu3=vpa(subs(Im*int(Nsho3,x,0,L)+Ia*Nshmo3));
% Longitudinal piezoelectric coupling
Pu1= -subs(Ra*int(Ndzhyno1,x,0,L));
Pu2= -subs(Ra*int(Ndzhyno2,x,0,L));
Pu3= -subs(Ra*int(Ndzhyno3,x,0,L));
%%%%%%%%%%%%%%%%%%%%%%%%%%%%%%%%%%%%%%%%%%%%%%%%%%%%%%%%%%%%%%%%%%%%%%%%
%%%%% Generations of FRFs electrical voltage, current, power, %%%%%
%%%%% optimal power, polar power, tip transverse displacement %%%%%
%%%%%                          and velocity                   %%%%%
%%%%%%%%%%%%%%%%%%%%%%%%%%%%%%%%%%%%%%%%%%%%%%%%%%%%%%%%%%%%%%%%%%%%%%%%
% Iterating input frequency range
freq_end=90; % input last frequency
hrqf=freq_end*2*pi;
hrqi=2*pi*60; % input initial frequency
deltahrq=1;
nhrq=fix((hrqf-hrqi)/deltahrq)+1; % the number of the generated
                                  % frequency
% Iteration of electromechanical FRFs
 plotsol=3 ;  % Input iteration
if plotsol==1 % iterating the tip absolute transverse displacement
              % with CEDRT model
zb1=0.0139;
zb2=0.015;
zb3=0.020;
za1=0.03;
```

```
za2=0.036;
za3=0.04;
wra1=sqrt(NKaa1);        % first longitudinal natural frequency
wra2=sqrt(NKaa2);        % second longitudinal natural frequency
wra3=sqrt(NKaa3);        % third longitudinal natural frequency
wrb1=sqrt(NKbb);         % first transverse natural frequency
wrb2=sqrt(NKbb2);        % second transverse natural frequency
wrb3=sqrt(NKbb3);        % third transverse natural frequency
FRVw1=zeros(10,nhrq);    % Initialisation of generated frequency
                         % response
    nl=0;
    s2=0;
% Iterating input load resistance
for Rdd=[560 5.6e3 20e3 30e3 51e3 60e3 79e3  150e3 200e3 602e3];
    nl=nl+1;
for n=hrqi:deltahrq:hrqf; % iterating input frequency
    Rl=1/Rdd;
    s2=s2+1;
FRVw1(nl,s2)=FRVw1(nl,s2)+(-3/(n^2)+(((-Nshm/(wrb1^2-
n^2+2*i*zb1*n*wrb1))*((Pd*i*n-Rl)*NQw1*3)/....
    ((Pd*i*n-Rl)-i*n*Pw1^2/(wrb1^2-n^2+2*i*zb1*n*wrb1)-
i*n*Pw2^2/(wrb2^2-n^2+2*i*zb2*n*wrb2)-i*n*Pw3^2/(wrb3^2-
n^2+2*i*zb3*n*wrb3)))+....
((-Nshm2/(wrb2^2-n^2+2*i*zb2*n*wrb2))*((Pd*i*n-Rl)*NQw2*3)/....
    ((Pd*i*n-Rl)-i*n*Pw1^2/(wrb1^2-n^2+2*i*zb1*n*wrb1)-
i*n*Pw2^2/(wrb2^2-n^2+2*i*zb2*n*wrb2)-i*n*Pw3^2/(wrb3^2-
n^2+2*i*zb3*n*wrb3)))+...
    ((-Nshm3/(wrb3^2-n^2+2*i*zb3*n*wrb3))*((Pd*i*n-Rl)*NQw3*3)/....
    ((Pd*i*n-Rl)-i*n*Pw1^2/(wrb1^2-n^2+2*i*zb1*n*wrb1)-
i*n*Pw2^2/(wrb2^2-n^2+2*i*zb2*n*wrb2)-i*n*Pw3^2/(wrb3^2-
n^2+2*i*zb3*n*wrb3)))));
end
    s2=0;
end
nqr=hrqi:deltahrq:hrqf;
semilogy(nqr/(2*pi),(abs(FRVw1)));


elseif plotsol==2 % iterating the tip absolute transverse
                  % velocity with CEDRT model
zb1=0.0139;
zb2=0.015;
zb3=0.020;
za1=0.03;
za2=0.036;
za3=0.04;
wra1=sqrt(NKaa1);        % first longitudinal natural frequency
wra2=sqrt(NKaa2);        % second longitudinal natural frequency
wra3=sqrt(NKaa3);        % third longitudinal natural frequency
wrb1=sqrt(NKbb);         % first transverse natural frequency
wrb2=sqrt(NKbb2);        % second transverse natural frequency
wrb3=sqrt(NKbb3);        % third transverse natural frequency
FRVw2=zeros(10,nhrq);    % Initialisation of generated frequency
                         % response
    nl=0;
    s2=0;
% iterating input load resistance
for Rdd=[560 5.6e3 20e3 30e3 51e3 60e3 79e3  150e3 200e3 602e3];
    nl=nl+1;
for n=hrqi:deltahrq:hrqf; % iterating input frequency
    Rl=1/Rdd;
    s2=s2+1;
```

```
FRVw2(nl,s2)=FRVw2(nl,s2)+(3/(i*n)+i*n*(((-Nshm/(wrb1^2-
n^2+2*i*zb1*n*wrb1))*((Pd*i*n-Rl)*NQw1*3)/....
    ((Pd*i*n-Rl)-i*n*Pw1^2/(wrb1^2-n^2+2*i*zb1*n*wrb1)-
i*n*Pw2^2/(wrb2^2-n^2+2*i*zb2*n*wrb2)-i*n*Pw3^2/(wrb3^2-
n^2+2*i*zb3*n*wrb3)))+....
((-Nshm2/(wrb2^2-n^2+2*i*zb2*n*wrb2))*((Pd*i*n-Rl)*NQw2*3)/....
    ((Pd*i*n-Rl)-i*n*Pw1^2/(wrb1^2-n^2+2*i*zb1*n*wrb1)-
i*n*Pw2^2/(wrb2^2-n^2+2*i*zb2*n*wrb2)-i*n*Pw3^2/(wrb3^2-
n^2+2*i*zb3*n*wrb3)))+...
    ((-Nshm3/(wrb3^2-n^2+2*i*zb3*n*wrb3))*((Pd*i*n-Rl)*NQw3*3)/....
    ((Pd*i*n-Rl)-i*n*Pw1^2/(wrb1^2-n^2+2*i*zb1*n*wrb1)-
i*n*Pw2^2/(wrb2^2-n^2+2*i*zb2*n*wrb2)-i*n*Pw3^2/(wrb3^2-
n^2+2*i*zb3*n*wrb3)))));
end
    s2=0;
end
nqr=hrqi:deltahrq:hrqf;
semilogy(nqr/(2*pi),(abs(FRVw2)));

elseif plotsol==3 % iterating the electrical voltage
                  % with CEDRT model
zb1=0.0139;
zb2=0.015;
zb3=0.020;
za1=0.03;
za2=0.036;
za3=0.04;
wra1=sqrt(NKaa1);      % first longitudinal natural frequency
wra2=sqrt(NKaa2);      % second longitudinal natural frequency
wra3=sqrt(NKaa3);      % third longitudinal natural frequency
wrb1=sqrt(NKbb);       % first transverse natural frequency
wrb2=sqrt(NKbb2);      % second transverse natural frequency
wrb3=sqrt(NKbb3);      % third transverse natural frequency
FRVw3=zeros(10,nhrq);  % Initialisation of generated frequency
                       % response
nl=0;
s2=0;
% iterating input load resistance
for Rdd=[560 5.6e3 20e3 30e3 51e3 60e3 79e3  150e3 200e3 602e3];
    nl=nl+1;
for n=hrqi:deltahrq:hrqf; % iterating input frequency
    Rl=1/Rdd;
    s2=s2+1;
FRVw3(nl,s2)=FRVw3(nl,s2)+((Pw1*i*n*NQw1*3/(wrb1^2-
n^2+2*i*zb1*n*wrb1)+Pw2*i*n*NQw2*3/(wrb2^2-
n^2+2*i*zb2*n*wrb2)+Pw3*i*n*NQw3*3/(wrb3^2-n^2+2*i*zb3*n*wrb3))/....
    ((Pd*i*n-Rl)-i*n*Pw1^2/(wrb1^2-n^2+2*i*zb1*n*wrb1)-
i*n*Pw2^2/(wrb2^2-n^2+2*i*zb2*n*wrb2)-i*n*Pw3^2/(wrb3^2-
n^2+2*i*zb3*n*wrb3)));
end
    s2=0;
end
nqr=hrqi:deltahrq:hrqf;
semilogy(nqr/(2*pi),(abs(FRVw3)));
elseif plotsol==4 % iterating the electrical voltage
                  % with CEDRT model
zb1=0.0139;
zb2=0.015;
zb3=0.020;
za1=0.03;
za2=0.036;
```

```
za3=0.04;
wra1=sqrt(NKaa1);        % first longitudinal natural frequency
wra2=sqrt(NKaa2);        % second longitudinal natural frequency
wra3=sqrt(NKaa3);        % third longitudinal natural frequency
wrb1=sqrt(NKbb);         % first transverse natural frequency
wrb2=sqrt(NKbb2);        % second transverse natural frequency
wrb3=sqrt(NKbb3);        % third transverse natural frequency
FRVw3=zeros(10,nhrq);    % Initialisation of generated frequency
                         % response
nl=0;
s2=0;
% iterating input load resistance
for Rdd=[560 5.6e3 20e3 30e3 51e3 60e3 79e3  150e3 200e3 602e3];
    nl=nl+1;
for n=hrqi:deltahrq:hrqf; % iterating input frequency
    Rl=1/Rdd;
    s2=s2+1;
FRVw3(nl,s2)=FRVw3(nl,s2)+((Pw1*i*n*NQw1*3/(wrb1^2-
n^2+2*i*zb1*n*wrb1)+Pw2*i*n*NQw2*3/(wrb2^2-
n^2+2*i*zb2*n*wrb2)+Pw3*i*n*NQw3*3/(wrb3^2-n^2+2*i*zb3*n*wrb3))/....
    ((Pd*i*n-Rl)-i*n*Pw1^2/(wrb1^2-n^2+2*i*zb1*n*wrb1)-
i*n*Pw2^2/(wrb2^2-n^2+2*i*zb2*n*wrb2)-i*n*Pw3^2/(wrb3^2-
n^2+2*i*zb3*n*wrb3)));
end
    s2=0;
end
nqr=hrqi:deltahrq:hrqf;
semilogy(nqr/(2*pi),(abs(FRVw3)));
elseif plotsol==5 % iterating the electrical current
                  % with CEDRT model
zb1=0.0139;
zb2=0.015;
zb3=0.020;
za1=0.03;
za2=0.036;
za3=0.04;
wra1=sqrt(NKaa1);        % first longitudinal natural frequency
wra2=sqrt(NKaa2);        % second longitudinal natural frequency
wra3=sqrt(NKaa3);        % third longitudinal natural frequency
wrb1=sqrt(NKbb);         % first transverse natural frequency
wrb2=sqrt(NKbb2);        % second transverse natural frequency
wrb3=sqrt(NKbb3);        % third transverse natural frequency
FRVw4=zeros(10,nhrq);    % Initialisation of generated frequency
                         % response
nl=0;
s2=0;
for Rdd=[560 5.6e3 20e3 30e3 51e3 60e3 79e3  150e3 200e3 602e3];
    nl=nl+1;
for n=hrqi:deltahrq:hrqf; % iterating input frequency
    Rl=1/Rdd;
    s2=s2+1;
FRVw4(nl,s2)=FRVw4(nl,s2)+((Pw1*i*n*NQw1*3/(wrb1^2-
n^2+2*i*zb1*n*wrb1)+Pw2*i*n*NQw2*3/(wrb2^2-
n^2+2*i*zb2*n*wrb2)+Pw3*i*n*NQw3*3/(wrb3^2-n^2+2*i*zb3*n*wrb3))/....
    ((Pd*i*n-Rl)-i*n*Pw1^2/(wrb1^2-n^2+2*i*zb1*n*wrb1)-
i*n*Pw2^2/(wrb2^2-n^2+2*i*zb2*n*wrb2)-i*n*Pw3^2/(wrb3^2-
n^2+2*i*zb3*n*wrb3)))/Rdd;
end
    s2=0;
end
nqr=hrqi:deltahrq:hrqf;
```

```
semilogy(nqr/(2*pi),(abs(FRVw4)));
elseif plotsol==5 % iterating the electrical Power
                  % with CEDRT model
zb1=0.0139;
zb2=0.015;
zb3=0.020;
za1=0.03;
za2=0.036;
za3=0.04;
wra1=sqrt(NKaa1);       % first longitudinal natural frequency
wra2=sqrt(NKaa2);       % second longitudinal natural frequency
wra3=sqrt(NKaa3);       % third longitudinal natural frequency
wrb1=sqrt(NKbb);        % first transverse natural frequency
wrb2=sqrt(NKbb2);       % second transverse natural frequency
wrb3=sqrt(NKbb3);       % third transverse natural frequency
FRVw5=zeros(10,nhrq);   % Initialisation of generated frequency
                        % response
nl=0;
s2=0;
for Rdd=[560 5.6e3 20e3 30e3 51e3 60e3 79e3  150e3 200e3 602e3];
    nl=nl+1;
for n=hrqi:deltahrq:hrqf; % iterating input frequency
    Rl=1/Rdd;
    s2=s2+1;
FRVw5(nl,s2)=FRVw5(nl,s2)+((Pw1*i*n*NQw1*3/(wrb1^2-
n^2+2*i*zb1*n*wrb1)+Pw2*i*n*NQw2*3/(wrb2^2-
n^2+2*i*zb2*n*wrb2)+Pw3*i*n*NQw3*3/(wrb3^2-n^2+2*i*zb3*n*wrb3))/....
    ((Pd*i*n-Rl)-i*n*Pw1^2/(wrb1^2-n^2+2*i*zb1*n*wrb1)-
i*n*Pw2^2/(wrb2^2-n^2+2*i*zb2*n*wrb2)-i*n*Pw3^2/(wrb3^2-
n^2+2*i*zb3*n*wrb3)))^2/Rdd;
end
    s2=0;
end
nqr=hrqi:deltahrq:hrqf;
semilogy(nqr/(2*pi),(abs(FRVw5)));


elseif plotsol==6 % iterating the tip absolute transverse
                  % displacement with CEDRTL model
zb1=0.0139;
zb2=0.015;
zb3=0.020;
za1=0.03;
za2=0.036;
za3=0.04;
wra1=sqrt(NKaa1);       % first longitudinal natural frequency
wra2=sqrt(NKaa2);       % second longitudinal natural frequency
wra3=sqrt(NKaa3);       % third longitudinal natural frequency
wrb1=sqrt(NKbb);        % first transverse natural frequency
wrb2=sqrt(NKbb2);       % second transverse natural frequency
wrb3=sqrt(NKbb3);       % third transverse natural frequency
FRVw6=zeros(10,nhrq);   % Initialisation of generated frequency
                        % response
nl=0;
s2=0;
for Rdd=[560 5.6e3 20e3 30e3 51e3 60e3 79e3  150e3 200e3 602e3];
nl=nl+1;
for n=hrqi:deltahrq:hrqf; % iterating input frequency
Rl=1/Rdd;
s2=s2+1;
FRVw6(nl,s2)=FRVw6(nl,s2)+(-3/(n^2)+(((-Nshm/(wrb1^2-
n^2+2*i*zb1*n*wrb1))*((Pd*i*n-Rl)*NQw1*3-Pu1^2*i*n*NQw1*3/(wra1^2-
```

```
n^2+2*i*za1*n*wra1)-Pu2^2*i*n*NQw2*3/(wra2^2-n^2+2*i*za2*n*wra2)-
Pu3^2*i*n*NQw3*3/(wra3^2-n^2+2*i*za3*n*wra3))/....
((Pd*i*n-Rl)-i*n*Pw1^2/(wrb1^2-n^2+2*i*zb1*n*wrb1)-
i*n*Pw2^2/(wrb2^2-n^2+2*i*zb2*n*wrb2)-i*n*Pw3^2/(wrb3^2-
n^2+2*i*zb3*n*wrb3)-....
i*n*Pu1^2/(wra1^2-n^2+2*i*za1*n*wra1)-i*n*Pu2^2/(wra2^2-
n^2+2*i*za2*n*wra2)-i*n*Pu3^2/(wra3^2-n^2+2*i*za3*n*wra3)))+....
((-Nshm2/(wrb2^2-n^2+2*i*zb2*n*wrb2))*((Pd*i*n-Rl)*NQw2*3-
Pu1^2*i*n*NQw1*3/(wra1^2-n^2+2*i*za1*n*wra1)-
Pu2^2*i*n*NQw2*3/(wra2^2-n^2+2*i*za2*n*wra2)-
Pu3^2*i*n*NQw3*3/(wra3^2-n^2+2*i*za3*n*wra3))/....
((Pd*i*n-Rl)-i*n*Pw1^2/(wrb1^2-n^2+2*i*zb1*n*wrb1)-
i*n*Pw2^2/(wrb2^2-n^2+2*i*zb2*n*wrb2)-i*n*Pw3^2/(wrb3^2-
n^2+2*i*zb3*n*wrb3)-....
i*n*Pu1^2/(wra1^2-n^2+2*i*za1*n*wra1)-i*n*Pu2^2/(wra2^2-
n^2+2*i*za2*n*wra2)-i*n*Pu3^2/(wra3^2-n^2+2*i*za3*n*wra3)))+...
((-Nshm3/(wrb3^2-n^2+2*i*zb3*n*wrb3))*((Pd*i*n-Rl)*NQw3*3-
Pu1^2*i*n*NQw1*3/(wra1^2-n^2+2*i*za1*n*wra1)-
Pu2^2*i*n*NQw2*3/(wra2^2-n^2+2*i*za2*n*wra2)-
Pu3^2*i*n*NQw3*3/(wra3^2-n^2+2*i*za3*n*wra3))/....
((Pd*i*n-Rl)-i*n*Pw1^2/(wrb1^2-n^2+2*i*zb1*n*wrb1)-
i*n*Pw2^2/(wrb2^2-n^2+2*i*zb2*n*wrb2)-i*n*Pw3^2/(wrb3^2-
n^2+2*i*zb3*n*wrb3)-....
i*n*Pu1^2/(wra1^2-n^2+2*i*za1*n*wra1)-i*n*Pu2^2/(wra2^2-
n^2+2*i*za2*n*wra2)-i*n*Pu3^2/(wra3^2-n^2+2*i*za3*n*wra3)))));
end
s2=0;
end
nqr=hrqi:deltahrq:hrqf;
semilogy(nqr/(2*pi),(abs(FRVw6)));


elseif plotsol==7 % iterating the tip absolute transverse
                  % velocity with CEDRTL model
zb1=0.0139;
zb2=0.015;
zb3=0.020;
za1=0.03;
za2=0.036;
za3=0.04;
wra1=sqrt(NKaa1);       % first longitudinal natural frequency
wra2=sqrt(NKaa2);       % second longitudinal natural frequency
wra3=sqrt(NKaa3);       % third longitudinal natural frequency
wrb1=sqrt(NKbb);        % first transverse natural frequency
wrb2=sqrt(NKbb2);       % second transverse natural frequency
wrb3=sqrt(NKbb3);       % third transverse natural frequency
FRVw6=zeros(10,nhrq);   % Initialisation of generated frequency
                        % response
nl=0;
s2=0;
for Rdd=[560 5.6e3 20e3 30e3 51e3 60e3 79e3  150e3 200e3 602e3];
nl=nl+1;
for n=hrqi:deltahrq:hrqf; % iterating input frequency
Rl=1/Rdd;
s2=s2+1;
FRVw6(nl,s2)=FRVw6(nl,s2)+(-3/(i*n)+i*n*(((-Nshm/(wrb1^2-
n^2+2*i*zb1*n*wrb1))*((Pd*i*n-Rl)*NQw1*3-Pu1^2*i*n*NQw1*3/(wra1^2-
n^2+2*i*za1*n*wra1)-Pu2^2*i*n*NQw2*3/(wra2^2-n^2+2*i*za2*n*wra2)-
Pu3^2*i*n*NQw3*3/(wra3^2-n^2+2*i*za3*n*wra3))/....
((Pd*i*n-Rl)-i*n*Pw1^2/(wrb1^2-n^2+2*i*zb1*n*wrb1)-
i*n*Pw2^2/(wrb2^2-n^2+2*i*zb2*n*wrb2)-i*n*Pw3^2/(wrb3^2-
n^2+2*i*zb3*n*wrb3)-....
```

```
i*n*Pu1^2/(wra1^2-n^2+2*i*za1*n*wra1)-i*n*Pu2^2/(wra2^2-
n^2+2*i*za2*n*wra2)-i*n*Pu3^2/(wra3^2-n^2+2*i*za3*n*wra3)))+....
((-Nshm2/(wrb2^2-n^2+2*i*zb2*n*wrb2))*((Pd*i*n-Rl)*NQw2*3-
Pu1^2*i*n*NQw1*3/(wra1^2-n^2+2*i*za1*n*wra1)-
Pu2^2*i*n*NQw2*3/(wra2^2-n^2+2*i*za2*n*wra2)-
Pu3^2*i*n*NQw3*3/(wra3^2-n^2+2*i*za3*n*wra3))/....
((Pd*i*n-Rl)-i*n*Pw1^2/(wrb1^2-n^2+2*i*zb1*n*wrb1)-
i*n*Pw2^2/(wrb2^2-n^2+2*i*zb2*n*wrb2)-i*n*Pw3^2/(wrb3^2-
n^2+2*i*zb3*n*wrb3)-....
i*n*Pu1^2/(wra1^2-n^2+2*i*za1*n*wra1)-i*n*Pu2^2/(wra2^2-
n^2+2*i*za2*n*wra2)-i*n*Pu3^2/(wra3^2-n^2+2*i*za3*n*wra3)))+...
((-Nshm3/(wrb3^2-n^2+2*i*zb3*n*wrb3))*((Pd*i*n-Rl)*NQw3*3-
Pu1^2*i*n*NQw1*3/(wra1^2-n^2+2*i*za1*n*wra1)-
Pu2^2*i*n*NQw2*3/(wra2^2-n^2+2*i*za2*n*wra2)-
Pu3^2*i*n*NQw3*3/(wra3^2-n^2+2*i*za3*n*wra3))/....
((Pd*i*n-Rl)-i*n*Pw1^2/(wrb1^2-n^2+2*i*zb1*n*wrb1)-
i*n*Pw2^2/(wrb2^2-n^2+2*i*zb2*n*wrb2)-i*n*Pw3^2/(wrb3^2-
n^2+2*i*zb3*n*wrb3)-....
i*n*Pu1^2/(wra1^2-n^2+2*i*za1*n*wra1)-i*n*Pu2^2/(wra2^2-
n^2+2*i*za2*n*wra2)-i*n*Pu3^2/(wra3^2-n^2+2*i*za3*n*wra3)))));
end
s2=0;
end
nqr=hrqi:deltahrq:hrqf;
semilogy(nqr/(2*pi),(abs(FRVw7)));
elseif plotsol==8 % iterating the electrical voltage
                  % with CEDRTL model
zb1=0.0139;
zb2=0.015;
zb3=0.020;
za1=0.03;
za2=0.036;
za3=0.04;
wra1=sqrt(NKaa1);        % first longitudinal natural frequency
wra2=sqrt(NKaa2);        % second longitudinal natural frequency
wra3=sqrt(NKaa3);        % third longitudinal natural frequency
wrb1=sqrt(NKbb);         % first transverse natural frequency
wrb2=sqrt(NKbb2);        % second transverse natural frequency
wrb3=sqrt(NKbb3);        % third transverse natural frequency
FRVw8=zeros(10,nhrq);    % Initialisation of generated frequency
                         % response
nl=0;
s2=0;
for Rdd=[560 5.6e3 20e3 30e3 51e3 60e3 79e3  150e3 200e3 602e3];
    nl=nl+1;
for n=hrqi:deltahrq:hrqf; % iterating input frequency
    Rl=1/Rdd;
    s2=s2+1;
FRVw8(nl,s2)=FRVw8(nl,s2) +((Pw1*i*n*NQw1*3/(wrb1^2-
n^2+2*i*zb1*n*wrb1)+Pw2*i*n*NQw2*3/(wrb2^2-
n^2+2*i*zb2*n*wrb2)+Pw3*i*n*NQw3*3/(wrb3^2-n^2+2*i*zb3*n*wrb3))/....
    ((Pd*i*n+Rl)-i*n*Pw1^2/(wrb1^2-n^2+2*i*zb1*n*wrb1)-
i*n*Pw2^2/(wrb2^2-n^2+2*i*zb2*n*wrb2)-i*n*Pw3^2/(wrb3^2-
n^2+2*i*zb3*n*wrb3)-....
    i*n*Pu1^2/(wra1^2-n^2+2*i*za1*n*wra1)-i*n*Pu2^2/(wra2^2-
n^2+2*i*za2*n*wra2)-i*n*Pu3^2/(wra3^2-n^2+2*i*za3*n*wra3)));
end
    s2=0;
end
nqr=hrqi:deltahrq:hrqf;
semilogy(nqr/(2*pi),(abs(FRVw8)));
```

```
elseif plotsol==9 % iterating the electrical Current
                  % with CEDRTL model
zb1=0.0139;
zb2=0.015;
zb3=0.020;
za1=0.03;
za2=0.036;
za3=0.04;
wra1=sqrt(NKaa1);        % first longitudinal natural frequency
wra2=sqrt(NKaa2);        % second longitudinal natural frequency
wra3=sqrt(NKaa3);        % third longitudinal natural frequency
wrb1=sqrt(NKbb);         % first transverse natural frequency
wrb2=sqrt(NKbb2);        % second transverse natural frequency
wrb3=sqrt(NKbb3);        % third transverse natural frequency
FRVw9=zeros(10,nhrq);    % Initialisation of generated frequency
                         % response
nl=0;
s2=0;
for Rdd=[560 5.6e3 20e3 30e3 51e3 60e3 79e3  150e3 200e3 602e3];
    nl=nl+1;
for n=hrqi:deltahrq:hrqf; % iterating input frequency
    Rl=1/Rdd;
    s2=s2+1;
FRVw9(nl,s2)=FRVw9(nl,s2) +((Pw1*i*n*NQw1*3/(wrb1^2-
n^2+2*i*zb1*n*wrb1)+Pw2*i*n*NQw2*3/(wrb2^2-
n^2+2*i*zb2*n*wrb2)+Pw3*i*n*NQw3*3/(wrb3^2-n^2+2*i*zb3*n*wrb3))/....
    ((Pd*i*n+Rl)-i*n*Pw1^2/(wrb1^2-n^2+2*i*zb1*n*wrb1)-
i*n*Pw2^2/(wrb2^2-n^2+2*i*zb2*n*wrb2)-i*n*Pw3^2/(wrb3^2-
n^2+2*i*zb3*n*wrb3)-....
    i*n*Pu1^2/(wra1^2-n^2+2*i*za1*n*wra1)-i*n*Pu2^2/(wra2^2-
n^2+2*i*za2*n*wra2)-i*n*Pu3^2/(wra3^2-n^2+2*i*za3*n*wra3)))/Rdd;
end
    s2=0;
end
nqr=hrqi:deltahrq:hrqf;
semilogy(nqr/(2*pi),(abs(FRVw9)));
elseif plotsol==10 % iterating the electrical power
                   % with CEDRTL model
zb1=0.0139;
zb2=0.015;
zb3=0.020;
za1=0.03;
za2=0.036;
za3=0.04;
wra1=sqrt(NKaa1);        % first longitudinal natural frequency
wra2=sqrt(NKaa2);        % second longitudinal natural frequency
wra3=sqrt(NKaa3);        % third longitudinal natural frequency
wrb1=sqrt(NKbb);         % first transverse natural frequency
wrb2=sqrt(NKbb2);        % second transverse natural frequency
wrb3=sqrt(NKbb3);        % third transverse natural frequency
FRVw10=zeros(10,nhrq);   % Initialisation of generated frequency
                         % response
nl=0;
s2=0;
for Rdd=[560 5.6e3 20e3 30e3 51e3 60e3 79e3  150e3 200e3 602e3];
    nl=nl+1;
for n=hrqi:deltahrq:hrqf; % iterating input frequency
    Rl=1/Rdd;
    s2=s2+1;
```

```
FRVw10(nl,s2)=FRVw10(nl,s2) +((Pw1*i*n*NQw1*3/(wrb1^2-
n^2+2*i*zb1*n*wrb1)+Pw2*i*n*NQw2*3/(wrb2^2-
n^2+2*i*zb2*n*wrb2)+Pw3*i*n*NQw3*3/(wrb3^2-n^2+2*i*zb3*n*wrb3))/....
     ((Pd*i*n+Rl)-i*n*Pw1^2/(wrb1^2-n^2+2*i*zb1*n*wrb1)-
i*n*Pw2^2/(wrb2^2-n^2+2*i*zb2*n*wrb2)-i*n*Pw3^2/(wrb3^2-
n^2+2*i*zb3*n*wrb3)-....
     i*n*Pu1^2/(wra1^2-n^2+2*i*za1*n*wra1)-i*n*Pu2^2/(wra2^2-
n^2+2*i*za2*n*wra2)-i*n*Pu3^2/(wra3^2-n^2+2*i*za3*n*wra3)))^2/Rdd;
end
     s2=0;
end
nqr=hrqi:deltahrq:hrqf;
semilogy(nqr/(2*pi),(abs(FRVw10)));
elseif plotsol==11 % iterating the polar tip absolute transverse
                   % displacement with CEDRTL model
UWc=3; % input acceleration
n=77.71*2*pi; % input frequency
UW=UWc/(n)^2;
s2=0;
zb1=0.0139;
zb2=0.015;
zb3=0.020;
za1=0.03;
za2=0.036;
za3=0.04;
wra1=sqrt(NKaa1);      % first longitudinal natural frequency
wra2=sqrt(NKaa2);      % second longitudinal natural frequency
wra3=sqrt(NKaa3);      % third longitudinal natural frequency
wrb1=sqrt(NKbb);       % first transverse natural frequency
wrb2=sqrt(NKbb2);      % second transverse natural frequency
wrb3=sqrt(NKbb3);      % third transverse natural frequency
freq_end=0.05; % the number of the generated time history (second)
frqf=freq_end;
frqi=0; % the initial input time (second)
deltahrq=1/1000; % the incremental time (second)
fhrq=fix((frqf-frqi)/deltahrq)+1;
fr=180; % the number of the generated angle (degree)
hf=fr;
hi=0; % the initial input angle (degree)
drq=1; % the incremental angle (degree)
hrq=fix((hf-hi)/drq)+1;
FRVw11=zeros(hrq,fhrq);
nl=0;
Rdd=[60e3]; % input load resistance (ohm)
Rl=1/Rdd;
for thetapz=(hi:drq:hf)*(pi*2)/360; % iterating input angle
    nl=nl+1;
  for k=frqi:deltahrq:frqf; % iterating input time history
        s2=s2+1;
FRVw11(nl,s2)=FRVw11(nl,s2)+(UW*sin(thetapz)*exp(i*n*k)+(((-
Nshm/(wrb1^2-n^2+2*i*zb1*n*wrb1))*(Pu1*Pw1*i*n*NQu1/(wra1^2-
n^2+2*i*za1*n*wra1)+Pu2*Pw2*i*n*NQu2/(wra2^2-
n^2+2*i*za2*n*wra2)+Pu3*Pw3*i*n*NQu3/(wra3^2-
n^2+2*i*za3*n*wra3))/....
     ((Pd*i*n-Rl)-i*n*Pw1^2/(wrb1^2-n^2+2*i*zb1*n*wrb1)-
i*n*Pw2^2/(wrb2^2-n^2+2*i*zb2*n*wrb2)-i*n*Pw3^2/(wrb3^2-
n^2+2*i*zb3*n*wrb3)-....
     i*n*Pu1^2/(wra1^2-n^2+2*i*za1*n*wra1)-i*n*Pu2^2/(wra2^2-
n^2+2*i*za2*n*wra2)-i*n*Pu3^2/(wra3^2-n^2+2*i*za3*n*wra3)))+....
((-Nshm2/(wrb2^2-n^2+2*i*zb2*n*wrb2))*(Pu1*Pw1*i*n*NQu1/(wra1^2-
n^2+2*i*za1*n*wra1)+Pu2*Pw2*i*n*NQu2/(wra2^2-
```

```
n^2+2*i*za2*n*wra2)+Pu3*Pw3*i*n*NQu3/(wra3^2-
n^2+2*i*za3*n*wra3))/....
     ((Pd*i*n-Rl)-i*n*Pw1^2/(wrb1^2-n^2+2*i*zb1*n*wrb1)-
i*n*Pw2^2/(wrb2^2-n^2+2*i*zb2*n*wrb2)-i*n*Pw3^2/(wrb3^2-
n^2+2*i*zb3*n*wrb3)-....
     i*n*Pu1^2/(wra1^2-n^2+2*i*za1*n*wra1)-i*n*Pu2^2/(wra2^2-
n^2+2*i*za2*n*wra2)-i*n*Pu3^2/(wra3^2-n^2+2*i*za3*n*wra3)))+...
     ((-Nshm3/(wrb3^2-n^2+2*i*zb3*n*wrb3))*(Pu1*Pw1*i*n*NQu1/(wra1^2-
n^2+2*i*za1*n*wra1)+Pu2*Pw2*i*n*NQu2/(wra2^2-
n^2+2*i*za2*n*wra2)+Pu3*Pw3*i*n*NQu3/(wra3^2-
n^2+2*i*za3*n*wra3))/....
     ((Pd*i*n-Rl)-i*n*Pw1^2/(wrb1^2-n^2+2*i*zb1*n*wrb1)-
i*n*Pw2^2/(wrb2^2-n^2+2*i*zb2*n*wrb2)-i*n*Pw3^2/(wrb3^2-
n^2+2*i*zb3*n*wrb3)-....
     i*n*Pu1^2/(wra1^2-n^2+2*i*za1*n*wra1)-i*n*Pu2^2/(wra2^2-
n^2+2*i*za2*n*wra2)-i*n*Pu3^2/(wra3^2-n^2+2*i*za3*n*wra3))))*(-
n^2*UW*cos(thetapz)*exp(i*n*k))+....
     (((-Nshm/(wrb1^2-n^2+2*i*zb1*n*wrb1))*((Pd*i*n-Rl)*NQw1-
Pu1^2*i*n*NQw1/(wra1^2-n^2+2*i*za1*n*wra1)-Pu2^2*i*n*NQw2/(wra2^2-
n^2+2*i*za2*n*wra2)-Pu3^2*i*n*NQw3/(wra3^2-n^2+2*i*za3*n*wra3))/....
((Pd*i*n-Rl)-i*n*Pw1^2/(wrb1^2-n^2+2*i*zb1*n*wrb1)-
i*n*Pw2^2/(wrb2^2-n^2+2*i*zb2*n*wrb2)-i*n*Pw3^2/(wrb3^2-
n^2+2*i*zb3*n*wrb3)-....
i*n*Pu1^2/(wra1^2-n^2+2*i*za1*n*wra1)-i*n*Pu2^2/(wra2^2-
n^2+2*i*za2*n*wra2)-i*n*Pu3^2/(wra3^2-n^2+2*i*za3*n*wra3)))+....
((-Nshm2/(wrb2^2-n^2+2*i*zb2*n*wrb2))*((Pd*i*n-Rl)*NQw2-
Pu1^2*i*n*NQw1/(wra1^2-n^2+2*i*za1*n*wra1)-Pu2^2*i*n*NQw2/(wra2^2-
n^2+2*i*za2*n*wra2)-Pu3^2*i*n*NQw3/(wra3^2-n^2+2*i*za3*n*wra3))/....
((Pd*i*n-Rl)-i*n*Pw1^2/(wrb1^2-n^2+2*i*zb1*n*wrb1)-
i*n*Pw2^2/(wrb2^2-n^2+2*i*zb2*n*wrb2)-i*n*Pw3^2/(wrb3^2-
n^2+2*i*zb3*n*wrb3)-....
i*n*Pu1^2/(wra1^2-n^2+2*i*za1*n*wra1)-i*n*Pu2^2/(wra2^2-
n^2+2*i*za2*n*wra2)-i*n*Pu3^2/(wra3^2-n^2+2*i*za3*n*wra3)))+...
((-Nshm3/(wrb3^2-n^2+2*i*zb3*n*wrb3))*((Pd*i*n-Rl)*NQw3-
Pu1^2*i*n*NQw1/(wra1^2-n^2+2*i*za1*n*wra1)-Pu2^2*i*n*NQw2/(wra2^2-
n^2+2*i*za2*n*wra2)-Pu3^2*i*n*NQw3/(wra3^2-n^2+2*i*za3*n*wra3))/....
((Pd*i*n-Rl)-i*n*Pw1^2/(wrb1^2-n^2+2*i*zb1*n*wrb1)-
i*n*Pw2^2/(wrb2^2-n^2+2*i*zb2*n*wrb2)-i*n*Pw3^2/(wrb3^2-
n^2+2*i*zb3*n*wrb3)-....
i*n*Pu1^2/(wra1^2-n^2+2*i*za1*n*wra1)-i*n*Pu2^2/(wra2^2-
n^2+2*i*za2*n*wra2)-i*n*Pu3^2/(wra3^2-n^2+2*i*za3*n*wra3))))*(-
n^2*UW)*sin(thetapz)*exp(i*n*k));
   end
     s2=0;
end


nqr=frqi:deltahrq:frqf;
k=0;
for thetapz=(hi:drq:hf)*(pi*2)/360;
    k=k+1;
    Fw11(k,:)=max(real(FRVw11(k,:)));
end
dw11=Fw11';
thetapz=(hi:drq:hf)*(pi*2)/360;
polar (thetapz,dw11);
elseif plotsol==12 % iterating the polar tip absolute transverse
                   % velocity with CEDRTL model

UWc=3; % input acceleration
n=77.71*2*pi; % input frequency
UW=UWc/(n)^2;
```

```matlab
s2=0;
zb1=0.0139;
zb2=0.015;
zb3=0.020;
za1=0.03;
za2=0.036;
za3=0.04;
wra1=sqrt(NKaa1);        % first longitudinal natural frequency
wra2=sqrt(NKaa2);        % second longitudinal natural frequency
wra3=sqrt(NKaa3);        % third longitudinal natural frequency
wrb1=sqrt(NKbb);         % first transverse natural frequency
wrb2=sqrt(NKbb2);        % second transverse natural frequency
wrb3=sqrt(NKbb3);        % third transverse natural frequency
freq_end=0.05; % the number of the generated time history (second)
frqf=freq_end;
frqi=0; % the initial input time (second)
deltahrq=1/1000; % the incremental time (second)
fhrq=fix((frqf-frqi)/deltahrq)+1;
fr=180; % the number of the generated angle (degree)
hf=fr;
hi=0; % the initial input angle (degree)
drq=1; % the incremental angle (degree)
hrq=fix((hf-hi)/drq)+1;
FRVw12=zeros(hrq,fhrq);
nl=0;
Rdd=[60e3]; % input load resistance (ohm)
Rl=1/Rdd;
for thetapz=(hi:drq:hf)*(pi*2)/360; % iterating input angle
    nl=nl+1;
  for k=frqi:deltahrq:frqf; % iterating input time history
        s2=s2+1;
FRVw12(nl,s2)=FRVw12(nl,s2) +(UW*sin(thetapz)*i*n*exp(i*n*k)+(((-
Nshm/(wrb1^2-n^2+2*i*zb1*n*wrb1))*(Pu1*Pw1*i*n*NQu1/(wra1^2-
n^2+2*i*za1*n*wra1)+Pu2*Pw2*i*n*NQu2/(wra2^2-
n^2+2*i*za2*n*wra2)+Pu3*Pw3*i*n*NQu3/(wra3^2-
n^2+2*i*za3*n*wra3))/....
    ((Pd*i*n-Rl)-i*n*Pw1^2/(wrb1^2-n^2+2*i*zb1*n*wrb1)-
i*n*Pw2^2/(wrb2^2-n^2+2*i*zb2*n*wrb2)-i*n*Pw3^2/(wrb3^2-
n^2+2*i*zb3*n*wrb3)-....
    i*n*Pu1^2/(wra1^2-n^2+2*i*za1*n*wra1)-i*n*Pu2^2/(wra2^2-
n^2+2*i*za2*n*wra2)-i*n*Pu3^2/(wra3^2-n^2+2*i*za3*n*wra3)))+....
((-Nshm2/(wrb2^2-n^2+2*i*zb2*n*wrb2))*(Pu1*Pw1*i*n*NQu1/(wra1^2-
n^2+2*i*za1*n*wra1)+Pu2*Pw2*i*n*NQu2/(wra2^2-
n^2+2*i*za2*n*wra2)+Pu3*Pw3*i*n*NQu3/(wra3^2-
n^2+2*i*za3*n*wra3))/....
    ((Pd*i*n-Rl)-i*n*Pw1^2/(wrb1^2-n^2+2*i*zb1*n*wrb1)-
i*n*Pw2^2/(wrb2^2-n^2+2*i*zb2*n*wrb2)-i*n*Pw3^2/(wrb3^2-
n^2+2*i*zb3*n*wrb3)-....
    i*n*Pu1^2/(wra1^2-n^2+2*i*za1*n*wra1)-i*n*Pu2^2/(wra2^2-
n^2+2*i*za2*n*wra2)-i*n*Pu3^2/(wra3^2-n^2+2*i*za3*n*wra3)))+...
    ((-Nshm3/(wrb3^2-n^2+2*i*zb3*n*wrb3))*(Pu1*Pw1*i*n*NQu1/(wra1^2-
n^2+2*i*za1*n*wra1)+Pu2*Pw2*i*n*NQu2/(wra2^2-
n^2+2*i*za2*n*wra2)+Pu3*Pw3*i*n*NQu3/(wra3^2-
n^2+2*i*za3*n*wra3))/....
    ((Pd*i*n-Rl)-i*n*Pw1^2/(wrb1^2-n^2+2*i*zb1*n*wrb1)-
i*n*Pw2^2/(wrb2^2-n^2+2*i*zb2*n*wrb2)-i*n*Pw3^2/(wrb3^2-
n^2+2*i*zb3*n*wrb3)-....
    i*n*Pu1^2/(wra1^2-n^2+2*i*za1*n*wra1)-i*n*Pu2^2/(wra2^2-
n^2+2*i*za2*n*wra2)-i*n*Pu3^2/(wra3^2-n^2+2*i*za3*n*wra3))))*(-
n^3*i*UW*cos(thetapz)*exp(i*n*k))+....
```

```
    (((-Nshm/(wrb1^2-n^2+2*i*zb1*n*wrb1))*((Pd*i*n-Rl)*NQw1-
Pu1^2*i*n*NQw1/(wra1^2-n^2+2*i*za1*n*wra1)-Pu2^2*i*n*NQw2/(wra2^2-
n^2+2*i*za2*n*wra2)-Pu3^2*i*n*NQw3/(wra3^2-n^2+2*i*za3*n*wra3)))/....
((Pd*i*n-Rl)-i*n*Pw1^2/(wrb1^2-n^2+2*i*zb1*n*wrb1)-
i*n*Pw2^2/(wrb2^2-n^2+2*i*zb2*n*wrb2)-i*n*Pw3^2/(wrb3^2-
n^2+2*i*zb3*n*wrb3)-....
i*n*Pu1^2/(wra1^2-n^2+2*i*za1*n*wra1)-i*n*Pu2^2/(wra2^2-
n^2+2*i*za2*n*wra2)-i*n*Pu3^2/(wra3^2-n^2+2*i*za3*n*wra3)))+....
((-Nshm2/(wrb2^2-n^2+2*i*zb2*n*wrb2))*((Pd*i*n-Rl)*NQw2-
Pu1^2*i*n*NQw1/(wra1^2-n^2+2*i*za1*n*wra1)-Pu2^2*i*n*NQw2/(wra2^2-
n^2+2*i*za2*n*wra2)-Pu3^2*i*n*NQw3/(wra3^2-n^2+2*i*za3*n*wra3)))/....
((Pd*i*n-Rl)-i*n*Pw1^2/(wrb1^2-n^2+2*i*zb1*n*wrb1)-
i*n*Pw2^2/(wrb2^2-n^2+2*i*zb2*n*wrb2)-i*n*Pw3^2/(wrb3^2-
n^2+2*i*zb3*n*wrb3)-....
i*n*Pu1^2/(wra1^2-n^2+2*i*za1*n*wra1)-i*n*Pu2^2/(wra2^2-
n^2+2*i*za2*n*wra2)-i*n*Pu3^2/(wra3^2-n^2+2*i*za3*n*wra3)))+...
((-Nshm3/(wrb3^2-n^2+2*i*zb3*n*wrb3))*((Pd*i*n-Rl)*NQw3-
Pu1^2*i*n*NQw1/(wra1^2-n^2+2*i*za1*n*wra1)-Pu2^2*i*n*NQw2/(wra2^2-
n^2+2*i*za2*n*wra2)-Pu3^2*i*n*NQw3/(wra3^2-n^2+2*i*za3*n*wra3)))/....
((Pd*i*n-Rl)-i*n*Pw1^2/(wrb1^2-n^2+2*i*zb1*n*wrb1)-
i*n*Pw2^2/(wrb2^2-n^2+2*i*zb2*n*wrb2)-i*n*Pw3^2/(wrb3^2-
n^2+2*i*zb3*n*wrb3)-....
i*n*Pu1^2/(wra1^2-n^2+2*i*za1*n*wra1)-i*n*Pu2^2/(wra2^2-
n^2+2*i*za2*n*wra2)-i*n*Pu3^2/(wra3^2-n^2+2*i*za3*n*wra3))))*(-
n^3*i*UW*sin(thetapz)*exp(i*n*k)));
    end
        s2=0;
end
nqr=frqi:deltahrq:frqf;
k=0;
for thetapz=(hi:drq:hf)*(pi*2)/360;
    k=k+1;
    Fw12(k,:)=max(real(FRVw12(k,:)));
end
dw12=Fw12';
thetapz=(hi:drq:hf)*(pi*2)/360;
polar (thetapz,dw12);
elseif plotsol==13 % iterating the polar electrical voltage
                    % with CEDRTL model
UWc=3; % input acceleration
n=77.71*2*pi; % input frequency
UW=UWc/(n)^2;
s2=0;
zb1=0.0139;
zb2=0.015;
zb3=0.020;
za1=0.03;
za2=0.036;
za3=0.04;
wra1=sqrt(NKaa1);       % first longitudinal natural frequency
wra2=sqrt(NKaa2);       % second longitudinal natural frequency
wra3=sqrt(NKaa3);       % third longitudinal natural frequency
wrb1=sqrt(NKbb);        % first transverse natural frequency
wrb2=sqrt(NKbb2);       % second transverse natural frequency
wrb3=sqrt(NKbb3);       % third transverse natural frequency
freq_end=0.05; % the number of the generated time history (second)
frqf=freq_end;
frqi=0; % the initial input time (second)
deltahrq=1/1000; % the incremental time (second)
fhrq=fix((frqf-frqi)/deltahrq)+1;
fr=180; % the number of the generated angle (degree)
```

```
hf=fr;
hi=0; % the initial input angle (degree)
drq=1; % the incremental angle (degree)
hrq=fix((hf-hi)/drq)+1;
FRVw13=zeros(hrq,fhrq);
nl=0;
Rdd=[60e3]; % input load resistance (ohm)
Rl=1/Rdd;
for thetapz=(hi:drq:hf)*(pi*2)/360; % iterating input angle
    nl=nl+1;
  for k=frqi:deltahrq:frqf; % iterating input time history
        s2=s2+1;
FRVw13(nl,s2)=FRVw13(nl,s2)+(((((Pw1*i*n*NQw1/(wrb1^2-
n^2+2*i*zb1*n*wrb1)+Pw2*i*n*NQw2/(wrb2^2-
n^2+2*i*zb2*n*wrb2)+Pw3*i*n*NQw3/(wrb3^2-n^2+2*i*zb3*n*wrb3))/....
            ((Pd*i*n+Rl)-i*n*Pw1^2/(wrb1^2-n^2+2*i*zb1*n*wrb1)-
i*n*Pw2^2/(wrb2^2-n^2+2*i*zb2*n*wrb2)-i*n*Pw3^2/(wrb3^2-
n^2+2*i*zb3*n*wrb3)-....
        i*n*Pu1^2/(wra1^2-n^2+2*i*za1*n*wra1)-i*n*Pu2^2/(wra2^2-
n^2+2*i*za2*n*wra2)-i*n*Pu3^2/(wra3^2-n^2+2*i*za3*n*wra3)))*(-
n^2)*UW*sin(thetapz)))*(exp(i*n*k))+....
        (((Pu1*i*n*NQu1/(wra1^2-
n^2+2*i*za1*n*wra1)+Pu2*i*n*NQu2/(wra2^2-
n^2+2*i*za2*n*wra2)+Pu3*i*n*NQu3/(wra3^2-n^2+2*i*za3*n*wra3))/....
        ((Pd*i*n+Rl)-i*n*Pw1^2/(wrb1^2-n^2+2*i*zb1*n*wrb1)-
i*n*Pw2^2/(wrb2^2-n^2+2*i*zb2*n*wrb2)-i*n*Pw3^2/(wrb3^2-
n^2+2*i*zb3*n*wrb3)-....
        i*n*Pu1^2/(wra1^2-n^2+2*i*za1*n*wra1)-i*n*Pu2^2/(wra2^2-
n^2+2*i*za2*n*wra2)-i*n*Pu3^2/(wra3^2-n^2+2*i*za3*n*wra3)))*(-
n^2)*UW*cos(thetapz)))*(exp(i*n*k)));
   end
    s2=0;
end
nqr=frqi:deltahrq:frqf;
k=0;
for thetapz=(hi:drq:hf)*(pi*2)/360;
    k=k+1;
    Fw13(k,:)=max(real(FRVw13(k,:)));
end
dw13=Fw13';
thetapz=(hi:drq:hf)*(pi*2)/360;
polar (thetapz,dw13);
elseif plotsol==14 % iterating the polar electrical current
                   % with CEDRTL model
UWc=3; % input acceleration
n=77.71*2*pi; % input frequency
UW=UWc/(n)^2;
s2=0;
zb1=0.0139;
zb2=0.015;
zb3=0.020;
za1=0.03;
za2=0.036;
za3=0.04;
wra1=sqrt(NKaa1);        % first longitudinal natural frequency
wra2=sqrt(NKaa2);        % second longitudinal natural frequency
wra3=sqrt(NKaa3);        % third longitudinal natural frequency
wrb1=sqrt(NKbb);         % first transverse natural frequency
wrb2=sqrt(NKbb2);        % second transverse natural frequency
wrb3=sqrt(NKbb3);        % third transverse natural frequency
freq_end=0.05; % the number of the generated time history (second)
```

```
frqf=freq_end;
frqi=0; % the initial input time (second)
deltahrq=1/1000; % the incremental time (second)
fhrq=fix((frqf-frqi)/deltahrq)+1;
fr=180; % the number of the generated angle (degree)
hf=fr;
hi=0; % the initial input angle (degree)
drq=1; % the incremental angle (degree)
hrq=fix((hf-hi)/drq)+1;
FRVw14=zeros(hrq,fhrq);
nl=0;
Rdd=[60e3]; % input load resistance (ohm)
Rl=1/Rdd;
for thetapz=(hi:drq:hf)*(pi*2)/360; % iterating input angle
    nl=nl+1;
  for k=frqi:deltahrq:frqf; % iterating input time history
        s2=s2+1;
FRVw14(nl,s2)=FRVw14(nl,s2)+(((((Pw1*i*n*NQw1/(wrb1^2-
n^2+2*i*zb1*n*wrb1)+Pw2*i*n*NQw2/(wrb2^2-
n^2+2*i*zb2*n*wrb2)+Pw3*i*n*NQw3/(wrb3^2-n^2+2*i*zb3*n*wrb3)))/....
        ((Pd*i*n+Rl)-i*n*Pw1^2/(wrb1^2-n^2+2*i*zb1*n*wrb1)-
i*n*Pw2^2/(wrb2^2-n^2+2*i*zb2*n*wrb2)-i*n*Pw3^2/(wrb3^2-
n^2+2*i*zb3*n*wrb3)-....
      i*n*Pu1^2/(wra1^2-n^2+2*i*za1*n*wra1)-i*n*Pu2^2/(wra2^2-
n^2+2*i*za2*n*wra2)-i*n*Pu3^2/(wra3^2-n^2+2*i*za3*n*wra3)))*(-
n^2)*UW*sin(thetapz))/Rdd)*(exp(i*n*k))+....
      ((((Pu1*i*n*NQu1/(wra1^2-
n^2+2*i*za1*n*wra1)+Pu2*i*n*NQu2/(wra2^2-
n^2+2*i*za2*n*wra2)+Pu3*i*n*NQu3/(wra3^2-n^2+2*i*za3*n*wra3)))/....
      ((Pd*i*n+Rl)-i*n*Pw1^2/(wrb1^2-n^2+2*i*zb1*n*wrb1)-
i*n*Pw2^2/(wrb2^2-n^2+2*i*zb2*n*wrb2)-i*n*Pw3^2/(wrb3^2-
n^2+2*i*zb3*n*wrb3)-....
      i*n*Pu1^2/(wra1^2-n^2+2*i*za1*n*wra1)-i*n*Pu2^2/(wra2^2-
n^2+2*i*za2*n*wra2)-i*n*Pu3^2/(wra3^2-n^2+2*i*za3*n*wra3)))*(-
n^2)*UW*cos(thetapz))/Rdd)*(exp(i*n*k)));
  end
    s2=0;
end
nqr=frqi:deltahrq:frqf;
k=0;
for thetapz=(hi:drq:hf)*(pi*2)/360;
    k=k+1;
    Fw14(k,:)=max(real(FRVw14(k,:)));
end
dw14=Fw14';
thetapz=(hi:drq:hf)*(pi*2)/360;
polar (thetapz,dw14);
elseif plotsol==15 % iterating the polar electrical power
                   % with CEDRTL model
UWc=3; % input acceleration
n=77.71*2*pi; % input frequency
UW=UWc/(n)^2;
s2=0;
zb1=0.0139;
zb2=0.015;
zb3=0.020;
za1=0.03;
za2=0.036;
za3=0.04;
wra1=sqrt(NKaa1);        % first longitudinal natural frequency
wra2=sqrt(NKaa2);        % second longitudinal natural frequency
```

```
wra3=sqrt(NKaa3);        % third longitudinal natural frequency
wrb1=sqrt(NKbb);         % first transverse natural frequency
wrb2=sqrt(NKbb2);        % second transverse natural frequency
wrb3=sqrt(NKbb3);        % third transverse natural frequency
freq_end=0.05; % the number of the generated time history (second)
frqf=freq_end;
frqi=0; % the initial input time (second)
deltahrq=1/1000; % the incremental time (second)
fhrq=fix((frqf-frqi)/deltahrq)+1;
fr=180; % the number of the generated angle (degree)
hf=fr;
hi=0; % the initial input angle (degree)
drq=1; % the incremental angle (degree)
hrq=fix((hf-hi)/drq)+1;
FRVw14=zeros(hrq,fhrq);
nl=0;
Rdd=[60e3]; % input load resistance (ohm)
Rl=1/Rdd;
for thetapz=(hi:drq:hf)*(pi*2)/360;  % iterating input angle
    nl=nl+1;
  for k=frqi:deltahrq:frqf;     % iterating input time history
        s2=s2+1;
FRVw15(nl,s2)=FRVw15(nl,s2)+(((((Pw1*i*n*NQw1/(wrb1^2-
n^2+2*i*zb1*n*wrb1)+Pw2*i*n*NQw2/(wrb2^2-
n^2+2*i*zb2*n*wrb2)+Pw3*i*n*NQw3/(wrb3^2-n^2+2*i*zb3*n*wrb3))/....
        ((Pd*i*n+Rl)-i*n*Pw1^2/(wrb1^2-n^2+2*i*zb1*n*wrb1)-
i*n*Pw2^2/(wrb2^2-n^2+2*i*zb2*n*wrb2)-i*n*Pw3^2/(wrb3^2-
n^2+2*i*zb3*n*wrb3)-....
        i*n*Pu1^2/(wra1^2-n^2+2*i*za1*n*wra1)-i*n*Pu2^2/(wra2^2-
n^2+2*i*za2*n*wra2)-i*n*Pu3^2/(wra3^2-n^2+2*i*za3*n*wra3)))*(-
n^2)*UW*sin(thetapz))^2/Rdd)*(exp(i*n*k))+....
        ((((Pu1*i*n*NQu1/(wra1^2-
n^2+2*i*za1*n*wra1)+Pu2*i*n*NQu2/(wra2^2-
n^2+2*i*za2*n*wra2)+Pu3*i*n*NQu3/(wra3^2-n^2+2*i*za3*n*wra3))/....
        ((Pd*i*n+Rl)-i*n*Pw1^2/(wrb1^2-n^2+2*i*zb1*n*wrb1)-
i*n*Pw2^2/(wrb2^2-n^2+2*i*zb2*n*wrb2)-i*n*Pw3^2/(wrb3^2-
n^2+2*i*zb3*n*wrb3)-....
        i*n*Pu1^2/(wra1^2-n^2+2*i*za1*n*wra1)-i*n*Pu2^2/(wra2^2-
n^2+2*i*za2*n*wra2)-i*n*Pu3^2/(wra3^2-n^2+2*i*za3*n*wra3)))*(-
n^2)*UW*cos(thetapz))^2/Rdd)*(exp(i*n*k)));
  end
    s2=0;
end
nqr=frqi:deltahrq:frqf;
k=0;
for thetapz=(hi:drq:hf)*(pi*2)/360;
    k=k+1;
    Fw15(k,:)=max(real(FRVw15(k,:)));
end
dw15=Fw15';
thetapz=(hi:drq:hf)*(pi*2)/360;
polar (thetapz,dw15);


else    % iterating the optimal power
        % with CEDRTL model
zb1=0.0139;
zb2=0.015;
zb3=0.020;
za1=0.03;
za2=0.036;
za3=0.04;
```

```matlab
wra1=sqrt(NKaa1);        % first longitudinal natural frequency
wra2=sqrt(NKaa2);        % second longitudinal natural frequency
wra3=sqrt(NKaa3);        % third longitudinal natural frequency
wrb1=sqrt(NKbb);         % first transverse natural frequency
wrb2=sqrt(NKbb2);        % second transverse natural frequency
wrb3=sqrt(NKbb3);        % third transverse natural frequency
FRVw16=zeros(1,nhrq);    % Initialisation of generated frequency
                         % response
nl=0;
s2=0;
 for n=hrqi:deltahrq:hrqf; % iterating input frequency
     Rl=sqrt(((Pd*n-n*Pw1^2*(wrb1^2-n^2)/((wrb1^2-
n^2)^2+(2*zb1*n*wrb1)^2)-n*Pw2^2*(wrb2^2-n^2)/((wrb2^2-
n^2)^2+(2*zb2*n*wrb2)^2)-n*Pw3^2*(wrb3^2-n^2)/((wrb3^2-
n^2)^2+(2*zb3*n*wrb3)^2)-n*Pu1^2*(wra1^2-n^2)/((wra1^2-
n^2)^2+(2*za1*n*wra1)^2)-n*Pu2^2*(wra2^2-n^2)/((wra2^2-
n^2)^2+(2*za2*n*wra2)^2)-n*Pu3^2*(wra3^2-n^2)/((wra3^2-
n^2)^2+(2*za3*n*wra3)^2))^2+......
         (n*Pw1^2*2*zb1*n*wrb1/((wrb1^2-
n^2)^2+(2*zb1*n*wrb1)^2)+n*Pw2^2*2*zb2*n*wrb2/((wrb2^2-
n^2)^2+(2*zb2*n*wrb2)^2)+n*Pw3^2*2*zb3*n*wrb3/((wrb3^2-
n^2)^2+(2*zb3*n*wrb3)^2)+n*Pu1^2*2*za1*n*wra1/((wra1^2-
n^2)^2+(2*za1*n*wra1)^2)+n*Pu2^2*2*za2*n*wra2/((wra2^2-
n^2)^2+(2*za2*n*wra2)^2)+n*Pu3^2*2*za3*n*wra3/((wra3^2-
n^2)^2+(2*za3*n*wra3)^2))^2))/......
         ((Pd*n-n*Pw1^2*(wrb1^2-n^2)/((wrb1^2-
n^2)^2+(2*zb1*n*wrb1)^2)-n*Pw2^2*(wrb2^2-n^2)/((wrb2^2-
n^2)^2+(2*zb2*n*wrb2)^2)-n*Pw3^2*(wrb3^2-n^2)/((wrb3^2-
n^2)^2+(2*zb3*n*wrb3)^2)-n*Pu1^2*(wra1^2-n^2)/((wra1^2-
n^2)^2+(2*za1*n*wra1)^2)-n*Pu2^2*(wra2^2-n^2)/((wra2^2-
n^2)^2+(2*za2*n*wra2)^2)-n*Pu3^2*(wra3^2-n^2)/((wra3^2-
n^2)^2+(2*za3*n*wra3)^2))^2+......
         (n*Pw1^2*2*zb1*n*wrb1/((wrb1^2-
n^2)^2+(2*zb1*n*wrb1)^2)+n*Pw2^2*2*zb2*n*wrb2/((wrb2^2-
n^2)^2+(2*zb2*n*wrb2)^2)+n*Pw3^2*2*zb3*n*wrb3/((wrb3^2-
n^2)^2+(2*zb3*n*wrb3)^2)+n*Pu1^2*2*za1*n*wra1/((wra1^2-
n^2)^2+(2*za1*n*wra1)^2)+n*Pu2^2*2*za2*n*wra2/((wra2^2-
n^2)^2+(2*za2*n*wra2)^2)+n*Pu3^2*2*za3*n*wra3/((wra3^2-
n^2)^2+(2*za3*n*wra3)^2))^2) ;
     s2=s2+1;
FRVw16(1,s2)=FRVw16(1,s2)+((Pw1*i*n*NQw1*3/(wrb1^2-
n^2+2*i*zb1*n*wrb1)+Pw2*i*n*NQw2*3/(wrb2^2-
n^2+2*i*zb2*n*wrb2)+Pw3*i*n*NQw3*3/(wrb3^2-n^2+2*i*zb3*n*wrb3))/....
     ((Pd*i*n-1/Rl)-i*n*Pw1^2/(wrb1^2-n^2+2*i*zb1*n*wrb1)-
i*n*Pw2^2/(wrb2^2-n^2+2*i*zb2*n*wrb2)-i*n*Pw3^2/(wrb3^2-
n^2+2*i*zb3*n*wrb3)-....
     i*n*Pu1^2/(wra1^2-n^2+2*i*za1*n*wra1)-i*n*Pu2^2/(wra2^2-
n^2+2*i*za2*n*wra2)-i*n*Pu3^2/(wra3^2-n^2+2*i*za3*n*wra3)))^2/Rl;
end
nqr=hrqi:deltahrq:hrqf;
semilogy(nqr/(2*pi),(abs(FRVw16)))
end
```